NEUTRINO-NUCLEUS INTERACTIONS IN A COUPLED-CHANNEL HADRONIC TRANSPORT MODEL

TINA J. LEITNER

Dissertation

Justus-Liebig-Universität Gießen
Fachbereich 07 (Mathematik und Informatik, Physik, Geographie)
Institut für Theoretische Physik

2009

Acknowledgments

It is a pleasure to thank all the people whose support and advice have helped me to complete this dissertation. First of all, I wish to express my deep gratitude to my advisor Prof. Dr. Ulrich Mosel. Thanks for giving me the opportunity to work on such a fascinating project, for the continuous guidance, encouragement, and support, but also for giving me the great freedom to pursue independent work. Moreover, he made it possible for me to present my results on many occasions and discuss them with colleagues from other institutions.

I am especially grateful to Dr. Oliver Buß for the excellent and close collaboration, for his expertise, and also for the great atmosphere in our office. I am no less grateful to Dr. Luis Alvarez-Ruso for countless fruitful and inspiring discussions and his valuable advice. Special thanks to Dr. Kai Gallmeister not only, but in particular, for sharing his extraordinary computing skills. I wish to extend my gratitude to Dr. Theodoros Gaitanos, Dr. Murat Kaskulov, Dr. Olga Lalakulich, Dr. Alexei Larionov, and Janus Weil. I also would like to acknowledge stimulating discussions with PD Dr. Stefan Leupold. Thanks to Luis, Oliver, Kai, Dr. Hendrik van Hees and Ivan Lappo-Danilevski for proofreading parts of this thesis and for valuable feedback. I am especially indebted to Prof. Dr. Karlheinz Langanke for kindly agreeing to review this dissertation.

I have benefited a lot from numerous discussions with many colleagues on their models and event generators, on experiments and data. I would like to offer my sincere thanks to everyone of them, in particular to Dr. Geralyn Zeller for answering all my questions on the MiniBooNE data analysis. Furthermore, I am grateful to Prof. Dr. Gerald Garvey for initiating my interest in the radiative Δ decay and to Dr. Lothar Tiator for providing the MAID results.

This thesis would not have been possible without a high-performance computer cluster — and thus not without our local administrators Dr. Oliver Buss, Fabian Eichstädt, Dr. Frank Frömel and Janus Weil. Thanks!

I am obliged to all my colleagues in the institute for many interesting physics and non-physics discussions, entertaining lunch and coffee breaks, and for many joint undertakings. All this made my PhD time a very enjoyable experience for me. Elke Jung deserves special acknowledgment for helping me with any kind of paperwork.

Above all, I am deeply indebted to my parents, Jutta and Roland Leitner for the constant support and for believing in me and my work. Last, but far from least, I would like to thank Sven Kuhlbörsch for his tolerance and permanent encouragement.

Reviewer:
Prof. Dr. Ulrich Mosel (Justus-Liebig-Universität Gießen)
Prof. Dr. Karlheinz Langanke (GSI Darmstadt)

Contents

I Preface **1**

1 Introduction **3**
1.1 Motivation 3
1.2 Survey 8
1.3 Overview: neutrino-nucleus scattering in the GiBUU approach 9
1.4 Outline 9

II Lepton-nucleon interactions **11**

2 Electroweak interactions, symmetries and currents **13**
2.1 Electroweak interactions of quarks and leptons 13
2.1.1 Interaction Lagrangian 13
2.1.2 Quark currents 14
2.2 Strong interactions and isospin symmetry 17
2.2.1 Quantum Chromodynamics 17
2.2.2 Isospin symmetry and conserved flavor currents 17
2.2.3 Chiral symmetry and axial currents 18
2.3 Hadronic currents 20
2.3.1 Conserved vector current hypothesis 20
2.3.2 Partially conserved axial current hypothesis 20

3 General properties of the lepton-nucleon interaction **23**
3.1 Contributions to the lepton-nucleon interaction 23
3.2 Dynamics of the lepton-nucleon interaction 27
3.3 Kinematics of the lepton-nucleon interaction 28

4 Quasielastic scattering **29**
4.1 Hadronic current 29
4.2 Form factors of the nucleon 30

4.3 Cross section 36

5 Excitation of baryon resonances **39**
5.1 Excitation of spin 1/2 resonances 39
5.1.1 Hadronic current 39
5.1.2 Nucleon–resonance transition form factors 41
5.2 Excitation of spin 3/2 resonances 45
5.2.1 Hadronic current 45
5.2.2 Nucleon-resonance transition form factors 46
5.3 Resonances with spin $> 3/2$ 55
5.4 Cross sections 55
5.4.1 Resonance-excitation cross sections 55
5.4.2 Pion production through resonance excitation 57
5.5 Comparison to other approaches 60
5.5.1 Phenomenological models 60
5.5.2 Quark models 63

6 Single-π non-resonant background **69**
6.1 Vector part 70
6.2 Non-vector part 73

III Lepton-nucleus interactions in the GiBUU model **77**

7 GiBUU transport model **79**
7.1 Introduction 79
7.2 Particle species 80
7.3 BUU equation 82
7.3.1 General properties 82
7.3.2 Approximations 84
7.3.3 Test-particle ansatz 84
7.4 Potentials 85
7.4.1 Hadronic potentials 85
7.4.2 Coulomb potential 87
7.5 Nuclear ground state 87
7.5.1 Local Thomas-Fermi approximation 87
7.5.2 Ground-state stability 91
7.6 Collision term 91
7.6.1 Resonance decays 92
7.6.2 Two-body collisions 93
7.6.3 Three-body collisions 97

7.7 Spectral functions and self energies . . . 97
7.7.1 Formalism . . . 97
7.7.2 Numerical implementation . . . 100
7.7.3 Results and discussion . . . 100
7.7.4 Approximations . . . 104
7.8 Off-shell transport . . . 104
7.8.1 Off-shell potential method . . . 105
7.8.2 Numerical implementation and discussion . . . 106

8 Nuclear electroweak cross sections 113
8.1 Lepton-nucleon interaction in the nuclear medium . . . 113
8.1.1 Quasielastic scattering . . . 114
8.1.2 Resonance excitations . . . 115
8.1.3 Non-resonant single-pion background . . . 115
8.2 Lepton-nucleus interactions . . . 116
8.3 Numerical implementation . . . 116

9 Inclusive cross sections 119
9.1 Introduction . . . 119
9.2 Results and their model dependence . . . 120
9.2.1 Double differential cross sections . . . 120
9.2.2 Integrated cross sections . . . 129
9.3 Modeling in-medium cross sections . . . 129
9.3.1 Preliminaries . . . 131
9.3.2 Models . . . 133
9.3.3 Results . . . 136
9.4 Model validation: electron scattering . . . 138
9.5 Comparison to other approaches . . . 141

10 Pion production on nuclei 147
10.1 Introduction . . . 147
10.2 CC pion production . . . 148
10.2.1 Double differential pion cross sections . . . 148
10.2.2 Total pion cross sections . . . 148
10.2.3 Pion kinetic-energy spectra . . . 154
10.3 NC pion production . . . 157
10.3.1 Total cross sections . . . 157
10.3.2 Kinetic-energy spectra . . . 159
10.4 Model dependencies . . . 159
10.5 Model validation . . . 164

10.6 Comparisons . . . 166
10.6.1 Charged currents . . . 167
10.6.2 Neutral currents . . . 168

11 Nucleon knockout **173**
11.1 Introduction . . . 173
11.2 CC nucleon knockout . . . 174
11.2.1 Double differential pion cross sections . . . 175
11.2.2 Total cross section . . . 176
11.2.3 Nucleon kinetic-energy spectra . . . 179
11.3 NC nucleon knockout . . . 183
11.3.1 Total cross section . . . 183
11.3.2 Nucleon kinetic-energy spectra . . . 188
11.4 Model dependencies . . . 189
11.5 Comparisons . . . 190

IV Applications, predictions and comparisons **197**

12 Experimental status **199**
12.1 Neutrino experiments . . . 199
12.2 Monte Carlo event generators . . . 203
12.2.1 Generator overview . . . 205
12.2.2 Conclusion . . . 210

13 CCQE/CC1π^+ entanglement and neutrino energy reconstruction **211**
13.1 Introduction . . . 211
13.2 Event selection . . . 212
13.3 Topologies . . . 213
13.3.1 CCQE identification . . . 213
13.3.2 CC1π^+ identification . . . 217
13.4 Neutrino energy reconstruction . . . 217

14 NC neutrino-nucleus reactions: implications for MiniBooNE's ν_e appearance searches **225**
14.1 Introduction . . . 225
14.2 Search for electron-neutrino appearance . . . 226
14.3 Estimate of radiative Δ decay in the medium . . . 227

15 Predictions and comparison with data **231**
15.1 CCQE measurements . . . 231
15.1.1 Q^2 distribution and axial mass . . . 231
15.1.2 Absolute CCQE cross section . . . 238
15.2 CC1π^+ measurements . . . 241
15.2.1 Single-π^+/QE ratio . . . 242
15.2.2 Absolute CCπ^+ cross section . . . 244
15.3 NCπ^0 measurements . . . 245
15.4 Possible origins of the discrepancies and conclusion . . . 247

V Conclusion **255**

16 Summary and conclusive remarks **257**
16.1 Summary . . . 257
16.2 Outlook and future improvements . . . 261
16.3 Conclusion . . . 262

Appendices **263**

A Reference formulae **265**
A.1 Units and constants . . . 265
A.2 Notation and definitions . . . 265
A.3 Metric and conventions . . . 267
A.4 Isospin operators . . . 270

B Cross sections and kinematics **273**
B.1 General expression for the cross section . . . 273
B.2 Kinematics of the lepton-nucleon interaction . . . 273
B.3 Kinematics . . . 277

C Feynman rules and electro-weak transition matrix elements **283**
C.1 Feynman rules . . . 283
C.2 Electro-weak transition matrix elements . . . 284

D Isospin relations **287**
D.1 QE scattering and excitation of nucleon resonances: isospin 1/2 to isospin 1/2 transition . . . 287
D.2 Excitation of Δ resonances: isospin 1/2 to isospin 3/2 transition . . . 290
D.3 Isospin relations for the non-resonant background . . . 292

E Form factors and helicity amplitudes **293**
E.1 Spin 1/2 resonances 294
E.2 Spin 3/2 resonances 295

F Derivation of axial couplings **297**
F.1 Resonance interaction Lagrangians and widths 297
F.2 PCAC relations 299

G Uncertainties in the neutrino-nucleon cross section **303**
G.1 W dependence of the resonance form factors 303
G.2 Neglect of DIS 304

Bibliography **309**

Deutsche Zusammenfassung **335**

Part I

Preface

1 Introduction

More than 75 years ago, Wolfgang Pauli concluded "I have done a terrible thing, I have postulated a particle that cannot be detected." Indeed, it took Reines and Cowan a quarter of a century to prove the existence of the neutrino in the "Poltergeist" experiment [RC53, Rei95]. Even today, neutrinos remain elusive particles, only weakly interacting and thus hard to detect. They can only be observed by detecting the secondary particles they create when interacting with matter. This thesis is devoted to the study of the interaction of neutrinos with matter.

1.1 Motivation

Since the early days of neutrino physics we have learned much about these objects. We now know that the neutrino appears as (at least) three different species, all uncharged with spin 1/2. Only since recently, we know that neutrinos change their flavor and have non-zero masses — in contrast to the predictions of the Standard Model of particle physics and interactions. These findings have triggered a tremendous theoretical and experimental interest in the last years. Given that the neutrino interaction cross sections are tiny, neutrino experiments are very challenging, or, as Haim Harari put it: "Neutrino physics is largely an art of learning a great deal by observing nothing."

Neutrino oscillations and the Standard Model

The Standard Model of particle physics combines the theory of the strong interactions of quarks, named Quantum Chromodynamics (QCD), with the theory of the

electroweak interactions of quarks and leptons. It has been proven to be extremely successful in describing experimental data with high precision.

The Standard Model incorporates three neutrino flavors, ν_e, ν_μ and ν_τ, which are all experimentally observed. The number of light neutrinos can be predicted from the Z^0 decay width and it was measured to equal 3, long before the tau-neutrino was detected not even 10 years ago [DONUT01]. Neutrinos are massless and purely left-handed, i.e., their spin is anti-parallel to their momentum, (anti-neutrinos are right-handed) which reflects the fact that parity is maximally violated in weak interactions. Charged leptons appear left- and right-handed.

Our picture of neutrinos has changed dramatically in the last decade. In 1998, the Super-Kamiokande collaboration reported the observation of atmospheric neutrinos changing flavor [Super-K98]. Next, the SNO experiment showed that the long-standing solar neutrino problem — the observation that less solar-ν_e than expected reach the earth — is due to neutrino oscillations [SNO01]. In the following years, these findings were confirmed with man-made neutrinos from reactors [KamLAND03] and particle accelerators [K2K03].

Neutrinos change their flavor when their weak eigenstates, ν_e, ν_μ and ν_τ, differ from their mass eigenstates, ν_1, ν_2 and ν_3, which evolve in time. Like the Cabbibo-Kobayashi-Maskawa matrix in the quark sector, there is a neutrino mass-mixing matrix which relates both sets of eigenstates in terms of three mixing angles, θ_{13}, θ_{23} and θ_{12}, and a possible CP-violating phase δ. The oscillation probability further depends on the two mass-squared differences, $\Delta m^2_{21} = m^2_2 - m^2_1$ and Δm^2_{32}, but also on the traveled distance, L, and the neutrino energy, E_ν. The conclusive evidence that neutrino oscillations exist implies that neutrinos are massive.

The discovery of neutrino oscillations opens many more questions including[1]

- How many neutrino species are there? Do sterile neutrinos exist?
  The findings of the LSND experiment imply the existence of a forth neutrino, a non-interacting sterile neutrino [LSND01]. The MiniBooNE experiment was built to confirm or reject this claim [MiniBooNE07b].

- What are the masses of the mass eigenstates ν_i?
  Oscillation experiments can access only the mass-squared differences but not the absolute neutrino masses. Present values are $\Delta m^2_{21} = (7.59 \pm 0.20) \cdot 10^{-5}\,\text{eV}$ and $|\Delta m^2_{32}| = (2.43 \pm 0.13) \cdot 10^{-3}\,\text{eV}$ [PDG08]. Still unknown is the sign of Δm^2_{32} and thus the mass hierarchy.

  Using the kinematics of nuclear β decay, one can determine directly the mass of the electron neutrino by studying the endpoint of the β spectrum. The KATRIN experiment, currently under construction, with its expected sub-eV sensitivity

[1] Taken from the review article of B. Kayser in Ref. [PDG08].

[KATRIN01] will significantly improve the current upper limit of $m_{\nu_e} < 2.3\,\text{eV}$ [K$^+$05].

By measuring the half-life of neutrinoless double-beta decay or from current cosmological data one gains further information about absolute neutrino masses, but as of today, the masses are still unknown.

- Are the neutrino mass eigenstates Majorana particles?
  This question can be conclusively answered when one observes neutrinoless double-beta decay. This process can only take place if the neutrino is its own anti-particle, i.e., it is not a Dirac but a Majorana particle.

- What are the mixing angles in the leptonic mixing matrix?
  Only the solar mixing angle θ_{12} is rather well determined ($\sin^2(2\theta_{12}) = 0.87 \pm 0.03$). The atmospheric mixing angle θ_{23} is only constrained by $\sin^2(2\theta_{23}) > 0.92$. θ_{13} is still unknown, only upper limits have been placed at $\sin^2(2\theta_{13}) < 0.19$ (all numbers taken from Ref. [PDG08]).

- Does the behavior of neutrinos violate CP?
  One knows that CP violation in the quark sector is not sufficient to cause the baryon asymmetry of the universe. Possible leptonic CP violation could be responsible for this asymmetry.

  However, CP violation, driven by the phase δ, can only be measured when θ_{13} turns out to be non-vanishing (in the mixing matrix, this phase appears only proportional to $\sin\theta_{13}$).

To address these questions, an extensive experimental program is being developed around the world. Among them are several long-baseline (LBL) experiments, i.e., accelerator oscillation experiments, aiming at the precise determination of the mixing parameters [K2K, MiniBooNE, MINOS, OPERA, T2K]. All of them use heavy nuclei as target material. The success of these experiments depends critically on a good knowledge of the neutrino-nucleus interactions as we will explicate in the following.

Neutrino-nucleus interactions

Neutrinos interact with matter only weakly with very small cross sections and can be identified solely through the particles produced in the reaction. Neutrino interactions are classified as charged-current (CC) or neutral-current (NC) processes depending on whether a W or a Z boson is exchanged. In the first case, a charged lepton is emitted, whereas the neutrino preserves its nature in the second one. The experimental study of NC neutrino interactions is an even more demanding task than the study of CC reactions due to the considerable difficulties of collecting data on reactions with cross

sections even smaller than those of CC processes, and in which the outgoing neutrino leaves no signal, so that the event identification has to rely on the detection of one or more hadrons.

To increase the neutrino cross section, experiments often use targets with a large atomic mass number A, e.g., current and future LBL experiments use carbon, oxygen, iron and lead [K2K, MiniBooNE, MINOS, OPERA, T2K]. This causes a major difficulty: particles produced in neutrino interactions can reinteract before leaving the nucleus and can be absorbed, change their kinematics or even charge before being detected. Nuclear reinteractions limit our ability to identify the reaction channel and they change the topology of the measured hadronic final state. Consequently, the detected rates on nuclei are changed significantly compared to the ones on free nucleons.

Nuclear effects are known to be the largest source of systematic error in LBL experiments [NUINT09]. The discovery of neutrino oscillations has therefore renewed the interest in and the need for a better determination of the neutrino-nucleus cross sections. The SciBooNE and the MINERνA experiments have been constructed to this aim [SciBooNE, MINERvA04].

The oscillation probability depends directly on the neutrino energy: ν_μ disappearance experiments for example search for a distortion in the neutrino flux in the detector positioned far away from the source. By comparing the un-oscillated with the oscillated flux, one gains information about the oscillation probability and with that about mixing angles and mass squared differences. However, the neutrino energy cannot be measured directly but has to be reconstructed from the final-state particles that are detected. But, as we have pointed out before, they are affected by in-medium effects and final-state interactions in the nucleus. Appearance experiments, for instance, search for a specific neutrino flavor in a neutrino beam of different flavor. The flavor of the neutrino can only be determined from the charged lepton it produces in the interaction. π^0 production events in neutral current reactions are a source of background in ν_e appearance searches in a ν_μ beam because they might be misidentified as charge current (ν_e, e^-) interactions.

To extract the oscillation parameters from the measured particle yields, the experimental analyses have to rely on models for the neutrino-nucleus interaction. Thus, the theoretical understanding of nuclear effects is essential for the interpretation of the data and represents both a challenge and an opportunity. Only with precise and well-tested models it is possible to minimize the systematic uncertainties in neutrino fluxes, backgrounds and detector responses.

The interest in neutrinos goes beyond the study of their oscillations and extends to a variety of topics in astro-, nuclear and hadronic physics. In particular, they are a valuable tool for nuclear and hadronic physics. By studying the scattering of electrons off the nucleon, a wealth of information on nucleon properties such as

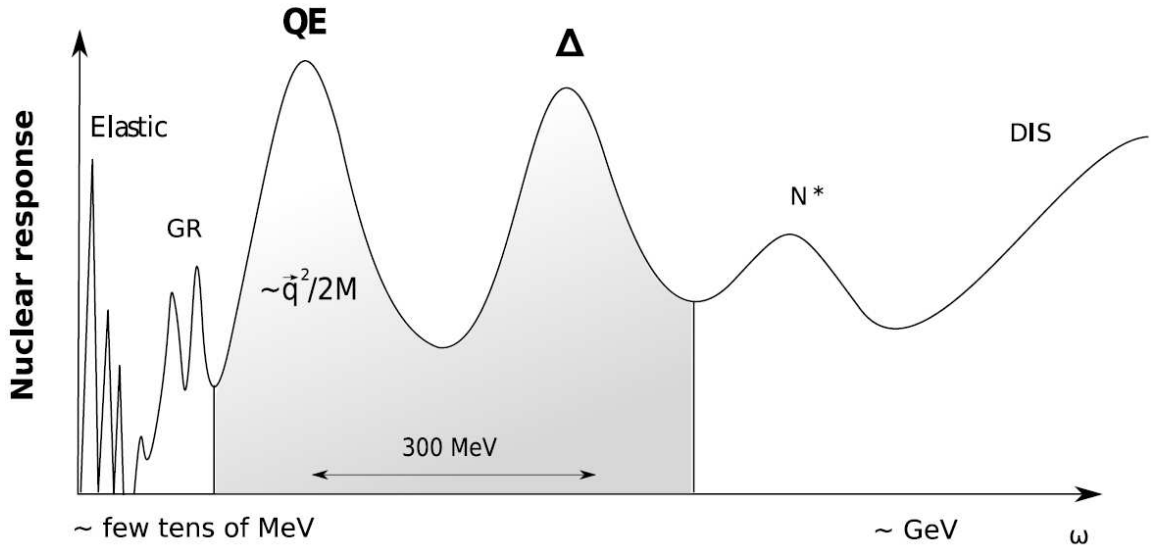

Figure 1.1: Schematic overview of the nuclear response to a electroweak probe as a function of the energy transfer ω. Taken from Ref. [Pra09].

its structure functions and charge radius, as the distribution of its quark and gluon constituents, and its excitation spectrum has been gathered. Neutrinos provide a unique opportunity to gain even more information on the structure of the nucleon and baryonic resonances since they probe not only the vector but also the axial structure. Current and future experiments address relevant problems like the extraction of the nucleon and $N - \Delta$ axial form factors. NC neutrino-nucleus interactions are also relevant to answer a fundamental question of hadronic structure, namely, the strange-quark contribution to the nucleon spin.

Fig. 1.1 shows schematically what processes contribute to the neutrino-nucleus reaction in the few-GeV region. There, the nuclear response is plotted as a function of the energy ω that is transferred from the neutrino to the system. At very small energy transfers of only a few MeV, one scatters into discrete nuclear states and excites so-called giant resonances. We focus on the energy region of the quasielastic (QE), Δ and N^* peaks with energy transfers of few hundred MeV up to about a GeV. The QE peak is caused by processes like $\ell N \to \ell' N'$ where one has only nucleons, both in the initial and final state. With increasing ω, one can excite the Δ resonance (second peak) or even higher lying resonances (third peak) via $\ell N \to \ell' R$. At even higher ω, one reaches the deep-inelastic scattering (DIS) region where one starts to probe quark degrees of freedom.

1.2 Survey

Inclusive quasielastic scattering on nuclei has been investigated within relativistic Fermi-gas models [SM72, DP79, HKMP93, BDPD$^+$96, ABB$^+$97, ABB$^+$98]. Other approaches go beyond the plane-wave approximation and apply more realistic wave functions [ABB$^+$97, ABB$^+$98, MGP04a, MLJ$^+$06, vdVP06, MGP06, JRHR99] or a so-called "scaling analysis" of electron data to predict neutrino cross sections [ABC$^+$05]. Realistic nuclear spectral functions have been used as well [BFN$^+$05].

The treatment of semi-inclusive quasielastic nucleon knockout reactions requires a good understanding of the final-state interactions. Often they are fully neglected [HKMP93, BDPD$^+$96, vdVP06] or purely absorptive [ABB$^+$97, ABB$^+$98, MGP04a, vdVP04, MGP06, MLJ$^+$06]. However, in these approaches the nucleons that go into unobserved states as a result of an interaction are lost, while, in fact, they are ejected with a different energy, angle and maybe charge. Monte Carlo methods permit to take into account interactions of nucleons leading to energy losses, charge exchange and multiple nucleon emission [NVVV06]. All these theoretical models consider only QE processes, but one should bear in mind that the excitation of resonances also contributes to nucleon knockout; those resonance excitation events where a nucleon is emitted but there are no pions in the final state (or they are produced but not detected) represent a source of background for the neutrino energy reconstruction which commonly relies on the QE reaction. Only coupled-channel models can provide a realistic description of this scenario, but none of the ones mentioned.

A good knowledge of pion production is essential for the interpretation of neutrino oscillation experiments, not only for the flavor identification: charged-current π^+ production represents the major background to the QE "signal channel". If the pion is absorbed in the nucleus, the event appears QE-like. However, the available literature on neutrino-induced pion production is scarce: medium-modification for the Δ excitation have been discussed [SVVO98] as well as the rescattering and absorption of the pions inside the nucleus [SVVO98, PPY00].

The available models focus either on QE scattering or on pion production, but none includes both simultaneously. However, in particular the entanglement between both has important implications for LBL experiments as outlined before. Hence, the experimental collaborations have developed their own Monte Carlo event generators [Cas02, Hay02, A$^+$09] in order to quantify these effects. Their nuclear-physics modeling, however, is simplistic and has not been tested extensively for similar problems like electron scattering.

The intention of this thesis has been to develop a model that provides a combined description of neutrino-nucleus scattering from the quasielastic to the resonance region, i.e., which is applicable for neutrino energies from a few hundred MeV to about 2 GeV. Our approach is based on two pillars, both equally important: a good descrip-

tion of the neutrino-*nucleon* reaction and a realistic treatment of in-medium effects and final-state interactions.

1.3 Overview: neutrino-nucleus scattering in the GiBUU approach

Since the wavelength of the exchanged boson is small compared to intra-nucleon distances in the nucleus, we treat the nuclear reaction in impulse approximation which assumes that the lepton interacts with a single nucleon embedded in the nuclear medium. We divide the lepton-nucleus reactions into a two-step process: In the *initial step* the elementary projectile scatters off one single bound nucleon and generates a quasielastic event, excites a resonance, or a non-resonant background process within the nucleus. Thus, the first essential ingredient is a reliable description of the νN collision. For that we use a fully relativistic formalism with state-of-the-art parametrizations of the form factors.

When scattering off bound nucleons, the elementary cross section has to be modified in order to account for nuclear effects. We describe the nucleus by a local Fermi gas, leading to density dependent Fermi momenta. We further account for the binding of the nucleons in a density and momentum-dependent mean field. Pauli blocking of the final-state nucleons is also considered as well as collisional broadening.

Once produced the particles are propagated out of the nucleus undergoing *final-state interactions*. A realistic treatment of the final-state interactions can be achieved in the framework of a coupled-channel transport theory — the Giessen BUU model — which allows the investigation of semi-inclusive channels. The GiBUU transport approach is a microscopic description of the final-state process with all kind of coupled channel effects included, e.g., elastic and inelastic scattering, charge-exchange scattering, resonance production and decays in the medium. All particles are propagated in hadronic mean fields, and full off-shell propagation of the hadronic resonances has been implemented.

1.4 Outline

This work is organized as follows. In Part II, we first present our model for lepton-nucleon scattering. An introduction to electroweak interactions is given in Chapter 2. Chapter 3 explains how leptons interact with nucleons and gives an estimate of the relative importance of the various contributions. Starting in Chapter 4 we discuss in detail lepton scattering in the case of the free nucleon beginning with quasielastic scattering. Chapter 5 introduces our model for resonance excitation focussing on the

extraction of form factors. Finally, Chapter 6 is devoted to the non-resonant pion background and its phenomenological implementation in our approach.

Proceeding from nucleons to nuclei in Part III, we present in Chapter 7 the main relevant features of the GiBUU transport model. Chapter 8 specifies the in-medium modifications that apply when the neutrino scatters with a bound nucleon.

First results for electron and neutrino scattering on nuclei are presented in Chapter 9 where we focus in particular on model dependencies in the leptonic observables. Our main results for semi-inclusive scattering on nuclei are given in Chapter 10 for pion production and in Chapter 11 for nucleon knockout. There we investigate in particular the influence of final-state interactions.

Applications of the model are presented in Part IV. Chapter 12 gives a brief overview over current neutrino experiments and the Monte Carlo event generators used by the experiments to interpret their data. All present experiments use nuclear targets, thus, Chapter 13 covers CC neutrino-nucleus reactions and their importance for ν_μ disappearance measurements while Chapter 14 focuses on NC neutrino-nucleus reactions and their importance for ν_e appearance searches. Both chapters address the question how nuclear effects influence the oscillation measurements and we discuss specific examples. We give predictions and compare to available data in Chapter 15.

We close with a summary, conclusions and outlook in Chapter 16. The appendices complete the discussion by giving all necessary details.

Part II

Lepton-nucleon interactions

2

Electroweak interactions, symmetries and currents

The electroweak interaction as part of the Standard Model is covered in full detail in any textbook on Quantum Field Theory or High Energy Physics, e.g., in Refs. [TW01, MS93, AH96, Mos99], and will not be repeated here. Nonetheless, it is the theoretical basis for large parts of this work, thus, we briefly present the basics of the electroweak interaction and summarize basic facts on the currents and their relations.

2.1 Electroweak interactions of quarks and leptons

2.1.1 Interaction Lagrangian

According to the Standard model of particle physics, there are three mass-less neutrinos, ν_e, ν_μ and ν_τ. Neutrinos appear only left-handed, i.e., have spin anti-parallel to their momentum, while anti-neutrinos are right-handed.[1]

The Standard Model of the electroweak interaction is based on a local $SU(2) \times U(1)$

[1] Throughout this thesis, neutrinos are considered mass-less and purely left-handed. This is in contrast to the experimental evidence for non-zero neutrino masses as discussed in the introduction, but a very good approximation for neutrino-nucleon scattering — the neutrino mass is too small to be relevant or even visible in neutrino-nucleon reaction cross sections at neutrino energies of about 1 GeV.

gauge symmetry and its interaction Lagrangian reads (cf., e.g., Ref. [TW01])

$$\mathcal{L}_{\text{int}} = -eJ^{\mu}_{\text{EM}}A_{\mu} - \frac{g}{2\sqrt{2}}\left(J^{\mu}_{\text{CC}}{W_{\mu}}^{\dagger} + \text{h. c.}\right) - \frac{g}{2\cos\theta_W}J^{\mu}_{\text{NC}}Z_{\mu}. \tag{2.1}$$

The electromagnetic current (EM) J^{μ}_{EM}, the weak charged current (CC) J^{μ}_{CC} and the weak neutral current (NC) J^{μ}_{NC} couple to the photon field A_{μ}, the charged W-boson fields $W^{\pm}_{\mu}$, and the neutral Z-boson field Z_{μ}. Since parity is maximal violated in weak interactions, the weak currents have to have a vector-axialvector $(V-A)$ structure. Note that the electroweak currents in Eq. (2.1) include sums over all quarks and leptons. The quark currents are specified below, for the leptonic currents, we refer the reader to Section 3.2. The Feynman rules and the relations between the coupling constants are summarized in Appendix C.

The resulting interactions of leptons with quarks are sketched in Fig. 2.1: charged leptons, i.e., electrons, muons and tau leptons, scatter electromagnetically exchanging a photon (EM: $\ell^- q \to \ell^- q$). This process, which only probes the vector part of the currents, is visualized in Fig. 2.1a. For neutrino-induced reactions, we have to distinguish two cases depending on the nature of the exchanged gauge boson. In charged-current scattering (CC: $\nu_\ell q \to \ell^- q'$), indicated in Fig. 2.1b, the neutrino turns into a charged lepton via W exchange affecting also the charge of the final quark. No charge is transferred in neutral-current scattering mediated by the Z boson (NC: $\nu q \to \nu q$) shown in Fig. 2.1c. Also possible but not of interest for this work (and therefore not shown) is the scattering of charged leptons and quarks via Z exchange instead of EM scattering.

2.1.2 Quark currents

We now specify the quark currents J^{μ}_{EM}, J^{μ}_{CC} and J^{μ}_{NC}.[2] Omitting the heavy quark sector, u-, d- and s-quarks are the building blocks of matter. They form a triplet field

$$q = \begin{pmatrix} q_u \\ q_d \\ q_s \end{pmatrix} \tag{2.2}$$

with charges $Q_u = +2/3$, $Q_d = Q_s = -1/3$. With a charge matrix, defined as

$$Q = \begin{pmatrix} 2/3 & 0 & 0 \\ 0 & -1/3 & 0 \\ 0 & 0 & -1/3 \end{pmatrix}, \tag{2.3}$$

[2] For details, we refer the reader to Chapter 1 of Ref. [TW01] and to Chapters 11 and 12 of Ref. [Mos99].

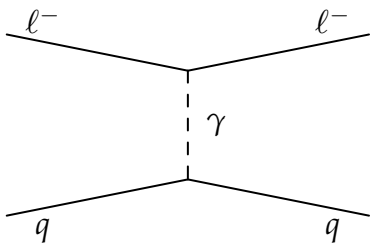

(a) Electromagnetic scattering

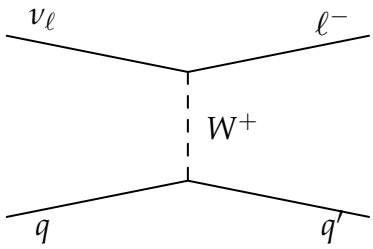

(b) Charged-current scattering

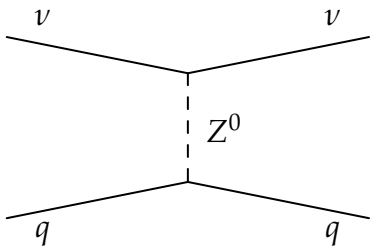

(c) Neutral-current scattering

Figure 2.1: Possible interactions of leptons with quarks.

the electromagnetic current reads

$$\begin{aligned} J^{\mu}_{\mathrm{EM}} &= \bar{q} Q \gamma^{\mu} q \\ &= \frac{2}{3}\bar{q}_u \gamma^{\mu} q_u - \frac{1}{3}\left(\bar{q}_d \gamma^{\mu} q_d + \bar{q}_s \gamma \mu q_s\right). \end{aligned} \tag{2.4}$$

(see Appendix A.3 for our metric and conventions).

For neutral currents, the coupling depends on the helicity of the quarks fields and the current reads

$$J^{\mu}_{\mathrm{NC}} = \sum_q \bar{q}\gamma^{\mu}\left[(t_3 - e_q \sin^2\theta_W)(1-\gamma^5) - e_q \sin^2\theta_W (1+\gamma^5)\right] q, \tag{2.5}$$

with e_q being the electric charge and t_3 the third component of the weak isospin. For up quarks we have $t_3 = 1/2$, for down and strange quarks $t_3 = -1/2$. Thus, the neutral current is explicitly written as

$$\begin{aligned} J^{\mu}_{\mathrm{NC}} = {} & \bar{q}_u \gamma^{\mu}\left[\frac{1}{2} - 2\frac{2}{3}\sin^2\theta_W - \frac{1}{2}\gamma^5\right] q_u \\ & + \bar{q}_d \gamma^{\mu}\left[-\frac{1}{2} - 2\left(-\frac{1}{3}\right)\sin^2\theta_W + \frac{1}{2}\gamma^5\right] q_d \\ & + \bar{q}_s \gamma^{\mu}\left[-\frac{1}{2} - 2\left(-\frac{1}{3}\right)\sin^2\theta_W + \frac{1}{2}\gamma^5\right] q_s. \end{aligned} \tag{2.6}$$

For the charged current, we have to consider that the mass eigenstates with weak isospin $-1/2$ (the d and s quark) are not the weak eigenstates. However, both sets of eigenstates are connected through a unitary transformation with the Cabbibo mixing matrix

$$\begin{pmatrix} q'_d \\ q'_s \end{pmatrix} = \begin{pmatrix} \cos\theta_C & \sin\theta_C \\ -\sin\theta_C & \cos\theta_C \end{pmatrix} \begin{pmatrix} q_d \\ q_s \end{pmatrix}, \tag{2.7}$$

where θ_C is the Cabbibo mixing angle with $\cos\theta_C = 0.9745$ (note that we later include $\cos\theta_C$ into the coupling). The charged current then reads

$$\begin{aligned} J^{\mu}_{\mathrm{CC}} &= \bar{q}\gamma^{\mu}(1-\gamma^5) q' \\ &= \bar{q}_u \gamma^{\mu}(1-\gamma^5)\left(\cos\theta_C q_d + \sin\theta_C q_s\right), \end{aligned} \tag{2.8}$$

which reflects the $(V-A)$ structure: we define the vector current as

$$V^{\mu}_{\mathrm{CC}} = \bar{q}\gamma^{\mu} q', \tag{2.9}$$

and the axial current

$$A^{\mu}_{\mathrm{CC}} = \bar{q}\gamma^{\mu}\gamma^5 q', \tag{2.10}$$

so that $J^{\mu}_{\mathrm{CC}} = V^{\mu}_{\mathrm{CC}} - A^{\mu}_{\mathrm{CC}}$.

2.2 Strong interactions and isospin symmetry

In the following, we discuss general properties and symmetries of the introduced currents.

2.2.1 Quantum Chromodynamics

Quantum Chromodynamics (QCD) is the theory of quarks and gluons and their interactions. The QCD Lagrangian is built upon a local $SU(3)$ color gauge invariance and has the form

$$\mathcal{L} = \bar{\psi}\left(\mathrm{i}\gamma^\mu D_\mu - m\right)\psi - \frac{1}{4}G^a_{\mu\nu}G^{\mu\nu}_a \tag{2.11}$$

with the quark field ψ and the non-Abelian gluon field tensor $G^{\mu\nu}_a$, $a = 1, \ldots, 8$. The couplings of the quarks and gluons is contained in the gauge covariant derivative D_μ. The interaction of quarks is independent of their flavor, the only difference comes from their different masses. We refer the reader to Chapter 5.1 in Ref. [TW01] or any other textbook for details.

Apart from its local color gauge symmetry, QCD has global unitary symmetries. They imply conserved currents, which impose constraints on the dynamics of strongly interacting systems, regardless of whether those are quarks, gluons or composite hadrons.

2.2.2 Isospin symmetry and conserved flavor currents

In the limit of $m_u = m_d = m_s$, the QCD Lagrangian has a global $SU(3)$ flavor symmetry and is invariant under[3]

$$q \to \exp\left(\mathrm{i}\theta^a \frac{\lambda_a}{2}\right) q, \tag{2.12}$$

where λ_a are the Gell-Mann matrices listed in Appendix A.3 and θ^a denotes a set of arbitrary rotations independent of the space-time coordinate. q is given in Eq. (2.2). The corresponding eight conserved Noether currents are

$$V^\mu_a = \bar{q}\gamma^\mu \frac{\lambda_a}{2} q, \tag{2.13}$$

with $\partial_\mu V^\mu_a = 0$.

Combinations of these flavor currents appear in the quark electromagnetic current. Q in Eq. (2.4) can be written as

$$Q = \frac{Y}{2} + I_3, \tag{2.14}$$

[3] We closely follow the discussion in Chapter 6 of Ref. [TW01].

where Y stands for the hypercharge $Y = B + S = \lambda_8/\sqrt{3}$ with the baryon number B and the third component of the strong isospin $I_3 = \lambda_3/2$. Applying this to Eq. (2.4) yields

$$J^\mu_{\mathrm{EM}} = \frac{1}{2} V^\mu_Y + V^\mu_3. \tag{2.15}$$

V^μ_3 is the isovector (isospin) current,

$$V^\mu_3 = \bar{q}\gamma^\mu \frac{\lambda_3}{2} q, \tag{2.16}$$

and V^μ_Y is the isoscalar (hypercharge) current,

$$V^\mu_Y = \bar{q}\gamma^\mu \frac{\lambda_8}{\sqrt{3}} q \tag{2.17}$$

Also the vector part of the charged current, V^μ_{CC} (cf., Eq. (2.9)), can be expressed in terms of V^μ_a, namely

$$V^\mu_{\mathrm{CC}} = \bar{q}\gamma^\mu \frac{\lambda_1 + \mathrm{i}\lambda_2}{2} q = \bar{q}\gamma^\mu \frac{\lambda_+}{2} q = V^\mu_1 + \mathrm{i} V^\mu_2. \tag{2.18}$$

Finally, we rewrite the vector part of the neutral current given in Eq. (2.5) in terms of the flavor currents and obtain

$$V^\mu_{\mathrm{NC}} = (1 - 2\sin^2\theta_W) V^\mu_3 - 2\sin^2\theta_W \frac{1}{2} V^\mu_Y - \frac{1}{2} V^\mu_S, \tag{2.19}$$

with V^μ_3 and V^μ_Y as above and V^μ_S given by

$$V^\mu_S = \bar{q}_s \gamma^\mu q_s. \tag{2.20}$$

To conclude, we have shown that the isovector part of the electromagnetic current, V^μ_3, and the vector part of the weak currents, $V^\mu_{1,2}$, are components of the same conserved $SU(3)_f$ vector current.

2.2.3 Chiral symmetry and axial currents

QCD has an additional global symmetry in the limit of mass-less quarks, i.e., $m_u = m_d = m_s = 0$, the so-called chiral symmetry. Then, the QCD Lagrangian is invariant under the transformations

$$q_L \to \exp\left(\mathrm{i}\theta^a_L \frac{\lambda_a}{2}\right) q_L, \qquad q_R \to \exp\left(\mathrm{i}\theta^a_R \frac{\lambda_a}{2}\right) q_R, \tag{2.21}$$

where q_L and q_R are the left and right-handed quark fields defined as

$$q_{L,R} = \frac{1}{2}\left(1 \mp \gamma^5\right) q. \tag{2.22}$$

The corresponding sixteen conserved Noether currents are

$$J^\mu_{a,L} = \bar{q}_L \gamma^\mu \frac{\lambda_a}{2} q_L, \qquad J^\mu_{a,R} = \bar{q}_R \gamma^\mu \frac{\lambda_a}{2} q_R, \tag{2.23}$$

with $\partial_\mu J^\mu_{a,L} = \partial_\mu J^\mu_{a,R} = 0$.

Combining $J^\mu_{a,L}$ and $J^\mu_{a,R}$ gives the already introduced vector current

$$V^\mu_a = J^\mu_{a,R} + J^\mu_{a,L} = \bar{q}\gamma^\mu \frac{\lambda_a}{2} q \tag{2.24}$$

and the axial current

$$A^\mu_a = J^\mu_{a,R} - J^\mu_{a,L} = \bar{q}\gamma^\mu\gamma^5 \frac{\lambda_a}{2} q. \tag{2.25}$$

The weak axial charged current introduced in Eq. (2.10) is written in terms of A^μ_a as

$$A^\mu_{\mathrm{CC}} = \bar{q}\gamma^\mu\gamma^5 \frac{\lambda_+}{2} q = A^\mu_1 + \mathrm{i}A^\mu_2. \tag{2.26}$$

Similarly, we obtain for the axial part of the neutral current given in Eq. (2.5)

$$A^\mu_{\mathrm{NC}} = A^\mu_3 + \frac{1}{2} A^\mu_S, \tag{2.27}$$

with

$$A^\mu_3 = \bar{q}\gamma^\mu\gamma^5 \frac{\lambda_3}{2} q \tag{2.28}$$

and

$$A^\mu_S = \bar{q}_s\gamma^\mu\gamma^5 q_s. \tag{2.29}$$

Chiral symmetry is explicitly broken by the non-zero quark masses, and the divergence of the axial current becomes

$$\partial_\mu A^\mu_a = \mathrm{i}\bar{q}\left\{m, \frac{\lambda_a}{2}\right\}\gamma^5 q, \tag{2.30}$$

with $m = \mathrm{diag}(m_u, m_d, m_s)$. For example, the divergence of A^μ_{CC} reads

$$\partial_\mu A^\mu_{\mathrm{CC}} = (m_u + m_d)\bar{q}_u \mathrm{i}\gamma^5 q_d, \tag{2.31}$$

and is thus conserved only in the chiral limit $m_u \to 0$ and $m_d \to 0$.

2.3 Hadronic currents

2.3.1 Conserved vector current hypothesis

In the previous section it has been shown, that, at the quark level, one can directly relate the electromagnetic and the weak vector currents assuming only isospin symmetry of the strong interactions. If isospin symmetry is a good symmetry of the particular hadronic system, one expects the obtained relations to be independent of the details of the hadronic structure, or, in other words, the relations hold also for hadrons.

Then, we find the following structure for the electromagnetic current

$$J^\mu_{\mathrm{EM}} = \frac{1}{2} V^\mu_Y + V^\mu_3 . \tag{2.32}$$

V^μ_3 is the third component of the isovector (isospin) current and V^μ_Y the isoscalar (hypercharge) current. The vector part of the charged current is given by

$$V^\mu_{\mathrm{CC}} = V^\mu_1 + \mathrm{i} V^\mu_2 , \tag{2.33}$$

and the vector part of the neutral current by

$$V^\mu_{\mathrm{NC}} = (1 - 2\sin^2\theta_W) V^\mu_3 - \sin^2\theta_W V^\mu_Y - \frac{1}{2} V^\mu_S , \tag{2.34}$$

where V^μ_Y is the hypercharge, V^μ_S the strange (both isoscalar), and $V^\mu_{1,2,3}$ the isovector current.

We assume that $V^\mu_{1,2}$ and V^μ_3 form a vector in isospin space, i.e., the weak hadronic vector current can be identified with the isospin current. This is known as "conserved vector current hypothesis" (CVC). An immediate consequence of CVC is the conservation of the weak hadronic vector current.

Further predictions of CVC and possible measurements are reviewed in Ref. [TH95]; altogether, there is impressive experimental support for the validity of CVC.

2.3.2 Partially conserved axial current hypothesis

Also for the axial part, we assume the hadronic currents to have the same structure as the quark current discussed in the previous section and find

$$A^\mu_{\mathrm{CC}} = A^\mu_1 + \mathrm{i} A^\mu_2 , \tag{2.35}$$

for charged currents, and

$$A^\mu_{\mathrm{NC}} = A^\mu_3 + \frac{1}{2} A^\mu_S , \tag{2.36}$$

for neutral currents. Eq. (2.36) includes the isoscalar strange axial current A^μ_S. $A^\mu_{1,2}$ and A^μ_3 are components of the same isospin vector.

The divergence of the axial current A^μ can be connected to the pion field ϕ via

$$\partial_\mu A^\mu = -f_\pi m_\pi^2 \phi. \tag{2.37}$$

A detailed discussion and derivation is given in Chapter 9 of Ref. [EW88]. This relation implies that the axial current is conserved in the chiral limit $m_\pi \to 0$ which is known as "partially conserved axial current hypothesis" (PCAC).

Predictions of PCAC and their experimental verifications are discussed, e.g., in the review article by Towner and Hardy [TH95]. Overall, the predictions are found to deviate from the measurements by a few percent to at most 10%[4] which reflects the accuracy to which PCAC is realized.

[4] See also the discussion on page 33.

3

General properties of the lepton-nucleon interaction

In this and in the following three chapters we explain in detail our model for neutrino scattering off *nucleons*. We shall start with a general section giving an overview about the neutrino nucleon reaction while the following chapters address the various reaction channels considered in this thesis.

3.1 Contributions to the lepton-nucleon interaction

Leptons interact with nucleons in various ways (compare Fig. 2.1 where we have discussed the interactions of leptons with quarks): charged leptons, i.e., electrons, muons and tau leptons, exchange a photon[1] (EM: $\ell^- N \to \ell^- X$) as sketched in Fig. 3.1a. Neutrino-induced reactions are very similar; however, here the nucleon is not probed by a (virtual) photon but by a weak gauge boson and the coupling now contains both vector and axial-vector parts. In charged-current scattering (CC: $\nu_\ell N \to \ell^- X$) mediated by W exchange (cf., Fig. 3.1b) the neutrino turns into a charged lepton and also the charge of the final hadronic system is changed. No charge is transferred in neutral-current scattering via the Z boson (NC: $\nu N \to \nu X$) shown in Fig. 3.1c. In this work, we treat EM, CC and NC scattering within the same formalism.

[1] Charged leptons can also scatter via Z^0 exchange which is highly suppressed by the smallness of the coupling although relevant for experiments with polarized beams and/or targets. It is disregarded in this work.

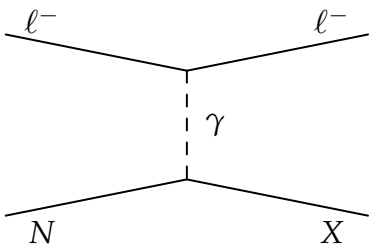

(a) Electromagnetic scattering

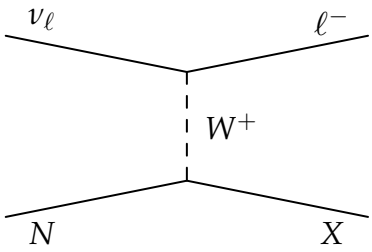

(b) Charged-current scattering

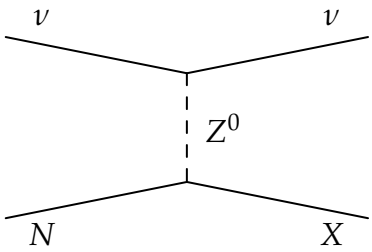

(c) Neutral-current scattering

Figure 3.1: Possible interactions of leptons with nucleons.

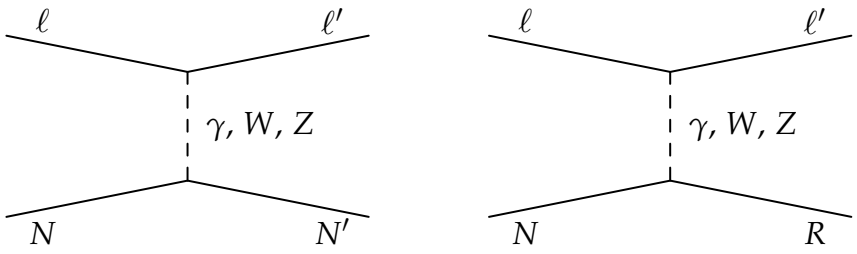

(a) Quasielastic scattering

(b) Resonance excitation

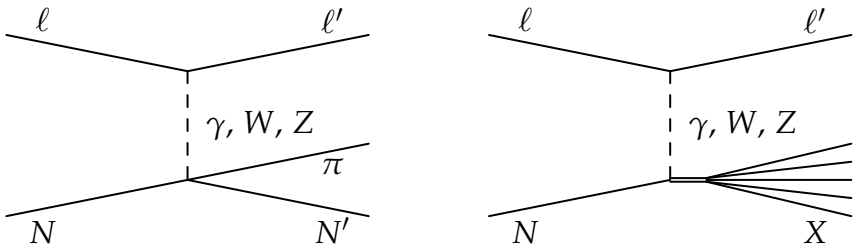

(c) Non-resonant single-pion production (background)

(d) Deep-inelastic scattering

Figure 3.2: Contributions to ℓN scattering

The total lepton-nucleon cross section contains contributions from different possible final states which are outlined in Fig. 3.2. Most important in the region of intermediate lepton beam energies ($E_{\text{beam}} \sim 0.5 - 2\,\text{GeV}$) is quasielastic scattering (QE: $\ell N \to \ell' N'$), where one has only nucleons, both in the initial and final state. In CC scattering, a neutron is turned into a proton while the charge of the nucleon is not changed in NC and EM scattering. QE scattering is discussed in detail in Chapter 4. A significant contribution to the total cross section comes from resonance excitation (R: $\ell N \to \ell' R$) covered in Chapter 5 where the nucleon is excited to a baryonic resonance in the final state. Resonances decay into baryons and mesons, mainly pions.[2] A prominent channel at intermediate energies is single-pion production, but also the decay into multiple pions or other mesons, e.g., etas, is possible (and taken into account in this work). Besides pion production through resonance decay, also direct, i.e., non-resonant single-pion production (BG: $\ell N \to \ell' \pi N'$), treated in our description as background, is significant in some cases as will be discussed in Chapter 6. A non-resonant two-pion background is neglected because its contribution is only minor for

[2] In the nuclear medium, the resonances may also interact with nucleons which leads to "pion-less decay modes". For example, the Δ can scatter via $\Delta N \to NN$ and contributes, therefore, not only to single-π production. These processes will be discussed in Chapter 7.

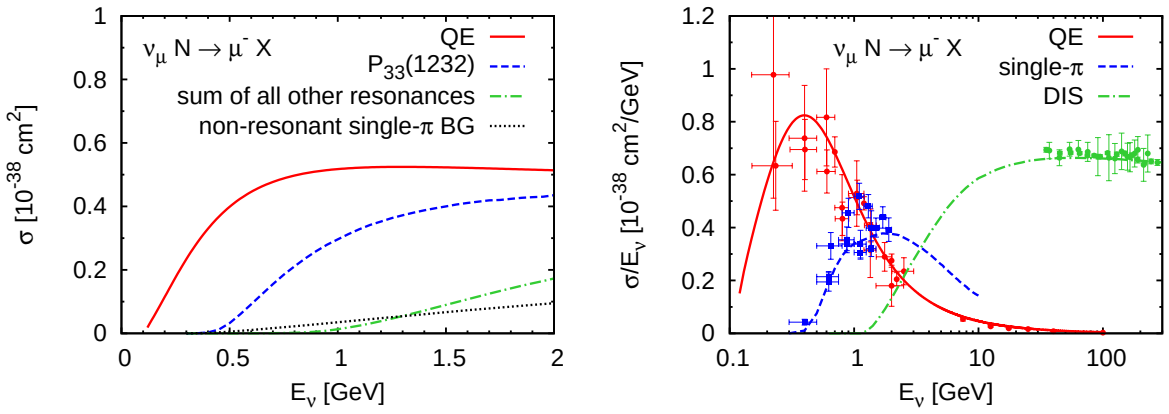

Figure 3.3: Total neutrino cross sections for $\nu_\mu N \to \mu^- X$ for an isoscalar target as a function of the neutrino energy. The curves are averaged over protons and neutrons: $\sigma = (\sigma_{\nu_\mu p} + \sigma_{\nu_\mu n})/2$. Left panel: contributions to the total neutrino-nucleon cross section according to Eq. (3.1), namely quasielastic scattering (solid line), $P_{33}(1232)$ resonance excitation (dashed line), the sum of the excitation of all other resonances (dash-dotted line) and the non-resonant single-π background (dotted line). Right panel: cross sections, divided by E_ν, for quasielastic scattering, single-π production and deep-inelastic scattering (DIS) compared to data. The data are taken from Refs. [B$^+$77, M$^+$73, B$^+$81, B$^+$79, R$^+$82, K$^+$86, A$^+$90, M$^+$84, Sel97].

the energy region discussed in this work [ADT81b, ADT81a, HNS$^+$08].[3]

Altogether, the present model assumes

$$\mathrm{d}\sigma_{\mathrm{tot}} = \mathrm{d}\sigma_{\mathrm{QE}} + \sum_{\mathrm{R}} \mathrm{d}\sigma_{\mathrm{R}} + \mathrm{d}\sigma_{\mathrm{BG}}. \tag{3.1}$$

The relative importance of these contributions is illustrated in the left panel of Fig. 3.3 where the corresponding CC cross section are shown as a function of the neutrino energy.

In the right panel of Fig. 3.3 we show the QE cross section, the total single-π production cross section and also the contribution from deep-inelastic scattering (DIS), a process visualized in Fig. 3.2d where one scatters off partonic degrees of freedom. Note that we divided the cross section by the neutrino energy, thus, the DIS part increases linearly with energy and is by far the most important process for energies above $\approx 5\,\mathrm{GeV}$.

As we focus on neutrino scattering up to about 2 GeV, an energy regime where DIS is not very important, we neglect this contribution. The uncertainties related with

[3] Note, however, that it is not negligible in photon-induced reactions.

the neglect of DIS are discussed in Appendix G.2 where also more details on the calculation are given.

From Fig. 3.3, we conclude that our νN model characterized by Eq. (3.1) contains the most important ingredients for neutrino scattering at medium energies and can be reliably applied to nucleon-knockout reactions and pion production on nuclei.

3.2 Dynamics of the lepton-nucleon interaction

The dynamics of the lepton-nucleon interaction is encoded in the absolute value of the matrix element squared, summed and averaged over initial and final spins,

$$|\bar{\mathcal{M}}_{\mathrm{QE,R,BG}}|^2 = C^2\, L_{\mu\nu}\, H^{\mu\nu}_{\mathrm{QE,R,BG}}\,, \tag{3.2}$$

where the coupling C stands either for $C_{\mathrm{EM}} = 4\pi\alpha/q^2$, $C_{\mathrm{CC}} = G_F \cos\theta_C/\sqrt{2}$, or $C_{\mathrm{NC}} = G_F/\sqrt{2}$ (cf. Appendix C) and q^2 stands for the four-momentum transfer squared. $L_{\mu\nu}$ and $H^{\mu\nu}$ are the leptonic and hadronic tensors, respectively.

Throughout this work, the incoming lepton defines the z-axis and all quantities, if not stated otherwise, are given in the laboratory (lab) frame, i.e., in the target rest frame. Our notation is summarized in Table A.3.

The leptonic tensor $L_{\mu\nu}$ is constructed from the leptonic current, $j_\mu = \bar{u}(k')l_\mu u(k)$, as

$$\begin{aligned} L_{\mu\nu} &= \frac{1+|a|}{2}\sum_{s_i}\sum_{s_f} {j_\mu}^\dagger j_\nu = \frac{1+|a|}{2}\sum_{s_i}\sum_{s_f} \bar{u}(k)\widetilde{l_\mu}u(k')\bar{u}(k')l_\nu u(k) \\ &= \frac{1+|a|}{2}\mathrm{Tr}\left[(\not{k}+m_\ell)\widetilde{l_\mu}(\not{k}'+m_{\ell'})l_\nu\right], \end{aligned} \tag{3.3}$$

where

$$l_\mu = \gamma_\mu(1-a\gamma^5), \tag{3.4}$$

and

$$\tilde{l}_\mu = \gamma_0 l_\mu^\dagger \gamma_0. \tag{3.5}$$

Here, k (k') denotes the four-vector of the incoming (outgoing) lepton and m_ℓ ($m_{\ell'}$) the corresponding masses. The parameter a depends on the reaction process: $a = 0$ for EM and $a = 1$ (-1) for CC and NC (anti-)neutrino scattering. For incoming neutrinos there is no averaging over initial neutrino helicities since they are left-handed. For this reason, we include the factor $(1+|a|)/2$. However, one can formally sum over both helicity states, since the factor $(1-\gamma^5)$ guarantees anyhow that neither right-handed neutrinos nor left-handed anti-neutrinos contribute to the cross section.

The hadronic currents in $H^{\mu\nu}_{\mathrm{QE,R,BG}}$ have to be parametrized in terms of form factors. They depend not only on the final state but also on the specific process, namely

EM, CC or NC. This will be discussed in Chapters 4 to 6. Contracting the hadronic tensor $H^{\mu\nu}_{\mathrm{QE,R,BG}}$ with the leptonic tensor given in (3.3), one obtains the matrix element $|\bar{\mathcal{M}}_{\mathrm{QE,R,BG}}|$ (see Eq. (3.2)).[4]

3.3 Kinematics of the lepton-nucleon interaction

A detailed derivation of the cross section formula is given in Section B.2; here, we summarize the final results.

The cross section for quasielastic scattering $\ell(k)N(p) \to \ell'(k')N'(p')$ reads [cf. Eq. (B.11) on page 275 with $M = M' = M_N$ where M_N denotes the nucleon mass]

$$\frac{\mathrm{d}\sigma_{\mathrm{QE}}}{\mathrm{d}\omega\,\mathrm{d}\Omega_{k'}} = \frac{|\mathbf{k}'|}{32\pi^2}\,\frac{\delta(p'^2 - M_N^2)}{\left[(k\cdot p)^2 - m_\ell^2 M_N^2\right]^{1/2}}\,|\bar{\mathcal{M}}_{\mathrm{QE}}|^2, \tag{3.6}$$

where $\omega = k^0 - k'^0$ is the energy transfer and $\mathrm{d}\Omega_{k'} = \mathrm{d}\phi\,\mathrm{d}\cos\theta$ includes the angles between incoming and outgoing leptons. In the lab frame the initial nucleon is at rest, hence $p^\mu = (M_N, \mathbf{0})$.

A similar expression holds for resonance excitation $\ell(k)N(p) \to \ell'(k')R(p')$ [cf. Eq. (B.11) on page 275 with $M = M_N$]

$$\frac{\mathrm{d}\sigma_{\mathrm{R}}}{\mathrm{d}\omega\,\mathrm{d}\Omega_{k'}} = \frac{|\mathbf{k}'|}{32\pi^2}\,\frac{\mathcal{A}(p')}{\left[(k\cdot p)^2 - m_\ell^2 M_N^2\right]^{1/2}}\,|\bar{\mathcal{M}}_{\mathrm{R}}|^2, \tag{3.7}$$

where we have replaced

$$\delta(p'^2 - M'^2) \to \mathcal{A}(p'). \tag{3.8}$$

$\mathcal{A}(p')$ denotes the vacuum spectral function of the particle given by a Breit-Wigner distribution

$$\mathcal{A}(p') = \frac{\sqrt{p'^2}}{\pi}\frac{\Gamma(p')}{(p'^2 - M_R^2)^2 + p'^2\Gamma^2(p')}\,, \tag{3.9}$$

with the momentum-dependent width Γ and the Breit-Wigner masses M_R. The explicit functional form of Γ is be given in Section 7.6.1. We refer the reader to Section 7.7 for further details, in particular for a discussion on the normalization of Eq. (3.9).

For the cross section for the non-resonant pion background, we refer the reader to Chapter 6.

[4] In our numerical realization, we calculate and contract both tensors during run-time numerically. An analytic expression for the matrix elements is not needed and therefore not given.

4 Quasielastic scattering

This chapter is devoted to quasielastic scattering. At neutrino energies up to about 2 GeV, QE scattering is the dominant contribution to the total cross section as we have seen in Fig. 3.3.

4.1 Hadronic current

The hadronic tensor $H^{\mu\nu}_{\mathrm{QE}}$ for quasielastic scattering, $\ell N \to \ell' N'$, is determined by the hadronic current

$$J^{\mu}_{\mathrm{QE}} = \left\langle N'(p') \left| J^{\mu}_{\mathrm{QE}}(0) \right| N(p) \right\rangle = \bar{u}(p')\Gamma^{\mu}_{\mathrm{QE}} u(p) \tag{4.1}$$

as

$$\begin{aligned} H^{\mu\nu}_{\mathrm{QE}} &= \frac{1}{2}\sum_{s_i}\sum_{s_f} J^{\mu\,\dagger}_{\mathrm{QE}} J^{\nu}_{\mathrm{QE}} = \frac{1}{2}\sum_{s_i}\sum_{s_f} \bar{u}(p)\tilde{\Gamma}^{\mu}_{\mathrm{QE}} u(p')\bar{u}(p')\Gamma^{\nu}_{\mathrm{QE}} u(p) \\ &= \frac{1}{2}\mathrm{Tr}\left[(\not{p} + M)\tilde{\Gamma}^{\mu}_{\mathrm{QE}}(\not{p}' + M')\Gamma^{\nu}_{\mathrm{QE}}\right], \end{aligned} \tag{4.2}$$

with $\tilde{\Gamma}^{\mu}_{\mathrm{QE}} = \gamma_0 \Gamma^{\mu\,\dagger}_{\mathrm{QE}} \gamma_0$, and $M = \sqrt{p^2}$ and $M' = \sqrt{p'^2}$. In the case of free nucleons, we have $M = M' = M_N$. The prefactor $1/2$ stems from the averaging over the initial nucleon spin.

The vertex function $\Gamma^{\mu}_{\mathrm{QE}}$ has a vector−axial ($V - A$) Lorentz structure

$$\Gamma^{\mu}_{\mathrm{QE}} = \mathcal{V}^{\mu}_{\mathrm{QE}} - \mathcal{A}^{\mu}_{\mathrm{QE}} \,. \tag{4.3}$$

We construct the most general form for $\mathcal{V}^\mu_{\rm QE}$ out of the four vectors at our disposal: p^μ, p'^μ and $q^\mu = p'^\mu - p^\mu$. Gordon identities (cf., e.g., Appendix A.2 in Ref. [IZ05]) limit the number of terms and we find for the vector part

$$\mathcal{V}^\mu_{\rm QE} = \mathcal{F}_1\gamma^\mu + \frac{\mathcal{F}_2}{2M_N}\mathrm{i}\sigma^{\mu\alpha}q_\alpha + \frac{q^\mu}{M}\mathcal{F}_3\,. \tag{4.4}$$

Current conservation, i.e., $q_\mu\left(\bar{u}(p')\mathcal{V}^\mu_{\rm QE}u(p)\right) = 0$, gives

$$\begin{aligned} 0 &= \bar{u}(p')\left(\mathcal{F}_1\not{q} + \frac{\mathcal{F}_2}{2M_N}\mathrm{i}\sigma^{\mu\alpha}q_\mu q_\alpha + \frac{q^2}{M}\mathcal{F}_3\right)u(p) \\ &= \bar{u}(p')\left(\mathcal{F}_1\not{q} + \frac{q^2}{M}\mathcal{F}_3\right)u(p), \end{aligned} \tag{4.5}$$

where we have used that the term $\sigma^{\mu\alpha}q_\mu q_\alpha$, antisymmetric in μ and α, vanishes. Then, we get

$$\mathcal{F}_1\not{q} + \frac{q^2}{M}\mathcal{F}_3 = 0 \quad\Leftrightarrow\quad \mathcal{F}_3 = -\mathcal{F}_1\frac{\not{q}M}{q^2}, \tag{4.6}$$

which leads to

$$\mathcal{V}^\mu_{\rm QE} = \mathcal{F}_1\left(\gamma^\mu + \frac{\not{q}q^\mu}{Q^2}\right) + \frac{\mathcal{F}_2}{2M_N}\mathrm{i}\sigma^{\mu\alpha}q_\alpha\,. \tag{4.7}$$

The term $\not{q}q^\mu/Q^2$ in Eq. (4.7) vanishes when $M = M'$ since $\bar{u}(p')\not{q}u(p) = \bar{u}(p')(M' - M)u(p)$. In the nuclear medium, M and M' are in general not equal due to the momentum dependence of the mean-field potential. We come back to this discussion in Section 8.1.1 and Section 9.3.

For the axial part, we find

$$-\mathcal{A}^\mu_{\rm QE} = \mathcal{F}_A\gamma^\mu\gamma^5 + \frac{\mathcal{F}_P}{M_N}q^\mu\gamma^5\,. \tag{4.8}$$

$\mathcal{F}_i$ ($i = 1,2$) denotes either the CC form factors, F_i^V, the NC form factors, $\tilde{F}_i^N$, or the EM form factors, F_i^N, with $N = p,n$; $\mathcal{F}_A$ the CC form factor, F_A, or the NC form factor, $\tilde{F}_A^N$, (analogous for the pseudoscalar form factor $\mathcal{F}_P$) as detailed below. All form factors depend on $Q^2 = -q^2$.

4.2 Form factors of the nucleon

Vector form factors

The vector form factors, F_i^V and $\tilde{F}_i^N$, can be related to the electromagnetic Dirac and Pauli form factors, F_i^N, with $N = p,n$ as listed in Table 4.1: the conserved vector current hypothesis (CVC) implies that the vector part of the current in Eq. (4.7) and the

Table 4.1: Relations for the vector form factors; details are given in Appendix D.1. Note that CCQE scattering is not possible on protons. The strangeness form factors F_i^s are defined on page 35.

reaction	replace $\mathcal{F}_i$ in Eq. (4.7) with
$\ell^- p \to \ell^- p$	F_i^p
$\ell^- n \to \ell^- n$	F_i^n
$\nu n \to \ell^- p$	$F_i^V = F_i^p - F_i^n$
$\nu p \to \nu p$	$\tilde{F}_i^p = (\frac{1}{2} - 2\sin^2\theta_W)F_i^p - \frac{1}{2}F_i^n - \frac{1}{2}F_i^s$
$\nu n \to \nu n$	$\tilde{F}_i^n = (\frac{1}{2} - 2\sin^2\theta_W)F_i^n - \frac{1}{2}F_i^p - \frac{1}{2}F_i^s$

electromagnetic current are components of the same isospin multiplet of conserved currents, and that therefore their form factors are related. Details are given in Appendix D.1.

Rewriting F_i^p and F_i^n in terms of Sachs form factors defined, e.g., in Ref. [Sto93], one gets

$$F_1^{p,n} = \left[G_E^{p,n} + \frac{Q^2}{4M_N^2} G_M^{p,n}\right] \left[1 + \frac{Q^2}{4M_N^2}\right]^{-1}, \tag{4.9}$$

$$F_2^{p,n} = \left[G_M^{p,n} - G_E^{p,n}\right] \left[1 + \frac{Q^2}{4M_N^2}\right]^{-1}. \tag{4.10}$$

Here, $G_M(Q^2)$ and $G_E(Q^2)$ are the magnetic and the electric form factors of the nucleon, respectively. In the following, we use the updated BBBA-2007 parametrization [BABB08] which includes recent electron scattering data from JLab and accounts for deviations from the dipole Q^2-dependence.

In Fig. 4.1, the electromagnetic form factors F_i^p and F_i^n (upper panel) and the vector form factors for CC and NC scattering (cf. Table 4.1; middle and lower panel, respectively) are shown as a function of Q^2. At zero momentum transfer the vector form factors are fixed by the electric charge and the magnetic moment of the nucleon.

Axial form factors

The axial form factors $\mathcal{F}_A$ and $\mathcal{F}_P$ introduced in Eq. (4.8) — present in CC and NC scattering — depend also on the process under consideration as indicated in Table 4.2. Contracting leptonic and hadronic tensors, one finds that $\mathcal{F}_P$ appears only multiplied by the mass of the outgoing lepton. Thus, it does not contribute for NC interactions.

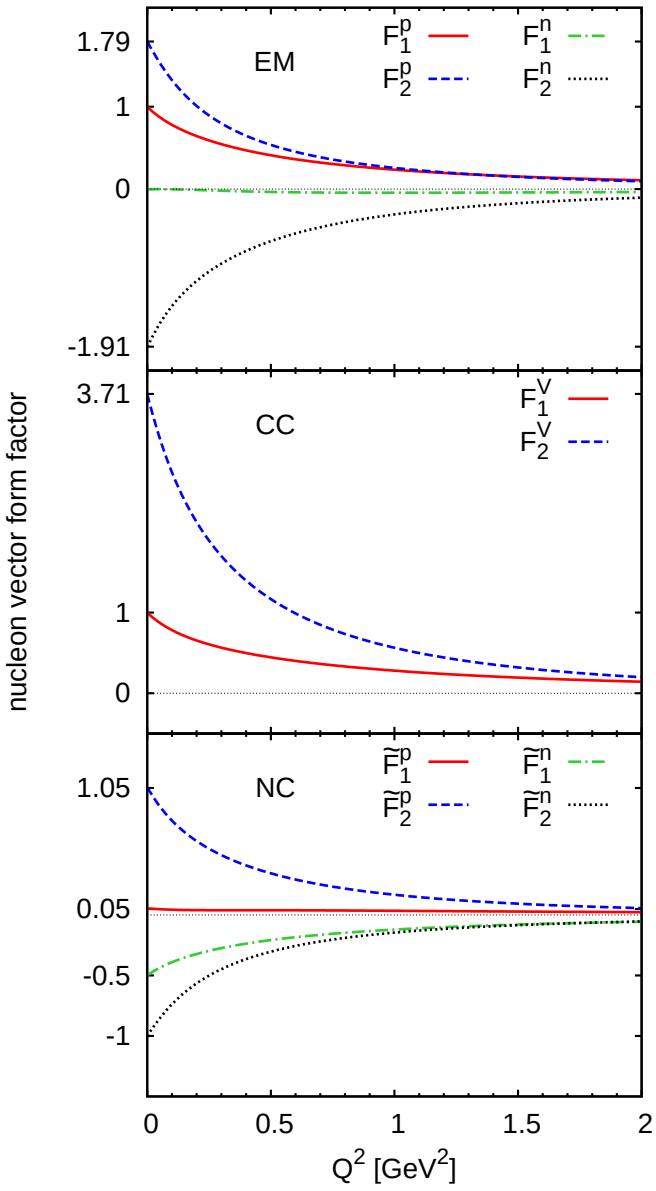

Figure 4.1: Nucleonic vector form factors as a function of Q^2. The upper panel shows the Dirac and Pauli form factors F_i^N with $N = p, n$, the middle panel the form factors F_i^V for CC, the lower panel $\tilde{F}_i^N$ for NC scattering as given in Table 4.1.

Table 4.2: Relations for the axial form factors; details are given in Section D.1. Note that CCQE scattering is not possible on protons. The strangeness form factor F_A^s is defined on page 35.

reaction	replace $\mathcal{F}_A$ in Eq. (4.8) with	replace $\mathcal{F}_P$ in Eq. (4.8) with
$\ell^- p \to \ell^- p$	-	-
$\ell^- n \to \ell^- p$	-	-
$\nu n \to \ell^- p$	F_A	$\frac{2M_N^2}{Q^2+m_\pi^2} F_A$
$\nu p \to \nu p$	$\tilde{F}_A^p = \frac{1}{2}F_A + \frac{1}{2}F_A^s$	-
$\nu n \to \nu n$	$\tilde{F}_A^n = -\frac{1}{2}F_A + \frac{1}{2}F_A^s$	-

In the case of CC reactions, we assume pion-pole dominance and use the partial conservation of the axial current (PCAC) to relate F_A and F_P (details are given in Appendix F.2.1), so that[1]

$$F_P(Q^2) = \frac{2M_N^2}{Q^2 + m_\pi^2} F_A(Q^2). \tag{4.11}$$

The axial vector coupling constant $F_A(0)$ is obtained using Eq. (F.17) with $C_{\text{iso}} = \sqrt{2}$, so that

$$F_A(0) = -2 f_\pi \frac{f}{m_\pi} \equiv -g_A. \tag{4.12}$$

This is known as the Goldberger-Treiman relation (see, e.g., Eq. (9.61) in Ref. [EW88]). It predicts the axial coupling g_A constant with a 2% accuracy compared to the value measured from neutron beta decay [BEM02, TH95]. These experiments obtained $g_A = 1.267$ [PDG08], which is the value we adopt throughout this work.

For the axial form factor we assume a standard dipole form

$$F_A(Q^2) = F_A(0) \left(1 + \frac{Q^2}{M_A^2}\right)^{-2}. \tag{4.13}$$

There are two methods to determine the so-called axial mass M_A: QE neutrino scattering or charged pion electroproduction. The former method has been applied by Kuzmin and collaborators to refit M_A using the recent BBBA-2007 parametrization

[1] Experimentally, PCAC and the assumption of pion-pole dominance have been tested by measuring muon capture in Hydrogen [MuCap07] where good agreement with the predicted values has been found (see also the review article by Towner and Hardy [TH95]). We note that we neglect a small non-pion pole correction in F_P (see, e.g., Section 4.1 in Ref. [BEM02]).

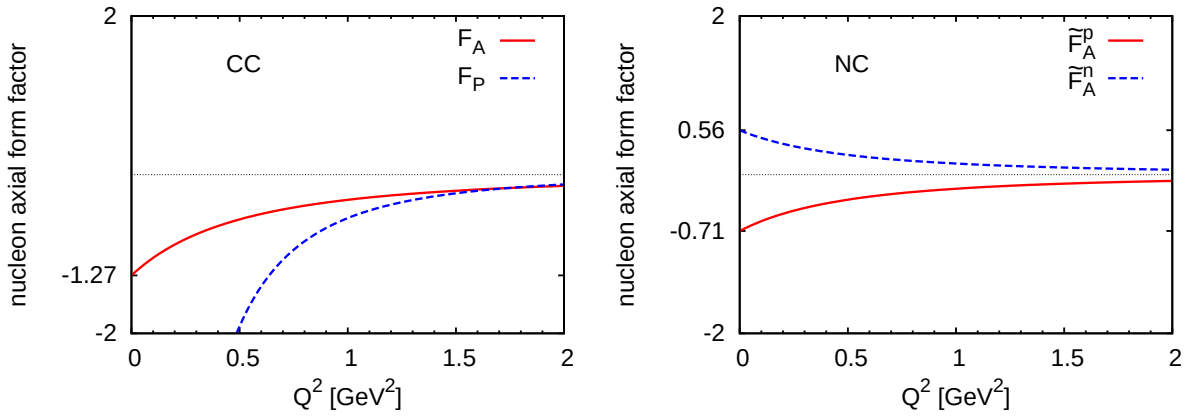

Figure 4.2: Nucleonic axial form factors as a function of Q^2. In the left panel, we show the CC axial form factors F_A and F_P; in the right panel $\tilde{F}_A^p$ and $\tilde{F}_A^n$ present in NC scattering (using the strange contribution F_A^s with $\Delta s = -0.15$ discussed on page 35).

for the vector form factors [KLN08]. They analyzed all available experimental data on the total and differential charged-current cross sections for quasielastic $\nu_\mu N$ and $\bar{\nu}_\mu N$ scattering, obtained in the accelerator experiments at ANL, BNL, FNAL, CERN, and IHEP over the the last decades. We take their best fit value

$$M_A = 0.999 \pm 0.011\,\text{GeV}. \tag{4.14}$$

This value is consistent with the one extracted from pion electroproduction data which gives $M_A = 1.014\,\text{GeV}$ (Ref. [BEM02], their Eq. (10) together with the correction in their Eq. (53)). These numbers seem to be in conflict with the recent findings of the K2K and MiniBooNE experiments [K2K06, MiniBooNE08b]. The new data, obtained from reactions on nuclei, seem to prefer an axial mass of around 1.2 GeVand higher. We return to this issue in Section 15.1.

The axial form factors are shown in Fig. 4.2 as a function of Q^2 for both, CC and NC scattering. Note that even though the absolute value of F_P becomes very large (≈ -120 at $Q^2 = 0$), this form factor contributes only very little to the ν_e and ν_μ CCQE cross section since it appears only multiplied by $m_{\ell'}^2$ (cf., e.g., Fig. 4.5 and 4.6 in Ref. [Lei05]).

Strange form factors

The strangeness content of the nucleon is contained in $F_{1,2}^s$ and F_A^s, which play a role in NC scattering (see Table 4.1 and 4.2). It can be investigated in a combined study of parity-violating polarized electron scattering and neutral-current neutrino

scattering. Parity-violating electron scattering is sensitive to the strange electric and magnetic form factors (i.e., to the strange vector form factors) and much less to the strange axial-vector form factor (cf., e.g., Ref. [TW01]). The opposite holds for NC neutrino scattering. An extensive program studying parity violation experimentally has evolved in the last years: the SAMPLE experiment at MIT/Bates [SAMPLE04], HAPPEX [HAPPEX01, HAPPEX06] and G0 [G005] at JLab, and PVA4 [A404] in Mainz have extracted linear combinations of the strange electric and magnetic form factors at different Q^2 values. Recently, the strange electric and magnetic form factors were extracted from a combined set of available parity-violating electron scattering data by Young *et al.* [YRCT06]. However, data for NC neutrino-nucleon scattering, needed to determine the strange axial form factor, are scarce. The best measurement to date has been performed by the E734 experiment at BNL [A$^+$87] which measured neutrino-proton and anti-neutrino-proton elastic scattering, albeit with large systematical errors and only small statistics. Former attempts to extract the strange axial form factor from these data [GLW93, ABB$^+$99] faced the fact that, as pointed out by Alberico *et al.* [ABB$^+$99], the experimental uncertainty is still too large to be conclusive about specific values of the strange form factors of the nucleon and a rather wide range of values for the strange parameters is compatible with the BNL E734 data. The advent of new polarized electron scattering data from the above mentioned experiments changes appreciably the situation because, as shown by Pate [Pat04, PMP08, Pat05], it allows to perform a simultaneous determination of all (electric, magnetic and axial) strange form factors with small error bars, in spite of the uncertainties of the E734 data. But this is only possible in the region of $0.45 < Q^2 < 1.05\ \mathrm{GeV}^2$ where the E734 differential cross sections were measured, so new NC neutrino-nucleon scattering data at low Q^2 are needed for a reliable extrapolation down to $Q^2 = 0$.

At present, no definite conclusion can be drawn from data, thus we set for simplicity[2]

$$F_1^s(0) = 0, \tag{4.15}$$

$$F_2^s(0) = 0, \tag{4.16}$$

and

$$F_A^s(Q^2) = \frac{\Delta s}{\left(1 + \frac{Q^2}{M_A^2}\right)^2}\,, \tag{4.17}$$

assuming that the strange axial mass is equal to the non-strange one. Here Δs denotes the strange contribution to the nucleon spin. In line with Ref. [ABB$^+$97] we use $\Delta s = -0.15$ and $\Delta s = 0$ as representative values. If not stated otherwise, the former value is used by default.

[2]The NC cross section is more sensitive to the strange axial form factor than to the strange vector form factors. This has been discussed in detail in Ref. [Lei05].

4.3 Cross section

Contracting the hadronic tensor defined in Eq. (4.2) at the beginning of this chapter with the leptonic tensor given in Eq. (3.3) on page 27, one obtains the matrix element $|\bar{\mathcal{M}}_{\mathrm{QE}}|$ (see Eq. (3.2)), which, together with Eq. (3.6) (page 28) yields the QE cross section. Rewriting Eq. (3.6) in terms of $t = -Q^2$ using $\mathrm{d}t = 2|\mathbf{k}||\mathbf{k}'|\,\mathrm{d}\cos\theta$, we arrive at

$$\frac{\mathrm{d}\sigma_{\mathrm{QE}}}{\mathrm{d}Q^2} = \frac{1}{16\pi}\frac{1}{(s-M_N^2)^2}\,|\bar{\mathcal{M}}_{\mathrm{QE}}|^2, \tag{4.18}$$

with $s = M_N^2 + 2M_N k^0$ and the Q^2 limits given by

$$Q^2_{\mathrm{min,max}} = -m_{\ell'}^2 + 2E_{\mathrm{cm}}(E'_{\mathrm{cm}} \mp \sqrt{E'^2_{\mathrm{cm}} - m_{\ell'}^2}), \tag{4.19}$$

where

$$E_{\mathrm{cm}} = \frac{s-M_N^2}{2\sqrt{s}}, \quad E'_{\mathrm{cm}} = \frac{s-M_N^2+m_{\ell'}^2}{2\sqrt{s}}. \tag{4.20}$$

The resulting CCQE cross section for ν_μ scattering on the neutron is presented in Fig. 4.3. The left panel shows $\mathrm{d}\sigma/\mathrm{d}Q^2$ for various neutrino energies. There, the lines for the different energies end at the kinematical limits. The right panel shows the integrated cross section, σ, in comparison with the available data on H_2 and D_2 targets. In our calculations the main source of uncertainty comes from the axial form factor whose Q^2 dependence has to be extracted from ν scattering data. Thus, we have varied M_A within the error band given in Eq. (4.14) but the impact of this error is not resolvable within the line thickness and consequently not shown.

In Fig. 4.4, we plot the cross sections for NC QE scattering on proton (upper panels) and neutron (lower panels). The left panels show $\mathrm{d}\sigma/\mathrm{d}Q^2$ for different neutrino energies with $\Delta s = -0.15$; Δs is varied in the right panels where the integrated cross section σ is presented. We emphasize that the strange spin causes opposite effects on the cross sections for protons and neutrons because it is an isoscalar contribution (compare the different signs in the NC axial form factor given in the last two lines in Table 4.2). In the left panels, as in Fig. 4.3, the lines end at the kinematical limits.

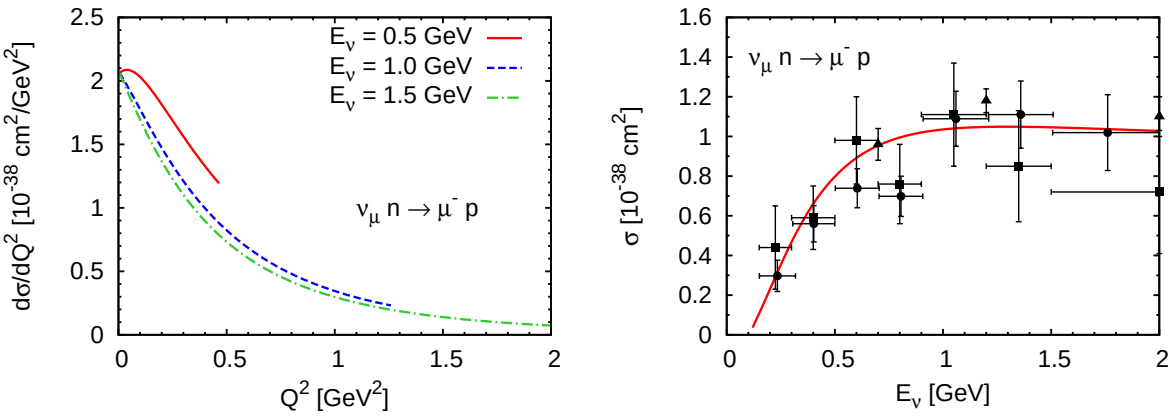

Figure 4.3: CCQE cross section for ν_μ scattering off neutrons. Left panel: $\mathrm{d}\sigma/\mathrm{d}Q^2$ as a function of Q^2 for different neutrino energies. Right panel: σ as a function of the neutrino energy. Data taken from Refs. [B$^+$77] (●), [M$^+$73] (■), [B$^+$81] (▲).

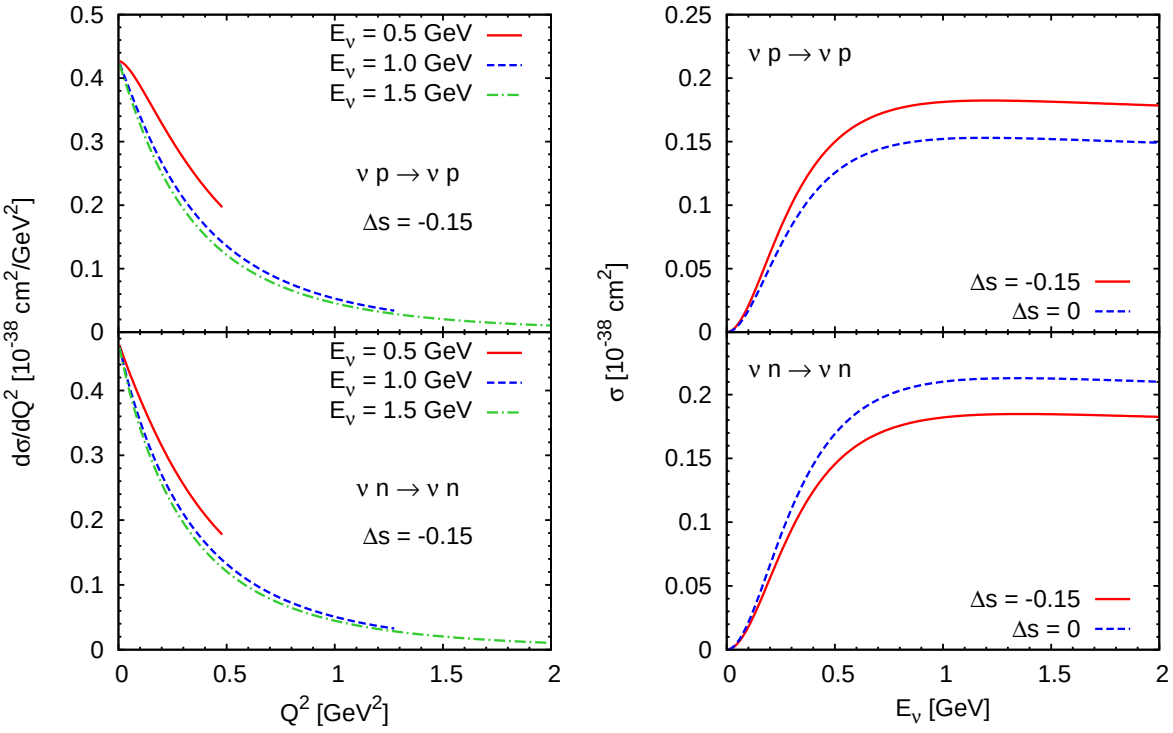

Figure 4.4: NC QE scattering on proton (upper panels) and neutron (lower panels). Left panels: $\mathrm{d}\sigma/\mathrm{d}Q^2$ as a function of Q^2 for different neutrino energies using $\Delta s = -0.15$. Right panels: σ as a function of the neutrino energy; the solid (dashed) lines denote the results with $\Delta s = -0.15$ ($\Delta s = 0$).

5 Excitation of baryon resonances

This chapter is devoted to the second part of our general decomposition of the cross section given in Eq. (3.1), namely the excitation of resonances, $\ell N \to \ell' R$. As will be shown, the electromagnetic form factors are taken from the MAID analysis where 13 resonances with invariant masses of less than 2 GeV are included. Consequently, this restricts the number of resonances in our model to 13 — they are listed in Table 5.1. In the following, we will split the description according to the spin of the resonances.

5.1 Excitation of spin 1/2 resonances

This section covers the lepton-induced excitation of spin 1/2 resonances. We include in our model five spin 1/2 resonances, namely the positive parity states, $P_{11}(1440)$ and $P_{31}(1910)$, and the negative parity states, $S_{11}(1535)$, $S_{31}(1620)$ and $S_{11}(1650)$.

5.1.1 Hadronic current

The hadronic current for the excitation of a spin 1/2 final state is given by

$$J^{\mu}_{1/2} = \left\langle R(p') \left| J^{\mu}_{1/2}(0) \right| N(p) \right\rangle = \bar{u}(p') \Gamma^{\mu}_{1/2} u(p), \tag{5.1}$$

and the hadronic tensor reads

$$H^{\mu\nu}_{1/2} = \frac{1}{2} \mathrm{Tr} \left[(\not{p} + M) \tilde{\Gamma}^{\mu}_{1/2} (\not{p}' + M') \Gamma^{\nu}_{1/2} \right], \tag{5.2}$$

Table 5.1: Properties of the resonances included in our model for the ℓN scattering. The Breit-Wigner mass, M_R, spin, J, isospin, I, parity, P, the vacuum total decay width, Γ_0, at the pole, the branching ratio into πN, b_R, and the axial coupling ($F_A(0)$ for spin 1/2 states; $C_5^A(0)$ for states with spin 3/2 or higher) are listed. The resonance parameters are taken from the analysis of Manley *et al.* [MS92], the axial couplings are derived in Appendix F.

	M_R [GeV]	J	I	P	Γ_0 [GeV]	b_R	$F_A(0)$ or $C_5^A(0)$
$P_{33}(1232)$	1.232	3/2	3/2	+	0.118	1.00	1.17
$P_{11}(1440)$	1.462	1/2	1/2	+	0.391	0.69	−0.52
$D_{13}(1520)$	1.524	3/2	1/2	−	0.124	0.59	−2.15
$S_{11}(1535)$	1.534	1/2	1/2	−	0.151	0.51	−0.23
$S_{31}(1620)$	1.672	1/2	3/2	−	0.154	0.09	0.05
$S_{11}(1650)$	1.659	1/2	1/2	−	0.173	0.89	−0.25
$D_{15}(1675)$	1.676	5/2	1/2	−	0.159	0.47	−1.38
$F_{15}(1680)$	1.684	5/2	1/2	+	0.139	0.70	−0.43
$D_{33}(1700)$	1.762	3/2	3/2	−	0.599	0.14	0.84
$P_{13}(1720)$	1.717	3/2	1/2	+	0.383	0.13	−0.29
$F_{35}(1905)$	1.881	5/2	3/2	+	0.327	0.12	0.15
$P_{31}(1910)$	1.882	1/2	3/2	+	0.239	0.23	0.08
$F_{37}(1950)$	1.945	7/2	3/2	+	0.300	0.38	0.24

with $M = \sqrt{p^2}$ and $M' = \sqrt{p'^2}$, and $\tilde{\Gamma}^\mu_{1/2} = \gamma_0 \Gamma^{\mu\,\dagger}_{1/2} \gamma^0$.

The vertex function Γ^μ for states with positive parity (e.g., $P_{11}(1440)$) is given by

$$\Gamma^\mu_{1/2+} = \mathcal{V}^\mu_{1/2} - \mathcal{A}^\mu_{1/2}\,, \tag{5.3}$$

and for states with negative parity (e.g., $S_{11}(1535)$) by

$$\Gamma^\mu_{1/2-} = \left[\mathcal{V}^\mu_{1/2} - \mathcal{A}^\mu_{1/2}\right]\gamma^5. \tag{5.4}$$

Both the vector part, $\mathcal{V}^\mu_{1/2}$, and the axial part, $\mathcal{A}^\mu_{1/2}$, are parametrized in terms of form factors as

$$\mathcal{V}^\mu_{1/2} = \frac{\mathcal{F}_1}{(2M_N)^2}\left(Q^2\gamma^\mu + \not{q} q^\mu\right) + \frac{\mathcal{F}_2}{2M_N} i\sigma^{\mu\alpha} q_\alpha \tag{5.5}$$

$$-\mathcal{A}^\mu_{1/2} = \mathcal{F}_A \gamma^\mu \gamma^5 + \frac{\mathcal{F}_P}{M_N} q^\mu \gamma^5. \tag{5.6}$$

Table 5.2: Isospin relations for the vector form factors. R stands for N^* ($I = 1/2$) or Δ ($I = 3/2$) resonances. $\mathcal{F}_i$ is the generalized vector form factor in Eq. (5.5), which has — depending on the process — to be substituted following the prescription in the table. Note that in the case of an isospin $1/2 \to 3/2$ transition, the form factors are equal for proton and neutron which is indicated by the index N (instead of p or n). A detailed derivation of these relations is given in Appendix D.1 for $I = 1/2$ resonances and in Appendix D.2 for $I = 3/2$ resonances.

	replace $\mathcal{F}_i$ in Eq. (5.5) with	
	for $I = 1/2$	for $I = 3/2$
$e^- p \to e^- R^+$	F_i^p	F_i^N
$e^- n \to e^- R^0$	F_i^n	F_i^N
$\nu p \to \ell^- R^{++}$	-	$\sqrt{3}F_i^V = -\sqrt{3}F_i^N$
$\nu n \to \ell^- R^+$	$F_i^V = F_i^p - F_i^n$	$F_i^V = -F_i^N$
$\nu p \to \nu R^+$	$\tilde{F}_i^p = (\frac{1}{2} - 2\sin^2\theta_W)F_i^p - \frac{1}{2}F_i^n - \frac{1}{2}F_i^s$	$\tilde{F}_i^N = (1 - 2\sin^2\theta_W)F_i^N$
$\nu n \to \nu R^0$	$\tilde{F}_i^n = (\frac{1}{2} - 2\sin^2\theta_W)F_i^n - \frac{1}{2}F_i^p - \frac{1}{2}F_i^s$	$\tilde{F}_i^N = (1 - 2\sin^2\theta_W)F_i^N$

Precisely as in the QE case, $\mathcal{F}_i$ ($i = 1, 2$) stands either for the CC form factors, F_i^V, for the NC form factors, $\tilde{F}_i^N$, or the EM form factors, F_i^N, with $N = p, n$; analogous for $\mathcal{F}_A$ and $\mathcal{F}_P$. The form factors are functions of $Q^2 = -q^2$.

5.1.2 Nucleon–resonance transition form factors

Vector form factors

The vector form factors F_i^V are related to the electromagnetic transition form factors F_i^N with $N = p, n$ as listed in Table 5.2, hence, the form factors for neutrino and electron scattering are related (details are given in Appendix D.1 and D.2).

The form factors $F_i^{p,n}$ can be derived from helicity amplitudes extracted from electron scattering experiments. The explicit relations between the form factors $F_i^{p,n}$ and the helicity amplitudes $A_{1/2}^{p,n}$, and $S_{1/2}^{p,n}$ are given in Appendix E.1 for both, positive and negative parity states. We use these relations to extract the form factors from the results of the recent MAID analysis [TAR, MAID, TK06, DT92, TDK$^+$04, DKT07] for the helicity amplitudes and their Q^2-dependence. The helicity amplitudes from MAID2005 are shown in Fig. 5.1 for the positive parity $P_{11}(1440)$ (left panel) and the negative parity $S_{11}(1535)$ (right panel). The extracted form factors are plotted in Fig. 5.2 for the $P_{11}(1440)$ (left panel) and the $S_{11}(1535)$ (right panel).

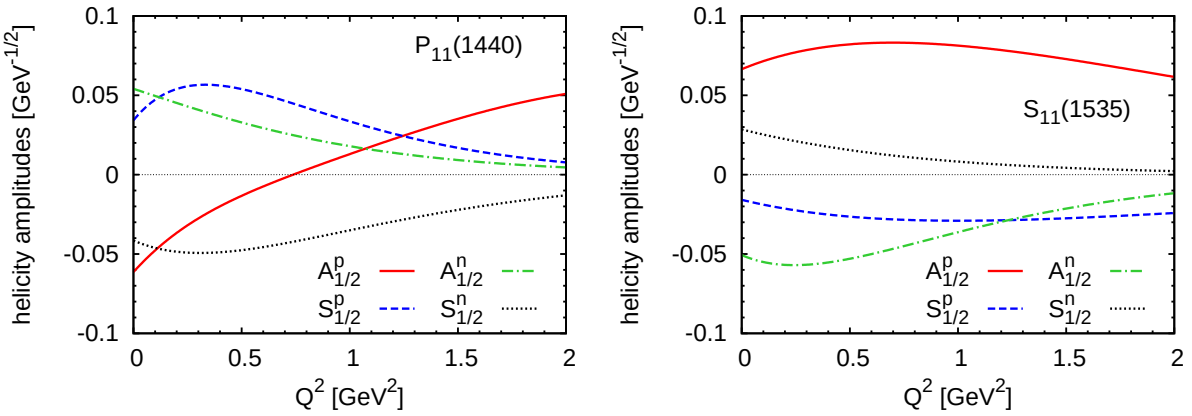

Figure 5.1: Helicity amplitudes $S_{1/2}$ and $A_{1/2}$ from MAID2005 for the positive parity $P_{11}(1440)$ (left panel) and the negative parity $S_{11}(1535)$ (right panel) for both, protons and neutrons.

Axial form factors

The meaning of the axial form factor $\mathcal{F}_A$ in Eq. (5.6) is given in Table 5.3 for each reaction channel. As in QE scattering, $\mathcal{F}_P$ appears only multiplied by the mass of the outgoing lepton, hence, it is not present in NC interactions. In the case of CC reactions, $\mathcal{F}_P$ is replaced by F_P.

Experimental information on the $N - R$ axial transition form factors F_A and F_P is very limited. Goldberger-Treiman relations have been derived for the axial couplings [FN79], but there is no information about the Q^2-dependence. We will follow this approach and apply PCAC and pion pole dominance to derive the axial couplings $F_A(0)$ and to relate F_A and F_P. The derivation, performed in Appendix F.2.1, leads to

$$F_P(Q^2) = \frac{(M_R \pm M_N)M_N}{Q^2 + m_\pi^2} F_A(Q^2), \tag{5.7}$$

with $+$ $(-)$ for positive (negative) parity resonances. The Q^2-dependence of the axial form factor is neither fully constrained by theory nor by experiment, so we assume — as in the QE case — a dipole dependence

$$F_A(Q^2) = F_A(0)\left(1 + \frac{Q^2}{M_A^{*\,2}}\right)^{-2}; \tag{5.8}$$

with $M_A^* = 1\,\text{GeV}$ as for the nucleon. The coupling $F_A(0)$ can be related to the πNR-coupling as detailed in Appendix F.2.1 (off-diagonal Goldberger-Treiman relation) and we obtain the results summarized in Table 5.4.

The axial form factors for the two lowest lying states are plotted in Fig. 5.3 for the $P_{11}(1440)$ (left panel) and the $S_{11}(1535)$ (right panel).

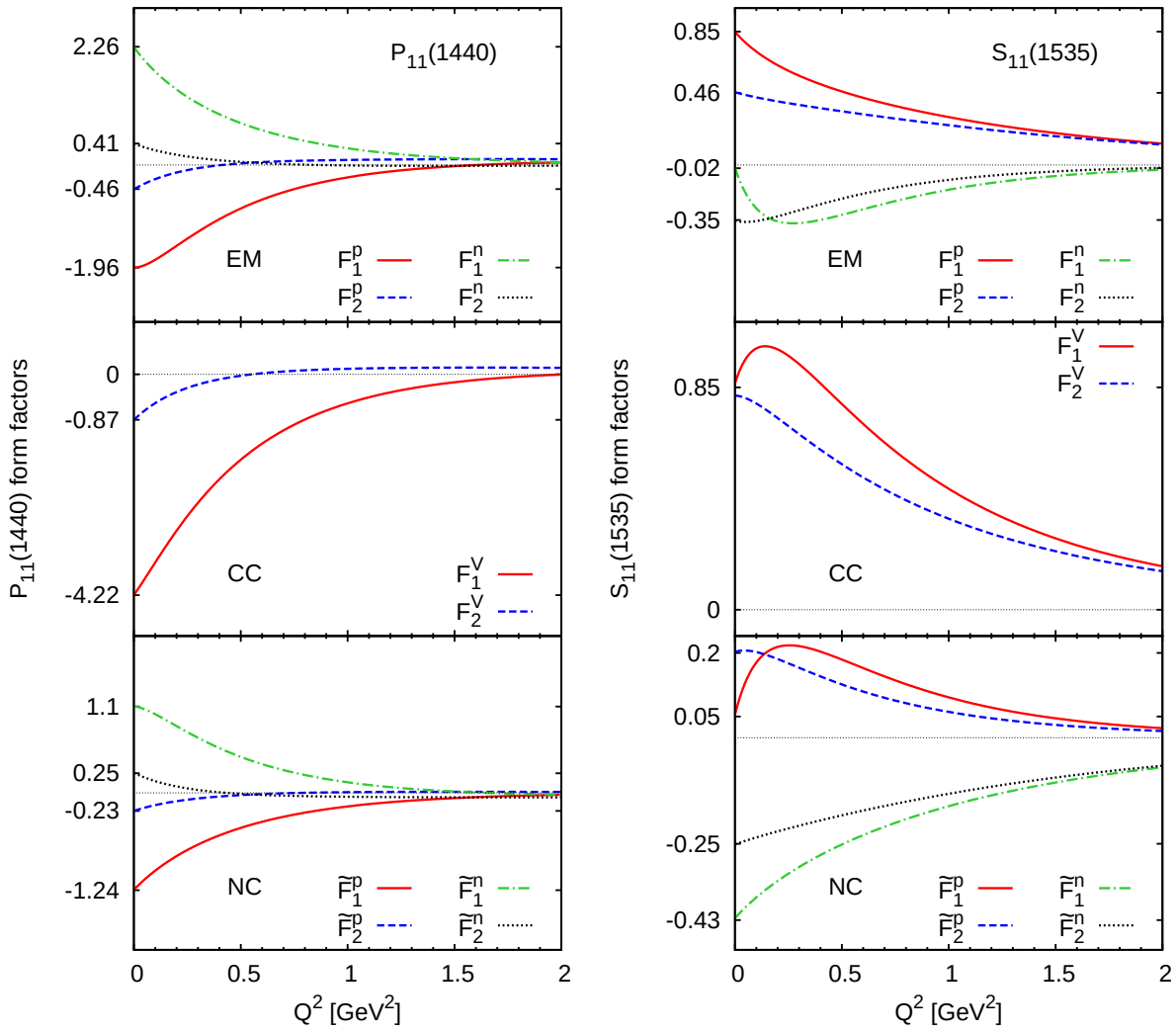

Figure 5.2: Form factors for the $P_{11}(1440)$ (right panels) and $S_{11}(1535)$ (left panels) resonances as a function of Q^2. The upper panels show the form factors $F_i^{p,n}$, the middle panels the form factors for CC, the lower panels the ones for NC scattering as given in Table 5.2.

Table 5.3: Isospin relations for the axial form factors. R stands for N^* ($I = 1/2$) or Δ ($I = 3/2$) resonances. $\mathcal{F}_A$ is the generalized axial form factor in Eq. (5.6), which has — depending on the process — to be substituted following the prescription in the table. Note that in the case of an isospin $1/2 \to 3/2$ transition, the form factors are equal for proton and neutron which is indicated by the index N (instead of p or n). A detailed derivation of these relations is given in Appendix D.1 for $I = 1/2$ resonances and in Appendix D.2 for $I = 3/2$ resonances.

	replace $\mathcal{F}_A$ in Eq. (5.6) with	
	for $I = 1/2$	for $I = 3/2$
$e^- p \to e^- R^+$	-	-
$e^- n \to e^- R^0$	-	-
$\nu p \to \ell^- R^{++}$	-	$\sqrt{3} F_A$
$\nu n \to \ell^- R^+$	F_A	F_A
$\nu p \to \nu R^+$	$\tilde{F}_A^p = \frac{1}{2} F_A + \frac{1}{2} F_A^s$	$\tilde{F}_A^N = -F_A$
$\nu n \to \nu R^0$	$\tilde{F}_A^n = -\frac{1}{2} F_A + \frac{1}{2} F_A^s$	$\tilde{F}_A^N = -F_A$

Table 5.4: πNR coupling f and axial coupling $F_A(0)$ for the resonances with spin 1/2. See Appendix F.2.1 for details.

	f	$F_A(0)$
$P_{11}(1440)$	0.39	$-2 f_\pi \frac{f}{m_\pi} = -0.52$
$S_{11}(1535)$	0.17	$-2 f_\pi \frac{f}{m_\pi} = -0.23$
$S_{31}(1620)$	0.09	$\sqrt{\frac{2}{3}}\, f_\pi \frac{f}{m_\pi} = 0.05$
$S_{11}(1650)$	0.19	$-2 f_\pi \frac{f}{m_\pi} = -0.25$
$P_{31}(1910)$	0.14	$\sqrt{\frac{2}{3}}\, f_\pi \frac{f}{m_\pi} = 0.08$

Strange form factors

As in the nucleon case, strange form factors can contribute for isospin $1/2 \to 1/2$ transitions (cf. Appendix D.1; and also Table 5.2 and Table 5.3). However, the present experimental status does not allow any conclusions on the strange transition form factors, thus, we neglect them in this work and set F_i^s and F_A^s to zero.

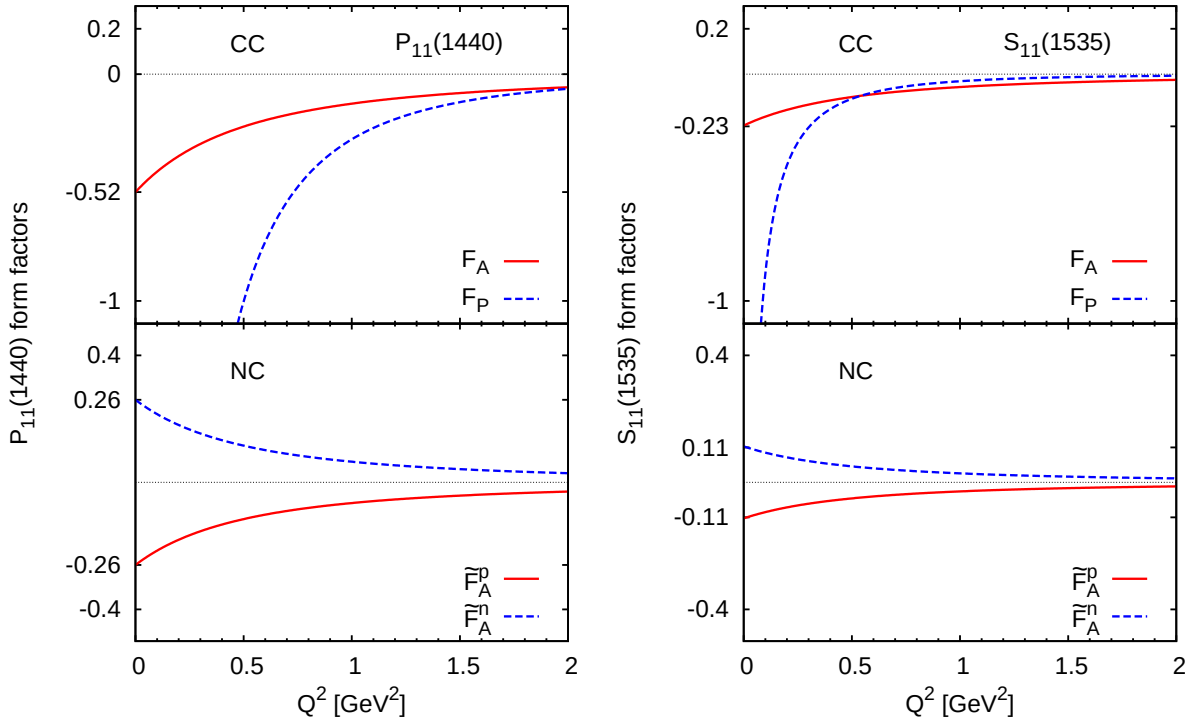

Figure 5.3: Axial form factors for the $P_{11}(1440)$ (right panels) and $S_{11}(1535)$ (left panels) resonances as a function of Q^2. The upper panels show the form factors for CC, the lower panels the ones for NC scattering as given in Table 5.3.

5.2 Excitation of spin 3/2 resonances

In this section we discuss the lepton-induced excitation of spin 3/2 resonances. We include the following set: $P_{33}(1232)$ and $P_{13}(1720)$ with positive parity, and $D_{13}(1520)$ and $D_{33}(1700)$ with negative parity.

5.2.1 Hadronic current

The excitation of a spin 3/2 final state is described within a Rarita-Schwinger formalism where the hadronic current is given by

$$J^{\mu}_{3/2} = \left\langle R(p') \left| J^{\mu}_{3/2}(0) \right| N(p) \right\rangle = \bar{\psi}_{\alpha}(p') \Gamma^{\alpha\mu}_{3/2} u(p) \tag{5.9}$$

with the Rarita-Schwinger spinor $\bar{\psi}_{\alpha}$ describing the resonance state.

We deduce the hadronic tensor

$$H^{\mu\nu}_{3/2} = \frac{1}{2}\sum_{s_i}\sum_{s_f} J^{\mu\,\dagger}_{3/2} J^{\nu}_{3/2} = \frac{1}{2}\sum_{s_i}\sum_{s_f} \bar{u}(p)\tilde{\Gamma}^{\alpha\mu}_{3/2}\psi_\alpha(p')\bar{\psi}_\beta(p')\Gamma^{\beta\nu}_{3/2}u(p)$$
$$= \frac{1}{2}\mathrm{Tr}\left[(\not{p}+M)\tilde{\Gamma}^{\alpha\mu}_{3/2}\Lambda_{\alpha\beta}\Gamma^{\beta\nu}_{3/2}\right], \tag{5.10}$$

with the spin 3/2 projector

$$\Lambda_{\alpha\beta} = -\left(\not{p}'+M'\right)\left(g_{\alpha\beta} - \frac{2}{3}\frac{p'_\alpha p'_\beta}{M'^2} + \frac{1}{3}\frac{p'_\alpha\gamma_\beta - p'_\beta\gamma_\alpha}{M'} - \frac{1}{3}\gamma_\alpha\gamma_\beta\right), \tag{5.11}$$

where $M = \sqrt{p^2}$ and $M' = \sqrt{p'^2}$, and $\tilde{\Gamma}^{\alpha\mu}_{3/2} = \gamma_0\Gamma^{\alpha\mu\,\dagger}_{3/2}\gamma_0$. For states with positive parity as the $P_{33}(1232)$, we have

$$\Gamma^{\alpha\mu}_{3/2+} = \left[\mathcal{V}^{\alpha\mu}_{3/2} - \mathcal{A}^{\alpha\mu}_{3/2}\right]\gamma^5, \tag{5.12}$$

and for the negative parity ones (e.g., $D_{13}(1535)$),

$$\Gamma^{\alpha\mu}_{3/2-} = \mathcal{V}^{\alpha\mu}_{3/2} - \mathcal{A}^{\alpha\mu}_{3/2}\,. \tag{5.13}$$

In terms of form factors, the vector part is given by

$$\mathcal{V}^{\alpha\mu}_{3/2} = \frac{\mathcal{C}^V_3}{M_N}(g^{\alpha\mu}\not{q} - q^\alpha\gamma^\mu) + \frac{\mathcal{C}^V_4}{M^2_N}(g^{\alpha\mu}q\cdot p' - q^\alpha p'^\mu) + \frac{\mathcal{C}^V_5}{M^2_N}(g^{\alpha\mu}q\cdot p - q^\alpha p^\mu) + g^{\alpha\mu}\mathcal{C}^V_6 \tag{5.14}$$

and the axial part by

$$-\mathcal{A}^{\alpha\mu}_{3/2} = \left[\frac{\mathcal{C}^A_3}{M_N}(g^{\alpha\mu}\not{q} - q^\alpha\gamma^\mu) + \frac{\mathcal{C}^A_4}{M^2_N}(g^{\alpha\mu}q\cdot p' - q^\alpha p'^\mu) + \mathcal{C}^A_5 g^{\alpha\mu} + \frac{\mathcal{C}^A_6}{M^2_N}q^\alpha q^\mu\right]\gamma^5. \tag{5.15}$$

As before, the calligraphic $\mathcal{C}^V_i$, $i = 3,\ldots,6$, stands either for the CC form factors C^V_i, the electromagnetic transition form factors C^N_i with $N = p, n$ or the NC form factors ${}_N\tilde{C}^V_i$, analogous for $\mathcal{C}^A_i$.

5.2.2 Nucleon-resonance transition form factors

Vector form factors

The vector form factors C^V_i and ${}_N\tilde{C}^V_i$ can be related to the electromagnetic transition form factors $C^{p,n}_i$ as detailed in Table 5.5. Note that current conservation implies $C^N_6 = 0$ for EM transitions. Using information from electron scattering, $C^{p,n}_i$ can

Table 5.5: Isospin relations for the vector form factors. R stands for N^* ($I = 1/2$) or Δ ($I = 3/2$) resonances. C_i^V, $i = 3,\ldots,6$, is the generalized vector form factor in Eq. (5.14), which has — depending on the process — to be substituted following the prescription in the table. Note that in the case of an isospin $1/2 \to 3/2$ transition, the form factors are equal for proton and neutron which is indicated by the index N (instead of p or n). A detailed derivation of these relations is given in Appendix D.1 for $I = 1/2$ resonances and in Appendix D.2 for $I = 3/2$ resonances.

	replace C_i^V in Eq. (5.14) with	
	for $I = 1/2$	for $I = 3/2$
$e^- p \to e^- R^+$	C_i^p	C_i^N
$e^- n \to e^- R^0$	C_i^n	C_i^N
$\nu p \to \ell^- R^{++}$	-	$\sqrt{3} C_i^V = -\sqrt{3} C_i^N$
$\nu n \to \ell^- R^+$	$C_i^V = C_i^p - C_i^n$	$C_i^V = -C_i^N$
$\nu p \to \nu R^+$	${}_p\tilde{C}_i^V = (\frac{1}{2} - 2\sin^2\theta_W) C_i^p - \frac{1}{2} C_i^n - \frac{1}{2} C_i^{s_V}$	${}_N\tilde{C}_i^V = (1 - 2\sin^2\theta_W) C_i^N$
$\nu n \to \nu R^0$	${}_n\tilde{C}_i^V = (\frac{1}{2} - 2\sin^2\theta_W) C_i^n - \frac{1}{2} C_i^p - \frac{1}{2} C_i^{s_V}$	${}_N\tilde{C}_i^V = (1 - 2\sin^2\theta_W) C_i^N$

be parametrized in the same way as in the previous section for spin 1/2 resonances by relating them to the MAID helicity amplitudes. The explicit relations between the form factors $C_i^{p,n}$ and the helicity amplitudes $A_{1/2}^{p,n}$, $A_{3/2}^{p,n}$ and $S_{1/2}^{p,n}$ are given in Appendix E.2. Note that in the case of isovector transitions, i.e., isospin $1/2 \to 3/2$ transitions, proton and neutron form factors are identical.

The helicity amplitudes obtained in MAID2005 are plotted in Fig. 5.4 as a function of Q^2 for the positive parity $P_{33}(1232)$ (left panel) and the negative parity $D_{13}(1520)$ (right panel). The extracted form factors are plotted in Fig. 5.5 for the $P_{33}(1232)$ (left panel) and the $D_{13}(1520)$ (right panel).

Axial form factors

The substitutions for the axial form factors are summarized in Table 5.6. Pion pole dominance and PCAC allow us on one side to fix the coupling $C_5^A(Q^2 = 0)$ by using an off-diagonal Goldberger-Treiman relation to the values displayed in Table 5.7, and on the other side to relate C_5^A and C_6^A (see Appendix F.2.2),

$$C_6^A(Q^2) = \frac{M_N^2}{Q^2 + m_\pi^2}\, C_5^A(Q^2), \tag{5.16}$$

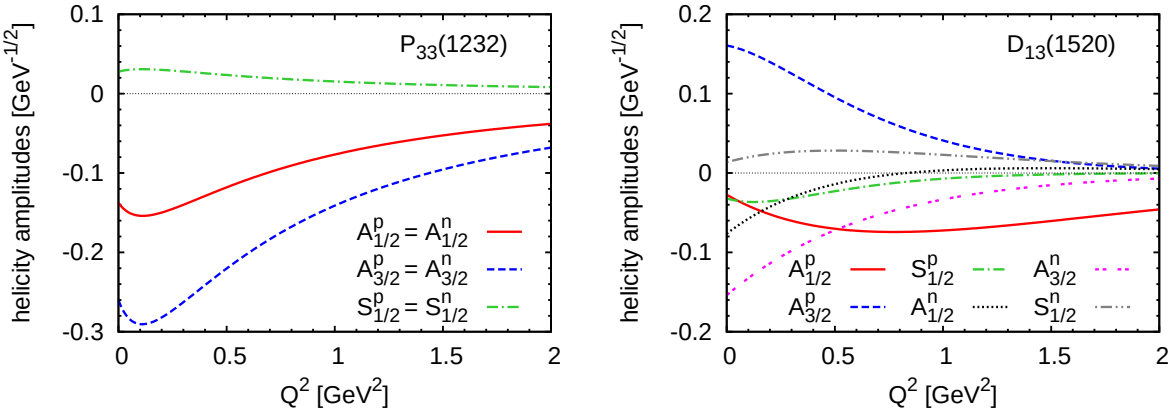

Figure 5.4: Helicity amplitudes $S_{1/2}$, $A_{1/2}$ and $A_{3/2}$ from MAID2005 for the positive parity $P_{33}(1232)$ (left panel) and the negative parity $D_{13}(1520)$ (right panel) for both, protons and neutrons.

Table 5.6: Isospin relations for the axial form factors. R stands for N^* ($I = 1/2$) or Δ ($I = 3/2$) resonances. C_i^A, $i = 3, \ldots, 6$, is the generalized axial form factor in Eq. (5.15), which has — depending on the process — to be substituted following the prescription in the table. Note that in the case of an isospin $1/2 \to 3/2$ transition, the form factors are equal for proton and neutron which is indicated by the index N (instead of p or n). A detailed derivation of these relations is given in Appendix D.1 for $I = 1/2$ resonances and in Appendix D.2 for $I = 3/2$ resonances.

	replace C_i^A in Eq. (5.15) with	
	for $I = 1/2$	for $I = 3/2$
$e^- p \to e^- R^+$	-	-
$e^- n \to e^- R^0$	-	-
$\nu p \to \ell^- R^{++}$	-	$\sqrt{3} C_i^A$
$\nu n \to \ell^- R^+$	C_i^A	C_i^A
$\nu p \to \nu R^+$	${}_p\tilde{C}_i^A = \frac{1}{2} C_i^A + \frac{1}{2} C_i^{s_A}$	${}_N\tilde{C}_i^A = -C_i^A$
$\nu n \to \nu R^0$	${}_n\tilde{C}_i^A = -\frac{1}{2} C_i^A + \frac{1}{2} C_i^{s_A}$	${}_N\tilde{C}_i^A = -C_i^A$

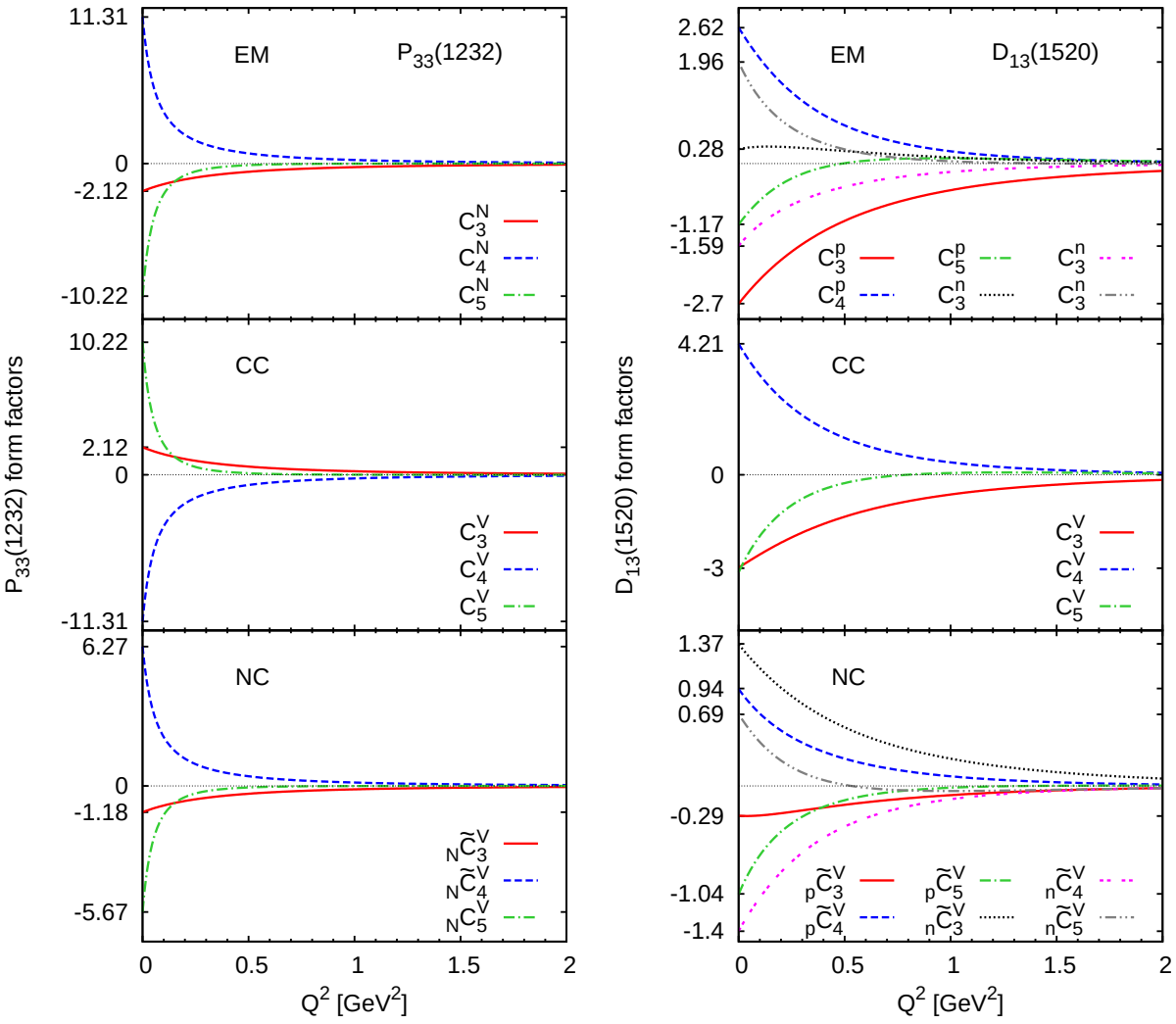

Figure 5.5: Vector form factors for the $P_{33}(1232)$ (left panels) and the $D_{13}(1520)$ resonances (right panels) as a function of Q^2. The upper panels show the EM form factors C_i^N with $N = p, n$, the middle panels the form factors C_i^V for CC, the lower panels ${}_N\tilde{C}_i^V$ for NC scattering as given in Table 5.5.

Table 5.7: πNR coupling f and axial coupling $C_5^A(0)$ for the resonances with spin 3/2. The derivation is performed in Appendix F.2.2.

	f	$C_5^A(0)$
$P_{33}(1232)$	2.15	$\sqrt{\frac{2}{3}}\, f_\pi\, \frac{f}{m_\pi} = 1.17$
$D_{13}(1520)$	1.61	$-2\, f_\pi\, \frac{f}{m_\pi} = -2.15$
$D_{33}(1700)$	1.54	$\sqrt{\frac{2}{3}}\, f_\pi\, \frac{f}{m_\pi} = 0.84$
$P_{13}(1720)$	0.22	$-2\, f_\pi\, \frac{f}{m_\pi} = -0.29$

which holds for both parity states. The C_6^A form factor appears in the cross section only multiplied by the mass of the outgoing lepton, such that its contribution vanishes in NC and is rather small even in CC reactions (except for ν_τ).

$P_{33}(1232)$. We adopt the Adler model [Adl68] for the axial form factors of the Δ where

$$C_4^A(Q^2) = -\frac{C_5^A(Q^2)}{4} \quad \text{and} \quad C_3^A(Q^2) = 0. \tag{5.17}$$

Then, the only unknown is the Q^2-dependence of C_5^A because $C_5^A(0)$ is fixed by PCAC (see Appendix F.2.2). We will show in Section 5.4 that the cross section for the isospin 3/2 reaction $\nu p \to l^- p\pi^+$ is in very good approximation described by the excitation of the Δ and its subsequent decay. Thus, we can use these data to extract the Q^2-dependence of C_5^A. The available data comes mainly from two bubble-chamber experiments: the 12-ft bubble chamber at Argonne (ANL) [B$^+$79, R$^+$82] and the 7-ft bubble chamber at Brookhaven (BNL) [K$^+$86, K$^+$90]. The ANL neutrino energy flux peaks at about 0.5 GeV [B$^+$77] while the BNL one peaks at about 1 GeV [Fur02].

The simplest ansatz, which has also been used for the spin 1/2 states, is a dipole form, and reads

$$\left(C_5^A\right)^{\mathrm{DP}}(Q^2) = C_5^A(0)\left(1 + \frac{Q^2}{M_A^{\mathrm{DP}\,2}}\right)^{-2}, \tag{5.18}$$

with $M_A^{\mathrm{DP}} = 1\,\mathrm{GeV}$ in analogy to the nucleon and the spin 1/2 resonances, and $C_5^A(0) = 1.17$ (see Table 5.7).

A alternative parametrization, widely used in the analysis of the neutrino experiments [K$^+$86, K$^+$90, B$^+$79, R$^+$82], is a modified dipole

$$C_5^A(Q^2) = C_5^A(0)\left[1 + \frac{aQ^2}{b+Q^2}\right]\left(1 + \frac{Q^2}{M_A^{\Delta\,2}}\right)^{-2}; \tag{5.19}$$

a, b and M_A^Δ have to be extracted from data, and $C_5^A(0) = 1.17$ fixed by PCAC (see Table 5.7). A fit to the shape of the ANL and BNL $\mathrm{d}\sigma/\mathrm{d}Q^2$ data gives $a = -0.25$, $b = 0.04\,\mathrm{GeV}^2$ and $M_A^\Delta = 0.95\,\mathrm{GeV}$.

The resulting cross sections for both, the dipole form of Eq. (5.18) and the modified dipole of Eq. (5.19) are compared to ANL and BNL data in Fig. 5.6. The shape of the BNL distribution (note: normalized to unit area) is described well by both form factors (right panel of Fig. 5.6) while the ANL data, which are available as normalized cross sections, are overestimated by the dipole form, but well described by the modified dipole form factor.

PCAC, used to fix $C_5^A(0)$, is exact only in the chiral limit of vanishing pion mass. The left panel of Fig. 5.7 shows C_5^A as in Eq. (5.19) and in Eq. (5.18) with an assumed error of 10% for the $N-\Delta$ transition axial coupling, i.e., with $C_5^A(0) = 1.17 \pm 10\%$.[1] The comparison of both form factor shows a steeper behavior for the modified dipole one. This translates also in a larger axial radius. The resulting integrated cross section is displayed in the right panel of Fig. 5.7 together with the data of ANL and BNL. The dipole form factor describes well the BNL data while good agreement to the ANL data is reached with the modified dipole form. All axial form factors of the Δ are plotted in Fig. 5.8.

Describing the ANL and BNL data simultaneously with the same form factors is impossible and a choice has to be made: thus, if not stated otherwise, we use the modified dipole form of Eq. (5.19) in the following.

We end this paragraph by stressing known uncertainties. First of all, we have neglected a non-resonant background in the isospin 3/2 channel $\nu p \to \mu^- \pi^+ p$. Both, Sato *et al.* [SUL03] and Hernandez *et al.* [HNV07] find within their microscopic models for the non-resonant pion background a correction of the order of 10% in this channel. We shall return to this discussion in Chapter 6. We have also neglected the effect of the deuteron structure: Fig. 5.9 shows our calculation on the proton together with a result including deuterium effects using the Argonne V18 NN potential (details on the implementation are given in Sec. 8.4.1 of Ref. [Bus08]). We find only a minor correction — the correction is even smaller in the BNL case because of the higher neutrino energy. This agrees with the findings of Alvarez-Ruso *et al.* [ARSVV99] who state that the correction does not exceed 8% even at low Q^2 (they have used the Hulthen, Bonn and Paris NN potentials).

We note that Hernandez *et al.* [HNV07] take $C_5^A(0)$ as a free parameter in their refit of C_5^A. As we rely on PCAC for all other resonance couplings (where no data are available) we prefer to keep it also here. In addition, this coupling was extracted from the BNL data in Ref. [ARSVV99] and found to be consistent with the PCAC prediction; our value of $C_5^A(0) = 1.17$ agrees also with the one calculated in chiral

[1] On the nucleon, the Goldberger-Treiman relation derived from PCAC is satisfied at the level of 2% (cf., Ref. [TH95] and references therein and our discussion on page 33).

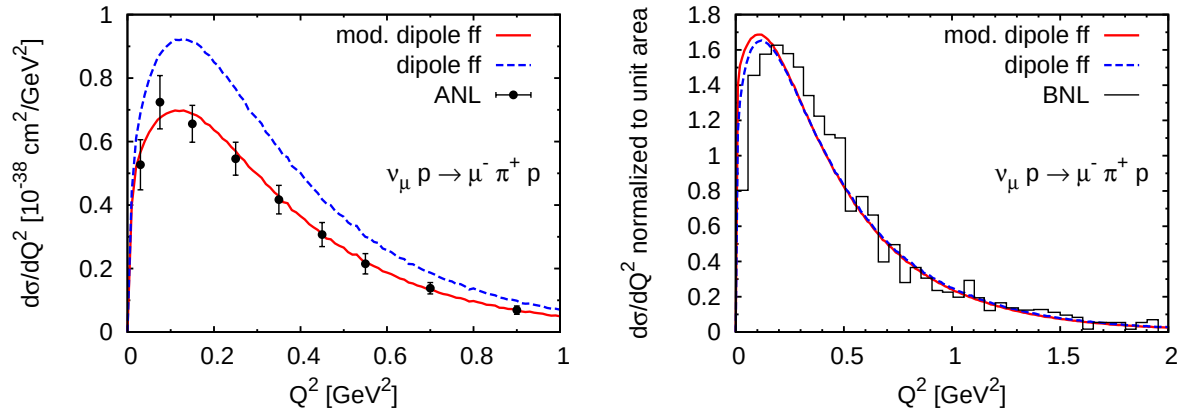

Figure 5.6: Differential cross section $d\sigma/dQ^2$ averaged over the ANL flux (left panel) and the BNL flux (right panel) compared to ANL (left) and BNL data (right). To compare with data, we apply an invariant mass cut at $W < 1.4\,\text{GeV}$. The solid lines are obtained with C_5^A as in Eq. (5.19), the dashed lines with Eq. (5.18). $C_5^A(0) = 1.17$ in both cases. The ANL data are taken from Ref. [R$^+$82] (their Fig. 12), the BNL data from Fig. 10 of Ref. [K$^+$86]; the ANL flux is taken from Ref. [B$^+$77] and the BNL flux from Ref. [Fur02].

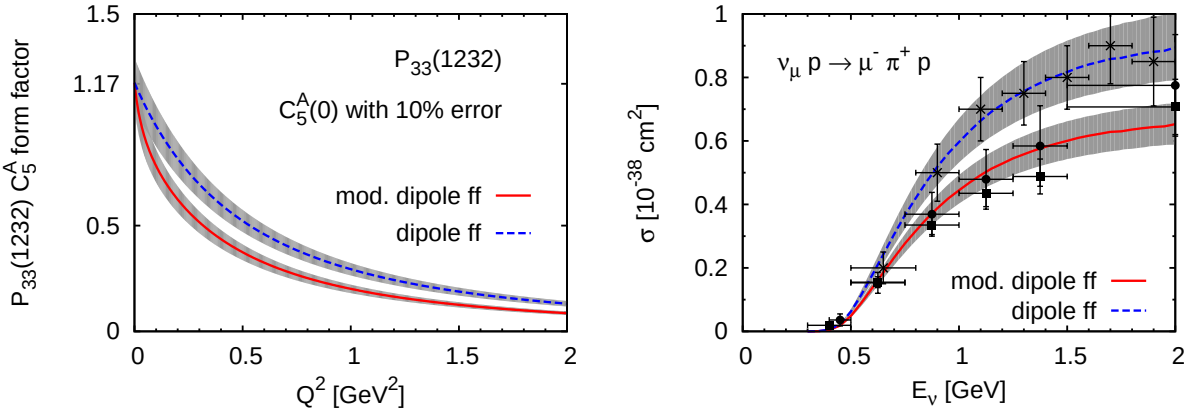

Figure 5.7: Left panel: axial form factor C_5^A. Right panel: total CC $\pi^+ p$ production cross sections compared to data of ANL [Refs. [B$^+$79] (•), [R$^+$82] (■)] and BNL [[K$^+$86] (×)]. The solid lines are obtained with C_5^A as in Eq. (5.19), the dashed lines with Eq. (5.18). The shaded areas denote a 10% error in $C_5^A(0)$.

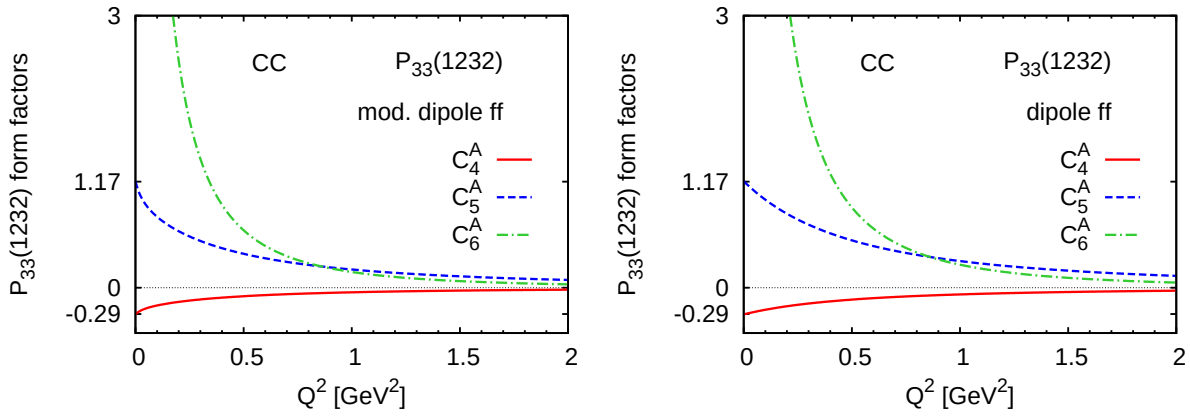

Figure 5.8: Axial form factors for the $P_{33}(1232)$ resonance as a function of Q^2. Shown are the form factors C_i^A for CC (the NC form factors ${}_N\tilde{C}_i^A$ are identical up to the minus sign, see Table 5.6). The left panel shows the form factors based on Eq. (5.19), the right panel the ones based on Eq. (5.18).

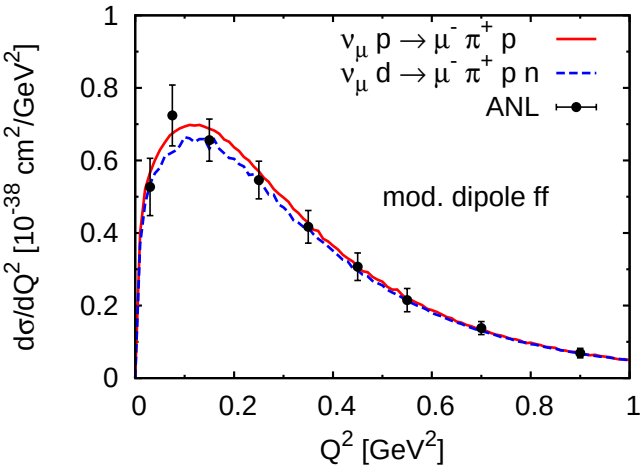

Figure 5.9: Differential cross section $d\sigma/dQ^2$ averaged over the ANL flux compared to ANL data [R+82] (invariant mass cut at $W < 1.4\,\text{GeV}$). The solid line corresponds to the solid line in the left panel of Fig. 5.6 while the dashed line shows the result including deuterium effects (see text for details).

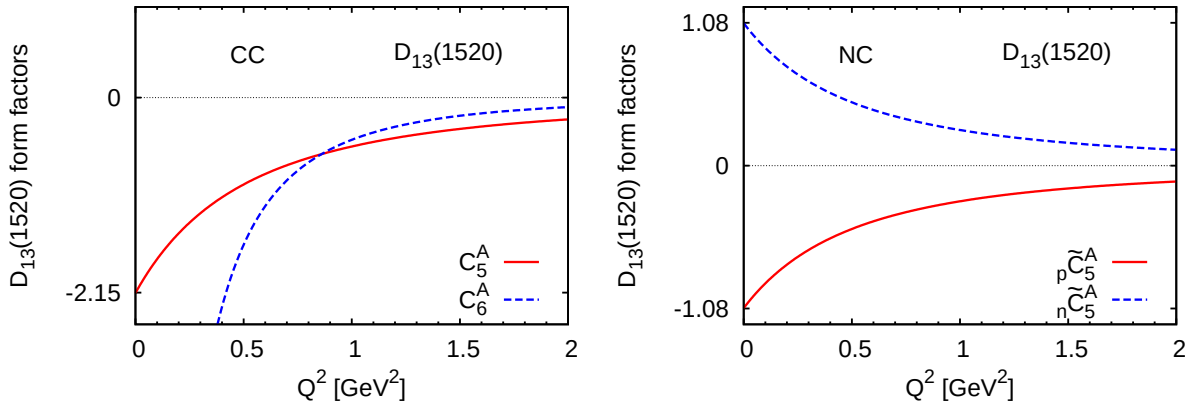

Figure 5.10: Axial form factors for the $D_{13}(1520)$ resonance as a function of Q^2. Shown are the form factors C_i^A for CC (left panel) and ${}_N\tilde{C}_i^A$ (right panel) for NC scattering as given in Table 5.6.

perturbation theory [GMCARVV08] ($(C_5^A(0))_{\chi PT} = 1.16$). Moreover, recent lattice results seem to support the off-diagonal Goldberger-Treiman relation [ALNT07] but the chiral extrapolation has to be handled with great care.

$D_{13}(1520)$, $D_{33}(1700)$ and $P_{13}(1720)$. As the $P_{33}(1232)$ dominates the cross section (see Section 5.4), the extraction of the Q^2-dependence of the axial form factor from data is only possible for this state but not for the other resonances. Therefore, we assume for the other resonances a simple dipole behavior as done for the spin 1/2 resonances,

$$C_5^A(Q^2) = C_5^A(0)\left(1 + \frac{Q^2}{M_A^{*\,2}}\right)^{-2}; \tag{5.20}$$

with $M_A^* = 1\,\text{GeV}$ in analogy to the nucleon. The couplings $C_5^A(0)$, extracted by using PCAC (see Appendix F.2.2), are summarized in Table 5.7. On the basis of various quark models and dispersion relations, C_3^A and C_4^A are expected to be minor and thus are neglected [Adl68]. The form factors for the $D_{13}(1520)$ are plotted in Fig. 5.10.

Strange form factors

For isospin $1/2 \to 1/2$ transitions, strange form factors can contribute (cf. Table 5.5 and Table 5.6), but are neglected in this work due to the lack of experimental information, i.e., we set C_i^{sV} and C_i^{sA} to zero.

Table 5.8: πNR coupling f and axial coupling $C_5^A(0)$ for the resonances with spin higher than 3/2. They are derived in Appendix F.2.2.

	f	$C_5^A(0)$
$D_{15}(1675)$	1.03	$-2\, f_\pi\, \frac{f}{m_\pi} = -1.38$
$F_{15}(1680)$	0.32	$-2\, f_\pi\, \frac{f}{m_\pi} = -0.43$
$F_{35}(1905)$	0.27	$\sqrt{\frac{2}{3}}\, f_\pi\, \frac{f}{m_\pi} = 0.15$
$F_{37}(1950)$	0.43	$\sqrt{\frac{2}{3}}\, f_\pi\, \frac{f}{m_\pi} = 0.24$

5.3 Resonances with spin $>$ 3/2

Any formalism describing resonances with spin greater than 3/2 is highly complicated [SLMP05]. We thus make as simplifying assumption that all resonances with spin $> 3/2$ — we include in our model four spin $>3/2$ resonances: $D_{15}(1675)$, $F_{15}(1680)$, $F_{35}(1905)$, and $F_{37}(1950)$ — can be treated with the spin 3/2 formalism. As we will show, their contributions are anyway negligible in the energy region of interest for this work.

The axial couplings $C_5^A(0)$ are summarized in Table 5.8; Eq. (5.20) is used for the Q^2 dependence.

5.4 Cross sections

5.4.1 Resonance-excitation cross sections

Contracting the hadronic tensor defined in Eq. (5.2) for spin 1/2 resonances and in Eq. (5.10) for spin 3/2 resonances with the leptonic tensor given in Eq. (3.3) on page 27, one obtains the matrix element $|\bar{\mathcal{M}}_R|$ (see Eq. (3.2)) and, together with Eq. (3.7) (page 28) the resonance excitation cross section for the reaction $\ell(k)N(p) \to \ell'(k')R(p')$.

In Fig. 5.11, we show the integrated cross section for CC (top panels) and NC (bottom panels) induced resonance production on the proton (left panels) and on the neutron (right panels). The dominant contribution comes from the excitation of the Δ resonance (solid line).

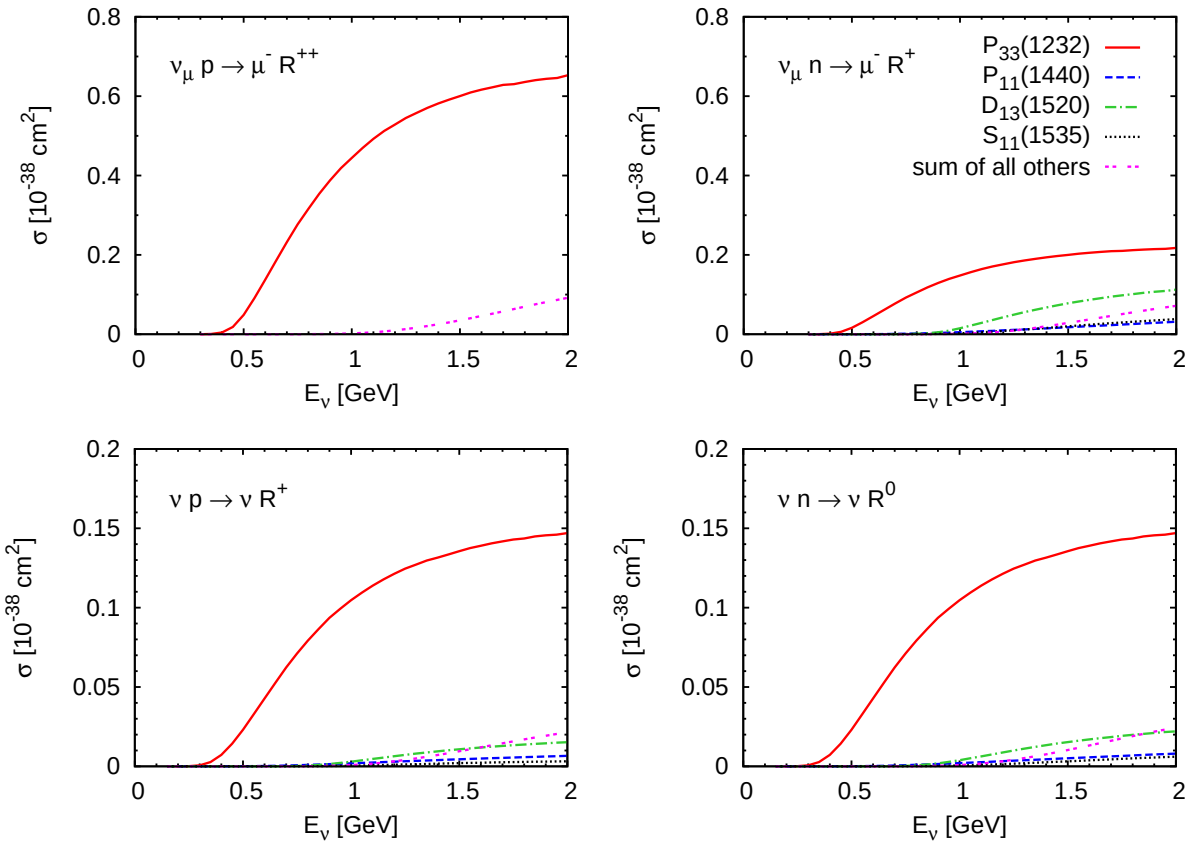

Figure 5.11: Integrated cross section for CC (top panels) and NC (bottom panels) induced resonance production on the proton (left panels) and on the neutron (right panels). The different lines indicate the different resonances. Explicitly shown are the results for the four lowest lying resonances — the sum of the remaining 9 resonances gives the double-dashed line. In the case of CC scattering on protons (upper left panel) only the excitation of isospin 3/2 resonances is possible.

5.4.2 Pion production through resonance excitation

Here, we consider pion production via resonance excitation and their subsequent decay[2]. By νN scattering one can excite an isospin 3/2 resonance (e.g., $P_{33}(1232)$) or an isospin 1/2 resonance (e.g., $P_{11}(1440)$). They decay, among other channels, with a certain branching ratio into πN pairs. We neglect possible interferences between the resonances. By including the appropriate Clebsch-Gordan coefficients, we obtain in the case of *charged-current scattering* for the cross sections of the three possible one-pion production channels

$$\mathrm{d}\sigma(\nu p \to \ell^- p\pi^+) = \sum_{\substack{I=3/2\\ \text{resonances}}} b_i \, \mathrm{d}\sigma_{R_i^{++}}, \tag{5.21}$$

$$\mathrm{d}\sigma(\nu n \to \ell^- n\pi^+) = \frac{1}{3} \sum_{\substack{I=3/2\\ \text{resonances}}} b_i \, \mathrm{d}\sigma_{R_i^{+}} + \frac{2}{3} \sum_{\substack{I=1/2\\ \text{resonances}}} b_i \, \mathrm{d}\sigma_{R_i^{+}} \,, \tag{5.22}$$

$$\mathrm{d}\sigma(\nu n \to \ell^- p\pi^0) = \frac{2}{3} \sum_{\substack{I=3/2\\ \text{resonances}}} b_i \, \mathrm{d}\sigma_{R_i^{+}} + \frac{1}{3} \sum_{\substack{I=1/2\\ \text{resonances}}} b_i \, \mathrm{d}\sigma_{R_i^{+}} \,, \tag{5.23}$$

and for the *neutral-current* ones

$$\mathrm{d}\sigma(\nu p \to \nu n\pi^+) = \frac{1}{3} \sum_{\substack{I=3/2\\ \text{resonances}}} b_i \, \mathrm{d}\sigma_{R_i^{+}} + \frac{2}{3} \sum_{\substack{I=1/2\\ \text{resonances}}} b_i \, \mathrm{d}\sigma_{R_i^{+}} \,, \tag{5.24}$$

$$\mathrm{d}\sigma(\nu p \to \nu p\pi^0) = \frac{2}{3} \sum_{\substack{I=3/2\\ \text{resonances}}} b_i \, \mathrm{d}\sigma_{R_i^{+}} + \frac{1}{3} \sum_{\substack{I=1/2\\ \text{resonances}}} b_i \, \mathrm{d}\sigma_{R_i^{+}} \,, \tag{5.25}$$

$$\mathrm{d}\sigma(\nu n \to \nu p\pi^-) = \frac{1}{3} \sum_{\substack{I=3/2\\ \text{resonances}}} b_i \, \mathrm{d}\sigma_{R_i^{0}} + \frac{2}{3} \sum_{\substack{I=1/2\\ \text{resonances}}} b_i \, \mathrm{d}\sigma_{R_i^{0}} \,, \tag{5.26}$$

$$\mathrm{d}\sigma(\nu n \to \nu n\pi^0) = \frac{2}{3} \sum_{\substack{I=3/2\\ \text{resonances}}} b_i \, \mathrm{d}\sigma_{R_i^{0}} + \frac{1}{3} \sum_{\substack{I=1/2\\ \text{resonances}}} b_i \, \mathrm{d}\sigma_{R_i^{0}} \,, \tag{5.27}$$

where $\sigma_{R_i^{++}}$, $\sigma_{R_i^{+}}$ and $\sigma_{R_i^{0}}$ are the cross sections for resonance excitation on protons or neutrons as discussed before. The branching ratios $b_i = \Gamma_{\pi N}/\Gamma_{\mathrm{tot}}$ are taken from the analysis of Manley and Saleski [MS92] (cf. Table 5.1 for their values).

The three charged-current channels are plotted in Fig. 5.12 together with pion-production data from ANL and BNL on H_2 and D_2. The solid line includes all resonances, while only the Δ is considered in the dashed line. One can see that the isospin

[2]We note that in the nuclear medium resonances can undergo "pion-less decay" which will be discussed in later chapters.

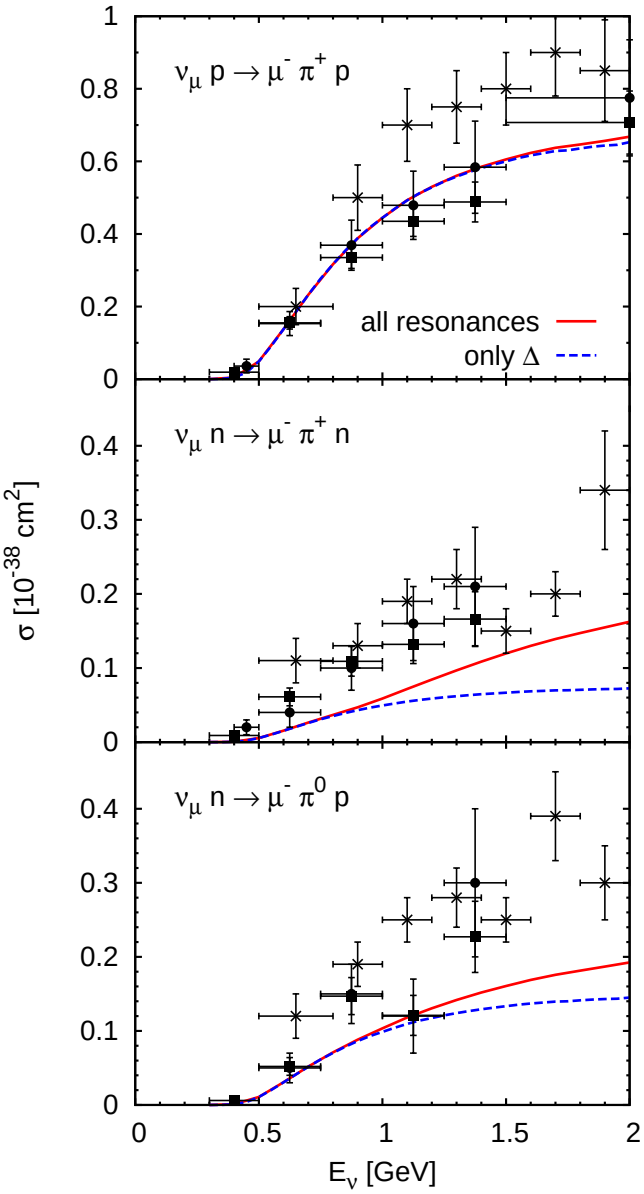

Figure 5.12: Total CC pion production cross sections through resonance excitation as a function of the neutrino energy (solid lines) compared to the pion production data of ANL (Refs. [B^+79] (•) and [R^+82] (■)) and BNL ([K^+86] (×)). The contribution from the Δ resonance is indicated by the dashed lines. No cut on the invariant mass is applied.

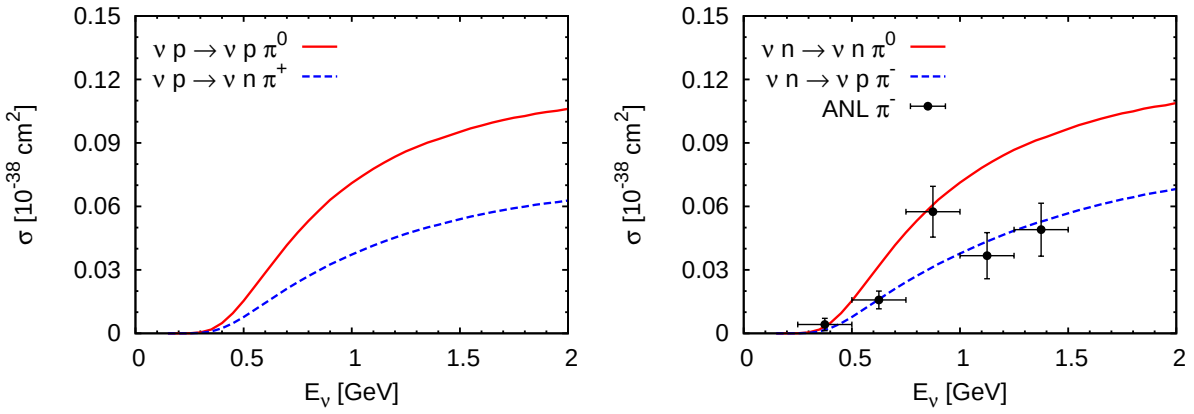

Figure 5.13: Total NC cross sections for pion production through the excitation and the subsequent decay of all included resonances as a function of the neutrino energy. The left panel shows the cross sections on protons, the right one on neutrons. In addition, we show the data of ANL [D$^+$80] which have to be compared with the $\nu n \to \nu p \pi^-$ channel (dashed line in right panel). No cut on the invariant mass is applied.

3/2 channel $\nu_\mu p \to \mu^- \pi^+ p$ (upper panel; note also the different scale there) is totally dominated by the Δ resonance. A good agreement with the ANL data is reached (note that we use the modified dipole form for the Δ axial form factor C_5^A).

In the case of the $\pi^+ n$ and $\pi^0 p$ channels our results lie systematically below the data (middle and lower panel). This is mainly due to the non-negligible contribution from the non-resonant πN background which will be discussed in the next chapter. Note, however, that the isospin-averaged total π^+ production cross section is dominated by the isospin 3/2 channel $\pi^+ p$, thus, the underestimate in the (small) $\pi^+ n$ channel translates into an error of only $\approx 10\%$ at $E_\nu = 1$ GeV.

To conclude, we find that the CC pion production cross section is dominated by the excitation and subsequent decay of the Δ resonance. The contribution of higher-lying resonances at neutrino energies $\lesssim 2$ GeV is rather small compared to the total pion yield. The underestimate in the isospin 1/2 channels, in particular in the $\pi^0 p$ channel, indicates that a non-resonant pion background is needed.

Our results for NC pion production are shown in Fig. 5.13 for protons (left) and neutrons (right). Data on NC pion production is extremely sparse. A measurement was performed on D_2 at the ANL bubble chamber for the $\nu n \to \nu p \pi^-$ channel [D$^+$80] — our calculation agrees well with these data (dashed line in the right panel of Fig. 5.13). The remaining channels have only been measured at the Gargamelle bubble chamber [K$^+$78] (see also the reanalysis by Hawker [Haw02]) on a propane-freon mixture and not on "elementary targets". Thus, we do not show them here.

5.5 Comparison to other approaches

Basically, two approaches are considered in the literature for the $N - R$ transition form factors: a phenomenological one with parameters extracted from neutrino and electron scattering data or a microscopical one using quark models. As discussed before, we have chosen the first approach and use phenomenological form factors.

5.5.1 Phenomenological models

Several studies have addressed the properties of the $P_{11}(1440)$ as well as its electromagnetic and weak production [LBL92, CG98, AFGM01, CPSS97, ARSVV98, DSFB99, ARBDM03, HNS$^+$08]. In the works of Refs. [FN79, LPP06] the form factors of the four lowest lying resonances, $P_{33}(1232)$, $P_{11}(1440)$, $D_{13}(1520)$ and $S_{11}(1535)$, are extracted using helicity amplitudes for the vector form factors and PCAC for the determination of the axial couplings.

We compare our form factors to the most recent works by Lalakulich *et al.* [LPP06] and Hernandez *et al.* [HNS$^+$08]. To perform a meaningful comparison, we have corrected for different normalizations[3] and sign conventions: both use a different sign in the definition of the axial current. The result after these corrections for the $P_{11}(1440)$ and $S_{11}(1535)$ resonance is shown in Table 5.9. We agree in all signs with Hernandez *et al.*, but with little differences in the numerical values. For the vector form factors, these differences can be attributed to the different analysis of helicity amplitudes used, since their Eqs. (28) and (29) coincide with our Eqs. (E.5) and (E.6)[4]. We also agree in the expressions for the Goldberger-Treiman relation (their Eq. (21) vs. our Eq. (F.17) — note the different sign convention); the difference in the axial coupling comes from a different value for the πNR-coupling.

Comparing to Lalakulich *et al.*, we find major differences. Ignoring a global sign difference — we and also Hernandez *et al.* take $F_i^V = F_i^p - F_i^n$ while Lalakulich uses $F_i^V = F_i^n - F_i^p$ —, a relative sign difference between F_1^V and F_A remains for the $P_{11}(1440)$ resonance. This is mainly caused by the different sign of F_1^p, which can be attributed — as already pointed out by Hernandez *et al.* [HNS$^+$08] — to the extra minus sign in the $S_{1/2}$ amplitude adopted in the analysis of experimental data which is missing in the work of Lalakulich *et al*. Furthermore, they perform the calculation in the lab frame, while it should be done in the cm frame as stated by Refs. [Tia, ABL08] (this affects $S_{1/2}$, see also the remarks in Appendix E).

[3] which, in both cases, introduces factors $\frac{(2M_N)^2}{\mu^2}\left(\frac{2M_N}{\mu}\right)$ with $\mu = M_N + M_R$ in front of the vector form factors F_1^V (F_2^V)

[4] While we include the minus sign in the $S_{1/2}$ amplitude explicitly, they account for it when fitting to the helicity amplitudes extracted from data.

Table 5.9: Comparison of our couplings for the $P_{11}(1440)$ and the $S_{11}(1535)$ to those compiled by Hernandez *et al.* [HNS+08] and Lalakulich *et al.* [LPP06]. The $S_{11}(1535)$ resonance is not considered in the work of Hernandez. F_i^N with $N = p, n$ stands for the EM form factors and F_i^V for the CC form factors. In our work (see discussions in connection with Table 5.2), and also in the work of Hernandez, F_i^V is taken as $F_i^V = F_i^p - F_i^n$ while Lalakulich uses $F_i^V = F_i^n - F_i^p$. F_A stands for the axial form factor. We have corrected for different normalizations and sign conventions in the axial current.

		this work	Hernandez *et al.*	Lalakulich *et al.*
$P_{11}(1440)$	$F_1^p(0)$	-1.96	-3.55	1.43
	$F_1^n(0)$	2.26	0.26	-1.43
	$F_1^V(0)$	-4.22	-3.81	-2.86
	$F_2^p(0)$	-0.46	-0.50	-0.60
	$F_2^n(0)$	0.41	0.34	0.60
	$F_2^V(0)$	-0.87	-0.84	1.20
	$F_A(0)$	-0.52	-0.63	0.51
$S_{11}(1535)$	$F_1^p(0)$	0.85	–	-1.24
	$F_1^n(0)$	-0.02	–	1.24
	$F_1^V(0)$	0.87	–	-2.49
	$F_2^p(0)$	0.46	–	-0.66
	$F_2^n(0)$	-0.35	–	0.66
	$F_2^V(0)$	0.82	–	-1.32
	$F_A(0)$	-0.23	–	0.21

Lalakulich *et al*. use a modified dipole form for the Q^2 dependence of their axial form factors, F_A and C_5^A, which reads

$$\left\{ \begin{array}{c} F_A(Q^2) \\ C_5^A(Q^2) \end{array} \right\}_{\mathrm{LPP}} = \left\{ \begin{array}{c} F_A(0) \\ C_5^A(0) \end{array} \right\} \left(1 + \frac{Q^2}{3{M'_A}^2}\right)^{-1} \left(1 + \frac{Q^2}{{M'_A}^2}\right)^{-2}, \qquad (5.28)$$

with $M'_A = 1.05\,\mathrm{GeV}$ for all four included resonances.

In Table 5.10 we compare our couplings for the $P_{33}(1232)$ and $D_{13}(1520)$ resonance to the recent compilation of Lalakulich *et al.* [LPP06]. The agreement is better than in the spin 1/2 case (cf. Table 5.9): focussing on the dominating form factor C_3, we still

Table 5.10: Comparison of our couplings for the $P_{33}(1232)$ and $D_{13}(1520)$ to those compiled by Lalakulich *et al.* [LPP06]. C_i^N with $N = p, n$ denotes the electromagnetic transition form factor while C_i^V stands for the CC form factor. In the case of the $P_{33}(1232)$, the electromagnetic form factors are equal for proton and neutron which is indicated by the index N (instead of p and n as for the $D_{13}(1520)$); furthermore, C_i^N and C_i^V differ only by their sign (in the table, the upper sign stands for C_i^N, the lower one for C_i^V, see Table 5.5). Note that both have the same sign in the work of Lalakulich *et al.* C_i^A denotes the axial form factor.

		this work	Lalakulich *et al.*
$P_{33}(1232)$	$C_3^{N,V}(0)$	∓ 2.12	2.13
	$C_4^{N,V}(0)$	± 11.31	-1.51
	$C_5^{N,V}(0)$	∓ 10.22	0.48
	$C_5^A(0)$	1.17	1.20
$D_{13}(1520)$	$C_3^p(0)$	-2.70	2.95
	$C_3^n(0)$	0.28	-1.13
	$C_3^V(0)$	-2.98	-4.08
	$C_4^p(0)$	2.62	-1.05
	$C_4^n(0)$	-1.59	0.46
	$C_4^V(0)$	4.21	1.51
	$C_5^p(0)$	-1.17	-0.48
	$C_5^n(0)$	1.96	-0.17
	$C_5^V(0)$	-3.13	0.31
	$C_5^A(0)$	-2.15	-2.10

do not agree in the sign of the EM form factors. However, in this case no relative sign difference remains for the CC form factors as it has been in the case of the $P_{11}(1440)$.

For the Δ resonance, we show in Fig. 5.14 the differential cross section obtained with our form factors (solid line) and with the form factor set of Lalakulich *et al.* [LPP06] (dashed line). With their form factors, no satisfactory agreement with the ANL data can be reached since the improvement on the vector form factors has not been applied to refit the axial form factors.

The difference in the Δ-resonance channel is also present in the integrated cross section shown in the upper left panel of Fig. 5.15. The solid lines denote the calculation

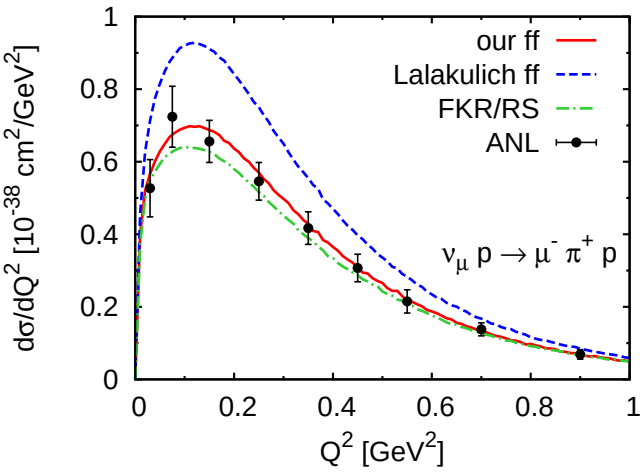

Figure 5.14: Differential cross section $d\sigma/dQ^2$ averaged over the ANL flux taken from [B$^+$77] as function of Q^2 compared to the ANL data taken from Radecky *et al.* [R$^+$82] (their Fig. 12). Our result is denoted by the solid line, the dashed line has been obtained with the form factors of Lalakulich *et al.* [LPP06], and the dash-dotted one with the FKR/RS model [RS81]. To compare with data, we apply an invariant mass cut at $W < 1.4\,\text{GeV}$.

using our form factors based on the MAID analysis and Eq. (5.19) while the dashed lines were calculated using the form factors of Lalakulich *et al.* [LPP06]. In this figure, we further investigate the impact of the different sets of form factors on the $P_{11}(1440)$, $D_{13}(1520)$ and $S_{11}(1535)$ integrated cross sections.

5.5.2 Quark models

Early attempts for quark-model form factors are reviewed in Ref. [SvH73] (see also references therein); more recent ones are summarized in Ref. [LMZ95]. Among them, the most widely used approach — which we shall briefly introduce here — is based on helicity amplitudes derived in a relativistic quark model by Feynman, Kislinger and Ravndal [FKR71] (FKR). Those have been used to describe the electroproduction of resonances [Rav71]. Later, Rein and Sehgal [RS81] (RS) applied the FKR model to describe the excitation of resonances up to $W = 2\,\text{GeV}$ via CC and NC interactions, but they also provide the helicity amplitudes for EM interactions in their work (which from now on we denote by FKR/RS model).

The FKR/RS model in its original version has been widely used in the simulation and analysis of many neutrino experiments as it is implemented in many neutrino event generators (see, e.g., Refs. [Cas02, Gal02, Hay02]). The FKR/RS model is very easy to program in a computer code and is really fast during run-time, which made it

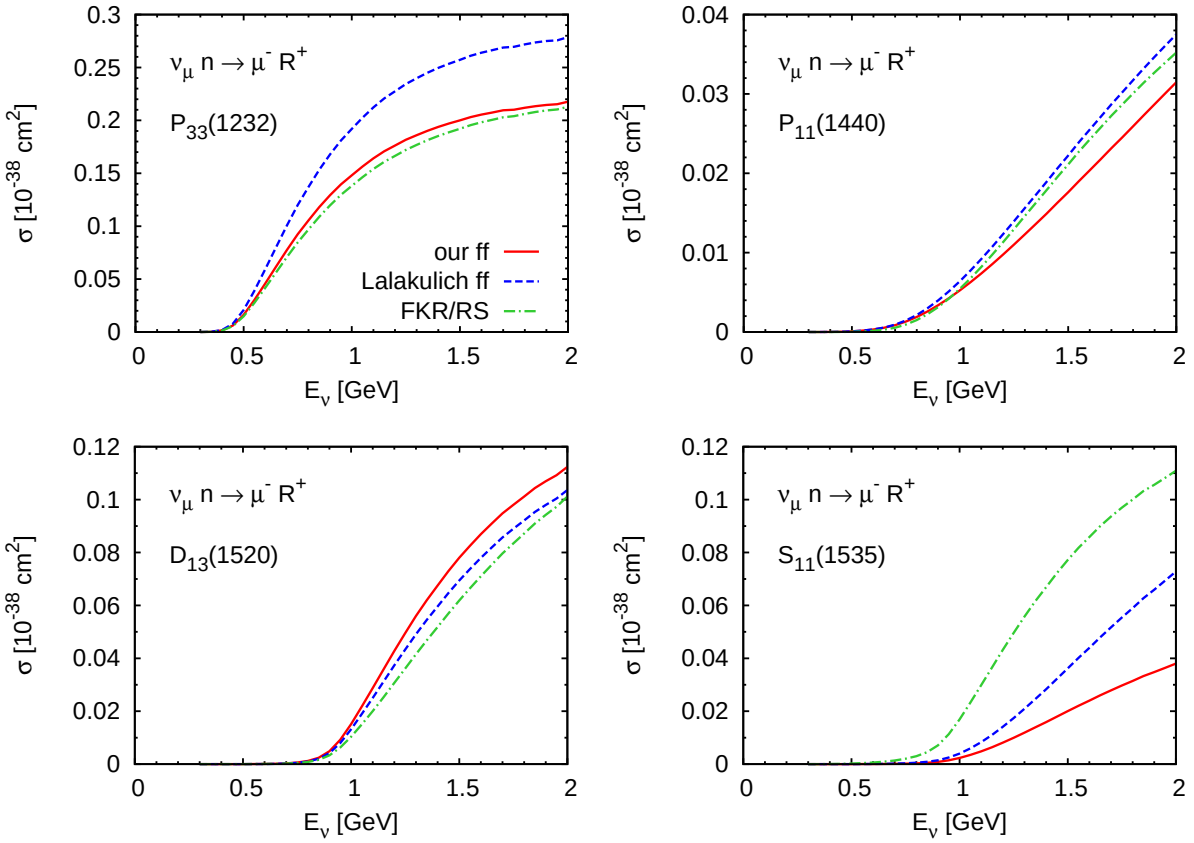

Figure 5.15: Integrated resonance excitation cross sections on the neutron for the $P_{33}(1232)$ (upper left panel), $P_{11}(1440)$ (upper right panel), $D_{13}(1520)$ and $S_{11}(1535)$ resonances. The curves are obtained with different sets of form factors: the solid lines indicate the calculation with our form factors based on the MAID helicity amplitudes as described in the previous sections, the dashed lines are calculated with the form factors of Lalakulich *et al.* [LPP06], and the dash-dotted ones with the FKR/RS model.

the first choice for many neutrino codes. But, one should keep in mind, that the lepton masses set to zero in this model which already imposes some corrections in the case of CC muon neutrino scattering, in the case of CC tau neutrino scattering, however, the FKR/RS model should not be used without modifications [GS08b, BS07, KLN04].

To compare directly our approach to the FKR/RS model, we simply replace the matrix element in Eq. (3.7) by the one derived in the FKR/RS model. One obtains the FKR/RS matrix element in the following way: comparing Eq. (2.13) in Ref. [RS81] to our Eq. (B.11) (page 275) after substituting $\mathrm{d}t = 2k_0|\mathbf{k}'|\,\mathrm{d}\cos\theta$, we find

$$|\bar{\mathcal{M}}_{\mathrm{FKR/RS}}|^2 = \frac{1}{2}\sum_{\mathrm{spins}} |T(\nu N \to \ell N^*)|^2, \tag{5.29}$$

with $T(\nu N \to \ell N^*)$ defined in their Eq. (2.11) in terms of the transition currents $F_{\pm,0}$ by

$$T = -4\,\sqrt{2}\,C_{\mathrm{CC,NC}}\,M_R\,E_\nu \left[\sqrt{\frac{Q^2}{|\mathbf{q}|^2}}\,\langle N^*\,|uF_- - vF_+|\,N\rangle + \frac{M_N}{M_R}\sqrt{2uv}\,\langle N^*\,|F_0|\,N\rangle\right], \tag{5.30}$$

with $q^\mu = (\omega, 0, 0, |\mathbf{q}|)$ and

$$u = \frac{E_\nu + E_\ell + |\mathbf{q}|}{2E_\nu}, \quad v = \frac{E_\nu + E_\ell - |\mathbf{q}|}{2E_\nu}. \tag{5.31}$$

We obtain

$$\begin{aligned}|\bar{\mathcal{M}}_{\mathrm{FKR/RS}}|^2 &= 16\,C^2_{\mathrm{CC,NC}}\,M_R^2\,E_\nu^2\frac{Q^2}{|\mathbf{q}|^2}\\ &\times\left[u^2\left(|f_{-3}|^2 + |f_{-1}|^2\right) + v^2\left(|f_{+3}|^2 + |f_{+1}|^2\right) + 2uv\frac{M_N^2}{M_R^2}\frac{|\mathbf{q}|^2}{Q^2}\left(|f_{0+}|^2 + |f_{0-}|^2\right)\right].\end{aligned} \tag{5.32}$$

The amplitudes f depend on the transition currents $F_{\pm,0}$ and on the spin projection of the initial and final states. They are defined as (cf. Eq. (3.19) in Ref. [RS81])

$$\begin{aligned} f_{-3} &= \langle N, J_z = 1/2\,|F_-|\,R, J_z = 3/2\rangle\,, & f_{-1} &= \langle N, J_z = -1/2\,|F_-|\,R, J_z = 1/2\rangle\,,\\ f_{+1} &= \langle N, J_z = 1/2\,|F_+|\,R, J_z = -1/2\rangle\,, & f_{+3} &= \langle N, J_z = -1/2\,|F_+|\,R, J_z = -3/2\rangle\,,\\ f_{0\pm} &= \langle N, J_z = \pm 1/2\,|F_0|\,R, J_z = \pm 1/2\rangle\,. \end{aligned} \tag{5.33}$$

F_+ (F_-, F_0) corresponds to photons with positive (negative, zero) helicity. They are determined using the FKR quark model;[5] the final result is listed in Table II in Ref. [RS81].

[5] For calculational details, we refer the reader to Refs. [FKR71, RS81]

In Fig. 5.15 we compare the integrated cross sections on the neutron obtained in the FKR/RS model (dash-dotted lines) to the one obtained with our default form factor set (solid lines) for the four lowest lying resonances. To further investigate the differences, we focus on the CC excitation of the $P_{33}(1232)$ resonance. For the helicity amplitudes, one finds in the FKR/RS model (cf. Table II in Ref. [RS81])

$$f_{\pm 3}^{\Delta,V} = \mp\sqrt{6}\, R^{\pm}, \tag{5.34}$$

$$f_{\pm 1}^{\Delta,V} = \mp\sqrt{2}\, R^{\pm}, \tag{5.35}$$

$$f_{\pm 0}^{\Delta,V} = -2\sqrt{2}\, C, \tag{5.36}$$

where $R^{\pm}$ includes both vector and axial vector components (cf. Eq. (3.11) in Ref. [RS81] with $n = 0$ for the Δ resonance)

$$R^{\pm} = -(R^V \pm R^A), \tag{5.37}$$

with

$$R^V = \sqrt{2}\frac{M_N}{M_R}\frac{|\mathbf{q}|(M_N + M_R)}{Q^2 + (M_R + M_N)^2} G_{\mathrm{FKR/RS}}^V \tag{5.38}$$

and

$$R^A = \frac{Z\sqrt{2}}{6M_R}(M_R + M_N) G_{\mathrm{FKR/RS}}^A. \tag{5.39}$$

The variable C depends only on the axial form factor via

$$C = \frac{Z}{6M_N|\mathbf{q}|}(M_R^2 - M_N^2) G_{\mathrm{FKR/RS}}^A. \tag{5.40}$$

For the form factors, they use

$$G_{\mathrm{FKR/RS}}^{V,A}(Q^2) = \left(1 + \frac{Q^2}{4M_N^2}\right)^{\frac{1}{2}} \left(1 + \frac{Q^2}{M_{V,A}^2}\right)^{-2}. \tag{5.41}$$

with $M_V = 0.84\,\mathrm{GeV}$ and $M_A = 1.032\,\mathrm{GeV}$, respectively.[6] The value of the axial vector renormalization constant Z has been chosen to be $3/4$ in order to, in the words of Rein and Sehgal, compensate for the difference between the SU_6 predicted value $5/3$ for the nucleon's axial vector form factor at $Q^2 = 0$ and its experimental value of about $5/4$.

In Fig. 5.14 on page 63 we show in addition to the total cross section already seen in Fig. 5.15 also the FKR/RS prediction for $\mathrm{d}\sigma/\mathrm{d}Q^2$ (dash-dotted line) for the Δ resonance excitation. From both figures we find reasonable agreement to our results for CC scattering. Good agreement is also found for NC scattering.

[6] Rein and Sehgal originally proposed an axial mass of $M_A = 0.95\,\mathrm{GeV}$, however, we use the value commonly used in the neutrino event generators [Zel03].

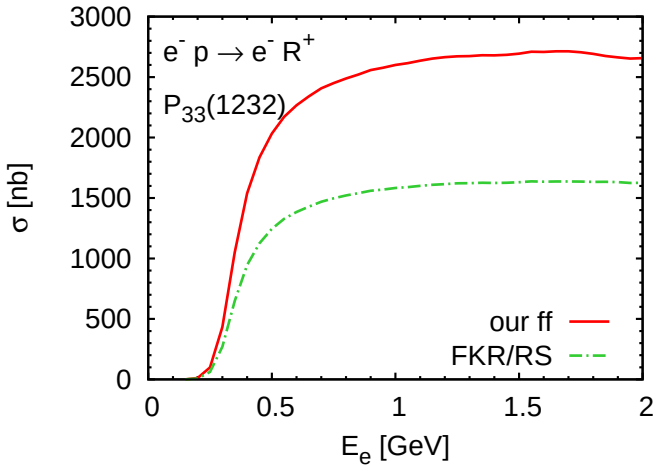

Figure 5.16: Integrated EM Δ excitation cross sections on the proton versus the electron energy. The solid line indicates the calculation with our form factors while the dash-dotted one is obtained with the FKR/RS model.

A different picture emerges when we look at the electron proton cross section shown in Fig. 5.16. Our result is denoted by the solid line, the one obtained in the FKR/RS model by the dash-dotted line. The comparison yields a clear discrepancy in EM scattering.[7] This has also been observed by Graczyk *et al.* [GS08a] who, as a consequence, refit the FKR/RS form factors. We therefore conclude that the vector contribution of the FKR/RS model is smaller than ours, but, consequently, their axial part must be larger than ours to obtain agreement in the CC case when both axial and vector form factors are important. And indeed, this can be verified from the comparison shown in Fig. 5.17. The left (right) panel shows in addition to the full curve the result when only the vector (axial) part is taken into account. We find that the FKR/RS form factors lead to significantly smaller cross sections than our vector form factors based on the MAID analysis (left panel, dashed versus dotted lines). We further note that the FKR/RS model is based on a single vector form factor only ($G_V^{\mathrm{FKR/RS}}$) while our model incorporates three independent vector form factors (C_i^V, $i = 3, 4, 5$). The opposite behavior is found in the axial channel: there, the FKR/RS overshoots our prediction. Note that both our vector and axial parts alone give very similar contributions. Axial and vector parts alone do not add up to the full cross section as interference between vector and axial part are also important.

To conclude, the FKR/RS model gives reasonable results for neutrino-induced reactions, however, one should be aware of its limitations: the major drawbacks are

[7] See also our comparison to JLAB data at higher energies shown in Fig. 2 of Ref. [LBMAR08] leading to the same conclusion.

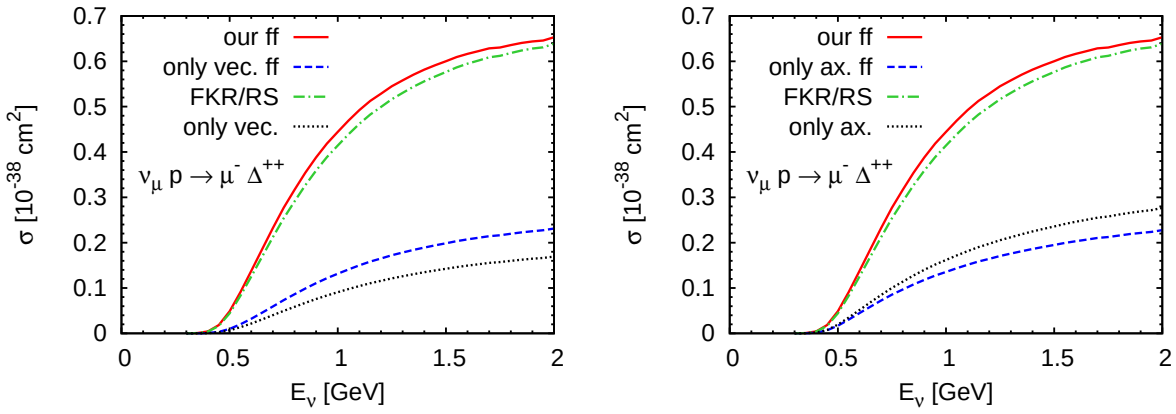

Figure 5.17: Integrated CC Δ excitation cross sections on the proton versus the neutrino energy calculated with our form factors (solid lines) and within the FKR/RS model (dash-dotted lines). The left (right) panel shows, in addition, the result when only the vector (axial) form factors are included. Here, the dashed lines stand for our result and the dotted ones for the FKR/RS model.

the neglect of the lepton masses and the outdated and too small vector form factors leading to too small electron cross sections.

6

Single-π non-resonant background

The need of a single-π non-resonant background contribution in neutrino scattering is justified by the fact that we underestimate the total pion production cross section in the isospin 1/2 channels. We know from the comparison to ANL and BNL data that the resonance excitation alone does not account for all the pion strength (cf. the discussion Section 5.4). However, the discrepancy is small compared to the total pion-production cross section which is dominated by the isospin 3/2 channel.

Early ideas for the non-resonant single-pion background have been formulated by Fogli and Nardulli [FN79, FN80], and also by Rein and Sehgal [RS81] who include only a simple nucleon pole term which accounts for the missing strength in the isospin 1/2 channels. Recently, microscopic models for the elementary reaction have been developed. Nieves and collaborators have extended their model for $eN \rightarrow e'N'\pi$ [GNO97] to describe CC and NC pion production on the nucleon [HNV07]. Besides the dominant Δ contribution they have included background terms required by chiral symmetry. Also the model of Sato and Lee for neutrino-induced pion production on the nucleon including Δ excitation and non-resonant background terms [SUL03] is based on their approach for electrons [SL01]. However, both approaches, include besides non-resonant terms only the Δ as intermediate resonance state.

In this chapter, we thus discuss the remaining contribution to the total cross section as given in Eq. (3.1): the single-π non-resonant background cross section $\mathrm{d}\sigma_{\mathrm{BG}}$. It is essential to realize that the background must be known for all kinematic variables if one is interested in calculating also differential cross sections. Therefore, we heavily rely on models applied to electron-/photon scattering where the background contribution is even more important and rather well understood.

In contrast to the aforementioned models, our ansatz is phenomenological: the single-π non-resonant background cross section $\mathrm{d}\sigma_{\mathrm{BG}}$ includes vector, axial and also interference contributions

$$\begin{aligned}\mathrm{d}\sigma_{\mathrm{BG}} &= \mathrm{d}\sigma_{\mathrm{BG}}^{\mathrm{V}} + \mathrm{d}\sigma_{\mathrm{BG}}^{\mathrm{A}} + \mathrm{d}\sigma_{\mathrm{BG}}^{\mathrm{V/A}} \\ &= \mathrm{d}\sigma_{\mathrm{BG}}^{\mathrm{V}} + \mathrm{d}\sigma_{\mathrm{BG}}^{\text{non-V}}. \end{aligned} \tag{6.1}$$

The vector part is fully determined by electron scattering data. The axial and the interference term collected under the label "non-V" are only present in neutrino scattering and will be fitted to the available neutrino data.

6.1 Vector part

We first discuss the vector part of the non-resonant pion cross section, $\mathrm{d}\sigma_{\mathrm{BG}}^{\mathrm{V}}$. Our strategy will be to evaluate the unpolarized pion production cross section $\ell(k)N(p) \to \ell'(k')\pi(k_\pi)N(p')$, $\mathrm{d}\sigma_{N\pi}^{\mathrm{V}}$, and to subtract afterwards the resonance contribution. We understand this subtracted contribution, which then includes also the resonance-background interference terms, as a single-π background denoted as $\mathrm{d}\sigma_{\mathrm{BG}}^{\mathrm{V}}$. We are actually assuming that the resonances do not interfere among themselves or with the background, so that

$$\frac{\mathrm{d}\sigma_{\mathrm{BG}}^{\mathrm{V}}}{\mathrm{d}\omega \mathrm{d}\Omega_{k'} \mathrm{d}\Omega_{k_\pi}} = \frac{\mathrm{d}\sigma_{N\pi}^{\mathrm{V}}}{\mathrm{d}\omega \mathrm{d}\Omega_{k'} \mathrm{d}\Omega_{k_\pi}} - \sum_R \frac{\mathrm{d}\sigma_{\ell N \to \ell R \to \ell N\pi}^{\mathrm{V}}}{\mathrm{d}\omega \mathrm{d}\Omega_{k'} \mathrm{d}\Omega_{k_\pi}} \,. \tag{6.2}$$

We note that with this procedure the background may become negative since it absorbs the interferences.[1]

The first term of the rhs, the cross section for $\ell(k)N(p) \to \ell'(k')\pi(k_\pi)N(p')$, $\mathrm{d}\sigma_{N\pi}^{\mathrm{V}}$, is given by (cf. Appendix B.2)

$$\frac{\mathrm{d}\sigma_{N\pi}^{\mathrm{V}}}{\mathrm{d}\omega \mathrm{d}\Omega_{k'} \mathrm{d}\Omega_{k_\pi}} = \int \mathrm{d}k_\pi^0 \, \frac{|\mathbf{k}'||\mathbf{k}_{\boldsymbol{\pi}}|}{512\pi^5} \left[(k\cdot p)^2 - m_\ell^2 M_N^2\right]^{-1/2} \delta(p'^2 - M_N^2) \, |\bar{\mathcal{M}}_{N\pi}|^2, \tag{6.3}$$

with $p' = k + p - k' - k_\pi$, $|\mathbf{k}'| = \sqrt{{k_0'}^2 - m_{\ell'}^2}$ and $|\mathbf{k}_{\boldsymbol{\pi}}| = \sqrt{{k_\pi^0}^2 - m_\pi^2}$ and with Ω_{k_π} denoting the solid angle of the pion. Note that the lepton mass is kept explicitly in our work. The δ-function $\delta(p'^2 - M_N^2)$ eliminates the $\mathrm{d}k_\pi^0$ integration. The hadronic tensor $H_{N\pi}^{\mu\nu}$ entering the matrix element in Eq. (6.3) is written in a form similar to that of resonance production

$$H_{N\pi}^{\mu\nu} = \frac{1}{2}\mathrm{Tr}\left[(\not{p} + M)\, \tilde{\mathcal{V}}_{N\pi}^{\mu} \left(\not{p}' + M'\right) \mathcal{V}_{N\pi}^{\nu}\right], \tag{6.4}$$

[1] We come back to this issue in Section 8.3.

with $M = \sqrt{p^2}$ and $M' = \sqrt{p'^2}$, and

$$\tilde{\mathcal{V}}^{\mu}_{N\pi} = \gamma_0 \mathcal{V}^{\mu\,\dagger}_{N\pi} \gamma_0. \tag{6.5}$$

The hadronic vertex can be parametrized in the most general way as [BDW67]

$$\mathcal{V}^{\mu}_{N\pi} = \sum_{i=1}^{6} A_i^{N\pi} M_i^{\mu}, \tag{6.6}$$

with (in the notation of MAID [PDT07])

$$\begin{aligned}
M_1^{\mu} &= \frac{-\mathrm{i}}{2}\gamma^5(\gamma^{\mu}\not{q} - \not{q}\gamma^{\mu}) = -\mathrm{i}\gamma^5(\gamma^{\mu}\not{q} - q^{\mu}) \,, \\
M_2^{\mu} &= 2\mathrm{i}\gamma^5 \left(P^{\mu} q \cdot \left(k_{\pi} - \frac{q}{2} \right) - P \cdot q \left(k_{\pi} - \frac{q}{2} \right)^{\mu} \right) \,, \\
M_3^{\mu} &= -\mathrm{i}\,\gamma^5(\gamma^{\mu} k_{\pi} \cdot q - \not{q} k_{\pi}^{\mu}) \,, \\
M_4^{\mu} &= -2\mathrm{i}\,\gamma^5(\gamma^{\mu} q \cdot P - \not{q} P^{\mu}) - 2M_N M_1^{\mu} \,, \\
M_5^{\mu} &= \mathrm{i}\,\gamma^5(q^{\mu} k_{\pi} \cdot q - q^2 k_{\pi}^{\mu}) \,, \\
M_6^{\mu} &= -\mathrm{i}\,\gamma^5(\not{q} q^{\mu} - q^2 \gamma^{\mu})
\end{aligned} \tag{6.7}$$

and $P^{\mu} = (p + p')^{\mu}/2$. The so-called invariant amplitudes $A_1^{N\pi}, \ldots, A_6^{N\pi}$, depending both on the probe and the reaction channel, are functions of three scalars which completely determine all the four-vectors at the vertex. We choose $W = \sqrt{s}$, $Q^2 = -q_{\mu} q^{\mu}$ and the cm scattering angle θ between $\mathbf{q}$ and $\mathbf{k_{\pi}}$ as such a set of independent scalars.

The second part of Eq. (6.2) is obtained in the following way: the resonances are assumed to decay isotropically in their rest-frame, i.e.,

$$\frac{\mathrm{d}\Gamma_{R\to N\pi}}{\mathrm{d}\Omega^{\mathrm{cm}}_{k_{\pi}}} = \frac{\Gamma_{R\to N\pi}}{4\pi}, \tag{6.8}$$

and consequently the single resonance contributions are given by

$$\frac{\mathrm{d}\sigma^{\mathrm{V}}_{\ell N\to \ell R\to \ell N\pi}}{\mathrm{d}\omega \mathrm{d}\Omega_{k'} \mathrm{d}\Omega_{k_{\pi}}} = \frac{\mathrm{d}\sigma^{\mathrm{V}}_{R}}{\mathrm{d}\omega \mathrm{d}\Omega_{k'}} \frac{1}{4\pi} \frac{\Gamma_{R\to N\pi}}{\Gamma_R} \frac{\mathrm{d}\Omega^{\mathrm{cm}}_{k_{\pi}}}{\mathrm{d}\Omega_{k_{\pi}}} \,. \tag{6.9}$$

The vector part of the resonance cross section has been introduced in the previous section and the solid-angle transformation is given by [BK73]

$$\frac{\mathrm{d}\Omega^{\mathrm{cm}}_{k_{\pi}}}{\mathrm{d}\Omega_{k_{\pi}}} = \frac{\sqrt{p'^2}\,\mathbf{k}_{\boldsymbol{\pi}}^2}{|\mathbf{k}^{\mathrm{cm}}_{\boldsymbol{\pi}}| \left(|\mathbf{k}_{\boldsymbol{\pi}}| p'^0 - |\mathbf{p}'| k^0_{\pi} \cos\theta_{\pi} \right)} \,, \tag{6.10}$$

where $\theta_{\pi} = \measuredangle(\mathbf{k}_{\boldsymbol{\pi}}, \mathbf{p}')$.

Electron scattering

In the case of electron scattering, the possible channels are

$$\begin{aligned} e^- p &\to e^- p \pi^0, \\ e^- p &\to e^- n \pi^+, \\ e^- n &\to e^- n \pi^0, \\ e^- n &\to e^- p \pi^-. \end{aligned}$$

For each of these channels, a set of invariant amplitudes $A_i^{N\pi,\mathrm{EM}}$ can be fitted to data. We use the MAID parametrization [MAID, TK06, DT92]. More details are given in Chapter 4.5 of Ref. [Bus08].

Charged-current scattering

In the case of charged-current neutrino scattering, there are three pion production channels, namely

$$\begin{aligned} \nu p &\to \ell^- p \pi^+, \\ \nu n &\to \ell^- n \pi^+, \\ \nu n &\to \ell^- p \pi^0. \end{aligned}$$

Applying isospin relations to relate $A_i^{N\pi,\mathrm{CC}}$ to the known $A_i^{N\pi,\mathrm{EM}}$, one gets (for details, see Appendix D.3)

$$A_i^{p\pi^+,\mathrm{CC}} = \sqrt{2} A_i^{n\pi^0,\mathrm{EM}} + A_i^{p\pi^-,\mathrm{EM}}, \tag{6.11}$$

$$A_i^{n\pi^+,\mathrm{CC}} = \sqrt{2} A_i^{p\pi^0,\mathrm{EM}} - A_i^{p\pi^-,\mathrm{EM}}, \tag{6.12}$$

$$A_i^{p\pi^0,\mathrm{CC}} = A_i^{p\pi^0,\mathrm{EM}} - A_i^{n\pi^0,\mathrm{EM}} - \sqrt{2} A_i^{p\pi^-,\mathrm{EM}}, \tag{6.13}$$

so that the CC vector part is fully determined.

Neutral-current scattering

The following channels contribute to neutral-current pion production

$$\begin{aligned} \nu p &\to \nu p \pi^0, \\ \nu p &\to \nu n \pi^+, \\ \nu n &\to \nu n \pi^0, \\ \nu n &\to \nu p \pi^-. \end{aligned} \tag{6.14}$$

Isospin relations required to relate the invariant amplitudes $A_i^{N\pi,\mathrm{NC}}$ to the known $A_i^{N\pi,\mathrm{EM}}$ are more complicated than in the CC case and can be found, e.g., in Section III of Ref. [HNV07]. However, they are not needed here since we do not include any background in the NC channels (see below).

6.2 Non-vector part

In the case of neutrino scattering, a non-vector background is present. In principle, one can write down a similar expression as Eq. (6.6) for the axial current. This would lead to a large number of unknown amplitudes A_i to be fixed by data, but, the scarcity of available data makes this option impracticable.

However, as pointed out before, the background contribution to the *total* pion production cross section is small because of the dominant isospin 3/2 channel. Thus, in the present work, we rather use a simple ansatz for the non-vector background expecting that the final results in nuclei are not sensitive to the background details.

Charged-current scattering

As already discussed in Section 5.2.2, we neglect a non-resonant background in the isospin 3/2 channel, $\nu p \to \mu^- \pi^+ p$, where it is only a small correction. Furthermore, we assume that $\mathrm{d}\sigma_{\mathrm{BG}}^{\mathrm{V}}$ and $\mathrm{d}\sigma_{\mathrm{BG}}^{\text{non-V}}$ have the same functional form, i.e.,

$$\mathrm{d}\sigma_{\mathrm{BG}} = \mathrm{d}\sigma_{\mathrm{BG}}^{\mathrm{V}} + \mathrm{d}\sigma_{\mathrm{BG}}^{\text{non-V}} = (1 + b^{N\pi})\, \mathrm{d}\sigma_{\mathrm{BG}}^{\mathrm{V}} \,, \tag{6.15}$$

where the global factor $b^{N\pi}$ depends on the channel, $\nu n \to \ell^- n \pi^+$ or $\nu n \to \ell^- p \pi^0$. The data sets for the two CC scattering channels off neutrons allow then the fit of the two parameters. The influence of this fit parameter for ν_μ-induced pion production is shown in Fig. 6.1. With $b^{p\pi^0} = 3$ and $b^{n\pi^+} = 1.5$ a reasonable agreement with the ANL data is achieved as can be seen from Fig. 6.2 where the solid line denotes our full calculation and the dashed (dash-dotted) one includes only the resonance (Δ) contribution.

Our numbers are in agreement with general isospin considerations. The dominant contribution to the non-resonant background comes from the nucleon-pole term [Val, HNV07], an isospin 1/2 channel. Using Clebsch-Gordon coefficients, we find for the yields $\pi^0/\pi^+ = 2$, which nicely corresponds to $b^{p\pi^0}/b^{n\pi^+} = 2$.

Even though these parameters were extracted for muon neutrinos, they can safely be applied for electron neutrinos, since the cross sections for both are almost identical in this energy region. However, they should not be used for ν_τ where the cross sections differ significantly.

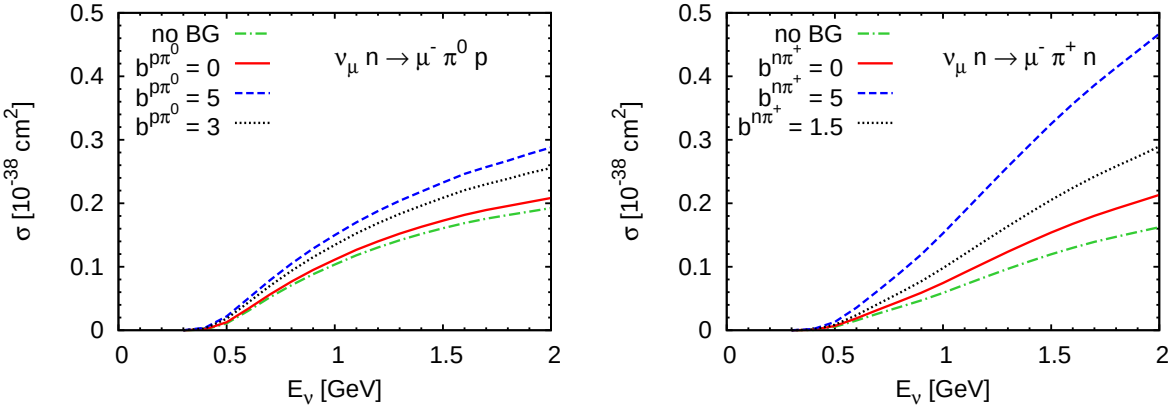

Figure 6.1: Influence of the fit parameter $b^{N\pi}$ on the total pion production cross sections in the mixed isospin channels.

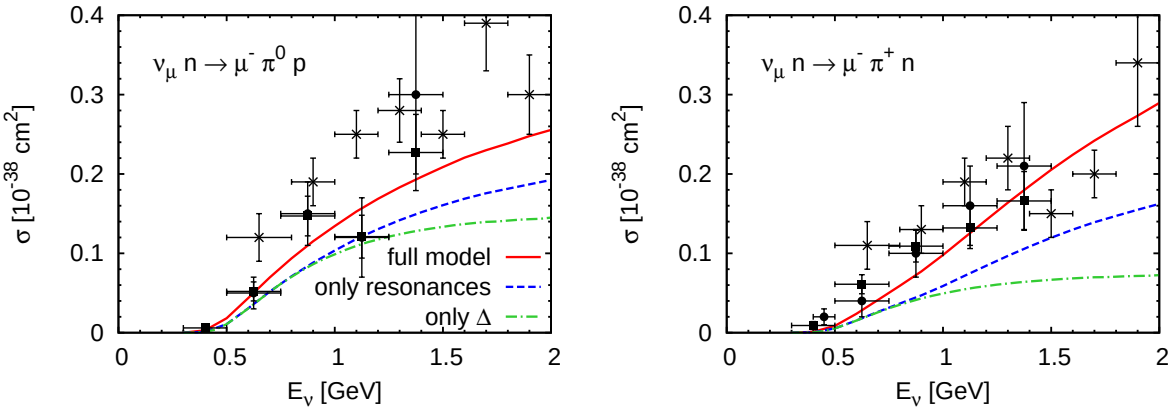

Figure 6.2: Total CC pion production cross sections for the mixed isospin channels as a function of the neutrino energy compared to the pion production data measured at ANL (Refs. [B^+79] (•) and [R^+82] (■)) and BNL ([K^+86] (×)). The solid lines denote the our full result including the non-resonant background following Eq. (6.15) with $b^{p\pi^0} = 3$ and $b^{n\pi^+} = 1.5$. Furthermore, we show the results for pion production only through the excitation and the subsequent decay of all resonances (dashed lines) or through the Δ alone (dash-dotted lines). No cut on the invariant mass is applied.

Neutral-current scattering

Pion data for NC scattering are even more scarce than for the CC case. The available data are compared to our results for the resonance induced pion production in Fig. 5.13 on page 59 and we find a good agreement (compare the dashed line in the right panel to the data) already without non-resonant background. In view of this, we abstain from fitting the non-vector part to these data and neglect a NC background.

Part III

Lepton-nucleus interactions in the GiBUU model

7 GiBUU transport model

This chapter introduces the semi-classical Giessen Boltzmann-Uehling-Uhlenbeck (GiBUU) transport model [GiBUU, BGG$^+$]. It describes the space-time evolution of a many-particle system in a mean-field potential including a collision term, and hereby allows for a realistic treatment of in-medium modifications and for a full microscopic coupled-channel description of final-state interactions inside the nucleus.

7.1 Introduction

Originally developed to describe heavy-ion collisions [TCE$^+$97, HCTM99, LM03, LM05, WLM05], the Giessen BUU model has been extended to describe high-energy non-resonant electron-induced reactions [FCGM04, GF05], photon-, pion- and electron-induced processes in the resonance region [ECM$^+$94, EBM99, LEM00, LPM03, MFM04, BARMM06, MM06, Bus08, LBARM09],[1] and — presented in this thesis — neutrino-induced reactions.[2] The study of νA scattering is a natural extension of the previous work and does not introduce any new free nuclear parameters. The applicability to and validation in many different nuclear reactions is a major strength of our model, which describes all the different processes using the same physics input. In particular, the test against existing data on the interaction of photons and electrons with nuclei is

[1] An overview of the GiBUU history, which goes back to the 1980s, is collected at http://gibuu.physik.uni-giessen.de/GiBUU/wiki/GiBUU_Code_history.

[2] Partly published in Refs. [LARM06a, LARM06b, BLMAR07, LBMAR08, LBARM09, LBMAR09].

an important prerequisite for any model aiming at a description of neutrino-nucleus interactions.

The numerical implementation of the GiBUU model is based on Fortran2003 using modern programming paradigms and a version control management (Subversion).[3] The code runs and has been tested with numerous compilers on different platforms, details are given on our website [GiBUU]. From 2007, the GiBUU code is open source under the GPL license and can be downloaded after registration [GiBUU].

In the following, we introduce the GiBUU model focussing on the issues relevant to this work — for further details on the theoretical foundations and their numerical implementations we refer to Refs. [Tei97, Eff99, Leh03, Bus08].

7.2 Particle species

The GiBUU model includes a large variety of different particle species, namely 61 baryons and 21 mesons with their corresponding antiparticles. Isospin degrees of freedom are treated explicitly, while the spin enters only via a statistical factor. In the energy region of interest for this work, i.e., beam energies of about 0.5 - 2 GeV, the most relevant states are nucleon, the nucleon resonances (isospin 1/2), the Δ resonances (isospin 3/2) and the light mesons, in particular the pion. The parameters for all particles without strangeness and charm, are taken from the πN scattering phase-shift analysis of Manley and Saleski [MS92]; the parameters for all other particles are taken from the PDG group [PDG08].

The properties of the included 31 non-strange/non-charm resonances are listed in Table 7.1 together with their decay channels. We use the common notation which reads l_{ij} with the spin $J = \frac{j}{2}$ and isospin $I = \frac{i}{2}$. l denotes the relative angular momentum of the πN system. The parity follows from $P = (-1)^{l+1}$. The light mesons and their properties are listed in Table 7.2. Their quantum numbers and decay channels are given explicitly.

At higher energies, particles with higher strangeness and charm quantum numbers could play a role, thus, in addition to the above listed particles, 30 baryonic and 8 mesonic states of the strange-/charm-sector are included in the GiBUU model (cf. Tables 3.2, 3.3, A.1 and A.2 in Ref. [Bus08] for their properties and decays).

Leptons are not explicitly propagated in our model; due to their small couplings we assume that they interact only once in the initial reaction (e.g., $\nu A \to \mu^- X$) and that the final lepton leaves the nucleus undisturbed.

[3] See the GiBUU website [GiBUU] and Section 3.1 and Appendix C in the dissertation of O. Buss [Bus08] for detailed information on the current code structure and its programming history.

Table 7.1: Properties and decay channels for the non-strange/non-charm baryons as in the Manley analysis [MS92]. Given are the Breit-Wigner masses, M_B, the width at M_B, Γ_0, and the branching ratios into the various decay channels.

	M_B	Γ_0	branching ratio in %								
	[MeV]	[MeV]	$N\pi$	$N\eta$	$N\omega$	$K\Lambda$	$\Delta\pi$	$N\rho$	$N\sigma$	$N^*\pi$	$\Delta\rho$
N(938)	938	0	0	0	0	0	0	0	0	0	0
P_{33}(1232)	1232	118	100	0	0	0	0	0	0	0	0
P_{11}(1440)	1462	391	69	0	0	0	22	0	9	0	0
S_{11}(1535)	1534	151	51	43	0	0	0	3	1	2	0
S_{11}(1650)	1659	173	89	3	0	0	2	3	2	1	0
S_{11}(2090)	1928	414	10	0	0	0	6	49	5	30	0
D_{13}(1520)	1524	124	59	0	0	0	20	21	0	0	0
D_{13}(1700)	1737	249	1	0	0	0	84	13	2	0	0
D_{13}(2080)	1804	447	23	0	0	0	24	26	27	0	0
D_{15}(1675)	1676	159	47	0	0	0	53	0	0	0	0
G_{17}(2190)	2127	547	22	0	49	0	0	29	0	0	0
P_{11}(1710)	1717	478	9	0	0	37	49	3	2	0	0
P_{11}(2100)	1885	113	15	0	0	2	24	27	32	0	0
P_{13}(1720)	1717	383	13	0	0	0	0	87	0	0	0
P_{13}()	1879	498	26	0	30	0	0	44	0	0	0
F_{15}(1680)	1684	139	70	0	0	0	11	7	12	0	0
F_{15}(2000)	1903	494	8	0	0	0	12	75	5	0	0
F_{17}(1990)	2086	535	6	94	0	0	0	0	0	0	0
S_{31}(1620)	1672	154	9	0	0	0	62	29	0	0	0
S_{31}(1900)	1920	263	4	0	0	0	16	38	0	6	0
D_{33}(1700)	1762	599	14	0	0	0	78	8	0	0	0
D_{33}(1940)	2057	460	18	0	0	0	47	35	0	0	0
D_{35}(1930)	1956	526	18	0	0	0	0	0	0	0	82
D_{35}(2350)	2171	264	2	0	0	0	0	0	0	0	98
P_{31}()	1744	299	8	0	0	0	0	0	0	28	64
P_{31}(1910)	1882	239	23	0	0	0	0	10	0	67	0
P_{33}(1600)	1706	430	12	0	0	0	68	0	0	20	0
P_{33}(1920)	2014	152	2	0	0	0	83	0	0	15	0
F_{35}()	1752	251	2	0	0	0	76	22	0	0	0
F_{35}(1905)	1881	327	12	0	0	0	1	87	0	0	0
F_{37}(1950)	1945	300	38	0	0	0	18	0	0	0	44

Table 7.2: Properties and decay channels for the light mesons. Given are the pole masses, m_m, the width at m_m, Γ_0, spin, J, isospin, I, strangeness, S, and the branching ratios into the various decay channels.

meson	m_m [MeV]	Γ_0 [MeV]	J	I	S	decay channels
π	138	0	0	1	0	
η	547	$1.2 \cdot 10^{-3}$	0	0	0	$\gamma\gamma$ (40%), $\pi^+\pi^-\pi^0$ (28%), $3\pi^0$ (32%)
ρ	770	151	1	1	0	$\pi\pi$
σ	800	800	0	0	0	$\pi\pi$
ω	782	8.4	1	0	0	$\pi\pi$ (2%), $\pi^0\gamma$ (9%), $\pi^+\pi^-\pi^0$ (89%)
η'	958	0.2	0	0	0	$\rho^0\gamma$ (31%), $\pi\pi\eta$ (69%)
ϕ	1020	4.4	1	0	0	$\rho\pi$ (13%), $K\bar{K}$ (84%), $\pi^+\pi^-\pi^0$ (3%)
K	496	0	0	1/2	1	
$\bar{K}$	496	0	0	1/2	-1	
K^*	892	50	1	1/2	1	$K\pi$
$\bar{K}^*$	892	50	1	1/2	-1	$\bar{K}\pi$

7.3 BUU equation

The Boltzmann-Uehling-Uhlenbeck (BUU) equation describes the space-time evolution of a many-particle system under the influence of mean-field potentials and a collision term, or more precisely, the time evolution of the Wigner transform of the real-time Green's function which is a generalization of the classical phase-space density. For each particle species, one gets within the BUU approach an additional differential equation. All these equations are coupled through the gain and loss terms which represent scattering processes, and by the mean fields being included in the Hamiltonians. In this section, we present the generalized BUU equation and discuss its approximations.

7.3.1 General properties

The BUU equation can be derived from the Kadanoff-Baym equation, which is based on quantum-field theory, applying special assumptions. We refer the reader to the book of Kadanoff and Baym for details [KB94].[4] Since the BUU equation has been extensively discussed in the literature (cf., e.g., Refs. [Nor28, UU33, BK84, BG88, Eff99, Leh03, Leu00]), we focus in the following on issues relevant to this work.

[4] A detailed overview is also given in Section 2.2 of Ref. [Leh03].

The generalized BUU equation for particle species i, suited also for particles off their mass shell, is given by [Eff99, Leu00]

$$\left[p_0 - H_i, \bar{g}_i^<\right] + A_{\text{off-shell}} = I_{\text{coll}}, \tag{7.1}$$

where

$$A_{\text{off-shell}} = \left[\text{Re}(g_i), \Sigma_i^<\right], \tag{7.2}$$

with the Poisson brackets

$$[a, b] = \frac{\partial a}{\partial p_\mu}\frac{\partial b}{\partial x^\mu} - \frac{\partial a}{\partial x_\mu}\frac{\partial b}{\partial p^\mu}. \tag{7.3}$$

The collision term reads

$$I_{\text{coll}} = -\Sigma_i^> \bar{g}_i^< + \Sigma_i^< \bar{g}_i^>. \tag{7.4}$$

$\bar{g}_i^<(r,p)$ $\left(\bar{g}_i^>(r,p)\right)$ denotes the Wigner transform of the real-time Green's function and is interpreted as a generalized particle (hole) phase-space density; g_i is the retarded Green's function. $\Sigma_i^<$ $\left(\Sigma_i^>\right)$ stands for the gain (loss) term of the phase-space density and are explained in Section 7.6. H_i represents the Hamilton function — note that the phase space variable p_0 and H_i are distinct entities — which is in its relativistic form given by

$$H_i = \sqrt{m_i^2 + \mathbf{p}^2} + V_i(r,p), \tag{7.5}$$

where m_i is the pole mass of the ith particle species which is under the influence of a mean-field potential V_i. For later use, we introduce a scalar potential U_i,

$$U_i(r,p) = \sqrt{\left(\sqrt{m_i^2 + \mathbf{p}^2} + V_i(r,p)\right)^2 - \mathbf{p}^2} - m_i, \tag{7.6}$$

such that we can rewrite the Hamiltonian as

$$H_i = \sqrt{m_i^2 + \mathbf{p}^2} + V_i(r,p) \equiv \sqrt{\left(m_i + U_i(r,p)\right)^2 + \mathbf{p}^2}. \tag{7.7}$$

In general, the potentials may depend on $r = (t, \mathbf{r})$ and $p = (p^0, \mathbf{p})$, i.e., time, position, energy and momentum. Additionally, they may depend on the phase-space densities of all other particle species and thus couple the BUU equations. Much more important, however, is the coupling through the collision term I_{coll} (see Section 7.6).

We can now introduce a spectral function by

$$\mathcal{A}_i(r,p) = \bar{g}_i^>(r,p) \mp \bar{g}_i^<(r,p), \tag{7.8}$$

and assume that there exits a function $f(\mathbf{r}, t, \mathbf{p})$ fulfilling

$$\bar{g}_i^<(r,p) = f_i(\mathbf{r}, t, \mathbf{p})\mathcal{A}_i(r,p), \tag{7.9}$$

$$\bar{g}_i^>(r,p) = \left(1 \pm f_i(\mathbf{r}, t, \mathbf{p})\right)\mathcal{A}_i(r,p), \tag{7.10}$$

which can be considered as a phase space distribution function. The upper (lower) sign holds for bosons (fermions). The structure of the spectral function is discussed in detail in Section 7.7.

7.3.2 Approximations

The BUU equation (7.1) is written in a general form and holds also for broad, i.e., unstable states and thus allows, e.g., to transport resonances [Leu00]. In this work, however, we do not solve the full problem of Eq. (7.1) but follow the lines of Effenberger [Eff99] and work with the so-called off-shell potential (OSP) ansatz which we introduce in detail in Section 7.8. Within this ansatz, we set $A_{\text{off-shell}} = 0$ in the BUU equation (7.1), so that its left side reads (for simplicity, we omit the particle-species index, i, from now on)

$$\begin{aligned}\left[p_0 - H, \bar{g}^<\right] &\overset{\text{Eq. (7.3)}}{=} \frac{\partial(p_0 - H)}{\partial p_\mu}\frac{\partial \bar{g}^<}{\partial x^\mu} - \frac{\partial(p_0 - H)}{\partial x_\mu}\frac{\partial \bar{g}^<}{\partial p^\mu} \\ &= \left[\left(1 - \frac{\partial H}{\partial p_0}\right)\frac{\partial}{\partial t} + \frac{\partial H}{\partial \mathbf{p}}\frac{\partial}{\partial \mathbf{r}} - \frac{\partial H}{\partial \mathbf{r}}\frac{\partial}{\partial \mathbf{p}} + \frac{\partial H}{\partial t}\frac{\partial}{\partial p^0}\right]\bar{g}^<(r,p). \quad (7.11)\end{aligned}$$

The BUU equation can be further simplified for the case of particles with vanishing or very small width. Then, the spectral function becomes a δ-function and after integration over p_0 one finds the BUU equation in on-shell approximation

$$\left[\frac{\partial}{\partial t} + \frac{\partial H}{\partial \mathbf{p}}\frac{\partial}{\partial \mathbf{r}} - \frac{\partial H}{\partial \mathbf{r}}\frac{\partial}{\partial \mathbf{p}}\right] f(\mathbf{r},t,\mathbf{p}) = -\Sigma^> f + \Sigma^<(1 \pm f). \quad (7.12)$$

This equation is the "standard BUU equation" widely used for simulations in nuclear physics. Basically, it is the classical Boltzmann equation with some modifications in the collision term for fermions added by Nordheim [Nor28] and later by Uehling and Uhlenbeck [UU33].

Setting the right hand side of the BUU equation (7.1) or (7.12) to zero, i.e., $I_{\text{coll}} = 0$, one obtains the so-called Vlasov equation which describes the phase-space evolution of particles in a mean field without collision term.

7.3.3 Test-particle ansatz

The next step is to solve the generalized BUU equation (7.1) with $A_{\text{off-shell}} = 0$ [see Eq. (7.11)] numerically. This can be achieved using the so-called test-particle ansatz, i.e., the continuous phase-space density is replaced by discrete test particles represented by δ-functions,

$$\bar{g}^<(\mathbf{r},t,p) = \lim_{n(t)\to\infty} \frac{(2\pi)^4}{N}\sum_{j=1}^{n(t)} \delta(\mathbf{r} - \mathbf{r}_j(t))\delta(\mathbf{p} - \mathbf{p}_j(t))\delta(p^0 - p_j^0(t)), \quad (7.13)$$

where $n(t)$ denotes the number of test particles at time t, and $\mathbf{r}_j(t)$ and $p_j(t)$ are the coordinates and the four-momenta of test particle j at time t. As the phase-space density changes in time due to both, collisions and the Vlasov dynamics, also the number of test particles changes throughout the simulation: in the collision term, test particles are deleted and new ones are created. At $t = 0$ we start with $n(0) = N \cdot A$ test particles where A is the number of physical particles and N is the number of ensembles (test particles per physical particle).

Combining the time derivative of Eq. (7.13) and the one obtained from Eq. (7.11), we find the equations of motion

$$\frac{\partial \mathbf{r}_j}{\partial t} = \left(1 - \frac{\partial H}{\partial p_0}\right)^{-1} \frac{\partial H}{\partial \mathbf{p}} \,, \tag{7.14}$$

$$\frac{\partial \mathbf{p}_j}{\partial t} = -\left(1 - \frac{\partial H}{\partial p_0}\right)^{-1} \frac{\partial H}{\partial \mathbf{r}} \,, \tag{7.15}$$

$$\frac{\partial p_j^0}{\partial t} = \left(1 - \frac{\partial H}{\partial p_0}\right)^{-1} \frac{\partial H}{\partial t} \,. \tag{7.16}$$

Within the so-called off-shell potential ansatz — discussed in detail in Section 7.8 — the Hamiltonian depends on p_0. Only then, the term $\partial H/\partial p_0$ remains. If $\partial H/\partial p_0 = 0$, Eqs. (7.14) and (7.15) are simply the Hamilton equations of motion which describe the propagation of the test particles between the collisions. Energy conservation is enforced by Eq. (7.16) when $\partial p_j^0/\partial t = 0$ if $\partial H/\partial t = 0$. Numerically, the Hamilton equations of motion are solved with a predictor-corrector algorithm.

7.4 Potentials

Besides medium modifications like Fermi motion and Pauli blocking (cf. Section 7.5) we include hadronic mean-field potentials and also a Coulomb potential.

7.4.1 Hadronic potentials

The relativistic single-particle Hamiltonian given by Eq. (7.5) includes a mean-field potential V_i for a particle of species i. The nucleon mean-field potential V_N, which describes many-body interactions of the nucleons, can be parametrized according to Welke *et al.* [WPK$^+$88] as a sum of a Skyrme term depending only on density and a momentum-dependent contribution of Yukawa-type interaction

$$V_N(\mathbf{p}, \mathbf{r}) = A\,\frac{\rho(\mathbf{r})}{\rho_0} + B\,\left(\frac{\rho(\mathbf{r})}{\rho_0}\right)^{\tau} + \frac{2C}{\rho_0}\int \frac{\mathrm{d}^3\mathbf{p}'}{(2\pi)^3}\frac{g\left(f_n(\mathbf{r},\mathbf{p}') + f_p(\mathbf{r},\mathbf{p}')\right)}{1 + \left(\frac{\mathbf{p}-\mathbf{p}'}{\Lambda}\right)^2} \,, \tag{7.17}$$

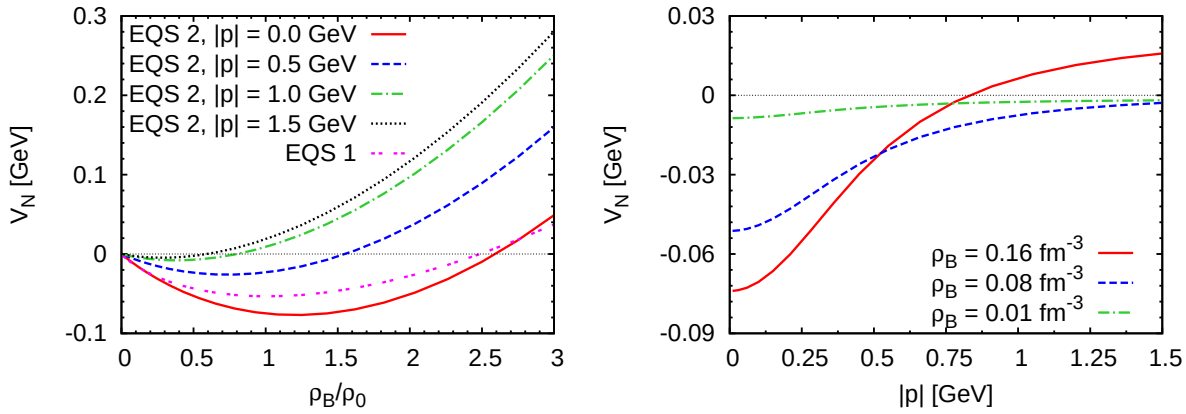

Figure 7.1: Left panel: density dependence of the nucleon mean-field potential for the sets EQS 2 (different momenta) and EQS 1. Right panel: momentum dependence of set EQS 2 for various densities.

Table 7.3: Parameter sets for the nuclear mean-field potential according to Eq. (7.17) as fitted by Teis [Tei97].

EQS	K [MeV]	A [MeV]	B [MeV]	C [MeV]	τ	Λ [fm^{-1}]
1	215	-287.0	233.7	0	1.23	-
2	290	-29.3	57.2	-63.5	1.76	2.13

with $\rho_0 = 0.168$ fm^{-3} and the spin degeneracy factor $g = 2$. Two parameter sets, used throughout this work, are given in Table 7.3. They were fitted to the saturation density of nuclear matter, and also to the momentum dependence of the nucleon-optical potential as measured in pA collisions [Tei97, TCE+97]. If not stated otherwise we use the set labeled EQS 2 which gives a medium momentum-dependent potential with a nuclear-matter compressibility of $K = 290$ MeV. For comparison, we also apply set 1 which yields a momentum-independent potential with $K = 215$ MeV. Their dependence on density and, in the case of EQS 2, on momentum are illustrated in Fig. 7.1.

Photon-nucleus scattering experiments indicate that the potential of the Δ resonance has a depth of about -30 MeV at ρ_0 [EW88, PLM98]. Comparing to a momentum-independent nucleon potential, which is approximately -50 MeV deep, the Δ potential is, therefore, approximated by

$$V_\Delta(\mathbf{p},\mathbf{r}) = \frac{2}{3}\, V_N(\mathbf{p},\mathbf{r}). \tag{7.18}$$

We assume for all spin 3/2 resonances the same potential as for the Δ resonance.

For all spin 1/2 and spin $> 3/2$ resonances we assume the same potential as for the nucleon.

7.4.2 Coulomb potential

The explicit treatment of the isospin degrees of freedom in our model requires that we include also the effect of the electromagnetic forces on charged particles. The Coulomb potential for a given charge distribution $\rho_c(\mathbf{r})$ is given by

$$\Phi(\mathbf{r}) = \int \mathrm{d}^3 r' \, \frac{\rho_c(\mathbf{r}')}{|\mathbf{r} - \mathbf{r}'|} \,, \tag{7.19}$$

however, for technical reasons, instead of the integral we solve the Poisson equation,

$$-\nabla^2 \Phi(\mathbf{r}) = 4\pi \rho_c(\mathbf{r}), \tag{7.20}$$

using the ADI algorithm discussed in detail in Appendix B of Ref. [Tei97].

7.5 Nuclear ground state

The BUU equation (7.1) is a first order differential equation in time, thus, to solve this equation, the phase-space distributions of all particle species need to be known at time $t = 0$. This concerns the initial distribution of the nucleons in the nucleus (nuclear ground state), but also the hadrons produced in the initial lepton-nucleon reaction. We now focus on the nuclear ground state and postpone the latter to Chapter 8.

7.5.1 Local Thomas-Fermi approximation

The phase-space density of the nucleons bound in a nucleus is treated within a local Thomas-Fermi (LTF) approximation, i.e., at each space point the nucleon momentum distribution is given by a Fermi sphere

$$f_{n,p}(\mathbf{r}, \mathbf{p}) = \Theta\left(p_F^{n,p}(\mathbf{r}) - |\mathbf{p}|\right). \tag{7.21}$$

with the radius in momentum space determined by the local Fermi momentum

$$p_F^{n,p}(\mathbf{r}) = (3\pi^2 \rho_{n,p}(\mathbf{r}))^{1/3}. \tag{7.22}$$

The normalization is chosen such that the particle density is retrieved by

$$\rho_{n,p}(\mathbf{r}) = g \int f_{n,p}(\mathbf{r}, \mathbf{p}) \, \frac{\mathrm{d}^3 \mathbf{p}}{(2\pi)^3} \,, \tag{7.23}$$

Table 7.4: Density parameters R_p, a_p for protons and R_n, a_n for neutrons used in Eqs. (7.27) and (7.28).

nucleus	R_p [fm]	a_p [fm]	R_n [fm]	a_n [fm]
^{12}C	1.692	1.082	R_p	a_p
^{16}O	1.833	1.544	1.815	1.529
^{56}Fe	3.971	0.5935	4.05	a_p

where $g = 2$ denotes the spin degeneracy factor. The single-particle phase-space density $f(\mathbf{r}, \mathbf{p})$ is then fully determined and the momentum density reads

$$n_{n,p}(\mathbf{p}) = g \int f_{n,p}(\mathbf{r}, \mathbf{p}) \frac{\mathrm{d}^3\mathbf{r}}{(2\pi)^3} \,. \tag{7.24}$$

with the normalization $\int \mathrm{d}^3\mathbf{p}\; n(\mathbf{p}) = A$.

In the LTF approximation, the Pauli blocking factor is given by

$$P_{\text{PB}}^{n,p}(\mathbf{r}, \mathbf{p}) = 1 - f_{n,p}(\mathbf{r}, \mathbf{p}) \,. \tag{7.25}$$

The Fermi energy reads

$$\epsilon_F = \sqrt{p_F^2 + M_N^2} - M_N + V_N(\mathbf{r}, p_F). \tag{7.26}$$

Provided that the density parameters are known, we can define the initial state for any nucleus. Later, we shall present results mainly for C, O and Fe nuclei. The density profiles $\rho(\mathbf{r}) = \rho(r)$ for ^{12}C and ^{16}O are parametrized in a harmonic oscillator form [NOGR93]

$$\rho_{n,p}(r) = \rho_0 \left[1 + a_{n,p} \left(\frac{r}{R_{n,p}}\right)^2\right] \exp\left[-\left(\frac{r}{R_{n,p}}\right)^2\right], \tag{7.27}$$

for ^{56}Fe a Fermi ansatz is used,

$$\rho_{n,p}(r) = \frac{\rho_0}{1 + \exp\left(\frac{r - R_{n,p}}{a_{n,p}}\right)} \,. \tag{7.28}$$

The parameters are collected in Table 7.4: the proton density is based on the compilation of Ref. [DJDVDV74] from electron scattering; the neutron density is provided by Hartree-Fock calculations.

In Fig. 7.2 we show the density and the Fermi momentum together with the mean-field potential and the resulting Fermi energy for ^{12}C, ^{16}O and ^{56}Fe as a function of the radius. The test particles are distributed in position and momentum space with

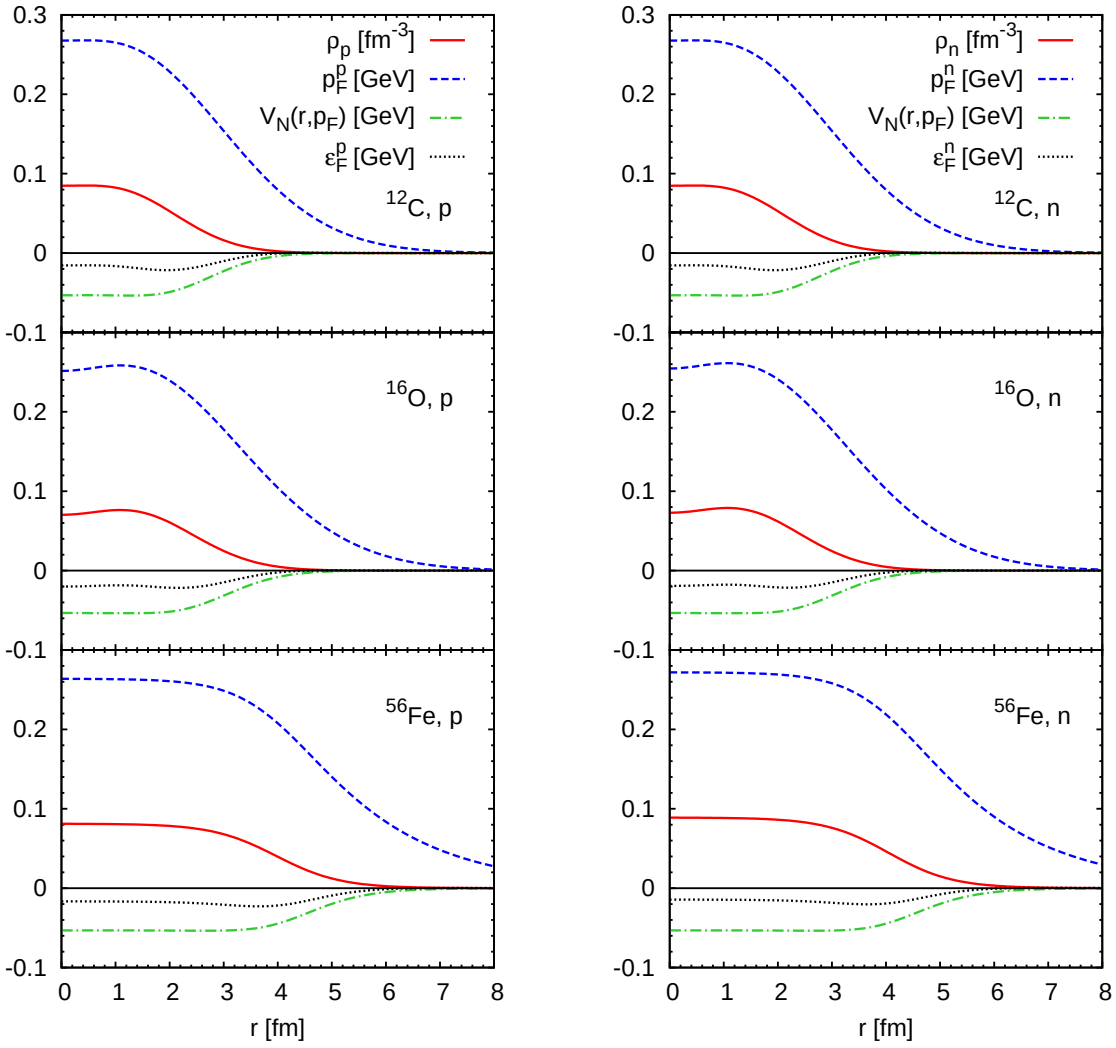

Figure 7.2: Density, Fermi momentum, mean-field potential and Fermi energy of protons (left panel) and neutrons (right panel) for ^{12}C, ^{16}O and ^{56}Fe as a function of radius.

the probabilities $4\pi r^2 \rho_p(r)$ and $4\pi p^2 n_p(p)$, respectively, which are plotted in Fig. 7.3. We emphasize that both distributions are not independent but strongly correlated: in Fig. 7.4 one observes that the probability $N(p,\rho)$ to find a nucleon with absolute momentum p in a nuclear environment of density ρ has a ridge structure. The low-momentum nucleons tend to sit at low densities while the high-momentum nucleons tend to sit at higher densities.

For comparison, we briefly introduce a model widely used in the literature (see

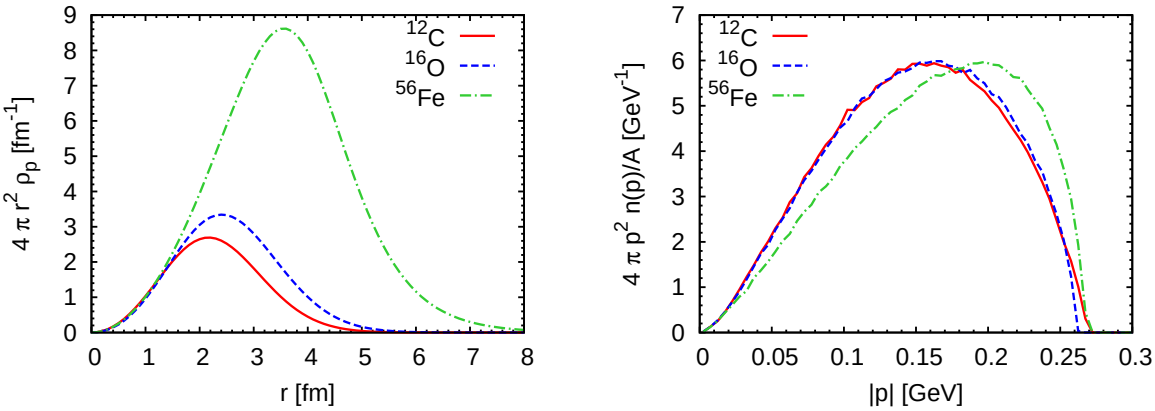

Figure 7.3: Radial (left panel) and momentum (right panel) density distribution of protons in ^{12}C, ^{16}O and ^{56}Fe.

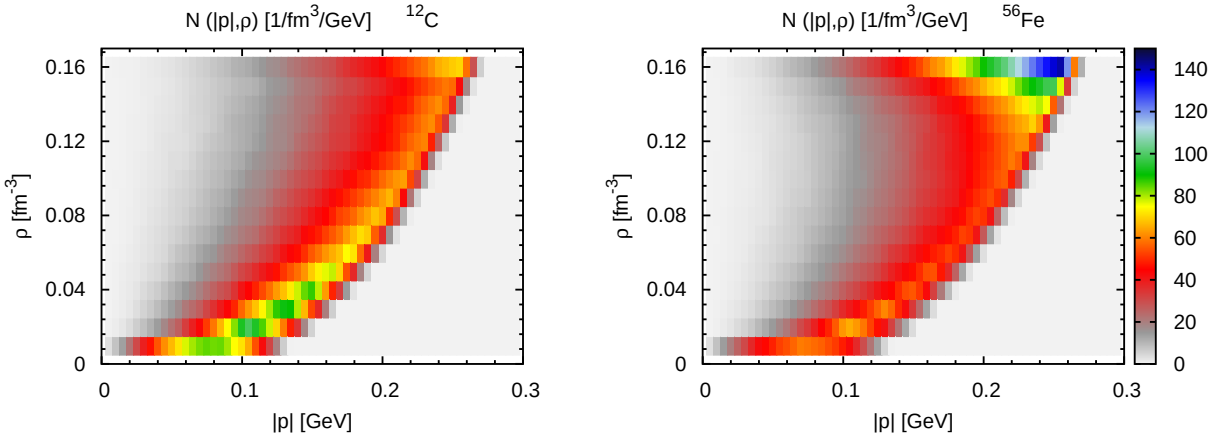

Figure 7.4: Probability density $N(|\mathbf{p}|, \rho)$ of finding a nucleon with absolute momentum $|\mathbf{p}|$ at a position with density ρ in ^{12}C (left panel) and ^{56}Fe (right panel).

also Section 12.2), the global Fermi gas model (GFG).[5] In this approach, the Fermi momentum is constant over the whole nucleus. With Eq. (7.22), also the density is constant and the nucleus is just a sphere of radius R with

$$f_{n,p}^{\mathrm{GFG}}(\mathbf{r},\mathbf{p}) = \Theta(R-r)\Theta\left(p_F^{n,p} - |\mathbf{p}|\right). \tag{7.29}$$

The probability to find a test particle of momentum p is then given by $4\pi p^2 n_p(p) \propto p^2\,\Theta\left(p_F^{n,p} - |\mathbf{p}|\right)$. Thus, the distribution peaks at p_F while it is less peaked in the LTF approach shown in the left panel of Fig. 7.3. Furthermore, $4\pi r^2\rho_p(r)$ and $4\pi p^2 n_p(p)$ are not correlated in the GFG model.

7.5.2 Ground-state stability

Finally, we address the problem of the ground-state stability discussed in detail in Section 3.2 of Effenberger's thesis [Eff99] and in the diploma thesis of Steinmüller [Ste07]. The density distributions of Eqs. (7.27) and (7.28) do not coincide with the ground-state density distribution according to the mean-field potential. The latter requires the ground state to be perfect spheres of constant density. This discrepancy leads to oscillations of the root-mean-square radius in time (cf., e.g., Figs. 3.2 and 3.6 in Ref. [Eff99]). Effenberger also showed that the influence on observables in photon-induced reactions is only minor. However, we circumvent this problem by working in the so-called "frozen approximation". This means that the test particles which define the initial particle distribution of the nucleus (the so-called "real particles") are not propagated and are not allowed to undergo any collisions — they are frozen. Thus, by definition, we obtain a stable ground state. This treatment is justified by the fact that in lepton-induced reactions at around 1 GeV beam energy the nucleus stays close to its ground state which means that its phase-space density almost stays constant during the simulation. Only the reaction products of the lepton-nucleon reactions are propagated and undergo final-state interactions. Those test particles and also their reaction products are called "pertubative particles", and they do not influence the nucleus phase-space density.[6]

7.6 Collision term

The BUU equations for the different particle species are coupled through the collision term I_{coll} (r.h.s. of Eq. (7.1)),

$$I_{\mathrm{coll}}(r,p) = -\Sigma^{>}(r,p)\bar{g}^{<}(r,p) + \Sigma^{<}(r,p)\bar{g}^{>}(r,p), \tag{7.30}$$

[5] We refer the reader to pages 133ff. of Ref. [Bus08] for an extended discussion and observable consequences.

[6] The concept of real and pertubative particles is explained, e.g., in Appendix B.1 of [Bus08].

which comprises all kinds of scattering processes among the particles. The first term, $-\Sigma^{>}(r,p)\bar{g}^{<}(r,p)$, describes the loss of particles (loss term) while $\Sigma^{<}(r,p)\bar{g}^{>}(r,p)$ describes the gain of strength (gain term) caused by scattering into the phase space element at point $(\mathbf{r},p)$ at time t. We account for one-body (i.e., resonance decay), two-body and three-body interactions, but neglect processes of higher order. This assumption is justified by the fact that in lepton-nucleus reactions — as just pointed out — the nucleus stays close to its ground state, in contrast to, e.g., heavy-ion collisions, and very high densities cannot be reached at which those many-body processes become may important [LBGM07].

7.6.1 Resonance decays

The one-body loss term describes the rate at which particles decay, and reads

$$\Sigma^{>,1} = 1/\tau = \Gamma, \tag{7.31}$$

where $\tau = 1/\Gamma$ is the resonance life time and Γ the decay width in the calculation frame. Thus, the loss term gives a probability that a certain test particle is absorbed, i.e., deleted from the simulation. Its possible decay products and their kinematics are determined with a Monte-Carlo method; these test particles are then added to the simulation and hereby preserve energy and the quantum numbers. Details on the algorithm are given, e.g., in Ref. [Bus08].

Decay widths

The properties of the 30 non-strange/non-charm resonances listed in Table 7.1 are, as outlined already in Section 7.2, taken from the analysis of Manley and Saleski [MS92]. They may decay into the following two-body final states: $N\pi$, $N\eta$, ΛK, $N\omega$, $\Delta\pi$, $N\sigma$, $N\rho$, $P_{11}(1440)\pi$ and $\Delta\rho$. Any decay into more than two particles, e.g., $R \to N\pi\pi$, is treated as a two-step process, e.g., $R \to N\rho \to N\pi\pi$. The energy dependence of the vacuum-decay widths, also taken from Manley and Saleski, is given by

$$\Gamma_{R\to ab}(W) = \Gamma^0_{R\to ab}\frac{\rho_{ab}(W)}{\rho_{ab}(M_R)}\,, \tag{7.32}$$

where $\Gamma^0_{R\to ab}$ is the decay width of the resonance R into the final state ab at the pole (given in Table 7.1). W is the invariant mass of the resonance and M_R its pole mass. ρ_{ab} is given by

$$\rho_{ab}(W) = \int \mathrm{d}p_a^2\,\mathrm{d}p_b^2\,\mathcal{A}_a(p_a)\mathcal{A}_b(p_b)\,\frac{p_{ab}}{W}\,B^2_{l_{ab}}(p_{ab}R)\mathcal{F}^2_{ab}(W). \tag{7.33}$$

$\mathcal{A}_{a,b}$ are the vacuum spectral functions of the final-state particles a, b (δ-function for stable final-state particles), p_{ab} is the cm momentum of the particles a and b, l_{ab} the relative angular momentum, and $R = 1\,\mathrm{fm}$ an interaction radius. $B^2_{l_{ab}}$ is a Blatt-Weisskopf barrier-penetration factor given by

$$B_0(x) = 1, \tag{7.34}$$

$$B_1(x) = \frac{x}{(1+x^2)^{1/2}}\,, \tag{7.35}$$

$$B_2(x) = \frac{x^2}{(9+3x^2+x^4)^{1/2}}\,, \tag{7.36}$$

$$B_3(x) = \frac{x^3}{(225+45x^2+6x^4+x^6)^{1/2}}\,. \tag{7.37}$$

Thus, the partial widths have the proper analytic threshold behavior, i.e., $\sim p_{ab}^{2l_{ab}+1}$. In the work of Buss [Bus08] (cf., in particular his Sections 3.2.2 and 3.7), the form factor $\mathcal{F}_{ab}(W)$ has been introduced for decays into non-stable particles ($\mathcal{F}_{ab}(W) = 1$ for stable final states) to prevent the arbitrarily growing of the widths at large invariant masses W. This became necessary for calculating the self energies with dispersion relations.

7.6.2 Two-body collisions

The two-body contribution to the collision term includes both gain and loss terms describing the scattering into and out of a certain phase-space element. Considering, e.g., the two-body process at point $\mathbf{r}$,

$$A(p_A)\; B(p_B) \longrightarrow a(p_a)\; b(p_b), \tag{7.38}$$

the phase-space density decreases at $(\mathbf{r}, p_A)$ and $(\mathbf{r}, p_B)$ while it increases around $(\mathbf{r}, p_a)$ and $(\mathbf{r}, p_b)$. The loss and gain terms are given by

$$\begin{aligned} I_{\text{2-body, loss}}(\mathbf{r},t,p_A) &= -\Sigma^{>,2}(\mathbf{r},t,p_A)\bar{g}^{<}(\mathbf{r},t,p_A) \\ &= -\int \frac{\mathrm{d}^4 p_B}{(2\pi)^4} \int \mathrm{d}\Omega_{\text{cm}} \frac{\mathrm{d}\sigma_{AB\to ab}}{\mathrm{d}\Omega_{\text{cm}}}\; v_{AB}\;\; \bar{g}^{<}(\mathbf{r},t,p_B)\bar{g}^{<}(\mathbf{r},t,p_A) P_a P_b \end{aligned} \tag{7.39}$$

and

$$\begin{aligned} I_{\text{2-body, gain}}(\mathbf{r},t,p_A) &= \Sigma^{<,2}(\mathbf{r},t,p_A)\bar{g}^{>}(\mathbf{r},t,p_A) \\ &= \int \frac{\mathrm{d}^4 p_a}{(2\pi)^4} \frac{\mathrm{d}^4 p_b}{(2\pi)^4} (2\pi)^3 \frac{\mathrm{d}\sigma_{ab\to AB}}{\mathrm{d}^4 p_A}\; v_{ab}\; \bar{g}^{<}(\mathbf{r},t,p_a)\; \bar{g}^{<}(\mathbf{r},t,p_b) P_A P_B, \end{aligned} \tag{7.40}$$

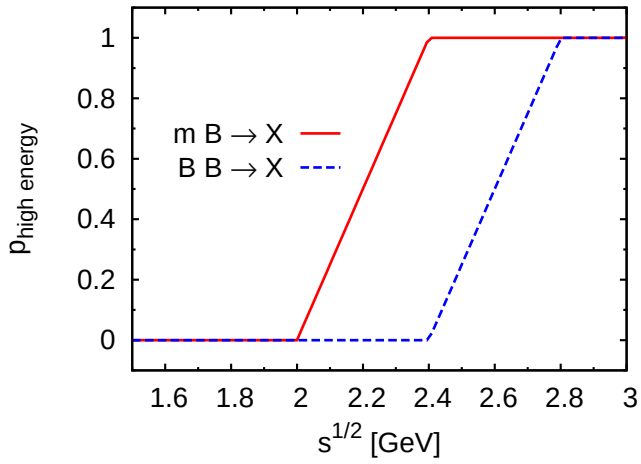

Figure 7.5: Probability that a high-energy event is simulated with PYTHIA for meson-baryon (solid) and baryon-baryon scattering (dashed line) as a function of $\sqrt{s}$.

with the angular- and the momentum-differential cross sections $\mathrm{d}\sigma_{AB\to ab}/\mathrm{d}\Omega_{\mathrm{cm}}$ and $\mathrm{d}\sigma_{ab\to AB}/\mathrm{d}^4p_A$ for the processes $AB \to ab$ and $ab \to AB$, respectively. v_{AB} and v_{ab} are the relative velocities of the scattering partners AB and ab.

The Pauli principle forbids scattering of fermions into occupied states, leading to factors of $P_X = 1 - f(\mathbf{r}, \mathbf{p}_X, t)$ with $X = A, B, a, b$. In the case of bosons, scattering into occupied states is allowed, leading to factors of $P_X = 1 + f(\mathbf{r}, \mathbf{p}_X, t)$. Besides Pauli blocking and Fermi motion, the hadronic potentials also affect the collision rates and have to be accounted for (cf. Section 3.5 in Ref. [Bus08]).

Cross section model

Our model for the two-body cross sections entering the collision term above is based on two pillars: at low energies up to center of mass energies of $\sqrt{s} \approx 2.4\,\mathrm{GeV}$ resonance contributions and a small non-resonant background are most important. At higher energies, hard scattering processes described by pertubative QCD dominate the interaction. In our model they are simulated with the help of PYTHIA which is based on the Lund string model (for details cf. Refs. [FCGM04, GF05]). To prevent a sharp cut between the low and the high energy treatment of the cross sections, K. Gallmeister has introduced a smooth transition using a Monte-Carlo decision on the probability for a high energy event [Galb]. This probability function is shown in Fig. 7.5 for both meson-baryon and baryon-baryon scattering. Instead of having a sharp step, the probability increases linearly in an interval of 0.4 GeV. More relevant at the energies considered in this thesis are the low-energy cross section treated in the resonance model which we discuss in the following.

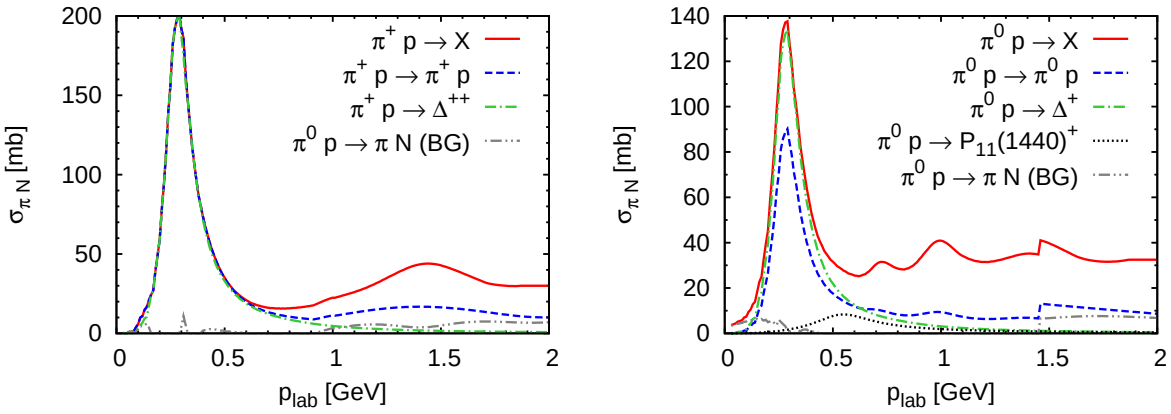

Figure 7.6: Cross sections for $\pi^+ p \to X$ (left panel) and $\pi^0 p \to X$ (right panel) as function of $p_{\rm lab}$.

Meson-baryon scattering. Meson-baryon cross sections are implemented by means of a resonance model, i.e., reactions of the type $mB \to R$ which are added incoherently.[7] Interactions are possible between all particles. The resonance cross sections have been derived in detail in Chapter 2.4 of Ref. [Eff99] and are not repeated here. Furthermore, a small non-resonant background has been introduced and fitted so that we reach agreement with data or reliable models. Details on the extraction and a full list of all included background channels are given in Appendix A.3 of Ref. [Bus08].

As an example, we show in Fig. 7.6 the cross sections for πN scattering. The total cross sections are shown by the solid lines, while the elastic contributions, i.e.,

$$\sigma_{\pi N \to \pi N} = \sum_R \sigma_{\pi N \to R \to \pi N} + \sigma^{\rm BG}_{\pi N \to \pi N} \,, \tag{7.41}$$

are shown by the dashed lines. In addition, the non-resonant background contributions and the scattering into the two lowest resonances are plotted.

Baryon-baryon scattering. In the GiBUU model, cross sections for the following reactions have been implemented: $NN \leftrightarrow NN$, $NN \leftrightarrow NR$, $NR \leftrightarrow NR'$, $NN \leftrightarrow \Delta\Delta$ and a non-resonant background to $NN \to NN\pi$. The explicit expressions are collected in Appendix A.2 of Ref. [Bus08] — here we focus on the channels that are relevant to this work.

The parametrization for the $NN \to NN$ cross section is taken from Cugnon *et al.* [CVL96]. At low $p_{\rm lab}$ it has been modified by A. Larionov [Lar] to improve the correspondence with the data. The cross sections $pn \to pn$, $nn \to nn$ and $pp \to pp$ are plotted as a function of $p_{\rm lab}$ in Fig. 7.7.

[7] Detailed balance requires that the cross sections for $mB \to R$ are consistent with the ones for $R \to mB$.

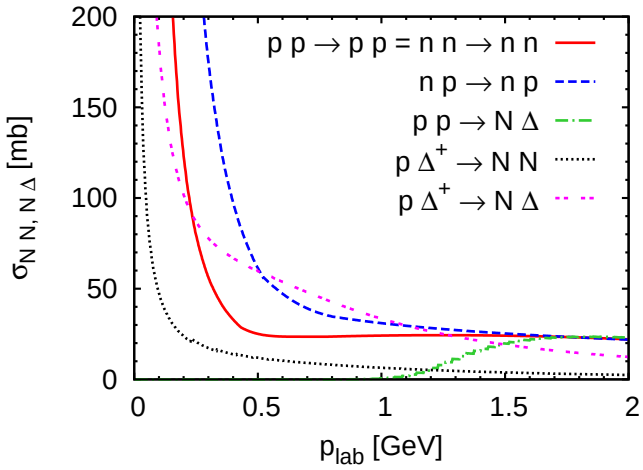

Figure 7.7: Cross sections for $NN \to X$ and $N\Delta \to X$ as indicated in the plot as function of p_{lab}.

The $NN \to N\Delta$ cross section is based on a model by Dmitriev *et al.* [DSG86] and the result is also shown in Fig. 7.7. For the inverse reaction, $N\Delta \to NN$, and for the process $N\Delta \to N\Delta$ the GiBUU model includes two options. One choice is to use again a one-pion exchange model similar to that of Dmitriev *et al.* [DSG86]; the outcome is plotted in Fig. 7.7. However, if one chooses to use the Oset prescription for the in-medium width of the Δ (cf., Section 7.7), then for consistency, also the cross sections for $N\Delta \to NN$ and $N\Delta \to N\Delta$ are evaluated based on the model of Oset *et al.* [OS87]. If not stated otherwise, the Oset model is used as our default. Full details on both options are given on pages 193–200 in Ref. [Bus08].

Meson-meson scattering. Meson-meson interactions are also included in the simulation [WLM05] but are negligible for lepton-nucleus scattering under investigation in this work.

Numerical implementation

Numerically, the BUU equation can be solved, e.g., by using the so-called parallel or full ensemble method both described in Section 2.5 of Ref. [Bus08]. They differ in the locality of the scattering processes. In the parallel ensemble method, all test particles are subdivided into groups (ensembles), where the number of test particles in each ensemble equals the number of physical particles. Only particles of the same ensemble are allowed to collide; the mean field is averaged over all ensembles. While this method is numerically simpler and faster (and therefore commonly used in many approaches), it does not converge to the exact solution — in the BUU equation, the

interactions are local in space-time — in the limit of a large number of test particles. The exact solution is resembled within the full ensemble method, where collisions between all test particles are allowed. This method is numerically very demanding. An approximation to the full ensemble method is the so-called local ensemble method which is used throughout this work.

7.6.3 Three-body collisions

Two three-body processes are considered in GiBUU: $NN\pi \to NN$ and $NN\Delta \to NNN$. The matrix element for the former is obtained via detailed balance from the $NN \to NN\pi$ cross section, and the latter is based on the model of Oset *et al.* [OS87].

7.7 Spectral functions and self energies

7.7.1 Formalism

The spectral function — introduced in Eq. (7.8) — is given by

$$\mathcal{A}(p,r) = \frac{1}{\pi} \frac{-\operatorname{Im}\Pi(p,r)}{\left(p^2 - m^2 - \operatorname{Re}\Pi(p,r)\right)^2 + \left(\operatorname{Im}\Pi(p,r)\right)^2}\,, \tag{7.42}$$

with the four-momentum p and the self energy $\Pi(p,r) = \Pi(p_0, \mathbf{p}, r)$. In the medium, Π depends on p_0 and $\mathbf{p}$ separately.

The vacuum spectral function of a stable particle is — due to the vanishing width — simply a δ-function situated at its pole mass m. Unstable particles, however, have a finite lifetime and therefore a non-vanishing width. In the nuclear medium, the lifetime of all particles is affected by collisions leading to an additional width, or, in other words, to modifications of the imaginary part of the self energy Π. Thus, the imaginary part of the self energy is closely connected to the collision term and therefore to the width by

$$\begin{aligned} \operatorname{Im}\Pi &= -\sqrt{p^\mu p_\mu}\left(\Sigma^> - \Sigma^<\right) \\ &= -\sqrt{p^\mu p_\mu}\,\Gamma_{\text{med}}. \end{aligned} \tag{7.43}$$

To deduce $\operatorname{Im}\Pi$ of a particle in the medium, we have to consider the modification of its free decay width due to Pauli blocking of the final-state nucleons and the collisional broadening due to its interactions with the surrounding nucleons. Both contributions sum up to the in-medium width Γ_{med}. In the medium, the spectral function peaks at

$$p^2_{\text{pole}} = m^2_{\text{pole}} = m^2 + \operatorname{Re}\Pi(p_0, \mathbf{p}, \mathbf{r}), \tag{7.44}$$

and is thus centered at a mass different from its vacuum pole mass m. The real part can be calculated via dispersion relations where a mean-field contribution can also be included using a subtraction constant. Both, real and imaginary part of the self energy are discussed in the following.

The spectral function is normalized as

$$\int_0^\infty \mathrm{d}p^2 \mathcal{A}(p,r) = 1. \tag{7.45}$$

For the spectral function of the initial-state nucleons, we consider only the real part of the self energy generated by the mean-field potential and neglect the small imaginary part. We further neglect the self energies of all mesons.

Imaginary part

To estimate the collisional broadening of a particle with momentum $\mathbf{p}$ and energy p_0, we employ the low-density approximation

$$\Gamma_{\mathrm{coll}}(p_0,\mathbf{p},\mathbf{r}) = g \sum_{i=n,p} \int f_i(\mathbf{p}',\mathbf{r}) \sigma_i(p_0,\mathbf{p},\mathbf{p}') v_{\mathrm{rel}}(p_0,\mathbf{p},\mathbf{p}') \ \mathrm{d}^3\mathbf{p}'. \tag{7.46}$$

Here, the variable v_{rel} denotes the relative velocity of the regarded particle and a nucleon with momentum $\mathbf{p}'$; the nucleon phase-space densities f_i have been introduced in Eq. (7.21). The total nucleon-particle scattering cross sections σ_i are chosen according to the GiBUU collision term discussed in Section 7.6. Thus, the collisional width Γ_{coll} accounts for additional decay channels of the particle inside the nucleus.

Let us take the Δ resonance as an example: besides its usual decay, $\Delta \to \pi N$, there are also two-body and three-body interaction mechanisms in the nuclear medium such as $\Delta N \to \Delta N$, $\Delta N \to NN$ or $\Delta NN \to NNN$. On the other hand, the medium width is decreased by Pauli blocking. While the nucleons inside the nucleus are constrained to have momenta below the Fermi momentum, there is no such constraint for the production of the Δ resonances. Their decay, however, is influenced by Pauli blocking, e.g., a Δ decaying into a pion-nucleon pair is Pauli blocked if the resulting nucleon's momentum is lower than the Fermi momentum.

Altogether, the imaginary part of the self energy in the rest-frame of the particle is given by

$$\mathrm{Im}\,\Pi(p_0,\mathbf{p},\mathbf{r}) = -\sqrt{p^2}\left\{\Gamma_{\text{free,Pauli blocked}}\left(p_0,\mathbf{p},\mathbf{r}\right) + \gamma\Gamma_{\mathrm{coll}}\left(p_0,\mathbf{p},\mathbf{r}\right)\right\}, \tag{7.47}$$

so that

$$\Gamma_{\mathrm{med}} = \Gamma_{\text{free,Pauli blocked}} + \gamma\Gamma_{\mathrm{coll}}\,. \tag{7.48}$$

γ denotes the boost factor from the nucleus rest-frame to the particle rest-frame (details are given in Ref. [Bus08]). The vacuum decay widths Γ_{free} are listed in Section 7.6.1. If the invariant mass of the particle is less than the mass of its lightest decay products, then $\Gamma_{\text{free}} = 0$.

Real part

Since the self energy is an analytic function of p_0, we can use dispersion relations to deduce the off-shell behavior of the real parts from the imaginary part. We apply a once-subtracted dispersion relation with the energy at the pole, given by Eq. (7.44),

$$p_0^{\text{pole}} = \sqrt{\mathbf{p}^2 + m^2 + \text{Re}\,\Pi(p_0^{\text{pole}}, \mathbf{p}, \mathbf{r})}\,, \tag{7.49}$$

as a subtraction point. This yields

$$\text{Re}\,\Pi(p_0, \mathbf{p}, \mathbf{r}) = \text{Re}\,\Pi(p_0^{\text{pole}}, \mathbf{p}, \mathbf{r}) + \frac{p_0 - p_0^{\text{pole}}}{\pi}\, \wp \int_{-\infty}^{\infty} \mathrm{d}p_0' \frac{\text{Im}\,\Pi(p_0', \mathbf{p}, \mathbf{r})}{(p_0' - p_0^{\text{pole}})(p_0' - p_0)} + \text{Re}\ C_\infty. \tag{7.50}$$

In line with Lehr *et al.* [LLLM02, Leh03], we demand that the in-medium shift of the on-shell energy is determined by the mean fields, so that

$$p_0^{\text{pole}} = \sqrt{\mathbf{p}^{\,2} + (m + U(\mathbf{p}, \mathbf{r}))^2}\,, \tag{7.51}$$

with the scalar potential U defined in Eq. (7.6). Consequently, the non-dispersive contribution to $\text{Re}\,\Pi$ is given by

$$\text{Re}\,\Pi(p_0^{\text{pole}}, \mathbf{p}, \mathbf{r}) = 2mU(\mathbf{p}, \mathbf{r}) + U(\mathbf{p}, \mathbf{r})^2\,. \tag{7.52}$$

In the numerical realization, we approximate the dispersion integral (7.50) for $\text{Re}\,\Pi$ by [Bus08]

$$\begin{aligned}\text{Re}\,\Pi(p_0, \mathbf{p}, \mathbf{r}) = \text{Re}\,\Pi(p_0^{\text{pole}}, \mathbf{p}, \mathbf{r}) + \frac{p_0 - p_0^{\text{pole}}}{\pi} \times \\ \wp \left(\int_{E_{\text{min}}}^{E_1} \mathrm{d}p_0' \frac{\text{Im}\,\Pi(p_0', \mathbf{p}, \mathbf{r})}{(p_0' - p_0^{\text{pole}})(p_0' - p_0)} + \int_{E_1}^{E_2} \mathrm{d}p_0' \frac{\text{Im}\,\Pi(p_0', \mathbf{p}, \mathbf{r})}{(p_0' - p_0^{\text{pole}})(p_0' - p_0)} \frac{E_2 - p_0'}{E_2 - E_1} \right)\end{aligned} \tag{7.53}$$

with the cutoff parameters $E_1 = 5\,\text{GeV}$ and $E_2 = 7\,\text{GeV}$. E_{min} is determined by the mass of the lightest decay product of the particle. The dependence of the results on the cutoffs has been investigated in Ref. [Bus08] and only a marginal impact has been found. The whole procedure guarantees analytical self energies and, therefore, normalized spectral functions.

7.7.2 Numerical implementation

Evaluating the imaginary and real parts for all non-strange baryons is numerically a highly demanding task — the integral for the collisional widths, Eq. (7.46), is calculated using a Monte-Carlo method — and cannot be performed during run time. Thus, we tabulated them on a multi-dimensional grid as a function of proton and neutron density, mass and absolute three-momentum assuming that the nuclear phase-space density is in its ground state during all the process. The advantage is a fast access to the in-medium width at the cost of a large memory need.[8]

7.7.3 Results and discussion

Nucleon

For the calculation of Γ_{coll} in Eq. (7.46), we assume — since the *off-shell* NN cross sections are not known — that the cross sections are independent of the nucleon mass (see page 95 for the implemented cross sections). Consequently, also Γ_{coll} depends only on density and the absolute momentum, but not on the mass. The left panel of Fig. 7.8 shows the collisional width as a function of momentum for various densities. The threshold is determined by Pauli blocking: collisions are forbidden when $p_{\text{lab}} < p_F(\rho) \propto \rho^{1/3}$ (see (Eq. (7.22)) and the width vanishes below the Fermi momentum. Increasing p_{lab} from threshold to the kink seen in the curves, one slowly overcomes Pauli blocking. At even larger momentum, the width is approximately linear in density, or, in other words, it scales with the number of scattering partners.

The right panel of Fig. 7.8 visualizes the spectral function of the nucleon according to Eq. (7.42) as a function of its energy for different momentum cuts and a fixed density of $\rho = 0.16\,\text{fm}^{-3}$. The spectral function broadens for larger momenta caused by the increasing width. The norm differs from unity only at the 1% level as can be seen from Table 7.5 where the normalization is given for some momenta at $\rho = 0.16\,\text{fm}^{-3}$.

Δ resonance

As already indicated in Section 7.6.2, we have included two different approaches to the in-medium width of the Δ. Within the first one (in the following denoted as "one-pion exchange approach") we evaluate the imaginary part of the self energy using the $\rho\sigma v$ ansatz as in Eq. (7.46), and the ΔN cross sections are calculated in the one-pion exchange model as outlined in Section 7.6.2. The real parts are then determined via Eq. (7.53). We obtain a good normalization within a few percent (cf., the second line

[8] Roughly 1 GB of memory is needed for the grids.

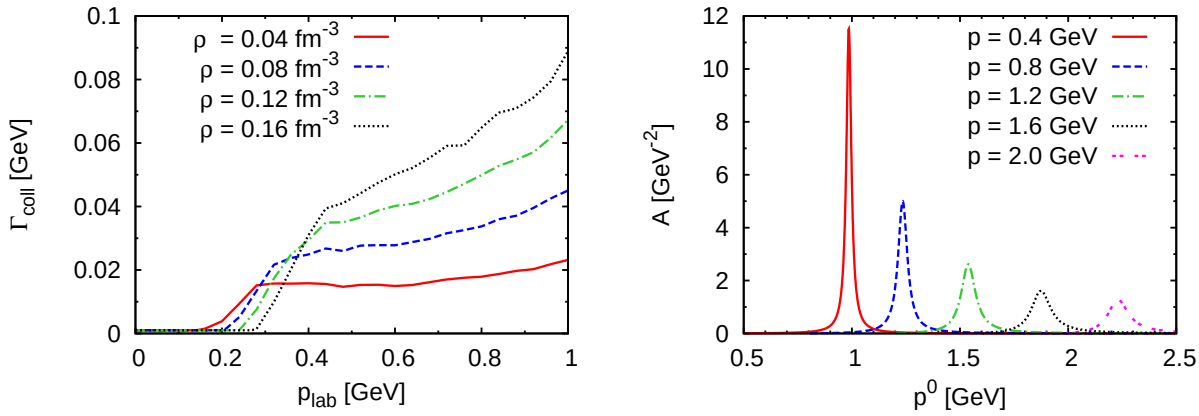

Figure 7.8: Left panel: collisional width of the nucleon vs. its momentum for different nuclear densities. Right panel: resulting nucleon spectral function as a function of its energy for different fixed momenta at $\rho = 0.16\,\mathrm{fm}^{-3}$.

Table 7.5: Normalization of the nucleon and Δ spectral functions at various momenta for $\rho = 0.16\,\mathrm{fm}^{-3}$. For the Δ resonance, we show the results for both the one-pion exchange based and the Oset parametrization of the width.

	$\int_0^\infty \mathrm{d}p^0 2p^0 \mathcal{A}(p^0, \mathbf{p})$				
$\lvert\mathbf{p}\rvert =$	0.2 GeV	0.4 GeV	0.6 GeV	0.8 GeV	1.0 GeV
nucleon	1.000	0.999	0.995	0.994	0.994
$P_{33}(1232)$ (1π-ex. approach)	0.975	0.974	0.975	0.977	0.981
$P_{33}(1232)$ (Oset approach)	0.952	0.911	0.879	0.868	0.868

in Table 7.5). The missing strength is caused by our finite integration interval — we integrate up to $M_{\max} = 10.5\,\text{GeV}$.

The second approach, which we will call "Oset approach", is based on the model of Oset and Salcedo [OS87]. They evaluate the Δ self energy in the nuclear medium using a many-body expansion in terms of ph and Δh excitations. Quasielastic corrections, two-body and three-body absorption is included. The latter two are roughly similar in size. However, this model is only applicable to lower energies up to $T_\pi \approx 0.35\,\text{GeV}$ where T_π is the kinetic energy of the pion which creates the Δ in an $N\pi$ collision. In our implementation, we use the parametrization given in their Eq. (4.4) up to $T_\pi = 0.45\,\text{GeV}$, and then "freeze" the width at this value. Therefore, the dispersion integrals needed for the determination of the real part cannot be evaluated, so that the real parts are given solely by the mean fields. This then leads to normalization errors as indicated in the last line in Table 7.5. For the above reasons, the integration interval extends only up to $M_{\max} = 2.5\,\text{GeV}$.

It has been shown by Effenberger [Eff99] and later by Buss [Bus08] that the numerical outcome of both approaches differs (cf., in particular, Fig. 4.3 in Ref. [Eff99] and left panel of Fig. 3.3 in Ref. [Bus08]). Qualitative agreement is found for the two-body contribution, $\Delta N \to NN$, with differences of the order of 25%. The three-body channel, $\Delta NN \to NNN$ is completely missing in the one-pion exchange approach for the in-medium width. The major disagreement, however, comes from the quasielastic term ($\Delta N \to \Delta N$) which is the dominating contribution in the one-pion exchange approach. This problem has been investigated further in Ref. [Bus08] (see right panel of his Fig. 3.3 and the discussion) by comparing different choices for calculating the $\Delta N \to \Delta N$ cross section. In former code versions, as, e.g., described in Effenberger's thesis [Eff99], this cross section has been replaced by the one for $NN \to NN$ which leads to a much smaller contribution in the collisional width. However, the large difference between the Oset approach and our simple 1π-exchange model tree-level ansatz for $\Delta N \to \Delta N$ is not yet understood and has to be further investigated.

In Fig. 7.9 we compare the resulting collisional widths of both approaches. In the left panel, we keep the mass W fixed and vary the absolute momentum, and vice versa in the right panel. We have chosen two representative values: in the left panel, W is close to the Δ pole, while $|\mathbf{p}| = 0.6\,\text{GeV}$ is a characteristic value which can be reached in lepton-nucleus scattering (compare also Fig. B.3). Overall, the BUU approach leads to smaller widths at low momentum and mass than the Oset approach — which is constant in $|\mathbf{p}|$ — caused in particular by the larger $\Delta N \to NN$ contribution of Oset and Salcedo. The opposite behavior is found at high momentum/mass where the BUU approach is dominated by the $\Delta N \to \Delta N$ contribution.

The impact of the choice of the Δ in-medium width on observables in lepton-nucleus scattering will be investigated in Chapters 9, 10 and 11 for inclusive cross sections, pion production and nucleon knockout.

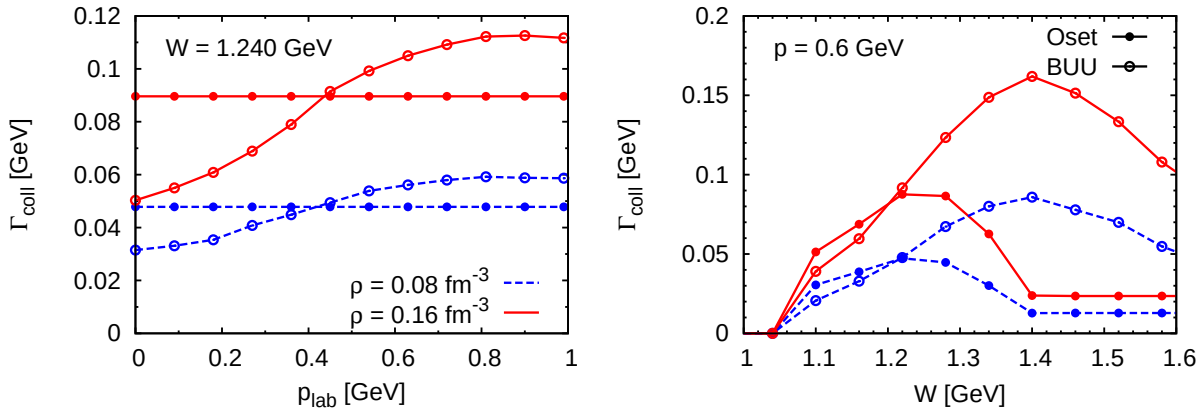

Figure 7.9: Collisional width of the Δ resonance as a function of momentum for $W = 1.240\,\text{GeV}$ (left panel) and as a function of invariant mass for $|\mathbf{p}| = 0.6\,\text{GeV}$ (right panel), respectively. The solid (dashed) lines stand for a density of $\rho = 0.16\,\text{fm}^{-3}$ ($\rho = 0.08\,\text{fm}^{-3}$). The filled circles denote the results obtained with the Oset model while the open circles stand for the one-pion exchange approach.

Table 7.6: Normalization of the spectral functions for the $P_{11}(1440)$, the $D_{13}(1520)$ and the $S_{11}(1535)$ resonances at various momenta for $\rho = 0.16\,\text{fm}^{-3}$.

	$\int_0^\infty \mathrm{d}p^0 2p^0 \mathcal{A}(p^0, \mathbf{p})$				
$\lvert\mathbf{p}\rvert =$	0.2 GeV	0.4 GeV	0.6 GeV	0.8 GeV	1.0 GeV
$P_{11}(1440)$	0.972	0.975	0.976	0.979	0.981
$D_{13}(1520)$	0.987	0.989	0.989	0.990	0.992
$S_{11}(1535)$	0.982	0.985	0.984	0.986	0.988

Other baryonic resonances

The in-medium width of all other non-strange/non-charm baryonic resonances is implemented in the same way as for the nucleon and the Δ resonance using the GiBUU collision term. The normalization is fulfilled at the 1-3% level as seen from Table 7.6. Overall, we find that the collisional width causes a broadening of the spectral functions (cf., e.g., Fig. 3.6 in Ref. [Bus08]).

Table 7.7: Normalization of the vacuum spectral functions for the nucleon, the $P_{33}(1232)$, the $P_{11}(1440)$, the $D_{13}(1520)$ and the $S_{11}(1535)$ resonances at $\rho = 0$.

	$\int_0^\infty \mathrm{d}p^2 \mathcal{A}^{\mathrm{noColl}}(p,r)$
nucleon	1.000
$P_{33}(1232)$	1.112
$P_{11}(1440)$	0.935
$D_{13}(1520)$	1.097
$S_{11}(1535)$	1.061

7.7.4 Approximations

Neglecting collisional broadening, we can approximate the in-medium spectral function, $\mathcal{A}$, defined in Eq. (7.42) by

$$\mathcal{A}(p,r) \to \mathcal{A}^{\mathrm{noColl}}(p,r) = \frac{\sqrt{p^2}}{\pi} \frac{\Gamma(p)}{(p^2 - (m + U(p,r))^2)^2 + p^2\Gamma^2(p)} \,, \tag{7.54}$$

with the vacuum width Γ given in Section 7.6.1. The vacuum spectral function of the nucleon is a δ-function; however, for numerical reasons, we replace this δ-function by a Breit-Wigner distribution of vanishing width

$$\mathcal{A}_N^{\mathrm{noColl}}(p,r) = \lim_{\Gamma \to 0} \frac{\sqrt{p^2}}{\pi} \frac{\Gamma}{(p^2 - (m + U(p,r))^2)^2 + p^2\Gamma^2} \,. \tag{7.55}$$

We choose $\Gamma = 1\,\mathrm{MeV}$ and have checked that the observables are not sensitive to the choice of Γ if it is small enough.

These expressions have already been applied to calculate the neutrino-induced resonance excitation off the nucleon, i.e., at $\rho = 0$ (see Eq. (3.9) on page 28). Table 7.7 indicates that the normalization is fulfilled at a 10% level.

7.8 Off-shell transport

We have seen in the previous section, that particles in the medium have a finite life time due to collisional broadening even if they are stable in the vacuum. We have also seen that the spectral functions depend on $\rho(\mathbf{r})$ and p, i.e., they change over the nuclear volume, e.g., when going from high- to low-density regions. Therefore, one must ensure that particles leaving the nucleus have returned to their vacuum pole mass (in case they are stable in the vacuum as the nucleon) or to their free spectral function (for baryonic resonances for example). This immediately raises the question

of how to propagate broad states. Up to now the propagation of the test particles via Eqs. (7.14)-(7.16) is only influenced by the mean fields but unaffected by $\mathrm{Im}\,\Pi$ since we neglected $A_{\text{off-shell}}$ in Eq. (7.1).

In this section, we present an ansatz based on an "educated guess" by Mosel and Effenberger [EM99, Eff99] which restores proper off-shell propagation without the need of solving the generalized BUU equation — the so-called off-shell potential ansatz (OSP). The full solution is an highly advanced task and has been addressed for example in Refs. [Leu00, EM99, Eff99, CJ00, Leh03].

7.8.1 Off-shell potential method

To introduce the OSP method we start by defining the offshellness (or off-shell potential), $\Delta\mu_j$, of the jth test particle by

$$\sqrt{p_j^2} = m + U + \Delta\mu_j \,, \tag{7.56}$$

where m is the pole mass of the particle species under consideration and U the scalar potential.[9] Thus, $m + U$ corresponds to the in-medium pole mass $(m+U)^2 = m^2 + \mathrm{Re}\,\Pi$ (compare Eq. (7.49) and Eq. (7.51)) and, consequently, $\Delta\mu_j$ is a measure of how far the test particle mass $\sqrt{p_j^2}$ is off the pole $m + U$. Rewriting Eq. (7.56) yields for the energy of the test particle

$$p_j^0 = \sqrt{(m + U + \Delta\mu_j)^2 + \mathbf{p}^2} \,. \tag{7.57}$$

The OSP ansatz now consists in regulating the offshellness $\Delta\mu_j$ in a way that the vacuum behavior is restored when the particles leave the nucleus. Our choice is that $\Delta\mu_j$ depends linearly on the full in-medium width Γ_{tot}, so that

$$\Delta\mu_j(\mathbf{r}, p) = \chi_j^{\text{os}}\, \Gamma_{\text{tot}}(\mathbf{r}, p), \tag{7.58}$$

where we define the off-shell parameter as

$$\chi_j^{\text{os}} = \frac{\Delta\mu_j(\mathbf{r}_j(t_0), p_j(t_0))}{\Gamma_{\text{tot}}(\mathbf{r}_j(t_0), p_j(t_0))}. \tag{7.59}$$

The widths have to be calculated in the lab frame since only then the ratio $\Gamma_{\text{tot}}(\mathbf{r}, p)/\Gamma_{\text{tot}}(\mathbf{r}_j(t_0), p_j(t_0))$ is a scalar for all times.[10]

[9] Remember that we suppress the particle species index i while we keep the index j which denotes the jth test particle.

[10] For the derivation we refer the reader to the footnote on page 18 in Ref. [Bus08].

At production time t_0 each test particle j is assigned its specific off-shell parameter $\chi_j^{\rm os}$ which stays constant in time. Its value is less than zero for particles below the pole and larger than zero for the ones above the pole. As each test particle has its own off-shell parameter, we require a separate Hamilton function H_j for each test particle and replace

$$H = \sqrt{(m+U)^2 + \mathbf{p}^2} \rightarrow H_j = \sqrt{(m+U+\Delta\mu_j)^2 + \mathbf{p}^2}. \tag{7.60}$$

Each test particle is thus propagated also under the influence of the off-shell potential $\Delta\mu_j$. Note that within the OSP ansatz the Hamiltonian depends on the test particle, but, since $H_j(t_0) = p_j^0$ and $\partial_t H_j = 0$, it is constant, i.e., $H_j(t) = p_j^0(t)$ for all times. Thus, by construction of the off-shell potential, the single-particle energy is conserved and we find $\partial p_j^0/\partial t = 0$ [Eq. (7.16)].

The OSP ansatz as applied by Effenberger [Eff99] and later by Lehr [Leh03] has been even simpler: they have chosen a linear dependence in density instead of the full in-medium width in Eq. (7.59), which is from the numerical point of view a huge simplification as we shall see in the next section. In addition, they have introduced a back-coupling term stemming from the influence of the OSP on the residual nucleus which restores also the overall energy conservation. Since the nucleus stays approximately in its ground state in lepton-induced reactions, the back-coupling term leads only to minor modifications and can be neglected.

Finally, we briefly address the justification of the OSP method which is an effective way of simulating the full off-shell solution to the generalized BUU equation (7.1). The full equations of motion have been derived in non-relativistic kinematics by Leupold [Leu00] and relativistically by Cassing and Juchem [CJ00]. The three approaches were compared to each other by Lehr (cf. Section 5.2 in Ref. [Leh03]) who has found good agreement of the OSP ansatz (their realization using the densities) with the full solution by Leupold within the low-density approximation. Lehr has further compared numerically the OSP method to the relativistic solution and has found only minor differences that are negligible for practical purposes (see Figs. 5.1-5.3 in Ref. [Leh03]).

7.8.2 Numerical implementation and discussion

We store the off-shell parameter $\chi_j^{\rm os}$, defined in Eq. (7.59), of each test particle j when it is produced. It can be produced either in the initial lepton-nucleon interaction or in secondary collisions (cf. Section 7.6).[11] These test particles are then propagated in both the mean-field potential and the off-shell potential following Eqs. (7.14)-(7.16) according to their Hamilton function given in Eq. (7.60).

[11] Note that we had to adjust the collision term, in particular the treatment of the kinematics, to account for broad nucleons.

Since $\partial p_j^0/\partial t = 0$ [Eq. (7.16)], the single-particle energy is conserved in the propagation. As the off-shell potential depends on $\mathbf{r}$ and p, we have to evaluate for Eqs. (7.14) and (7.15) also the derivatives acting on $\Delta\mu_j(\mathbf{r}, p)$ leading to

$$\frac{\partial \Delta\mu_j(\mathbf{r}, p)}{\partial \mathbf{p}} = \chi_j^{\text{os}} \frac{\partial \Gamma_{\text{tot}}(\mathbf{r}, p)}{\partial \mathbf{p}}, \tag{7.61}$$

$$\frac{\partial \Delta\mu_j(\mathbf{r}, p)}{\partial \mathbf{r}} = \chi_j^{\text{os}} \frac{\partial \Gamma_{\text{tot}}(\mathbf{r}, p)}{\partial \mathbf{r}}. \tag{7.62}$$

As a test of the off-shell propagation we let nucleons and Δ resonances of different kinematics propagate out of and Δ resonances propagate also through a ^{12}C nucleus. In detail, consider the following scenarios:

(1) nucleon initialized at $\mathbf{r} = \mathbf{0}$ with $M = 1.1\,\text{GeV}$ and $\mathbf{p} = 1\,\text{GeV}\,\mathbf{e}_z$

(2) nucleon initialized at $\mathbf{r} = \mathbf{0}$ with $M = 1.1\,\text{GeV}$ and $\mathbf{p} = 0.5\,\text{GeV}\,\mathbf{e}_z$

(3) nucleon initialized at $\mathbf{r} = \mathbf{0}$ with $M = 0.8\,\text{GeV}$ and $\mathbf{p} = 1\,\text{GeV}\,\mathbf{e}_z$

(4) nucleon initialized at $\mathbf{r} = \mathbf{0}$ with $M = 0.8\,\text{GeV}$ and $\mathbf{p} = 0.5\,\text{GeV}\,\mathbf{e}_z$

(5) $P_{33}(1232)$ initialized at $\mathbf{r} = \mathbf{0}$ with $M = 1.1\,\text{GeV}$ and $\mathbf{p} = 1\,\text{GeV}\,\mathbf{e}_z$

(6) $P_{33}(1232)$ initialized at $\mathbf{r} = \mathbf{0}$ with $M = 1.1\,\text{GeV}$ and $\mathbf{p} = 0.5\,\text{GeV}\,\mathbf{e}_z$

(7) $P_{33}(1232)$ initialized at $\mathbf{r} = \mathbf{0}$ with $M = 1.5\,\text{GeV}$ and $\mathbf{p} = 1\,\text{GeV}\,\mathbf{e}_z$

(8) $P_{33}(1232)$ initialized at $\mathbf{r} = \mathbf{0}$ with $M = 1.5\,\text{GeV}$ and $\mathbf{p} = 0.5\,\text{GeV}\,\mathbf{e}_z$

(9) $P_{33}(1232)$ initialized at $\mathbf{r} = -4\,\text{fm}\,\mathbf{e}_z$ with $M = 1.1\,\text{GeV}$ and $\mathbf{p} = 1\,\text{GeV}\,\mathbf{e}_z$

(10) $P_{33}(1232)$ initialized at $\mathbf{r} = -4\,\text{fm}\,\mathbf{e}_z$ with $M = 1.1\,\text{GeV}$ and $\mathbf{p} = 0.5\,\text{GeV}\,\mathbf{e}_z$

(11) $P_{33}(1232)$ initialized at $\mathbf{r} = -4\,\text{fm}\,\mathbf{e}_z$ with $M = 1.5\,\text{GeV}$ and $\mathbf{p} = 1\,\text{GeV}\,\mathbf{e}_z$

(12) $P_{33}(1232)$ initialized at $\mathbf{r} = -4\,\text{fm}\,\mathbf{e}_z$ with $M = 1.5\,\text{GeV}$ and $\mathbf{p} = 0.5\,\text{GeV}\,\mathbf{e}_z$

Collisions are "switched off" and the Oset prescription is used for the Δ width. If not stated otherwise, we include the full hadronic potentials in the propagation. The simulation stops either after $t = 50\,\text{fm}$ or if $r > 7\,\text{fm}$. In the following plots we always show the time evolution of the absolute momentum $|\mathbf{p}| = p$, the radial distance from the center of the nucleus $|\mathbf{r}| = r$, the full in-medium width Γ_{tot}, the energy E, the particle's bare mass $M = \sqrt{p^2} - U = m + \Delta\mu_j$. The value of the off-shell parameter χ^{os} is indicated in the plots.

We start with scenarios (1)-(3) shown in Fig. 7.10. Here the nucleons propagate out of a ^{12}C nucleus (increase of dashed lines). In (1) and (2) the nucleons are initialized

with a mass larger than M_N (positive $\chi^{\rm os}$), while the mass is smaller in (3). In all cases, $M \to M_N$ when propagating out (double-dashed lines) — at the same time, the momentum p is adjusted accordingly (solid lines) and the collisional width tends to zero (dash-dotted lines). The energy stays constant as it should (dotted lines). Very similar results are found when the mean-field potential is set to zero.

A completely different behavior is observed in Fig. 7.11 for case (4). In the left panel, we show the results without mean-field potential while the results shown in the right panel are obtained including the mean-field potential. The dashed lines show that the nucleon propagates out about 3 fm (after $t = 10\,\text{fm}$), but after a while it returns, passes the origin at $t \approx 32\,\text{fm}$ and propagates out again to about 3 fm (dashed lines). The mass (double-dashed), momentum (solid) and the in-medium width (dash-dotted lines) oscillate accordingly. Thus, for setup (4), the nucleon is bound in the nucleus by the off-shell potential which is attractive for very negative off-shell parameters. The effect of the mean-field potential can be appreciated by comparing both panels: it does not change the overall picture but slightly affects the propagation.

The left panel of Fig. 7.12 shows scenarios (5)-(7) where a $P_{33}(1232)$ resonance propagates out of a ^{12}C nucleus (increase of dashed lines in time). In (5) and (6) the $P_{33}(1232)$ resonances are initialized with a mass smaller than the Breit-Wigner mass (negative $\chi^{\rm os}$), while the mass is larger in (7). In the first two scenarios, M increases with increasing distance from the nuclear center (double-dashed lines); at the same time, $|\mathbf{p}|$ (solid) and the full in-medium width $\Gamma_{\rm tot}$ (dash-dotted lines) decrease. The opposite is found for scenario (7). The single-particle energy stays constant in all cases (dotted lines).

The propagation of a $P_{33}(1232)$ resonance *through* a ^{12}C nucleus is addressed in the right panel of Fig. 7.12. Here, the radial distance decreases from 4 fm to 0, then the particle passes the nuclear center and the distance increases again. For particles with negative off-shell parameter, M decreases (double-dashed lines) while $|\mathbf{p}|$ (solid lines) increases when propagating through the nucleus (the width is very small and thus not shown in the two upper plots). For particles with positive off-shell parameter, the picture is reversed.

For specific choices of the kinematics, cf., e.g., Fig. 7.13, the Δ resonances are bound in the nucleus by the OSP (dashed line in the left panel, similar effect as seen in Fig. 7.11) which, however, is very sensitive to minor changes (effect vanishes in the right panel when the hadronic mean-field potential is included). In the same way, particles can be reflected from nuclei by the OSP alone.

We conclude, that for both, the nucleon and the Δ — the most important baryons in our work —, we find the correct behavior in time which proves the correct implementation of the OSP method.

Let us finally discuss the main problems of this method. Equations (7.61) and (7.62) reveal on one hand the simplicity of implementing the OSP method but on the other

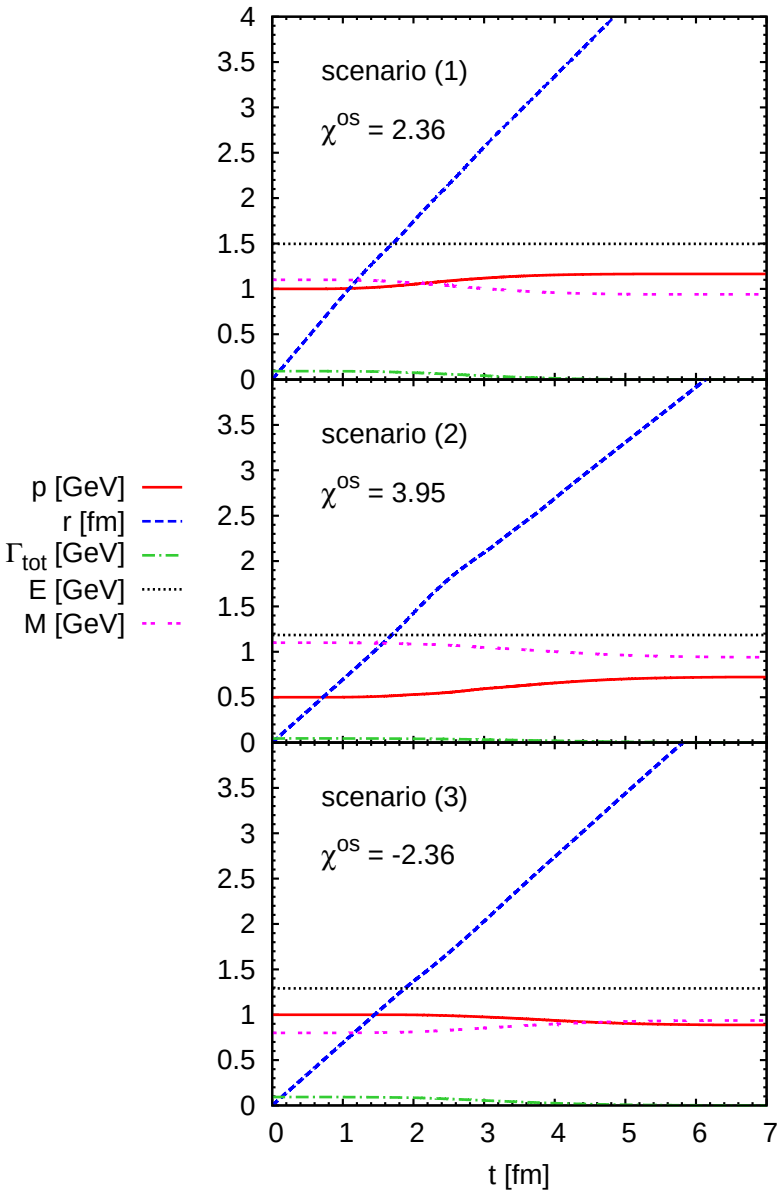

Figure 7.10: Off-shell propagation of nucleons out of a ^{12}C nucleus with different kinematic settings as detailed in the text. The time evolution of various quantities is shown (see labels).

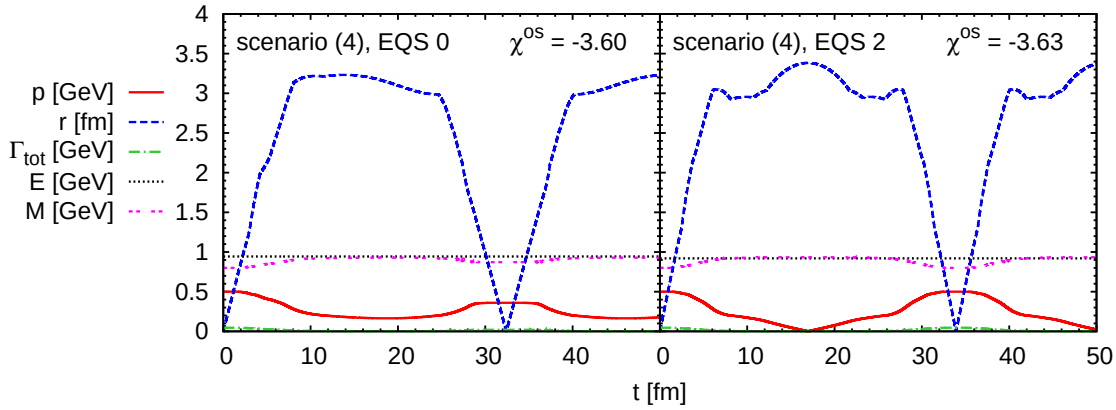

Figure 7.11: Off-shell propagation of nucleons out of a ^{12}C nucleus for scenario (4). In the left panel, the mean-field potential is "switched off".

hand show its major difficulties: a large sensitivity on the in-medium width. As outlined in Section 7.7, the widths are calculated using a Monte Carlo method with a certain precision for the integral in Eq. (7.46) and then stored on a grid. If these widths are not smooth enough, the numerical evaluation of the gradients can give unrealistic values, which, since $\dot{r} = \partial H/\partial p$, leads to particles faster than light (tachyons). Thus, we have to ensure high precision in the tabulation of the width and in solving the equations of motion. For example, to avoid rapid changes we have to decrease the time step size from 0.1 fm to at least half and also Δp in the numerical evaluation of the derivatives from 0.01 to 0.002. Similar numerical problems arise at the borders of the tabulation grid. We circumvent them by extrapolating the width or by doing forward or backward derivatives instead.

Difficulties are not only caused by numerical problems in the gradients but also by the properties of the width itself. We eventually observe tachyons if the off-shell potential becomes too stiff, which is the case for large off-shell parameters. The off-shell parameter directly translates into a maximal (if positive) or minimal mass (if negative) at production time and, since the cross section is suppressed by the spectral function away from the pole, particles with a large off-shell parameter do not contribute significantly to any observable. Thus, to avoid problems in the gradients we introduce a cut on the off-shell parameter by requiring $\left|\chi_j^{os}\right| < 5$ which corresponds to cutting particles more than 5Γ away from the pole mass. Furthermore, we do not allow the production of arbitrarily light particles, i.e., we cut the spectral function such that the nucleon in-medium mass is at least 0.7 GeV and the resonance masses are larger than the vacuum limit $M_N + m_\pi$.

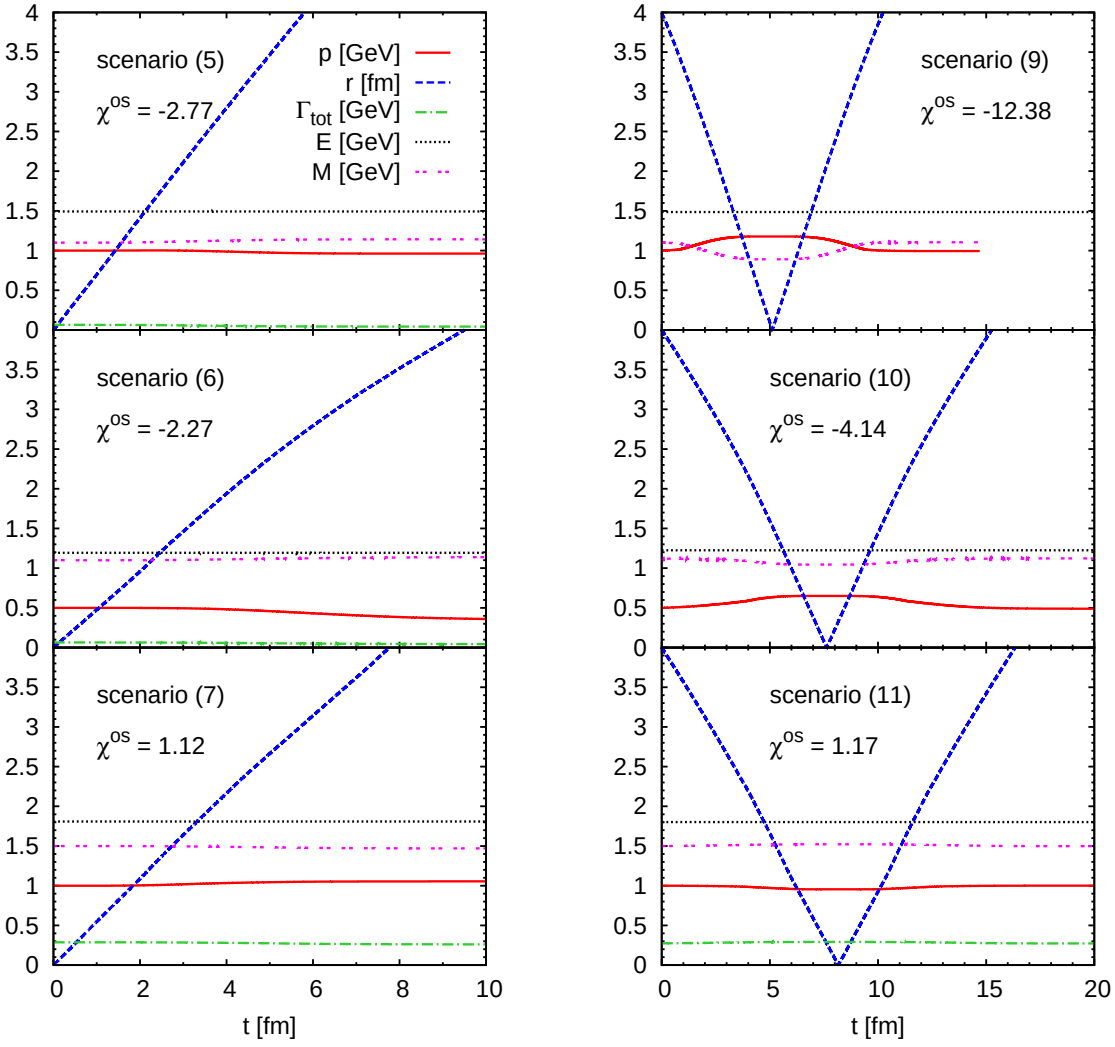

Figure 7.12: Off-shell propagation of $P_{33}(1232)$ resonances out of (left panels) and through (right panels) a ^{12}C nucleus with different kinematic settings as detailed in the text. The time evolution of various quantities is shown (see labels).

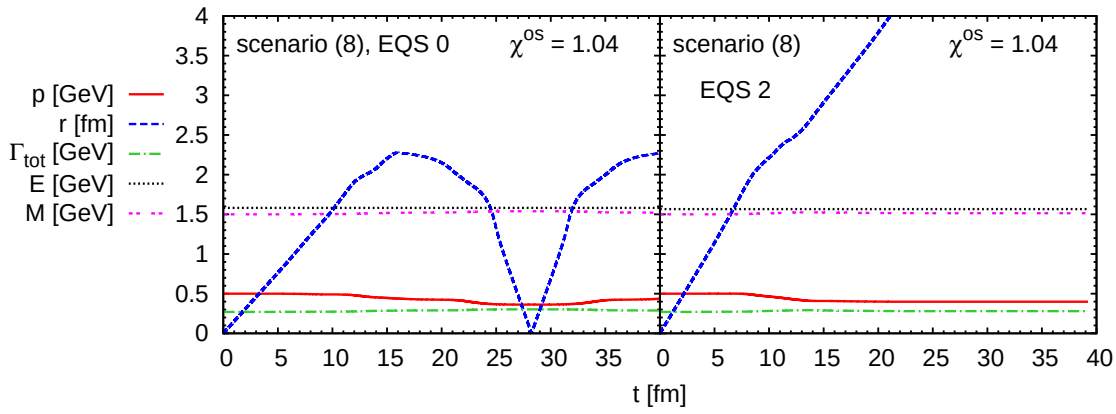

Figure 7.13: Off-shell propagation of $P_{33}(1232)$ resonances out of a ^{12}C nucleus for scenario (8). In the left panel, the mean-field potential is "switched off".

As stated above, most numerical problems, i.e., the appearance of tachyons,[12] are caused by our ansatz Eq. (7.59), where we have chosen to use the widths, and by the momentum dependence of the width. If one instead uses the densities in Eq. (7.59), i.e., ρ/ρ_0 as done by Effenberger and Lehr, or takes a width which is constant in momentum and mass, all of the aforementioned problems with tachyons disappear since the off-shell potential does not affect $\dot{r} = \partial H/\partial p$.

A major disadvantage of the OSP method from the computing point of view is the huge increase of needed CPU-time. First, the in-medium width needs to be interpolated in four dimensions for calculating the derivatives. Then, as pointed out above, the number of time steps had to be reduced. Overall, the OSP method slows down the propagation part by roughly a factor of 10.

Thus, it is of importance to discuss the impact of the off-shell transport on observables, or, in other words, the conditions under which it can be neglected. For example, particles with high interaction rates have only a short life time, hence they propagate only shortly under the influence of the off-shell potential. Thus, its impact is only minor in such cases. In Chapters 10 and 11, we show that its impact is indeed negligible for lepton-induced pion production and nucleon knockout.

[12] We emphasize again that the appearance of tachyons is not physical but caused by unphysical structures leading to numerical problems — they have no influence on physical observables.

8

Nuclear electroweak cross sections

In our approach, the lepton-nucleus reaction is treated as a two-step process: in the initial step the elementary projectile scatters — assuming impulse approximation — off one single bound nucleon whereby a quasielastic event takes place, a resonance is excited, or a non-resonant background process is initiated. Afterwards, the resulting particle yield of this initial-state interaction propagates through the nucleus undergoing final-state interactions.

In this chapter, we give the connection between the lepton-nucleon cross section derived in the first part of this thesis and the GiBUU transport model introduced in the preceding chapter. We discuss in particular the medium modifications of the initial lepton-nucleon scattering cross section and derive the lepton-nucleus cross section and explain its numerical implementation.

8.1 Lepton-nucleon interaction in the nuclear medium

In the first part of this thesis, we have discussed the scattering of leptons with free nucleons. Now we proceed to the scattering of leptons with nuclei, i.e., in our assumption of impulse approximation off an ensemble of bound nucleons. Thus, we have to account for medium effects: the nucleons which build the nucleus acquire a certain, in our approach density-dependent, Fermi momentum (cf., Section 7.5). In- and outgoing baryons are further affected by mean-field potentials (see Section 7.4) which modify their dispersion relations. The spectral functions of the outgoing baryons contain, in addition, the collisional broadening caused by the scattering with the residual

nucleons (see Section 7.7). These effects require modifications of both, the cross section formulas and the matrix elements.

In the medium, the four-vectors of the incoming nucleons are given by [see also Eq. (7.6) on page 83]

$$p = \left(\sqrt{\left(M_N + U_N(\mathbf{p}, \mathbf{r})\right)^2 + \mathbf{p}^2} \, , \mathbf{p} \right), \tag{8.1}$$

which defines their invariant masses (also called effective masses)

$$M = \sqrt{p^2} = M_N + U_N(\mathbf{p}, \mathbf{r}). \tag{8.2}$$

In the following we discuss how the different contributions to $\mathrm{d}\sigma_{\mathrm{tot}}$ (see Eq. (3.1) on page 26) are modified when the nucleon is bound in a nucleus, i.e.,

$$\mathrm{d}\sigma_{\mathrm{tot}} = \mathrm{d}\sigma_{\mathrm{QE}} + \sum_{\mathrm{R}} \mathrm{d}\sigma_{\mathrm{R}} + \mathrm{d}\sigma_{\mathrm{BG}} \rightarrow \mathrm{d}\sigma_{\mathrm{tot}}^{\mathrm{med}} = \mathrm{d}\sigma_{\mathrm{QE}}^{\mathrm{med}} + \sum_{\mathrm{R}} \mathrm{d}\sigma_{\mathrm{R}}^{\mathrm{med}} + \mathrm{d}\sigma_{\mathrm{BG}}^{\mathrm{med}}, \tag{8.3}$$

where $\mathrm{d}\sigma_{\mathrm{tot}}^{\mathrm{med}}$ stands for the medium-modified cross section to be discussed below.

8.1.1 Quasielastic scattering

The in-medium cross section for QE scattering is derived in Appendix B.2.1 and reads [Eq. (B.11) with Eq. (B.14)]

$$\frac{\mathrm{d}\sigma_{\mathrm{QE}}^{\mathrm{med}}}{\mathrm{d}k'^0 \, \mathrm{d}\Omega_{k'}} = \frac{|\mathbf{k}'|}{32\pi^2} \left[(k \cdot p)^2 - m_\ell^2 M^2 \right]^{-1/2} \mathcal{A}_N(p', r) \, |\bar{\mathcal{M}}_{\mathrm{QE}}^{\mathrm{med}}|^2. \tag{8.4}$$

The in-medium four-momentum p' of the outgoing nucleon is directly given by energy and momentum conservation using the in-medium four-vector p defined above; M is given in Eq. (8.2) and $M' = M_N + U_N(\mathbf{p}', \mathbf{r})$. We emphasize that in our model not only the initial-state nucleon is affected by the mean-field potential but also the final-state nucleon. Thus, also p' includes modifications from the potential. This means that a struck nucleon is not necessarily knocked out, but can also stay bound in the nucleus. This is different, e.g., from the model of Benhar *et al.* [BFN$^+$05], where the outgoing nucleon does not feel any potential and is always assumed to be knocked out, described in terms of a single parameter, an average removal energy.

$\mathcal{A}_N(p', r)$ in Eq. (8.4) stands for the in-medium spectral function of the nucleon introduced in Section 7.7. Hereby, we account for the fact that the outgoing nucleon acquires a collisional width in the medium.

Already in the simplest case of QE scattering, the most general in-medium vertex for $\gamma^\star N \rightarrow N'$ can be expressed in terms of 12 linearly independent Lorentz structures, leading to 12 different form factors [NPKO90]. While in the vacuum, the form

factors are only functions of q^2, in the medium they may depend on all the possible independent Lorentz scalars, i.e., e.g., q^2, P^2 and $P \cdot q$ where $P = p + p'$. However, the present experimental situation does not allow to fix these parameters, therefore, we follow the common assumption that the vertex structure, given in Eqs. (4.7) and (4.8) on page 30, and the form factors are not modified by the medium and that the latter depend only on q^2 (We will expand this discussion in Section 9.3.). Consequently, the matrix element $|\bar{\mathcal{M}}^{\text{med}}_{\text{QE}}|$ in Eq. (8.4) is the same as the one derived in Chapter 4 for unbound nucleons, *but* calculated with the full medium-modified four-vectors, p and p', affecting the hadronic tensor.

8.1.2 Resonance excitations

For resonance excitations, the implementation of medium modifications is straight forward. The cross section is given by [Eq. (B.11) with Eq. (B.14)]

$$\frac{\mathrm{d}\sigma^{\text{med}}_{\text{R}}}{\mathrm{d}k'^0\,\mathrm{d}\Omega_{k'}} = \frac{|\mathbf{k}'|}{32\pi^2}\,\left[(k\cdot p)^2 - m_\ell^2 M^2\right]^{-1/2}\,\mathcal{A}_{\text{R}}(p',r)\,|\bar{\mathcal{M}}^{\text{med}}_{\text{R}}|^2. \tag{8.5}$$

As for QE scattering, the in-medium four-momentum p' of the outgoing resonance is given by $p' = p + q$ with the in-medium four-vector p of Eq. (8.1); M is given in Eq. (8.2). The in-medium spectral function for the resonances, $\mathcal{A}_{\text{R}}(p',r)$, is given in Section 7.7.

As in the quasielastic case, we also assume that for resonance production the in-medium vertex structure and the form factors are not modified by the medium. Thus, the matrix elements $|\bar{\mathcal{M}}^{\text{med}}_{\text{R}}|$ in Eq. (8.5) are the same as derived in Chapter 5 for scattering off free nucleons, *but* calculated with the full medium-modified four-vectors p and p'.

8.1.3 Non-resonant single-pion background

We have outlined in Chapter 6 that the cross section for the non-resonant single-pion background is based on the MAID parametrization of available electron-induced single-pion production data on the nucleon. The background is defined by the difference between these *vacuum* data and the resonance contributions. Thus, we use vacuum kinematics (only Fermi motion is considered, no potentials) to construct both parts of $\mathrm{d}\sigma_{\text{BG}}$ given in Eq. (6.2) on page 70, the total single-pion cross section using the MAID input and the contribution of the resonances to single-pion production. This means for the in-medium background cross section that

$$\mathrm{d}\sigma^{\text{med}}_{\text{BG}}(p,q) = \mathrm{d}\sigma^{\text{vac}}_{\text{BG}}(p_{\text{vac}},q), \tag{8.6}$$

with $p_{\text{vac}} = \left(\sqrt{M_N^2 + \mathbf{p}^2}, \mathbf{p}\right)$.

8.2 Lepton-nucleus interactions

Assuming impulse approximation, we can take the nuclear-current operator as a sum of one-body currents, and also the nucleus wave function is simply a sum over all single-particle wave functions, for which we take plane waves. This allows us to express the cross section for lepton scattering on nuclei as an integral over the nucleus of the lepton-nucleon cross sections, and we obtain for the inclusive cross section (i.e., summed over all hadronic final states)

$$\mathrm{d}\sigma_{\mathrm{tot}}^{\ell A\to\ell' X} = \int\limits_{\text{nucleus}} \mathrm{d}^3 r \int \frac{\mathrm{d}^3 p}{(2\pi)^3}\,\Theta(p_F(r)-p)\; f_{\mathrm{corr}}\;\mathrm{d}\sigma_{\mathrm{tot}}^{\mathrm{med}}\; P_{\text{PB}}(\mathbf{r},\mathbf{p}). \tag{8.7}$$

The term $\mathrm{d}\sigma_{\mathrm{tot}}^{\mathrm{med}}$ stands for the total cross section on nucleons including nuclear medium corrections as discussed in the previous section. The Pauli-blocking factor, P_{PB}, and the local Fermi momentum, $p_F(r)$, are both given in Section 7.5. The factor f_{corr} is a flux correction and reads

$$f_{\mathrm{corr}} = \frac{|v_N - v_\ell|}{|v_A - v_\ell|} \approx \frac{|v_N - v_\ell|}{1} = \frac{k\cdot p}{k^0 p^0}\,, \tag{8.8}$$

where $v_{N,A,\ell}$ denotes the velocity of the corresponding nucleon, the nucleus and the incoming lepton, all in the frame where the nucleus is at rest.

The semi-inclusive cross section, i.e., the cross section for a specific final state f can now be written down as

$$\mathrm{d}\sigma_{\mathrm{tot}}^{\ell A\to\ell' f X} = \int\limits_{\text{nucleus}} \mathrm{d}^3 r \int \frac{\mathrm{d}^3 p}{(2\pi)^3}\,\Theta(p_F(r)-p)\; f_{\mathrm{corr}}\;\mathrm{d}\sigma_{\mathrm{tot}}^{\mathrm{med}}\; P_{\text{PB}}(\mathbf{r},\mathbf{p})\; M_f(\mathbf{r},\mathbf{p}). \tag{8.9}$$

M_f is the multiplicity of the final state f given an initial state i. This mapping $i \to f$ is determined by the GiBUU transport simulation.

8.3 Numerical implementation

The integrals in Eqs. (8.7) and (8.9) are solved numerically using a Monte Carlo sampling method. In terms of test particles the integral reads [Bus08]

$$\begin{aligned}
\int \mathrm{d}^3 r\,\frac{\mathrm{d}^3 p}{(2\pi)^3}\,\Theta(p_F-p)\ldots &= \int \mathrm{d}^3 r\,\frac{\mathrm{d}^3 p}{(2\pi)^3}\; f(\mathbf{r},\mathbf{p},t=0)\ldots \\
&= \int \mathrm{d}^3 r\,\frac{\mathrm{d}^4 p}{(2\pi)^4}\; g^{<}(\mathbf{r},p,t=0)\ldots \\
&= \int \mathrm{d}^3 r\;\mathrm{d}^4 p\;\frac{1}{N}\sum_{j=1}^{N\times A}\delta^4(p-p_j)\;\delta^3(r-r_j)\ldots .
\end{aligned} \tag{8.10}$$

Each nucleon test particle gives a distinct contribution to the integrals so that

$$\mathrm{d}\sigma_{\mathrm{tot}}^{\ell A\to\ell' X} = \frac{1}{N}\sum_{j=1}^{N\times A} f_{\mathrm{corr}}(p_j)\ \mathrm{d}\sigma_{\mathrm{tot}}^{\mathrm{med}}(\mathbf{r}_j, p_j)\ P_{\mathrm{PB}}(\mathbf{r}_j, \mathbf{p}_j), \tag{8.11}$$

where $\mathrm{d}\sigma_{\mathrm{tot}}^{\mathrm{med}}(\mathbf{r}_j, p_j)$ is the cross section for the jth test particle.

The numerical implementation has been presented in detail in Section 5.5 of Ref. [Bus08]; for completeness we shall review the major steps. First, we formally rewrite Eq. (8.3) so that

$$\mathrm{d}\sigma_{\mathrm{tot}}^{\mathrm{med}}(\mathbf{r}_j, p_j) = \sum_{f\in\{N,\pi N,\mathrm{P}_{33}(1232),\mathrm{P}_{11}(1440),\ldots\}} \mathrm{d}\sigma_f(\mathbf{r}_j, p_j). \tag{8.12}$$

Since the πN background cross section may become negative as pointed out on page 70, we have to apply a modified importance-sampling algorithm as developed in Ref. [Bus08]. We first evaluate the cross section for each channel f using one random phase-space point $(\mathbf{r}_j, p_j)$. Then, one specific final state is chosen with a Monte Carlo method. The probability according to the modified importance sampling algorithm is [Bus08]

$$P(f) = \frac{|\mathrm{d}\sigma_f(\mathbf{r}_j, p_j)|}{\sum_{f\in\{N,\pi N,\mathrm{P}_{33}(1232),\mathrm{P}_{11}(1440),\ldots\}} |\mathrm{d}\sigma_f(\mathbf{r}_j, p_j)|}\ . \tag{8.13}$$

The event then gets a Monte-Carlo weight which includes the sign of the partial cross section

$$w_j = \underbrace{\frac{\mathrm{d}\sigma_f(\mathbf{r}_j, p_j)}{|\mathrm{d}\sigma_f(\mathbf{r}_j, p_j)|}}_{=\mathrm{sign}(\mathrm{d}\sigma_f)} \sum_{f\in\{N,\pi N,\mathrm{P}_{33}(1232),\mathrm{P}_{11}(1440),\ldots\}} |\mathrm{d}\sigma_f(\mathbf{r}_j, p_j)|. \tag{8.14}$$

It has been shown in Ref. [Bus08] that with this modification the correct cross sections are sampled.

We assume that the final lepton does not interact any more, thus, we only propagate the hadrons produced in this initial reaction. After the transport simulation, we evaluate their final multiplicities to calculate semi-exclusive cross sections (cf., Eq. (8.9)).

9 Inclusive cross sections

In this chapter, we present our results for inclusive neutrino scattering off nuclei focussing on the quasielastic and the resonance region, taking into account various nuclear effects: the local density approximation for the nuclear ground state, mean-field potentials and in-medium spectral functions. As a benchmark we also present results for electron-induced reactions which represent a model validation due to the available high-precision nuclear data.

9.1 Introduction

At intermediate energies the lepton-nucleon cross section is, as we have seen, dominated by QE scattering and pion production via resonance excitations or non-resonant processes. Many authors investigated electron *or* neutrino scattering on nucleons, but only a few study both within the same model. Quasielastic collisions have been investigated using a relativistic treatment of the matrix elements in Fermi-gas models [SM72, DP79, HKMP93], that take into account Fermi motion, Pauli blocking and binding energies. The influence of nuclear effects on both, electron- and neutrino-scattering cross sections, has been investigated by Benhar *et al.* using an impulse-approximation model with realistic spectral functions obtained from nuclear many-body theory calculations [BFN$^+$05, NSNB07]. Nuclear effects in the QE region have also been investigated in detail by Nieves and collaborators for electrons [GNO97] and neutrinos [NAV04, NVVV06] where they have included, among other nuclear corrections, long-range nuclear correlations. The importance of these strong renormalization effects on the weak transition strengths in the nuclear medium has also

been emphasized by [SO92, SSAA06b, Mar99]. A relativistic Green's function approach has been applied by Meucci *et al.* [MCGP03, MGP04b] to inclusive electron- as well as to inclusive neutrino-nucleus QE reactions. Butkevich *et al.* [BM05, BK07] address both, neutrino and electron QE scattering, with special emphasis on the impact of different impulse-approximation (IA) schemes: plane-wave IA (PWIA) and relativistic distorted-wave IA (RDWIA). The Ghent group applies RPWIA and RDWIA models to neutrino and electron scattering in the QE region [MLJ$^+$06]; lately they have extended their framework to the Δ region [PLJR09] where they employ realistic bound-state wave functions and find a good agreement to relativistic Fermi-gas calculations at neutrino energies around 1 GeV.

Within our model we are able to address the QE and the resonance region simultaneously and, unlike most of the models mentioned above, are not restricted to the QE region only. In the following, we focus on two issues: first, we present results for lepton scattering off nuclei focussing on neutrino — both charged (CC) and neutral current (NC) — reactions. In particular, we investigate the influence of the nuclear medium on inclusive cross sections. Then, to validate our model for neutrinos, we calculate inclusive electron spectra with the very same approach and compare them to electron-scattering data. Finally, we compare our model to others.

The main results of this chapter have been published in Ref. [LBARM09]; first results, where we have included only QE and Δ excitations, can be found in Refs. [LARM06a, LARM06b, BLMAR07] for CC and NC neutrino-induced reactions.

9.2 Results and their model dependence

By inclusive scattering we understand the process where only the outgoing lepton is detected, i.e., we sum over all hadronic final states. The corresponding cross section has been derived in Chapter 8 — for the reader's convenience we repeat here the final expression [Eq. (8.7)]

$$\mathrm{d}\sigma_{\mathrm{tot}}^{\ell A\to\ell' X} = \int\limits_{\text{nucleus}} \mathrm{d}^3 r \int \frac{\mathrm{d}^3 p}{(2\pi)^3}\Theta(p_F(r)-p)\,\frac{k\cdot p}{k^0 p^0}\,\mathrm{d}\sigma_{\mathrm{tot}}^{\mathrm{med}}\,P_{\text{PB}}(\mathbf{r},\mathbf{p}), \tag{9.1}$$

with the medium-modified cross section $\mathrm{d}\sigma_{\mathrm{tot}}^{\mathrm{med}}$ discussed in Chapter 8.

9.2.1 Double differential cross sections

In Fig. 9.1 we show a contour plot of the inclusive cross section for ν_μ CC scattering on ^{16}O as a function of energy transfer $\omega = k^0 - k'^0$ and scattering angle θ at a fixed neutrino energy of $E_\nu = 1\,\mathrm{GeV}$. In this calculation, we take into account Fermi motion,

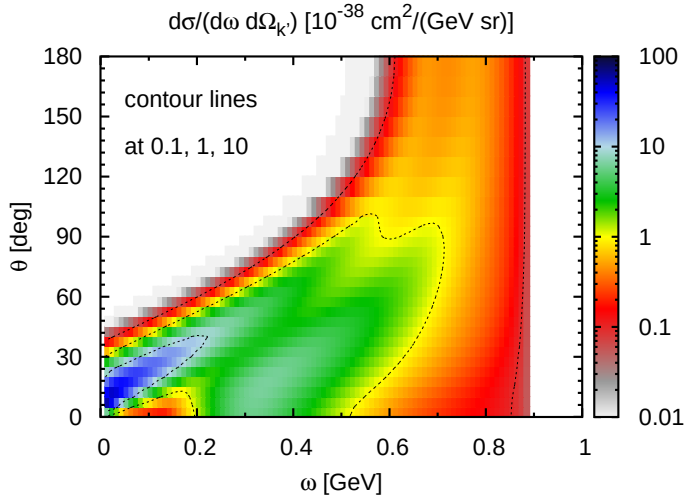

Figure 9.1: Total inclusive ν_μ CC cross section $\mathrm{d}\sigma/(\mathrm{d}\omega\mathrm{d}\Omega_{k'})$ on ^{16}O as a function of energy transfer $\omega = k^0 - k'^0$ and scattering angle θ for a fixed neutrino energy of $E_\nu = 1\,\mathrm{GeV}$.

Pauli blocking, binding potentials and in-medium spectral functions, i.e., our full model. At low energy transfer ω and small scattering angles θ (which corresponds to lower Q^2 as can be appreciated by comparing with Fig. B.1 on page 278), two peaks can be clearly distinguished. The left-upper ridge is due to QE scattering, while the right-lower ridge is dominated by the excitation of the Δ resonance. At higher ω and larger θ (higher Q^2), the two peaks overlap and the distinct peak structure vanishes and the inclusive cross section tends to zero.

To visualize the single contributions according to Eq. (3.1) (see page 26), i.e., QE, resonance or single-π background, more quantitatively, we show on the left panels of Fig. 9.2 cuts at various scattering angles for a fixed neutrino energy. In the right panel, we plot the single contributions for various neutrino energies at a fixed scattering angle. The left peaks have their origin in QE scattering (compare the total yield given by the solid lines to the QE yield given by the dashed ones). With increasing energy transfer, ω, one enters the pion-production region, which is dominated by initial Δ excitation (solid vs. dash-dotted lines). The non-resonant single pion background also contributes in this region (dotted lines) while the impact of the higher resonances is only visible as a minor contribution at high beam energies and at large scattering angles (double dashed lines in the lowest panels). The same behavior is obtained also for NC scattering as can be seen in Fig. 9.3.

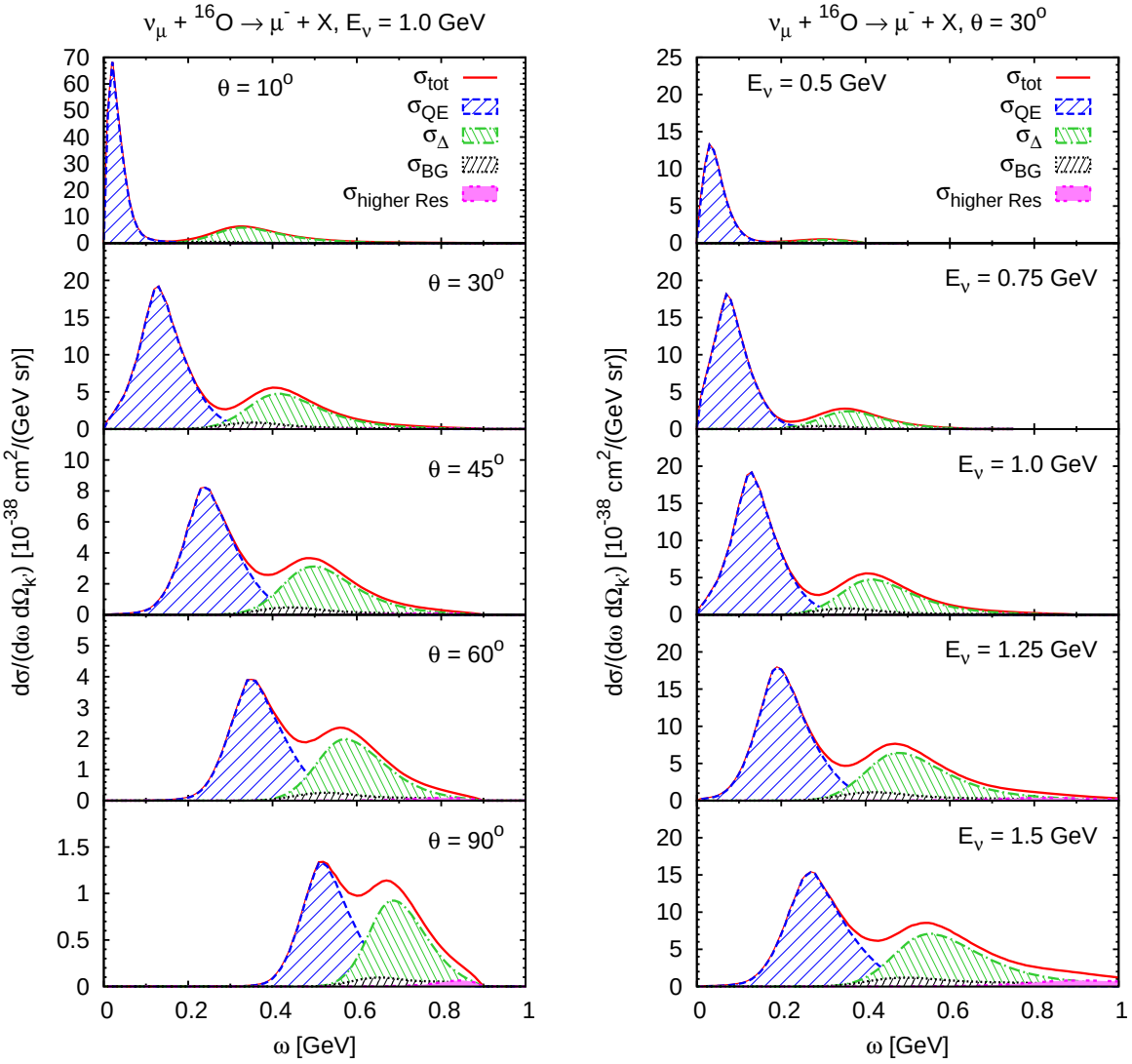

Figure 9.2: Left panel: inclusive CC neutrino cross section $d\sigma/(d\omega d\Omega_{k'})$ on ^{16}O as a function of the energy transfer ω for a fixed neutrino energy of 1 GeV and five distinct scattering angles (10, 30, 45, 60 and 90 degrees). *Note the different scales.* Right panel: same but for five distinct neutrino energies (0.5, 0.75, 1.0, 1.25 and 1.5 GeV) and a fixed scattering angle of $\theta_{\mathbf{k}'} = 30°$. In both panels, the solid lines denote our full result, where we include all in-medium modifications and in particular in-medium changes of the width. The dashed lines show the quasielastic contribution, the dotted ones the single-π background and the dash-dotted ones the contribution coming from an initial Δ excitation. Higher resonance contributions are indicated by the double-dashed lines.

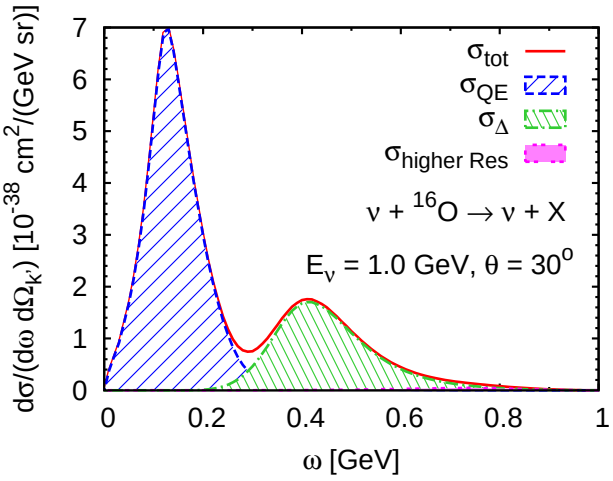

Figure 9.3: Inclusive NC neutrino cross section $d\sigma/(d\omega d\Omega_{k'})$ on ^{16}O as a function of the energy transfer ω at a fixed neutrino energy of 1 GeV and a scattering angle of $\theta_{\mathbf{k}'} = 30°$. The solid lines denote our full result, where we include all in-medium modifications and in particular in-medium changes of the width. The dashed lines show the quasielastic contribution, the dash-dotted ones the contribution coming from an initial Δ excitation and the double-dashed ones the contributions from higher resonances.

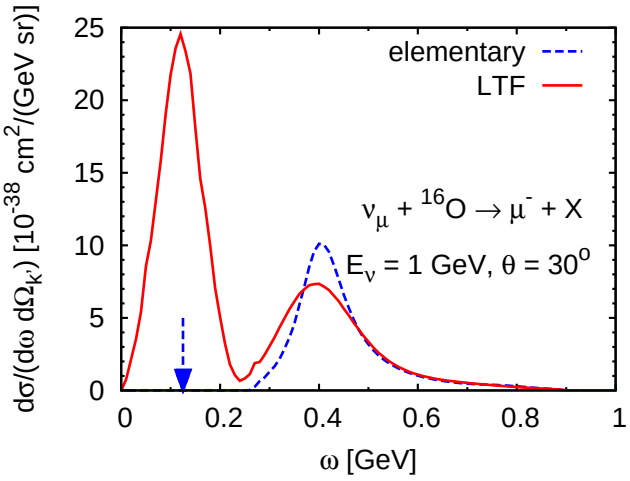

Figure 9.4: Inclusive CC cross section $d\sigma/(d\omega d\Omega_{k'})$ on ^{16}O as a function of the energy transfer ω at $E_\nu = 1\,\text{GeV}$ and a fixed scattering angle of $\theta_{\mathbf{k}'} = 30°$. The right peak is dominated by Δ excitation, the left one is due to QE scattering. The dashed line shows the elementary cross section — the position of the δ-function of the QE cross section is indicated by the arrow. The solid line includes Fermi motion and Pauli blocking.

Influence of Fermi motion and Pauli blocking

To understand the influence of the different in-medium effects, we cut again the double differential cross section at a fixed value of $E_\nu = 1\,\mathrm{GeV}$ and $\theta = 30°$. Fig. 9.4 shows the inclusive CC cross section $\mathrm{d}\sigma/(\mathrm{d}\omega \mathrm{d}\Omega_{k'})$ for ν_μ scattering on ^{16}O. First, we pay attention to the QE peak (left peak). The line denoted with "elementary" is the vacuum cross section, which can be obtained from Eq. (3.6) (see page 28). In the case of QE scattering, the differential cross section is a δ-function in ω, its position is marked by an arrow. This position is given by (cf. Eq. (B.29) on page 278)

$$\omega = \frac{-m_{\ell'}^2 + 2k^0(k'^0 - |\mathbf{k}'|\cos\theta)}{2M_N}. \tag{9.2}$$

If we "switch on" Fermi motion and Pauli blocking, denoted as "LTF" in Fig. 9.4 (solid line), we find that QE scattering is now possible for a range of values of ω with E_ν and θ fixed. This can be understood from the on-shell condition

$$(p+q)^2 = M_N^2 - Q^2 + 2p^0\omega - 2\mathbf{p}\cdot\mathbf{q} \equiv M_N^2, \tag{9.3}$$

which has multiple solutions for ω due to the Fermi momentum $\mathbf{p}$ of the nucleons. Turning to the right peak which is mainly due to Δ excitations (see Fig. 9.2), we obtain the vacuum cross section (dotted lines) by summing Eq. (3.7) (see page 28) over all resonances and adding a non-resonant contribution as described in Chapter 6. We also find a broadening of the peak when Fermi motion is included (solid line).

Influence of the mean-field potential

We now focus on the impact of the choice of the mean-field potential on the inclusive cross section. In the left panel of Fig. 9.5 we present results for the inclusive reaction $^{16}\mathrm{O}\left(\nu_\mu, \mu^-\right) X$ at various neutrino energies from 0.5 to 1.5 GeV. The different curves indicate calculations with different nucleon mean-field potentials, in-medium changes to the width are not included in this plot. The dash-dotted curves denote the results without potentials, including only Fermi motion and Pauli blocking. In the dashed curves we include a density-dependent but momentum-independent potential (EQS 1, see Section 7.4). The presence of such a momentum-independent potential has practically no impact on the QE peak because both, in- and outgoing nucleons experience the same potential. The single-pion region is slightly modified, which is caused by the fact that the Δ — dominating this region — is less strongly bound than the nucleon and, consequently, more energy must be transferred to the nucleon to compensate the binding.

Including a momentum-dependent mean field (EQS 2, solid curves), we find a broadening and a shift to higher ω. As the momenta of the initial and final nucleons

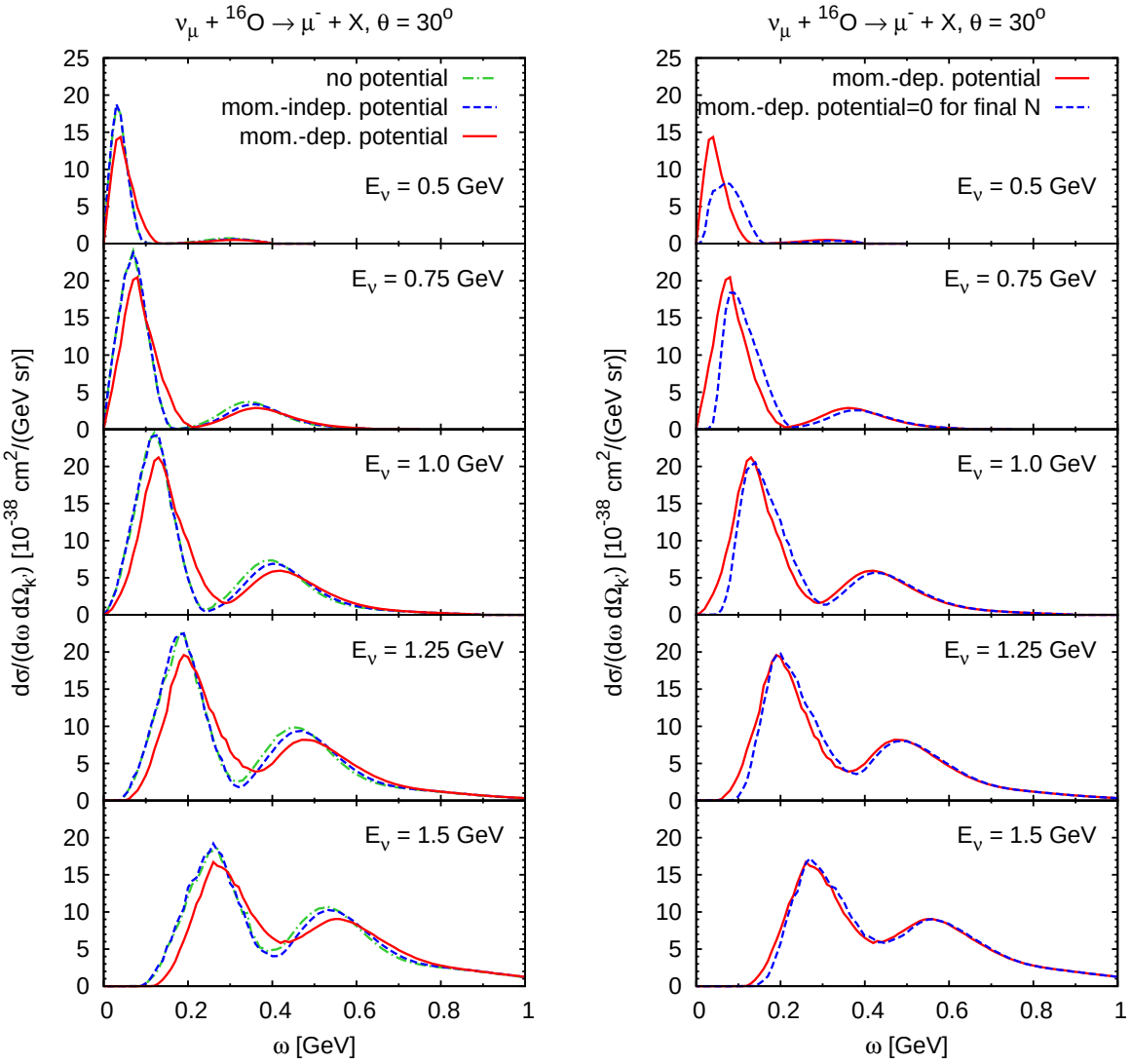

Figure 9.5: Inclusive CC cross section $d\sigma/(d\omega d\Omega_{k'})$ on ^{16}O as a function of the energy transfer ω for various beam energies and a scattering angle of $\theta_{\mathbf{k}'} = 30°$. Left panel: the plots show the results for different nucleon potentials: no potential (dash-dotted lines), momentum-independent potential (dashed lines) and momentum-dependent potential (solid lines). The calculations do not include in-medium changes of the widths. Right panel: the dashed lines show the results where we assume that the outgoing nucleon feels no potential (solid lines are identical in both panels).

differ, they now experience a different potential: the faster (on average) final-state nucleons experience a shallower potential than the initial-state ones. The same holds for the resonances. Thus, even more energy must be transferred to the initial bound nucleon which causes both the broadening and shift of the peaks towards a higher energy transfer ω. As can be seen from the right panel of Fig. 9.5, this effect is enhanced if we take the outgoing nucleon as free, i.e., if we set the potential of the outgoing nucleon to zero.

Influence of the spectral function

Finally, we investigate the influence of the in-medium spectral function and the choice for the Δ width. In Fig. 9.6, we show the calculations obtained with the vacuum spectral functions (dash-dotted lines). To get to the dashed and solid lines, the vacuum spectral function is replaced by the in-medium spectral function, i.e., the vacuum width is replaced by a sum of the vacuum width, modified due to Pauli blocking, and a collisional width accounting for additional channels in the medium (cf., Section 7.7). Since the cross section scales with the inverse of the width this replacement lowers the peak. We compare two different scenarios for the Δ width: in the first case, the Δ width is based on the one-pion exchange model, while in the second case it is calculated using the model of Oset and Salcedo [OS87]. We refer the reader to Section 7.7 for the necessary details. As appreciated from the figure, the observable consequence of this choice is only minor. Note that is due to the fact that the difference is mostly absorbed in the background via Eq. (6.2): our background is defined as data minus resonance contribution, thus, changing the resonance cross section shifts strength to the background.

We emphasize that we neglect the imaginary part of the hole self energy. Its influence for QE scattering has been investigated by Kalok [Kal07] and only a minor effect could be seen (cf., e.g., his Fig. 5.6; compare dotted and solid line) which can safely be neglected. Neglecting the imaginary part of the hole self energy is also supported by the work of Gil *et al.* [GNO97] who achieve impressive agreement with data for electron-nucleus scattering within this approximation. Non-negligible effects are caused by the real part of the hole spectral function which we account for by the mean-field potential and by the particle spectral function, where we use the full in-medium spectral function including both, real and imaginary part.

Dependence on nuclei

The left panel of Fig. 9.7 shows the inclusive CC cross section $1/N \; \mathrm{d}\sigma/(\mathrm{d}\omega \mathrm{d}\Omega_{k'})$ for ^{16}O while the right panel presents the corresponding results for ^{56}Fe. The cross section is scaled by the number of neutrons N: CCQE scattering is only possible on neutrons, thus, N should be the correct scaling variable in the region of the quasielastic peak.

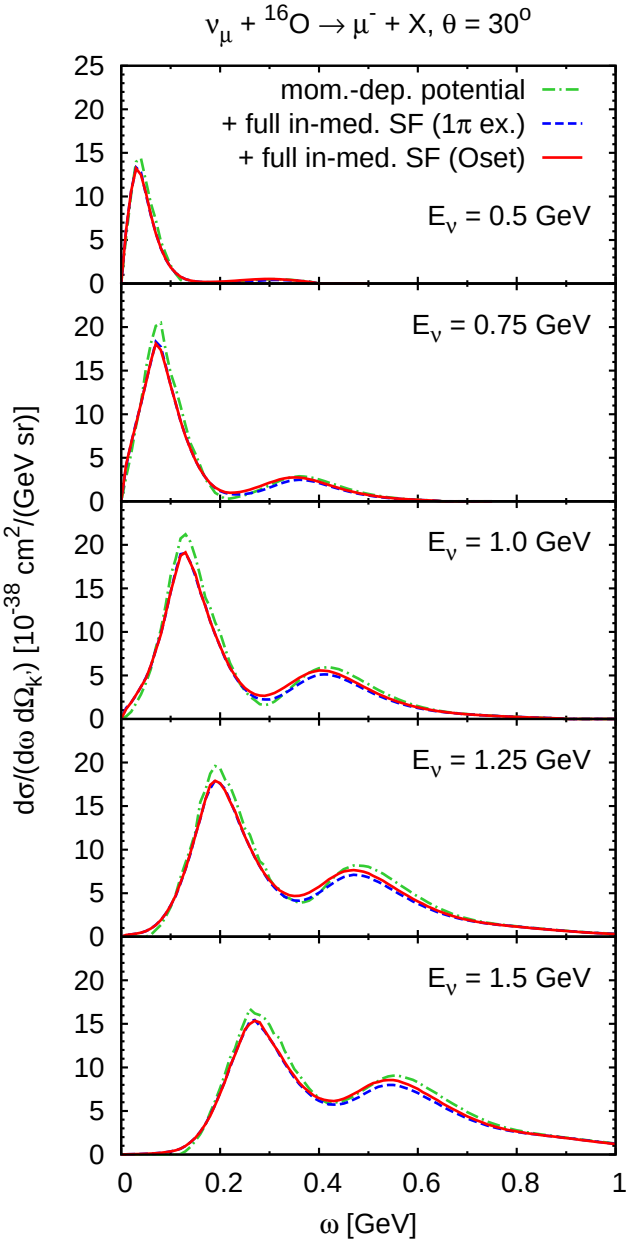

Figure 9.6: Inclusive CC cross section $d\sigma/(d\omega d\Omega_{k'})$ on ^{16}O as a function of the energy transfer ω for various beam energies and a scattering angle of $\theta_{\mathbf{k}'} = 30°$. The plots show the influence of the spectral function and in addition results for different choices of the in-medium width of the Δ resonance. The dash-dotted lines correspond to the solid lines of Fig. 9.5. In the calculation shown by the dashed lines, the Δ width is based the one-pion exchange model while the Oset prescription is applied to obtain the solid lines (difference only visible in the right peak).

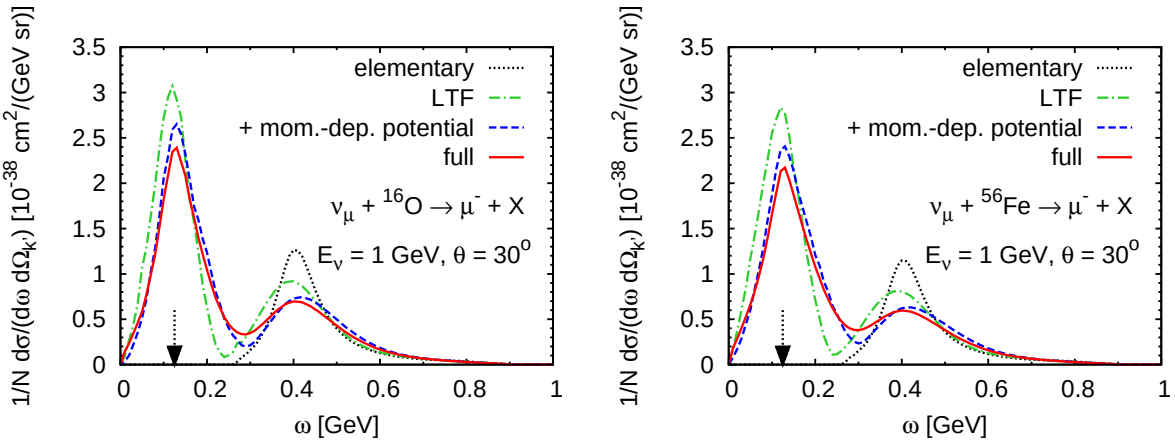

Figure 9.7: Inclusive CC cross section $1/N\ \mathrm{d}\sigma/(\mathrm{d}\omega\mathrm{d}\Omega_{k'})$ on ^{16}O (left panel) and ^{56}Fe (right panel) per neutron as a function of the energy transfer ω at $E_\nu = 1\,\mathrm{GeV}$ and a scattering angle of $\theta_{\mathbf{k}'} = 30°$. The dotted lines show the elementary cross section — the position of the δ-function of the QE cross section is indicated by the arrow. The dash-dotted lines include Fermi motion and Pauli blocking, the dashed ones in addition a momentum-dependent potential. The solid lines include also the in-medium broadening of the widths.

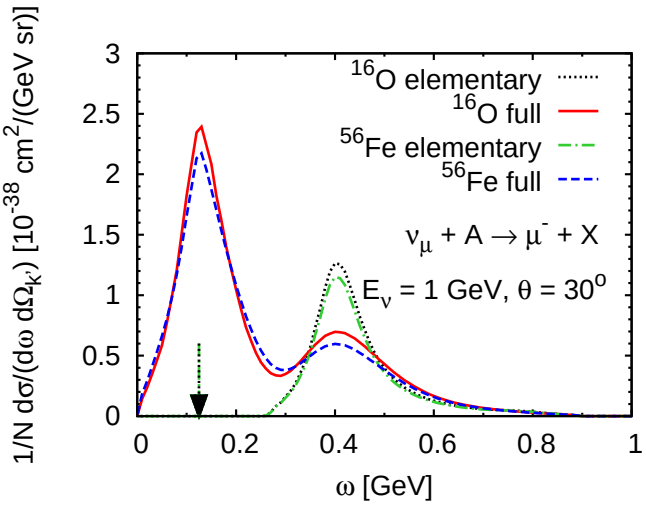

Figure 9.8: Inclusive CC cross section $1/N\ \mathrm{d}\sigma/(\mathrm{d}\omega\mathrm{d}\Omega_{k'})$ per neutron as a function of the energy transfer ω at $E_\nu = 1\,\mathrm{GeV}$ and a scattering angle of $\theta_{\mathbf{k}'} = 30°$. Shown are the elementary (dotted and dash-dotted, both coincide at the QE peak denoted by the arrow) and the full in-medium (solid and dashed lines) cross sections for both ^{16}O and ^{56}Fe.

The nuclear corrections discussed before are added subsequently: we start with the elementary cross section, then include Fermi motion and Pauli blocking ("LTF", dash-dotted lines), mean-field potentials (dashed lines) and in-medium modifications of the spectral functions (solid lines).

The elementary and the full in-medium cross sections for both nuclei are directly compared in Fig. 9.8. The difference in the resonance region on the elementary level (dotted vs. dash-dotted lines) is caused by the different proton to neutron ratio in both nuclei (e.g., the cross section for Δ excitation on protons is a factor of three larger than on neutrons, cf. Section 5.2). The QE peak is broader for Fe than for O. Overall, the difference between both nuclei is only minor.

9.2.2 Integrated cross sections

The integration over leptonic degrees of freedom yields the differential cross section, $\mathrm{d}\sigma/\mathrm{d}Q^2$, and the total cross section, σ; they are shown in Fig. 9.9. In the figure, the in-medium modifications are included subsequently as indicated in the caption; their explanation has been given above. In the lower panels, we show the effect of including the in-medium width for the Δ using either the Oset (solid) or the one-pion exchange based prescription (double-dashed lines, *only in the lower panels*).

The reduction from the free cross section to the one denoted with "LTF" in the QE case is caused by Pauli blocking; both curves agree for the Δ excitation where Pauli blocking plays no role. Overall, the cross sections are reduced in the medium (solid or double-dashed lines) compared to the ones for scattering on a free nucleon ($\sigma_{\mathrm{ele}} = Z\ \sigma_p + N\ \sigma_n$ with the neutron number N and the proton number Z; dash-dotted lines), so that $\sigma < \sigma_{\mathrm{ele}}$ (same for $\mathrm{d}\sigma/\mathrm{d}Q^2$). Note that CCQE scattering is only possible on neutrons, thus, $\sigma_{\mathrm{ele}}^{\mathrm{QE}} = N\ \sigma_n^{\mathrm{QE}}$.

9.3 Modeling in-medium cross sections

In Chapter 8, we have discussed the general form of the cross section for lepton-induced reactions on nuclei and how the cross sections for scattering off bound nucleons are calculated within our model. Many approaches have been developed to describe off-shell cross sections (cf., e.g., Refs. [NPKO90, PNK96, DF83, FK97, M$^+$76, BFN$^+$05, BDS08]). In this section, we present the most common ones and compare them to our approach.

For simplicity, we restrict ourselves to the simplest case of inclusive electron cross sections taking into account only QE scattering and neglecting collisional broadening.

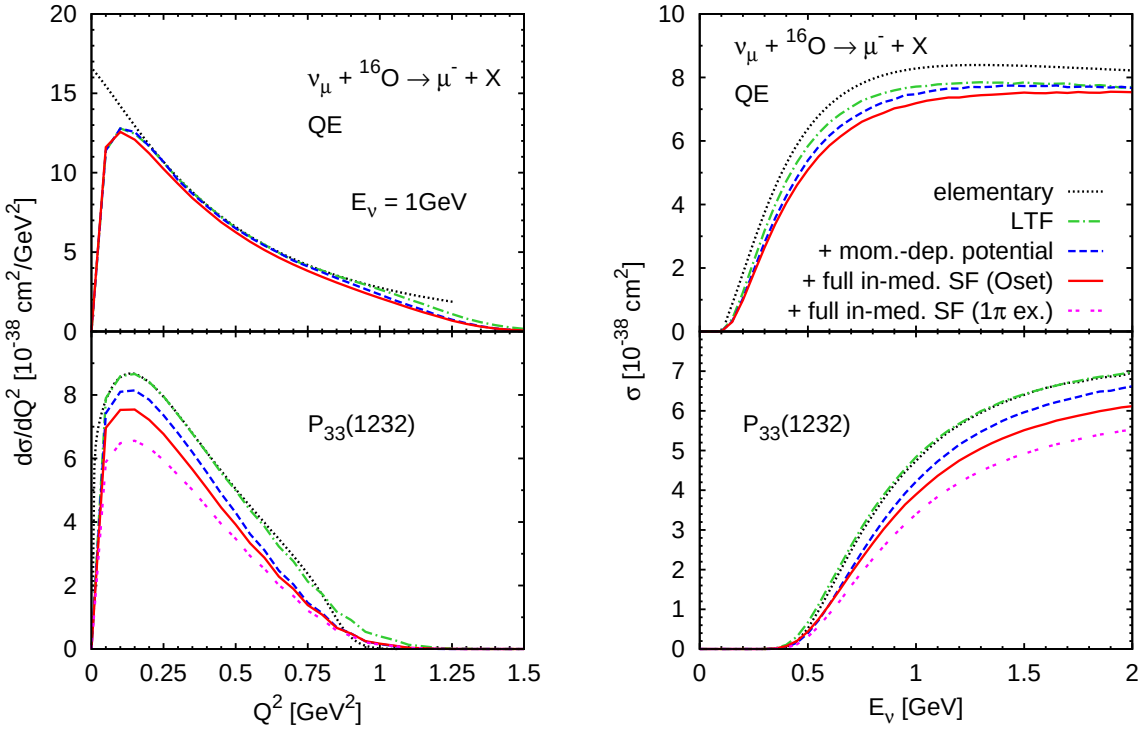

Figure 9.9: Inclusive CC cross sections on ^{16}O: the left panels show the differential cross sections $d\sigma/dQ^2$ at $E_\nu = 1\,\text{GeV}$, the right panels the total cross section σ as a function of E_ν. The upper panels include only QE scattering, while the lower ones include only the excitation of the Δ resonance. The in-medium modifications as labeled in the plot are added subsequently to the calculation, and two alternatives for the Δ in-medium spectral function are shown in the lower panels: either based on the model of Oset (solid lines) or on the one-pion exchange model (double-dashed lines). "Elementary" denotes the scaled vacuum cross section, i.e., $\sigma_{\text{ele}} = Z\,\sigma_p + N\,\sigma_n$ with the neutron number N and the proton number Z.

9.3.1 Preliminaries

We shall now discuss how the QE hadronic tensor for scattering off a bound nucleon within the above simplifications is determined in various models. We start with some general remarks.

Wave function. The first uncertainty concerns the choice of a wave function for the initial bound nucleon. A common approximation is to use a free spinor $u(p)$, which is determined by the three-momentum of the nucleon and its energy $p^0 = E_{\text{on}} = \sqrt{\mathbf{p}^2 + M_N^2}$ (on-shell energy). A different ansatz uses free spinors describing nucleons of mass $\sqrt{p^2} = M = M_N + U_N \neq M_N$, which means, that the binding potential is already included in the effective mass M, and the energy is $p^0 = \sqrt{\mathbf{p}^2 + M^2}$.

Kinematics. Closely related to the question of wave functions is the kinematics. Defined by the lepton kinematics are the energy and momentum transfer $\omega = k_0 - k_0'$ and $\mathbf{q}$, respectively. The energy transfer at the nucleon vertex is given by

$$\omega = p_0' - p_0. \tag{9.4}$$

However, if the nucleon were free, i.e., on its mass shell, with energy E_{on}, then the equivalent energy transfer $\tilde{\omega}$ would be given by

$$\tilde{\omega} = p_0' - E_{\text{on}}. \tag{9.5}$$

Thus,

$$\Delta\omega = \omega - \tilde{\omega} = E_{\text{on}} - p_0 \tag{9.6}$$

determines, how far one is from free scattering.

Vertex operator and current conservation. Further assumptions have to be made for the vertex operator. Here, we shall demonstrate the difficulties for the simplest case of a QE (e, e') reaction. The most general form for the EM vertex of an off-shell nucleon consists of 12 terms and can for example be written as [NPKO90]

$$\begin{aligned}\Gamma^{\mu}_{\text{off}} = {} & \Lambda_+(p') \left[f_1^{++}\gamma^\mu + f_2^{++}\Sigma^\mu + f_3^{++}q^\mu\right] \Lambda_+(p) \\ & + \Lambda_+(p') \left[f_1^{+-}\gamma^\mu + f_2^{+-}\Sigma^\mu + f_3^{+-}q^\mu\right] \Lambda_-(p) \\ & + \Lambda_-(p') \left[f_1^{-+}\gamma^\mu + f_2^{-+}\Sigma^\mu + f_3^{-+}q^\mu\right] \Lambda_+(p) \\ & + \Lambda_-(p') \left[f_1^{--}\gamma^\mu + f_2^{--}\Sigma^\mu + f_3^{--}q^\mu\right] \Lambda_-(p),\end{aligned} \tag{9.7}$$

with

$$\Sigma^\mu = \frac{\mathrm{i}\sigma^{\mu\nu}q_\nu}{2M_N} \tag{9.8}$$

and

$$\Lambda_{\pm}(p) = M \pm \not{p}, \tag{9.9}$$

where $M = \sqrt{p^2}$. The form factors f_i, $i = 1, \ldots, 3$, are functions of three scalar variables, e.g., $f_i(p'^2, p^2, q^2)$, with some constraints from C, P, T and gauge invariance. Until now, it is not possible to constrain them with electron scattering data. However, there has been some effort to calculate the off-shell form factors in a simplified dynamical model [NPKO90] and estimate the size of the off-shell effects.

If we take the outgoing nucleon on-shell, we can write the vertex in a simpler form of only 4 form factors depending now on only 2 scalar variables.

For the full on-shell case, i.e., both incoming and outgoing nucleon on-shell, we can further simplify Eq. (9.7) to

$$\Gamma_2^\mu = F_1 \gamma^\mu + F_2 \Sigma^\mu, \tag{9.10}$$

with the Dirac and Pauli form factors F_1 and F_2,

$$F_1(q^2) = f_1^{++}(M_N^2, M_N^2, q^2) \tag{9.11}$$

$$F_2(q^2) = f_2^{++}(M_N^2, M_N^2, q^2). \tag{9.12}$$

Γ_2^μ corresponds to our QE hadronic vector current of Eq. (4.7). Using Gordon identities for on-shell nucleons, we can rewrite Γ_2^μ so that

$$\Gamma_2^\mu \to \Gamma_1^\mu = (F_1 + F_2)\gamma^\mu - (p' + p)^\mu \frac{F_2}{2M_N}\,. \tag{9.13}$$

A common approximation is to use the free nucleon current Γ_1^μ or Γ_2^μ with the free Dirac and Pauli form factors also in the medium. Γ_1^μ and Γ_2^μ are equivalent for on-shell nucleons, but the results differ when one applies them to the off-shell case.

A further problem arises with current conservation: the vector part of the current has to be conserved. However, using the simpler forms Γ_1^μ or Γ_2^μ instead of Γ_{off}^μ, we find that

$$q_\mu j_i^\mu \neq 0, \tag{9.14}$$

with $j_i^\mu = \bar{u}(p')\Gamma_i^\mu u(p)$, $i = 1, 2$, and therefore, the current is not conserved.

Different recipes to restore current conservation on the nucleon or nucleus level are discussed in Refs. [NPKO90, DF83, M$^+$76, BFN$^+$05] — in Ref. [PNK96], it is shown, that the different methods can be understood as a choice of gauge. Some of them are introduced in the following and compared to our approach. We further show that our current fulfills $q_\mu j^\mu = 0$.

Before we continue, we briefly repeat how the hadronic tensor $H^{\mu\nu}$ is constructed out of the currents, namely

$$H^{\mu\nu} = \frac{1}{2}\mathrm{Tr}\left[(\not{p} + M)\tilde{\Gamma}_i^\mu (\not{p}' + M')\Gamma_i^\nu\right], \tag{9.15}$$

where M (M') is the mass of the initial (final) nucleon. Alternatively, but fully equivalent, it can also be written in terms of two structure functions, W_1 and W_2, as

$$H^{\mu\nu} = W_1 \left(-g^{\mu\nu} + \frac{q^\mu q^\nu}{q^2} \right) + \frac{W_2}{M^2} \left(p^\mu - \frac{(pq)}{q^2} q^\mu \right) \left(p^\nu - \frac{(pq)}{q^2} q^\nu \right) , \tag{9.16}$$

where M is the mass of the initial nucleon. The structure functions depend on the two scalars, Q^2 and (pq). This expression is most general and can be applied to all inelastic contributions. In the case of quasielastic scattering, the two structure functions, W_1 and W_2, are simply related to the measured electric and magnetic nucleon form factors, G_E and G_M (Sachs form factors), which depend only on q^2.

9.3.2 Models

We shall now discuss the recipes for off-shell cross sections used in the literature and compare them to our approach.

Our approach. For completeness, we briefly review our approach introduced in Section 8.1.1: we use free spinors for the wave function of initial and final states describing nucleons of mass $M = \sqrt{p^2}$ and $M' = \sqrt{p'^2}$, i.e., not necessarily on-shell nucleons of mass M_N. p and p' are the full off-shell in-medium four-vectors; we use full in-medium momentum conservation with $p' = p + q$ with q fully determined by the lepton kinematics. Thus, the binding effects are already taken into account there. Our QE hadronic tensor then reads [Eq. (4.2) on page 29]

$$H^{\mu\nu}_{\mathrm{QE}} = \frac{1}{2} \mathrm{Tr} \left[(\not{p} + M) \tilde{\Gamma}^\mu (\not{p}' + M') \Gamma^\nu \right] , \tag{9.17}$$

with [Eq. (4.7) on page 30]

$$\Gamma^\mu = F_1 \left(\gamma^\mu + \frac{\not{q} q^\mu}{Q^2} \right) + \frac{F_2}{2M_N} \mathrm{i} \sigma^{\mu\alpha} q_\alpha \, . \tag{9.18}$$

The term $\not{q} q^\mu / Q^2$ ensures that $q_\mu \bar{u}(p') \Gamma^\mu u(p) = 0$ is fulfilled even when $M \neq M'$:

$$\bar{u}(p') \left(F_1 \left(\not{q} + \frac{\not{q} q^2}{Q^2} \right) + \frac{F_2}{2M_N} \mathrm{i} \sigma^{\mu\alpha} q_\mu q_\alpha \right) u(p) = \bar{u}(p') F_1 \left(\not{q} - \frac{Q^2}{Q^2} \not{q} \right) u(p) = 0 \, , \tag{9.19}$$

because the term $\sigma^{\mu\alpha} q_\mu q_\alpha$, antisymmetric in μ and α, vanishes.

De Forest. The assumption made by De Forest [DF83] is that the wave functions of both the plane-wave final nucleon (unbound) and also the initial bound nucleon are given by the Dirac spinor for an on-shell nucleon. For the initial nucleon it is assumed that this spinor is determined through its three-momentum, $\mathbf{p}$, the missing momentum of the initial nucleon, and the corresponding on-shell energy, E_{on}.

A measure of how far one is from the on-shell kinematics is provided by the energy transfer. The actual energy transfer to the nucleon, ω, is determined by the lepton kinematics. If the initial nucleon were on its mass shell, its energy would be $E_{\text{on}} = \sqrt{\mathbf{p}^2 + M_N^2}$, where $\mathbf{p}$ is the missing momentum. The energy transfer, $\tilde{\omega}$, which one would have in that case is given by

$$\tilde{\omega} = p_0' - E_{\text{on}}. \tag{9.20}$$

Assuming that the current operators are not modified by the nuclear environment, the off-shell extrapolation of the currents Γ_1 (leading to De Forest's σ_1^{CC}) and Γ_2 (leading to De Forest's σ_2^{CC}) is simply done by shifting ω and p_0 whenever the latter appear explicitly, i.e., lepton scattering off a bound nucleon with momentum transfer q can be described by lepton scattering off a free nucleon with momentum transfer $\tilde{q} = (\tilde{\omega}, \mathbf{q})$. Hence, binding effects are taken into account through the replacement

$$q = (\omega, \mathbf{q}) \rightarrow \tilde{q} = (\tilde{\omega}, \mathbf{q}), \tag{9.21}$$

and,

$$p_0 \rightarrow E_{\text{on}}. \tag{9.22}$$

De Forest's hadronic tensor then reads

$$H^{\mu\nu}_{\text{DF1,2}} = \frac{1}{2}\text{Tr}\left[(\not{p} + M_N)\tilde{\Gamma}^{\mu}_{1,2}(\tilde{q})(\not{p}' + M_N)\Gamma^{\nu}_{1,2}(\tilde{q})\right]. \tag{9.23}$$

The replacement of ω with $\tilde{\omega}$ poses a considerable conceptual problem in that it leads to a violation of current conservation. A prescription chosen by De Forest to overcome this difficulty is to replace the longitudinal component J_l, parallel to $\mathbf{q}$, by the charge density J_0 so that

$$J_l \rightarrow J_l' = \frac{\omega J_0}{|\mathbf{q}|}, \tag{9.24}$$

and thus work with a four-current

$$J_\mu = \left(J_0, \mathbf{J}_t, \frac{\omega J_0}{|\mathbf{q}|}\right), \tag{9.25}$$

with the transverse component $\mathbf{J}_t = (J_1, J_2)$. Pollock *et al.* [PNK96] state, that this would be correct and of no consequence if the current indeed was conserved. However, the above prescription is non-unique. For example, one might have just as well chosen the opposite way by eliminating the charge density instead: different recipes are discussed and compared for different experimental scenarios in Ref. [PNK96].

Saclay. The prescription used by the Saclay collaboration [M$^+$76] is very similar to our approach. They also use free spinors for the wave functions of initial and final states, describing nucleons of effective mass $M = \sqrt{p^2}$, and take the outgoing nucleon on-shell. Their hadronic tensor then reads

$$H^{\mu\nu}_{\text{Sac}} = \frac{1}{2}\text{Tr}\left[(\not{p} + M)\tilde{\Gamma}^{\mu}_{\text{Sac}}(\not{p}' + M_N)\Gamma^{\nu}_{\text{Sac}}\right]. \tag{9.26}$$

For the current they use, based on Γ^{μ}_1,

$$\Gamma^{\mu}_{\text{Sac}} = G_M\gamma^{\mu} + \frac{p^{\mu} + p'^{\mu}}{M + M_N}\frac{G_E - G_M}{1 - \frac{q^2}{(M+M_N)^2}} - \frac{M_N - M}{q^2}q^{\mu}\frac{G_E - \frac{q^2}{(M+M_N)^2}G_M}{1 - \frac{q^2}{(M+M_N)^2}}. \tag{9.27}$$

$G_{E,M}(q^2, M)$ are two a priori unknown form factors; in the limit $M = M_N$ they correspond to the free Sachs form factors which are then used in this approach. The last summand corresponds to our current-conserving factor. The only difference to our case is, when we put p' on-shell, the form factor normalization $M + M_N$ instead of $2M_N$.

Benhar. De Forest's prescription discussed in [DF83] has been widely used, e.g., by Benhar *et al.* [BFN$^+$05, BDS08]. They apply De Forest's replacement $q = (\omega, \mathbf{q}) \to \tilde{q} = (\tilde{\omega}, \mathbf{q})$, $p_0 \to E_{\text{on}}$ not at the current level but at the tensor level (cf. Eq. (9.16)) which is totally equivalent. $H^{\mu\nu}_{\text{Ben}}$ then reads

$$H^{\mu\nu}_{\text{Ben}} = W_1\left(-g^{\mu\nu} + \frac{\tilde{q}^{\mu}\tilde{q}^{\nu}}{\tilde{q}^2}\right) + \frac{W_2}{M_N^2}\left(p^{\mu} - \frac{(p\tilde{q})}{\tilde{q}^2}\tilde{q}^{\mu}\right)\left(p^{\nu} - \frac{(p\tilde{q})}{\tilde{q}^2}\tilde{q}^{\nu}\right), \tag{9.28}$$

with W_1 and W_2 also taken at $\tilde{q}$ and $M = M_N$.

Ferree/Koltun. The approach of Ref. [FK97] is comparable to the previous one by the Saclay group: the effective mass is used for the bound initial nucleon (and thus also the energy); the outgoing nucleon is treated on-shell. However, they do not modify the current, but, as Benhar, the hadronic tensor of Eq. (9.16):

$$H^{\mu\nu}_{\text{Fer}} = W_1\left(-g^{\mu\nu} + \frac{q^{\mu}q^{\nu}}{q^2}\right) + \frac{W_2}{M^2}\left(p^{\mu} - \frac{(pq)}{q^2}q^{\mu}\right)\left(p^{\nu} - \frac{(pq)}{q^2}q^{\nu}\right), \tag{9.29}$$

with

$$W_1 = -\frac{q^2}{4M^2}\,\delta\left(\omega + \frac{q^2}{2M}\right)\,G^2_{M_N}, \tag{9.30}$$

$$W_2 = \frac{1}{1 - q^2/4M^2}\,\delta\left(\omega + \frac{q^2}{2M}\right)\left(G^2_{E_N} - \frac{q^2}{4M^2}G^2_{M_N}\right). \tag{9.31}$$

$M = M_N + U_N = \sqrt{p^2}$ and p is the full in-medium four-vector — no shift to on-shell properties has been done here. It is worthwhile to mention that the effective mass also enters the form factor relations between W_i and F_i.

9.3.3 Results

In the following we compare the above approaches for inclusive QE electron scattering off ^{16}O only at beam energies ranging from 700 to 1500 MeV and a fixed electron-scattering angle of $\theta_{k'} = 32^\circ$. Since some recipes are restricted to the half off-shell case, i.e., the final nucleon is on-shell, we perform the comparison under this restriction. The meaning of the different curves is as follows:

(1) our standard approach with the current-conserving term

(2) our standard approach without the current-conserving term

(3) De Forest approach with current Γ_2 and q shift, but without current-conserving term Eq. (9.24)

(4) De Forest approach with current Γ_2 and $q, p(0)$ shift with current-conserving term Eq. (9.24)

(5) De Forest approach with current Γ_1 and $q, p(0)$ shift, but without current-conserving term Eq. (9.24)

(6) De Forest approach with current Γ_1 and $q, p(0)$ shift with current-conserving term Eq. (9.24)

(7) Saclay approach

(8) Benhar approach

(9) Ferree/Koltun approach

We have checked that all models agree on-shell as they should. In Fig. 9.10 we show the calculation with the momentum-dependent mean-field potential included. Even then, the difference between the curves is only minor, except for the Koltun approach, which is above all others.

We conclude from this discussion that there are in principle two approaches to the off-shell extrapolation: one is to shift the kinematical variables to their on-shell values and use them to calculate the hadron tensor derived from on-shell formulae; the other one replaces the original on-shell quantities in the hadron tensor by the in-medium variables. Current conservation can be restored in many different ways as discussed. However, we find almost no influence on the cross section. Here we agree with the findings of Rosenfelder [Ros80].

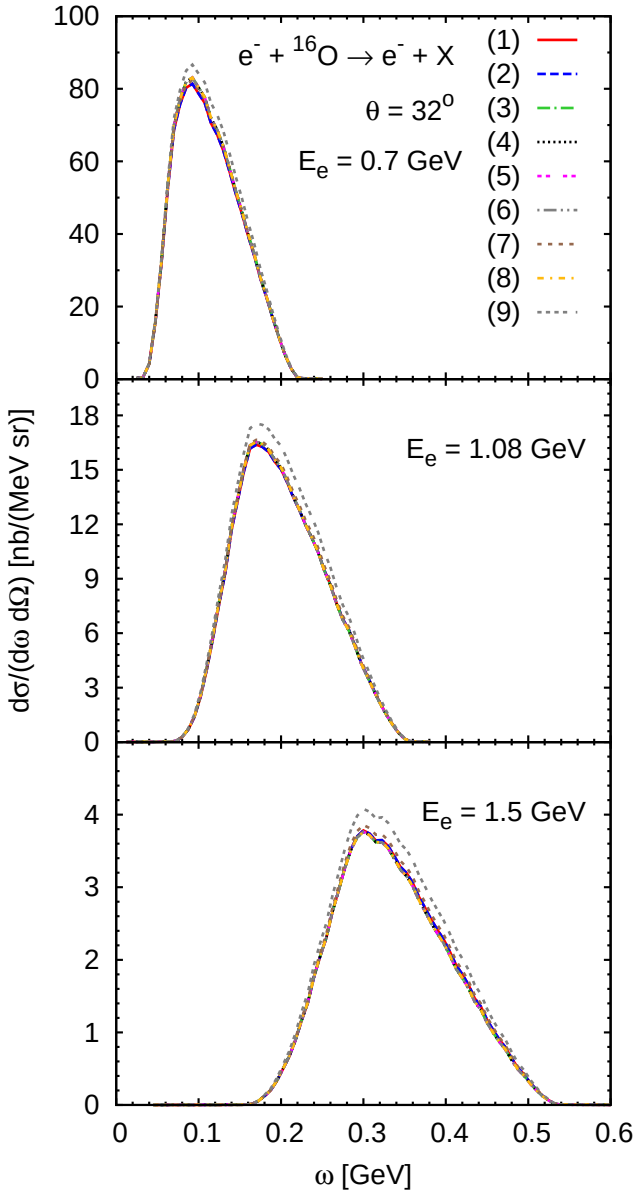

Figure 9.10: Inclusive electron cross section $\mathrm{d}\sigma_{\mathrm{EM}}/\mathrm{d}\omega\mathrm{d}\Omega$ on ^{16}O a function of the energy transfer $\omega = k_0 - k'_0$ at a scattering angle of $\theta_{k'} = 32^\circ$ including a momentum-dependent mean-field potential for the initial nucleons. We show the results for various beam energies. The different lines stand for different QE in-medium recipes and are detailed in the text.

9.4 Model validation: electron scattering

Until now, a detailed comparison to inclusive neutrino-nucleus scattering data is not possible. In principle, there are data are taken for Neon, Propane and Freon targets at Gargamelle (CERN) [P$^+$79b, P$^+$79a] and at the Serpukhov bubble chamber SKAT [B$^+$85, B$^+$90], but these experiments were limited in statistics with large neutrino-flux uncertainties with the consequence that the large error bars do not allow to draw any conclusion about the role of nuclear effects. Future data, in particular those from the MINERνA experiment [MINERvA04], will become more sensitive to in-medium processes so that a meaningful comparison will be possible (cf., also the discussion in Section 12.1).

We have discussed in Part II the relation between electromagnetic and weak transitions in detail, in particular, we have shown that the vector part of the current is probed by electrons and neutrinos. The axial part, however, is only probed by neutrinos. But inclusive electron scattering does not only provide a test of the vector part but also of the nuclear effects. The nuclear model applied in this work is independent of the incoming lepton, and high-statistics electron data can be used for a conclusive check.

Therefore, at this stage, the successful description of electron-scattering cross sections is a necessary, but not sufficient, condition for our neutrino model. In the following, we present results for inclusive electron spectra and compare them to electron-nucleus scattering data. The results are obtained using the very same model (and code!) as for the neutrinos with differences only at the lepton-nucleon vertex, i.e., without the axial current.[1]

In Fig. 9.11 we show the inclusive electron cross section $\mathrm{d}\sigma/(\mathrm{d}\omega\mathrm{d}\Omega_{k'})$ on ^{16}O (left panels) and ^{12}C (right panels) as a function of the energy transfer for various beam energies, but at a fixed scattering angle of $\theta = 32^\circ$ and $\theta = 37.5^\circ$, respectively. Good overall agreement to the experimental electron scattering data is achieved both in the QE and in the pion-production region by taking into account mean fields and in-medium spectral functions (Oset prescription for the Δ in-medium width) in addition to a local Fermi-gas momentum distribution. As discussed in connection with Fig. 9.5, we find that the momentum dependence of the mean field broadens and shifts the QE peak due to the target-momentum dependent energy loss and that the inclusion of in-medium widths leads to a further broadening (see also Fig. 9.6).

Our results are supported by the work of Rosenfelder [Ros80] who finds within a local Thomas-Fermi model with a Walecka-type mean-field potential that the momentum dependence of the potential is required to obtain the shift of the QE peak. An important quantity in this model is the effective nucleon mass, $M^\star$, so that the momentum-dependent potential for small momenta ($|\mathbf{p}| \ll M^\star$, $|\mathbf{p}| \ll M$) can be

[1] For an extensive investigation of electron scattering off complex nuclei, we refer to Ref. [Bus08].

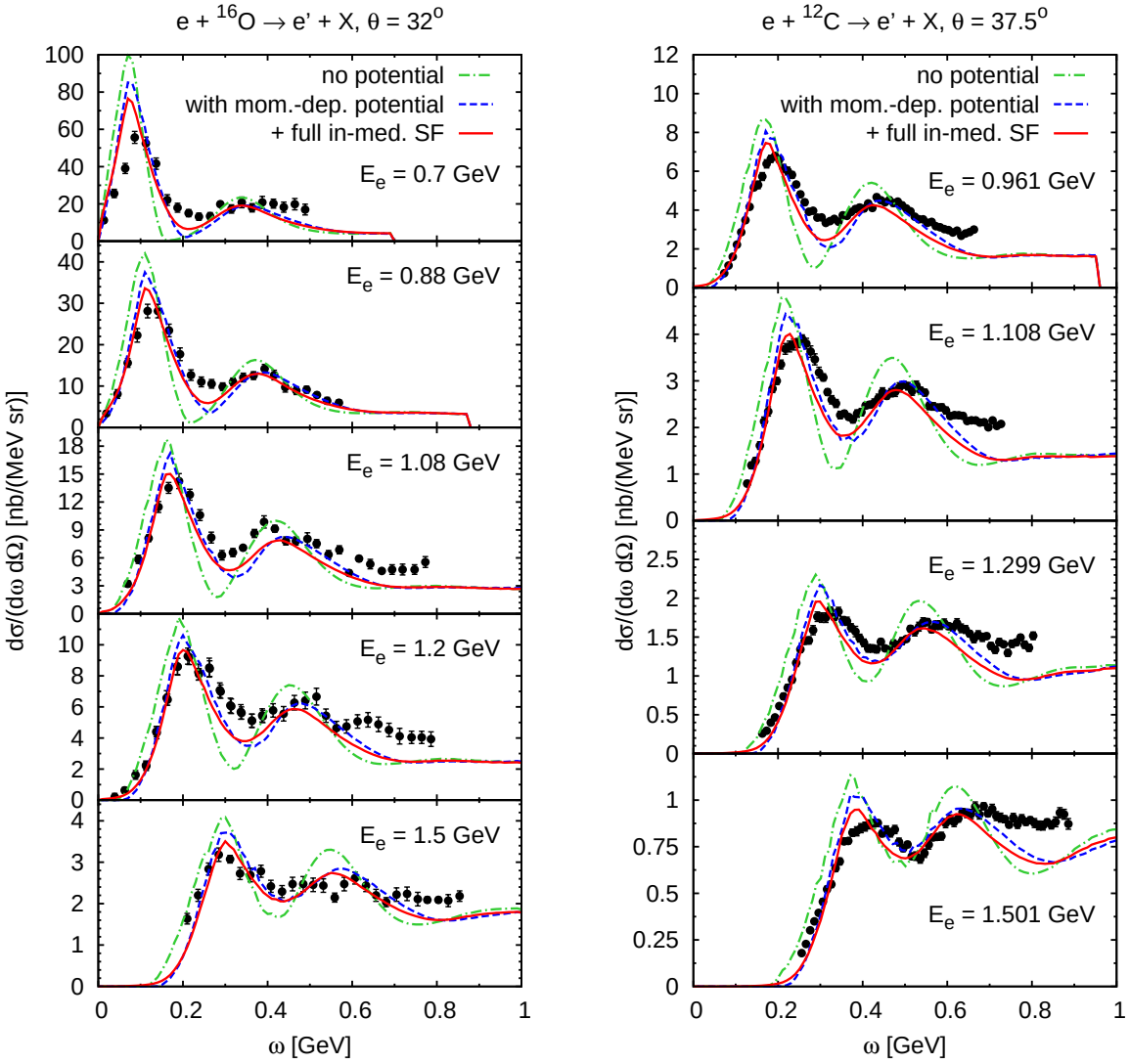

Figure 9.11: Left panel: inclusive electron cross section $\mathrm{d}\sigma/(\mathrm{d}\omega\mathrm{d}\Omega_{k'})$ on ^{16}O as a function of the energy transfer ω at five distinct fixed electron energies (0.7, 0.88, 1.08, 1.2 and 1.5 GeV) and a scattering angle of $\theta = 32^\circ$. This corresponds to $Q^2 = 0.134, 0.205, 0.302, 0.366, 0.550\,\mathrm{GeV}^2$. No potential has been included in the dash-dotted lines; the dashed lines denote the result, where we include all in-medium modifications except collisional broadening. The solid lines are obtained with our full model. The data are taken from Refs. [A$^+$96, A$^+$95]. Right panel: same on ^{12}C at four distinct electron energies (0.961, 1.108, 1.299 and 1.501 GeV) and a scattering angle of $\theta = 37.5^\circ$ ($Q^2 = 0.315, 0.408, 0.542, 0.700\,\mathrm{GeV}^2$). The data are taken from Ref. [S$^+$89].

written as (for a derivation, see page 129 of Ref. [Bus08])

$$V(\mathbf{r},\mathbf{p}) \approx p^2 \frac{M - M^\star(\mathbf{r})}{2MM^\star(\mathbf{r})} + M^\star(\mathbf{r}) - M. \tag{9.32}$$

Then, according to Rosenfelder, it is possible to adjust the value of $M^\star$ to fit the QE peak to electron-scattering data. We note, that the mean-field potential applied in our case has been fixed by nucleon-nucleus scattering as outlined in Section 7.4 and is not fitted to match the electron data. This possibility, however, has been investigated in detail in Section 7.2.3 of Ref. [Bus08]. Buss finds, that the correspondence with the data can only be improved with rather unrealistic potential parameters — within meaningful parameter ranges the improvement is only minor.

Even though the overall correspondence to the data is satisfactory, some problems remain: in particular at higher beam energies, the data are underestimated at ω due to the fact that non-resonant 2π-production channels have not yet been included. We further systematically underestimate the dip region between the QE and Δ peaks. Conventionally, it is attributed to 2N excitations not included in our model, but we note, that the description of this region is considerably improved by including collisional broadening of the QE peak which shuffles strength into the dip region.

We also find a discrepancy at the QE peak for very low $Q^2 \leq 0.15\,\mathrm{GeV}^2$ (cf., in particular, upper left plot corresponding to $Q^2 = 0.13\,\mathrm{GeV}^2$), where our model overestimates the data and does not fully resemble the peak shift. In view of this, the influence of the initial momentum distribution of the nucleons has been studied in [Bus08, LBARM09]. There, our local Thomas-Fermi approach has been compared to the widely used global Fermi-gas approximation, where the Fermi momentum does not depend on the density, and thus, nucleon momentum and position are not correlated as in the local Thomas-Fermi ansatz (cf., page 89 and in particular Figs. 7.3 and 7.4). Qualitative and quantitative differences have been found; in particular, the shift of the QE peak is easily obtained in the global Fermi-gas picture, while the peak shift is not sufficient in the local Thomas-Fermi picture. Additionally, Kalok found, that the inclusion of the imaginary part in the hole spectral function cannot cure the low-Q^2 discrepancy (cf., in particular, Figs. 5.2-5.4 in Ref. [Kal07]).

We conclude by comparing to electron-scattering data that our model is able to describe the QE region for beam energies above $\approx 1\,\mathrm{GeV}$ while there is room for improvement at lower beam energies, where nuclear many-body effects become important and the impulse approximation breaks down [Ank08]. The good agreement at higher energies at the QE peak and also in the single-π region shows that our low-density ansatz for the in-medium width and the inclusion of a proper potential incorporate the main nuclear corrections.

9.5 Comparison to other approaches

Finally, we compare our results to the ones obtained in other models, first focusing on the results obtained for ^{16}O nuclei. The work of Butkevich *et al.* [BK07, BM05] addresses the quasielastic peak region in a relativistic distorted-wave impulse approximation (RDWIA) approach. Their latest model for the ground state spectral function includes both a 75% shell-model and a 25% high-momentum contribution. When calculating inclusive cross sections, the final-state wave functions are obtained using a real optical potential. This procedure neglects the broadening of the outgoing nucleon in the medium but incorporates a shift of the outgoing nucleon energy. A direct comparison to models based on DWIA with *complex optical potentials* (*RDWIA exclusive* result in Butkevich *et al.* [BK07] or, e.g., calculations of Martinez *et al.* [MLJ$^+$06] and Maieron *et al.* [MMCU03]) is not possible since the imaginary part leads to a flux reduction in a particular channel. Thus, these models rather describe exclusive quasi-free single-nucleon knockout processes than fully inclusive scattering considered here.

Meucci *et al.* [MGP04b, MCGP03] apply a relativistic Green's function approach to both inclusive and exclusive processes. They achieve an impressive description of the data in the QE region. In the Green's function framework a complex optical potential can be incorporated when calculating inclusive cross sections without having the DWIA problem of flux reduction.

The model of Benhar, Nakamura and collaborators [BFN$^+$05, BM06, NSNB07, BM07] is based on non-relativistic nuclear many-body theory in the impulse approximation. It includes realistic spectral functions for the hole states obtained from $(e,e'p)$ data combined with theoretical nuclear-matter calculations using the local-density approximation. For the final-state spectral function, they rely on a correlated Glauber approximation, which leads to an energy shift of the cross section and to a redistribution of the strength (quenching of the peak and enhancement of the tail). Note that in this approach the outgoing nucleons are not bound any more — in our model they are still under the influence of the mean-field potential (see the comparison presented in Fig. 9.5 where we have shown that this leads to an additional shift of the peaks). In particular in the quasielastic peak region, they achieve good agreement to inclusive electron-scattering data. The framework of Benhar *et al.* provides a state-of-the-art description for the hole spectral functions including both real and imaginary parts of the self energy. However, more relevant for the observables discussed here is the real part while the impact of the imaginary part is minor due to the rather small width of the initial nucleons (see also Refs. [LLLM02, Kal07]). In our model, the real part of the hole self energy is taken into account for the initial nucleons through the mean-field potential while the imaginary part is neglected (we include both, real and imaginary part, in the spectral function of the final particle).

The model of Gil, Nieves and others, applicable to both inclusive electron [GNO97] and neutrino reactions [NAV04], takes into account nuclear corrections beyond Pauli blocking: they include both long and short range correlations as well as particle and hole spectral functions. These nuclear correlations are often taken into account as RPA resummation of particle-hole and Δ-hole states. As in our approach, they neglect the imaginary part of the self energy in the hole spectral function. Within their model Gil *et al.* [GNO97] achieve impressive agreement with data for electron-nucleus scattering. Nuclear correlations are also taken into account by Singh, Oset and collaborators [SSAA06b, SO92] for neutrino scattering. They renormalize the weak-transition strength, which is found to be very important at low momentum transfers. Singh *et al.* [SVVO98] have also pointed out that the in-medium modification of the Δ width causes a reduction of the $\nu A \to \Delta X$ cross section.

Fig. 9.12 shows a comparison of our full result (solid line) for inclusive electron scattering off ^{16}O with the results of other models. The dotted curves show the latest results of Nakamura, Benhar *et al.* [NSNB07]. Their model gives a better description of the QE-peak than ours at 880 MeV. However, at 1200 MeV both describe the data in the QE peak equally well. In the pion-production region, Nakamura tends to overshoot the data, and the Δ-peak position seems somewhat low in ω. This region is also underestimated by the model of Ref. [BM06] (dash-dotted line). Our model lacks strength in the dip region but describes properly the magnitude and position of the Δ peak. The framework of Butkevich *et al.* [BK07], which only includes QE scattering, fails in the same kinematical situation as our model (700 MeV, double-dashed line in upper panel) but leads to very good results at 880 MeV. The Green's function approach of Meucci *et al.* [MGP04b] is able to describe very well all the data in the QE region.

In Fig. 9.13 we compare our CC calculation to the models introduced above for the integrated inclusive cross section on ^{16}O as a function of the neutrino energy. The left panel shows the contribution from QE scattering while the right panel shows the pure Δ contribution. Our full result is denoted by the solid line labeled "GiBUU". The overall agreement with the other models is satisfactory. Focussing on the QE contribution, our curve is higher than other calculations at lower neutrino energies. Also, for the Δ our calculation is slightly higher. However, note that part of the differences are already present at the nucleon level and do not only arise from the different treatment of nuclear corrections.

Impressive agreement between very different approaches is found for ν_μ CCQE scattering off ^{12}C. In Fig. 9.14 we show the muon kinetic energy cross section for two fixed values of E_ν.[2] Our result is compared to results of Ankowski *et al.* [AS08], which is very similar to Benhar's approach, and of the Madrid group (cf., e.g., Ref. [MMCU03] for details). The shift of the threshold at the right hand side of the spectra is caused by

[2]This figure shows the outcome of comparing different models as shown at NUINT09 [Sob09].

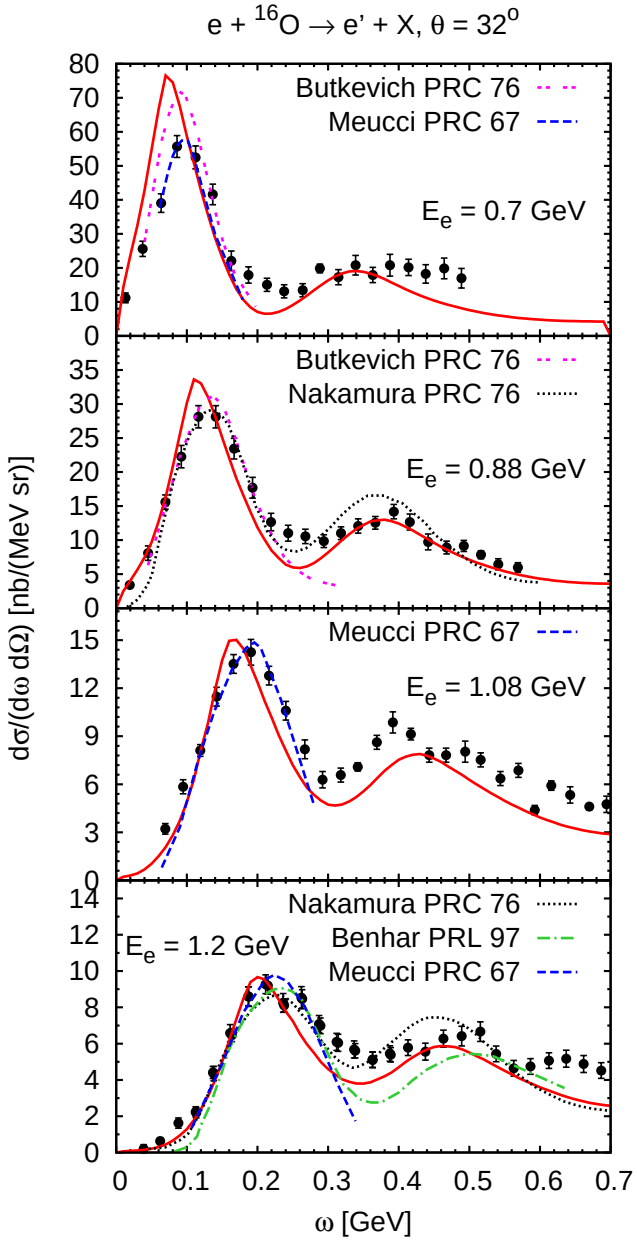

Figure 9.12: Inclusive electron cross section $\mathrm{d}\sigma/(\mathrm{d}\omega\mathrm{d}\Omega_{k'})$ on ^{16}O as a function of the energy transfer ω at four distinct fixed electron energies (0.7, 0.88, 1.08 and 1.2 GeV) and a scattering angle of $\theta_{\mathbf{k}'} = 32°$. The solid lines denote our full result, the dashed lines are taken from Meucci *et al.* [MGP04b], the double-dashed ones from Butkevich *et al.* [BK07] (RDWIA), the dotted ones from Nakamura *et al.* [NSNB07] and the dashed-dotted one from Benhar *et al.* [BM06]. The data are taken from Refs. [A$^+$96, A$^+$95].

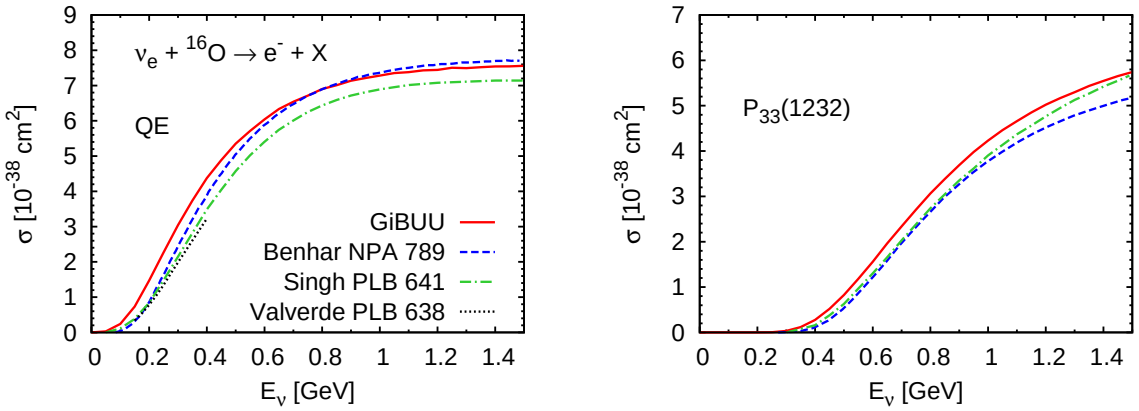

Figure 9.13: Inclusive CC electron neutrino cross section σ on ^{16}O as a function of the neutrino energy and integrated over the leptonic variables. The left panel shows the QE contribution, the right one the Δ contribution. Our results are denoted by the solid lines. We compare to Benhar *et al.* [BM07] (their "SF-PB" calculation), Singh *et al.* [SSAA06b] and Valverde, Nieves and others [VAN06] (their full model).

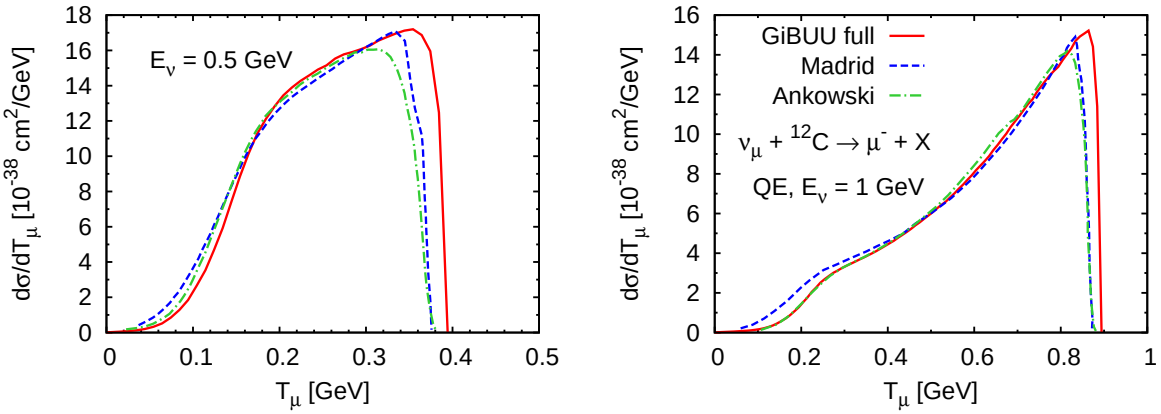

Figure 9.14: Inclusive CCQE cross section $d\sigma/dT_\mu$ on ^{12}C for $E_\nu = 0.5\,\text{GeV}$ and $1\,\text{GeV}$. Besides our result, calculations from Ankowski and from the Madrid group are shown (curves taken from Ref. [Sob09]).

the different treatment of the outgoing nucleons: in our model, the outgoing nucleons are still under the influence of the mean-field potential (see also Fig. 9.5).

10
Pion production on nuclei

10.1 Introduction

Neutrino-induced pion production on nucleons up to energies of about 1.5 GeV is dominated by the excitation and subsequent decay of the Δ resonance but, depending on the channel, non-resonant pion production is not negligible. At higher energies, more massive resonances become increasingly important as we have seen in Part II and as also stated in Refs. [FN79, RS81, SUL03, LPP06, HNV07, HNS$^+$08].

A realistic treatment of the FSI is an essential ingredient for modeling pion production off nuclei in a realistic manner. FSI may lead, e.g., to pionic final-state particles, even though the initial event was quasielastic scattering. However, the few available calculations deal with FSI in an oversimplified way. The study of semi-inclusive pion production presented by Paschos *et al.* [PPY00] includes pion absorption and charge exchange but does not properly take into account the important features of $\pi N\Delta$ dynamics, leading to unrealistic pion spectra as we shall see later. Extending the model of Ref. [SVVO98], Ahmad *et al.* [ASAS06] include, besides pion absorption, also elastic and charge-exchange rescattering using empirical vacuum πN cross sections.

In the following, we first present results for CC and NC neutrino scattering off nuclei. In particular, we focus on the influence of final-state interactions on pion production under different assumptions. Then, we compare our model to others.

The results of this chapter have been partly published in Refs. [LARM06a, LARM06b, LBMAR07, LBMAR08].

10.2 CC pion production

By pion production we understand the process where besides the outgoing lepton one or more pions are detected. The corresponding cross section has been given in Chapter 8 [Eq. (8.7)] and reads

$$\mathrm{d}\sigma_{\mathrm{tot}}^{\ell A\to\ell'\pi X} = \int\limits_{\text{nucleus}} \mathrm{d}^3 r \int \frac{\mathrm{d}^3 p}{(2\pi)^3}\Theta(p_F(r)-p)\,\frac{k\cdot p}{k^0 p^0}\,\mathrm{d}\sigma_{\mathrm{tot}}^{\mathrm{med}}\,P_{\mathrm{PB}}(\mathbf{r},\mathbf{p})\,M_\pi(\mathbf{r},\mathbf{p}), \quad (10.1)$$

with the medium modified cross section $\mathrm{d}\sigma_{\mathrm{tot}}^{\mathrm{med}}$ discussed in Chapter 8. The pion multiplicities M_π are determined with the GiBUU transport model.

10.2.1 Double differential pion cross sections

We start our discussion of pion production with the double differential cross sections shown in Fig. 10.1 and Fig. 10.2. There we plot the cross section for ν_μ-induced CC π^+ and π^0 production on ^{12}C at $E_\nu = 1\,\mathrm{GeV}$ as a function of energy transfer ω and muon scattering angle θ. In this calculation all medium modifications of the elementary cross section are included. The left panels show the results without FSI which are included in the right panels: once produced, the Δ — which dominates the pion production — can decay into πN or interact via $\Delta N \to NN$, $\Delta NN \to NNN$, $\Delta N \to \pi NN$ or $\Delta N \to \Delta N$. The produced pions interact through $\pi N \to \pi N$, $NN\pi \to NN$ and $\pi N \to \Delta$, i.e., they can scatter elastically, undergo charge exchange or be absorbed. This results in the creation of additional pions or their absorption.

The cross sections in Fig. 10.1 and Fig. 10.2 peak clearly at the position of the Δ (compare to the inclusive cross section shown in Fig. 9.1 on page 121). This clearly indicates that most of the produced pions come from the initially produced Δ resonances. Pions can also originate in multi-step processes initiated by QE scattering. There, the final-state nucleon can rescatter in the nucleus and create pions through $NN \to N\Delta$ or $NN \to NN\pi$. However, this effect, which can occur only at high momentum transfer Q^2, is less important as we will see later.

10.2.2 Total pion cross sections

In Fig. 10.3, we show the total cross section for π^+ (top) and π^0 production (bottom panels) on ^{12}C (left) and ^{56}Fe (right panels), i.e.,

$$\nu_\mu A \to \mu^- \pi^{+/0} X. \quad (10.2)$$

We compare different "counting schemes": the solid lines stand for the scenario with a single pion in the final state, i.e., where X does not contain any other pions. To

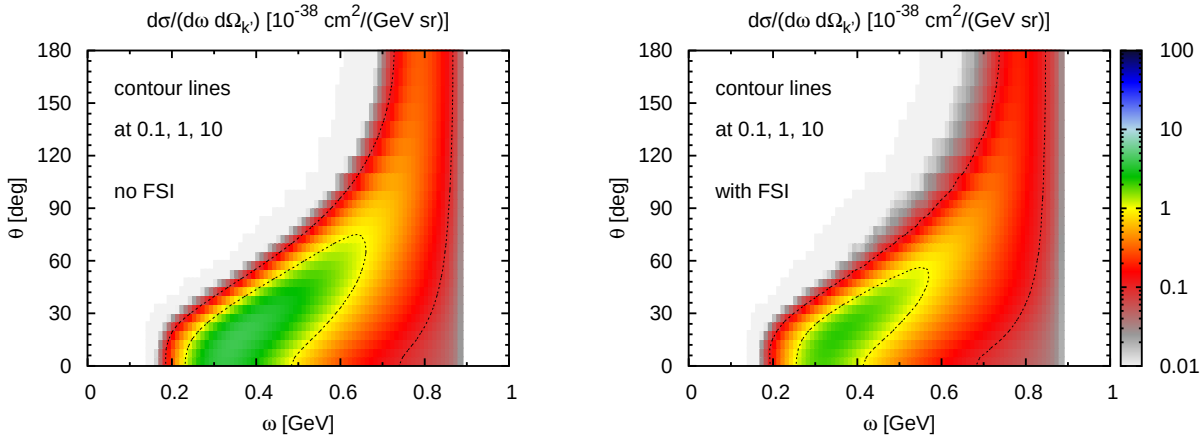

Figure 10.1: Double differential cross section $\mathrm{d}\sigma/(\mathrm{d}\omega\mathrm{d}\Omega_{k'})$ for ν_μ CC π^+ production on ^{12}C as a function of energy transfer $\omega = k^0 - k'^0$ and scattering angle θ at a fixed neutrino energy of $E_\nu = 1\,\mathrm{GeV}$. All in-medium modifications of the elementary cross section are included. The right panel additionally includes FSI.

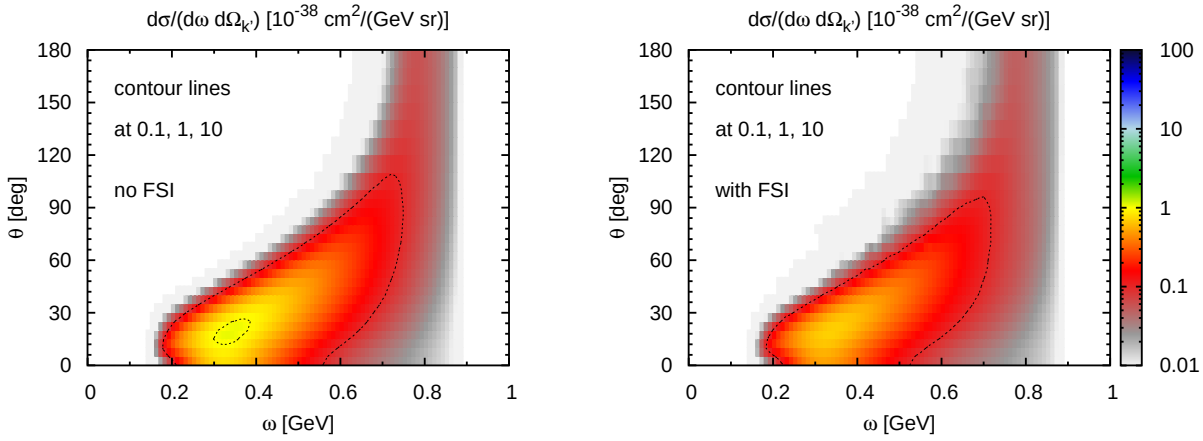

Figure 10.2: Same as Fig. 10.1 for CC π^0 production.

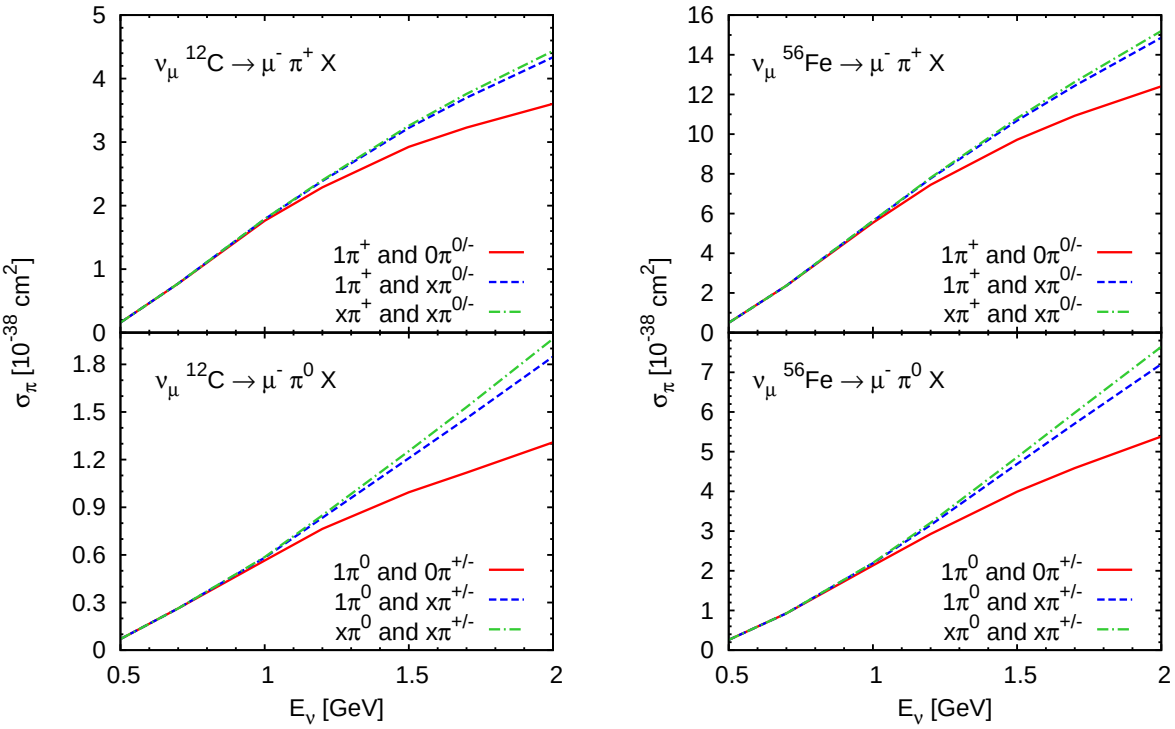

Figure 10.3: Total cross section for CC π^+ (top) and π^0 (bottom panels) production on ^{12}C (left) and ^{56}Fe (right panels) for different pion multiplicities versus the neutrino energy obtained in a full-model calculation including FSI.

obtain the dashed lines, we count all events which, besides the single-π of interest, may also contain pions of different charge. The dash-dotted lines are most inclusive. Here, the event may contain more than exactly one pion of the considered charge and, in addition, pions of different charge are allowed, too. Up to about 1 GeV neutrino energy, we observe no difference. A minor difference is visible for larger energies caused mainly by the fact that at these energies, the excitation of higher resonances is possible, which then may decay into 2π. In the following — justified also by the experiments (cf. Section 12.1) —, we restrict ourselves to the single-π case denoted by the solid lines, thus, X does not contain any other pions from now on.[1]

The influence of FSI on the pion yields and the origin of the emitted pions is shown in Fig. 10.4. The dashed lines show the result without final-state interactions (only the decay of the initially produced resonances is included), while the solid lines denote

[1]We note that the results presented in our previous work [LARM06a] correspond to the calculation leading to the dash-dotted line; but only Δ excitation and QE scattering have been considered in this work.

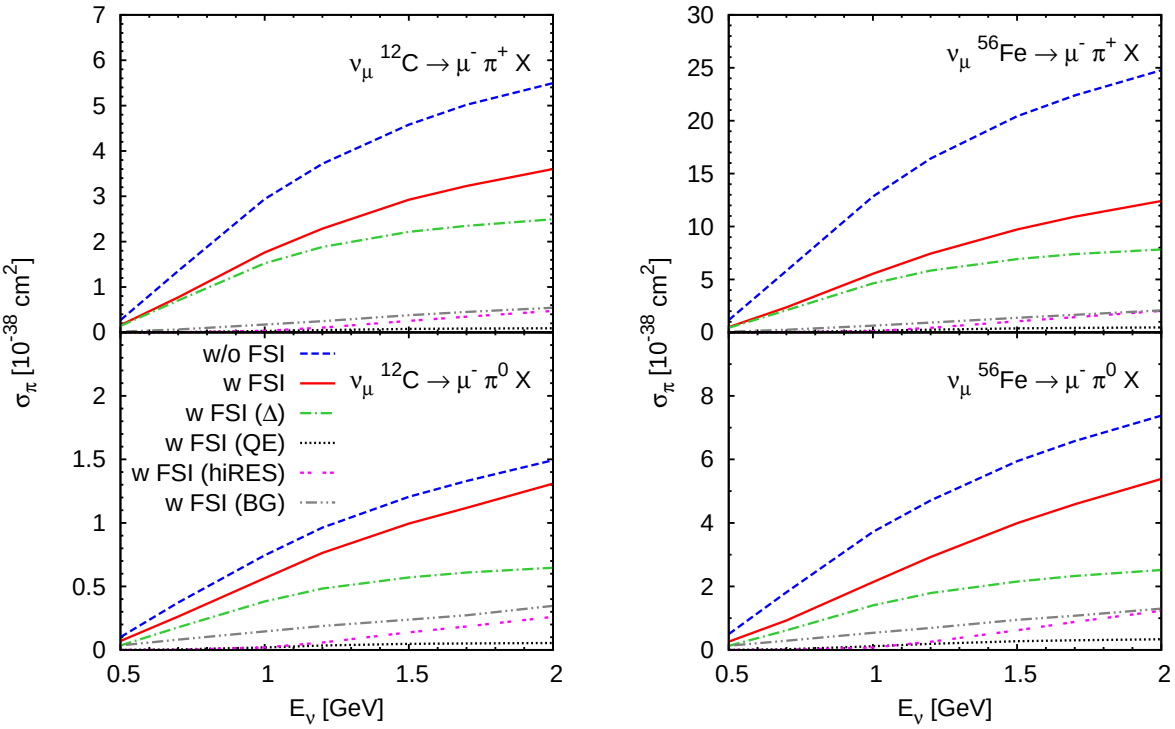

Figure 10.4: Total cross section for CC π^+ (top) and π^0 (bottom panels) production on ^{12}C (left) and ^{56}Fe (right panels). The dashed lines show the results without FSI (only the decay of resonances is possible); the results denoted by the solid lines include FSI. Furthermore, the origin of the pions is indicated (QE, Δ excitation, excitation of higher resonances, single-pion background).

the result of the full calculation. Furthermore, we show the contribution from initial Δ excitation (dash-dotted lines), from initial QE events (dotted), from initial excitation of the higher resonances (double-dashed) and from initial single-pion background events (dash-double dotted).

The cross sections for π^0 production without FSI is significantly lower than the one for π^+. This difference is a consequence of the primary interaction mechanism which is dominated by the Δ resonance excitation,

$$\begin{aligned} \nu_\ell p &\to \ell^- \Delta^{++}, \\ \nu_\ell n &\to \ell^- \Delta^{+}, \end{aligned}$$

where $\sigma_{\Delta^{++}} = 3\,\sigma_{\Delta^+}$ (cf., Section D.2). These Δ resonances decay into pions by (see also Eqs. (5.21)–(5.23) on page 57)

$$\begin{aligned} \Delta^{++} &\to p\pi^+, \\ \Delta^{+} &\to n\pi^+, \;\; p\pi^0. \end{aligned}$$

With the corresponding Clebsch-Gordan coefficients 1, $\sqrt{\frac{1}{3}}$, and $\sqrt{\frac{2}{3}}$, we obtain a ratio of

$$\pi^+ : \pi^0 = \left[3\,Z + \left(\sqrt{\frac{1}{3}}\right)^2 N\right] \left[\left(\sqrt{\frac{2}{3}}\right)^2 N\right]^{-1} = \begin{cases} 5:1 & \text{for } {}^{12}\text{C} \\ 4.4:1 & \text{for } {}^{56}\text{Fe} \end{cases} \tag{10.3}$$

(Z and N are the proton and neutron numbers) for the cross sections *without* final-state interactions. FSI, however, change this ratio. Indeed, the comparison of the π^+ channel to the π^0 channel (top and bottom panels of Fig. 10.4) reveals big differences. For π^+ we find a strong reduction of the cross section due to FSI, while in the π^0 channel this reduction is much smaller (compare solid and dashed lines). The additional strength in the π^0 channel is a consequence of charge exchange scattering, namely $\pi^+ n \to \pi^0 p$, which shuffles strength from the dominant π^+ channel in the subdominant π^0 channel. Side feeding in the opposite direction is strongly suppressed by the ratio of π^+ to π^0 production on the nucleon.

π^0 and π^+ production through FSI of QE scattering is not very sizable and happens only if the neutrino energy is high enough (dotted lines in Fig. 10.4). However, the effect is relatively more important in the π^0 channel than in the π^+ one. This follows from the fact that, while the production of both π^0 and π^+ from initial quasielastic scattering is basically the same, the π^0/π^+ ratio from initially produced Δ resonances is roughly a factor of 4–5 smaller as just outlined. Thus, this effect also enhances the π^0 channel due to FSI.

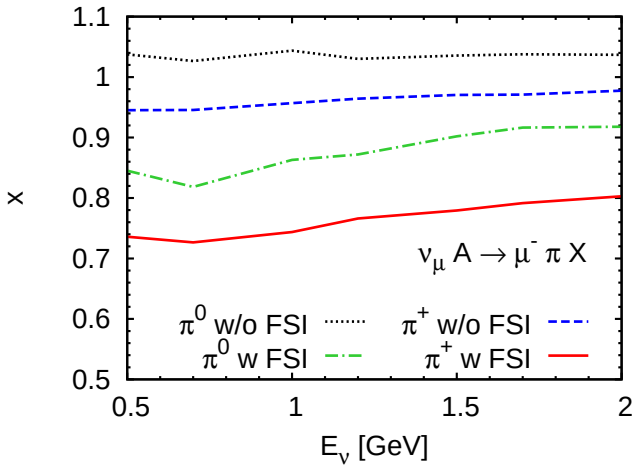

Figure 10.5: Scaling of the CC π^0 and π^+ cross sections with and without FSI as a function of the neutrino energy. x is defined in Eq. (10.4).

Comparing ^{56}Fe and ^{12}C clearly shows that the absorption is significantly larger in the heavier nucleus as expected. To quantify this effect, we show in Fig. 10.5 how the cross sections scale with the mass number A by plotting x, defined via

$$\frac{\sigma_\pi^{\mathrm{C}}}{\sigma_\pi^{\mathrm{Fe}}} = \left(\frac{A^{\mathrm{C}}}{A^{\mathrm{Fe}}}\right)^x , \tag{10.4}$$

versus the neutrino energy. In the case without FSI (dashed and dotted lines), x differs from 1 because π^0 and π^+ production depend, as discussed above, on the relative proton to neutron numbers which are different for Fe and C. π^+ is favored on protons causing the dashed line to lie slightly below 1 since the proton to neutron ratio is larger in C. Opposite behavior is seen for pi^0 production (dotted line slightly above 1) because it can only occur on neutrons and because the neutron to proton ratio is larger for Fe. With FSI, we find that the x value for the π^0 production is larger than for π^+ (dash-dotted vs. solid line). Note that also the difference is larger than in the case without FSI. This effect is caused by the side feeding from the π^+ into the π^0 channel which partly compensates for the π^0 absorption.

π^- cannot be produced directly in the CC neutrino-nucleon reactions, but only via final-state interactions. Thus, they play only a minor role as can be seen in Fig. 10.6 where we plot the total cross section for CC π^+, π^0 and π^- production including FSI. Note that this situation is reversed in anti-neutrino reactions where only Δ^- and Δ^0 can be produced in the initial interaction.

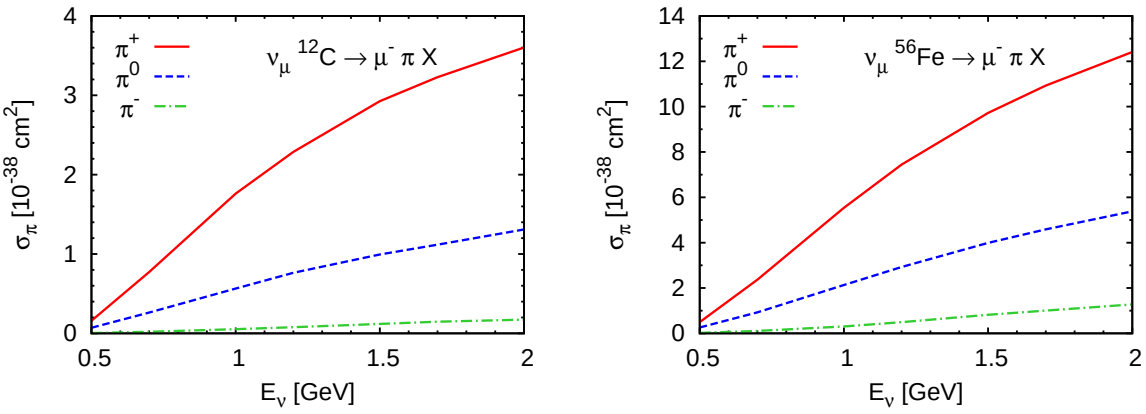

Figure 10.6: Total cross section for CC π^+ (dashed), π^0 (solid) and π^- (dash-dotted lines) production on ^{12}C (left) and ^{56}Fe (right panel) versus the neutrino energy. These results were obtained with a full-model calculation including FSI.

10.2.3 Pion kinetic-energy spectra

Further details on pion production can be brought up by studying the single-pion kinetic-energy distributions. They are shown in Fig. 10.7 (Fig. 10.8) for ν_μ CC π^+ (π^0) production at different values of E_ν for both, ^{12}C and ^{56}Fe. The dashed lines show the result without final-state interactions and the solid lines the result of the full calculation. The maximum of the solid curves (i.e., the calculation with final-state interactions) peaks at 0.05 - 0.1 GeV in all cases shown in Fig. 10.7 and in Fig. 10.8. This is due to the energy dependence of the pion absorption. The absorption is higher in the resonance region where the pions are mainly absorbed through the reaction $\pi N \to \Delta$, followed by $\Delta N \to NN$. This strong reduction for high-energy pions and the corresponding shift of the maximum to lower energies can be seen by comparing the dashed and the solid lines. These absorption processes equally affect π^+ and π^0 yields. But pions do not only undergo absorption when propagating through the nucleus. Of particular importance for pions of all energies is elastic scattering $\pi N \to \pi N$ which redistributes the kinetic energy, again shifting the maximum to lower energies.

The contributions from initial Δ excitation (dash-dotted line) and from initial QE events (dotted) are also plotted.[2] π^0 and π^+ production through FSI of QE scattering contributes mostly to the low energy region of the pion spectra because of the energy redistribution in the collisions.

[2]We only show these two contribution separately because they are most interesting: Δ excitation dominates the pion production and pion production through initial QE scattering is a pure coupled-channel effect. The size of the contribution from higher resonances and from the non-resonant single-pion background can be appreciated from Fig. 10.4.

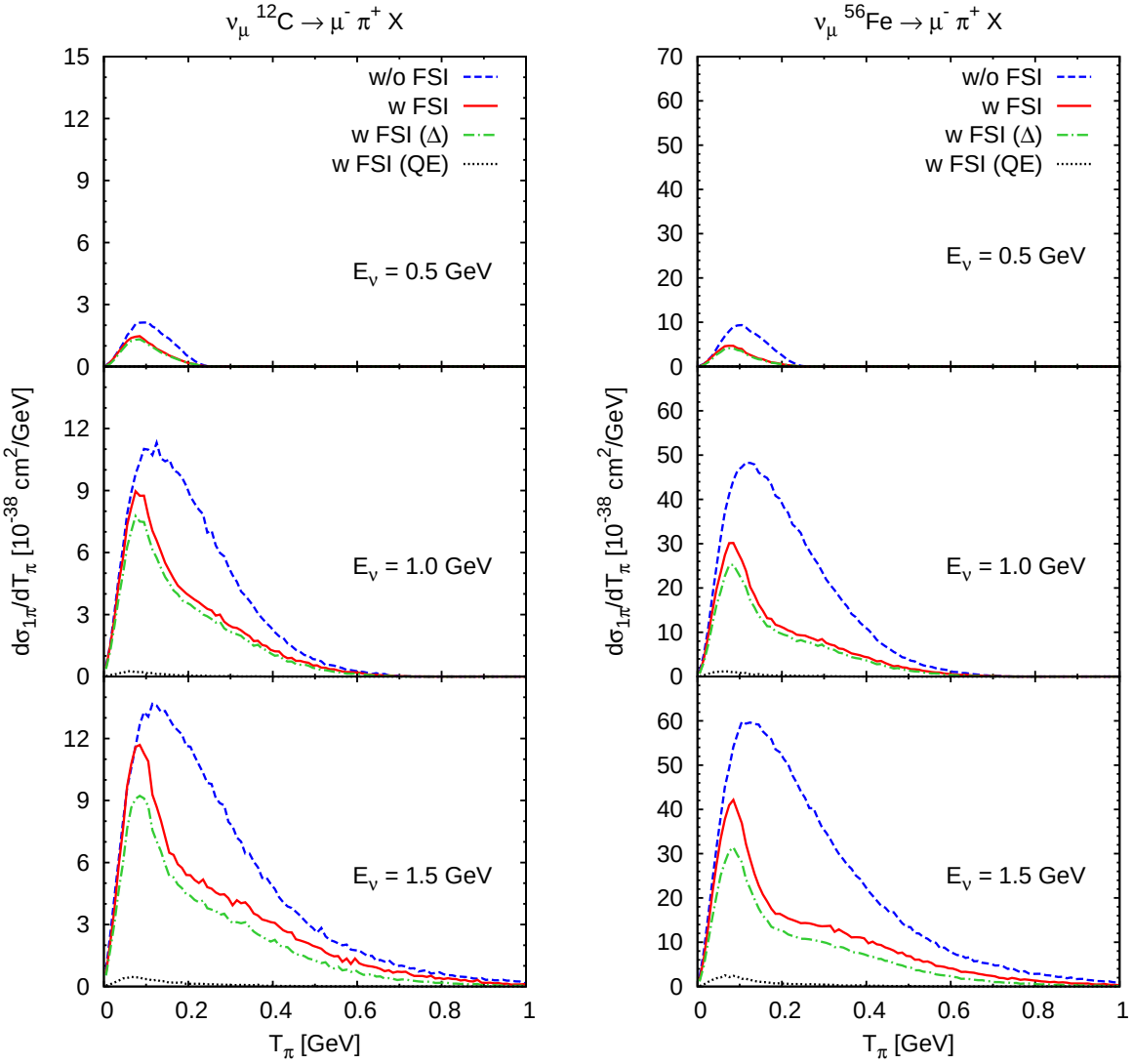

Figure 10.7: Kinetic-energy differential cross section for CC π^+ production on ^{12}C (left) and ^{56}Fe (right panels) versus the pion kinetic energy T_π at different values of E_ν. The dashed lines show the results without FSI interactions (only the decay of resonances is possible), the results denoted by the solid lines include FSI. Furthermore, the origin of the π^+ is indicated (QE or Δ excitation).

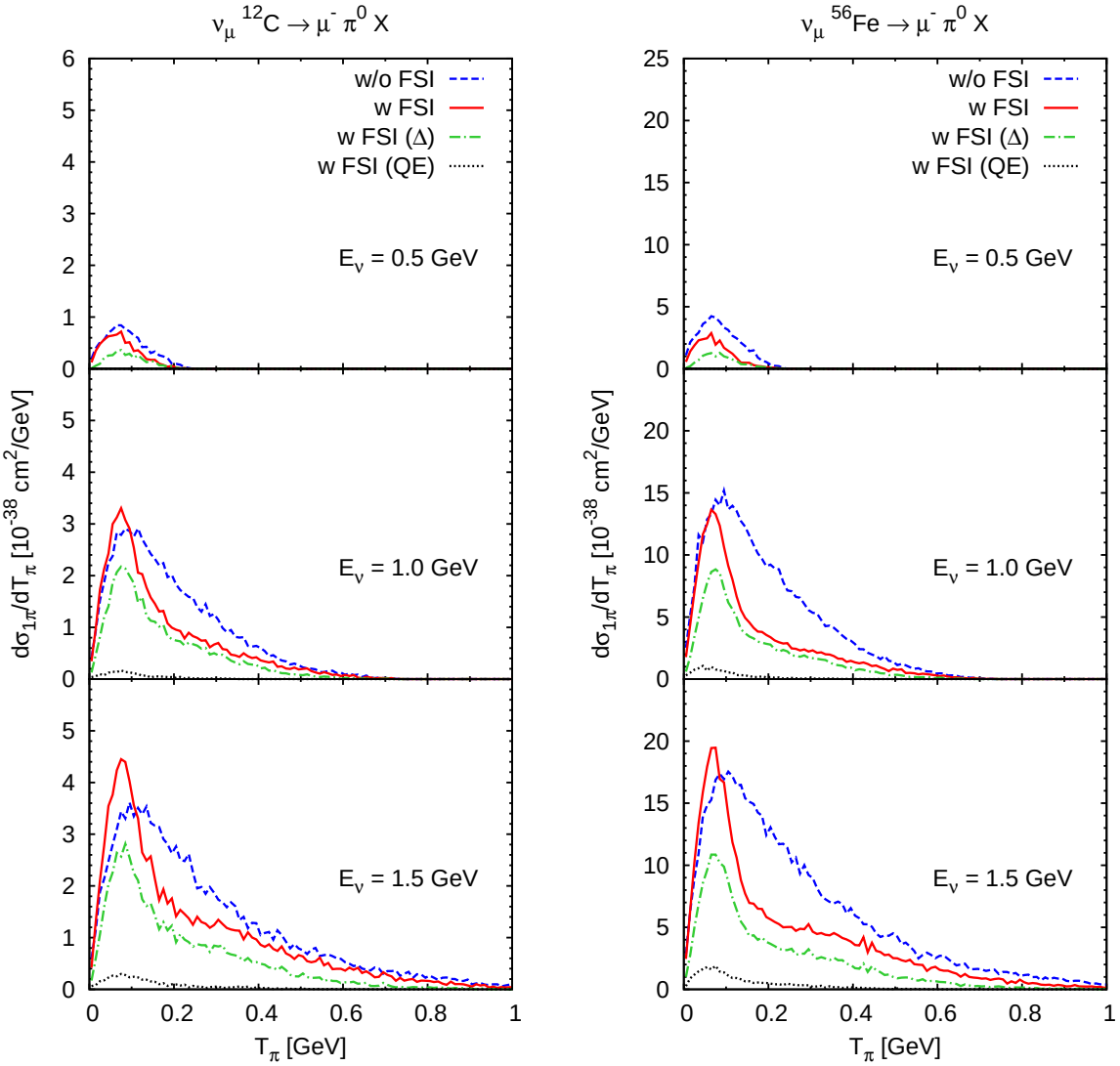

Figure 10.8: Same as Fig. 10.7 for CC π^0 production.

The different scale of CC π^+ and π^0 (Fig. 10.7 and Fig. 10.8) is a consequence of their different production rates in the neutrino-nucleon reaction. This leads to the already discussed side feeding from the dominant π^+ channel to the π^0 channel. Pions produced from initial QE events contribute relatively more to the π^0 channel. This together with the side feeding produces the enhancement in the π^0 cross section at low kinetic energies compared to the calculation without final-state interactions for $E_\nu \gtrsim 1\,\text{GeV}$.

Again, comparing results on C and on the considerable heavier Fe, we find larger absorption for the latter.

It is important to stress that similar patterns are obtained within our BUU model for π^0 photo-production in nuclei in a good agreement with data as can be seen in Fig. 14 of Ref. [K$^+$04].

10.3 NC pion production

10.3.1 Total cross sections

The total NC pion production cross sections for π^+, π^0 and π^- on ^{12}C and ^{56}Fe are shown in Fig. 10.9. The dashed line denotes the pions stemming from the decay of the initially produced resonances — no further FSI are taken into account here. The cross section for π^0 production (middle panels) is significantly higher than those of the charged channels. This is a direct consequence of the isospin dependence of the resonance decay and the ratio $\pi^0 : \pi^+ : \pi^-$ is obtained analogously to the CC case: assuming Δ dominance, pions can be produced by (see also Eqs. (5.24)-(5.27) on page 57)

$$\begin{aligned} \nu p &\to \nu\Delta^+ \to \nu p\pi^0,\ \ \nu n\pi^+, \\ \nu n &\to \nu\Delta^0 \to \nu n\pi^0,\ \ \nu p\pi^-, \end{aligned}$$

where $\sigma_{\Delta^+} = \sigma_{\Delta^0}$ (cf., Eq. (D.32) in Section D.2). With the corresponding Clebsch-Gordan coefficients $\sqrt{\frac{2}{3}}$, $\sqrt{\frac{1}{3}}$ (decay of Δ^+), and $\sqrt{\frac{2}{3}}$, $\sqrt{\frac{1}{3}}$ (decay of Δ^0), we obtain a ratio of

$$\begin{aligned} \pi^0 : \pi^+ : \pi^- &= \left[\left(\sqrt{\frac{2}{3}}\right)^2 Z + \left(\sqrt{\frac{2}{3}}\right)^2 N\right] : \left[\left(\sqrt{\frac{1}{3}}\right)^2 Z\right] : \left[\left(\sqrt{\frac{1}{3}}\right)^2 N\right] \\ &= \begin{cases} 4:1:1 & \text{for } ^{12}\text{C} \\ 3.7:0.9:1 & \text{for } ^{56}\text{Fe} \end{cases} \end{aligned} \tag{10.5}$$

(Z and N are the proton and neutron numbers) for the cross sections *without* final-state interactions assuming pure Δ excitation.

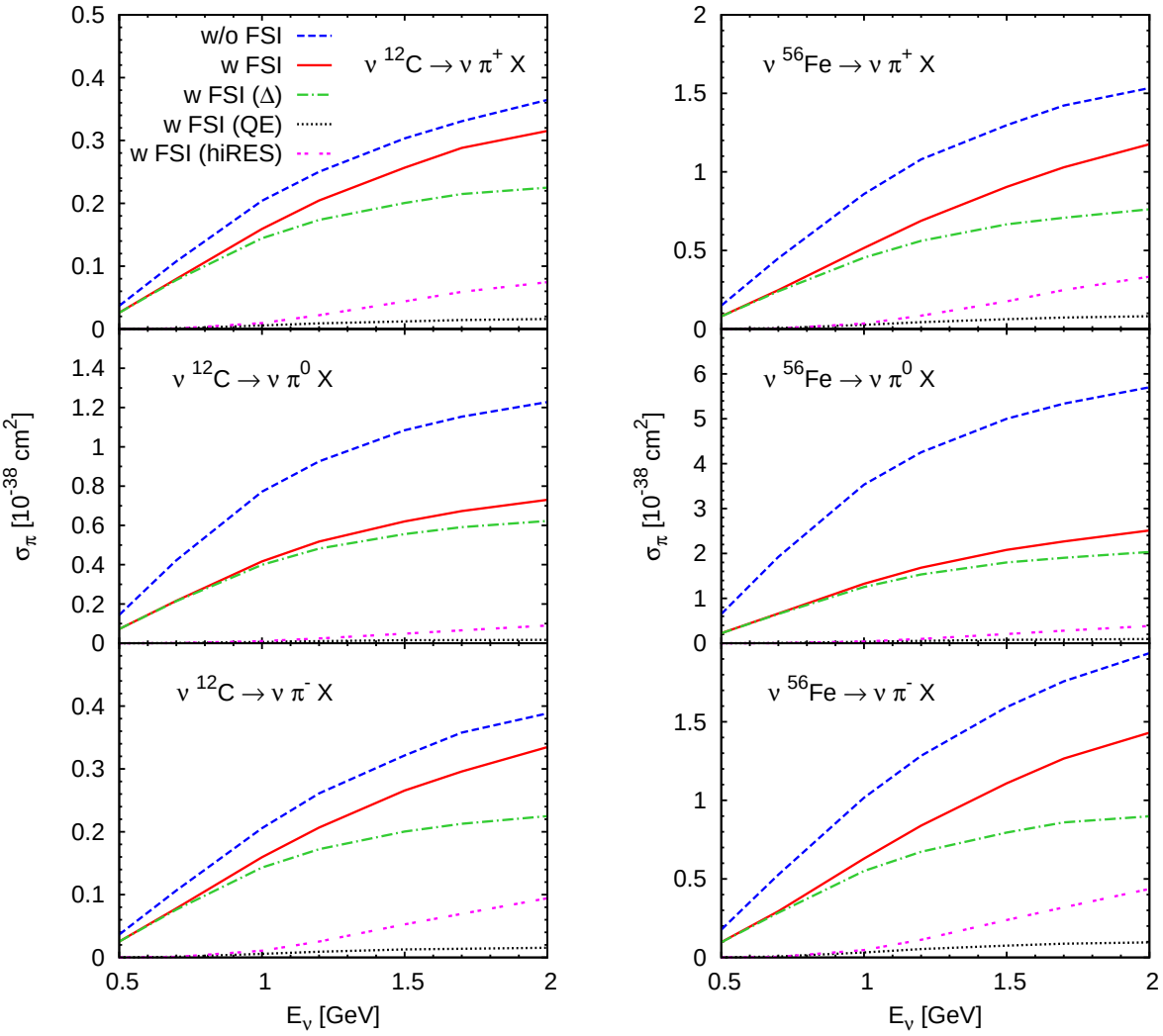

Figure 10.9: Total cross section for NC π^+ (top), π^0 (middle) and π^- (bottom panels) production on ^{12}C (left) and ^{56}Fe (right panels). The dashed lines show the results without FSI (only the decay of resonances is possible); the results denoted by the solid lines include FSI. Furthermore, the origin of the pions is indicated (QE, Δ excitation, excitation of higher resonances).

"Switching on" FSI allows the resonances to interact in different ways besides a simple decay, also the produced pions can interact further or undergo absorption. These FSI lead to a strong reduction of the total yield in the π^0 channel (compare solid and dashed lines in the middle panels of Fig. 10.9). The reduction is much smaller in the π^+ and π^- channels because the π^0 undergo charge-exchange scattering and thus contribute to the charged channels (side feeding). The effect in the opposite direction is less important due to the smaller elementary π^+ and π^- production cross section. The very same effect causes the side feeding from the dominant into the less dominant channel for CC reactions as discussed before.

Pions can also emerge from the initial QE neutrino-nucleon reaction when the produced nucleon rescatters producing a Δ or directly a pion. However, as can be seen from Fig. 10.9, this process is also not very sizable in NC scattering (dotted lines).

10.3.2 Kinetic-energy spectra

In Figs. 10.10, 10.11 and 10.12, we show the kinetic-energy spectra for NC π^0, π^+ and π^- production, respectively. The dashed lines denote again the result without final-state interactions and the solid lines the result of the full calculation. The contributions from initial Δ excitation (dash-dotted lines) and from initial QE events (dotted lines) are also shown. Pion production through FSI of initial QE processes contributes mostly to the low energy region of the pion spectra due to the energy redistribution in the collisions. While the overall shape of the dashed lines (without FSI) is dictated by the predominant p-wave production mechanism through the Δ resonance, the shape of the solid lines (full calculation) is influenced by the energy dependence of the pion absorption and rescattering in the same way as for CC: the main absorption mechanism for pions above $T_\pi \approx 0.1$ GeV is $\pi N \to \Delta$ followed by $\Delta N \to NN$ which leads to a considerable reduction of the cross section. Elastic scattering $\pi N \to \pi N$ redistributes the kinetic energies and thus also shifts the spectrum to lower energies. The absorption effects are larger for the heavier nucleus Fe. In the case of the smaller π^+ and π^- channels the already discussed side feeding enhances the peak in Fig. 10.11 and Fig. 10.12 over the value obtained without FSI. Again, note that these spectra are very similar in shape to those measured in (γ, π^0) reactions on nuclei (cf. Figs. 13 and 14 in Ref. [K$^+$04]).

10.4 Model dependencies

All results with FSI presented so far have been obtained using the full in-medium spectral function for all baryons with the Oset prescription for the Δ collisional broadening and the corresponding Δ reaction cross sections. Furthermore, the particles

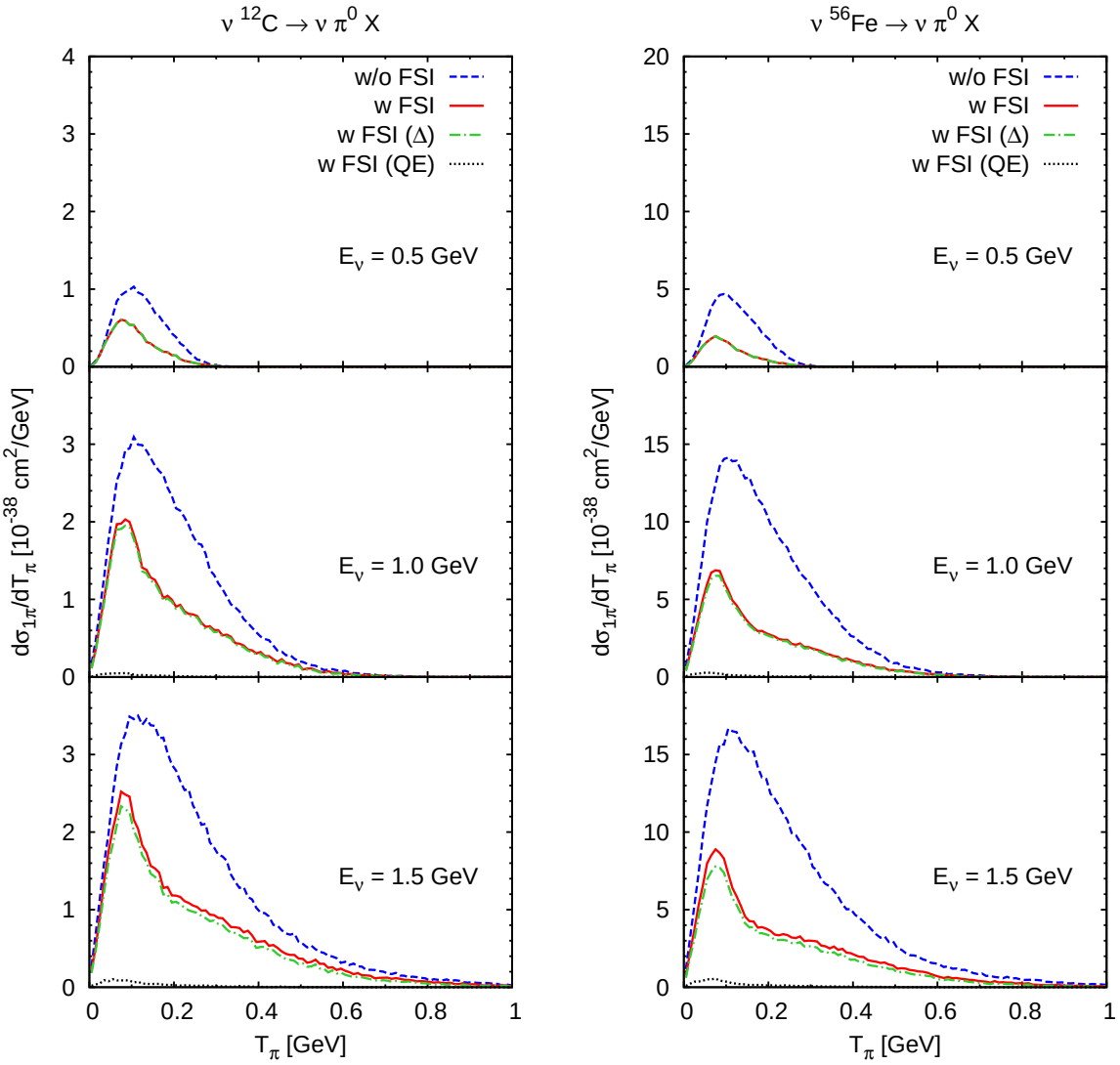

Figure 10.10: Kinetic-energy differential cross section for NC π^0 production on ^{12}C (left) and ^{56}Fe (right panels) versus the pion kinetic energy T_π at different values of E_ν. The dashed lines show the results without FSI interactions (only the decay of resonances is possible), the results denoted by the solid lines include FSI. Also indicated is whether the pion comes from initial QE or Δ excitation (dotted or dash-dotted lines).

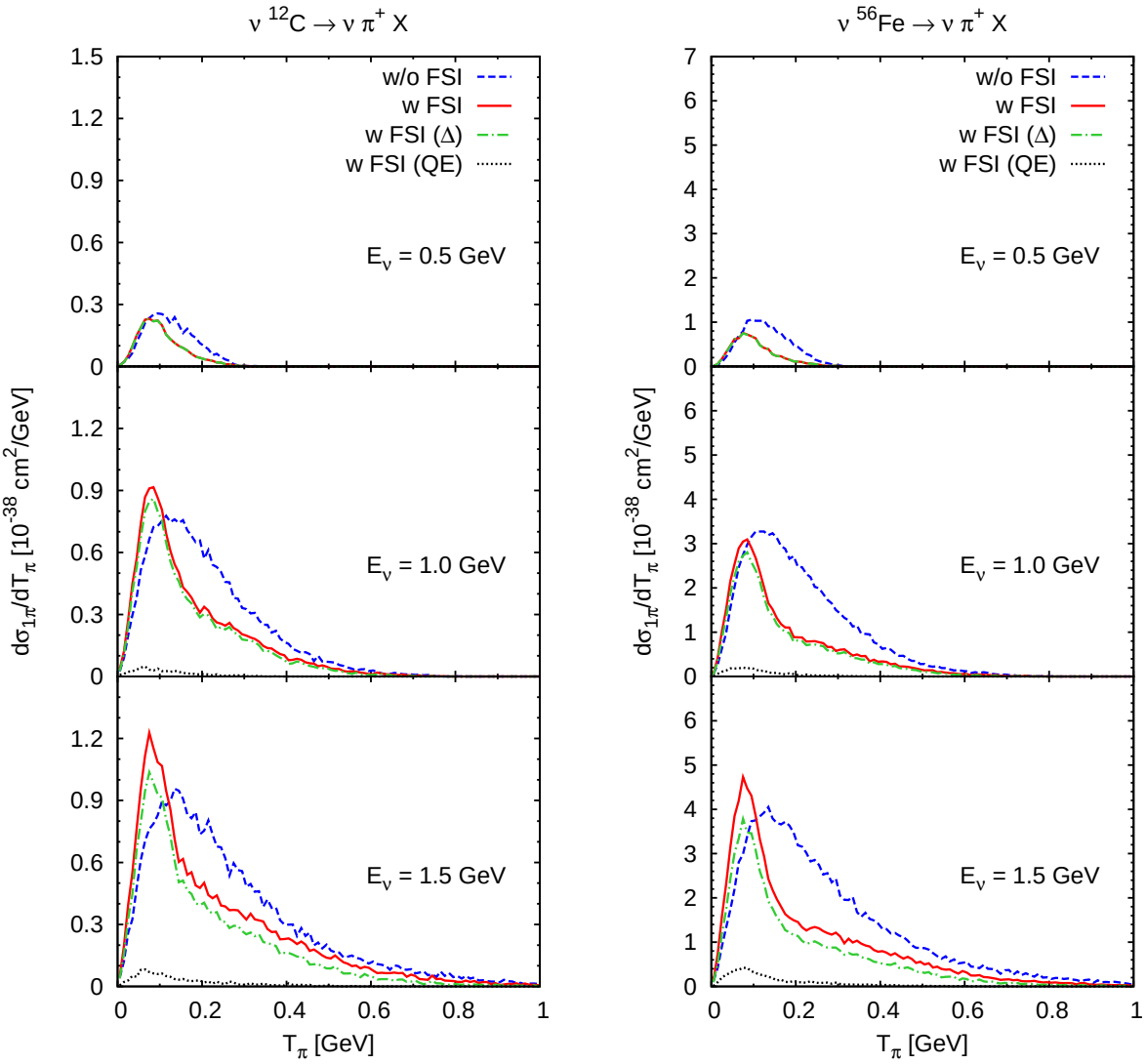

Figure 10.11: Same as Fig. 10.10 for NC π^+ production.

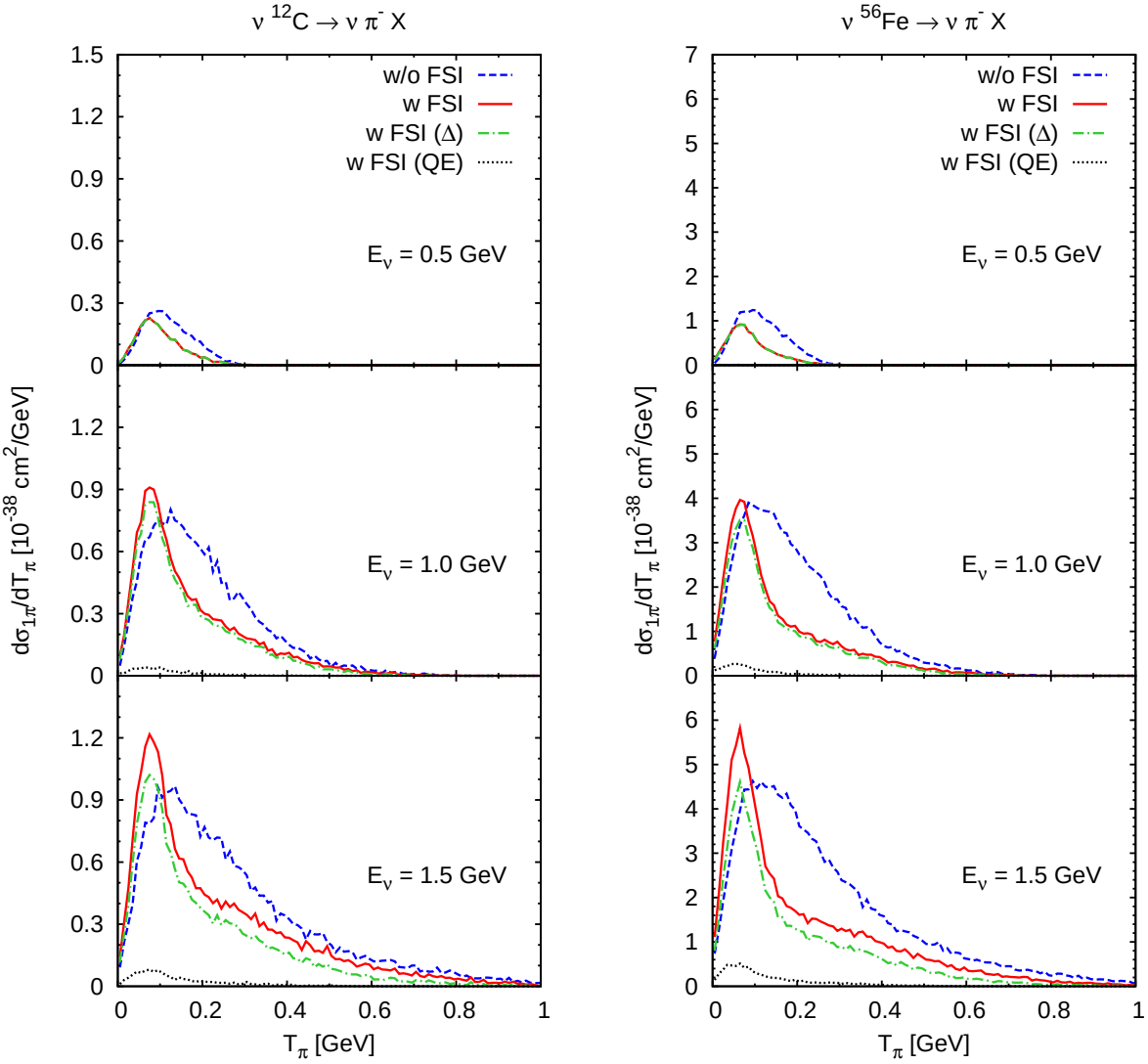

Figure 10.12: Same as Fig. 10.10 for NC π^- production.

were propagated applying the OSP method introduced in Section 7.8. In this section, we investigate the influence of this particular choice on observables. We choose as representative example a neutrino energy of 1 GeV and consider both, integrated cross sections and kinetic-energy distributions, for CC pion production.

As outlined in Section 7.7, we have two ways of including collisional broadening for the Δ resonance, either based on a one-pion exchange model or on the work of Oset. If collisional broadening is included, one needs to make sure that the particles are back on their mass-shell (or vacuum spectral function) when leaving the nucleus, thus, the OSP method is applied in the particle propagation. However, we have seen, that pion production proceeds mainly through the Δ resonance, so one may ask whether it is sufficient to include collisional broadening only for the Δ and whether it is feasible to neglect the OSP. These simplifications could save a significant amount of computing time and resources.

We compare the following scenarios:

(1) without FSI, without collisional broadening

(2) with FSI, without collisional broadening

(3) with FSI, with collisional broadening (one-pion exchange based model for Δ collisional width and cross sections), with OSP

(4) with FSI, with collisional broadening (Oset prescription for Δ collisional width and cross sections), with OSP

(5) with FSI, collisional broadening only for the Δ resonance (Oset prescription), without OSP

(6) with FSI, Oset based collisional broadening only for the Δ resonance, without OSP, here we do not further track the final nucleons after a $\Delta N \to NN$, $\Delta N \to \Delta N$ or $\Delta NN \to NNN$ reaction

Scenarios (1) and (4) have been applied so far. Scenario (6) has been added for comparison: the results published in Refs. [LARM06a, LARM06b] are based on this method.

We summarize the outcome for the total CC pion cross sections, σ_π, in Table 10.1 for both C and Fe. Furthermore, we plot the corresponding kinetic-energy distributions in Fig. 10.13. From both, we see that all scenarios involving the Oset width and the corresponding cross sections for the Δ rescattering agree impressively [scenarios (4)–(6)]. They differ significantly from the results obtained with the one-pion exchange cross sections and width [scenario (3)] and also from the ones where collisional broadening is fully neglected [scenario (2)]. This difference shows the sensitivity of our results to

Table 10.1: Total CC pion cross sections, σ_π, on ^{12}C and ^{56}Fe in units of $10^{-38}\,\mathrm{cm}^2$ at $E_\nu = 1\,\mathrm{GeV}$. The statistical error is negligible. Compared are the different scenarios as detailed in the text.

	^{12}C		^{56}Fe	
	π^0	π^+	π^0	π^+
(1)	0.74	2.94	3.72	12.84 0
(2)	0.71	2.06	2.71	6.54
(3)	0.68	1.80	2.72	6.01
(4)	0.56	1.76	2.13	5.54
(5)	0.57	1.74	2.10	5.48
(6)	0.56	1.75	2.07	5.45

the pion absorption model because the choice of the collisional width directly translates into the cross sections for $\Delta N \to NN$ and $\Delta N \to \Delta N$.[3] In addition, the process $\Delta NN \to NNN$ is only included in the Oset prescription. Thus, this model is more complete and therefore used as default.

The comparison shows that neglecting the collisional broadening of all particles except the Δ is a good approximation. Even the OSP is not needed: the life time of the Δ in the medium is too short to be significantly influenced by the rather small effects of the OSP in the propagation. Finally, also the deletion of the final nucleons as in scenario (6) has a negligible impact on pion observables. These nucleons are not likely to produce new pions by rescattering.

We conclude that scenario (5) is a very good approximation to the full model (4), in addition, it is numerically much simpler and faster. More important and visible in the observables is the realistic choice of the pion-absorption model rather than any off-shell effects.

10.5 Model validation

The treatment of pions, and the whole $\pi N\Delta$ dynamics, in the GiBUU model has undergone numerous previous tests in $A\,A \to \pi\,X$ [TCE$^+$97], $\pi\,A \to X$ [ECM$^+$94, BARMM06, BARLM06] and $\gamma\,A \to \pi\,X$ [LEM00] reactions. In particular, in Refs. [K$^+$04, Leh03, Bus08] quantitative comparisons of calculated $\gamma\,A \to \pi^0\,X$ cross sections to experiment have been given. This reaction directly tests the vector-interaction part of ν-induced π^0 production. These results, which contain the side feeding of

[3] See Sections 7.6 and 7.7 for details.

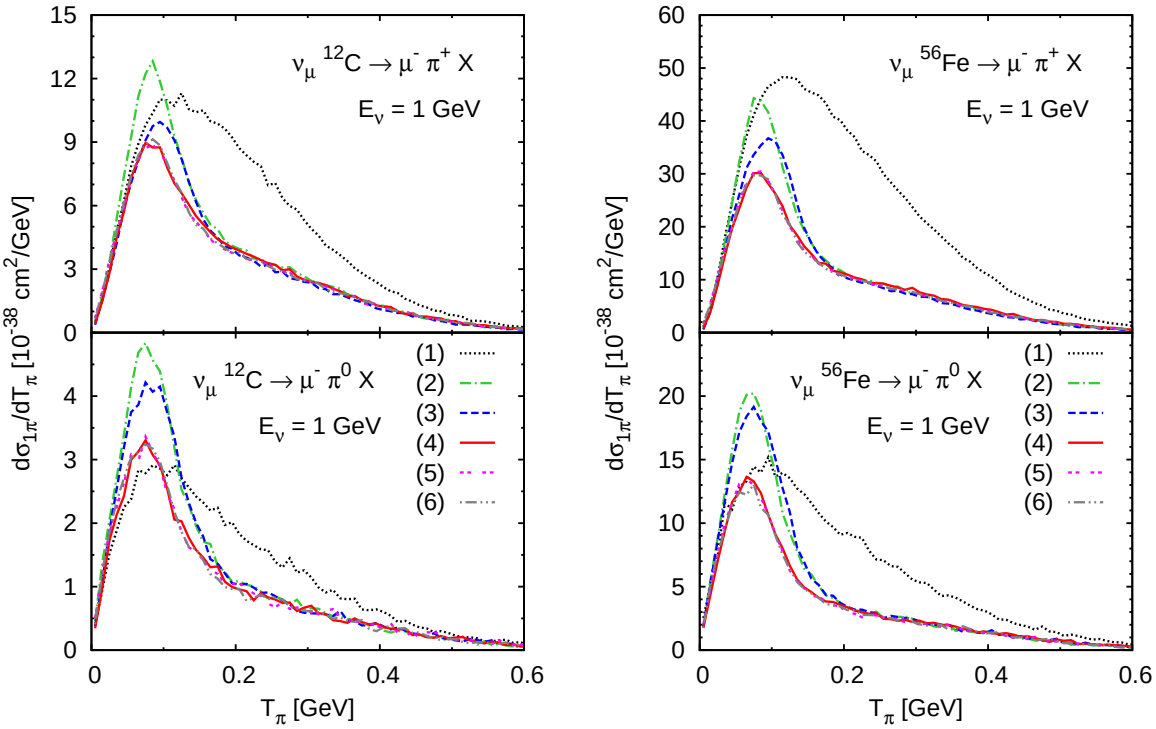

Figure 10.13: Kinetic-energy differential cross section for CC π^+ (top) and π^0 (bottom panels) production on ^{12}C (left) and ^{56}Fe (right panels) versus the pion kinetic energy T_π at $E_\nu = 1\,\text{GeV}$. The different scenarios (1)–(6) are detailed in the text.

the π^0 channel from charged pions produced in the primary reactions, show that the measured pion-momentum distributions are described very well by our theory as can be seen from Fig. 10.14. There we show the BUU results for Ca, Nb and Pb nuclei for various photon energies as a function of the pion momentum. Good agreement with the TAPS data [K$^+$04] is found, in particular the shape is reproduced (for more comparisons see Ref. [K$^+$04]). Also the results without FSI (dashed lines) and the deuterium data (open circles) show very similar shapes.

Because of its semi-classical nature, the method has a lower limit of validity of about 20–30 MeV pion kinetic energy [BARMM06]; this limitation is of no concern for the results discussed here. The comparison to data obtained with a few hundred MeV photon beam [K$^+$04, Leh03], roughly corresponding to the energy regime treated in this work, also shows that the deviations from experiment are typically of the order of 20%. We thus expect a similar systematic uncertainty in the pion results reported in this thesis.

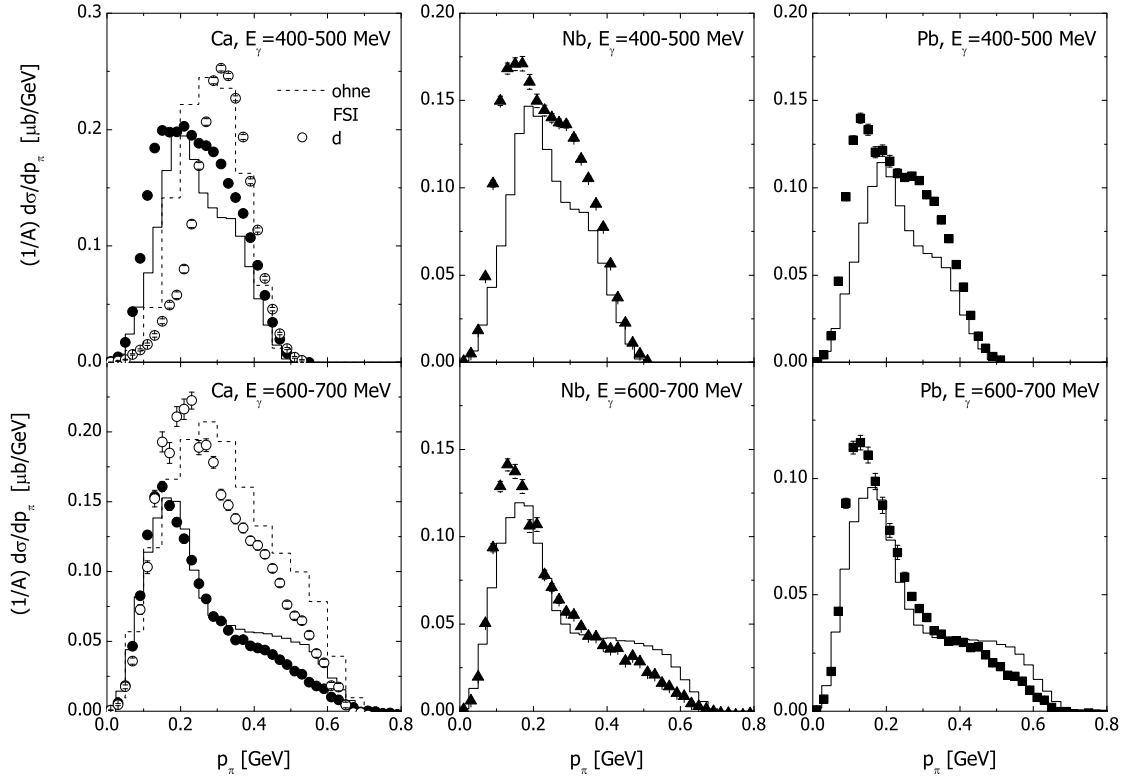

Figure 10.14: Momentum differential cross section for photon induced π^0 production for different nuclei and energies. For Ca also the results without FSI are shown (dashed curves) and compared to deuterium data (open circles). Data are from Ref. [K$^+$04]. The figure is taken from Ref. [Leh03].

10.6 Comparisons

The literature on neutrino-induced pion production is rather scarce.[4] We compare mainly with two different groups, namely Singh, Athar and collaborators for charged currents and Paschos *et al.* for neutral currents.

We emphasize that we are mostly interested in the comparison of nuclear effects, in particular FSI. However, one should keep in mind, that the various models already differ at the elementary lepton-nucleon vertex by including different processes, different form factors and so on. We have thus decided to compare observables, i.e., pion-production cross sections.

[4]We shall discuss the various Monte Carlo event generators used by the experimental communities in Section 12.2.

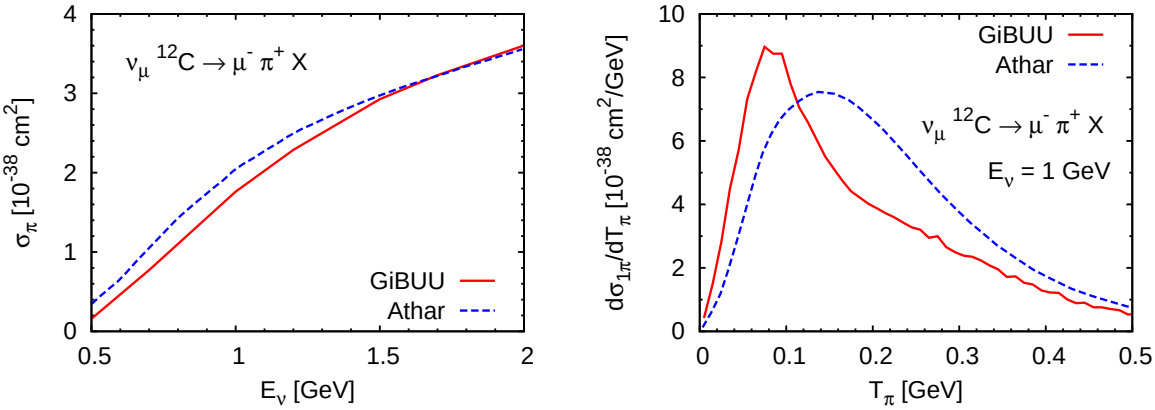

Figure 10.15: Left panel: total CC π^+ production on ^{12}C versus E_ν. Right panel: kinetic-energy differential cross section for CC π^+ production on ^{12}C versus the pion kinetic energy for $E_\nu = 1\,\text{GeV}$. In both panels, the solid lines denote our full calculation while the dashed lines are the result obtained by Athar *et al.* [SACSVV08] (note that we rescaled their p_π to T_π in the right panel).

10.6.1 Charged currents

Our calculations for charged currents can be compared to the weak pion-production model of Singh *et al.* [SVVO98], which has been extended over the last years by Athar, Singh and collaborators [SAA06, ASAS06]. For our comparison, we use their latest results presented in Ref. [SACSVV08].

In their model, pions are produced solely through the excitation of the Δ resonance for which they apply the same formalism as in our approach but with different form factors. In the nucleus, which is treated in the local-density approximation, they modify both the real and the imaginary part of the Δ spectral function according to Ref. [OS87] and therefore account for pion-less decays. The pion FSI are treated within a Monte Carlo approach described in Ref. [VVKM94], which considers besides pion absorption also elastic and charge-exchange scattering based on empirical vacuum πN cross sections.

In Fig. 10.15, we compare our full model for CC π^+ production on ^{12}C to the results of Athar *et al.* [SACSVV08]. Good agreement is found for the integrated cross section (left panel) but the shapes of the pion kinetic-energy distribution are very different (right panel). As pointed out before, the specific shape of our spectra is similar to those measured in (γ, π^0) reactions on nuclei (cf. Figs. 13 and 14 in Ref. [K$^+$04]).

10.6.2 Neutral currents

Finally, we compare our NC pion production results with earlier calculations of neutrino-induced pion production on nuclei by Paschos *et al.* [PPY00, PSY07]. There, pion final-state interactions are taken into account using the pion multiple-scattering model of Adler, Nussinov and Paschos (ANP model) [ANP74]. Paschos and collaborators treat the neutrino-nucleus reaction as a two-step process. The first step is the scattering of a neutrino off a bound nucleon, where they only consider Pauli blocking by including a "Pauli-production factor", a global suppression factor depending on W and Q^2, but neglect any other medium effects. The second step involves the FSI of the produced particles in the nucleus. In the ANP model the produced pions undergo a random walk in the nucleus which is described by a so-called "charge-exchange matrix". This matrix, derived in detail in Ref. [ANP74], takes into account elastic nucleon pion scattering and pion absorption under the assumption of an isoscalar target. Finally, we want to point out an important difference: Paschos *et al.* produce pions (through resonances) which then undergo FSI, while in our case the resonances themselves undergo FSI. In this way we account not only for their simple decay but also for many different reactions as pointed out earlier.

Their original publication [PPY00] contains an error in the elementary pion-production spectra [Pas] which affects their Figs. 8–14 for the pion-energy distribution.[5] Therefore, in the following, we compare only to the corrected results presented in Ref. [PSY07].

In Fig. 10.16 we show the kinetic-energy differential cross sections for NC pion production on ^{16}O (left) and ^{56}Fe (right panels) at $E_\nu = 1\,\text{GeV}$. The cross sections are scaled with the number of nucleons, which allows to compare directly pion production on different nuclei. Note that the scaled cross sections without FSI do not coincide exactly since the relative number of protons and neutrons is different in ^{56}Fe and ^{16}O, which has an influence on the production yields. Our results are labeled with "GiBUU" (the dashed (solid) lines denote the result without (with) FSI), the results of Paschos and collaborators with "Paschos". The lines labeled with "Paschos i" stand for their result without any nuclear correction, i.e., pion production on free nucleons, while "Paschos ig" includes a "Pauli-production factor" meant to account for Pauli blocking in the initial pion production. Finally, the lines denoted with "Paschos f" were obtained by Paschos *et al.* using the model introduced in Ref. [ANP74] in which the produced pions undergo a random walk through the nucleus where they can change directions but not energy. Pauli blocking appears only as a global factor com-

[5] At low E_π in the pion-energy spectra, the results presented in Ref. [PPY00] reach a maximal value whereas ours tend to zero. Due to the fact that the phase space approaches zero at threshold and in view of the dominant p-wave production mechanism of pions from the Δ resonance the former behavior is unexpected.

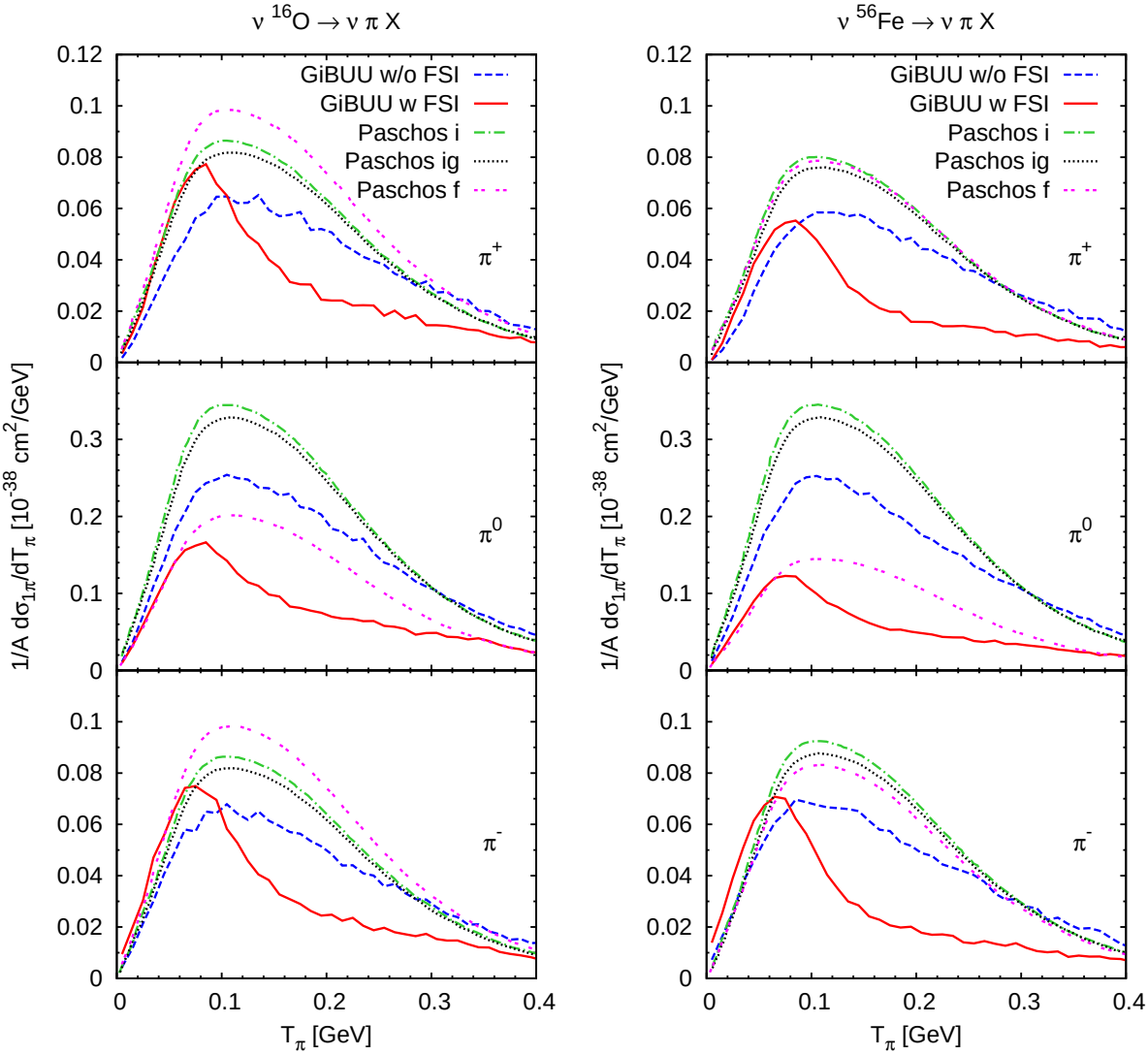

Figure 10.16: Kinetic-energy differential cross section for NC π production on ^{16}O (left) and ^{56}Fe (right) versus the pion kinetic energy for $E_\nu = 1\,\text{GeV}$. The cross sections are scaled with the number of nucleons. The dashed lines denote our result without FSI (only the decay of resonances is included) and the solid lines the full one with FSI. The lines indicated with "Paschos" are the results of Paschos *et al.* [PSY07] where we rescaled E_π to T_π: "i" stands for their result without any nuclear correction, "ig" includes a "Pauli-production factor" and "f" includes the rescattering of the pions in the nucleus (see discussion in the text).

mon to all collisions. Fermi motion is not taken into account in their work because, as stated in footnote 7 of Ref. [ANP74], its impact is rather small. If we compare our results without FSI and with FSI to these results ("ig" corresponds to our calculation without FSI and "f" to the one with FSI), we find considerable quantitative differences in all channels for both nuclei.

The impact of FSI is even more visible in the ratios obtained by dividing the differential cross section with FSI by the one without FSI. These ratios are plotted in Fig. 10.17 for ^{16}O and ^{56}Fe at $E_\nu = 1$ GeV versus the pion kinetic energy. They allow us to focus on the comparison of both FSI models, the ANP used by Paschos *et al.* and our GiBUU model, regardless of any discrepancies in the free cross section which cancel out in the ratio. In the model of Paschos *et al.* [PPY00], pions are produced through resonance excitation, with the Δ, the P_{11} and the S_{11} included. Higher resonances, non-resonant pion production and secondary pions through QE scattering are not included in their model.

Let us first focus on our results (solid for π^+, dashed for π^0 and dash-dotted lines for π^-). As seen before, the absorption is bigger in the heavier nucleus (^{56}Fe) than in the lighter one (^{16}O). For pions with kinetic energy $\gtrsim 0.1$ GeV we find strong effects of FSI. This is the region, where pion absorption and rescattering are most prominent due to the excitation of the Δ resonance around its peak position. At lower energies ($T_\pi \approx 0.07$ GeV) we find a peak, because pions of higher energy in average lose energy via rescattering. At still lower pion energies, the multi-nucleon pion-absorption mechanism takes over, leading to a small dip. We stress that a similar pattern has been experimentally observed by Krusche *et al.* [K$^+$04] in pion photoproduction (cf. Fig. 16 in Ref. [K$^+$04]). This particular dependence of the ratio reflects well-known features of the $\pi N\Delta$ dynamics in nuclei.

The ratios labeled with "Paschos" have been obtained by dividing their "ig" result (only including Pauli blocking in the initial pion production) by their "f" result (with all nuclear corrections) both taken from Ref. [PSY07] and rescaling E_π to T_π. We find that both FSI models are quantitatively and even qualitatively very different ("GiBUU" vs. "Paschos" curves). The ratios of Paschos *et al.* for the charged pions are considerably larger than ours for kinetic energies > 0.1 GeV. In addition, they are practically flat as a function of the pion energy in contrast to our results. In our calculation the ratio is much larger at low pion energies than at the higher ones because pions rescatter with the nucleons (with or without charge exchange) in the nuclear medium loosing energy. After the first collision, due to the energy redistribution, the probability of a second collision changes. The ANP model, on the contrary, assumes that the energy of the pion is constant during its random walk through the nucleus. Also, the ANP model uses vacuum cross sections to estimate the collision probability ignoring medium modifications. This is especially important for pions in the Δ region since this resonance is considerably broadened in the medium.

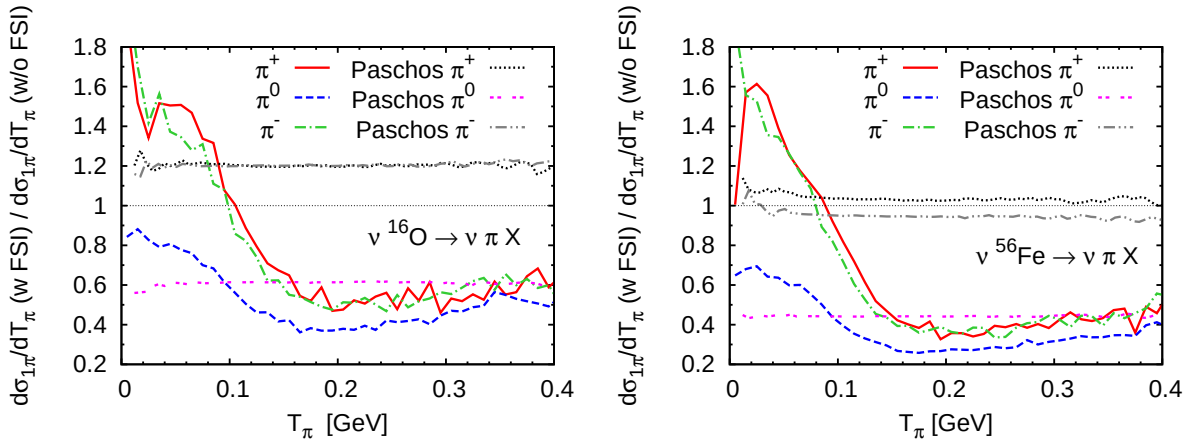

Figure 10.17: Ratio of the differential cross section (the cross section with FSI divided by the one without FSI) for NC pion production on ^{56}Fe (left) and ^{16}O (right) versus the pion kinetic energy for $E_\nu = 1\,\text{GeV}$. To compare with Paschos *et al.* [PPY00] we divided their "ig" result by their "f" result and rescaled E_π to T_π (see Fig. 10.16 and explanations in the text).

At its time, the ANP model represented a remarkable effort towards the description of neutrino-induced pion production, but with the present knowledge based on extensive studies of pion and photo-nuclear reactions, one has the tools to provide a more realistic quantitative description of neutrino-induced pion production in nuclei.

11 Nucleon knockout

11.1 Introduction

Neutrino-induced nucleon knockout has attracted considerable attention, mainly in connection with the possibility of extracting the axial strange content of the nucleon. Pure isovector CC processes do not depend on the strange form factors, hence, studying neutral-current neutrino-nucleus interactions promises insights to one of the fundamental questions of hadronic structure, namely, the strange-quark contribution to the nucleon spin. Because a non-zero strange axial form factor changes the NC QE cross section on protons and neutrons in different ways (see Chapter 4 for more details), the ratio $R(p/n)$ of these two cross sections is very sensitive to the strange spin, as pointed out by Garvey *et al.* [GKKL92]. Due to the technical difficulties of neutron detection, one can also measure the neutral to charged current ratio R(NC/CC) instead. In any case, the study of these ratios involves both neutrons and protons so it must be performed using nuclear targets. In Refs. [ABB$^+$98, ABM02, vdVP04], the authors state that nuclear effects approximately cancel for the ratios of cross sections. We will show that this is not the case for side-feeding effects caused by charge-exchange scattering, which are not negligible if the elementary cross sections on protons and neutrons differ.

Understanding strangeness within the nucleon has been the main motivation for a considerable amount of theoretical work aiming at the description of nuclear effects in NC (but also CC) nucleon-knockout reactions. The most straightforward approach to this problem is the plane-wave impulse approximation. It neglects all interactions between the outgoing nucleons and the nucleus [HKMP93, BDPD$^+$96,

vdVP06, vdVP04]. This situation can be improved by means of a distorted-wave impulse approximations, where the final nucleon-scattering state is computed using optical potentials [ABB$^+$97, ABB$^+$98, MGP04a, MLJ$^+$06, MGP06]. For energies above 1 GeV a multiple-scattering Glauber model, which is based on the eikonal and frozen spectator approximation, is a better alternative [MLJ$^+$06]. Furthermore, the input from a scaling analysis of electron-scattering data has been used to predict NC cross sections [ABCD06]. The shell model [ABB$^+$97, ABB$^+$98] and the continuum random-phase approximation [KLK94, JRHR99] have also been applied. However, all these approaches are purely absorptive, i.e., they have in common that the nucleons which go into unobserved states as a result of an interaction are lost, while, in fact, they may be ejected with a different energy, angle and maybe charge. Also, multiple-nucleon emissions cannot be treated within these models. Only Monte Carlo methods permit to take into account nucleon rescattering leading to energy loss, charge exchange and multiple nucleon emission [NVVV06]. We emphasize that also our approach falls into this category.

We emphasize that *all* of the above mentioned approaches consider only QE scattering in their knockout calculations, but — as we will see — for neutrinos of ~ 1 GeV, the excitation of resonances also contributes significantly to nucleon knockout. This, however, has major implications since it can lead to misidentified events, e.g., an initial Δ, whose decay pions are absorbed or which undergoes "pion-less decay", can count as QE event. The correct identification of QE events is not only important for strange axial form factor measurements but also for the reconstruction of the neutrino energy, which is the crucial quantity in oscillation experiments. We shall come back to this issue in Chapter 13.

This chapter is organized as follows. First, we present results for CC- and NC-induced nucleon knockout off nuclei. Our main focus will be on the influence of final-state interactions. Finally, we compare our model to other approaches.

The results of this chapter have been partly published in Refs. [LARM06a, LARM06b, LBMAR08].

11.2 CC nucleon knockout

By nucleon knockout we understand the process, where besides the outgoing lepton also one or more nucleons are detected. The corresponding cross section has been derived in Chapter 8 [Eq. (8.7)] and is given by

$$\mathrm{d}\sigma_{\mathrm{tot}}^{\ell A\to\ell' NX} = \int\limits_{\text{nucleus}} \mathrm{d}^3 r \int \frac{\mathrm{d}^3 p}{(2\pi)^3}\Theta(p_F(r)-p)\,\frac{k\cdot p}{k^0 p^0}\,\mathrm{d}\sigma_{\mathrm{tot}}^{\mathrm{med}}\,P_{\text{PB}}(\mathbf{r},\mathbf{p})\,M_N(\mathbf{r},\mathbf{p}). \quad (11.1)$$

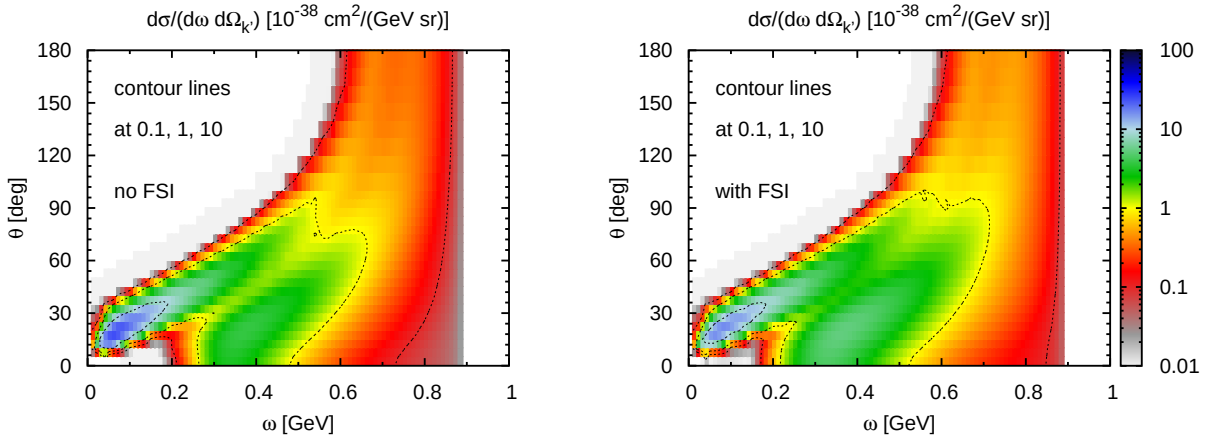

Figure 11.1: Double differential cross section $\mathrm{d}\sigma/(\mathrm{d}\omega\mathrm{d}\Omega_{k'})$ for CC ν_μ-induced proton knockout on ^{12}C as a function of energy transfer $\omega = k^0 - k'^0$ and the muon scattering angle θ at a fixed neutrino energy of $E_\nu = 1\,\mathrm{GeV}$. All in-medium modifications of the elementary cross section are included, the right panel additionally includes FSI.

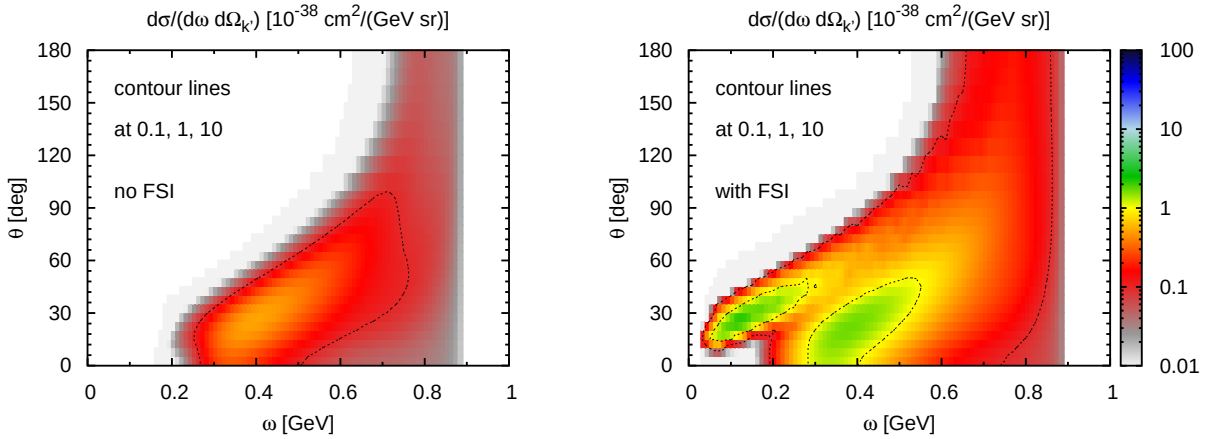

Figure 11.2: Same as shown in Fig. 11.1 for CC neutron knockout.

$M_N(\mathbf{r},\mathbf{p})$ is the multiplicity of the final-state nucleons and is determined by the GiBUU transport simulation. The term $\mathrm{d}\sigma_{\mathrm{tot}}^{\mathrm{med}}$ denotes the total cross section on a bound nucleon, i.e., including nuclear medium corrections as introduced in Chapter 8.

11.2.1 Double differential pion cross sections

We start our investigation with CC ν_μ-induced nucleon knockout on ^{12}C. In Fig. 11.1 (Fig. 11.2) we show the cross section for proton (neutron) knockout as a function of

energy transfer, ω, and the muon scattering angle, θ, for $E_\nu = 1\,\mathrm{GeV}$. For these results, we take into account all nucleons which leave the nucleus due to the νA reaction. FSI are included only in the right panels. Two clearly separated peaks can be seen at low ω and θ in both figures. The one at lower ω corresponds to initial quasielastic events, whereas the one at higher ω is caused mainly by resonance-induced nucleon knockout.[1] This clear separation is lost at higher momentum transfer. We have seen before that the inclusive cross section is smeared out with increasing Q^2 due to Fermi motion; the shape of the inclusive cross sections (cf. Fig. 9.1) is reflected in the proton- and neutron-knockout cross sections plotted here.

The significant difference in scale for proton and neutron knockout in the left panels, where FSI is not included, is generated by the initial neutrino-nucleon production process: QE scattering produces only protons via

$$\nu_\ell n \to \ell^- p;$$

neutrons cannot be produced in the initial quasielastic interactions (cf. left panel of Fig. 11.2). Also the Δ-production mechanism favors protons

$$\begin{aligned} \nu_\ell p &\to \ell^- \Delta^{++} \to \ell^- p\,\pi^+, \\ \nu_\ell n &\to \ell^- \Delta^{+} \to \ell^- p\,\pi^0,\ \ \ell^- n\,\pi^+, \end{aligned}$$

since $\sigma_{\Delta^{++}} = 3\,\sigma_{\Delta^+}$ (cf., Section D.2; compare Eq. (D.26) and Eq. (D.27) on page 291). With the corresponding Clebsch-Gordan coefficients 1, $\sqrt{\frac{2}{3}}$, and $\sqrt{\frac{1}{3}}$, we obtain a ratio of

$$p : n = \left[3\,Z + \left(\sqrt{\frac{2}{3}}\right)^2 N\right] \left[\left(\sqrt{\frac{1}{3}}\right)^2 N\right]^{-1} = \begin{cases} 11:1 & \text{for } {}^{12}\mathrm{C} \\ 9.8:1 & \text{for } {}^{56}\mathrm{Fe} \end{cases} \tag{11.2}$$

(Z and N are the proton and neutron numbers) for Δ dominance. Therefore, in a calculation *without* final-state interactions, proton and neutron knockout differ by about a factor of ten in the Δ region.

With final-state interactions, this scenario changes. In the right panel of Fig. 11.2 we clearly see that neutrons are knocked out in the quasielastic peak region through multi-step processes. Protons stemming from the initial neutrino-nucleon QE reaction undergo elastic and inelastic nucleon-nucleon collisions in the medium via $NN \to NN$, $NN \to NN\pi$ or $NN \to N\Delta$. This leads to charge exchange and thus to neutron knockout. The situation is similar in the pion region.

11.2.2 Total cross section

The total cross sections for proton and neutron knockout are shown in Fig. 11.3 for multiple-nucleon emission and in Fig. 11.4 for single-nucleon emission, both for ^{12}C

[1] We shall see later that the Δ is the dominant source of nucleon knockout in the pion region.

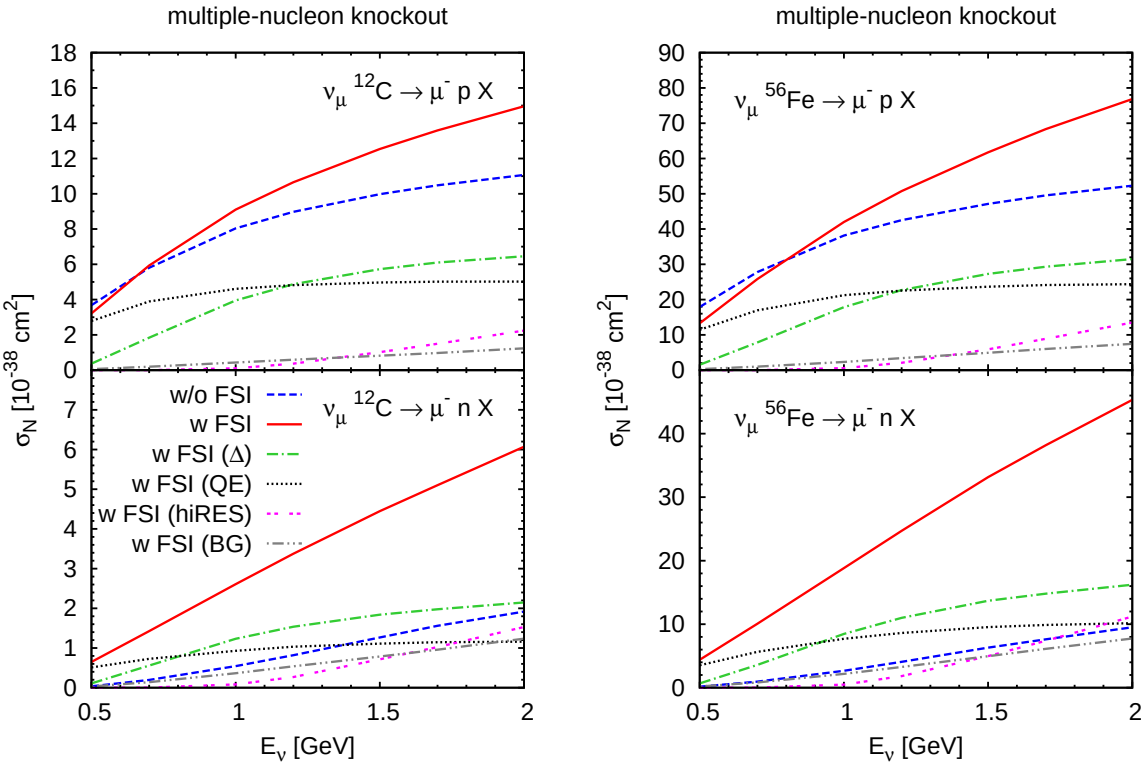

Figure 11.3: Total cross section for CC multiple-p (top) and n (bottom panels) knockout on ^{12}C (left) and ^{56}Fe (right panels). Multiple-nucleon knockout means that the final state may contain any number of knocked-out nucleons. The dashed lines show the results without FSI (only the decay of resonances is possible); the results denoted by the solid lines include FSI. Furthermore, the origin of the pions is indicated (QE, Δ excitation, excitation of higher resonances, single-pion background).

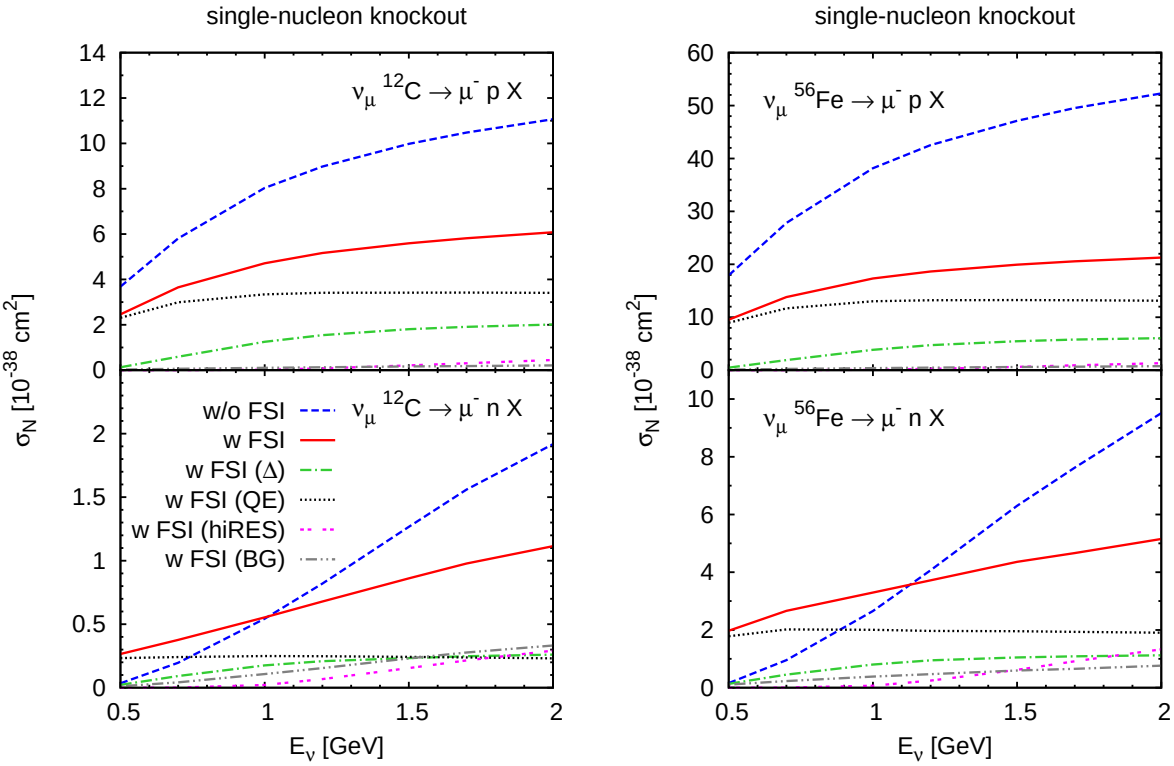

Figure 11.4: Total cross section for CC single-p (top) and n (bottom panels) knockout on ^{12}C (left) and ^{56}Fe (right panels). Single-nucleon knockout means that the final state does not contain any other knocked-out nucleons. The dashed lines show the results without FSI (only the decay of resonances is possible); the results denoted by the solid lines include FSI. Furthermore, the origin of the pions is indicated (QE, Δ excitation, excitation of higher resonances, single-pion background).

and ^{56}Fe. Single-nucleon knockout in the reaction

$$\nu_\mu A \to \mu^- N X \tag{11.3}$$

means, that we count only events where X does not contain any other knocked-out nucleon, which might be the case in our "multiple-knockout" definition. There, X may even contain knocked-out nucleons of different charge. In the following, nucleon knockout means multiple-nucleon knockout; we state explicitly when results for single-nucleon knockout are presented. For numerical simplicity, we only take nucleons with $T_N > 0.02\,\text{GeV}$ into account throughout this chapter.

In the case of multiple-nucleon knockout shown in Fig. 11.3, we find, that the solid line, showing the result with all final-state interactions included, lies well above the one without FSI (dashed line) already for the protons, but even more so for the neutrons. This enhancement is entirely caused by secondary interactions and cannot be obtained in a Glauber treatment or any other quantum-mechanical approach.

Furthermore, it is indicated in Fig. 11.3, whether the knocked out nucleon stems from initial QE scattering or Δ excitation (the contributions from higher resonances and from the non-resonant background are also shown). In contrast to the pion case, both contribute to the total cross section, even though with different weights depending on the neutrino energy. The phase space for Δ excitations opens later than for QE; this explains the small contribution of the Δ at $E_\nu = 0.5\,\text{GeV}$ which increases with energy.

Events with multiple nucleons in the final state are disregarded in Fig. 11.4. This leads to a very different behavior, in particular, the cross section without FSI is in general above the one with FSI included. Comparing both scenarios shows, that for single-nucleon knockout the Δ contribution is smaller than the QE one while it can be larger for the multiple-nucleon knockout. Through processes like $\Delta N \to NN$ and $\Delta \to \pi N$ followed by $\pi N \to \pi N$, the Δ contributes in large parts to the multiple-nucleon knockout.

11.2.3 Nucleon kinetic-energy spectra

In Fig. 11.5 and Fig. 11.6 we present the kinetic-energy differential cross section for CC proton and neutron knockout versus the kinetic energy for different values of E_ν. The line styles are as in the previous figures. FSI strongly modify the shape of the distribution. High-energy protons rescatter in the medium. As a consequence the flux at higher energies is reduced, and a large number of secondary protons at lower energies appear (cf., in particular, Fig. 11.5). Also low-energy secondary neutrons are produced through charge-changing FSI as can be seen in Fig. 11.6, where, in the case without FSI, the cross section is very small and even almost vanishes at lower neutrino energies. At $E_\nu = 0.5$ GeV, nucleon knockout is clearly dominated by QE processes,

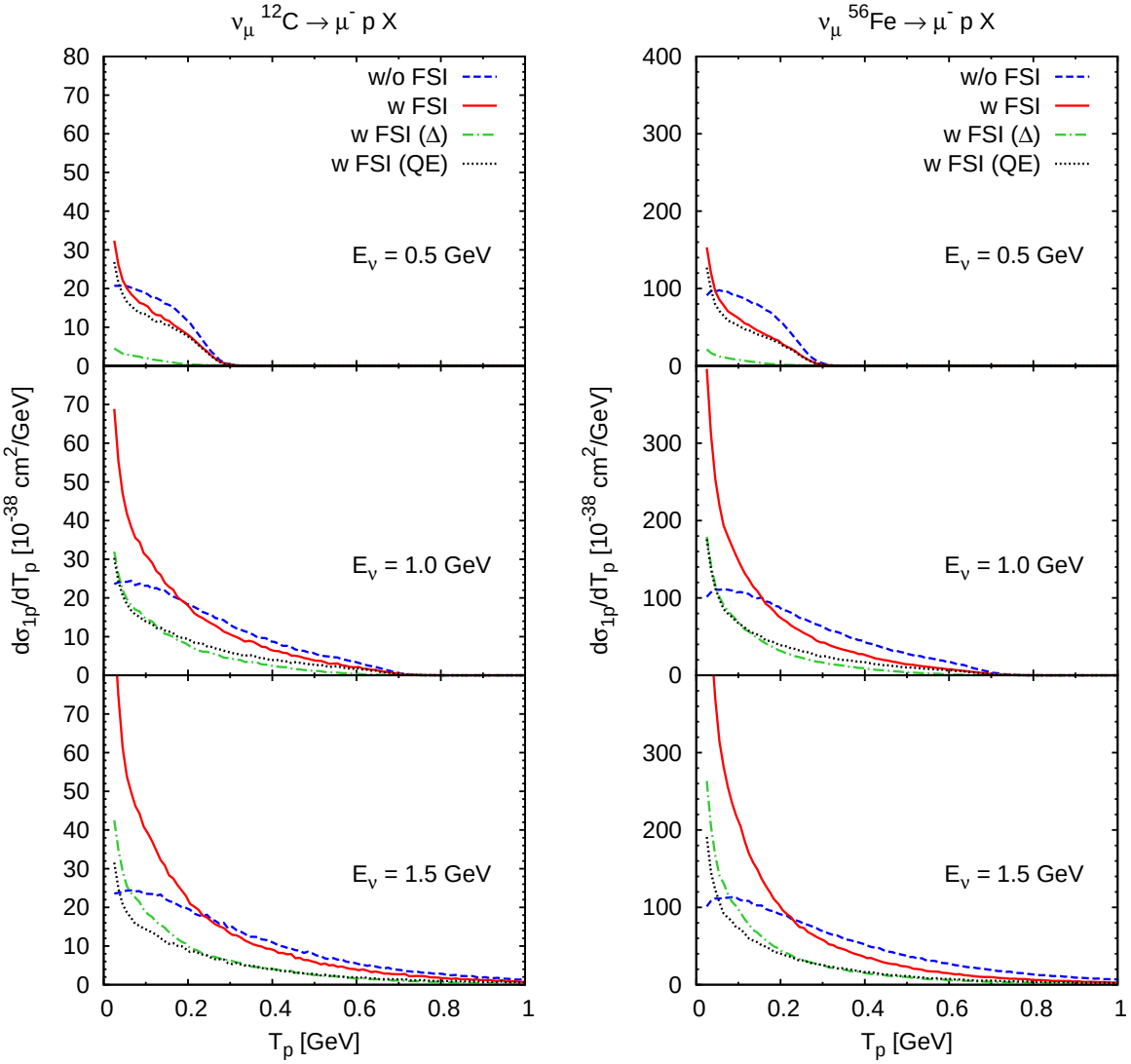

Figure 11.5: Kinetic-energy differential cross section for CC p knockout on ^{12}C (left) and ^{56}Fe (right panels) versus the proton kinetic energy T_p at different values of E_ν. The dashed lines show the results without FSI interactions (only the decay of resonances is possible), the results denoted by the solid lines include FSI. Furthermore, the origin of the proton is indicated (initial QE or Δ excitation).

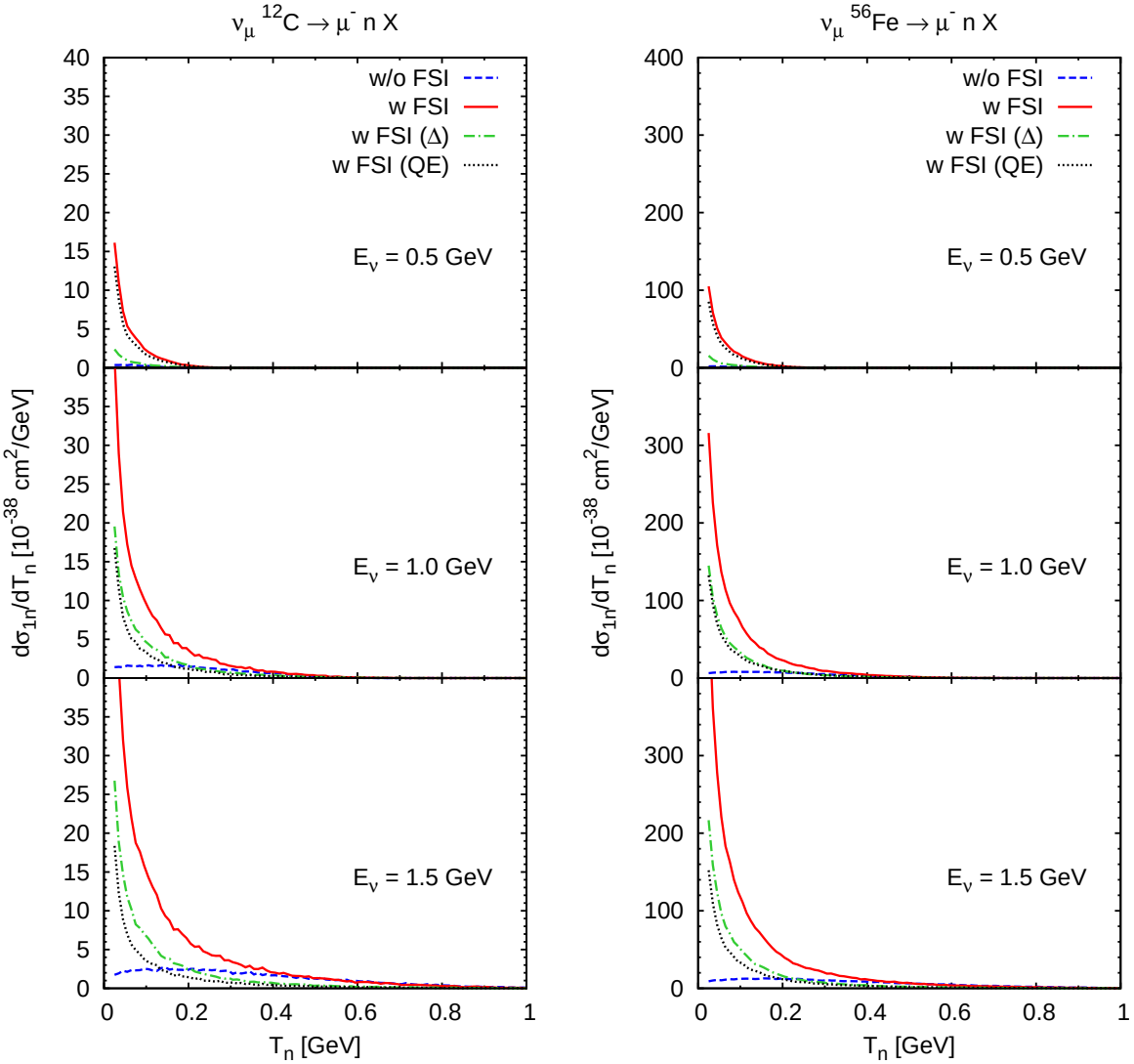

Figure 11.6: Same as Fig. 11.5 for CC *n* knockout.

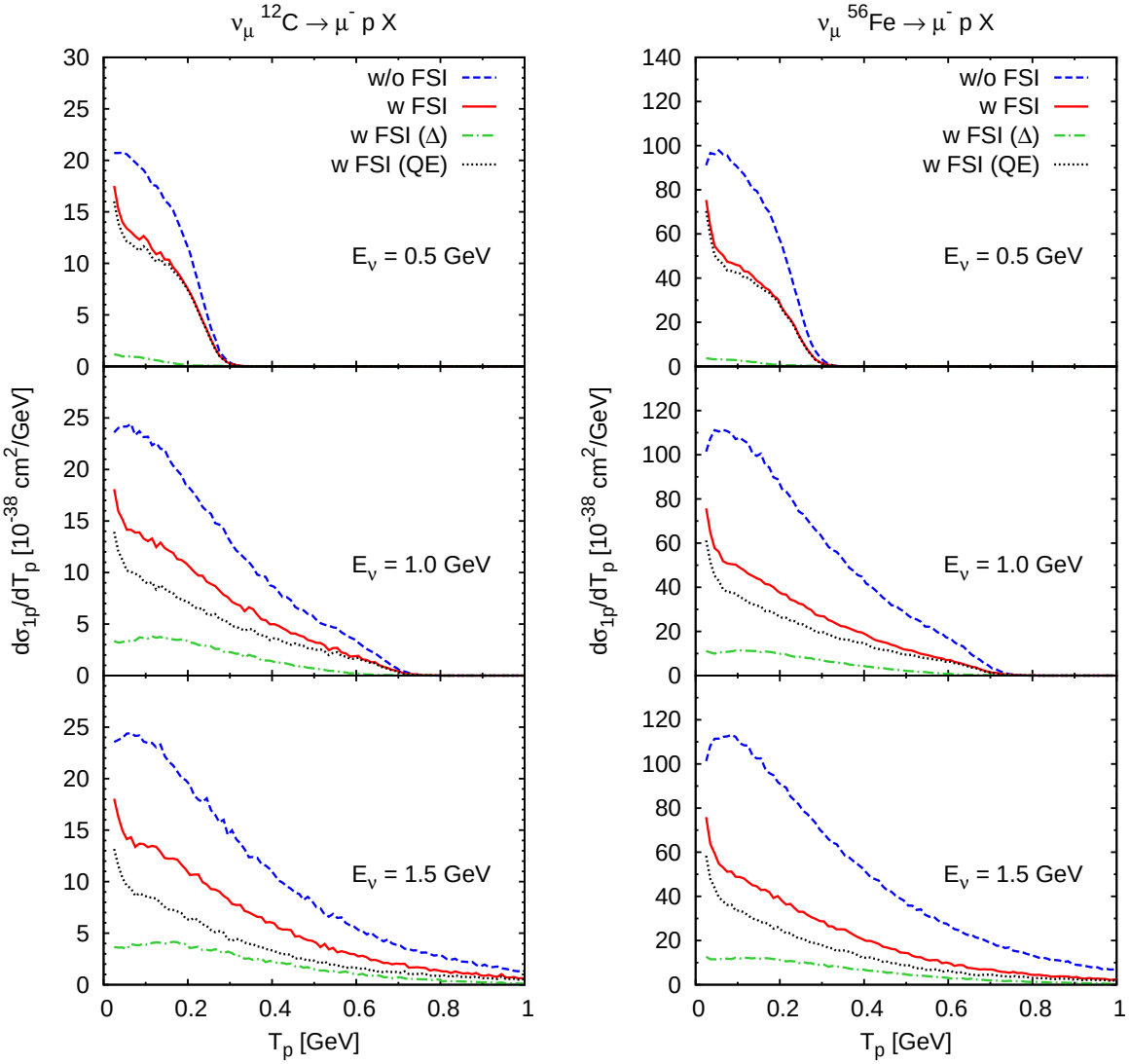

Figure 11.7: Same as Fig. 11.5 for CC single-p knockout.

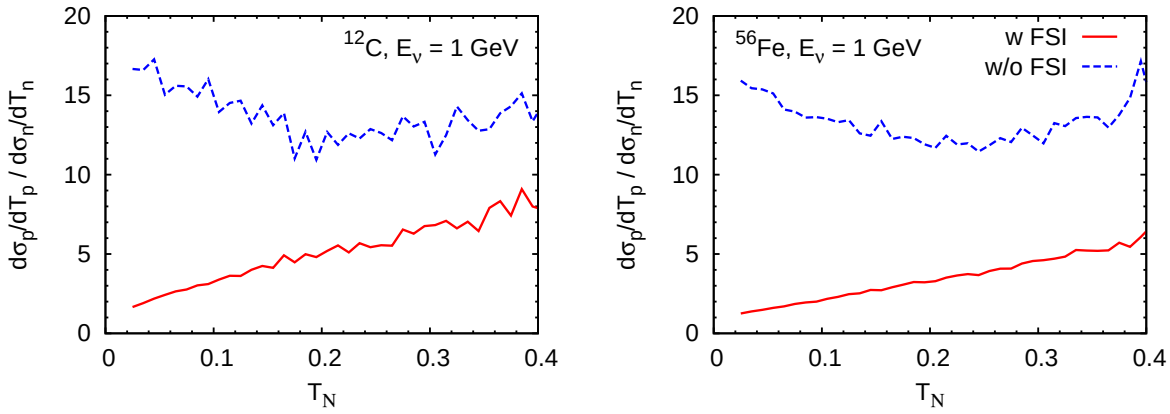

Figure 11.8: Ratio of proton to neutron CC kinetic-energy differential cross section on ^{12}C (left) and ^{56}Fe (right panel) versus the nucleon kinetic energy T_N at $E_\nu = 1\,\text{GeV}$. The solid and the long-dashed lines show the results with and without FSI.

however, the plots show a progressive increase of the Δ contribution with increasing E_ν.

For comparison, we show in Fig. 11.7 the kinetic-energy cross section for CC single-proton knockout. Obviously, the strong increase due to secondary particles at low kinetic energies is missing. Here, the Δ contribution is less important. This can be understood by the Δ FSI mechanism: the decay of the Δ into πN may contribute to the single-nucleon cross section depending on the FSI of the decay nucleon, but any other reaction of the Δ, like, e.g., $\Delta N \to NN$, contributes mostly to the multiple nucleon knockout.

In Fig. 11.8 we plot the ratio of CC proton to neutron cross sections as a function of the kinetic energy. The curves with and without FSI disagree; this shows clearly that final-state interactions do not cancel in the ratio — thus, measuring ratios instead of absolute yields still involves FSI. The disagreement is caused by the strong effects of side feeding through charge-exchange scattering from the dominant proton into the neutron channel. Since side feeding in the opposite direction is practically not present, the ratio is not the same with and without FSI.

11.3 NC nucleon knockout

11.3.1 Total cross section

We continue our discussion with NC nucleon knockout. In Fig. 11.9 we show the integrated cross sections for proton and neutron knockout on ^{12}C and ^{56}Fe. The solid lines, showing the results with FSI included, lie in both cases clearly above the ones

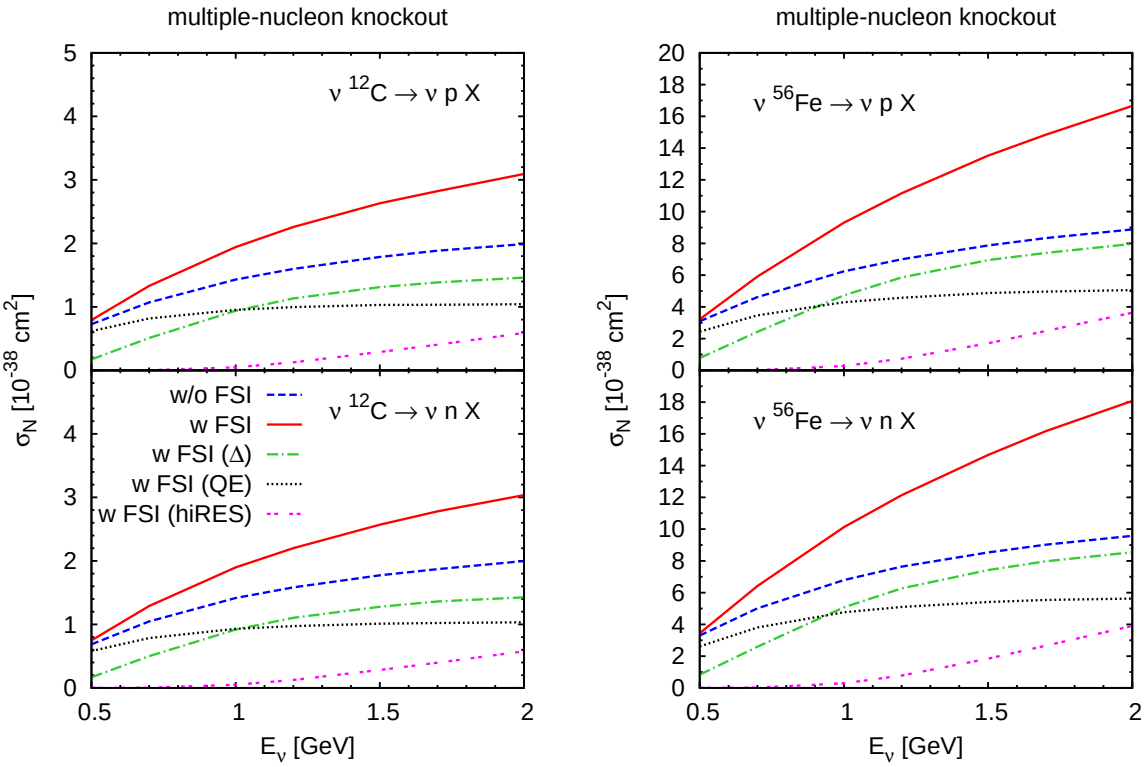

Figure 11.9: Total cross section for NC multiple p (top) and n (bottom panels) knockout on ^{12}C (left) and ^{56}Fe (right panels). The dashed lines show the results without FSI (only the decay of resonances is possible); the results denoted by the solid lines include FSI. Furthermore, the origin of the pions is indicated (QE, Δ excitation, excitation of higher resonances).

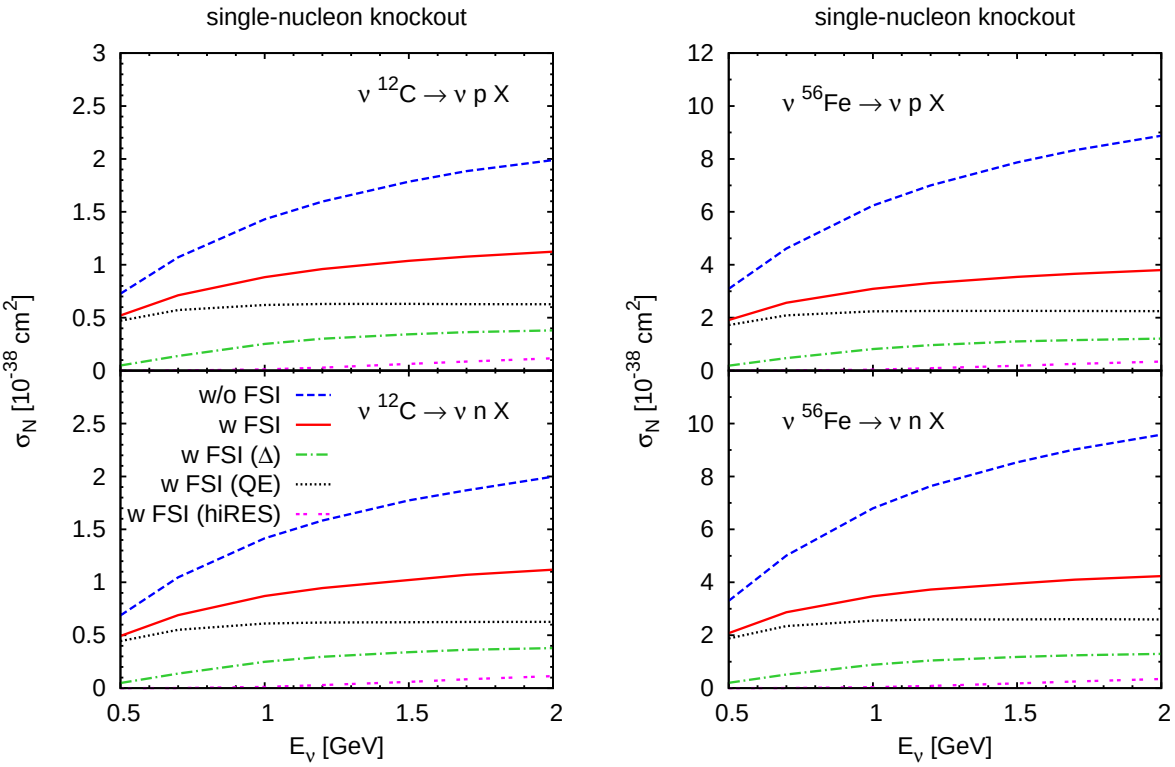

Figure 11.10: Same as Fig. 11.9 for NC single-nucleon knockout.

without FSI (dashed lines). As in the CC case, this enhancement is entirely caused by secondary interactions. Furthermore, the initial process leading to a knocked out nucleon is indicated. In the νN collision either QE scattering (dash-dotted), Δ (dotted), or the excitation of other resonances (double-dashed lines) is possible. Above $E_\nu \approx 1\,\text{GeV}$, the initial Δ excitation process contributes even more to the total knockout cross section than QE scattering. Only up to neutrino energies of $\approx 0.5\,\text{GeV}$, one may neglect the resonance contributions to nucleon knockout.

For comparison, we show the corresponding results for single-nucleon knockout in Fig. 11.10. Here, as also observed in CC scattering, the cross section after FSI is significantly smaller than without FSI, because events with more than one knocked-out nucleon are not counted. Note that also the Δ contribution is smaller than the QE one in contrast to the results of Fig. 11.9, since the Δ contributes in large parts to the multiple-nucleon knockout, e.g., through $\Delta N \to NN$ and $\Delta \to \pi N$ followed by $\pi N \to \pi N$.

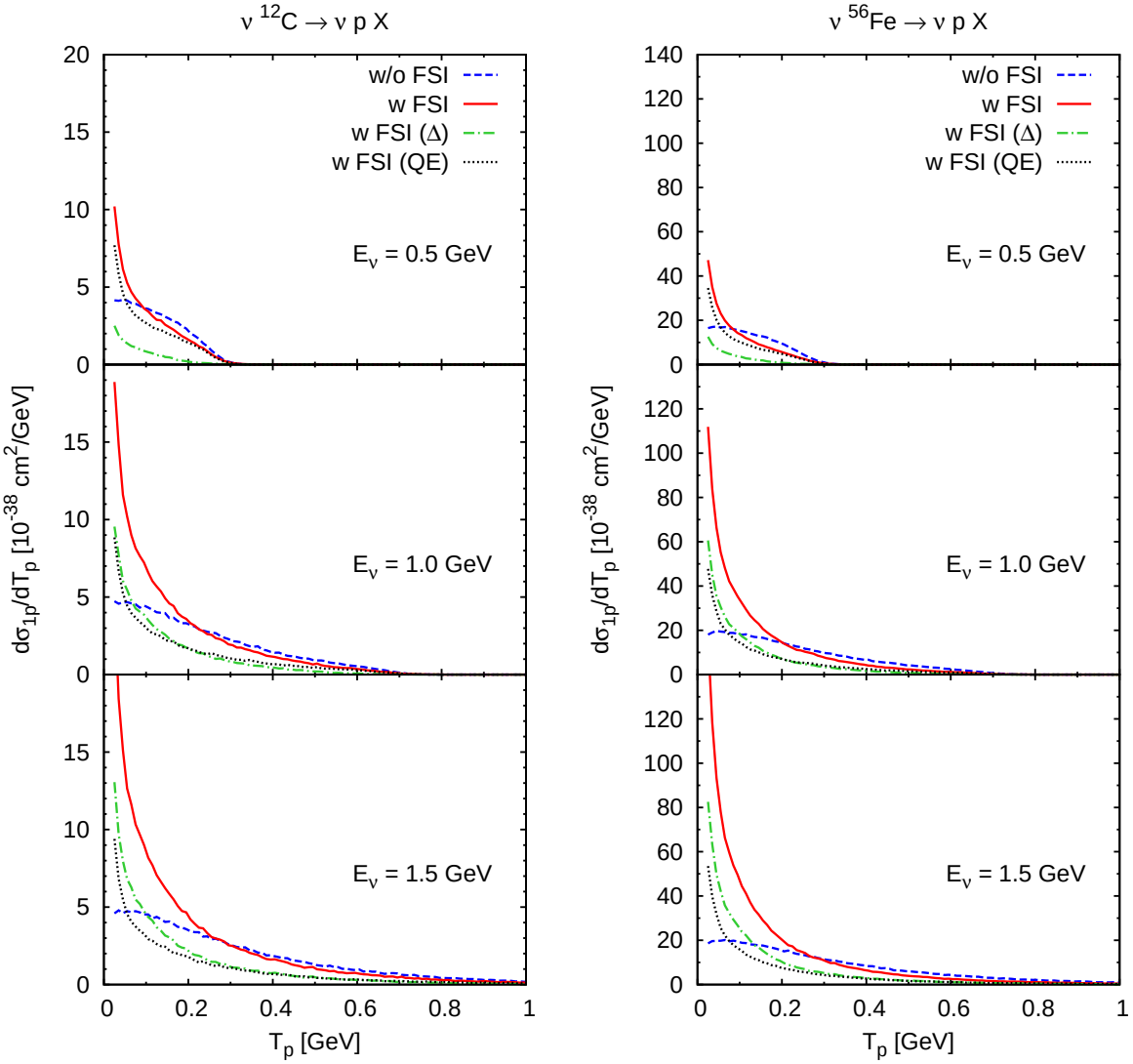

Figure 11.11: Kinetic-energy differential cross section for NC multiple-p knockout on ^{12}C (left) and ^{56}Fe (right panels) versus the proton kinetic energy T_p at different values of E_ν. The dashed lines show the results without FSI interactions (only the decay of resonances is possible), the results denoted by the solid lines include FSI. Furthermore, the origin of the proton is indicated (initial QE or Δ excitation).

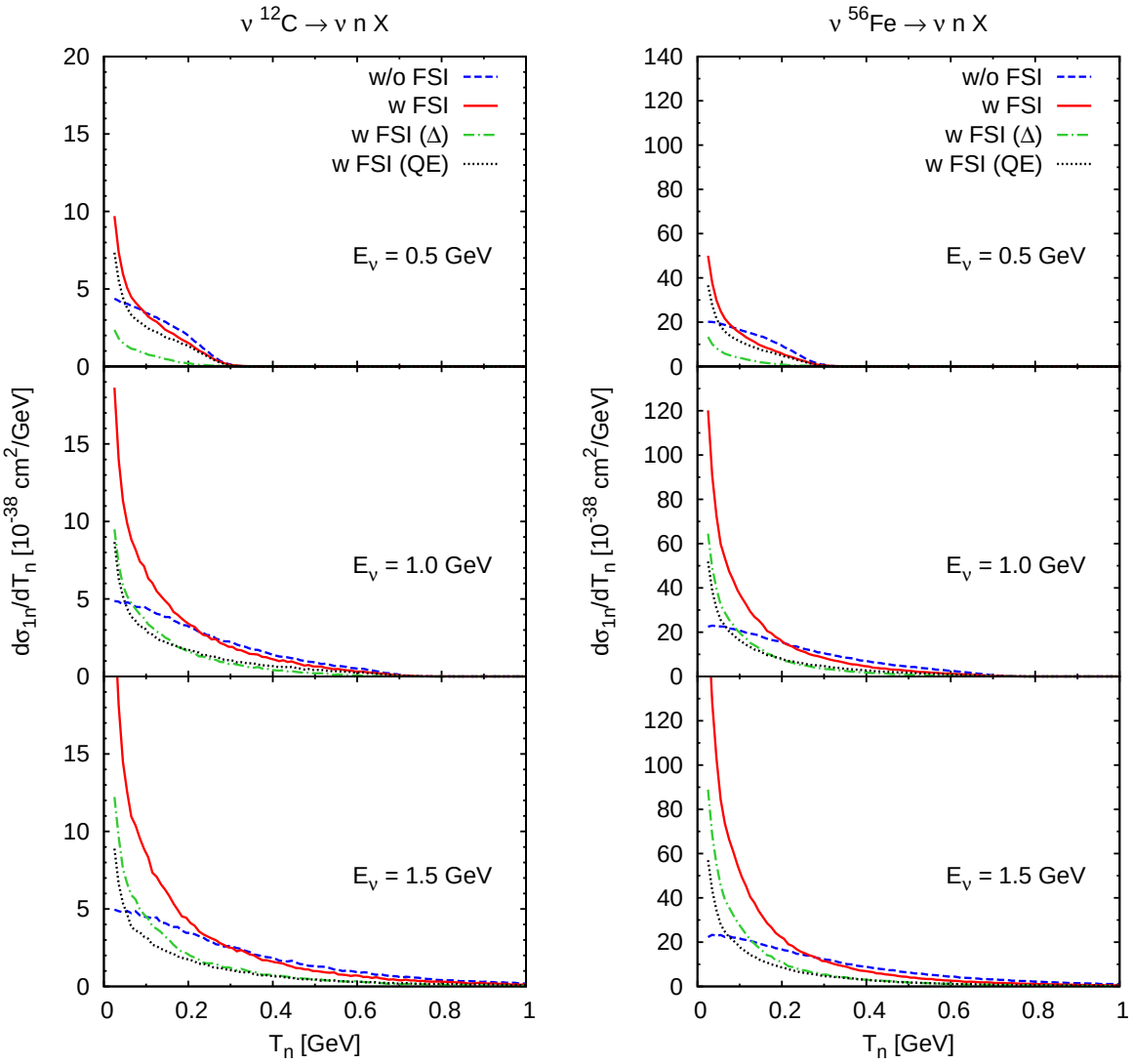

Figure 11.12: Same as Fig. 11.11 for NC *n* knockout.

11.3.2 Nucleon kinetic-energy spectra

In Fig. 11.11 and Fig. 11.12 we show the kinetic-energy differential cross section for NC multiple-proton and neutron knockout versus the kinetic energy for different values of E_ν. The inclusion of FSI strongly modifies the shape of the distribution (compare the dashed and the solid lines) in a similar way as in CC scattering: rescattering of high-energy nucleons in the medium reduces the flux at higher energies while, simultaneously, a large number of secondary nucleons at lower energies is emitted. Again, QE scattering and Δ excitation contribute in equal measure to nucleon knockout at $E_\nu \approx 1\,\mathrm{GeV}$; and the latter becomes increasingly important at higher energies. In contrast to the CC reaction, where neutrons are mainly emitted by secondary collisions, in the NC case, both the neutron and proton kinetic-energy distributions are equally affected by FSI since their total yields without FSI are comparable.

This can be seen also in Fig. 11.13, where we plot the ratio of the NC proton to neutron kinetic-energy differential cross section for ^{12}C and ^{56}Fe at $E_\nu = 0.5\,\mathrm{GeV}$. The calculations with and without FSI (solid and dashed lines) agree approximately if $\Delta s = -0.15$. This shows that the effect of the final-state interaction cancels out regardless of the nucleus. This is different in the CC case (cf. Fig. 11.8), where we have found strong effects of side feeding from the dominant p channel into the suppressed n channel. In fact, side feeding is only important when the initial proton and neutron yields are different. Otherwise the side feeding from proton to neutron is comparable with the opposite one from neutron to proton and then they compensate as just seen by comparing the solid and dashed lines. Indeed, when we set $\Delta s = 0$ in the strange axial form factor (see Eq. (4.17) on page 35), the elementary proton and neutron yields are different as shown in Fig. 4.4 (page 37): while the neutron cross section is enhanced, the proton cross section is reduced. Therefore, we expect side feeding from the neutron to the proton channel, which changes the p/n ratio as observed in Fig. 11.13 (dash-dotted versus dotted lines). Since nucleons lose energy in (charge-exchange) scattering, the effect is more pronounced at low kinetic energies.

Not only the side feeding is caused by differences in the elementary neutrino-nucleon cross section, but also the slight increase with T_N of the ratios. For $\Delta s = -0.15$, the cross section $\mathrm{d}\sigma/\mathrm{d}Q^2$ is bigger (smaller) for neutrons than for protons at low Q^2 (high Q^2) which directly translates into the kinetic energy of the nucleons. For $\Delta s = 0$, $\mathrm{d}\sigma/\mathrm{d}Q^2(\text{neutron}) \gg \mathrm{d}\sigma/\mathrm{d}Q^2(\text{proton})$ at low Q^2 and $\mathrm{d}\sigma/\mathrm{d}Q^2(\text{neutron}) \gtrsim \mathrm{d}\sigma/\mathrm{d}Q^2(\text{proton})$ at high Q^2. This explains both the increase with T_N and also the difference in the absolute magnitude between the two choices of Δs.

We conclude that FSI only cancel in specific cases but not at all in general. This is in contrast to the findings of Alberico *et al.* [ABB+98] who claim that this ratio depends very weakly on the nuclear model (see their Fig. 1). They presented calculations in plane-wave impulse approximation within two nuclear models: the relativistic Fermi

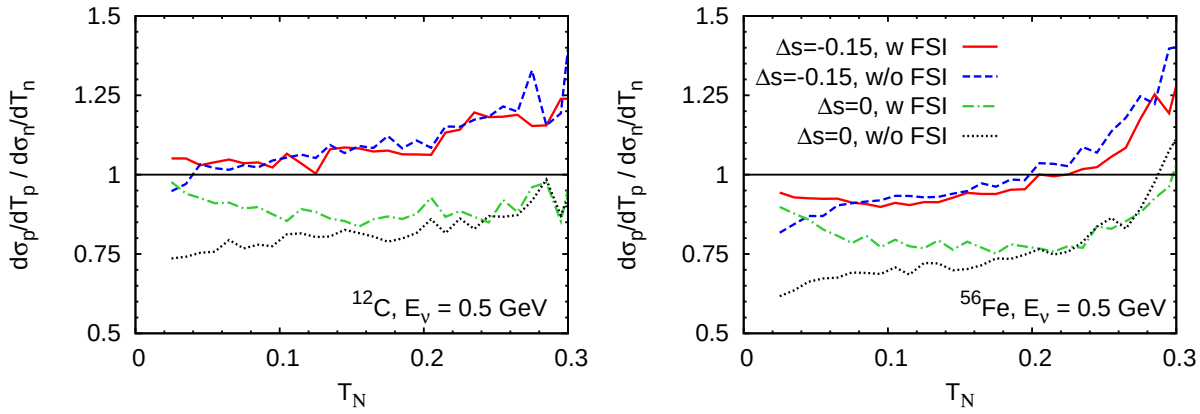

Figure 11.13: Ratio of proton to neutron NC kinetic-energy differential cross section on ^{12}C (left) and ^{56}Fe (right panel) versus the nucleon kinetic energy T_N at $E_\nu = 0.5\,\text{GeV}$. The solid and the long-dashed lines show the results with and without FSI for $\Delta s = -0.15$, the dash-dotted and the dotted lines the results for $\Delta s = 0$.

gas and a relativistic shell model. Calculations in distorted-wave impulse approximation were also included for the shell model, with FSI taken into account using a relativistic optical potential.

11.4 Model dependencies

Following up the discussion in Section 10.4 we now perform the corresponding comparison for CC nucleon knockout at $E_\nu = 1\,\text{GeV}$. We compare the very same cases:

(1) without FSI, without collisional broadening

(2) with FSI, without collisional broadening

(3) with FSI, with collisional broadening (one-pion exchange based model for Δ collisional width and cross sections), with OSP

(4) with FSI, with collisional broadening (Oset prescription for Δ collisional width and cross sections), with OSP

(5) with FSI, collisional broadening only for the Δ resonance (Oset prescription), without OSP

(6) with FSI, Oset based collisional broadening only for the Δ resonance, without OSP, here we do not further track the final nucleons after a $\Delta N \to NN$, $\Delta N \to \Delta N$ or $\Delta NN \to NNN$ reaction

Table 11.1: Total CC single-nucleon knockout cross sections, σ_{1N}, on ^{12}C and ^{56}Fe in units of $10^{-38}\,\mathrm{cm}^2$ at $E_\nu = 1\,\mathrm{GeV}$. The statistical error is negligible. Compared are the different scenarios as detailed in the text.

	^{12}C		^{56}Fe	
	$1p$	$1n$	$1p$	$1n$
(1)	8.04	0.54	38.16	2.65
(2)	5.11	0.62	18.69	3.77
(3)	4.65	0.57	17.13	3.39
(4)	4.71	0.55	17.32	3.31
(5)	4.99	0.58	18.37	3.60
(6)	5.11	0.66	18.97	4.07

Scenarios (1) and (4) have been used so far. Scenario (6) has been added for comparison: the results published in Refs. [LARM06a, LARM06b] are based on this method.

The results for the total CC knockout cross sections are summarized in Table 11.1 for single-nucleon knockout and in Table 11.2 for multiple-nucleon knockout, for both ^{12}C and ^{56}Fe. The kinetic-energy distributions are given in Figs. 11.14 and 11.15. Remarkable agreement of the order of 10% between all approaches is found for the single-nucleon knockout. Even neglecting the outgoing nucleons in the ΔN reactions has no visible impact on the single-nucleon knockout [scenario (6)]. In the multiple-nucleon knockout, however, this scenario slightly underestimates the cross section because most of the final-state nucleons in the ΔN scattering contribute to multiple knockout. Comparing scenarios (5) and (6), this difference is found to be between 15% and 25%.

As in the pion case, scenario (5) is a very good approximation to our best result obtained with the numerically much more complicated case (4). The neglect of the OSP in the propagation and even of the collisional broadening of every baryon besides the Δ has only a small impact.

11.5 Comparisons

One important result of our approach is the finding that already at $E_\nu \approx 1\,\mathrm{GeV}$ a large part of the ejected nucleons stems from Δ excitation and/or other processes different from QE, or, in other words, QE and non-QE processes are "mixed" during FSI.[2] This is an unique feature of a coupled-channel approach, such as the GiBUU

[2] An extended investigation of this entanglement is presented in Section 13.3.

Table 11.2: Total CC multiple-nucleon knockout cross sections, σ_N, on ^{12}C and ^{56}Fe in units of $10^{-38}\,\mathrm{cm}^2$ at $E_\nu = 1\,\mathrm{GeV}$. The statistical error is negligible. Compared are the different scenarios as detailed in the text.

	^{12}C		^{56}Fe	
	xp	xn	xp	xn
(1)	8.04	0.54	38.16	2.65
(2)	9.58	2.77	43.71	19.90
(3)	8.35	2.45	38.73	17.68
(4)	9.10	2.61	41.99	18.85
(5)	9.44	2.61	42.50	18.66
(6)	7.84	2.03	34.01	13.90

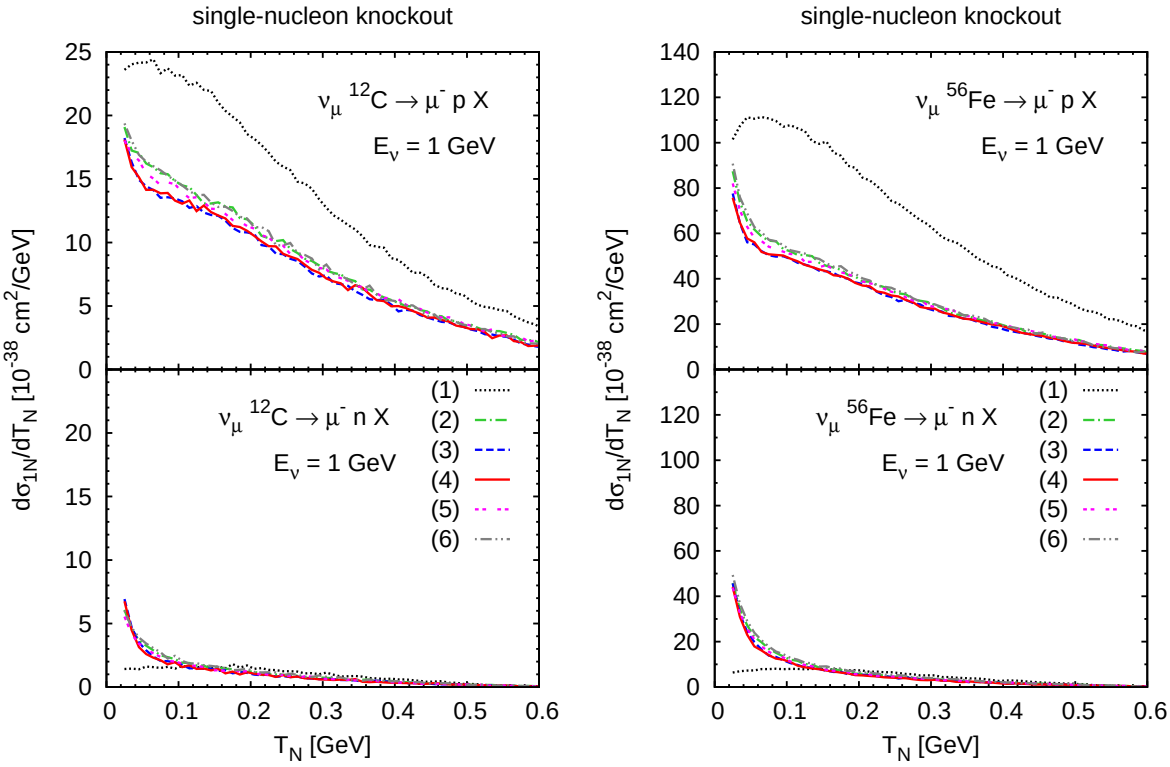

Figure 11.14: Kinetic-energy differential cross section for CC single-p (top) and single-n (bottom panels) knockout on ^{12}C (left) and ^{56}Fe (right panels) versus the nucleon kinetic energy T_N at $E_\nu = 1\,\mathrm{GeV}$. The different scenarios (1)–(6) are detailed in the text.

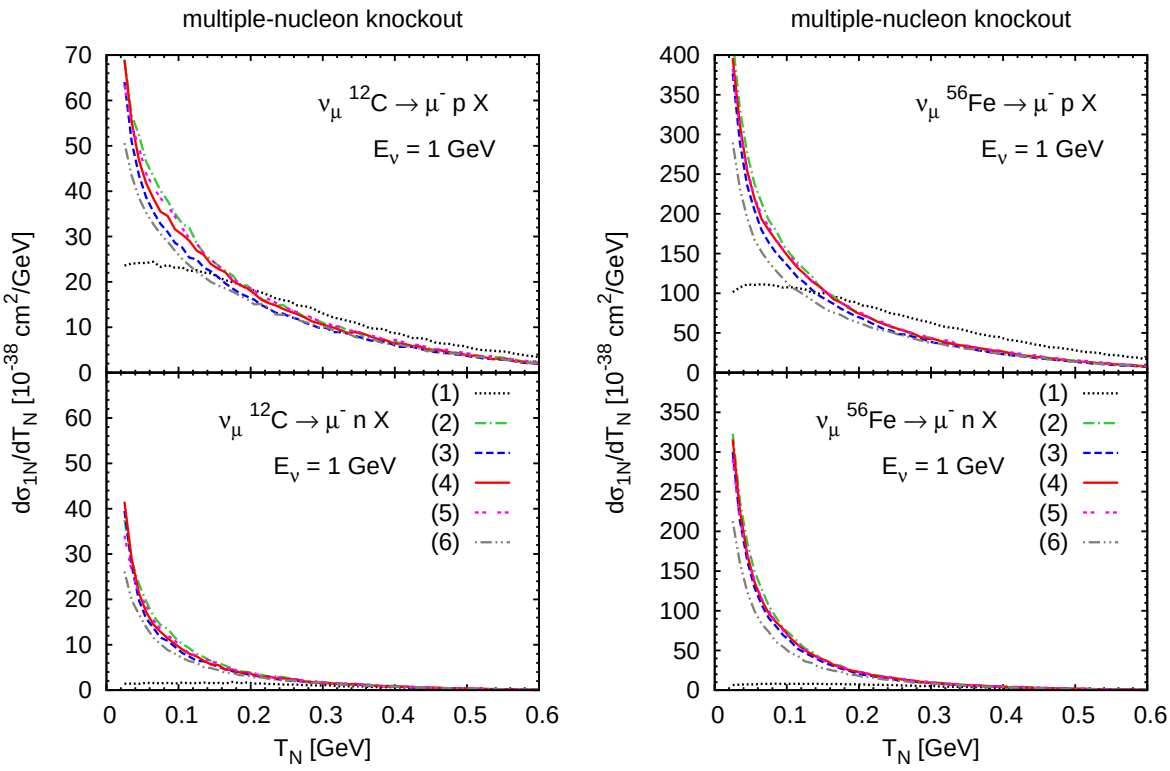

Figure 11.15: Same as Fig. 11.14 for CC multiple-nucleon knockout.

model, not present in any of the models mentioned in the introduction of this chapter. Except for the empirical event generators, we do not know of any other model for neutrino-induced nucleon knockout which accounts for QE and non-QE scattering simultaneously. Thus, for the following comparison, we restrict ourselves to QE scattering only.

We distinguish between two different model classes: first, a semi-classical Monte Carlo simulation which allows to follow the final nucleon hit in the QE process and also to include a large variety of possible final-state interactions. Besides our approach,[3] only the ansatz of Nieves *et al.* [NVVV06] falls into this category. Second, one can calculate nucleon knockout in full quantum mechanical models. Absorptive FSI can be included in a distorted-wave impulse approximation (DWIA) using optical potentials or Glauber models (see, e.g., Martinez *et al.* [MLJ$^+$06] as an example of both, Glauber and optical potential, and also references therein for more details on such kind of models).

We start our discussion by comparing to Nieves *et al.* [NVVV06]. In Figs. 11.16 and 11.17 we show our results for the CC and NC kinetic-energy differential cross section

[3] and the phenomenological event generators discussed in Section 12.2

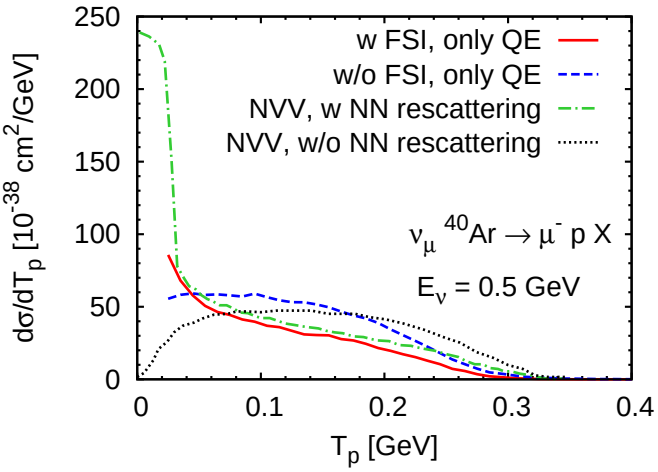

Figure 11.16: Differential cross section for CC proton knockout on ^{40}Ar at $E_\nu = 0.5\,\text{GeV}$. Only QE scattering is included. The dashed line denotes our result without FSI and the solid line the one with FSI. The dotted (dash-dotted) line denoted with "NVV" shows the result of Nieves *et al.* [NVVV06] without (with) NN rescattering.

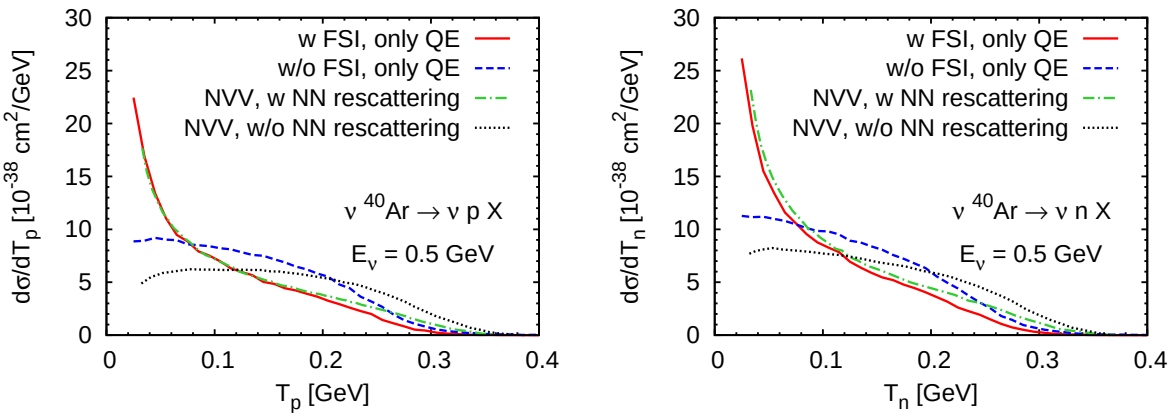

Figure 11.17: Same as Fig. 11.16 for NC. Note that the solid and the dash-dotted lines partly overlap.

together with those of Nieves *et al.* [NVVV06] (denoted with "NVV"). Since they do not include any resonances or background, we have "switched off" these processes in our calculation, so only nucleon knockout induced by initial QE events is considered. The discrepancy between our result without FSI and the result of Ref. [NVVV06] without NN rescattering (dashed versus dotted lines) can be attributed to — in addition to differences in the momentum distribution and the potentials — the RPA correlations included in their calculation which lead to a reduction of the cross section and a spreading of the spectrum. To model the rescattering of the primary nucleons in the nucleus, Nieves *et al.* use a Monte Carlo simulation with elastic NN cross sections similar to ours.[4] Therefore, we expect a similar behavior when FSI are included. Indeed, as one can see, when the rescattering of the outgoing nucleons is "turned on", both calculations lead to very similar results, namely a reduction of the flux for higher energetic nucleons and a large number of secondary low energy nucleons (solid versus dash-dotted lines). Also for the NC p/n ratios we find reasonable agreement: our ratios plotted in Fig. 11.13 show a behavior similar to the ones of Nieves *et al.* (cf. right panel of Fig. 17 in Ref. [NVVV06]).

Let us take the calculation of Martinez *et al.* [MLJ$^+$06] as an example for the full quantum mechanical models. There, nucleon FSI are considered within two frameworks. In one case, a relativistic optical potential in a distorted-wave impulse approximation (RDWIA) is used, in the other case a relativistic multiple-scattering Glauber approximation (RMSGA). Both can therefore account only for single-nucleon knockout. The flux reduction at higher kinetic energies is also observed in their calculations. However, by simple absorption of the nucleons they do not account for the rescattering in the medium which leads to the large number of secondary nucleons. Nucleons are not just absorbed but — through rescattering — ejected with a different energy, angle and/or charge. In particular, in a model not accounting for FSI in a realistic way, there would be no knocked-out neutrons for CCQE scattering.

Comparing directly to such kind of models is rather difficult as they not necessarily calculate the same observables. Already our calculations without FSI is not necessarily the same as PWIA. Thus, we abstain from a comparison.

We close this chapter with a word of caution related to this kind of comparisons. The meaning of "FSI" is interpreted differently in different approaches. We call FSI only the secondary interactions, everything connected with the initial vertex is not called FSI in our approach. For example, in GiBUU, both the initial and the final nucleon still experience a mean-field potential. Since the potential is momentum dependent and this momentum is different in the initial and final states, also the potential is different in both. The same holds for the collisional broadening of the final-state nucleon which we also do not call FSI for the same reason: it is still connected with the initial vertex. Therefore, FSI have in our case no influence at all on inclusive cross

[4] We emphasize that, in addition, we allow for inelastic NN collisions.

sections, e.g., muon observables, because they are not affected by what happens after the initial interaction to the final-state hadron.

Part IV

Applications, predictions and comparisons

12
Experimental status

After neutrino oscillations have first been observed in atmospheric and solar neutrinos [Super-K98, SNO01], an extensive experimental program has started aiming at the precise determination of ν masses and mixing angles, and to search for possible CP violation. Best suited for such precision experiments are long-baseline (LBL) experiments. This intensive search has renewed the interest in neutrino cross sections as they are an important ingredient in the analyses of neutrino-oscillation experiments. The target material of all modern detectors consists of heavy nuclei such as carbon, oxygen and iron. Thus, to interpret their data, the experiments have to rely on Monte Carlo event generator predictions for the final-state interactions in the target nucleus.

In this chapter, we first introduce the main LBL experiments and briefly describe the Monte Carlo event generators used in their analyses.

12.1 Neutrino experiments

We focus in the following on experiments using accelerator neutrino beams. These beams are all built along the same lines: first, a high energy proton beam is shot on a nuclear target producing pions and kaons. In a next step, the mesons, focused by a magnetic horn,[1] decay into charged leptons and neutrinos. A large absorber stops all particles but the weakly-interacting neutrinos. This neutrino beam is directed to the experiments which are located a few hundred meters from the neutrino source

[1] By changing its polarization, the horn switches between neutrino (from the decay of positive charge mesons) or anti-neutrino (from the decay of negative charged mesons) mode.

or even hundreds of kilometers away. A measure for the number of neutrinos, i.e., the statistics collected in an experiment, is the number of protons shot on the target ("protons on target" or POT).

A good understanding of the neutrino beam is critical for the success of the oscillation experiments. While the energy spectrum is most important for ν_μ disappearance experiments (cf., Chapter 13), a good knowledge of the beam composition is required in ν_e appearance searches (cf., Chapter 14). Thus, to limit flux uncertainties, an ideal setup for oscillation measurements consists of two identical detectors, one close to the neutrino production place (near detector) and one in the expected oscillation maximum or minimum (far detector). If such a setup is not possible one has to understand the neutrino production process to high precision. Also cross section experiments require a good knowledge of the absolute neutrino flux because it is the crucial quantity to relate measured count rates into cross sections. Since the uncertainties in the meson flux reflect directly to uncertainties in the neutrino flux, dedicated experiments have been set up to study the hadron production in pA collisions, for instance the HARP experiment [HARP].[2] These results then enter the flux predictions for the LBL experiments (cf., e.g., MiniBooNE's flux prediction in Ref. [MiniBooNE09c]).

We now present an brief overview on recent experiments[3]. The first three, K2K, MiniBooNE and SciBooNE, operating with beam energies around 1 GeV (see Fig. 12.1), are our primary interest.

K2K

The K2K experiment [K2K] in Japan was designed to confirm atmospheric neutrino oscillations using Super-Kamiokande as the far detector. A near detector was set up 300 m downstream to observe the initial, i.e., un-oscillated, spectrum and to measure neutrino cross sections. The near detector is schematically shown in Fig. 12.2. It consists of a 1 kt water Cherenkov detector, a scintillating-fiber/water target tracker (SciFi, oxygen target), a fully active scintillator-bar tracker (SciBar, carbon target) and a muon-range detector. By shooting 12 GeV protons on an Al target at the KEK facility, neutrinos with energies from 1 to 1.5 GeV are obtained; the resulting neutrino flux taken from Ref. [K2K05b] is displayed in Fig. 12.1. K2K collected in total about 1×10^{20} POT, but only 0.2×10^{20} in the SciBar detector because it was installed only later. This high statistics allows for precision cross section measurements: SciFi has measured CCQE cross sections [K2K06], CC1π^+ events have been measured in SciBar [K2K08] while NCπ^0 events have been observed in the 1 kt detector [K2K05b]. For detailed information on the event selection and performed cuts, we refer the reader

[2] The GiBUU model is also able to describe the HARP data [GM09].

[3] The bubble-chamber experiments performed at ANL and BNL in the 1970s to 1980s are not discussed any further.

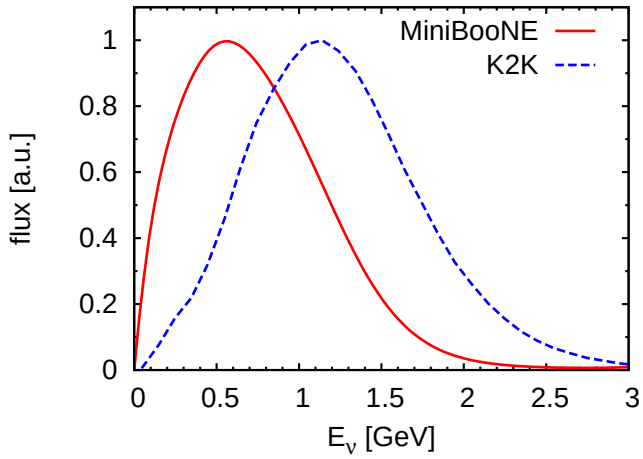

Figure 12.1: Neutrino energy flux for the K2K (dashed line, taken from Ref. [K2K05b]) and the MiniBooNE/SciBooNE experiments (solid line, taken from Ref. [MiniBooNE09c]).

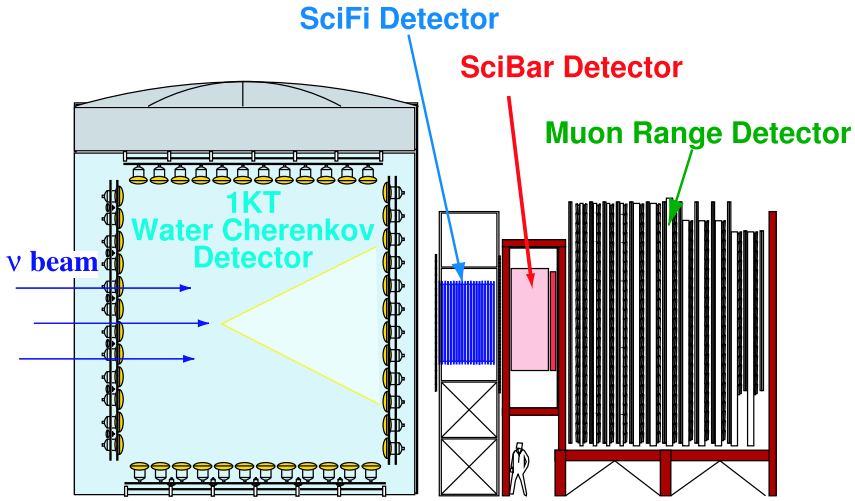

Figure 12.2: Schematic view of the K2K near detector. Taken from Ref. [K2K08].

to the cited references.

MiniBooNE

Two neutrino experiments make use of the 8 GeV Booster beam at the Fermi National Accelerator Laboratory (USA): MiniBooNE and SciBooNE. MiniBooNE [MiniBooNE] is a Cherenkov detector of 12 m diameter filled with around 800 tons of mineral oil, CH_2, and is located about 500 m downstream. Its primary goal was to check the neutrino-oscillation signal reported by the LSND experiment [LSND95, LSND01]. LSND reported strong evidence for $\bar{\nu}_\mu \to \bar{\nu}_e$ oscillations. This would require $\Delta m^2 \sim 1\,\mathrm{eV}^2$ which is much larger than what has been observed in atmospheric and solar neutrino oscillations (see Chapter 14 for an extended discussion).

However, with 7×10^{20} POT corresponding to about 10^6 neutrino interactions collected in the neutrino mode,[4] MiniBooNE is now also a high-statistics cross section experiment. The neutrino energy peaks at around 0.7 GeV as can be seen from Fig. 12.1. The primary mechanism at this energy is QE scattering, which thus dominates the MiniBooNE event sample. MiniBooNE has published results for CCQE scattering [MiniBooNE08b], CC1π^+ [MiniBooNE09a], and NCπ^0 production [MiniBooNE08a]. Many more cross section measurements, in particular measurements of absolute cross sections in many variables, are expected soon — first preliminary results were presented at NUINT09 [NUINT09], see in particular Refs. [And09a, Wil09]. The particle reconstruction is based primarily on the detection of Cherenkov radiation by the photo tubes at the tank surface: muons lead to full rings, electrons to fuzzy rings and neutral pions (via their decay into 2 photons) to double rings. Charged pions are also identified through their decay signature (Michel electrons). Again, for detailed information on MiniBooNE's event topology, we refer the reader to the above references.

SciBooNE

The second experiment in the Booster beam is SciBooNE [SciBooNE], located between MiniBooNE and the neutrino source. SciBooNE consists of a scintillator bar detector (carbon target) formerly used as the SciBar detector in the K2K experiment, a muon range detector and an electron catcher. SciBooNE is a dedicated experiment to measure cross sections. During its run time from June 2007 till Aug 2008, it collected 1×10^{20} POT in the neutrino mode which corresponds to about 10^4 CC ν interactions. First preliminary results for CCQE, NCQE, CCπ^+, and NCπ^0 cross sections were presented at the recent NUINT09 workshop [NUINT09].

[4] Currently, MiniBooNE is running in the anti-neutrino mode.

MINERνA

The MINERνA experiment [MINERvA04] is designed to study neutrino-nucleus interactions with unprecedented detail, it will measure inclusive and exclusive cross-sections for a wide variety of neutrino reactions over a 1-20 GeV range of neutrino energies. The detector is located in the NUMI beam line at Fermilab. It will be equipped with several different nuclear targets (C, Fe, Pb) such that a precise study of neutrino nuclear effects will be possible. The detector design, a fully active scintillator target, allows to track and reconstruct particles with a high precision. The prototype has already started to take data and full operation is expected to begin in early 2010.

T2K

The T2K experiment [T2K] is a long-baseline high-precision neutrino-oscillation experiment focussing on θ_{13} but also on improving θ_{23} and Δm^2_{23}. For this purpose JPARC's high intensity ν_μ beam with $\sim$700 MeV peak energy will be directed towards the Super-Kamiokande detector. The near high-resolution detector, presently under construction, aims at measuring the energy spectrum, the flavor content of the beam and also neutrino cross sections.

Others

Several other neutrino oscillation experiments are currently taking cross section data at higher neutrino energy. MINOS in the NUMI beam line collects data for neutrino iron scattering at energies around 5 GeV, NOMAD has recently published the most precise QE measurement between 3 and 100 GeV neutrino energy on a C target [NOMAD08].

12.2 Monte Carlo event generators

Neutrino event generators are crucial tools for experimental neutrino physics, and "in this sense, they serve as the gateway to a quantitative description of the physics of neutrino scattering" [Gal09]. They are further required to successfully envision, design and execute experiments. Thus, the neutrino experiments rely heavily on their Monte Carlo event generators. Their precision immediately limits the precision with which the oscillation parameters can be measured. For the extraction of electroweak parameters from such experiments it is, therefore, important to control the expected accuracy of these Monte Carlo analyses. While most event generators are similar in their treatment of the initial neutrino-nucleon interaction, they differ substantially in their treatment of nuclear effects and FSI (cf., e.g., Ref. [And07] and references

therein). Furthermore, first MiniBooNE and K2K results indicate a disagreement between the Monte Carlo predictions and the actual measurements [Zel08, NUINT09].

There are important differences between most Monte Carlo generators and the GiBUU approach that is used in this work. In the following, we address the main points. The GiBUU framework models the full space-time evolution of the phase space densities of all relevant particle species during a nuclear reaction within a consistent treatment of the initial vertex and the final-state processes; and we emphasize that these should not be treated separately. This is not true for all event generators. There, initial-state and final-state interactions are considered independently (e.g., a Fermi-gas model for the initial state but a Cascade model for the final-state interactions). As detailed in Chapter 7, the space-time evolution is determined by the so-called BUU equations, which describe the propagation of the particles in their potentials and the collisions between them — resonances are treated explicitly — however, at the price of a time-consuming numerical realization. A major strength of the GiBUU model is that it has been applied to many different reactions from heavy ion collisions to pion and electron induced processes [TCE$^+$97, GM09, LEM00, BARMM06] (see Refs. [GiBUU, BGG$^+$] for more applications). The comparison with data for the reactions mentioned allows to make estimates for the expected accuracy in neutrino-induced reactions. Unlike most Monte Carlo event generators, we do not tune any specific input (like for example pion absorption cross sections) to describe a specific reaction channel (like for example neutrino-induced pion production). On the contrary, we include as much physics as possible and are thus in a position to explain simultaneously a wide range of very different reactions. In our understanding, these are the main points where our approach differs from common event generators.

We emphasize that in particular the independent tests with photon or electron induced reactions, where accurate data are available, have not been performed by most of the generators. Mostly, they are tuned to describe pion-nucleus scattering. But this can only be a partial check since pions — unlike neutrinos — probe only the nuclear surface. Hence, this check is important and necessary but not sufficient: only reactions with (virtual) photons involved can be used as a meaningful "quality check", because, like neutrinos, they probe the full nuclear volume. Many high statistics electron- and photon-scattering data in a kinematical region relevant for the present neutrino experiments are available and allow precise tests of the nuclear model.

It has to be noted, that in a real experiment the event generator is only a small — though important — part in the simulation chain. In a first step, one has to understand the neutrino beam creation by shooting protons on a nuclear target. Then, after the neutrino-nucleus interaction, one has to track the outcome through the detector itself, commonly using the GEANT detector simulation. This involves questions like light propagation in Cherenkov detectors, pion detection abilities and so on. All these steps introduce additional uncertainties.

12.2.1 Generator overview

In the following, we briefly describe the generators used by MiniBooNE and K2K, namely NUANCE and NEUT. We also give some details about the GENIE project, which is used by MINOS and has the ability to serve as a coding framework into which other models can be implemented easily. FLUKA and NuWro, not connected with any of the experiments of our direct interest, are not discussed. Further details are given in Refs. [Ladek09, Gal09, GCHS05, And07] and references therein.

NUANCE

The NUANCE event generator [Cas02] was originally developed in the 1980s for the IMB experiment, a large water detector searching for proton decay but also able to detect neutrinos,[5] and is nowadays the event generator of MiniBooNE [Haw05]. NUANCE is able to handle ^{16}O and ^{12}C targets.

The modeling of the neutrino-nucleon vertex is based on inputs from Llewellyn-Smith for QE [LS72], Rein and Sehgal for the resonances [RS81], Bodek and Yang [BPY05] and the Lund hadronization model for DIS, each with some specific modifications. A model by Rein and Sehgal is also used for coherent pion production [RS83].

NUANCE uses a Fermi gas model to simulate the scattering off a bound target. Its implementation, however, is different from process to process. In general, the initial nucleons have a momentum distribution with a constant Fermi momentum (225 MeV for ^{16}O and 220 MeV for ^{12}C) with a constant binding energy (-27 MeV and -25 MeV).

For QE scattering, NUANCE applies the model of Smith and Moniz [SM72]. Recently, this has been modified to improve the agreement with MiniBooNE's QE data: the MiniBooNE collaboration introduced a parameter, κ, to shrink the phase space available for the outgoing proton [MiniBooNE08b].[6] The original QE implementation has been tested against inclusive electron scattering data by "switching off" the axial parts in the QE current (see their results in Refs. [Haw05, Haw04]). In Fig. 12.3 we show their results together with the ones of our model. Note that the height of their curves has been normalized to the height of the data points. The NUANCE curves show the typical shape of a Fermi gas calculation with a constant Fermi momentum (cf., our discussion in Section 9.4). It is enlightening to study the effects of Pauli blocking and the κ parameter in these observables. While Pauli blocking affects only the left outer part of the curves, the κ parameter cuts away all strength at the left side of

[5] A possible signature for proton decay is $p \to e^+\pi^0$; but the pions may reinteract in the nuclei in which the proton decays. A major background is caused by atmospheric neutrinos which also can produce π^0. Thus, to understand these processes and to estimate the detection efficiency, first neutrino event generators were developed.

[6] We will discuss the MiniBooNE QE result in more detail in Section 15.1.

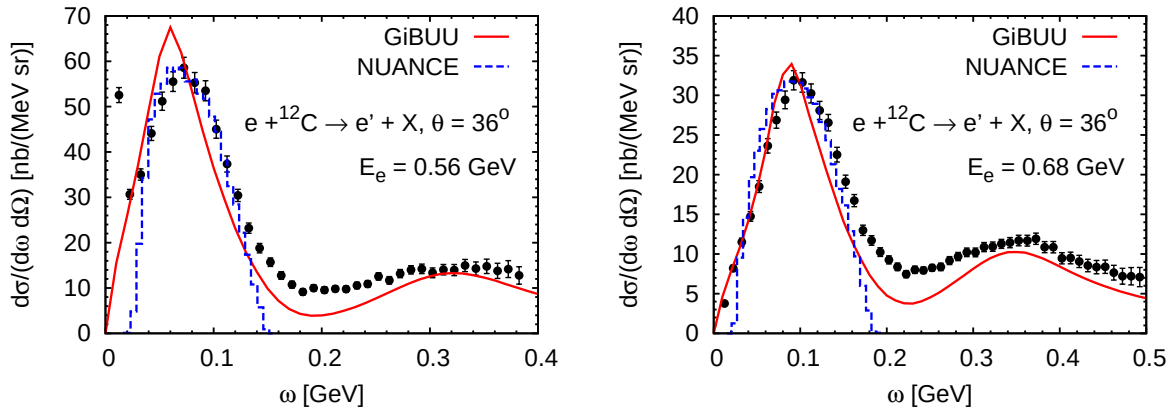

Figure 12.3: Inclusive electron cross section $\mathrm{d}\sigma/(\mathrm{d}\omega\mathrm{d}\Omega_{k'})$ on ^{12}C as a function of the energy transfer ω at two distinct fixed electron energies (0.56 and 0.68 GeV) and a scattering angle of $\theta_{\mathbf{k}'} = 36°$. The solid lines denote our full result while the dashed curves are obtained with NUANCE (taken from Refs. [Haw05, Haw04]). Note that the height of the NUANCE curves has been normalized to the height of the data points which are taken from Ref. [B$^+$83].

almost vertical lines of constant ω. Thus, from this observable it is clear, that κ cannot have any physical meaning.

In NUANCE, the original Rein-Sehgal model has been extended such that resonances may decay into final states other than πN. Decay nucleons are Pauli blocked when their momentum is below the Fermi momentum. In-medium effects on the resonance widths are not considered. However, to improve agreement with Super-Kamiokande and K2K data which favor a suppression of resonant pion production, NUANCE assumes a 20% (10%) suppression in the isospin 1/2 (3/2) channel and thus simulates in this way "pion-less" resonance decay.

For the FSI of the produced particles, mainly pions and nucleons (unlike in the GiBUU model, resonances decay immediately and do not undergo FSI), NUANCE applies an intranuclear cascade model. The starting position is chosen according to measured density profiles. Then, the hadrons are tracked through the nucleus in 0.2 fm steps. The interaction probability is calculated for each step using single-nucleon cross sections and the local density. Measured cross sections and angular distributions are used for πN and NN cross sections. No interactions are allowed in the first 1 fm. NUANCE further takes into account nuclear de-excitation by photon emission.

The cascade model has been tested by simulating p, π ^{16}O scattering. Here, the hadron is set in front of the nucleus and then propagated through. The pion absorption cross section is tuned to match available data. At intermediate energies, NUANCE describes the reaction $^{12}\mathrm{C}(p, p')$, rather well. Casper states [Cas02], that their

results agree also with the analytical approach of Paschos and collaborators which we discussed in Section 10.6.2.

NEUT

Like NUANCE, the NEUT event generator [Hay02, Mit07, Hay09] was initially developed for proton decay searches at Kamiokande. At present, it is used by K2K, SciBooNE and also Super-Kamiokande. It is applicable for neutrino energies from 100 MeV to 1 TeV and for proton and ^{16}O targets (extended to ^{12}C).

After fixing the neutrino energy, vacuum νN cross sections are used to select the interaction mode. The neutrino-nucleon cross section input is very similar to NUANCE: Llewellyn-Smith for QE [LS72], Rein-Sehgal for coherent and incoherent pion production [RS81, RS83], and Bodek and Yang [BPY05] parton distribution functions are used together with the standard DIS formula. Only since recently, NEUT accounts for lepton mass effects.

For quasielastic scattering, NEUT applies the relativistic Fermi gas model of Smith and Moniz [SM72] with a Fermi momentum of 225 MeV and a momentum-dependent nuclear potential. For resonance excitation, the pion-less decay of the Δ is simulated by generating final leptons and nucleons in only 80% of the events. This reduction is independent of energy. Pauli blocking of the resonance decay products is included. Like NUANCE, they have extended the original Rein-Sehgal model in a way such that resonances may decay into final states other than πN.

The rescattering of pions, kaons, etas, omegas and nucleons in the nucleus is described by a Cascade model. For example, the pions can undergo inelastic or charge-exchange scattering or be absorbed. Their initial position is chosen according to a Wood-Saxon density distribution. Then, for pions of momenta less than 500 MeV, the interaction mode is determined using the mean-free path calculated following Salcedo *et al.* [SOVVGR88] (includes both two-body and three-body contributions). Pauli blocking is also considered in the final-state interactions based on a local Fermi gas. The final nucleons after the pion absorption are not propagated.[7] For higher momentum pions, kaons, etas, omegas and nucleons, the cross sections are taken from various experiments and/or models. The nucleon, e.g., can scatter elastically, or via $NN \to \Delta N$ and $NN \to \Delta\Delta$.

The cascade model has been successfully tested against π^{12}C and π^{16}O (see the above references) but also against pion photo-production data (unpublished according to Hayato [Hay]). In Fig. 12.4 we compare NEUT to our approach (dashed vs. solid lines). From the total cross section, shown in the left panel, we find that NEUT has more π^+ after FSI. The difference is either due to larger elementary yields, less absorption or a different way of selecting the final states. The right panel, where the

[7] This is being improved at the moment [Hay].

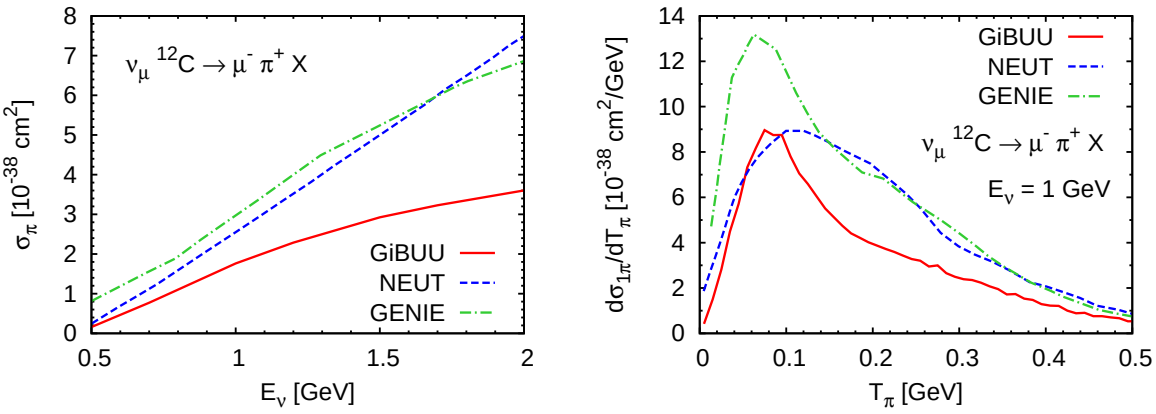

Figure 12.4: Left panel: total CC π^+ production on ^{12}C versus E_ν. Right panel: kinetic-energy differential cross section for CC π^+ production on ^{12}C versus the pion kinetic energy for $E_\nu = 1\,\text{GeV}$. In both panels, the solid lines denote our calculation while the dashed (dash-dotted) lines are the result obtained by NEUT (GENIE). Both are taken from Ref. [Sob09].

kinetic-energy distribution is shown, indicates a significant difference in the Δ region, where most of our pions are absorbed. This specific feature is not seen in the NEUT result.

GENIE

GENIE is a new neutrino event generator which started to be developed after the NUINT01 workshop; its goal is to become the "canonical" Monte Carlo code whose validity extends to all nuclear targets and neutrino energies [GENIE, A$^+$09, And09b]. Special emphasis is put on the software design which aims at providing a platform where others, in particular theorists, can contribute their models. GENIE is currently at use mainly for the MINOS experiment but also used in T2K, MINERνA, NOVA, ArgoNEUT and MicroBooNE and plans to extend its efforts also to other experiments. GENIE's physics models were synchronized to those in NEUGEN3 [Gal02], a generator used by Soudan 2 and MINOS. NEUGEN is superseded by GENIE and is therefore not being continued, while GENIE has been improved significantly in the last years.[8]

The neutrino-nucleon cross section model is similar to the two previous approaches: Llewellyn-Smith for QE [LS72], Rein-Sehgal for the coherent and incoherent pion production [RS81, RS83], and Bodek-Yang [BPY05] for DIS. The single-pion and two-pion channels in the transition region are tuned to match bubble chamber data. GENIE uses a home-grown hadronization model, the AGKY-model, which combines

[8]For example, NEUGEN had no baryon rescattering at all which is now implemented in GENIE.

PYTHIA/JETSET at higher invariant masses with the KNO-scaling at lower invariant masses (details are given in Ref. [A$^+$09]).

A Fermi-gas model with a constant Fermi momentum (221 MeV for C, 250 MeV for Fe) and constant binding energy (30 MeV) is used to describe the initial nucleons; it is modified to account for nucleon-nucleon correlations following the work of Bodek and Ritchie [BR81]. Currently, C. Andreopoulos is working on the implementation of Benhar's spectral function model for the nuclear ground state [And09b]. Pauli blocking is applied only for QE scattering, and no medium-modifications for the resonances are considered.

The rescattering of pions and nucleons is simulated with INTRANUKE/hA, an "effective" FSI model, which is anchored to a large body of experimental data, in particular π^{56}Fe and p^{56}Fe data (default model). In future releases, an alternative approach called INTRANUKE/hN will be available. INTRANUKE/hN is a cascade model based on nucleon cross sections.

We briefly introduce GENIE's default model, the INTRANUKE/hA. Here, the particles, i.e., pions and nucleons, are stepped through the nucleus in 0.1 fm steps. No interactions are possible during the first 0.5 fm. For each particle, only one interaction is allowed. The mean-free path is used to determine the interaction probability at a particular step. It is calculated from measured hadron-nucleon cross sections (taken from Ref. [CNS]) and charge densities. However, in GENIE the nuclear density distribution, through which a particle is tracked, is "stretched" by (half) the deBroglie wave length for nucleons (pions) to simulate quantum mechanical effects. Once it is decided that the nucleon/pion interacts, the corresponding reaction is chosen from a list of available π^{56}Fe or p^{56}Fe channels which include, e.g., proton elastic scattering, $p^{56}\text{Fe} \to p^{56}\text{Fe}$, charge exchange, $p^{56}\text{Fe} \to n^{56}\text{Co}$, pion production, $p^{56}\text{Fe} \to \pi^+ n^{56}\text{Fe}$, and so on. Details are given in Ref. [Dyt09]. Most cross sections are based on measurements performed on ^{56}Fe. GENIE has been applied also to other nuclei by scaling the cross sections with $A^{2/3}$.

The intranuclear rescattering model has been tested and tuned to π^{56}Fe and p^{56}Fe data running the simulation with hadrons instead of neutrinos. Tests with photons or electrons have not been done yet.

In Fig. 12.4 we compare GENIE to our approach (dash-dotted vs. solid lines). In both observables, the GENIE curve is much higher than ours. Part of this might be explained by the fact that GENIE overestimates the elementary pion-production bubble-chamber data in the resonance region [Gala] which is in their case not simply dominated by the Δ resonance but has a large contribution from their fit of pion production in the transition region which extends down to lower W.

12.2.2 Conclusion

We have seen that the common event generators agree in the description of the νN reaction (details are different: form factors, axial mass value, inclusion of lepton mass, inclusion of non-resonant background, transition region between resonance and DIS, ...). But there are obvious differences and levels of sophistication in the treatment of nuclear effects and final-state interactions. However, one should keep in mind that most neutrino event generators have been developed for a given experiment only — and different experiments are sensitive to different aspects of physics. For example, an event generator for a water Cherenkov detector with a proton threshold of more than 1 GeV does not need to model low-energy secondary nucleons with a high precision.

We close this section with a word of caution concerning the model consistency. Most event generators are now working on implementing recent theoretical models, e.g., spectral functions for the initial nucleons, RPA correlations, or new resonance excitation models. In general, those replace only a specific part of the simulation. We emphasize that consistency demands the same treatment for the initial and the final state. For example, self energies in the initial-state process (e.g., Δ spectral function) should match the FSI rates (e.g., $\Delta N \to NN$ cross sections). Thus, one has to be careful when merging various models in order to keep consistency and to avoid double-counting.

13

CCQE/CC1π^+ entanglement and neutrino energy reconstruction

13.1 Introduction

A good knowledge of the neutrino energy is required for a precise determination of oscillation parameters in ν_μ disappearance measurements. The neutrino beam is far from being mono-energetic in present experiments (cf., e.g., Fig. 12.1). External experiments are performed to help predict the beam profile, e.g., the HARP experiment [HARP]. ν_μ disappearance experiments now search for a distortion in the neutrino flux in the detector positioned far away from the source. Comparing both, unoscillated and oscillated flux, one gains information about the oscillation probability and with that about mixing angles and mass squared differences.

However, the neutrino energy is not measurable directly but has to be reconstructed from the reaction products. Present oscillation experiments use the CCQE reaction as signal event and reconstruct the energy with two-body kinematics from the outgoing muon assuming the target nucleon is at rest. Two immediate questions arise from this procedure: (1) How good is the identification of CCQE events? (2) How exact is the crucial assumption of two-body kinematics for nucleons bound in a nucleus where many in-medium modifications are present?

CCQE is defined as the process happening on the single nucleon; in the nucleus, CCQE is masked by FSI. Thus, the correct identification of CCQE is immediately related to the question of how FSI influence the event selection. The main background to CCQE is CC1π^+ production. If the pion is absorbed in the nucleus and/or not seen

in the detector, these events can be misidentified as CCQE. Consequently, a proper understanding of CCQE and CC1π^+ is essential for the reconstruction of the neutrino energy.

This chapter addresses the questions outlined above. We start with a general introduction into the event classification in typical neutrino detectors and discuss how possible thresholds influence the measured spectra. We further discuss both CCQE and CC1π^+ cross sections and their entanglement. Finally, we investigate how nuclear effects influence the reconstruction of the neutrino energy.

13.2 Event selection

The event selection in current neutrino experiments is a highly complicated subject (see, e.g., review talk given by M. Wascko [Was09]). Rather than presenting a quantitative discussion for each particular setup (if at all possible) we try to give a qualitative picture on how nuclear effects themselves modify the measured spectra in CC scattering assuming specific thresholds. Two "toy" detectors with the following properties are used to this aim:

Cherenkov detector. In a Cherenkov detector, e.g., MiniBooNE and K2K 1kt, CCQE events are identified by a single ring from the outgoing lepton. Muons can be tagged by their decay electron. If pions are produced, they lead to additional rings either from the γ decay of the π^0 or from the decay muon of the charged pions.

We define for our "toy" Cherenkov detector

CCQE:	$1\mu^-$	$0\pi^+$	$0\pi^-$	$0\pi^0$	xp	xn
CC1π^+:	$1\mu^-$	$1\pi^+$	$0\pi^-$	$0\pi^0$	xp	xn

where xp and xn indicates, that any number of protons or neutrons are allowed.

The lower momentum thresholds depend on the index of refraction n via

$$\beta_{\text{thres}} = \frac{1}{n} \Leftrightarrow |\mathbf{p}|_{\text{thres}} = \frac{m}{\sqrt{n^2-1}}\,, \tag{13.1}$$

where m is the particle mass. Typical values for water ($n = 1.33$) are $|\mathbf{p}|_{\text{thres}}$ =120 MeV for muons, 160 MeV for charged pions, 0 MeV for neutral pions (identified via their γ decay) and 1070 MeV for protons. Lower thresholds ($\approx$ 50 MeV for muons and charged pions, $\approx$ 350 MeV for protons) are reached with the MiniBooNE detector which is filled with mineral oil of $n = 1.47$ [MiniBooNE09b], and, in addition, produces also scintillation light.

Tracking detector. In a tracking detector, e.g., SciBooNE and K2K SciFi, all charged particles leave tracks which can be used to identify the particles and to determine their properties. Thus, highly advanced event selection procedures are applied. To keep it simple, we define

CCQE: $1\mu^-$ $0\pi^+$ $0\pi^-$ $0\pi^0$ $1p$ xn
CC1π^+: $1\mu^-$ $1\pi^+$ $0\pi^-$ $0\pi^0$ xp xn

The thresholds depend strongly on the experimental setup, e.g., the SciFi detector requires both muon and proton momentum to be above ≈600 MeV and the pion momentum above 200 MeV [K2K06]. Note that this proton threshold cuts away a significant part of the proton spectra as can be seen, e.g., from Fig. 11.5 (page 180) where $|\mathbf{p}|_{\text{thres}} \approx 600$ MeV corresponds to about 200 MeV kinetic energy (compare Fig. B.4). The same is true for the pions as can be appreciated, e.g., from Fig. 10.7 (page 155) where $|\mathbf{p}|_{\text{thres}} \approx 200$ MeV corresponds to about 100 MeV kinetic energy. We further note that the thresholds are much lower in the SciBar and SciBooNE detectors.

In the following, we assume perfect particle identification above threshold in both cases and neglect any other experimental restrictions.

13.3 Topologies

13.3.1 CCQE identification

The CCQE reaction, namely $\nu_\ell n \to \ell^- p$, is the dominant cross section at low energies (cf., Fig. 3.2), and commonly used to reconstruct the neutrino energy. In other words, CCQE is the signal event in present oscillation experiments.

The experimental challenge is to identify *true* CCQE events in the detector, i.e., muons originating from an initial QE process. To be more precise: true CCQE corresponds to the inclusive CCQE cross section including all medium effects, or, in other words, the CCQE cross section before FSI. The difficulty comes from the fact that the true CCQE events are masked by FSI in a detector built from nuclei. The FSI lead to misidentified events, e.g., an initial Δ whose decay pion is absorbed or which undergoes "pion-less decay" can count as CCQE event — we call this type of background events "fake CCQE" events. We denote every event which looks like a CCQE event by "CCQE-like".

As outlined above, at Cherenkov detectors CCQE-like events are all those where no pion is detected while in tracking detectors CCQE-like events are those where a single proton track is visible and at the same time no pions are detected. The two methods are compared in Fig. 13.1. The "true CCQE" events are denoted with the solid lines, the CCQE-like events by the dashed ones. The Cherenkov detector is able to detect

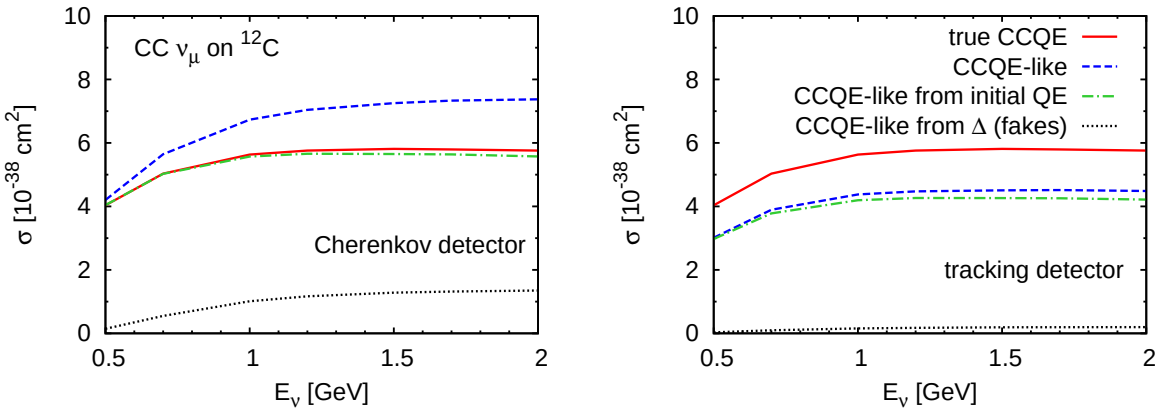

Figure 13.1: Total QE cross section on ^{12}C (solid lines) compared to different methods on how to identify CCQE-like events in experiments (dashed lines). The left panel shows the method commonly applied in Cherenkov detectors, the right panel the tracking detector method as described in the text. The contributions to the CCQE-like events are also classified (CCQE-like from initial QE (dash-dotted), from initial Δ (dotted lines)).

almost all true CCQE (left panel, solid vs. dash-dotted lines agree approximately) but sees also a considerable amount of "fake CCQE" (or "non-CCQE") events (left panel, the dashed line is roughly 20% higher than the solid line). They are caused mainly by initial Δ excitation as described in the previous paragraph (absorption of decay pion or "pion-less decay"); their contribution to the cross section is given by the dotted lines. On the contrary, less CCQE-like than true CCQE events are detected using the method applied in tracking detectors which trigger both on pions and protons (right panel, difference between dashed and solid line). The final-state interactions of the initial proton lead to secondary protons, or, via charge exchange to neutrons which are then not detected as CCQE-like any more (*single* proton track). We find that at tracking detectors the amount of fake events in the CCQE-like sample is less than at Cherenkov detectors (dashed and dash-dotted lines almost agree with each other in the right panel but not in the left panel). We conclude that even if the additional cut on the proton helps to restrict the background, an error of about 20% remains, since the measured CCQE cross section underestimates the true one by that amount.

To investigate further the relation between the CCQE-like and true CCQE cross section, we show their ratio as a function of proton and pion-momentum threshold in Fig. 13.2.[1] As the proton is not at all relevant for the CCQE identification in Cherenkov detectors, the ratio is independent of the proton momentum detection threshold (dashed line in left panel). This is very different in tracking detectors which

[1]See Section 13.2 for the thresholds applied in present experiments.

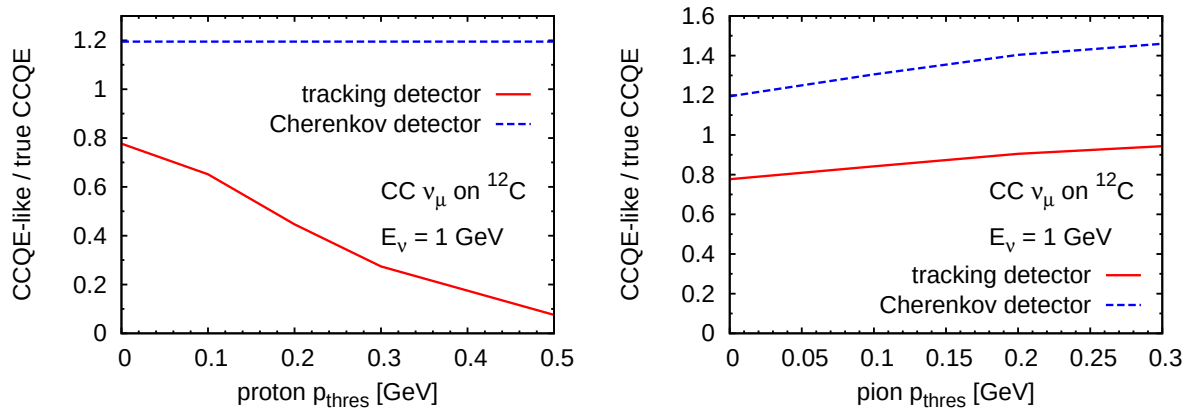

Figure 13.2: Ratio of the CCQE-like to the true CCQE cross section as a function of the proton (pion) detection momentum threshold for CC ν_μ on ^{12}C at $E_\nu = 1\,\text{GeV}$. The solid lines are obtained using the tracking detector identification, while the dashed lines are for Cherenkov detectors.

rely on the detected proton — here the efficiency is reduced to ≈10% at a proton momentum threshold of 0.5 GeV (solid line in left panel). Even at $|\mathbf{p}|^p_{\text{thres}} = 0$ the efficiency does not exceed 80% because of charge-exchange processes that lead to the emission of undetected neutrons and because of secondary proton knockout that leads to multiple-proton tracks. The same effects cause the difference between the solid and the dashed lines in the left panel of Fig. 13.1. Focussing on the right panel of Fig. 13.2 we find that the CCQE-like cross section increases for both detector types as $|\mathbf{p}|^\pi_{\text{thres}}$ increases. In this case even more events with pions in the final state appear as CCQE-like because then these pions are below threshold and thus not detected.

The CCQE-like cross section is splitted into QE and non-QE sources (like Δ excitation) in Fig. 13.3 and Fig. 13.4. The left panel of Fig. 13.3 shows again the ability of a Cherenkov-like detector to identify over 98% of the initial CCQE events (dashed line); the missing strength is mainly lost into pion channels, i.e., the nucleons rescatter and produce pions such that the event is not classified as CCQE-like any more. This fraction almost vanishes (the dashed line gets even closer to one in the right panel) when the pion momentum threshold increases because then the CCQE-induced pions are not detected any more and the event counts again as CCQE-like.

Let us now turn to the non-QE CCQE-like cross section displayed in Fig. 13.4. Different sources are indicated: initial Δ excitation and initial single-pion background reaction (higher resonances are negligible here and thus not shown). The left panel shows again the dependence on the proton-momentum threshold which is not relevant in the Cherenkov case: there the non-QE CCQE-like contribution adds up constantly to about 18%. However, this threshold is important for the tracking detector for

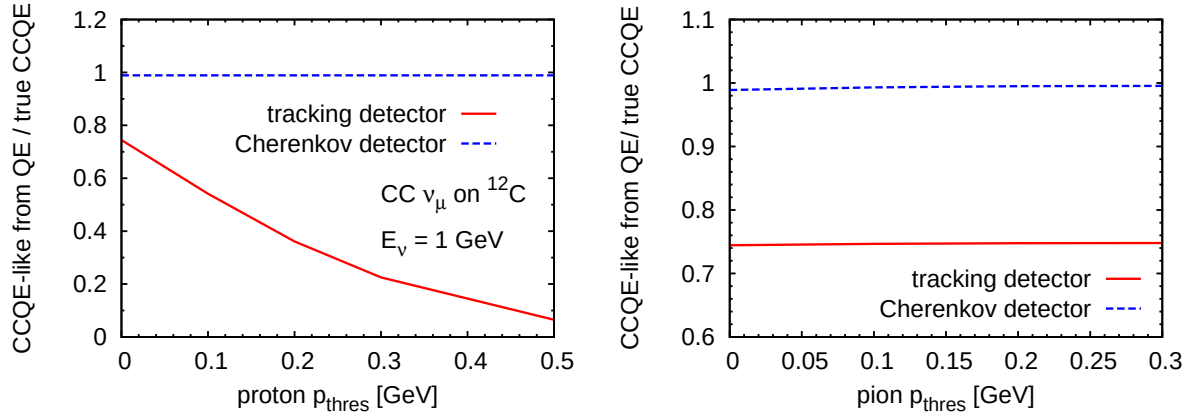

Figure 13.3: Ratio of the QE-induced CCQE-like (i.e., the fraction of the CCQE-like event where the initial interaction was QE: $\nu_\mu n \to \mu^- p$) to the true CCQE cross section as a function of the proton (pion) detection momentum threshold for CC ν_μ on ^{12}C at $E_\nu = 1\,\text{GeV}$. The solid lines are obtained using the tracking detector identification, while the dashed lines are for Cherenkov detectors.

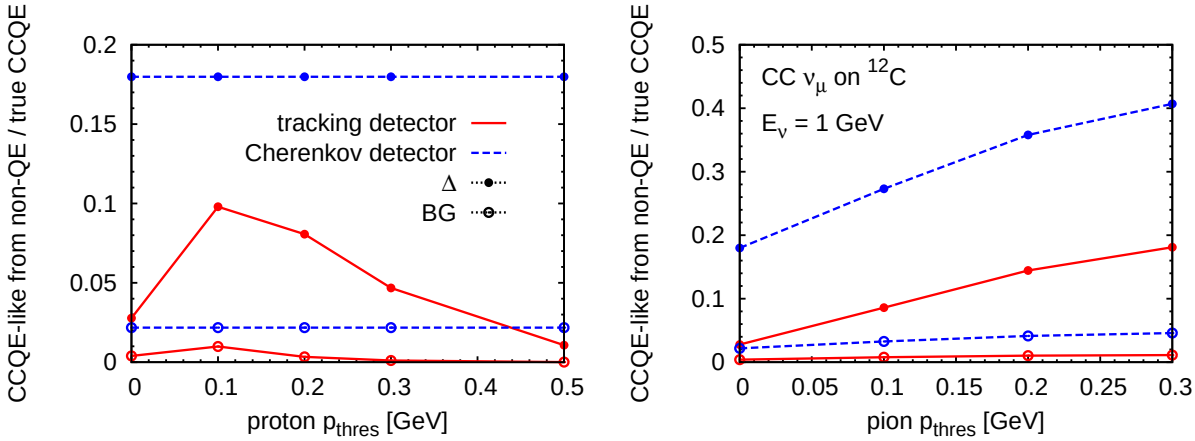

Figure 13.4: Ratio of the *non-QE induced* CCQE-like (i.e., the initial interaction was *not* $\nu_\mu n \to \mu^- p$) to the true CCQE cross section as a function of the proton (pion) detection momentum threshold for CC ν_μ on ^{12}C at $E_\nu = 1\,\text{GeV}$. The solid lines are obtained using the tracking detector identification, while the dashed lines are for Cherenkov detectors. The bullets symbolize the cross sections where the initial reaction is Δ excitation, while the open symbols stand for the initial single-pion background. The contribution from higher resonances is negligible and thus not shown.

the following reason. The non-QE processes lead not only to single-proton knockout but also to multi-nucleon knockout through pion absorption processes and rescattering. If the proton threshold is zero, these processes are not counted because there is more than one proton present. Increasing the threshold increases also the probability that only one proton is above threshold — then, the event is CCQE-like. From a certain momentum on ($\approx 0.1\,\text{GeV}$), more and more protons are below threshold and the ratio decreases again. The dependence on the pion momentum threshold is displayed in the right panel. Here the ratio increases because with increasing threshold for the outgoing pion more and more non-QE events are misidentified as CCQE.

We note that a realistic muon-momentum threshold in the same ballpark has no visible influence on the CCQE-like to true CCQE cross section ratio since the muon momentum is anyway larger in most cases.

13.3.2 CC1π^+ identification

The CC1π^+ reaction is the second largest cross section at the energies of interest in this work (see Fig. 3.2 on page 25), and the major background to the CCQE signal channel as we have seen in the previous section.

As in the case of CCQE, also the detected CC1π^+ events can be masked by FSI. However, as we will show now, the misidentification is minor and independent of the detector type: both of our "toy detectors" define CC1π^+ in the same way. Problematic, however, is the low efficiency caused by strong pion-absorption effects. The left panel of Fig. 13.5 shows that already without any threshold cuts only 60% of the pions leave the nucleus and can be detected.[2] Increasing the pion momentum threshold decreases clearly the CC1π^+ event rate in the detector. In the right panel we plot the different contributions separately and find that the Δ excitation dominates.

13.4 Neutrino energy reconstruction

In LBL experiments, CCQE events are commonly used to determine the ν_μ kinematics. Under the assumption that the nucleon is at rest within the nucleus, the neutrino energy has been reconstructed from QE events at the MiniBooNE experiment [MiniBooNE08b] using

$$E_\nu^{\text{rec}} = \frac{2(M_N - E_B)E_\mu - (E_B^2 - 2M_N E_B + m_\mu^2)}{2\left[(M_N - E_B) - E_\mu + |\mathbf{k}'|\cos\theta_\mu\right]}, \tag{13.2}$$

with a binding energy correction of $E_B = 34\,\text{MeV}$ and the measured muon energy, E_μ and scattering angle, θ_μ. The K2K experiment uses the same expression but with

[2] We have normalized the true CC1π^+ to the "no FSI" curve at $|\mathbf{p}|^\pi_{\text{thres}} = 0$.

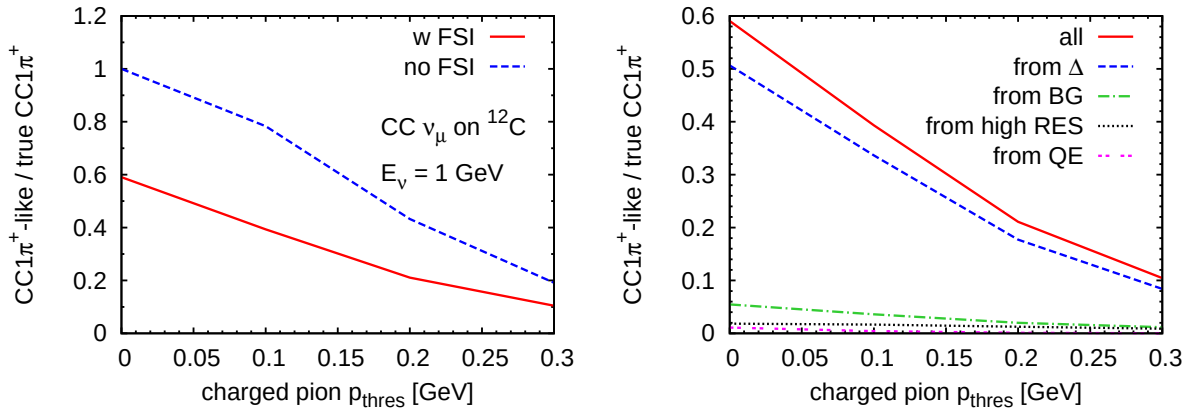

Figure 13.5: Ratio of the CC1π^+-like to the true CC1π^+ cross section as a function of the pion detection momentum threshold for CC ν_μ on ^{12}C at $E_\nu = 1\,\text{GeV}$. Left panel: the solid line is obtained with FSI, the dashed without FSI. Right panel: the different contributions to the full result (corresponds to the solid line in the left panel) are shown as indicated in the plot.

$E_B = 0$ [K2K03].

In Fig. 13.6 we plot the distribution of the reconstructed neutrino energy obtained using the MiniBooNE prescription in Eq. (13.2) for four fixed E_ν^{real} (0.5, 0.7, 1.0 and 1.5 GeV). The dashed lines show the true CCQE events only, the solid lines all CCQE-like events (using the Cherenkov definition, but without any threshold cuts). Both curves show a prominent peak around the real energy which is slightly shifted to higher E_ν^{rec}. This shift is caused by the difference between our potential and the specific choice of E_B.[3] The peak has a width of around 100 MeV (FWHM). This broadening is entirely caused by the Fermi motion of the nucleons — Eq. (13.2) assumes nucleons are rest.

While the distribution of the reconstructed energy for the true CCQE events is symmetric around the peak, this is not the case for the CCQE-like distribution. The reconstruction procedure now includes also non-CCQE events. However, Eq. (13.2) is entirely based on the muon kinematics and, in the case of Δ-induced non-CCQE events, more transferred energy is needed than for true CCQE, thus, the muon energy is smaller: taking Fig. 9.2 (see page 122) as an example, we find about $E_\mu = 0.6\,\text{GeV}$ at the Δ peak versus 0.9 GeV at the QE peak for $E_\nu = 1\,\text{GeV}$ and $\theta = 30°$. This lower muon energy leads then to the second smaller bump at lower reconstructed energies. Thus, the asymmetry is caused by the non-CCQE events identified as CCQE-like.

The reconstructed energy under tracking detector assumptions is plotted in Fig. 13.7. We have seen in the previous section that the tracking detector allows to extract a

[3] See Fig. 15.16 on page 250. The dash-dotted and dotted lines there have been obtained with $E_B = 0$.

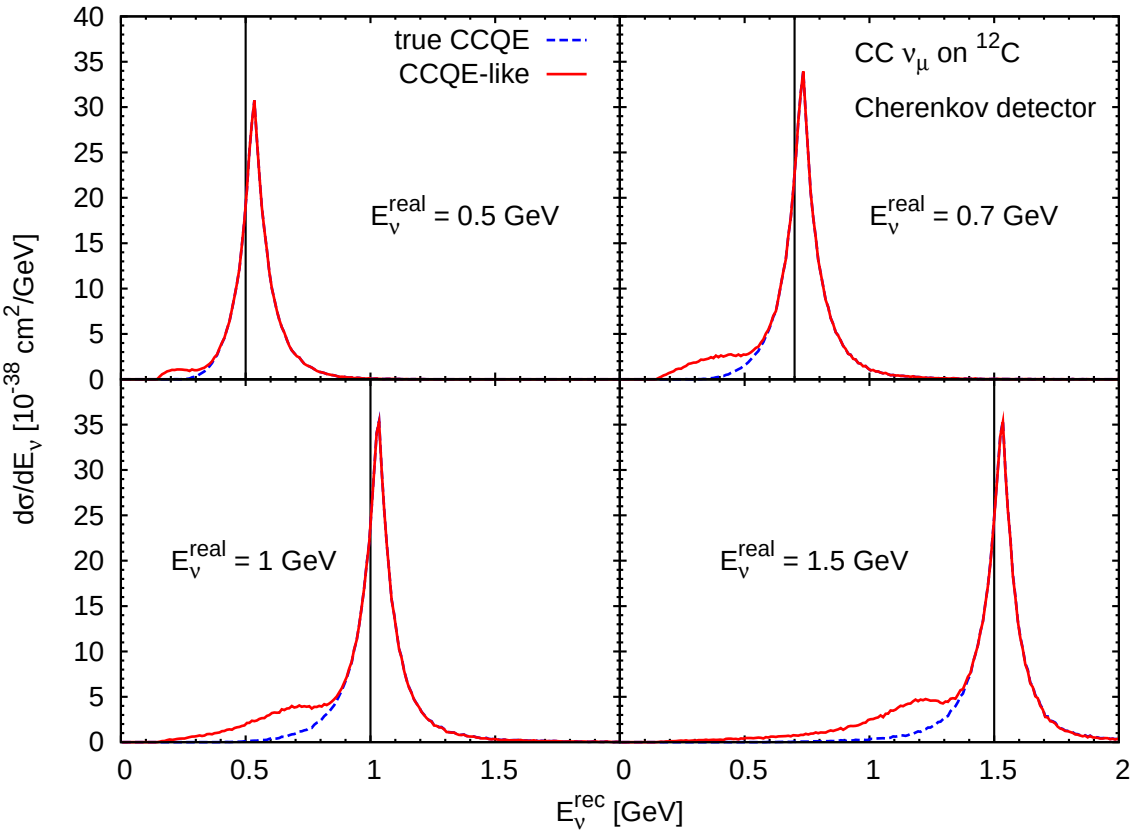

Figure 13.6: Distribution of the reconstructed neutrino energy according to Eq. (13.2) for $E_\nu^{\text{real}} = 0.5, 0.7, 1.0$ and $1.5\,\text{GeV}$. The reconstructed energy denoted by the dashed lines includes only true CCQE events, while the solid lines are obtained by reconstructing the energy with CCQE-like events under Cherenkov assumptions.

much cleaner CCQE-like sample than the Cherenkov detector — almost no fake, i.e., non-CCQE events spoil the CCQE-like sample. Consequently, the reconstructed distribution is again symmetric but at the cost of a lower detection rate.

The asymmetry is very sensitive to detection thresholds, in particular to the momentum threshold for charged pions (see Section 13.2 for the thresholds applied in present experiments). We have seen in the previous section, that increasing this threshold, increases also the CCQE-like cross section (via the non-CCQE events). Thus, a higher threshold leads to a more pronounced second bump as seen in Fig. 13.8.

The previous findings, without any threshold cuts, are summarized in Table 13.1 and in Fig. 13.9. The former lists the expected values for the reconstructed energy and the standard deviation, while the latter shows the relative discrepancy $(E_\nu^{\text{real}} - E_\nu^{\text{rec}})/E_\nu^{\text{real}}$ for 4 different real energies. We note that similar investigations by Blondel *et al.* [BCF04] and Butkevich [But08] result in smaller discrepancies. Both

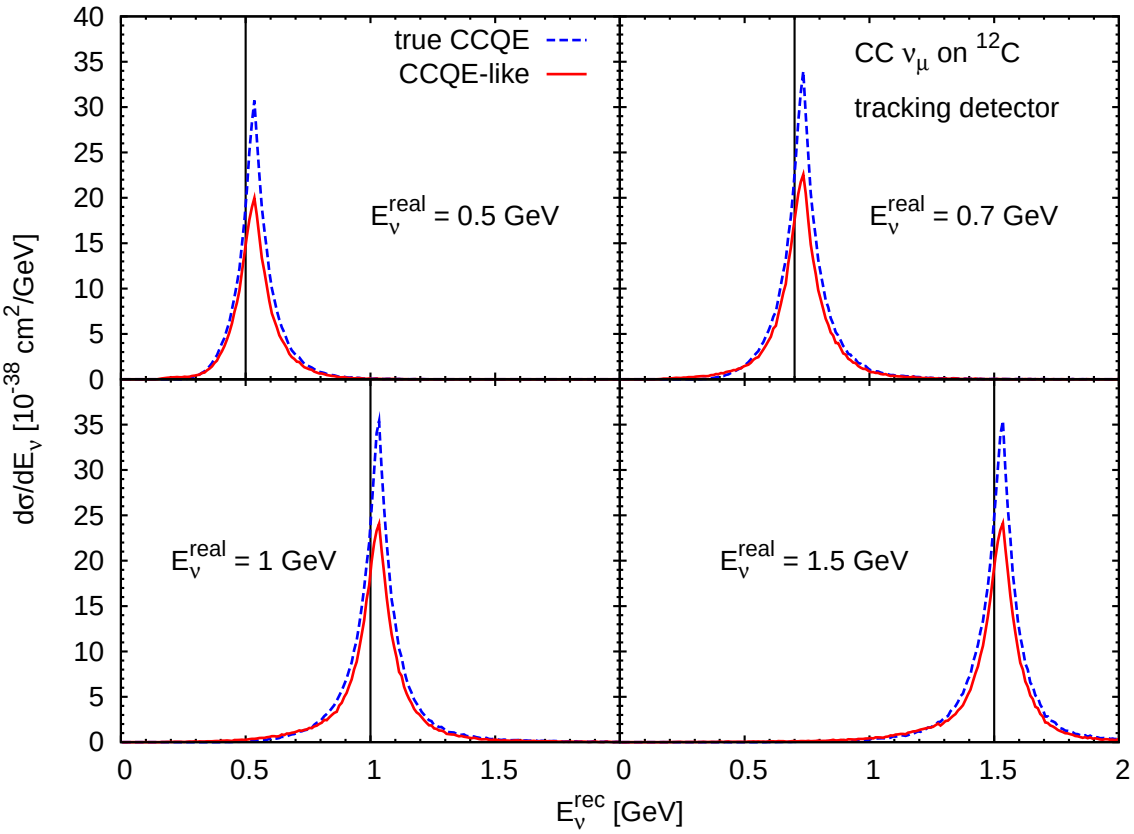

Figure 13.7: Same as Fig. 13.6 but under tracking detector assumptions for the CCQE-like events (solid lines).

works consider only CCQE in the initial state, and do not include, e.g., Δ excitation.

Finally, we show in Fig. 13.10 the reconstructed energy distribution for the MiniBooNE flux (left panel) and the K2K flux (right panel). Compared to the true CCQE we find a enhancement at low reconstructed energies caused by the non-CCQE induced CCQE-like events in a Cherenkov-like detector (dashed vs. solid lines; corresponding to the low-energy bump in Fig. 13.6). In a tracking detector, the event rates are reduced (dashed vs. dash-dotted lines).

Comparing the dashed lines in Fig. 13.10 with the neutrino energy flux (dashed lines in Fig. 13.11), one finds that, in particular for the MiniBooNE case, the spectrum is shifted to higher energies because we weight the events with their corresponding cross sections. Since the cross section is zero below the muon production threshold and still small at a few hundred MeV, this suppresses the lower part of the spectrum. For K2K this is not so important since the spectrum peaks at higher energy.

We close this section with a brief discussion on why the exact knowledge of the neutrino energy is of major importance. The oscillation probability for the transition

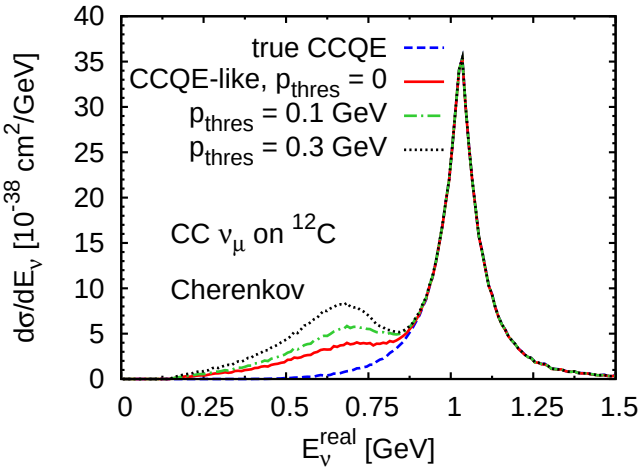

Figure 13.8: Distribution of the reconstructed neutrino energy according to Eq. (13.2) for $E_\nu^{\text{real}} = 1\,\text{GeV}$. Using only true CCQE events for the reconstruction leads to the dashed line. Including CCQE-like events (Cherenkov definition) with various charged pion detection thresholds one obtains the solid line (no pion threshold), the dash-dotted line (100 MeV) and the dotted line (300 MeV).

Table 13.1: Expected value, E, and standard deviation, S, for the distributions shown in Fig. 13.6 and Fig. 13.7.

	E_ν^{real}	$E = \int_0^\infty \mathrm{d}E_\nu^{\text{rec}} \, \frac{E_\nu^{\text{rec}}}{\sigma} \frac{\mathrm{d}\sigma}{\mathrm{d}E_\nu}$	$S = \left(\int_0^\infty \mathrm{d}E_\nu^{\text{rec}} \, \frac{(E_\nu^{\text{rec}} - E)^2}{\sigma} \frac{\mathrm{d}\sigma}{\mathrm{d}E_\nu} \right)^{1/2}$
true CCQE	0.5 GeV	0.55 GeV	0.09 GeV (17%)
	0.7 GeV	0.74 GeV	0.12 GeV (16%)
	1.0 GeV	1.03 GeV	0.15 GeV (15%)
	1.5 GeV	1.52 GeV	0.16 GeV (11%)
CCQE-like	0.5 GeV	0.53 GeV	0.11 GeV (20%)
(Cherenkov)	0.7 GeV	0.70 GeV	0.16 GeV (23%)
	1.0 GeV	0.96 GeV	0.22 GeV (23%)
	1.5 GeV	1.41 GeV	0.27 GeV (19%)
CCQE-like	0.5 GeV	0.54 GeV	0.10 GeV (18%)
(tracking)	0.7 GeV	0.73 GeV	0.13 GeV (18%)
	1.0 GeV	1.02 GeV	0.17 GeV (16%)
	1.5 GeV	1.50 GeV	0.19 GeV (13%)

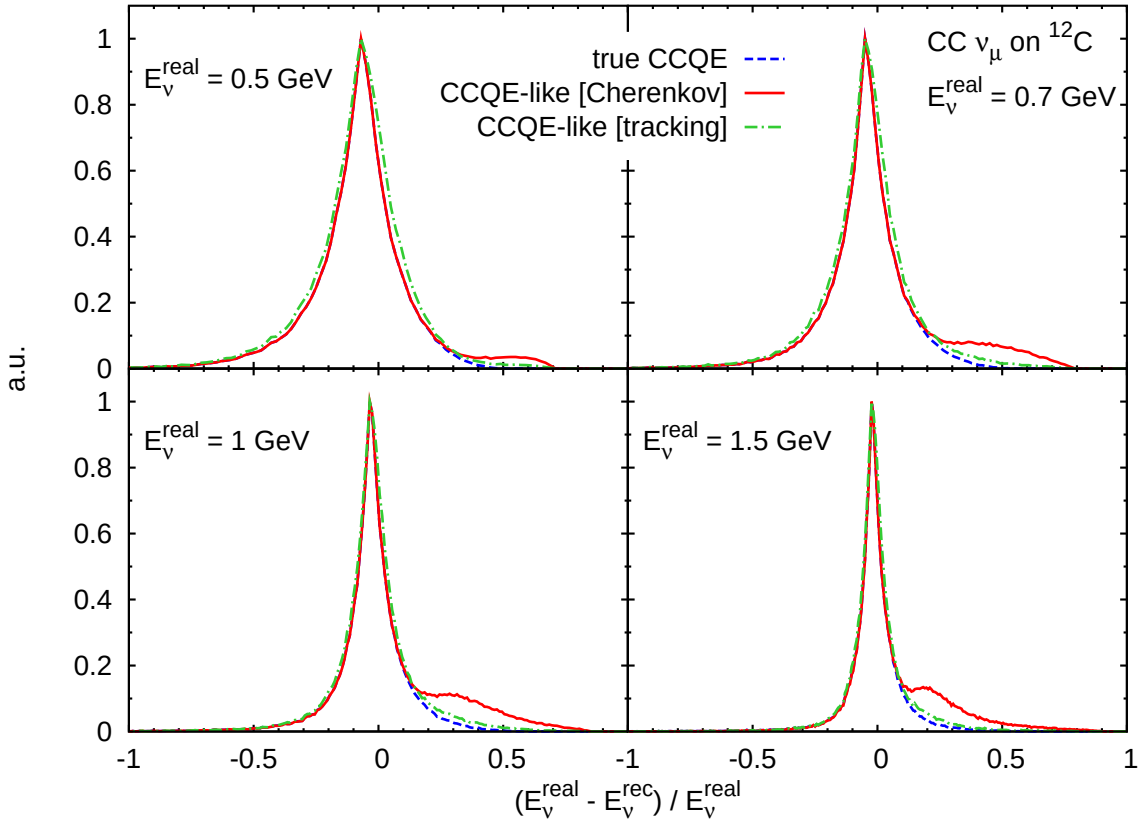

Figure 13.9: Relative discrepancy of the reconstructed neutrino energy obtained with Eq. (13.2) for $E_\nu^{\text{real}} = 0.5$, 0.7, 1.0, and 1.5 GeV. The dashed lines use true CCQE, the solid ones CCQE-like in a Cherenkov detector and the dash-dotted ones CCQE-like events in a tracking detector for the reconstruction.

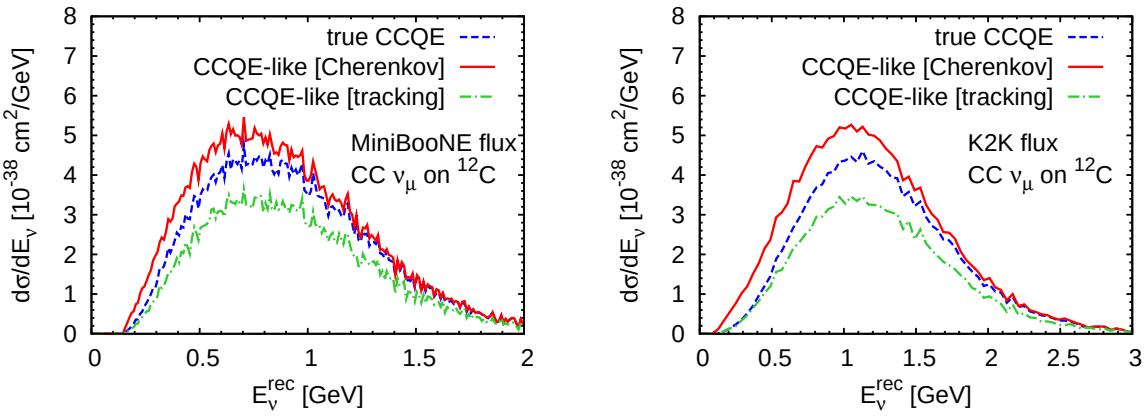

Figure 13.10: Reconstructed energy distribution for the MiniBooNE flux (left panel) and K2K flux (right panel) under different detector assumptions. Eq. (13.2) is used for the reconstruction, but with $E_B = 0$ in the K2K case.

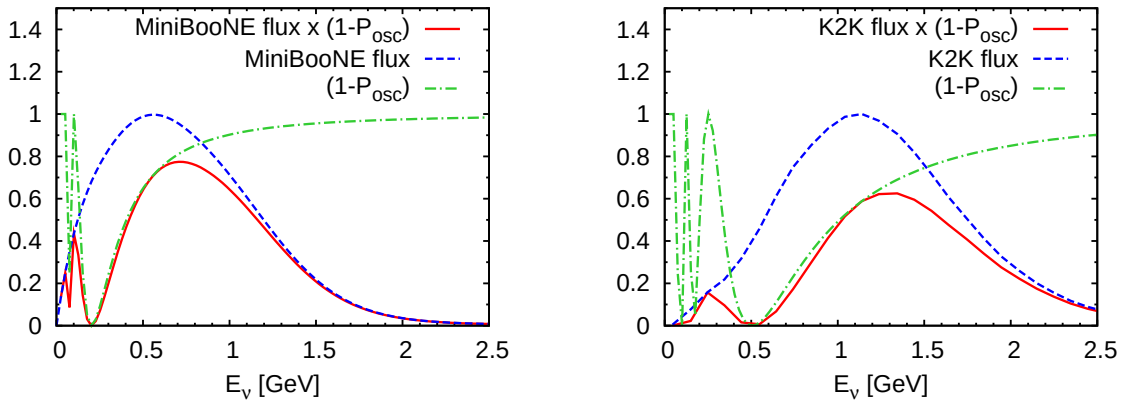

Figure 13.11: Sketch of the influence of neutrino oscillations on the neutrino flux (details are given in the text).

$\nu_\alpha \to \nu_\beta$ is given by (see, e.g., Chapter 13 in [PDG08] or any text book for details)

$$P_{\text{osc}}(\nu_\alpha \to \nu_\beta) = \sin^2 2\theta \sin^2 \left(\frac{\Delta m^2 L}{4E_\nu} \right), \tag{13.3}$$

where θ is the neutrino mixing angle, $\Delta m^2 = m_2^2 - m_1^2$ is the squared mass difference and L the traveled distance. Consequently,

$$P_{\text{no-osc}} = 1 - P_{\text{osc}}. \tag{13.4}$$

The probability depends on the neutrino energy E_ν. Measuring the oscillation parameters θ and Δm^2 requires the knowledge of both, L and E_ν. In LBL experiments, L and E_ν are typically chosen such that detector is placed in the oscillation maximum/minimum. To determine the oscillation probability in disappearance experiments, one has to measure the neutrino flux at that point and compare it to the un-oscillated spectrum at the production point.[4]

A schematic example is given in Fig. 13.11 for $\theta \approx 45^\circ$ and $\Delta m^2 = 2.5 \times 10^{-3}$ eV^2, i.e., the parameters measured in ν_μ disappearance [PDG08]. The left panel shows the MiniBooNE flux with $L = 100$ km, the right one the K2K flux with $L = 250$ km. The un-oscillated spectrum is given by the dashed lines, the survival probability by the dash-dotted lines and its convolution by the solid lines. A good measurement of the neutrino energy is thus necessary to resolve the difference between the un-oscillated and the oscillated flux, in particular the characteristic oscillation dip.

Furthermore, we have seen that the energy reconstruction based on the CCQE-like events tends to shift the energy spectrum to lower energies and causes an enhancement over the true CCQE distribution at low reconstructed energies (dashed vs. solid lines in Fig. 13.10). This effect is important for ν_μ disappearance searches since it fills in the characteristic oscillation dip shown in Fig. 13.11.

[4] Neutrino appearance experiments measure directly the appearance of a different neutrino flavor in the beam (see Chapter 14).

14

NC neutrino-nucleus reactions: implications for MiniBooNE's ν_e appearance searches

14.1 Introduction

The LSND experiment has reported the first evidence for appearance neutrino oscillations in the channel $\bar{\nu}_\mu \rightarrow \bar{\nu}_e$ which implied that at least one neutrino has a mass greater than 0.4 eV [LSND01]. This leads to a large mass squared difference of 1 eV^2 in addition to the much smaller mass squared differences observed in atmospheric and solar neutrino oscillations (10^{-3} and 10^{-5} eV^2). As this cannot be explained in a "standard" three-neutrino oscillation model the LSND result remains a long-standing puzzle. The most common solution to the LSND problem is to introduce one or more sterile neutrinos to explain the large mass squared difference. But also more exotic proposals such as CPT violation, extra dimensions, neutrino decay, quantum decoherence and others have been discussed (see, e.g., Ref. [Sch08b] for a brief review).

The MiniBooNE experiment was built to provide a definitive test of the LSND findings. MiniBooNE searches for $\nu_\mu \rightarrow \nu_e$ appearance with a very similar L/E_ν range as LSND. However, it found no evidence for ν_e appearance in a ν_μ beam in the energy region relevant for the LSND experiment ($E_\nu > 0.475\,\text{GeV}$) [MiniBooNE07b]. The data, so the MiniBooNE collaboration, are consistent with no oscillations within a two-neutrino appearance-only oscillation model which is thus excluded as an explanation of the LSND anomaly. But MiniBooNE observes a sizable excess of events over their

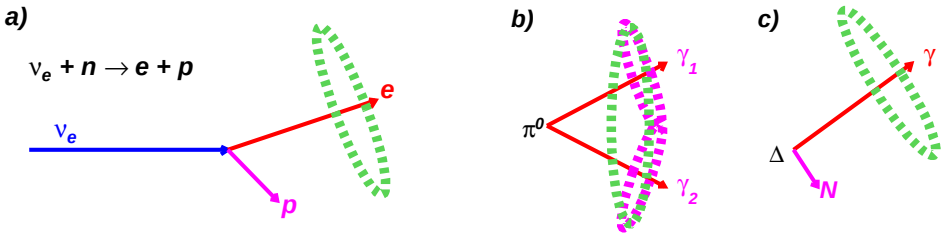

Figure 14.1: (a) indicates the "ν_e appearance signal" event in MiniBooNE while (b) and (c) are possible backgrounds. Taken from Ref. [Dju06].

Monte Carlo prediction below 475 MeV (see Fig. 14.2; see also Ref. [MiniBooNE07b] and the extended discussion in Refs. [MiniBooNE09e, Pol08]). This excess will be in the focus of our discussion in this chapter.[1]

14.2 Search for electron-neutrino appearance

To understand better the excess in the MiniBooNE neutrino signal [MiniBooNE09e, Pol08], let us introduce some more details. The main task in a ν_e appearance experiment is to detect electron neutrinos in a (almost) pure ν_μ beam. The signal event is the ν_e CCQE interaction as indicated in Fig. 14.1 (a). But the signal is dominated by background. Most of the detected ν_e events have their origin not in neutrino oscillations but are already present in the initial neutrino beam, e.g., through muon and kaon decays. As seen from Fig. 14.2 they contribute significantly to the measured ν_e events and dominate the spectrum above 475 MeV. A good understanding of the neutrino beam composition is therefore essential for ν_e appearance searches.

Even more significant at low reconstructed E_ν are misidentified events, mainly because of the fact, that the MiniBooNE detector cannot distinguish between a photon and an electron. Thus, ν_μ induced neutral current π^0 production,[2] where the π^0 decays into two γs, is the major source of background when one of the photons is not seen or both Cherenkov rings overlap. This process is illustrated in Fig. 14.1 (b). Additional background comes from the excitation of a Δ resonance via neutral current interaction followed by its radiative decay, $\Delta \rightarrow \gamma N$, which also leads to a final state with a photon (see Fig. 14.1 (c)). Of particular interest for experiments is to quantify how the photon to π^0 yield changes in the nuclear medium, depending on the

[1] We note that MiniBooNE recently released the first anti-neutrino results [MiniBooNE09d]. No significant excess of events over background in the full energy region has been observed. However, the result is inconclusive with respect to the LSND measurements.

[2] We recall that in NC events only the outgoing hadrons and/or their decay products are seen, but not the outgoing neutrino.

Δ momentum and also the nuclear density. Both, misidentified NCπ^0 and $\Delta \to \gamma N$, dominate the total background below 475 MeV, i.e., the excess region (see Fig. 14.2).

We stress that the background prediction and with that the magnitude of the excess of events is strongly model dependent. For instance, if the NUANCE Monte Carlo event generator predicted a larger π^0 yield, the difference between data and prediction, and with that the excess, would shrink. Models for photon detection efficiency in CH_2 are also crucial. Many sources of systematic errors and analysis updates are discussed in Ref. [Pol08].[3]

Let us emphasize one more problem: the major quantity in this measurement is the neutrino energy (see Fig. 14.2). However, it is not the "true" neutrino energy, but, as outlined in Section 13.4, the reconstructed energy. We have seen that the difference between both is significant in particular towards lower E_ν.

Finally, we note that the MiniBooNE findings have triggered many other explanations leading to photons at low neutrino energies, e.g., muon bremsstrahlung,[4] $\nu N \to \nu\gamma N$ interaction, but also explanations involving "new physics", e.g., introduction of a new gauge boson. Within the GiBUU model, however, we focus on the question, how the background changes when "standard nuclear physics" is applied, or in other words, on whether extraordinary effects (like Lorentz violation) survive after accounting for profane effects (like FSI).

In the following we study the in-medium modifications of the radiative Δ decay; the influence of nuclear effects and final-state interactions on NCπ^0 production is discussed in Section 15.3.

14.3 Estimate of radiative Δ decay in the medium

A small contribution to the ν_e appearance background is caused by the radiative decay of the Δ resonance excited in a NC reaction as discussed above. In the vacuum, a rough estimate for the photon to π^0 ratio through the Δ gives

$$\frac{\sigma^{\gamma}_{\text{tot}}}{\sigma^{\pi^0}_{\text{tot}}}(\Delta^{+/0}) = \frac{0.0056}{(2/3)} = 0.008, \tag{14.1}$$

where 0.0056 is the PDG branching fraction for $\Delta \to N\gamma$ and 2/3 comes from the appropriate Clebsch-Gordon coefficient for $\Delta^{+/0} \to \pi^0 + N$.

The complication arises when the Δ is produced in the nuclear medium, e.g., in ^{12}C as in MiniBooNE. Then the decay pion can either be absorbed or additional Δ

[3] A new experiment called MicroBooNE, a Liquid Argon Time Projection Chamber, has been proposed to address in particular the low energy excess [MicroBooNE]. Due to its design, MicroBooNE is capable of separating electrons and photons and can therefore improve the signal to background ratio significantly.

[4] Proved negligible in Ref. [MiniBooNE07a].

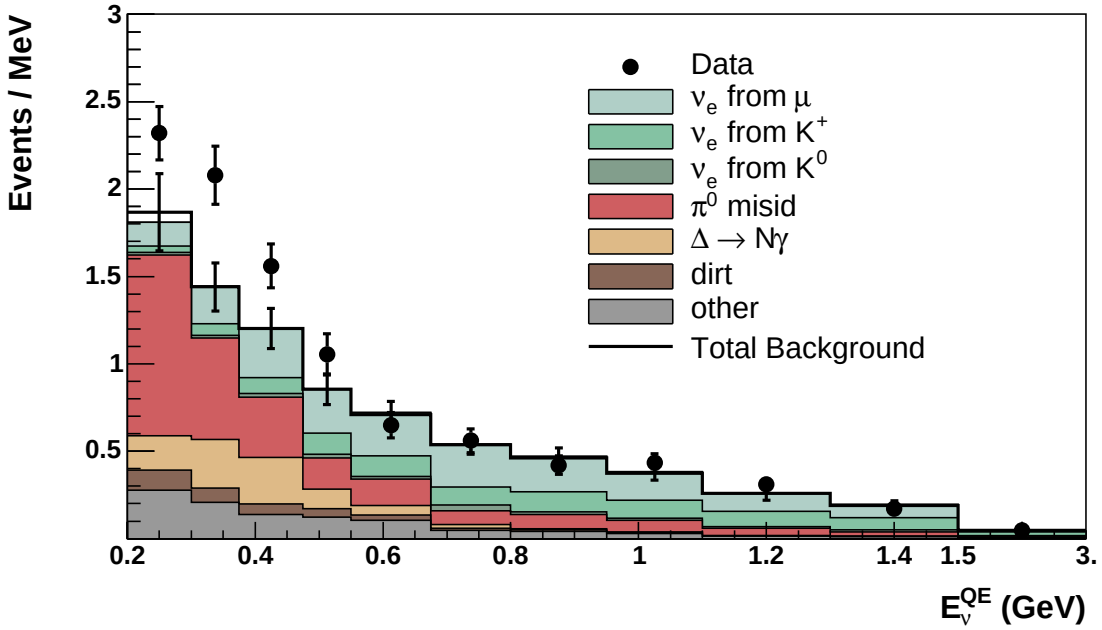

Figure 14.2: Measured ν_e events at MiniBooNE together with their prediction for the various backgrounds versus the reconstructed neutrino energy. Taken from Ref. [MiniBooNE09e].

resonances can be excited through FSI. These additional Δ can also decay into γN. Therefore, the probability of radiative decay to π^0 emission is modified in the nucleus.

The calculation has been performed as follows. First, Δ^0 and Δ^+ resonances are set inside the nucleus with momentum and position chosen randomly within a given range. Then, they are propagated out taking into account all possible decays and collisions. Afterwards, we calculate the total π^0 and the photon cross section as function of the *initial* momentum (radius) of the Δ, with which it has been initialized at the beginning of the simulation. We take into account only those π^0 which actually made it out of the nucleus after the final-state interactions. With that, we obtain in the medium for the above ratio 0.019, which represents an increase of about a factor of 2.4 compared to the free case.

Fig. 14.3 shows how the photon/π^0 rate changes in medium as a function of Δ position, momentum and mass (solid: initial Δ^0, dashed: initial Δ^+). In addition, the vacuum estimate is shown by the long dashed line. In the momentum dependence one observes typical final-state interaction effects: slow Δ's produce slow pions which are more likely to be absorbed in the medium than high-energy ones which might pass through undisturbed. As expected, the medium modification is largest for those Δs which have been put in the middle of the carbon nucleus. However, one might expect, that the solid/dashed lines approach the vacuum value at a radius larger than

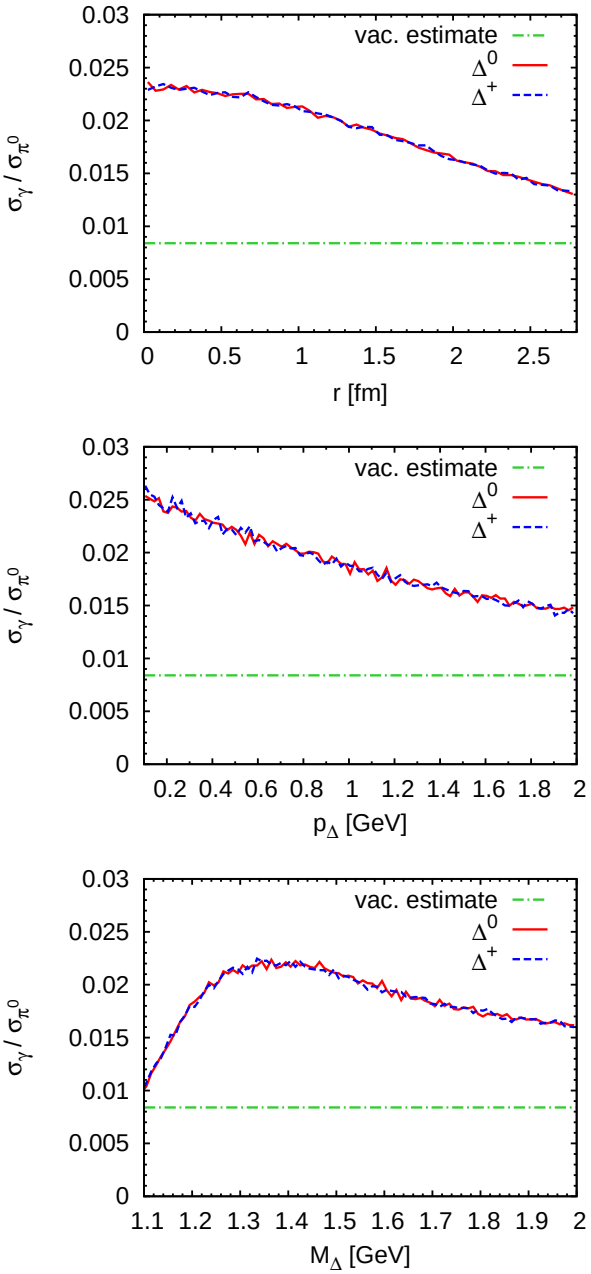

Figure 14.3: Photon/π^0 rate changes in ^{12}C as a function of the initial Δ position (top), momentum (middle) and mass (bottom panel).

the carbon radius. This does not happen here, because, as said before, we initialize the Δs at the beginning with a random momentum, therefore some of them can propagate into the nucleus and thus still undergo FSI which then again modify the spectrum.

To conclude, the production of photons vs. π^0 is enhanced in the nuclear medium due to complex pion final-state interactions reflecting a strong dependence of density, momentum and mass. This means also that one can expect an enhancement of single-γ events over two-γ (from π^0 decay) when scattering off nuclei. As the former are easier misidentified with electrons, one expects an increase of the background compared to the vacuum expectation. However, how this changes the absolute numbers in Fig. 14.2 cannot be easily obtained as there also detection efficiency and acceptance cuts are relevant.

15 Predictions and comparison with data

15.1 CCQE measurements

We outlined in Chapter 13 that CCQE scattering is the oscillation signal channel and also the channel used for the reconstruction of the neutrino energy. Thus, with the new generation of oscillation experiments which now aim at measuring the oscillation parameters with high precision, also the direct measurement of this channel again became important. In addition, CCQE scattering is also interesting on its own since it is the best approach to extract the axial mass of the nucleon and gives insight into the axial form factors.

15.1.1 Q^2 distribution and axial mass

If one assumes a dipole ansatz for the axial form factor, F_A, the axial mass, M_A, is the only free parameter in the QE nucleon hadronic current (see Eq. (4.3)). M_A affects both, the absolute value of the cross section and the shape of the Q^2 distribution (see Fig. 15.1). Thus, there are two ways of extracting M_A (we assume that the vector form factors are known): (1) Q^2-shape only fit which has the advantage that it does not require the absolute flux normalization, (2) fit to the total cross section. On nuclei, the extraction of M_A is much more complicated. Nuclear effects change the shape of the Q^2 distribution, and consequently, the extracted M_A depends on the model used to relate measured rates on nuclei to nucleonic form factors. Furthermore, we saw in the previous section, that FSI influence the CCQE identification. Misidentified events are likely to follow a different Q^2 distribution and also affect the total cross section

as discussed in connection with Fig. 13.1. Finally, we emphasize that Q^2 is not an observable but has to be reconstructed from the final state particles (see Section 13.4).

Before the era of K2K, all available CCQE data were obtained in bubble-chamber experiments at ANL and BNL which suffered from small statistics (≈2500 events in ANL and ≈3700 in BNL (from Table 1 in [NOMAD08])). However, most of the old experiments used Hydrogen or Deuterium targets instead of heavy nuclei which are used in all present experiments.

Assuming a dipole form for the vector form factors and F_A, the world average for M_A at low Q^2 obtained from bubble chamber data is $M_A = 1.026 \pm 0.021\,\text{GeV}$ [BEM02]. A refit by Kuzmin *et al.* [KLN08] using the BBBA-2007 parametrization for the vector form factors gives $M_A = 0.999 \pm 0.011\,\text{GeV}$, the value used throughout this work. At high Q^2 the NOMAD collaboration measured CCQE scattering on ^{12}C using ≈14,000 QE events in the energy interval of 3-100 GeV. They extracted $M_A = 1.05 \pm 0.06\,\text{GeV}$ from a fit of the Q^2 distribution in their high purity sample of 2-track events (reconstructed muon and proton track). These numbers are consistent with the value extracted from charged pion electroproduction off protons slightly above the pion threshold which gives $M_A = 1.014\,\text{GeV}$ (Eq. (10) together with the correction in Eq. (53) in Ref. [BEM02]).

The K2K collaboration reports a measurement of CCQE using the SciFi detector with an oxygen target taking their CCQE sample of ≈12,000 events. K2K finds, applying the NEUT Monte Carlo event generator, an axial mass of $1.20 \pm 0.12\,\text{GeV}$ [K2K06]. They performed a Q^2-shape fit but require $Q^2 > 0.2\,\text{GeV}^2$ to exclude the region most affected by nuclear effects. They further state, that they "have measured the effective M_A for oxygen".

MiniBooNE has collected the largest CCQE-like sample of to date ≈194,000 events. After subtracting the non-CCQE events based on their event generator, they observed a disagreement between data and the NUANCE Monte Carlo prediction at $Q^2 < 0.2\,\text{GeV}^2$. To restore the agreement, they introduced a new degree of freedom in their Fermi-gas model, the Pauli-blocking parameter κ. This parameter scales the lower integration bound over the initial nucleon energy which leads to a reduction of the cross section for $Q^2 < 0.25\,\text{GeV}^2$ and thus to a more pronounced dip in this region. In this way, according to the MiniBooNE collaboration, "it effectively controls the strength of Pauli blocking".[1] Fitting M_A and κ simultaneously to the shape of the Q^2 distribution, they report an effective axial mass of $M_A = 1.23 \pm 0.20\,\text{GeV}$ and $\kappa = 1.019 \pm 0.011$ [MiniBooNE08b].

Later, they observed that the CC1π data sample neither agrees in shape nor normalization with the NUANCE Monte Carlo prediction. In the former analysis, however,

[1] We remind the reader that Pauli blocking also causes a dip in the low Q^2 region (cf. upper left panel in Fig. 9.9 on page 130), but not as pronounced as seen in the MiniBooNE data (see the following discussion).

this NUANCE prediction has been used to subtract the non-CCQE background which is dominated by CC1π. In an updated analysis presented at NUINT09 [Kat09], the Monte Carlo code is tuned to restore the agreement to data in the CC1π sample, and then, this "new" Monte Carlo generator is used to subtract the non-CCQE background. Obviously, this procedure yields a different CCQE sample, in particular a different shape, than the one published in Ref. [MiniBooNE08b]. Performing the M_A-κ shape-only fit with this updated data set, now gives $M_A = 1.35 \pm 0.17\,\text{GeV}$ and $\kappa = 1.007 \pm 0.007$ [Kat09]. Due to the modified background subtraction, the axial mass is even larger than in their previous analysis, but the Pauli-blocking parameter is now consistent with 1.

Before presenting our results, we emphasize that all presented analyses to extract M_A fit the shape of the Q^2 distribution. Therefore, any nuclear effect, which modifies the shape, directly changes the extracted value of M_A. M_A is also sensitive to the CC1π background, which *cannot* be subtracted in a model independent way.[2] Consequently, the extracted M_A depends on the FSI modeling. Thus, the "measured" axial mass is not only effective, but a parameter within a very specific model and therefore not necessarily comparable between different experiments.[3]

The aim of the following is to study whether the MiniBooNE result can be explained when nuclear modifications are taken into account. For that reason, we focus on the Q^2 distribution.

Let us first investigate the effect of the axial mass on the inclusive, i.e., true CCQE Q^2 distribution. We show in Fig. 15.1 both the total and the normalized cross section for ^{12}C averaged over the MiniBooNE flux for various values of M_A. The calculation includes all medium-modifications discussed in Chapter 9 (compare in particular to the left panel of Fig. 9.9 where the influence of different in-medium effects on the Q^2 distribution is shown). We find that the shape becomes steeper with decreasing M_A (right panel) while the absolute cross section increases (left panel). The integrated values are given in Table 15.1, they also scale with M_A.

Let us assume for the moment, that the non-CCQE background subtraction from the MiniBooNE CCQE-like sample is perfect. Then, their true CCQE data are accurately described by a Smith-Moniz global Fermi-gas model with a binding energy of $E_b = 34\,\text{MeV}$, a constant Fermi momentum of $p_F = 220\,\text{MeV}$ and with $M_A = 1.35 \pm 0.17\,\text{GeV}$ and $\kappa = 1.007 \pm 0.007$ [Kat09]. *Thus, we can compare our calculation to the κ modified Smith-Moniz approach instead of comparing to data.*[4] This comparison is shown in Fig. 15.2 where our curves are given for two values of M_A: the

[2] We have just seen how the MiniBooNE parameters have changed with their modified background subtraction procedure.

[3] It has been outlined in Ref. [Zel09] that it is nevertheless very important for neutrino oscillation experiments.

[4] The code for the modified Smith-Moniz model has been provided by L. Alvarez-Ruso.

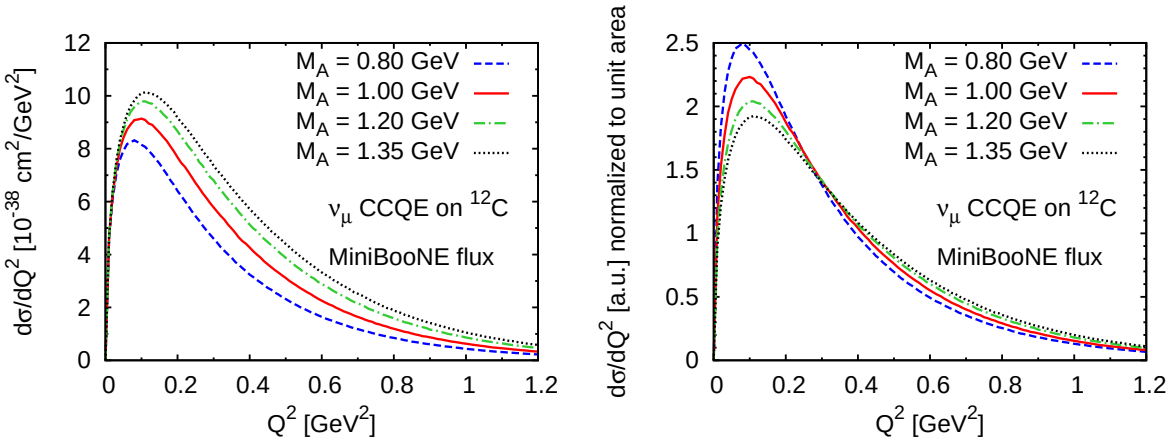

Figure 15.1: Q^2 distributions for inclusive CCQE scattering on ^{12}C averaged over the MiniBooNE flux. All nuclear corrections are considered. Various choices for the axial mass are compared. Left panel: absolute cross section, right panel: cross sections normalized to unit area.

Table 15.1: Integrated cross sections for true CCQE on ^{12}C averaged over the MiniBooNE flux divided by the number of nucleons.

	σ per nucleon $[10^{-38}\,\mathrm{cm}^2]$
GiBUU, $M_A = 0.80\,\mathrm{GeV}$	0.278
GiBUU, $M_A = 1.00\,\mathrm{GeV}$	0.341
GiBUU, $M_A = 1.20\,\mathrm{GeV}$	0.400
GiBUU, $M_A = 1.35\,\mathrm{GeV}$	0.439
GiBUU + RPA, $M_A = 1.00\,\mathrm{GeV}$	0.312
mod. Smith-Moniz	0.413

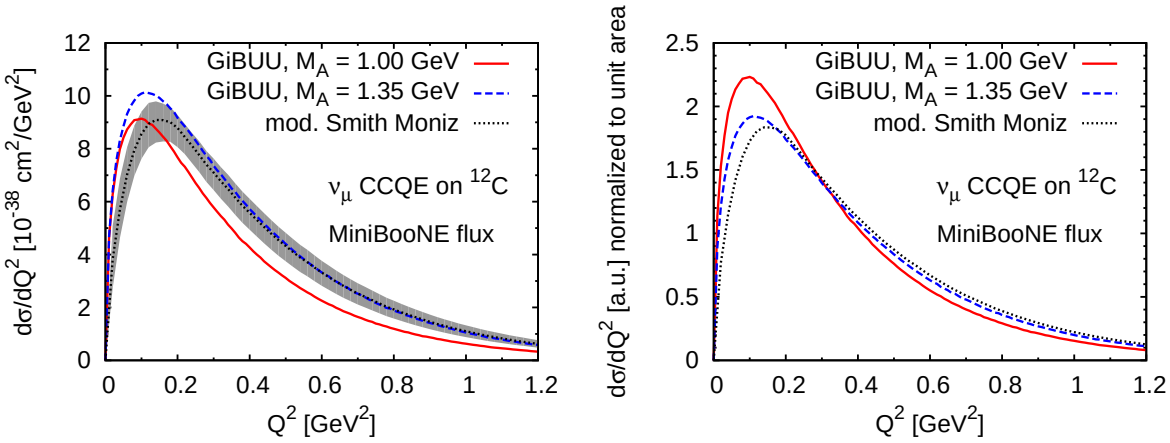

Figure 15.2: Q^2 distributions for inclusive CCQE scattering on ^{12}C averaged over the MiniBooNE flux. The solid and dashed lines denote our calculation for $M_A = 1.00\,\text{GeV}$ and $M_A = 1.35\,\text{GeV}$, respectively, while the dotted lines are obtained with a modified Smith-Moniz Fermi-gas model ($M_A = 1.35\,\text{GeV}$ and $\kappa = 1.007$). Left panel: absolute cross section where the shaded area denotes the experimental error in M_A and κ in the Smith-Moniz calculation, right panel: cross sections normalized to unit area.

default $M_A = 1.00\,\text{GeV}$ and the MiniBooNE best fit of $M_A = 1.35\,\text{GeV}$. The dotted lines are the Smith-Moniz calculation taken here as "data". The shaded area denotes the error: the upper bound is obtained by setting $M_A = 1.52\,\text{GeV}$ and $\kappa = 1.000$, the lower bound by setting $M_A = 1.18\,\text{GeV}$ and $\kappa = 1.014$. We observe that our standard calculation (solid lines) does not agree with the modified Smith-Moniz, but also our calculation with the higher M_A does neither reproduce the dip at low Q^2, present in the MiniBooNE data, nor the integral as can be seen from Table 15.1. The shape, however, is reproduced quite well with a higher M_A.

The next question to be asked — still under the assumption that MiniBooNE's non-CCQE background subtraction is perfect — is whether the shape can also be reproduced without changing M_A. To this aim, we account for medium polarization effects. Polarization effects due to the strong interaction among nucleons modify the QE hadronic tensor. Already in 1992, Singh and Oset have studied the influence of the nuclear medium on the axial form factor in CCQE reactions [SO92], and have found quite large effects of the medium polarization at low Q^2. They have taken into account strong renormalization effects in the spin-isospin channel. Recently, the effects have been calculated more accurately by Nieves *et al.* [NAV04]. The following results are obtained by including the RPA correlations taken from this work. For further details, we refer the reader to Ref. [ARBLM09].

In Fig. 15.3, the RPA result is compared to our "default" result (solid lines) and

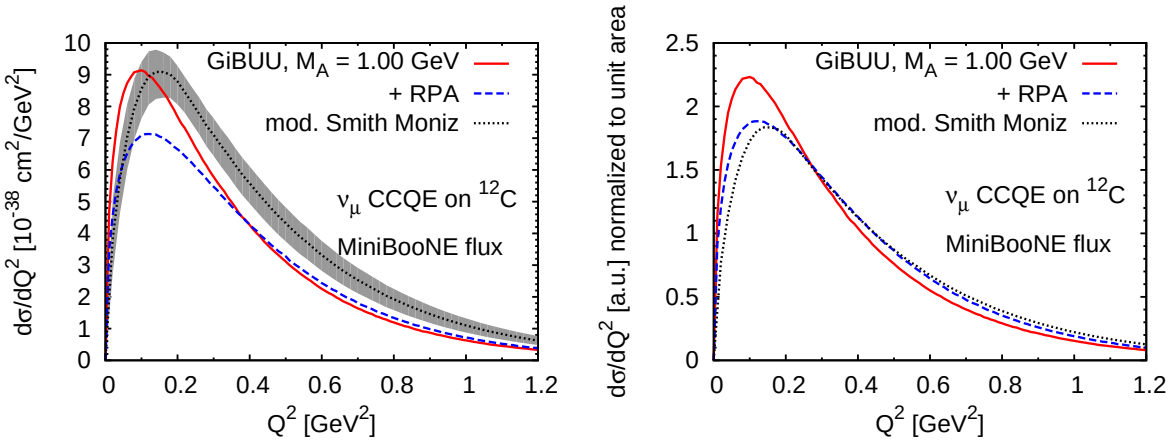

Figure 15.3: Q^2 distributions for inclusive CCQE scattering on ^{12}C averaged over the MiniBooNE flux. The solid lines denote our standard calculation, the dashed ones include in addition RPA correlations. The dotted lines are obtained with a modified Smith-Moniz Fermi-gas model ($M_A = 1.35\,\text{GeV}$ and $\kappa = 1.007$). Left panel: absolute cross section where the shaded area denotes the experimental error in the Smith-Moniz calculation, right panel: cross sections normalized to unit area.

the modified Fermi-gas model (dotted lines), the integrated values are given in Table 15.1. Focussing on the left panel, we find that the RPA correlations lower the cross section at small Q^2 (dash-dotted lines). Turning to the normalized curves presented in the right panel, we see good agreement in the shape for the Smith-Moniz and the RPA calculation down to $Q^2 = 0.15\,\text{GeV}^2$. The agreement is worse for our standard scenario.

We conclude from this exercise that the shape of the "experimental" Q^2 distribution is described well when medium polarizations are taken into account. The absolute cross section, however, is clearly underestimated and not at all reproduced with the RPA calculation.

Up to this point, we assumed not only that the non-CCQE background subtraction is perfect in MiniBooNE but also the reconstruction of Q^2. Both questions will be addressed now.

The flux averaged CCQE-like Q^2 distribution is shown in Fig. 15.4 assuming the Cherenkov identification. No charged pion detection threshold is applied in the left panel, while we choose it to be 100 MeV in the right panel. We show the CCQE-like Q^2 distribution (solid lines) separated into CCQE-induced CCQE-like (dashed lines) and fake CCQE (dash-dotted lines) compared to the modified Smith-Moniz model. The detection threshold directly changes the non-QE background (compare dash-dotted lines in both panels). Even though it increases in this way the CCQE-like cross section, our full result (solid line) still underestimates the "background-corrected

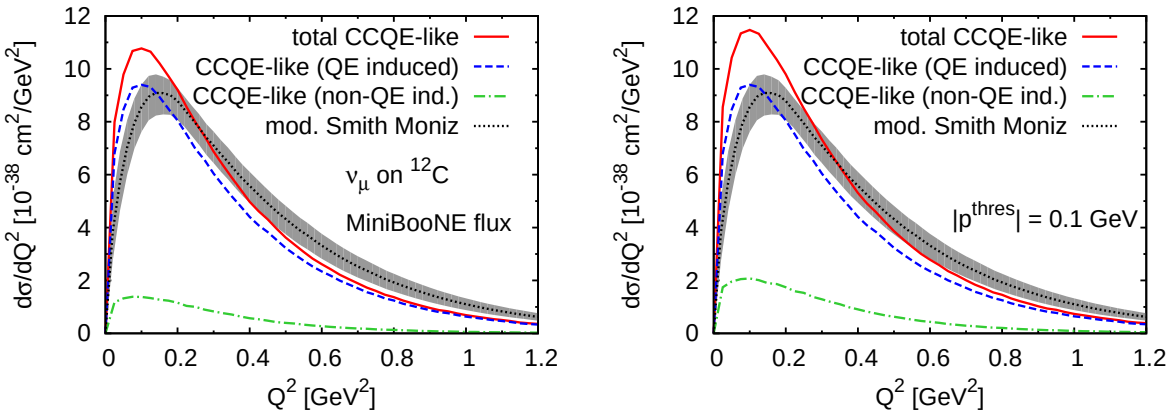

Figure 15.4: Flux averaged $d\sigma/dQ^2$ distribution of CCQE-like events (solid line) at MiniBooNE conditions without (left panel) and with (right panel) charged pion momentum threshold. In addition, we show the composition of the CCQE-like sample: the QE induced cross section is denoted by the dashed lines, the non-QE induced on by the dash-dotted lines. The dotted lines are obtained with a modified Smith-Moniz Fermi-gas model ($M_A = 1.35\,\text{GeV}$ and $\kappa = 1.007$) where the shaded area denotes the experimental error.

data" (dotted lines) at higher Q^2. Interestingly, we find the impact of the background, i.e., the non-QE induced cross section, to be most relevant at low Q^2 which is exactly the region where the MiniBooNE collaboration founds a large discrepancy between the data and their Monte Carlo prediction.

We have already stated before that Q^2 is not an observable — it has to be reconstructed from the measured muon properties. Using Eq. (13.2), we obtain the reconstructed Q^2 via

$$Q^2 = -m_\mu^2 + 2E_\nu(E_\mu - |\mathbf{k}'|\cos\theta_\mu). \tag{15.1}$$

The neutrino energy itself is reconstructed according to Eq. (13.2) (page 217). Fig. 15.5 shows the CCQE-like Q^2 distribution (solid line) separated into CCQE-induced CCQE-like (dashed line) and fake CCQE (dash-dotted line) together with the reconstructed cross section. If the background subtraction is perfect, i.e., when the true CCQE sample is isolated and only this sample is used to reconstruct Q^2, then the reconstructed spectrum almost reproduces the real spectrum (dashed and double-dashed line almost coincide). If background events, namely non-QE induced events, are also taken into account for the reconstruction, then, for the extreme case that no background at all is subtracted, we find an increase at lower Q^2 but then it falls off faster (solid vs. dotted line). The difference is caused by the different muon kinematics of the "fake" events. To conclude, we find that the reconstruction with the simplified formulas above turns out to be almost perfect when only true CCQE events are taken

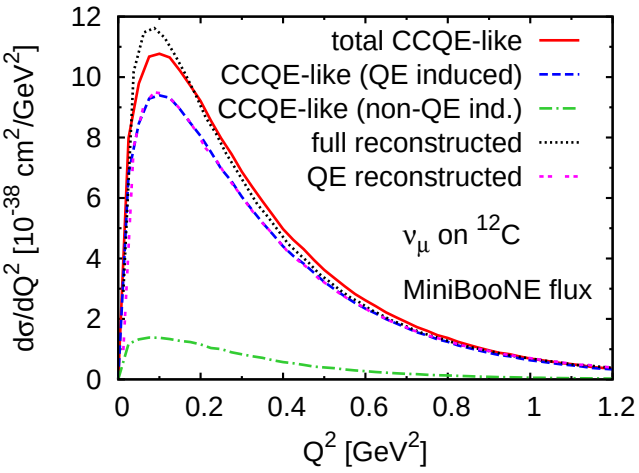

Figure 15.5: Flux averaged $d\sigma/dQ^2$ distribution of CCQE-like events (solid line) at MiniBooNE conditions. The dashed line shows the CCQE-like events induced by CCQE, the dash-dotted line the non-QE induced CCQE-like contribution. In addition, the reconstructed spectra are shown (dotted and double-dashed line).

into account but not if the whole CCQE-like sample is used to reconstruct Q^2.

15.1.2 Absolute CCQE cross section

Fixing the flux normalization with HARP's pion-production data, the MiniBooNE collaboration presented their first, preliminary absolutely normalized total, differential and double differential cross sections for CCQE very recently and finds an excess of about 35% compared to the total cross sections measured by NOMAD, ANL and BNL [Kat09].[5] Fig. 15.6 summarizes their findings. We strongly emphasize that MiniBooNE's absolute cross sections depend directly on the background subtraction which again is based on their Monte Carlo prediction (cf., pages 36 and 37 in Ref. [Kat09]). Furthermore, to obtain a flux-unfolded total cross section, i.e., σ as a function of E_ν, specific model assumptions for the energy reconstruction have to be made (see Section 13.4 for details).

As all of this introduces a model dependence in the data, a fully consistent comparison is not possible. Nonetheless, we show in the left panel of Fig. 15.7 our prediction for the true CCQE and the CCQE-like cross section together with the MiniBooNE CCQE data. As the MiniBooNE collaboration, in a way we have explained above, corrects for the non-CCQE events, one has to compare the solid line to the data. The

[5] It is interesting to note, that the modified Fermi-gas model also describes the total cross section up to 10% even though the parameters were fixed fully independent in a shape-only fit.

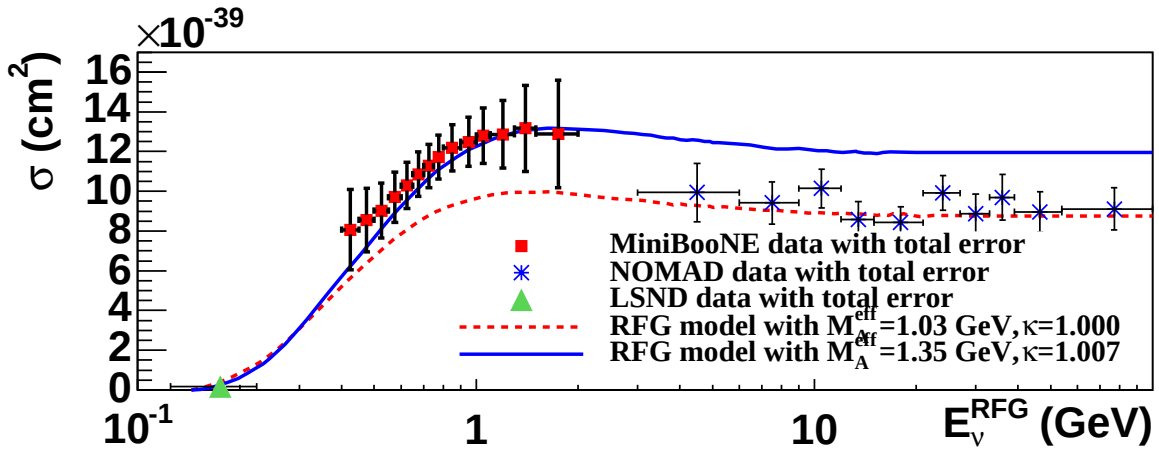

Figure 15.6: Flux unfolded CCQE cross section (*rescaled to the neutron*) as measured at LSND, MiniBooNE and NOMAD compared to a relativistic Fermi gas prediction for two values of M_A. Figure taken from Ref. [Kat09].

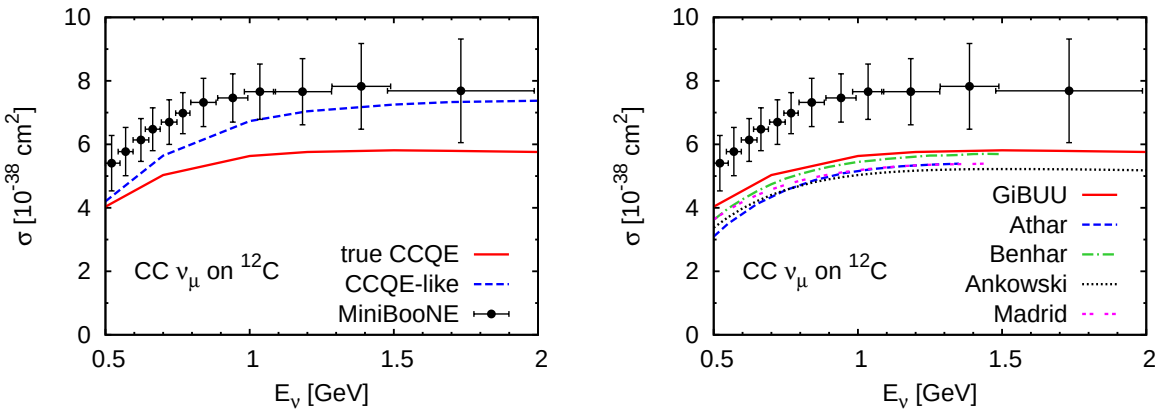

Figure 15.7: Left: true CCQE (solid line) and CCQE-like (dashed line) cross section for ν_μ scattering off ^{12}C together with the MiniBooNE data [Kat09] . Right: Besides our result for the true CCQE cross section and the MiniBooNE data we show calculations from Athar *et al.*, Benhar *et al.*, Ankowski and the Madrid group (for details on these models, we refer to Section 9.5). The numbers are taken from Refs. [ACS09, Sob09]. Compare also to Fig. 15.6.

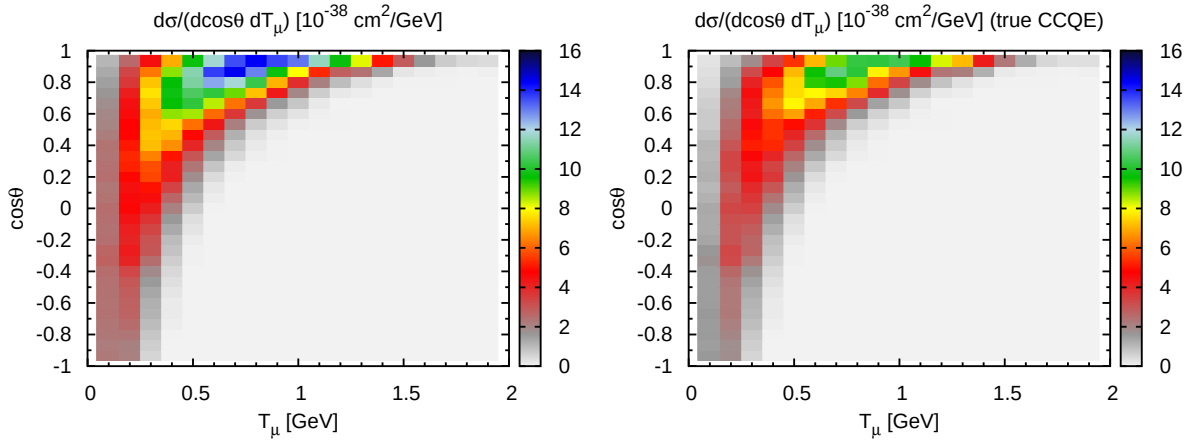

Figure 15.8: Double differential cross section on ^{12}C averaged over the MiniBooNE flux as a function of the muon kinetic energy and the muon scattering angle. The left panel shows the full inclusive cross section while the right one shows only the CCQE contribution (true CCQE).

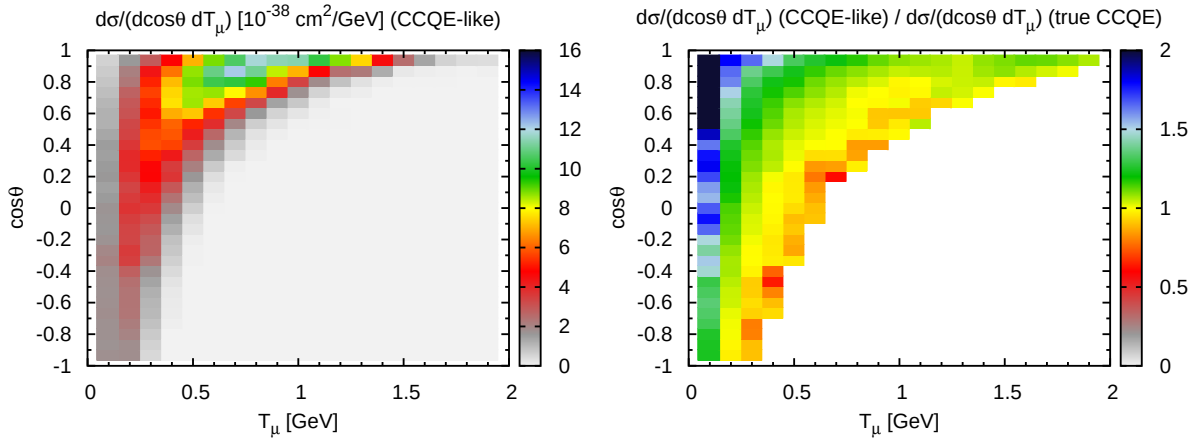

Figure 15.9: Double differential cross section on ^{12}C averaged over the MiniBooNE flux as a function of the muon kinetic energy and the muon scattering angle. The left panel shows the CCQE-like cross section, the right panel the ratio of the CCQE-like to the true CCQE cross section.

right panel shows our true CCQE result together with the prediction of various other models (for details on these models, we refer to Section 9.5). It is clear from this comparison that such a high cross section as measured by MiniBooNE seems hard to accommodate in our approach (or any of the available models) without increasing M_A. On the other hand, M_A should be around 1 GeV at least at low Q^2 according to pion-production data.

In the following we rather give our predictions and do not compare to the background corrected MiniBooNE data. Our result for $\mathrm{d}\sigma/\mathrm{d}Q^2$ has already been given in the left panel of Fig. 15.4.

In Fig. 15.8, we show our result for the double differential cross section at MiniBooNE in muon observables, all calculated with $M_A = 1.00$ GeV. The left plot shows the full inclusive double differential cross section averaged over the MiniBooNE flux. Unlike for monochromatic beams, QE and Δ peaks are not distinguishable any more (compare, e.g., to Fig. 9.1) but strongly overlap. This fact makes a model-independent cut on muon variables to subtract the non-CCQE background impossible. The right panel shows only the CCQE contribution to the full inclusive cross section (true CCQE).

The CCQE-like cross section is presented in the left panel of Fig. 15.9 — to better understand in what kinematic region the CCQE-like non-CCQE induced events ("fake" CCQE events) contribute and to appreciate their importance, we show the ratio CCQE-like/true CCQE in the right panel.

15.2 CC1π^+ measurements

We have shown in Chapter 13 that CC1π^+ is the major background to the CCQE signal channel in ν_μ disappearance experiments, its understanding is therefore crucial in the oscillation analyses. This direct connection has renewed the interest in pion cross section measurements in the last years [K2K08, MiniBooNE09a]. Until very recently, the ratio CC1π^+ to CCQE has only been measured to about 30% precision [MiniBooNE09a]. However, next generation oscillation experiments such as T2K require the pion cross section to be known to 5% accuracy [SciBooNE06].

On nuclei, pions can be produced either coherently, leaving the nucleus intact or, as described in our approach, incoherently. The former one has attracted considerable attention in the last years, both theoretically [SSAA06a, ARGHVV07, AHNV09, BS09, PS09] and experimentally [K2K05a, SciBooNE08, MiniBooNE08a]. While there is evidence for NC coherent pion production, no evidence for CC coherent pion production could be found. However, all these experimental analyses suffer from the fact that the coherent fraction is not accessible directly but has to be extracted from data assuming specific models for incoherent pion production. Furthermore, the theoretical models

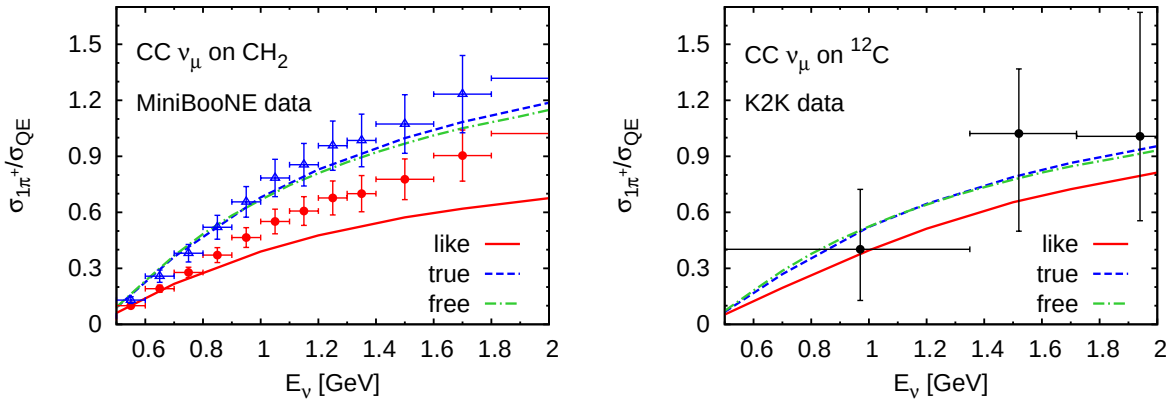

Figure 15.10: Single-π^+/QE cross section ratio for CC interactions vs. neutrino energy on mineral oil and on ^{12}C, respectively. The solid lines denote the CC1π^+-like/CCQE-like result (Cherenkov detector in the MiniBooNE case, tracking detector in the K2K case), the dashed lines stand for the true CC1π^+/true CCQE result, and the dash-dotted lines give the vacuum expectation, i.e., the sum of the nucleon cross sections (with two additional protons in the MiniBooNE case). The left panel shows recent data from MiniBooNE [MiniBooNE09a] (triangles: corrected for FSI, bullets: uncorrected for FSI); the right one K2K data [K2K08].

for coherent scattering used in the experimental analyses overpredict the measured rates. All mentioned calculations rely on the so-called local approximation for the pion production amplitude which allows one to factorize out the nuclear form factor. It has been shown by S. Winkelmann [Win08, LMW09], that the use of the local approximation leads to cross sections up to 100% higher than those obtained without this assumption.

In the following, we present our findings for CC incoherent pion production.

15.2.1 Single-π^+/QE ratio

In Fig. 15.10, we give our results for the single-π^+/QE ratio for CC interactions on mineral oil, CH_2, and on ^{12}C. We present different results for the scenarios discussed in Section 13.3: the solid lines denote the CC1π^+-like/CCQE-like result, the dashed lines stand for the true CC1π^+/true CCQE result, and the dash-dotted lines give the vacuum expectation. Note that we have applied the Cherenkov detection in the left panel and the tracking detector identifications in the right panel (cf., Section 13.2).

We emphasize that nuclear corrections cancel out in the ratio, as long as FSI are not considered ("true" vs. "free"). In general, the complexity of FSI prevent such cancellations as one can infer from the "like" results which both do not coincide with

the "true" and "free" ones.

We further compare to very recent MiniBooNE data [MiniBooNE09a] (Fig. 15.10 left) and to K2K data [K2K08] (Fig. 15.10 right). Let us first focus on the data by MiniBooNE shown by the triangles (upper data set). Those and the K2K data are corrected for FSI using specific Monte Carlo generators, i.e., they give the cross sections for bound nucleons "before FSI". This procedure introduces a model dependence in the data and prevents a conclusive comparison. Ignoring this inconsistency, our calculation denoted by "true" should be the one to compare with. In the MiniBooNE case, the agreement is perfect for energies up to 1.5 GeV, and still within their error bars for higher E_ν (cf. left panel of Fig. 15.10). We also reach a good agreement with the K2K data (cf. right panel of Fig. 15.10).

Let us now focus on the MiniBooNE data denoted with bullets (Fig. 15.10 left, lower data set). This, according to the MiniBooNE collaboration, is their result for the ratio of CC1π^+-like to CCQE-like using the very same notation as we do. These data are not corrected for FSI within a specific Monte Carlo event generator, so this observable is less model dependent (see Section 15.4 for a detailed discussion on the data extraction).

We find that our calculation clearly underestimates these data. The underestimate of the pion/quasielastic ratio in particular at higher energies could be due to either an underestimate of the pion production cross section (eventually already on the nucleon level), or an overestimate of the QE cross section.

It is interesting to note that while the agreement in the "like" distributions is not sufficient, the agreement with their corrected distribution is perfect. That indicates a significant difference between the pion absorption models. Indeed, a direct comparison shows that the FSI effects in our model are about 30% larger than the ones NUANCE predicts [Zel].

We outlined in Part II, that the ANL and BNL results differ with the BNL result approximately 30% higher. So far the ANL data have been used as a reference; and also MiniBooNE states, that their FSI-corrected result is consistent with the ANL result. Taking the BNL data as input, i.e., using a dipole form [Eq. (5.18)] instead of a modified dipole [Eq. (5.19)] for the axial form factor of the Δ (see page 50 for details), leads to a slight enhancement of the ratio but we still underestimate the data above 1 GeV neutrino energy (left panel of Fig. 15.11). Note that the enhancement is much more moderate than in the nucleon case (compare to the right panel of Fig. 5.7 shown on page 52). This is due to the fact, that both, numerator and denominator, i.e., also the CCQE-like cross section, are increased when the dipole form factor is used (see right panel of Fig. 15.11) and, as a consequence, the larger CCQE-like cross section partly compensates the enhancement in the pion cross section. From this comparison we conclude that an increase of the total pion production cross section on the nucleon compatible with the BNL data seems to be insufficient to describe this ratio at all

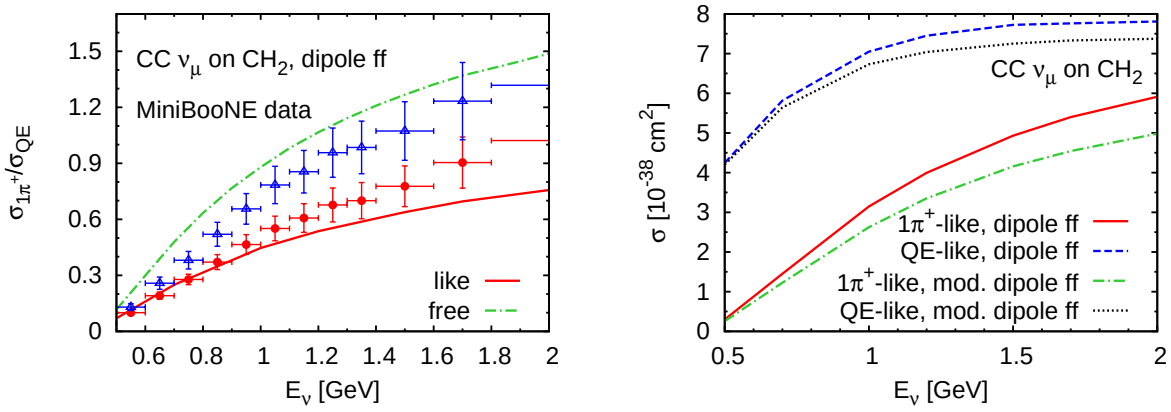

Figure 15.11: Left panel: same as Fig. 15.10 left but with a dipole form for the axial form factor of the Δ (see text). Right panel: single-π^+-like and CCQE-like cross sections obtained using a dipole or a modified dipole form for the Δ axial form factor.

energies.

We note that a similar result, namely an underestimate of the ratio, has been recently obtained by Athar *et al.* [ACS09].

15.2.2 Absolute CCπ^+ cross section

A first measurement of an absolute CC1π^+ cross section, uncorrected for FSI, has been presented at NUINT09 [Wil09]. Like the absolute CCQE measurement discussed above, it is based on the neutrino flux prediction which uses the HARP data as input [MiniBooNE09c]. We plot the MiniBooNE CCπ^+ data together with our result in Fig. 15.12. The solid line corresponds to our full model with our standard modified dipole axial form factor for the Δ — again, we clearly underestimate the data. FSI are "switched off" in the calculation leading to the dashed line: even without FSI, our calculation lies below the data for energies larger than 1 GeV![6] For comparison, we also show the full result with a dipole axial form factor for the Δ, but this curve clearly underestimates the data as well.

[6] Remember the CCQE data: also there, our model, and the models of everyone else, predict cross sections about 35% lower than the MiniBooNE data.

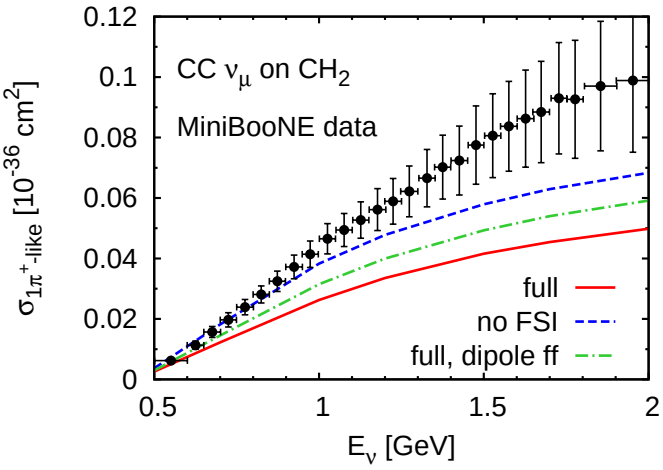

Figure 15.12: CC1π^+-like cross section on CH_2 as a function of the neutrino energy. The solid line includes FSI while the dashed line has been obtained without FSI. For comparison, we also show the full result with a dipole axial form factor for the Δ. The data are taken from Ref. [Wil09].

15.3 NCπ^0 measurements

We have outlined in Chapter 14 that a proper understanding of neutrino-induced pion production, especially NCπ^0, is essential in ν_e appearance experiments. Next generation experiments such as T2K require the NCπ^0 cross section to be known to 10% accuracy for the resulting error on the oscillation parameters to be comparable to that from statistical uncertainties [SciBooNE06]. This has triggered a lot of experimental activity towards direct NCπ^0 cross section measurements in the last years to be used as direct input for the oscillation analysis [K2K05b, MiniBooNE08a, Kur09, And09a].

As all of the present oscillations experiments use nuclear targets, it is mandatory for any calculation to consider FSI, in particular pion rescattering, with and without charge exchange, and absorption in the nuclear medium. In the left panel of Fig. 15.13, we show our results for NC single-π^0 production on CH_2 as a function of the pion momentum. We have averaged over the MiniBooNE energy flux which peaks at about 0.7 GeV neutrino energy [MiniBooNE09c] (see also Fig. 12.1). Comparing the dashed with the solid line (results without FSI and spectral function vs. full calculation), one finds also for the energy averaged spectra shown here a considerably change. The shape is — as we have seen — caused by the energy dependence of the pion absorption and rescattering cross sections. The vast majority of the pions comes from initial Δ excitation (dash-dotted line).

The right panel of Fig. 15.13 shows the results for NC single-π^0 production off ^{16}O averaged over the K2K energy flux which peaks at about 1.2 GeV neutrino energy

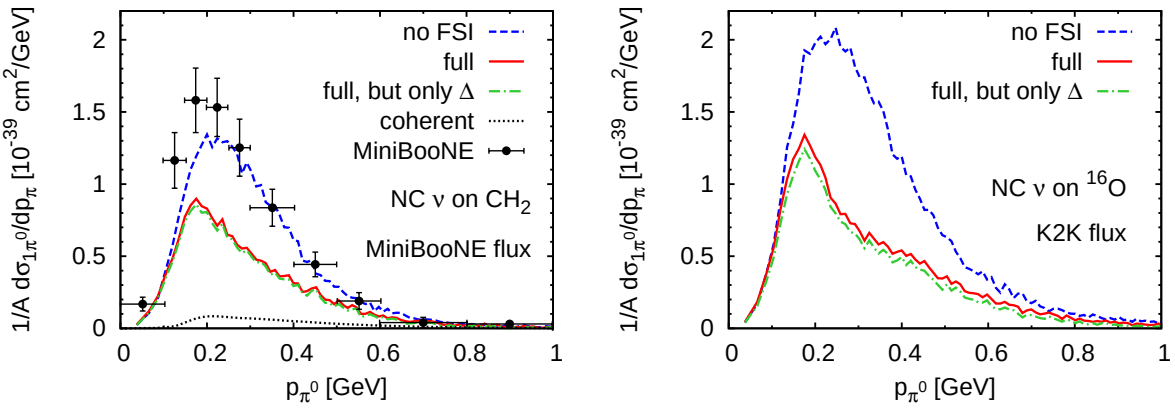

Figure 15.13: Left panel: NC induced single-π^0 production on CH_2 as a function of the pion momentum averaged over the MiniBooNE flux. Right panel: same on ^{16}O averaged over the K2K flux. The curves are scaled with the number of nucleons. The dashed lines show our calculation without FSI or spectral functions, both included in the full calculation denoted by the solid lines. The dash-dotted lines indicate the contribution from the Δ resonance to the full calculation. The MiniBooNE data are taken from Ref. [And09a]. In the left panel we show also the coherent contribution taken from [ARGVV07, AR].

[K2K05b] (see also Fig. 12.1). Compared to the left panel, the spectrum is broader and extends to larger p_π due to the higher neutrino energy. Also at these energies, the pion production is dominated by the Δ resonance. Both cross sections are scaled with the number of nucleons — the cross section for K2K is larger because of the higher neutrino energy.

NC single-π^0 spectra have been measured by the K2K collaboration [K2K05b]. Based on their Monte Carlo generator, the data are not only corrected for efficiency, but some background has already been subtracted, i.e., the data include a model dependence. Since K2K has not yet provided cross sections but only count rates, we cannot yet compare to these measurements directly.

MiniBooNE, however, has presented first results for acceptance corrected absolute cross sections [And09a]. The absolute normalization of the flux is fixed by the HARP measurement. For their NC1π^0 sample, MiniBooNE counts all events in which only one π^0 and no other mesons leave the target nucleus and they report cross sections uncorrected for FSI (see Section 15.4 for a detailed discussion on the data extraction). The MiniBooNE data are shown in the left panel of Fig. 15.13. Comparing to our full model (solid line) we find that we clearly underestimate the data — even our results without FSI (dashed line) lies below the data. However, the *shape of the distribution* is reproduced perfectly (when multiplying our solid curve by 2 we fully agree with the

data).

For the flux-averaged integrated NC1π^0 cross section on CH_2, MiniBooNE finds $(0.64 \pm 0.10) \cdot 10^{-38}\,\mathrm{cm}^2$ while we obtain $0.33 \cdot 10^{-38}\,\mathrm{cm}^2$.

π^0 can be produced in our approach not only through resonances but also through initial NC elastic scattering, i.e., final-state nucleons can rescatter in the nucleus and produce pions. But this accounts only for $\approx 1.5\%$. Missing is in our approach is DIS and any non-resonant single-π/double-π etc. background. But we do not expect a significant contribution of those at the rather low MiniBooNE energy. Coherent scattering can also contribute and we show in the left panel of Fig. 15.13 the prediction for coherent NCπ^0 production by Alvarez-Ruso *et al.* [ARGVV07, AR]. This contribution is even smaller in the model of Amaro *et al.* [AHNV09] ($0.02 \cdot 10^{-38}\,\mathrm{cm}^2$ vs. $0.04 \cdot 10^{-38}\,\mathrm{cm}^2$ for the integrated cross section). Furthermore, as already mentioned above, it has been shown by Winkelmann [Win08, LMW09] that all available calculations for the coherent cross section overestimate the cross section by up to a factor of 2. Thus, we believe that coherent scattering is only a small correction to the NCπ^0 cross section, or, in other words, we believe that our model accounts for the relevant contributions.

Still, a large discrepancy remains. As in the CC1π^+ case, a possible underestimate could come from the choice for the Δ axial form factor. The results in Fig. 15.13 have been obtained with a modified dipole form factor (see page 50 for details). In Fig. 15.14 we show the results for both form factors, dipole and modified dipole, for comparison. The pre-FSI curve with the dipole form factor (dash-dotted line) now lies slightly above the data. The full result with the dipole form factor, shown by the dotted line, still underestimates the data but less dramatic than the result obtained with the modified dipole form factor.

To better understand the source of the discrepancy we show in Fig. 15.15 our result for the pion angular distribution together with the MiniBooNE data [And09a]. Our standard modified dipole form factor has been applied in the left panel, and, like in the momentum distribution discussed before, we underestimate the data significantly — they rather agree with our calculation without FSI. The agreement is better in the right panel where the dipole axial form factor has been used for the Δ resonance. The obvious disagreement in shape at very small pion scattering angles can be attributed to coherent scattering which strongly peaks in forward direction.

15.4 Possible origins of the discrepancies and conclusion

Before going into detail, we summarize the previous sections. The comparison to the MiniBooNE data shows a obvious discrepancy — we clearly underestimate the measured CCQE, CC1π^+ and the NC1π^0 cross sections. By including nuclear effects,

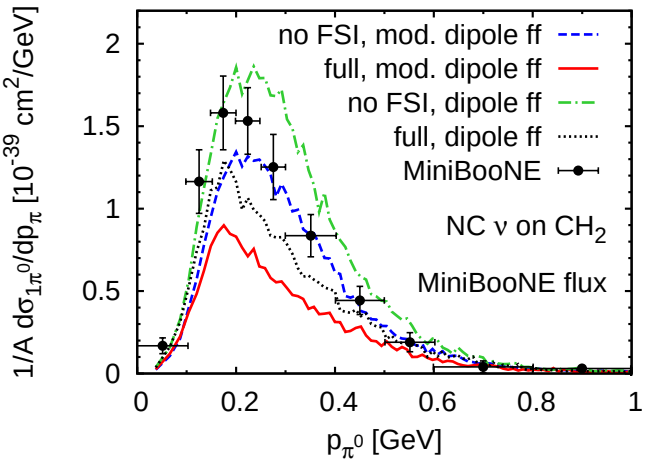

Figure 15.14: NC induced single-π^0 production on CH_2 as a function of the pion momentum averaged over the MiniBooNE flux. The dashed and the solid lines denote the calculation with a modified dipole form factor for the Δ resonance (identical to the result in the left panel of Fig. 15.13). The dash-dotted and dotted lines are obtained with a dipole form for the form factor. The MiniBooNE data are taken from Ref. [And09a].

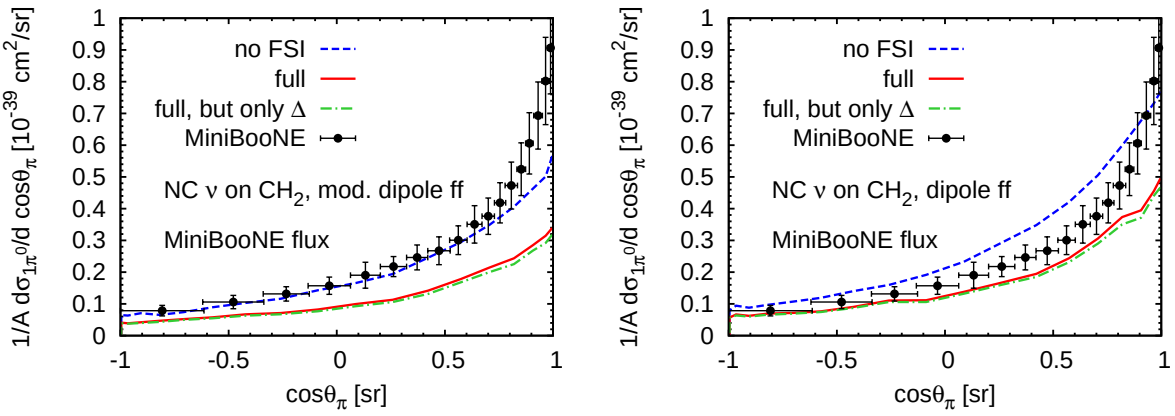

Figure 15.15: Left panel: NC induced single-π^0 production on CH_2 as a function of the pion scattering angle averaged over the MiniBooNE flux. The curves are scaled with the number of nucleons. The dashed line shows our calculation without FSI or spectral functions, both included in the full calculation denoted by the solid line. The dash-dotted line indicates the contribution from the Δ resonance to the full calculation. The MiniBooNE data are taken from Ref. [And09a]. Right panel: same but with a dipole axial form factor for the Δ resonance.

we have been able to describe the shape of the data, e.g., the CCQE Q^2 distribution (without increasing the axial mass) and the NCπ^0 momentum differential cross section. However, the absolute values of the cross sections are not reproduced. Interestingly, the FSI corrected contributions are well described by our method when we "switch off" FSI.

In the following, we discuss possible origins of the discrepancies.

Energy reconstruction

The ratio CC1π+/CCQE, the CCQE and the CC1π^+ cross section are presented in terms of the neutrino energy. We have discussed in Section 13.4 that the neutrino energy is not an observable but has to be reconstructed from the measured final-state particles, in case of CCQE from the outgoing muon according to Eq. (13.2) (see page 217).

In the case of the ratio, the MiniBooNE collaboration reconstructs the neutrino energy for both samples (CCQE and CC1π^+) from the observed muon kinematics, treating the interaction as a 2-body collision and assuming that the target nucleon is at rest inside the nucleus [MiniBooNE09a]:

$$E_\nu = \frac{1}{2}\frac{2M_N E_\mu + M_f^2 - M_N^2 - m_\mu^2}{M_N - E_\mu + \cos\theta_\mu \sqrt{E_\mu^2 - m_\mu^2}}. \tag{15.2}$$

M_N is the mass of the nucleon, m_μ is the mass of the muon, θ_μ its scattering angle and E_μ its energy. M_f is the mass of the neutron in CCQE events or the Breit-Wigner mass of the $P_{33}(1232)$ resonance in CC1π^+, respectively. This formula thus assumes that all pions are produced through the excitation of the Δ resonance which is taken to be a state of fixed mass, or, in other words, its spectral function is taken to be a δ-function. Binding effects are neglected here — for CCQE, this formula agrees with Eq. (13.2) for $E_B = 0$.

Fig. 15.16 shows the reconstructed energy distribution according to Eq. (15.2) for the CCQE-like sample and the CC1π^+ sample (before and after FSI). The shape of the dash-dotted and the dotted curves have been discussed already in Section 13.4: Fermi motion broadens the peak and the fake CCQE events cause the bump at lower reconstructed energies. Also the reconstructed energy from the pion sample is affected by Fermi motion (dashed and solid lines). A further broadening comes from the actual shape of the Δ resonance which is taken to be of δ-function-like shape in Eq. (15.2). Overall, the reconstructed energy is centered around the real energy for both samples even though with a slight tendency to lower reconstructed energies. Table 15.2 lists the expected values for the reconstructed energy and the standard deviation. This error, however, should be contained in the horizontal error bar of the data.

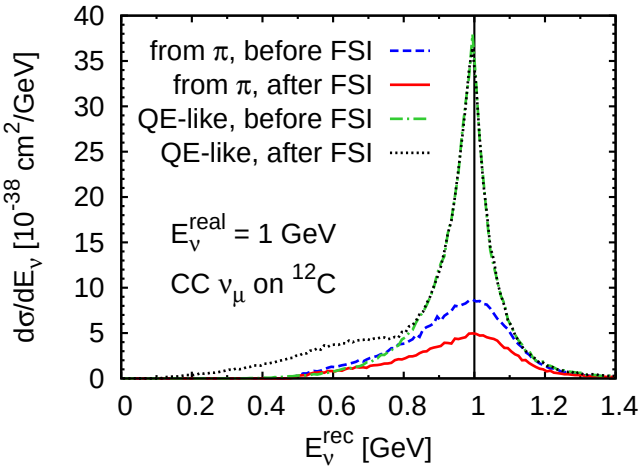

Figure 15.16: Distribution of the reconstructed neutrino energy according to Eq. (15.2) for $E_\nu^{\text{real}} = 1\,\text{GeV}$. Shown are the reconstruction based on the CCQE-like sample (before and after FSI, Cherenkov assumptions) and based on the CC1π^+ sample (before and after FSI).

Table 15.2: Expected value, E, and standard deviation, S, for the distributions shown in Fig. 15.16 for $E_\nu^{\text{real}} = 1\,\text{GeV}$.

	$E = \int_0^\infty \mathrm{d}E_\nu^{\text{rec}} \, \frac{E_\nu^{\text{rec}}}{\sigma} \frac{\mathrm{d}\sigma}{\mathrm{d}E_\nu}$	$S = \left(\int_0^\infty \mathrm{d}E_\nu^{\text{rec}} \, \frac{(E_\nu^{\text{rec}} - E)^2}{\sigma} \frac{\mathrm{d}\sigma}{\mathrm{d}E_\nu} \right)^{1/2}$
from π, before FSI	0.94 GeV	0.16 GeV (17%)
from π, after FSI	0.95 GeV	0.19 GeV (20%)
QE-like, before FSI	0.97 GeV	0.13 GeV (14%)
QE-like, after FSI	0.90 GeV	0.21 GeV (23%)

Underestimate of elementary cross sections

Our results on nuclei depend directly on the νN cross sections. We have demonstrated how the final pion results change when using the BNL pion data instead of the ANL ones as a reference. Both data sets suffer from bad statistics. The obvious difference between these data already indicates a possible problem, maybe even a flux problem. However, these data serve as a necessary input for our approach. While our value of the dominant axial coupling, $C_5^A(0)$ for the Δ resonance, is based on a PCAC prediction, the axial mass for the $N-\Delta$ transition form factor is fixed by the ANL or BNL data. Also the background is fitted to match the ANL data. Increasing M_A of the Δ and maybe also of the other resonances, and increasing the background would certainly improve the correspondence with the MiniBooNE data, but worsen the agreement with ANL and BNL.

Our transport model has been tested independently against many different measurements. Thus, we believe, that our pion absorption model gives realistic results. On this basis, we conclude that the MiniBooNE data are inconsistent with the finding of ANL and BNL.[7]

In the case of CCQE, the situation is different. Here, M_A is expected to be around 1 (see discussion before) and the freedom to change the elementary cross section is rather limited.

Data extraction

The MiniBooNE cross section measurements are based on Cherenkov light detection, therefore, they require a detailed model of light production and propagation in the tank.

We first focus on the NC1π^0 cross section as measured by MiniBooNE. According to G. Zeller [Zel], the events are selected as follows: any event in which there are (a) no pions, (b) more than one π^0, or (c) one π^0 and other mesons that leave the target nucleus are counted as background and subtracted. All events in which only one π^0 and no other mesons leave the target nucleus including events in which π^0's and other mesons are created elsewhere in the tank are counted as signal events and are not subtracted. Thus, the cross section includes only those events that had one and only one π^0 exiting the initial target, and no other mesons. So events where there was no π^0 exiting the target nucleus, but one was created in the tank are excluded. Events where one and only one π^0 exited the target nucleus but other particles were created in transit in the tank are included. The same event selection holds correspondingly for the CCπ^+ sample.

[7] Note that MiniBooNE's event generator has 30% less pion absorption than our approach and a coherent contribution much larger than current predictions [Zel] — they state that their data are consistent with the ANL data [MiniBooNE09a].

Since the cross section is defined based on what exited the target nucleus — the pions produced afterwards in the tank have been removed —, it is based on the NUANCE simulation which serves as an input for the detector simulation. The amount of pions produced in tank (i.e., the background they subtract) depends directly on the NUANCE ISI and FSI modeling — if this is not correct, then also the background prediction is not correct because, both, the neutrino event simulation and the detector simulation are not independent. For example, if NUANCE had less pion absorption than in reality, more pions would leave the nucleus. In the GEANT detector simulation, these additional pions, e.g., NCπ^+, could then undergo charge exchange in the tank and might be counted as NC1π^0 and would cause a wrong prediction of background events. Note that also knocked out nucleons can give rise to additional pions through reinteractions in the tank. The amount of pions produced in the tank is even comparable to that of pions produced inside the nucleus [MiniBooNE09f], so it is not a small correction.

It is clear, that these effects change the extracted pion cross sections, but without a detailed simulation of the MiniBooNE detector we cannot provide any numbers or conclusive statements and have to rely on the systematic error provided by the MiniBooNE collaboration.

For CCQE measurements, we already addressed the problem of the background subtraction in Section 15.1.

Neutrino flux

All absolute cross section measurements, CCQE, CC1π^+ and NC1π^0, are directly related to the predicted or measured neutrino flux. Changing the flux by a certain factor would immediately change all these cross sections by the same factor.

Predictions of the neutrino flux are strongly model dependent and very complex. Even if one only varies the proton-induced pion production cross section and keeps all other parts of the simulation identical, the largest flux estimate is about a factor of four higher than the lowest [Sch08a]! An accurate flux prediction is important for neutrino cross section measurements, thus, several experiments have been set up to measure the hadron production directly, e.g., the HARP experiment [HARP]. In the case of MiniBooNE and SciBooNE, the neutrino flux is predicted using the HARP pion production data [MiniBooNE09c].

However, it has been claimed that measuring the primary hadron production cross section is by far not enough to determine the neutrino flux [Kop09]. First, most particle experiments are performed on thin targets, while most neutrino cross section experiments use a thick target in their proton beam. The reinteractions are estimated to account for a 20–30% effect. Even the temperature of the target hall, beam degradations over time, downstream interactions, the earth magnetic field and more effects

can change the neutrino beam. Most of them are not even included in the flux calculations.

An *in situ* measurement of the neutrino flux itself in MiniBooNE based on CCQE events has shown a disagreement: the observed rate of interactions is a factor of about 1.2 higher than the predicted rate even after increasing M_A [MiniBooNE09c]. But, the MiniBooNE collaboration states that "the observed and predicted rates are compatible because of the large uncertainty in the predicted rates."

Conclusion

We have addressed some points which certainly influence either our predictions or even the data. No definite solution for the observed discrepancies has been found, and final conclusions cannot yet be drawn. More data, which are as model-independent as possible, are certainly needed. We emphasize that only with such model-independent acceptance-corrected data one can perform meaningful comparisons with theoretical calculations. The approach, started by MiniBooNE, to report "observed" cross sections instead of FSI corrected quantities is an important step in this direction even though the data still contain a lot of modeling.[8] Hopefully, upcoming data from MINERνA[9] will help to clarify the existing discrepancies and give further hints where to improve our modeling.

[8] See also the comments by G. Zeller [Zel09].

[9] Also SciBooNE will provide high-statistics cross section measurements. However, SciBooNE uses the same predicted flux as MiniBooNE.

Part V

Conclusion

16
Summary and conclusive remarks

In this thesis, we have investigated neutrino interactions with nucleons and nuclei at intermediate lepton energies, i.e., beam energies ranging from 0.5 to 2 GeV. To this aim we have developed a model able to describe neutrino reactions with nucleons and nuclei on the same basis as in electron-induced scattering.

First, we have presented our model for elementary lepton-nucleon scattering via EM, CC and NC where we have focused on the quasielastic and resonance region. The extension to finite nuclei has been done in the framework of a coupled-channel BUU transport theory which takes into account various in-medium modifications and final-state interactions. In particular, we have studied the influence of nuclear effects on inclusive scattering, pion-production mechanisms and nucleon knockout. Finally, this model has been applied to current and future neutrino long-baseline experiments. We have emphasized the importance of nuclear effects for neutrino oscillation measurements; furthermore, we have compared our results to recent cross section measurements and have presented various predictions.

16.1 Summary

After the introduction in Part I, we have introduced our model for the elementary ℓN reaction in Part II of this work. We treat EM, CC and NC within the same formalism which has been detailed in Chapter 2 and Chapter 3. In the energy regime from 0.5 to 2 GeV, the scattering process is dominated by three contributions: quasielastic scattering, resonance excitation and non-resonant pion production. QE scattering (cf.

Chapter 4) and resonance excitation — we include 13 N^* and Δ resonances with invariant masses less than 2 GeV — (cf. Chapter 5) are both described with a relativistic formalism that incorporates recent form factor parametrizations. EM, CC and NC form factors are connected via isospin relations. For the nucleon vector form factors we apply the latest BBBA-2007 analysis accounting for new electron scattering data; the $N-\Delta$ and $N-N^*$ vector form factors are based on the recent MAID analysis for the helicity amplitudes. The axial couplings has been obtained applying the PCAC theorem. The Q^2 dependence of the nucleon and the $N-\Delta$ axial form factors, F_A and C_5^A, is fitted to bubble chamber neutrino-scattering data. For the non-resonant pion background discussed in Chapter 6, we have used a technique based on invariant amplitudes taken from MAID, allowing us to incorporate background terms not only for EM, but also for CC processes, where the additional non-vector parts were fitted to the ANL data for total pion production cross sections.

All other available models for resonance excitation based on phenomenological form factors include at most the four lowest lying resonances while we have included the full set of MAID which includes 13 resonances. A similar set has been included in the Rein and Sehgal model, a microscopic approach based on a quark model; however, we have shown in Section 5.5.2 that their model fails for electron scattering.

Part III is devoted to the study of neutrino-nucleus scattering: in our approach, we treat neutrino-nucleus scattering as a two-step process. In the initial-state step, the neutrinos interact with nucleons embedded in the nuclear medium. In the final-state step, the outgoing particles of the initial reaction are propagated through the nucleus using a hadronic transport approach — the GiBUU coupled-channel transport model described in Chapter 7.

The neutrino-nucleon cross sections are modified in the nuclear medium (cf. Chapter 8). We use a local Thomas-Fermi approximation for the phase space density of the bound nucleons based on realistic nuclear densities. The nucleons are exposed to a mean-field potential which depends on density and momentum. We account for this by evaluating the νN cross sections with full in-medium kinematics, i.e., hadronic tensor and phase-space factors are evaluated with in-medium four-vectors. We also take Pauli blocking and in-medium spectral functions of the outgoing hadrons into account. The imaginary part of the self energies entering the spectral functions are calculated in a consistent way employing the low-density approximation, the real part of the self energies is obtained from dispersion relations.

After the initial neutrino-nucleon interaction, the produced particles propagate out of the nucleus. During propagation they undergo FSI which are simulated with the coupled-channel semi-classical GiBUU transport model (cf. Chapter 7). It models the full space-time evolution of the phase space densities of all relevant particle species during a nuclear reaction within a consistent treatment of the initial vertex and the final state processes. This space-time evolution is determined by the BUU equations,

which describe the propagation of the particles in their mean-field potentials and also the collisions between them — resonances are treated explicitly. Nucleons and resonances acquire medium-modified spectral functions and are propagated off-shell. Hereby we ensure, that vacuum spectral functions are recovered after leaving the nucleus. The collision term accounts for changes (gain and loss) in the phase-space density due to elastic and inelastic collisions between the particles, and also due to particle decays into other hadrons. Baryon-meson two-body interactions (e.g., $\pi N \to \pi N$) are described by resonance contributions and a small non-resonant background term; baryon-baryon cross sections (e.g., $NN \to NN$, $RN \to NN$, $RN \to R'N$, $NN \to \pi NN$) are either fitted to data or calculated, e.g., in pion exchange models. The three-body channels $\pi NN \to NN$ and $\Delta NN \to NNN$ are also included. The BUU equations for all particle species are thus coupled through the collision term and also through the potentials. Such a coupled-channel treatment is required to account for side feeding into different channels.

A major strength of the GiBUU model is that it has been applied to many different reactions from heavy ion collisions to pion and electron induced processes. Unlike most Monte Carlo event generators presented in Section 12.2, we do not tune any specific input (like for example pion absorption cross sections) to describe a specific reaction channel (like for example neutrino induced pion production). To the contrary, we include as much physics as possible and are thus in a position to explain simultaneously a wide range of very different reactions. We conclude from the successful comparison of the GiBUU calculations for pion, photon and electron induced reactions to experimental data, that the treatment of initial and final-state interactions is under good control and leads to reliable predictions. The comparison with data for the reactions mentioned allows to make estimates for the expected accuracy in neutrino-induced reactions.

Inclusive scattering of leptons off nuclei has been investigated in Chapter 9. We have shown how the inclusion of mean-field potentials and in-medium spectral functions modifies the cross sections. When comparing our results for electron induced processes to the experimental electron scattering data on Oxygen and Carbon, we achieve good agreement both in the QE region as well as in the pion production region. The overall agreement is improved by taking into account mean fields and in-medium spectral functions in addition to a local Fermi gas momentum distribution. Taking the in-medium modifications on the electron scattering results as a benchmark, we have made predictions for CC and NC inclusive scattering at beam energies ranging from 0.5 up to 2 GeV relevant for current and future neutrino oscillation experiments. We further have compared our CC and EM results to other, very different approaches and found reasonable agreement. In particular, a comparison to the results in the QE region obtained within a complex nuclear many-body calculation shows that our implementation of in-medium modifications provides an effective and

efficient treatment of nucleon properties in the medium.

Neutrino-induced pion production off nuclei has been the focus of Chapter 10. For CC neutrino-induced pion production, we have found that the in-medium corrections and, especially, final-state interactions reduce the pion cross sections and also give rise to a small fraction of π^- which cannot be produced in the initial νN reaction. Quasielastic scattering followed by π production in NN collisions contributes only weakly to the pion production cross section. In the kinematical region under investigation, the pions originate mainly from the initial Δ excitation. Furthermore, we have found an enhancement of the π^0 channel through side-feeding from the dominant π^+ channel. Also in the NC case, pion production cross sections are especially influenced by final-state interactions. In the elementary neutrino-nucleon reaction, more π^0 than charged pions are produced due to the isospin structure of resonance decay. When final-state interactions are included, those π^0 get absorbed or re-interact leading to side-feeding in the smaller $\pi^\pm$ channels. Quasielastic scattering followed by π production in NN collisions also accounts for a small fraction of the pion production cross section.

In Chapter 11 we have illustrated the importance of final-state interactions for nucleon knockout. High energy nucleons rescatter in the nucleus, which leads to a decrease of the flux at higher energies, but also to a large number of secondary knocked-out nucleons with low kinetic energies. Side feeding is important also for nucleon knockout: in the elementary CC quasielastic reaction, one the final state contains only protons, but no neutrons, however, we have found that, as a consequence of the final-state interactions, a large fraction of neutrons is knocked out. The same holds for in the Δ region where a large enhancement of neutrons due to final-state interactions is observed. Also for NC nucleon knockout the importance of FSI is evident: we have illustrated that for neutrino energies $\gtrsim$ 1 GeV initial resonance excitation (predominantly Δ) leads to a significant contribution to nucleon knockout.

Nucleon knockout is studied in many different models; only a few study pion production. But we do not know of any other theoretical model than the one presented here that considers both simultaneously. For example, Δ-induced nucleon knockout or QE-induced pion production are not described with any other model. In this respect, our approach is unique.

In Part IV of this work we have applied the model developed in Parts II and III to questions relevant for current and future neutrino long-baseline experiments. Chapter 12 serves as an introduction to the following chapters: here, we have summarized the main LBL experiments — all of them use nuclear targets — and the Monte Carlo event generators used in their analyses. In particular, we have emphasized the main points where our approach differs from the phenomenological event generators like NUANCE, NEUT and others and have stressed again the importance of neutrino independent quality checks of the nuclear model, e.g., by comparing to photon or electron

data.

Chapter 13 addresses the relevance of CC reactions for neutrino disappearance experiments. We have discussed that a correct identification of CCQE events is relevant for the neutrino energy reconstruction and thus for the oscillation result. A significant part of CC1π^+ events is detected as CCQE-like which is caused by the pion absorption in the nucleus. We have investigated their influence on the neutrino energy reconstruction and on the CCQE cross section which is the signal channel in oscillation experiments stressing the effect of final-state interactions.

The importance of NC reactions for ν_e appearance searches has been investigated in Chapter 14. After reviewing MiniBooNE's oscillation result we have discussed two examples, NC1π^0 production and radiative Δ decay, and how they can possibly influence the oscillation signal. Again, we have focused on the influence of final-state interactions.

Finally, in Chapter 15, we have presented our predictions and, where possible, compared our results for NC and CC induced reactions to recent data measured at MiniBooNE and K2K. Until recently, there has been a trend to "correct" the raw data using specific Monte Carlo event generator with specific assumptions on the initial neutrino nucleon cross section and the nuclear model. Now MiniBooNE started to provide more model independent data. However, our calculations underestimate the MiniBooNE data significantly. We have discussed several possible origins for these discrepancies. To solve this problem, more data also from other experiments are needed. These data should be as model-independent as possible to perform meaningful comparisons with theoretical calculations.

16.2 Outlook and future improvements

Finally, we discuss some possible future improvements. On the nucleon level, first priority has the improvement of the non-resonant single-pion background. As pointed out in Chapter 6, we use the same functional form for the vector and axial contributions which has no underlying justification except that this procedure succeeded in describing the data. One option would be to replace our phenomenological approach by a microscopical calculation, e.g., along the lines of Ref. [HNV07]. However, the advantage of our approach is that it includes much more contributions and that the vector part is directly constrained by electron data. A microscopical calculation beyond the Δ region is a highly non trivial task and has not yet been performed. Furthermore, our model on the nucleon still does not include a non-resonant two-pion background.

In view of the neutrino experiments operating at energies of a few GeV up to 20 GeV, a natural expansion of our model is the extension to higher energies, i.e., the

inclusion of DIS scattering off the nucleon. This is already in progress and we have shown first implications in Section G.2.

Concerning the transport part of our approach, a modification of the off-shell transport seems to be advisable. We have discussed the off-shell potential in detail in Section 7.8 and pointed out that this method is both time and computing resource consuming. In view of its little implication on observables (see Sections 10.4 and 11.4), this effort is not justified.

We have discussed in Chapter 9 that we do not fully resemble the peak shift for the lowest-energy electron-scattering QE data. Our local Thomas-Fermi ansatz leads to a r-dependent Fermi energy. Thus, nucleons close to the surface encounter a smaller Fermi energy than those in the center of the nucleus. Since most nucleons sit in the surface this could explain our missing peak shift. A possible improvement is to determine the local Fermi momentum not from measured density profiles via $p_F \sim \rho^{1/3}$ but by requiring the Fermi energy to be constant and hereby fix Fermi momentum and densities. However, this method would lead to densities which do not reach far enough out — they become zero at the classical turning point. Possible implications, e.g., for the particle propagation, need to be investigated.

16.3 Conclusion

Summarizing, we have presented in this thesis a consistent model for EM, CC and NC reactions off nucleons and nuclei in the energy regime of interest for current neutrino experiments. In-medium corrections, in particular the influence of final-state interactions, are found to be of considerable importance. Their understanding — within a well-tested transport model — is crucial for the interpretation of present and future experiments in order to distinguish extraordinary "new physics" from "profane" nuclear effects. We believe that our model with its unique features is well suited for this task.

Appendices

A
Reference formulae

A.1 Units and constants

Units with $\hbar = c = 1$ are used throughout this work. For all masses, energies and momenta we take "GeV" as standard unit, and cross sections have the dimension GeV^{-2}. Neutrino cross sections are commonly given in units of $10^{-38}\,\mathrm{cm}^2$. To convert to an area, one uses

$$1\,\mathrm{GeV}^{-2} = 3.8939 \cdot 10^{10} \cdot 10^{-38}\,\mathrm{cm}^2 = 0.38939\,\mathrm{mb}, \tag{A.1}$$

where $1\,\mathrm{mb} = 10^{-31}\,\mathrm{m}^2 = 0.1\,\mathrm{fm}^2$. Thus, we obtain the following relations:

- $10^{-38}\,\mathrm{cm}^2 = 10^{-11}\,\mathrm{mb} = 10^{-5}\,\mathrm{nb} = 10^{-2}\,\mathrm{pb}$
- $10^{-40}\,\mathrm{cm}^2\,/\,\mathrm{MeV} = 10 \cdot 10^{-38}\,\mathrm{cm}^2\,/\,\mathrm{GeV}$

Abbreviations are listed in Table A.1 and the numerical values of the constants used in this work are given in Table A.2.

A.2 Notation and definitions

The notations used throughout this thesis are summarized in Table A.3. Three-momenta are given by bold letters, e.g., $\mathbf{p}$; their absolute values by italic letters, e.g., $|\mathbf{p}| = p$. Four-momenta are given by italic letters, e.g., $p^\mu = p$ (the Lorentz index is not always written explicitly). The free nucleon mass is always denoted by M_N,

Table A.1: Abbreviations used throughout this work.

abbreviations	
BG	non-resonant single-pion background
CC	charged current
CVC	conserved vector current
DIS	deep inelastic scattering
FSI	final-state interaction
ISI	initial-state interaction
LBL	long-baseline
LTF	local Thomas-Fermi
NC	neutral current
OSP	off-shell potential
PCAC	partially conserved axial current
QE	quasielastic
R	resonance

Table A.2: Set of constants used throughout this work. The values are taken from the Particle Data Group [PDG08].

quantity	symbol	value
fine-structure constant	α	$\frac{e^2}{4\pi} = \frac{1}{137}$
Fermi coupling constant	G_F	$1.16637 \cdot 10^{-5}\,\mathrm{GeV}^{-2}$
axial coupling constant	g_A	1.267
Cabbibo mixing angle	$\cos\theta_C$	0.9745
weak-mixing angle	$\sin^2\theta_W$	0.2228
nucleon mass	M_N	0.938 GeV
resonance masses	M_R	values given in Table 5.1
pion mass	m_π	0.138 GeV
muon mass	m_μ	0.105658369 GeV
electron mass	m_e	0.00051099892 GeV
tau mass	m_τ	1.77699 GeV
neutrino mass	m_ν	0
pion decay constant	f_π	0.093 GeV

Table A.3: Notation used throughout this work.

	four-momentum	mass
incoming lepton ℓ or ν_ℓ	$k = (k^0, \lvert\mathbf{k}\rvert\mathbf{e_z})$	m_ℓ or m_ν
incoming nucleon N	$p = (p^0, \mathbf{p})$	M_N
outgoing lepton ℓ' or $\nu_{\ell'}$	$k' = (k'^0, \mathbf{k}')$	$m_{\ell'}$ or m_ν
outgoing nucleon N'	$p' = (p'^0, \mathbf{p}')$	M_N
outgoing resonance R	$p' = (p'^0, \mathbf{p}')$	pole mass M_R
		invariant mass $W = \sqrt{p'^2}$
outgoing pion π	$k_\pi = (k^0_\pi, \mathbf{k_\pi})$	m_π
boson γ, W or Z	$q = (\omega, \mathbf{q})$	

the Breit-Wigner mass of a resonance by M_R, its invariant mass by $W = \sqrt{p'^2}$. The incoming lepton defines the z-axis; the direction of the outgoing lepton is given by

$$\mathbf{k}' = (|\mathbf{k}'|\sin\theta\cos\phi, |\mathbf{k}'|\sin\theta\sin\phi, |\mathbf{k}'|\cos\theta). \tag{A.2}$$

The four-vector of the exchanged boson reads

$$q = k - k' = p' - p, \tag{A.3}$$

with the transferred energy

$$\omega = k^0 - k'^0. \tag{A.4}$$

Further, we define $Q^2 = -q^2$ and obtain

$$\begin{aligned} Q^2 = -q^2 &= -(k-k')^2 = -(p'-p)^2 \\ &= -k^2 - k'^2 + 2kk' \\ &= -m_\ell^2 - m_{\ell'}^2 + 2k^0k'^0 - 2\mathbf{k}\cdot\mathbf{k}' \\ &= -m_\ell^2 - m_{\ell'}^2 + 2k^0k'^0 - 2|\mathbf{k}||\mathbf{k}'|\cos\theta. \end{aligned} \tag{A.5}$$

The invariant mass, W, of the final hadronic system is given by

$$W^2 = p'^2 = (p+q)^2. \tag{A.6}$$

A.3 Metric and conventions

We generally follow the conventions of Bjorken and Drell [BD67] (except for the spinor normalization).

Metric tensor

$$g^{\mu\nu} = g_{\mu\nu} = \begin{pmatrix} 1 & 0 & 0 & 0 \\ 0 & -1 & 0 & 0 \\ 0 & 0 & -1 & 0 \\ 0 & 0 & 0 & -1 \end{pmatrix}. \tag{A.7}$$

Pauli matrices

The components of the Pauli spin vector $\boldsymbol{\sigma} = (\sigma^1, \sigma^2, \sigma^3)$ are

$$\sigma^1 = \begin{pmatrix} 0 & 1 \\ 1 & 0 \end{pmatrix}, \quad \sigma^2 = \begin{pmatrix} 0 & -\mathrm{i} \\ \mathrm{i} & 0 \end{pmatrix}, \quad \sigma^3 = \begin{pmatrix} 1 & 0 \\ 0 & -1 \end{pmatrix}. \tag{A.8}$$

Dirac matrices

$$\gamma^\mu = (\gamma^0, \boldsymbol{\gamma}), \quad \{\gamma^\mu, \gamma^\nu\} = 2g^{\mu\nu}, \tag{A.9}$$

(A.10)

$$\gamma^0 = \gamma_0 = \begin{pmatrix} \mathbb{1}_2 & 0 \\ 0 & -\mathbb{1}_2 \end{pmatrix}, \quad \boldsymbol{\gamma} = \begin{pmatrix} 0 & \boldsymbol{\sigma} \\ -\boldsymbol{\sigma} & 0 \end{pmatrix}. \tag{A.11}$$

Important combinations are

$$\gamma^5 = \gamma_5 = \mathrm{i}\gamma^0\gamma^1\gamma^2\gamma^3 = \begin{pmatrix} 0 & \mathbb{1}_2 \\ \mathbb{1}_2 & 0 \end{pmatrix}, \tag{A.12}$$

$$\left\{\gamma^\mu, \gamma^5\right\} = 0, \quad \gamma_5^2 = \mathbb{1}_4, \tag{A.13}$$

$$\sigma^{\mu\nu} = \frac{\mathrm{i}}{2}\left[\gamma^\mu, \gamma^n u\right]. \tag{A.14}$$

$\mathbb{1}_n$ stands for the $n \times n$ unit matrix.

Gell-Mann matrices

For the $SU(3)$ Gell-Mann matrices we use

$$\lambda_1 = \begin{pmatrix} 0 & 1 & 0 \\ 1 & 0 & 0 \\ 0 & 0 & 0 \end{pmatrix}, \ \lambda_2 = \begin{pmatrix} 0 & -\mathrm{i} & 0 \\ \mathrm{i} & 0 & 0 \\ 0 & 0 & 0 \end{pmatrix}, \tag{A.15}$$

$$\lambda_3 = \begin{pmatrix} 1 & 0 & 0 \\ 0 & -1 & 0 \\ 0 & 0 & 0 \end{pmatrix}, \ \lambda_8 = \frac{1}{\sqrt{3}}\begin{pmatrix} 1 & 0 & 0 \\ 0 & 1 & 0 \\ 0 & 0 & -2 \end{pmatrix}, \tag{A.16}$$

with

$$\lambda_{\pm} = (\lambda_1 \pm \mathrm{i}\lambda_2). \tag{A.17}$$

Normalization of spinors

For both, fermions and bosons, we choose the normalization in which we have $2E$ particles per unit volume, so that

$$\langle p'(s)|p(r)\rangle = 2E\,(2\pi)^3\,\delta^3\left(\mathbf{p}'-\mathbf{p}\right)\delta_{rs}. \tag{A.18}$$

The orthogonality relations thus reads

$$u^{\dagger}(p,s)u(p,r) = 2E\delta_{rs}, \tag{A.19}$$

and we get

$$\bar{u}(p,s)u(p,r) = 2m\delta_{rs}. \tag{A.20}$$

Completeness relation

For spin 1/2 particles:

$$\sum_s u(p,s)\bar{u}(p,s) = \not{p} + m. \tag{A.21}$$

For spin 3/2 particles:

$$\sum_s \psi_\alpha(p,s)\bar{\psi}_\beta(p,s) = \Lambda_{\alpha\beta}(p) \tag{A.22}$$

$$= -\left(\not{p}+m\right)\left(g_{\alpha\beta} - \frac{2}{3}\frac{p_\alpha p_\beta}{m^2} + \frac{p_\alpha\gamma_\beta - p_\beta\gamma_\alpha}{3m} - \frac{1}{3}\gamma_\alpha\gamma_\beta\right). \tag{A.23}$$

Dirac equation

The positive-energy four-component spinor u satisfies

$$\left(\not{p}-m\right)u(p,s) = 0, \tag{A.24}$$

with $\not{p} = \gamma_\mu p^\mu$.

Hermitian conjugate of spinor matrix elements

$$\left[\bar{u}(p',s')\Gamma u(p,s)\right]^{\dagger} = \bar{u}(p,s)\widetilde{\Gamma}u(p',s'), \tag{A.25}$$

where $\bar{u} = u^{\dagger}\gamma^0$; Γ is any combination of γ matrices and

$$\widetilde{\Gamma} = \gamma^0\Gamma^{\dagger}\gamma^0. \tag{A.26}$$

For example, we find $\widetilde{\gamma^\mu} = \gamma^\mu$ and $\widetilde{\gamma^\mu\gamma^5} = \gamma^\mu\gamma^5$.

A.4 Isospin operators

We use the conventions of Ericson and Weise (cf. Appendices 3 and 6 in Ref. [EW88]).

A.4.1 Nucleons and isospin 1/2 resonances

The proton and the neutron (and correspondingly, all isospin $1/2$ resonances) build an isospin doublet

$$|p\rangle = \begin{pmatrix} 1 \\ 0 \end{pmatrix}, \quad |n\rangle = \begin{pmatrix} 0 \\ 1 \end{pmatrix}. \tag{A.27}$$

The isospin matrices build a vector in isospin space

$$\boldsymbol{\tau} = (\tau_1, \tau_2, \tau_3), \tag{A.28}$$

where the definition of τ_i is as for the Pauli matrices given in Eq. (A.8). With the combination

$$\tau_\pm = \frac{1}{2}(\tau_1 \pm \mathrm{i}\tau_2) \tag{A.29}$$

we obtain

$$\tau_-|p\rangle = |n\rangle, \quad \tau_+|n\rangle = |p\rangle, \quad \tau_+|p\rangle = \tau_-|n\rangle = 0. \tag{A.30}$$

A.4.2 Pions

The charge components, $\phi_\pm$ and ϕ_0, of the pion field form an isovector $\boldsymbol{\phi}$ written in Cartesian isospin coordinates as

$$\boldsymbol{\phi} = (\phi_1, \phi_2, \phi_3). \tag{A.31}$$

We define

$$\phi_\pm = \frac{1}{\sqrt{2}}(\phi_1 \pm \mathrm{i}\,\phi_2), \quad \phi_0 = \phi_3, \tag{A.32}$$

where ϕ_- creates a π^- or annihilates a π^+, and ϕ_+ creates a π^+ or annihilates a π^-. The scalar product with the isospin $1/2$ matrix $\boldsymbol{\tau}$ follows to

$$\boldsymbol{\tau} \cdot \boldsymbol{\phi} = \tau_1\phi_1 + \tau_2\phi_2 + \tau_3\phi_3 = \sqrt{2}(\tau_+\phi_- + \tau_-\phi_+) + \tau_3\phi_0. \tag{A.33}$$

A.4.3 Isospin 3/2 resonances

The four charge states (R^{++}, R^+, R^0, R^-) form an isospin $3/2$ quartet. The isospin $1/2 \to 3/2$ transition operator $\mathbf{T}$ is defined by the matrix elements of its components T_λ ($\lambda = -1, 0, +1$) (cf. Eq. (A4.38) in Ref. [EW88])

$$\left\langle \frac{3}{2}M \left| \mathbf{T}^\dagger \right| \frac{1}{2}m \right\rangle = \sum_\lambda \left\langle \frac{3}{2}M \left| T_\lambda^\dagger \right| \frac{1}{2}m \right\rangle \mathbf{e}_\lambda^*, \tag{A.34}$$

with

$$\left\langle \frac{3}{2}M \left| T^\dagger_\lambda \right| \frac{1}{2}m \right\rangle = \left(\frac{1}{2}m1\lambda \,\middle|\, \frac{3}{2}M \right). \tag{A.35}$$

and

$$\mathbf{e}_{+1} = -\frac{1}{\sqrt{2}} \begin{pmatrix} 1 \\ \mathrm{i} \\ 0 \end{pmatrix}, \quad \mathbf{e}_0 = \begin{pmatrix} 0 \\ 0 \\ 1 \end{pmatrix}, \quad \mathbf{e}_{-1} = +\frac{1}{\sqrt{2}} \begin{pmatrix} 1 \\ -\mathrm{i} \\ 0 \end{pmatrix}. \tag{A.36}$$

We further define

$$T^\dagger_{\pm 1} = \mp \frac{T^\dagger_1 \pm \mathrm{i} T^\dagger_2}{\sqrt{2}}, \quad T^\dagger_0 = T^\dagger_3. \tag{A.37}$$

A.4.4 Derivation of isospin factors

With the above conventions, we can determine the following isospin factors — detailed compilations of the explicit forms can be found in Appendix A of Ref. [CSTL04], on pages 70–71 in [Mos99] or in Appendix F.2 in Ref. [Pen02].

For the isospin $1/2 \to 1/2$ transition, we find

$$\bar{\Psi}_\mathrm{R} \boldsymbol{\tau} \cdot \boldsymbol{\phi}\, \Psi_\mathrm{N} = \bar{R}^+ \bar{\pi}^0 p - \bar{R}^0 \bar{\pi}^0 n + \sqrt{2}\, \bar{R}^+ \bar{\pi}^- n + \sqrt{2}\, \bar{R}^0 \bar{\pi}^+ p. \tag{A.38}$$

In the same manner, we have for the isospin $1/2 \to 3/2$ transition

$$\begin{aligned} \bar{\Psi}_\mathrm{R} \mathbf{T}^\dagger \boldsymbol{\phi}\, \Psi_\mathrm{N} = &- \bar{R}^{++} \bar{\pi}^- p + \sqrt{\frac{2}{3}}\, \bar{R}^+ \bar{\pi}^0 p - \sqrt{\frac{1}{3}}\, \bar{R}^+ \bar{\pi}^- n \\ &+ \sqrt{\frac{1}{3}}\, \bar{R}^0 \bar{\pi}^+ p + \sqrt{\frac{2}{3}}\, \bar{R}^0 \bar{\pi}^0 n + \bar{R}^- \bar{\pi}^+ n. \end{aligned} \tag{A.39}$$

Note that $\bar{\pi}^{\pm,0} = \pi^{\pm,0}$.

B

Cross sections and kinematics

B.1 General expression for the cross section

The general expression of the differential cross section for the collision of two particles ($i = 1, 2$) and N outgoing particles ($f = 1, \ldots, N$) is given as (see, e.g., Ref. [IZ05]):

$$\mathrm{d}\sigma = \frac{(2\pi)^4}{4[(p_1 \cdot p_2)^2 - m_1^2 m_2^2]^{1/2}} \, \delta^4 \left(\sum_f p_f - \sum_i p_i \right) \left(\prod_f \frac{\mathrm{d}^4 p_f}{(2\pi)^3} \, \delta(p_f^2 - m_f^2) \right) \left| \bar{\mathcal{M}} \right|^2 , \tag{B.1}$$

where we adopt the normalization given on page 269. For particles on their mass-shell, we can further simplify this expression using that

$$\frac{\mathrm{d}^4 p}{(2\pi)^3} \, \delta(p^2 - m^2) = \frac{\mathrm{d}^3 p}{(2\pi)^3 \, 2p^0} = \frac{1}{(2\pi)^3} \, \frac{\sqrt{p^{0\,2} - m^2}}{2} \, \mathrm{d}\Omega \, \mathrm{d}p^0 . \tag{B.2}$$

B.2 Kinematics of the lepton-nucleon interaction

We shall now evaluate the cross section — suited also for scattering off bound nucleons and into broad states — for the general process

$$\ell(k) + N(p) \to \ell'(k') + \sum_f X_f(p'_f), \tag{B.3}$$

where X_f can be any final-state particle, e.g., a nucleon ($f = 1$), a resonance ($f = 1$) or a πN pair as in a background process ($f = 2$). We always assume that the incoming lepton moves in the z-direction, so that

$$k = (k^0, 0, 0, |\mathbf{k}|). \tag{B.4}$$

Following Eq. (B.1), the cross section is given by the most general expression

$$\begin{aligned} d\sigma = (2\pi)^4\, \delta^4 \left(k' + \sum_f p'_f - k - p \right)\, \frac{1}{4} \left[(k \cdot p)^2 - m_\ell^2 M^2 \right]^{-1/2} \\ \times \frac{\mathrm{d}^4 k'}{(2\pi)^3}\, \delta(k'^2 - m_{\ell'}^2) \prod_f \frac{\mathrm{d}^4 p'_f}{(2\pi)^3}\, \delta({p'_f}^2 - {M'_f}^2) |\bar{\mathcal{M}}|^2. \end{aligned} \tag{B.5}$$

With the outgoing lepton on-shell,

$$k'^0 = \sqrt{\mathbf{k}'^2 + m_{\ell'}^2}, \tag{B.6}$$

we can, using Eq. (B.2), further simplify the cross section formula and get

$$\begin{aligned} \mathrm{d}\sigma = (2\pi)^4\, \delta^4 \left(k' + \sum_f p'_f - k - p \right)\, \frac{1}{4} \left[(k \cdot p)^2 - m_\ell^2 M^2 \right]^{-1/2} \\ \times \frac{\sqrt{k'^{0 2} - m_{\ell'}^2}}{2(2\pi)^3}\, \mathrm{d}k'^0 \mathrm{d}\Omega_{k'} \prod_f \frac{\mathrm{d}^4 p'_f}{(2\pi)^3}\, \delta({p'_f}^2 - {M'_f}^2)\, |\bar{\mathcal{M}}|^2. \end{aligned} \tag{B.7}$$

In case of *scattering in the vacuum*, M denotes the free mass of the incoming nucleon, i.e., M_N, and M'_f the one of the outgoing hadron f. In *the nuclear medium* the particles are affected by the mean-field potential. Thus, all four-vectors appearing in these equations are in-medium four-vectors. Furthermore, M denotes the effective mass of the nucleon, i.e., $M = M_N + U_N(r, p)$ with the scalar potential defined in Eq. (7.6) (see page 83). The same applies to M'_f which, in the medium, is replaced by $M'_f = M_f + U_f(r', p')$. In general, the potentials may depend on position r and momentum p or r' and p', respectively.

B.2.1 Cross section for a single-hadron final state

Now let us have a closer look at the final state X. First, we focus on single-hadron final states as quasi-elastic scattering and resonance excitation, i.e., on processes like

$$\ell(k) + N(p) \to \ell'(k') + X(p'). \tag{B.8}$$

Starting from the general expression of Eq. (B.7) with $f = 1$ we obtain

$$\mathrm{d}\sigma = (2\pi)^4\,\delta^4\left(k' + p' - k - p\right)\;\frac{1}{4}\left[(k\cdot p)^2 - m_\ell^2 M^2\right]^{-1/2} \times \frac{\sqrt{k'^{0^2} - m_{\ell'}^2}}{2(2\pi)^3}\,\mathrm{d}k'^0\mathrm{d}\Omega_{k'}\;\frac{\mathrm{d}^4p'}{(2\pi)^3}\,\delta(p'^2 - M'^2)\;|\bar{\mathcal{M}}|^2, \tag{B.9}$$

and, performing the integral over d^4p',

$$\mathrm{d}\sigma = \frac{1}{32\pi^2}\left[(k\cdot p)^2 - m_\ell^2 M^2\right]^{-1/2}\sqrt{k'^{0^2} - m_{\ell'}^2}\;\mathrm{d}k'^0\mathrm{d}\Omega_{k'}\;\delta((k+p-k')^2 - M'^2)\;|\bar{\mathcal{M}}|^2, \tag{B.10}$$

we arrive at

$$\frac{\mathrm{d}\sigma}{\mathrm{d}k'^0\,\mathrm{d}\Omega_{k'}} = \frac{\mathrm{d}\sigma}{\mathrm{d}k'^0\,\mathrm{d}\phi\,\mathrm{d}\cos\theta} = \frac{|\mathbf{k}'|}{32\pi^2}\;\left[(k\cdot p)^2 - m_\ell^2 M^2\right]^{-1/2}\;\delta(p'^2 - M'^2)\;|\bar{\mathcal{M}}|^2, \tag{B.11}$$

with the limits $\cos\theta \in [-1,1]$, $\phi \in [0,2\pi]$ and $k'^0 \in \left[m_{\ell'}, k^0\right]$; k' and p' are fully defined for given k and p. M and M' are either the bare (free) or the effective masses of the particles as described on page 274.

Alternatively, one can express the cross section in terms of the Mandelstam variable t with $t = -Q^2 = m_\ell^2 + m_{\ell'}^2 - 2k^0k'^0 + 2|\mathbf{k}||\mathbf{k}'|\cos\theta$ (see Eq. (A.5)) which leads to

$$\mathrm{d}t = 2|\mathbf{k}||\mathbf{k}'|\;\mathrm{d}\cos\theta, \tag{B.12}$$

and we obtain

$$\frac{\mathrm{d}\sigma}{\mathrm{d}k'^0\,\mathrm{d}\phi\,\mathrm{d}t} = \frac{1}{64\pi^2}\;\left[(k\cdot p)^2 - m_\ell^2 M^2\right]^{-1/2}\;\frac{1}{|\mathbf{k}|}\;\delta(p'^2 - M'^2)\;|\bar{\mathcal{M}}|^2. \tag{B.13}$$

The limits in t are determined by setting $\cos\theta$ to 1 or -1, respectively.

For on-shell nucleons, the δ-function can be integrated out. For broad states (like resonances) in the final state, it is replaced by the spectral function of the particle,

$$\delta(p'^2 - M'^2) \to \mathcal{A}(p', r'), \tag{B.14}$$

with M' depending on position r' and momentum p' as defined on page 274. Hereby, the norm of $\mathcal{A}$ is fixed to

$$\int_0^\infty \mathrm{d}p'^2\mathcal{A}(p', r') = 1. \tag{B.15}$$

B.2.2 Cross section for a two-hadron final state

Now we proceed with the cross section for a two-hadron final state, X, e.g., the $N\pi$ background,

$$\ell(k) + N(p) \to \ell'(k') + N'(p') + \pi(k_\pi). \tag{B.16}$$

Starting from the general expression of Eq. (B.7), we set $f = 2$ (number of final-state particles) and begin with

$$\begin{aligned} \mathrm{d}\sigma = {} & (2\pi)^4\, \delta^4(k' + p' + k_\pi - k - p)\, \frac{1}{4} \left[(k\cdot p)^2 - m_\ell^2 M^2\right]^{-1/2} \\ & \times \frac{\sqrt{k'^{0^2} - m_{\ell'}^2}}{2(2\pi)^3}\, \mathrm{d}k'^0 \mathrm{d}\Omega_{k'}\, \frac{\mathrm{d}^4 p'}{(2\pi)^3}\, \delta(p'^2 - M'^2)\, \frac{\mathrm{d}^4 k_\pi}{(2\pi)^3}\, \delta(k_\pi^2 - m_\pi^2)\, |\bar{\mathcal{M}}|^2. \end{aligned} \tag{B.17}$$

Assuming that the outgoing pion is on the mass-shell, using Eq. (B.2), we can further simplify the cross section formula to

$$\begin{aligned} \mathrm{d}\sigma = {} & (2\pi)^4\, \delta^4(k' + p' + k_\pi - k - p)\, \frac{1}{4} \left[(k\cdot p)^2 - m_\ell^2 M^2\right]^{-1/2} \\ & \times \frac{\sqrt{k'^{0^2} - m_{\ell'}^2}}{2(2\pi)^3}\, \mathrm{d}k'^0 \mathrm{d}\Omega_{k'}\, \frac{\mathrm{d}^4 p'}{(2\pi)^3}\, \delta(p'^2 - M'^2)\, \frac{\sqrt{k_\pi^{0\,2} - m_\pi^2}}{2(2\pi)^3}\, \mathrm{d}k_\pi^0 \mathrm{d}\Omega_{k_\pi}\, |\bar{\mathcal{M}}|^2. \end{aligned} \tag{B.18}$$

Next, we perform the integral over $\mathrm{d}^4 p'$

$$\begin{aligned} \mathrm{d}\sigma = {} & \frac{1}{512\pi^5}\, \left[(k\cdot p)^2 - m_\ell^2 M^2\right]^{-1/2} \\ & \times \sqrt{k'^{0^2} - m_{\ell'}^2}\mathrm{d}k'^0 \mathrm{d}\Omega_{k'}\, \delta((k + p - k' - k_\pi)^2 - M'^2)\, \sqrt{k_\pi^{0\,2} - m_\pi^2}\, \mathrm{d}k_\pi^0 \mathrm{d}\Omega_{k_\pi}\, |\bar{\mathcal{M}}|^2, \end{aligned} \tag{B.19}$$

and we arrive at

$$\frac{\mathrm{d}\sigma}{\mathrm{d}k'^0 \mathrm{d}\Omega_{k'} \mathrm{d}k_\pi^0 \mathrm{d}\Omega_{k_\pi}} = \frac{|\mathbf{k}'||\mathbf{k}_{\boldsymbol{\pi}}|}{512\pi^5}\, \left[(k\cdot p)^2 - m_\ell^2 M^2\right]^{-1/2} \delta(p'^2 - M'^2)\, |\bar{\mathcal{M}}|^2 \tag{B.20}$$

with $p' = k + p - k' - k_\pi$, $|\mathbf{k}'| = \sqrt{k'^{0^2} - m_{\ell'}^2}$ and $|\mathbf{k}_{\boldsymbol{\pi}}| = \sqrt{k_\pi^{0\,2} - m_\pi^2}$. The δ-function $\delta(p'^2 - M'^2)$ is now either replaced by the spectral function of the final nucleon or, in case of on-shell nucleons, integrated out to eliminate the k_π^0 dependence. Depending on whether the scattering process happens in the vacuum or in the medium, M and M' are either the bare (free) or the effective masses of the participating nucleons, as explained on page 274.

Table B.1: Threshold energies according to Eq. (B.24) for different combinations of the final-state masses and $m_\ell = 0$.

	$M_{\text{hadr}} = M_N$	$M_{\text{hadr}} = M_N + m_\pi$
$m_{\ell'} = 0$	0 GeV	0.175 GeV
$m_{\ell'} = m_e$	~ 0 GeV	0.177 GeV
$m_{\ell'} = m_\mu$	0.111 GeV	0.305 GeV
$m_{\ell'} = m_\tau$	3.450 GeV	3.940 GeV

B.3 Kinematics

B.3.1 Energy thresholds for neutrino scattering

The total energy available for the reaction is given

$$s = (k + p)^2, \tag{B.21}$$

with the Mandelstam variable s. Energy conservation implies, that

$$s = (k + p)^2 = (k' + p')^2. \tag{B.22}$$

The minimal energy in the cm frame required for a given channel to be open is $m_{\ell'} + M_{\text{hadr}}$, thus, we have

$$(k + p)^2 = m_\ell^2 + M_N^2 + 2k^0 p^0 - 2\mathbf{k} \cdot \mathbf{p} = (m_{\ell'} + M_{\text{hadr}})^2. \tag{B.23}$$

Then, the minimal energy of the incoming lepton in the LAB frame reads

$$k^0 = \frac{(m_{\ell'} + M_{\text{hadr}})^2 - M_N^2 - m_\ell^2}{2(p^0 - p^3)} \,. \tag{B.24}$$

For a nucleon at rest, with $\mathbf{p} = \mathbf{0}$, we have $p^0 - p^3 = M_N$ and obtain the threshold energies given in Table B.1.

B.3.2 Useful relations

Leptonic reactions can be described with different sets of variables, e.g., the incoming lepton energy, k^0, the outgoing lepton energy, k'^0, and the scattering angle of the outgoing lepton, $\cos\theta$, or — fully equivalent — k^0, the lepton four-momentum transfer squared, Q^2, and the invariant mass, W, of the outgoing hadrons. In this section, we give the relations that connect them.

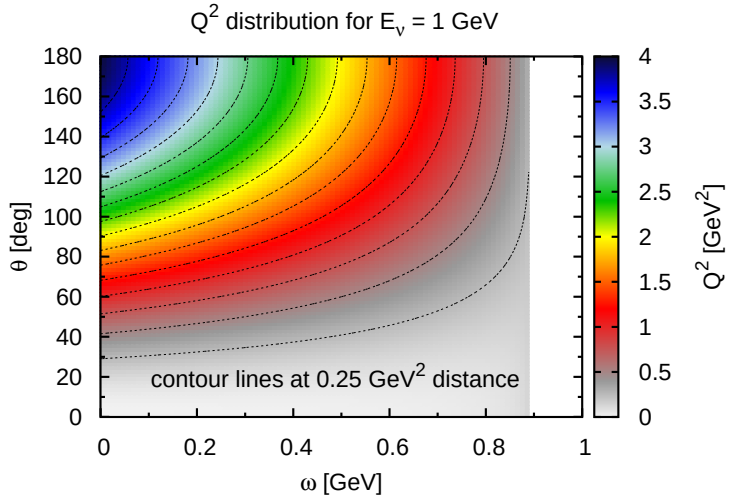

Figure B.1: Q^2 distribution for $k^0 = 1\,\mathrm{GeV}$, $m_\ell = 0$ and $m_{\ell'} = m_\mu$ as a function of the energy transfer ω and scattering angle θ.

We start by relating the leptonic variables k^0, k'^0, $\cos\theta$ to Q^2 so that (cf., Eq. (A.5))

$$Q^2 = -m_\ell^2 - m_{\ell'}^2 + 2k^0(k'^0 - |\mathbf{k}'|\cos\theta). \tag{B.25}$$

As an example, we show in Fig. B.1 the Q^2 distribution for $k^0 = 1\,\mathrm{GeV}$, $m_\ell = 0$ and $m_{\ell'} = m_\mu$.

For the following illustrations, we make the assumption, that the initial nucleon is at rest, i.e, $p = (M_N, \mathbf{0})$. Then, the invariant mass W of the final hadronic system is given by

$$W^2 = -Q^2 + M_N^2 + 2M_N\omega, \tag{B.26}$$

which is plotted in Fig. B.2 for the same sample as above. The absolute momentum of the final state reads

$$|\mathbf{p}'| = \sqrt{\mathbf{q}^2} = \sqrt{Q^2 + \omega^2}\,, \tag{B.27}$$

and is shown in Fig. B.3 for the same kinematics as above.

The value of Q^2 at the quasielastic peak or vice versa, the position of the peak in ω — in the nucleon rest frame and neglecting any binding — is then derived by setting in Eq. (B.26) $W = M_N$. We get

$$Q^2 = 2M_N\omega. \tag{B.28}$$

Rewriting Q^2 in terms of the variables ω and $\cos\theta$ according to Eq. (B.25) gives

$$\omega = \frac{Q^2}{2M_N} = \frac{-m_\ell^2 - m_{\ell'}^2 + 2k^0(k'^0 - |\mathbf{k}'|\cos\theta)}{2M_N}\,. \tag{B.29}$$

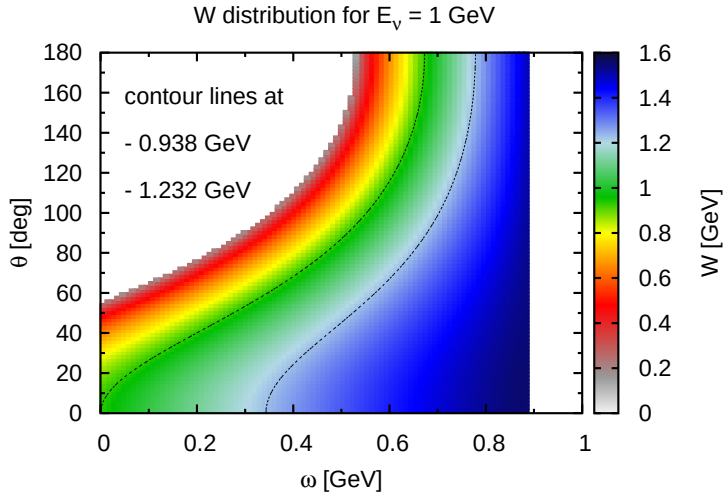

Figure B.2: W distribution for $k^0 = 1\,\text{GeV}$, $m_\ell = 0$ and $m_{\ell'} = m_\mu$ as a function of the energy transfer $\omega = k^0 - k'^0$ and scattering angle θ under the assumption that the initial nucleon is at rest.

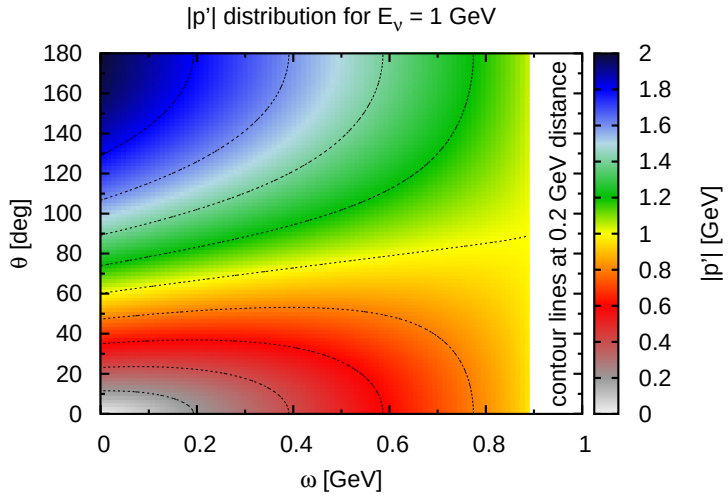

Figure B.3: $|\mathbf{p}'|$ distribution for $k^0 = 1\,\text{GeV}$, $m_\ell = 0$ and $m_{\ell'} = m_\mu$ as a function of the energy transfer $\omega = k^0 - k'^0$ and scattering angle θ under the assumption that the initial nucleon is at rest.

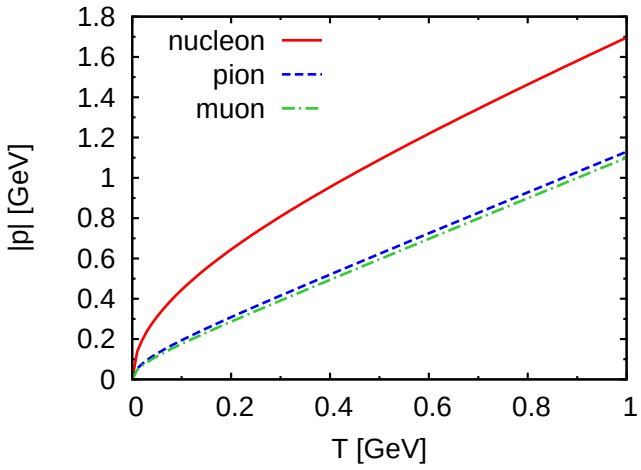

Figure B.4: Relation between kinetic energy and momentum for nucleons, pions and muons.

This can be further simplified for $m_\ell = m_{\ell'} = 0$, so that

$$\omega = \frac{k^0 k'^0}{M_N}(1 - \cos\theta). \tag{B.30}$$

Finally, we show in Fig. B.4 the relation between kinetic energy and momentum for nucleons, pions and muons according to

$$T = E - m = \sqrt{|\mathbf{p}|^2 + m^2} - m. \tag{B.31}$$

B.3.3 Limits

The limits in k'^0, $\cos\theta$ and ϕ are given by

$$m_{\ell'} \leq k'^0 \leq k^0, \tag{B.32}$$
$$-1 \leq \cos\theta \leq 1, \tag{B.33}$$
$$0 \leq \phi \leq 2\pi. \tag{B.34}$$

The limits in W and Q^2 are nicely derived on page 10 of Ref. [HNV07] (see also their Figure 3). In the following, we summarize the results. We take as independent variables k^0, W and Q^2. For a given incoming lepton energy, W is fixed in the range

$$M_{\text{hadr}} \leq W \leq \sqrt{s} - m_{\ell'}\,, \tag{B.35}$$

with $s = (k+p)^2 = M_N(M_N + 2k^0)$. M_{hadr} is the minimal mass of the final hadronic system, e.g., M_N or $M_N + m_\pi$. Then, $q^2 = -Q^2$ lies in the interval

$$\left[m_{\ell'}^2 - 2E_{\text{cm}}\left(E'_{\text{cm}} + \sqrt{E'^2_{\text{cm}} - m_{\ell'}^2}\right)\right] \leq q^2 \leq \left[m_{\ell'}^2 - 2E_{\text{cm}}\left(E'_{\text{cm}} - \sqrt{E'^2_{\text{cm}} - m_{\ell'}^2}\right)\right], \tag{B.36}$$

with $E_{\text{cm}} = (s - M_N^2)/(2\sqrt{s})$ and $E'_{\text{cm}} = (s - W^2 + m_{\ell'}^2)/(2\sqrt{s})$.

C

Feynman rules and electro-weak transition matrix elements

C.1 Feynman rules

External particle: An external line, representing a lepton or a quark, corresponds to a spinor $u(k,s)$ ($\bar{v}(k,s)$) for incoming (anti-)particles, or $\bar{u}(k',s')$ ($v(k',s')$) for outgoing (anti-)particles.

Propagators:

- Photon:
$$\frac{\mathrm{i}}{q^2}(-g^{\mu\nu}) \tag{C.1}$$
- Massive vector boson:
$$\frac{\mathrm{i}}{q^2 - M_V^2}\left(-g^{\mu\nu} + \frac{q^\mu q^\nu}{M_V^2}\right) \xrightarrow{|q^2| \ll M_V^2} \frac{\mathrm{i}\, g^{\mu\nu}}{M_V^2} \tag{C.2}$$
M_V is either the $W^\pm$ or of the Z boson mass.

Vertices:

- Electromagnetic vertex:
$$-\mathrm{i}e\gamma_\mu \equiv -\mathrm{i}\sqrt{4\pi\alpha}\gamma_\mu \tag{C.3}$$

- Weak vertex (W exchange):

$$-\mathrm{i}\frac{g}{\sqrt{2}}\, c\, \gamma_\mu \frac{1-\gamma^5}{2} \tag{C.4}$$

  with $c = 1$ for leptons, and $c = U_{qq'}$ for quarks, where $U_{qq'}$ is the appropriate entry of the Cabbibo-mixing matrix.

- Weak vertex (Z exchange):

$$\frac{-\mathrm{i}e}{\sin\theta_W \cos\theta_W}\gamma_\mu \left(c_L \frac{1-\gamma^5}{2} + c_R \frac{1+\gamma^5}{2} \right) \tag{C.5}$$

  c_L and c_R are defined as

	c_L	c_R
neutrinos	$\frac{1}{2}$	0
up quarks	$+\frac{1}{2} - \frac{2}{3}\sin^2\theta_W$	$-\frac{2}{3}\sin^2\theta_W$
down quarks	$-\frac{1}{2} + \frac{1}{3}\sin^2\theta_W$	$\frac{1}{3}\sin^2\theta_W$

Relations between electromagnetic and weak couplings. In the static limit of $|q^2| \ll M_V^2$, the weak coupling can be expressed in terms of Fermi's constant as

$$\frac{G_F}{\sqrt{2}} = \frac{g^2}{8M_W^2} = \frac{e^2}{8M_Z^2 \sin^2\theta_W \cos^2\theta_W}, \tag{C.6}$$

where

$$e = g\sin\theta_W, \quad \cos\theta_W = \frac{M_W}{M_Z}. \tag{C.7}$$

The values of the constants are given in Table A.2 on page 266.

C.2 Electro-weak transition matrix elements

Applying the Feynman rules summarized above one obtains the following amplitudes.

C.2.1 Electromagnetic transition (EM): $\ell^- N \longrightarrow \ell^- X$

The matrix element for EM reactions of charged leptons can be written as

$$\begin{aligned}\mathcal{M} &= 4\pi\alpha\bar{u}(k')\gamma_\mu u(k)\frac{-\mathrm{i}g^{\mu\nu}}{q^2}\left\langle X(p'_f)\left|J_\nu(0)\right|N(p)\right\rangle \\ &= \mathrm{i}\frac{4\pi\alpha}{Q^2}\bar{u}(k')\gamma_\mu u(k)\ \left\langle X(p'_f)\left|J_\nu(0)\right|N(p)\right\rangle, \end{aligned} \tag{C.8}$$

and one obtains

$$C_{\mathrm{EM}} = \frac{4\pi\alpha}{Q^2}. \tag{C.9}$$

C.2.2 Charged-current transition (CC): $\nu N \longrightarrow \ell^- X$

The matrix element for charged current reactions of neutrinos is given as

$$\begin{aligned}\mathcal{M} &= \left(\frac{g\cos\theta_C}{2\sqrt{2}}\right)^2\bar{u}(k')\gamma_\mu(1-\gamma^5)u(k)\frac{\mathrm{i}g^{\mu\nu}}{M_W^2}\left\langle X(p'_f)\left|J_\nu(0)\right|N(p)\right\rangle \\ &= \mathrm{i}\frac{G_F\cos\theta_C}{\sqrt{2}}\bar{u}(k')\gamma_\mu(1-\gamma^5)u(k)\ \left\langle X(p'_f)\left|J_\nu(0)\right|N(p)\right\rangle, \end{aligned} \tag{C.10}$$

so that

$$C_{\mathrm{CC}} = \frac{G_F\cos\theta_C}{\sqrt{2}}. \tag{C.11}$$

C.2.3 Neutral-current transition (NC): $\nu N \longrightarrow \nu X$

For neutral currents the matrix element is modified due to the different coupling and reads

$$\begin{aligned}\mathcal{M} &= \left(\frac{e}{2\sin\theta_W\cos\theta_W}\right)^2\bar{u}(k')\gamma_\mu\frac{1-\gamma^5}{2}u(k)\frac{\mathrm{i}g^{\mu\nu}}{M_Z^2}\left\langle X(p'_f)\left|J_\nu(0)\right|N(p)\right\rangle \\ &= \mathrm{i}\frac{G_F}{\sqrt{2}}\bar{u}(k')\gamma_\mu(1-\gamma^5)u(k)\ \left\langle X(p'_f)\left|J_\nu(0)\right|N(p)\right\rangle. \end{aligned} \tag{C.12}$$

Thus, the coupling reads

$$C_{\mathrm{NC}} = \frac{G_F}{\sqrt{2}}. \tag{C.13}$$

D
Isospin relations

D.1 QE scattering and excitation of nucleon resonances: isospin 1/2 to isospin 1/2 transition

In general, the isovector part of the current is given by

$$\mathbf{J}^\mu = (J_1^\mu, J_2^\mu, J_3^\mu) = \mathbf{V}^\mu - \mathbf{A}^\mu, \tag{D.1}$$

with

$$\mathbf{V}^\mu = (V_1^\mu, V_2^\mu, V_3^\mu) = \mathcal{V}^\mu \frac{\boldsymbol{\tau}}{2} \tag{D.2}$$

$$\mathbf{A}^\mu = (A_1^\mu, A_2^\mu, A_3^\mu) = \mathcal{A}^\mu \frac{\boldsymbol{\tau}}{2}, \tag{D.3}$$

where $\boldsymbol{\tau}$ is the isospin 1/2 transition operator given by the Pauli matrices (cf. Appendix A.4). $\mathcal{V}^\mu$ and $\mathcal{A}^\mu$ are given in Eqs. (4.7) and (4.8) for QE scattering (Eqs. (5.5) and (5.6) for spin 1/2 resonance excitation) where $\mathcal{F}_i$ ($i = 1, 2$) stands for the CC form factors, F_i^V, and $\mathcal{F}_A$ for F_A. For spin 3/2 resonances, $\mathcal{V}^\mu$ and $\mathcal{A}^\mu$ are given in Eqs. (5.14) and (5.15) where $C_i^{V,A}$, $i = 3, \ldots, 6$, stands for the CC form factors $C_i^{V,A}$.

In a transition between isospin 1/2 states, both, isoscalar and isovector parts of the current contribute as shown in Section 2.3. Therefore, we further define for the hypercharge part

$$V_Y^\mu = \mathcal{V}_Y^\mu \mathbb{1}_2, \tag{D.4}$$

which enters Eq. (2.32) and Eq. (2.34), and

$$V_S^\mu = \mathcal{V}_S^\mu \mathbb{1}_2, \tag{D.5}$$

$$A_S^\mu = \mathcal{A}_S^\mu \mathbb{1}_2, \tag{D.6}$$

for the strange component entering Eq. (2.34) and Eq. (2.36), respectively. $\mathbb{1}_2$ is the 2×2 unit matrix. $\mathcal{V}_Y^\mu$, $\mathcal{V}_S^\mu$ and $\mathcal{A}_S^\mu$ are given in Eqs. (4.7) and (4.8) for QE, in Eqs. (5.5) and (5.6) for spin $1/2$ and in Eqs. (5.14) and (5.15) for spin $3/2$, *but* with the corresponding form factors: $\mathcal{F}_i$ stands for either for F_i^Y or the strange form factor F_i^s, $\mathcal{F}_A$ for F_A^s; $\mathcal{C}_i^V$ stands either for C_i^Y or $C_i^{s_V}$, $\mathcal{C}_i^A$ for $C_i^{s_A}$.

We obtain for the electromagnetic transition matrix element using Eq. (2.32)

$$\begin{aligned}
\left\langle N^{*+} \left| J_{\mathrm{EM}}^\mu \right| p \right\rangle &= \left\langle N^{*+} \left| V_3^\mu + \frac{1}{2} V_Y^\mu \right| p \right\rangle \\
&= \left\langle N^{*+} \left| \mathcal{V}^\mu \frac{\tau_3}{2} + \mathcal{V}_Y^\mu \frac{\mathbb{1}_2}{2} \right| p \right\rangle \\
&= \frac{\mathcal{V}^\mu + \mathcal{V}_Y^\mu}{2} \\
&\equiv \mathcal{V}_p^\mu,
\end{aligned} \tag{D.7}$$

and, analogously,

$$\left\langle N^{*0} \left| J_{\mathrm{EM}}^\mu \right| n \right\rangle = \frac{-\mathcal{V}^\mu + \mathcal{V}_Y^\mu}{2} \equiv \mathcal{V}_n^\mu. \tag{D.8}$$

This yields the relations

$$\mathcal{V}^\mu = \mathcal{V}_p^\mu - \mathcal{V}_n^\mu, \tag{D.9}$$

$$\mathcal{V}_Y^\mu = \mathcal{V}_p^\mu + \mathcal{V}_n^\mu. \tag{D.10}$$

$\mathcal{V}_p^\mu$ and $\mathcal{V}_n^\mu$ are given in Eq. (4.7) for QE (Eq. (5.5) for spin $1/2$) but where $\mathcal{F}_i$ ($i = 1, 2$) stands for the EM form factors, F_i^p and F_i^n. For spin $3/2$ resonances, $\mathcal{V}_p^\mu$ and $\mathcal{V}_n^\mu$ are given in Eq. (5.14) with $\mathcal{C}_i^V$ replaced by C_i^p and C_i^n.

The vector part of the charged current transition matrix element is [Eq. (2.33)]

$$\begin{aligned}
\left\langle N^{*+} \left| V_{\mathrm{CC}}^\mu \right| n \right\rangle &= \left\langle N^{*+} \left| V_1^\mu + \mathrm{i} V_2^\mu \right| n \right\rangle \\
&= \left\langle N^{*+} \left| \mathcal{V}^\mu \tau_+ \right| n \right\rangle \\
&= \mathcal{V}^\mu,
\end{aligned} \tag{D.11}$$

which together with Eq. (D.9) relates EM and CC form factors: $\left\langle N^{*+} \left| V_{\mathrm{CC}}^\mu \right| n \right\rangle$ can be written as $\mathcal{V}_p^\mu - \mathcal{V}_n^\mu$ and thus, $F_i^V = F_i^p - F_i^n$ for nucleons and spin $1/2$ resonances and $C_i^V = C_i^p - C_i^n$ for spin $3/2$ resonances.

Applying the same procedure to NC, one gets with Eq. (2.34)

$$\begin{aligned}\left\langle N^{*+}\left|V^{\mu}_{\mathrm{NC}}\right|p\right\rangle &= \left\langle N^{*+}\left|(1-2\sin^2\theta_W)V^{\mu}_3 - \sin^2\theta_W V^{\mu}_Y - \frac{1}{2}V^{\mu}_S\right|p\right\rangle \\ &= \left\langle N^{*+}\left|(1-2\sin^2\theta_W)\mathcal{V}^{\mu}\frac{\tau_3}{2} - \sin^2\theta_W\mathcal{V}^{\mu}_Y\mathbb{1}_2 - \mathcal{V}^{\mu}_S\frac{\mathbb{1}_2}{2}\right|p\right\rangle \\ &= \left(\frac{1}{2}-\sin^2\theta_W\right)\mathcal{V}^{\mu} - \sin^2\theta_W\mathcal{V}^{\mu}_Y - \frac{1}{2}\mathcal{V}^{\mu}_S, \end{aligned} \tag{D.12}$$

and also

$$\left\langle N^{*0}\left|V^{\mu}_{\mathrm{NC}}\right|n\right\rangle = -\left(\frac{1}{2}-\sin^2\theta_W\right)\mathcal{V}^{\mu} - \sin^2\theta_W\mathcal{V}^{\mu}_Y - \mathcal{V}^{\mu}_S\frac{1}{2}. \tag{D.13}$$

The NC transition matrix elements are expressed in terms of $\mathcal{V}^{\mu}$, $\mathcal{V}^{\mu}_Y$ and $\mathcal{V}^{\mu}_S$. Hereby, we relate the NC form factors via Eq. (D.9) and Eq. (D.10) to the EM proton and neutron form factors — in addition, strange form factors coming from $\mathcal{V}_S$ have to be considered. We find for the neutral current form factors

$$\begin{aligned}\tilde{F}^p_i &= \left(\frac{1}{2}-\sin^2\theta_W\right)\left(F^p_i - F^n_i\right) - \sin^2\theta_W\left(F^p_i + F^n_i\right) - \frac{1}{2}F^s_i \\ &= \left(\frac{1}{2}-2\sin^2\theta_W\right)F^p_i - \frac{1}{2}F^n_i - \frac{1}{2}F^s_i, \end{aligned} \tag{D.14}$$

and

$$\begin{aligned}\tilde{F}^n_i &= -\left(\frac{1}{2}-\sin^2\theta_W\right)\left(F^p_i - F^n_i\right) - \sin^2\theta_W\left(F^p_i + F^n_i\right) - \frac{1}{2}F^s_i \\ &= \left(\frac{1}{2}-2\sin^2\theta_W\right)F^n_i - \frac{1}{2}F^p_i - \frac{1}{2}F^s_i, \end{aligned} \tag{D.15}$$

for spin 1/2 and analogous for spin 3/2 resonances.

One can proceed in the same way for the axial part and get with Eq. (2.35)

$$\begin{aligned}\left\langle N^{*+}\left|A^{\mu}_{\mathrm{CC}}\right|n\right\rangle &= \left\langle N^{*+}\left|A^{\mu}_1 + \mathrm{i}A^{\mu}_2\right|n\right\rangle \\ &= \left\langle N^{*+}\left|\mathcal{A}^{\mu}\tau_+\right|n\right\rangle \\ &= \mathcal{A}^{\mu}, \end{aligned} \tag{D.16}$$

while, for neutral currents, with Eq. (2.36)

$$\begin{aligned}\left\langle N^{*+}\left|A^{\mu}_{\mathrm{NC}}\right|p\right\rangle &= \left\langle N^{*+}\left|A^{\mu}_3 + \frac{1}{2}A^{\mu}_S\right|p\right\rangle \\ &= \left\langle N^{*+}\left|\mathcal{A}^{\mu}\frac{\tau_3}{2} + \mathcal{A}^{\mu}_S\frac{\mathbb{1}_2}{2}\right|p\right\rangle \\ &= \frac{\mathcal{A}^{\mu} + \mathcal{A}^{\mu}_S}{2}, \end{aligned} \tag{D.17}$$

and

$$\left\langle N^{*0} \left| A^{\mu}_{\mathrm{NC}} \right| n \right\rangle = \frac{-\mathcal{A}^{\mu} + \mathcal{A}^{\mu}_{S}}{2}, \tag{D.18}$$

which connects the NC axial form factors with the CC and the strange axial form factors such that $\tilde{F}^{p}_{A} = \frac{1}{2}F_A + \frac{1}{2}F^{s}_{A}$ and $\tilde{F}^{n}_{A} = -\frac{1}{2}F_A + \frac{1}{2}F^{s}_{A}$ for spin 1/2 (analogous for spin 3/2).

D.2 Excitation of Δ resonances: isospin 1/2 to isospin 3/2 transition

The full electroweak current can expressed as

$$\mathbf{J}^{\mu} = \mathbf{V}^{\mu} - \mathbf{A}^{\mu}, \tag{D.19}$$

with

$$\mathbf{V}^{\mu} = -\sqrt{\frac{3}{2}}\,\mathcal{V}^{\mu}\,\mathbf{T}^{+}, \tag{D.20}$$

$$\mathbf{A}^{\mu} = -\sqrt{\frac{3}{2}}\,\mathcal{A}^{\mu}\,\mathbf{T}^{+}, \tag{D.21}$$

where $\mathbf{T}^{+}$ is the $1/2 \to 3/2$ transition operator introduced in Appendix A.4. $\mathcal{V}^{\mu}$ and $\mathcal{A}^{\mu}$ are given in Eqs. (5.5) and (5.6) for spin 1/2 resonances where $\mathcal{F}_i$ ($i = 1, 2$) stands for the CC form factors, F^{V}_{i}, and $\mathcal{F}_A$ for F_A. For spin 3/2 resonances, $\mathcal{V}^{\mu}$ and $\mathcal{A}^{\mu}$ are given in Eqs. (5.14) and (5.15) where $\mathcal{C}^{V,A}_{i}$, $i = 3, \ldots, 6$, stands for the CC form factors $C^{V,A}_{i}$.

The transition current between $I = 1/2$ and $I = 3/2$ is purely isovector, so that Eq. (2.32) reads

$$J^{\mu}_{\mathrm{EM}} = V^{\mu}_{3} = V^{\mu}_{0} = -\sqrt{\frac{3}{2}}\,\mathcal{V}^{\mu} T^{+}_{0}. \tag{D.22}$$

This yields for the electromagnetic transition matrix element

$$\left\langle \Delta^{+} \left| J^{\mu}_{\mathrm{EM}} \right| p \right\rangle = -\sqrt{\frac{3}{2}}\,\mathcal{V}^{\mu} \left(\frac{1}{2}\,\frac{1}{2}\,1\,0 \,\middle|\, \frac{3}{2}\,\frac{1}{2} \right) = -\mathcal{V}^{\mu}, \tag{D.23}$$

$$\left\langle \Delta^{0} \left| J^{\mu}_{\mathrm{EM}} \right| n \right\rangle = -\sqrt{\frac{3}{2}}\,\mathcal{V}^{\mu} \left(\frac{1}{2}\,-\frac{1}{2}\,1\,0 \,\middle|\, \frac{3}{2}\,-\frac{1}{2} \right) = -\mathcal{V}^{\mu}. \tag{D.24}$$

The prefactor of $\sqrt{\frac{3}{2}}$ is chosen such that the electromagnetic matrix element carries no isospin factor. The minus-sign in front is convention — it is consistent with what is commonly found in the literature [SvH73].

For the vector part of the weak charged current, we obtain with Eq. (2.33)

$$V^\mu_{\mathrm{CC}} = V^\mu_1 + \mathrm{i}V^\mu_2 = -\sqrt{2}\left(-\sqrt{\frac{3}{2}}\,\mathcal{V}^\mu\right) T^+_{+1} = \sqrt{3}\,\mathcal{V}^\mu T^+_{+1}\,, \tag{D.25}$$

and therefore

$$\left\langle \Delta^{++}\left|V^\mu_{\mathrm{CC}}\right|p\right\rangle = \sqrt{3}\,\mathcal{V}^\mu \left(\frac{1}{2}\;\frac{1}{2}\;1\;1\,\middle|\,\frac{3}{2}\;\frac{3}{2}\right) = \sqrt{3}\mathcal{V}^\mu, \tag{D.26}$$

$$\left\langle \Delta^{+}\left|V^\mu_{\mathrm{CC}}\right|n\right\rangle = \sqrt{3}\,\mathcal{V}^\mu \left(\frac{1}{2}\;-\frac{1}{2}\;1\;1\,\middle|\,\frac{3}{2}\;\frac{1}{2}\right) = \mathcal{V}^\mu. \tag{D.27}$$

This agrees with the standard expression found in the literature (e.g., pages 144-145 in Ref. [FN79] and page 5 in Ref. [HNV07]). Since both the EM and the CC transition matrix elements are expressed in terms of $\mathcal{V}^\mu$, we can relate the form factors so that $F_i^V = -F_i^N$ for spin 1/2 and $C_i^V = -C_i^N$ for spin 3/2 (identical for $N = p, n$). In the case of Δ^{++} excitation, the form factors need to be multiplied by $\sqrt{3}$ (cf. Eq. (D.26)).

Analogously, we get for the axial part of the charged current with Eq. (2.35)

$$A^\mu_{\mathrm{CC}} = A^\mu_1 + \mathrm{i}A^\mu_2 = \sqrt{3}\,\mathcal{A}^\mu T^+_{+1}\,, \tag{D.28}$$

leading to

$$\left\langle \Delta^{++}\left|A^\mu_{\mathrm{CC}}\right|p\right\rangle = \sqrt{3}\mathcal{A}^\mu, \tag{D.29}$$

$$\left\langle \Delta^{+}\left|A^\mu_{\mathrm{CC}}\right|n\right\rangle = \mathcal{A}^\mu. \tag{D.30}$$

For neutral currents — again, only the isovector part of Eq. (2.34) and Eq. (2.36) is present — we have

$$V^\mu_{\mathrm{NC}} = (1 - 2\sin^2\theta_W)V^\mu_3 = (1 - 2\sin^2\theta_W)\left(-\sqrt{\frac{3}{2}}\,\mathcal{V}^\mu\right) T^+_0\,, \tag{D.31}$$

so that

$$\left\langle \Delta^{+}\left|V^\mu_{\mathrm{NC}}\right|p\right\rangle = \left\langle \Delta^{0}\left|V^\mu_{\mathrm{NC}}\right|n\right\rangle = -(1 - 2\sin^2\theta_W)\,\mathcal{V}^\mu, \tag{D.32}$$

and

$$A^\mu_{\mathrm{NC}} = A^\mu_3 = -\sqrt{\frac{3}{2}}\,\mathcal{A}^\mu T^+_0\,, \tag{D.33}$$

leading to

$$\left\langle \Delta^{+}\left|A^\mu_{\mathrm{NC}}\right|p\right\rangle = \left\langle \Delta^{0}\left|A^\mu_{\mathrm{NC}}\right|n\right\rangle = -\mathcal{A}^\mu. \tag{D.34}$$

Relating the form factors using Eqs. (D.24) and (D.30) gives $\tilde{F}_i^N = (1 - 2\sin^2\theta_W)F_i^N$ and $\tilde{F}_A^N = -F_A$ for spin 1/2, and ${}_N\tilde{C}_i^V = (1 - 2\sin^2\theta_W)C_i^N$ and ${}_N\tilde{C}_i^A = -C_i^A$ for spin 3/2.

D.3 Isospin relations for the non-resonant background

We obtain the following relations between the vector contribution V^{μ}_{CC} and the electromagnetic current J^{μ}_{EM}:

$$\langle p\pi^+ | V^{\mu}_{\mathrm{CC}} | p \rangle = \sqrt{2} \left\langle n\pi^0 \left| J^{\mu}_{\mathrm{EM}} \right| n \right\rangle + \langle p\pi^- | J^{\mu}_{\mathrm{EM}} | n \rangle , \tag{D.35}$$

$$\langle n\pi^+ | V^{\mu}_{\mathrm{CC}} | n \rangle = \sqrt{2} \left\langle p\pi^0 \left| J^{\mu}_{\mathrm{EM}} \right| p \right\rangle - \langle p\pi^- | J^{\mu}_{\mathrm{EM}} | n \rangle , \tag{D.36}$$

$$\left\langle p\pi^0 \left| V^{\mu}_{\mathrm{CC}} \right| n \right\rangle = \left\langle p\pi^0 \left| J^{\mu}_{\mathrm{EM}} \right| p \right\rangle - \left\langle n\pi^0 \left| J^{\mu}_{\mathrm{EM}} \right| n \right\rangle - \sqrt{2} \langle p\pi^- | J^{\mu}_{\mathrm{EM}} | n \rangle . \tag{D.37}$$

E

Form factors and helicity amplitudes

Here we give details on the connection between the electromagnetic resonance form factors and helicity amplitudes, which we apply to obtain the form factors from the helicity amplitudes provided by MAID [MAID, TK06, DKT07].

The helicity amplitudes describe the nucleon-resonance transition depending on the polarization of the incoming photon and the spins of the baryons; they can be defined in various ways [WSPR90, Sto93, ABL08]. We use the following notation

$$\begin{aligned} A^N_{1/2} &= \sqrt{\frac{2\pi\alpha}{k_R}} \left\langle R, J_z = 1/2 \left| \epsilon^+_\mu J^\mu_{\mathrm{EM}} \right| N, J_z = -1/2 \right\rangle \zeta, \\ A^N_{3/2} &= \sqrt{\frac{2\pi\alpha}{k_R}} \left\langle R, J_z = 3/2 \left| \epsilon^+_\mu J^\mu_{\mathrm{EM}} \right| N, J_z = 1/2 \right\rangle \zeta, \\ S^N_{1/2} &= -\sqrt{\frac{2\pi\alpha}{k_R}} \frac{|\mathbf{q}|}{\sqrt{Q^2}} \left\langle R, J_z = 1/2 \left| \epsilon^0_\mu J^\mu_{\mathrm{EM}} \right| N, J_z = 1/2 \right\rangle \zeta, \end{aligned} \tag{E.1}$$

where $k_R = (W^2 - M_N^2)/2W$ and

$$|\mathbf{q}|^2 = \frac{(W^2 - M_N^2 - Q^2)^2}{4W^2} + Q^2. \tag{E.2}$$

$W = \sqrt{p'^2}$ is the resonance mass; J^μ_{EM} is the electromagnetic transition current. The phase, ζ, is given by the relative sign between the πNN and πNR couplings [WSPR90, ABL08], which we have taken to be $+1$ (see also the discussion in Appendix F.1).

The photon polarization vectors are given by

$$\epsilon^{\mu}_{\pm} = \mp\frac{1}{\sqrt{2}}(0,1,\pm\mathrm{i},0) \qquad \text{(transverse)}, \tag{E.3}$$

and for a photon of momentum q moving along the z axis

$$\epsilon^{\mu}_{0} = \frac{1}{\sqrt{Q^2}}(|\mathbf{q}|,0,0,q^0) \qquad \text{(longitudinal)}. \tag{E.4}$$

Thus, $A_{1/2}$ ($A_{3/2}$, $S_{1/2}$) corresponds to photons with positive (negative, zero) helicity.

Our definition of the helicity amplitudes — note in particular the minus sign of the $S_{1/2}$ amplitude — is consistent with MAID (cf. Eq. (16) in Ref. [TDK+04] or Eq. (24) in Ref. [DKT07] where their $\rho = \mathbf{q}\cdot\mathbf{J}/q^0$ is introduced in Eq. (5) of Ref. [DT92]). While $A_{1/2}$ and $A_{3/2}$ are transverse and Lorentz invariant, $S_{1/2}$ is frame dependent. To be consistent with MAID, the resonance rest frame has to be used for the calculation [TAR]. We use the outcome of the MAID2005 analysis[1] which has been provided to us in form of a Fortran code by L. Tiator [Tia][2].

Note that the helicity amplitudes are taken at the Breit-Wigner mass M_R, thus we set $W = M_R$ in the following with the consequence that our resonance form factors are functions of Q^2 only. The uncertainties related with this assumption are discussed in Appendix G.1.

The explicit relations between the amplitudes and the form factors are summarized below.

E.1 Spin 1/2 resonances

For spin 1/2 resonances, only the $A_{1/2}$ and $S_{1/2}$ amplitudes are present.

E.1.1 Positive parity

In the case of positive parity, the electromagnetic current J^{μ}_{EM} is given by the one defined in Eq. (5.5) with $\mathcal{F}_i$ ($i = 1,2$) standing for the EM form factors, F_i^N, with $N = p,n$ denoting the initial particle. We obtain

$$A^{p,n}_{1/2} = \sqrt{\frac{2\pi\alpha}{M_N}\frac{(M_R-M_N)^2+Q^2}{M_R^2-M_N^2}}\left[\frac{Q^2}{4M_N^2}F_1^{p,n} + \frac{M_R+M_N}{2M_N}F_2^{p,n}\right] \tag{E.5}$$

[1] See Sec. 2 of Ref. [DKT07] for a history of MAID and the difference between different versions.

[2] see init/lepton/formfactors_ResProd/helicityAmplitudes.f90 in the GiBUU code directory.

and

$$S_{1/2}^{p,n} = -\sqrt{\frac{\pi\alpha}{M_N}\frac{(M_N+M_R)^2+Q^2}{M_R^2-M_N^2}}\frac{(M_R-M_N)^2+Q^2}{4M_RM_N}\left[\frac{M_R+M_N}{2M_N}F_1^{p,n}-F_2^{p,n}\right]. \quad \text{(E.6)}$$

E.1.2 Negative parity

In the case of negative parity, $J_{\rm EM}^{\mu}$ is defined in Eq. (5.5) with an additional γ^5 [Eq. (5.4)] and $\mathcal{F}_i$ $(i=1,2)$ standing for the EM form factors, F_i^N. We find

$$A_{1/2}^{p,n} = \sqrt{\frac{2\pi\alpha}{M_N}\frac{(M_R+M_N)^2+Q^2}{M_R^2-M_N^2}}\left[\frac{Q^2}{4M_N^2}F_1^{p,n}+\frac{M_R-M_N}{2M_N}F_2^{p,n}\right] \quad \text{(E.7)}$$

and

$$S_{1/2}^{p,n} = \sqrt{\frac{\pi\alpha}{M_N}\frac{(M_N-M_R)^2+Q^2}{M_R^2-M_N^2}}\frac{(M_R+M_N)^2+Q^2}{4M_RM_N}\left[\frac{M_R-M_N}{2M_N}F_1^{p,n}-F_2^{p,n}\right]. \quad \text{(E.8)}$$

E.2 Spin 3/2 resonances

E.2.1 Positive parity

In the case of positive parity, the electromagnetic current is defined in Eq. (5.14) with an additional γ^5 [Eq. (5.12)] and $\mathcal{C}_i^V$, $i=3,\ldots,6$, standing for the EM form factors C_i^N with $N=p,n$. This yields

$$A_{1/2}^{p,n} = \sqrt{\frac{\pi\alpha}{3M_N}\frac{(M_R-M_N)^2+Q^2}{M_R^2-M_N^2}} \times\left[\frac{C_3^{p,n}}{M_N}\frac{M_N^2+M_NM_R+Q^2}{M_R}-\frac{C_4^{p,n}}{M_N^2}\frac{M_R^2-M_N^2-Q^2}{2}-\frac{C_5^{p,n}}{M_N^2}\frac{M_R^2-M_N^2+Q^2}{2}\right], \quad \text{(E.9)}$$

$$A_{3/2}^{p,n} = \sqrt{\frac{\pi\alpha}{M_N}\frac{(M_R-M_N)^2+Q^2}{M_R^2-M_N^2}} \times\left[\frac{C_3^{p,n}}{M_N}(M_N+M_R)+\frac{C_4^{p,n}}{M_N^2}\frac{M_R^2-M_N^2-Q^2}{2}+\frac{C_5^{p,n}}{M_N^2}\frac{M_R^2-M_N^2+Q^2}{2}\right] \quad \text{(E.10)}$$

and

$$S_{1/2}^{p,n} = \sqrt{\frac{\pi\alpha}{6M_N}\frac{(M_R-M_N)^2+Q^2}{M_R^2-M_N^2}}\frac{\sqrt{[(M_R-M_N)^2+Q^2][(M_R+M_N)^2+Q^2]}}{M_R^2} \times \left[\frac{C_3^{p,n}}{M_N}M_R + \frac{C_4^{p,n}}{M_N^2}M_R^2 + \frac{C_5^{p,n}}{M_N^2}\frac{M_R^2+M_N^2+Q^2}{2}\right]. \tag{E.11}$$

E.2.2 Negative parity

In the case of negative parity, the electromagnetic current is defined in Eq. (5.14) with $\mathcal{C}_i^V$, $i = 3,\ldots,6$, standing for the EM form factors C_i^N with $N = p,n$, and we get

$$A_{1/2}^{p,n} = \sqrt{\frac{\pi\alpha}{3M_N}\frac{(M_R+M_N)^2+Q^2}{M_R^2-M_N^2}} \times \left[\frac{C_3^{p,n}}{M_N}\frac{M_N^2-M_NM_R+Q^2}{M_R} - \frac{C_4^{p,n}}{M_N^2}\frac{M_R^2-M_N^2-Q^2}{2} - \frac{C_5^{p,n}}{M_N^2}\frac{M_R^2-M_N^2+Q^2}{2}\right], \tag{E.12}$$

$$A_{3/2}^{p,n} = \sqrt{\frac{\pi\alpha}{M_N}\frac{(M_R+M_N)^2+Q^2}{M_R^2-M_N^2}} \times \left[\frac{C_3^{p,n}}{M_N}(M_N-M_R) - \frac{C_4^{p,n}}{M_N^2}\frac{M_R^2-M_N^2-Q^2}{2} - \frac{C_5^{p,n}}{M_N^2}\frac{M_R^2-M_N^2+Q^2}{2}\right] \tag{E.13}$$

and

$$S_{1/2}^{p,n} = -\sqrt{\frac{\pi\alpha}{6M_N}\frac{(M_R+M_N)^2+Q^2}{M_R^2-M_N^2}}\frac{\sqrt{[(M_R-M_N)^2+Q^2][(M_R+M_N)^2+Q^2]}}{M_R^2} \times \left[\frac{C_3^{p,n}}{M_N}M_R + \frac{C_4^{p,n}}{M_N^2}M_R^2 + \frac{C_5^{p,n}}{M_N^2}\frac{M_R^2+M_N^2+Q^2}{2}\right]. \tag{E.14}$$

F

Derivation of axial couplings

In this section, we derive the relations between the axial form factors and determine the axial couplings applying PCAC, according to which the divergence of the axial current is proportional to the pion mass squared (see Section 2.3.2). Thus, in the chiral limit the axial current is conserved if we assume pion-pole dominance, i.e., we assume that the pseudoscalar part is dominated by the one-pion exchange process, where a pion is created at the nucleon-resonance vertex and then couples to the lepton pair[1]. Its current is given by

$$A_\pi^\mu = (n \to R^+ \pi^-) \times \left(\frac{\mathrm{i}}{q^2 - m_\pi^2} \right) \times \left(-\mathrm{i}\sqrt{2} f_\pi q^\mu \right), \tag{F.1}$$

where $f_\pi = 93\,\mathrm{MeV}$ is the pion decay constant. The hadronic vertices are specified in the following.

F.1 Resonance interaction Lagrangians and widths

Here, we collect the relativistic Lagrangians used to extract the coupling of baryon resonances to nucleons and pions.

[1] For QE scattering, we have discussed this issue in detail in Chapter 4 of Ref. [Lei05].

F.1.1 Resonances with spin 1/2

The $R_{1/2}N\pi$ coupling is described by the pseudovector Lagrangian[2]

$$\mathcal{L}_{R_{1/2}N\pi} = \frac{f}{m_\pi}\bar{\Psi}_{R_{1/2}} \left\{ \begin{array}{c} \gamma^\mu\gamma^5 \\ \gamma^\mu \end{array} \right\} \partial_\mu \boldsymbol{\phi} \cdot \mathbf{t}\, \Psi, \tag{F.2}$$

where the upper (lower) operator holds for positive (negative) parity resonances and $\mathbf{t} = \boldsymbol{\tau}$ ($\mathbf{t} = \mathbf{T}^\dagger$) for $I = 1/2$ ($I = 3/2$) resonances (cf. Appendix A.4).

From this Lagrangian we deduce the following vertex factor

$$-\,\mathrm{i}\, C_{\mathrm{iso}}\, \frac{f}{m_\pi} \left\{ \begin{array}{c} \gamma^\mu\gamma^5 \\ \gamma^\mu \end{array} \right\}. \tag{F.3}$$

The isospin factor is $C_{\mathrm{iso}} = \sqrt{2}$ for $I = 1/2$ and $C_{\mathrm{iso}} = -\sqrt{1/3}$ for $I = 3/2$ resonances, respectively (cf. Appendix A.4).

The coupling f can be obtained from the $R_{1/2} \to \pi N$ partial decay width according to

$$\Gamma_{R_{1/2}\to\pi N} = \frac{I_R}{4\pi}\left(\frac{f}{m_\pi}\right)^2 (M_R \pm M_N)^2\, \frac{E_N \mp M_N}{M_R} |\mathbf{q}_{\mathrm{cm}}|, \tag{F.4}$$

where the upper (lower) sign is for positive (negative) parity. $|\mathbf{q}_{\mathrm{cm}}|$ is the momentum of the outgoing pion in the resonance rest frame

$$|\mathbf{q}_{\mathrm{cm}}| = \frac{\sqrt{(M_R^2 - m_\pi^2 - M_N^2)^2 - 4m_\pi^2 M_N^2}}{2M_R}. \tag{F.5}$$

$I_R = 1$ for isospin $3/2$ and $I_R = 3$ for isospin $1/2$ resonances, and E_N is the energy of the outgoing nucleon in the resonance rest frame, given by

$$E_N = \frac{M_R^2 + M_N^2 - m_\pi^2}{2M_R}. \tag{F.6}$$

The couplings f/m_π are determined via Eq. (F.4) using the resonance properties given in Table 5.1; the results are summarized in Table 5.4 on page 44. To be consistent with the choice of ζ in Eq. (E.1), f/m_π has to be positive [WSPR90, ABL08].

F.1.2 Resonances with spin 3/2

The $R_{3/2}N\pi$ coupling is described by the Lagrangian

$$\mathcal{L}_{R_{3/2}N\pi} = \frac{f}{m_\pi}\bar{\Psi}_\mu \left\{ \begin{array}{c} \mathbb{1}_4 \\ \gamma^5 \end{array} \right\} \partial^\mu \boldsymbol{\phi} \cdot \mathbf{t}\, \Psi, \tag{F.7}$$

[2] One might instead use a pseudoscalar Lagrangian for the coupling of negative-parity resonances; we refer the reader to Chapter 3.4.1 of Ref. [Pen02] and to page 50 of Ref. [BGPR96] for a discussion.

where Ψ_μ is a Rarita-Schwinger $J^\pi = 3/2^+$ field. The upper (lower) operator holds for positive (negative) parity resonances and and $\mathbf{t} = \boldsymbol{\tau}$ ($\mathbf{t} = \mathbf{T}^\dagger$) for $I = 1/2$ ($I = 3/2$) resonances (cf. Appendix A.4).

From this Lagrangian we obtain the vertex factor

$$-\,\mathrm{i}\,C_{\mathrm{iso}}\,\frac{f}{m_\pi}\,\left\{\begin{array}{c}\mathbb{1}_4\\ \gamma^5\end{array}\right\}, \tag{F.8}$$

with the isospin factor $C_{\mathrm{iso}} = \sqrt{2}$ for $I = 1/2$ and $C_{\mathrm{iso}} = -\sqrt{1/3}$ for $I = 3/2$ resonances (cf. Appendix A.4).

The decay width, needed to extract the coupling f, is — for resonances with $J^P = \frac{3}{2}^\pm$ — given by

$$\Gamma_{R_{3/2}\to\pi N} = \frac{I_R}{12\pi}\left(\frac{f}{m_\pi}\right)^2 \frac{E_N \pm M_N}{M_R}|\mathbf{q}_{\mathrm{cm}}|^3, \tag{F.9}$$

with $|\mathbf{q}_{\mathrm{cm}}|$, E_N and I_R as above.

Using the resonance properties given in Table 5.1, we obtain the couplings f/m_π summarized in Table 5.7 on page 50.

F.2 PCAC relations

F.2.1 Resonances with spin 1/2

The axial current for spin $1/2$ resonance excitation reads

$$\begin{aligned} A^\mu_{1/2\pm} &= \left\langle R(p')\left|A^\mu_{1/2\pm}(0)\right|N(p)\right\rangle \\ &= \bar{u}(p')A^\mu_{1/2}\left\{\begin{array}{c}\mathbb{1}_4\\ \gamma^5\end{array}\right\}u(p) \\ &= \bar{u}(p')\left(-\left[F_A\gamma^\mu\gamma^5 + \frac{F_P}{M_N}q^\mu\gamma^5\right]\right)\left\{\begin{array}{c}\mathbb{1}_4\\ \gamma^5\end{array}\right\}u(p), \end{aligned} \tag{F.10}$$

where we have used in the last line the definition of $A^\mu_{1/2}$ given in Eq. (5.6) on page 40. $A^\mu_{1/2}$ needs to be multiplied by γ^5 for negative parity states, thus, the upper (lower) operator holds for positive (negative) parity.

We then obtain for the divergence of the axial current $A^\mu_{1/2\pm}$

$$\begin{aligned} \partial_\mu A^\mu_{1/2\pm} = -\mathrm{i}q_\mu A^\mu_{1/2\pm} &= \mathrm{i}\bar{u}(p')\left[F_A q_\mu\gamma^\mu + \frac{F_P}{M_N}q^2\right]\left\{\begin{array}{c}\gamma^5\\ \mathbb{1}_4\end{array}\right\}u(p) \\ &= \mathrm{i}\bar{u}(p')\left[F_A(M_R \pm M_N) + \frac{F_P}{M_N}q^2\right]\left\{\begin{array}{c}\gamma^5\\ \mathbb{1}_4\end{array}\right\}u(p). \end{aligned} \tag{F.11}$$

The PCAC hypothesis introduced in Section 2.3.2 implies that this divergence should be proportional to the squared pion mass, m_π^2, and thus vanishes in the chiral limit ($m_\pi \to 0$). This cannot be fulfilled with the first term, $F_A(M_R \pm M_N)$, but when the induced pseudoscalar term has a pion pole. So the next step is to calculate the pion pole contribution to the current and compare that to the axial transition current. Starting from Eq. (F.1) and using Eq. (F.3) we find

$$\begin{aligned}
A^\mu_{\pi,1/2} &= \bar{u}(p')(-\mathrm{i})\, C_{\mathrm{iso}}\, \frac{f}{m_\pi} \left\{ \begin{array}{c} \gamma^\nu\gamma^5 \\ \gamma^\nu \end{array} \right\} \partial_\nu\phi\; u(p) \frac{\sqrt{2} f_\pi q^\mu}{q^2 - m_\pi^2} \\
&= \bar{u}(p')(-\mathrm{i})\, C_{\mathrm{iso}}\, \frac{f}{m_\pi}\, \gamma^\nu\, (-\mathrm{i} q_\nu) \left\{ \begin{array}{c} \gamma^5 \\ \mathbb{1}_4 \end{array} \right\} u(p) \frac{\sqrt{2} f_\pi q^\mu}{q^2 - m_\pi^2} \\
&= -\bar{u}(p')\, C_{\mathrm{iso}}\, \frac{f}{m_\pi}\, \gamma^\nu\, (p'_\nu - p_\nu) \left\{ \begin{array}{c} \gamma^5 \\ \mathbb{1}_4 \end{array} \right\} u(p) \frac{\sqrt{2} f_\pi q^\mu}{q^2 - m_\pi^2} \\
&= -\bar{u}(p')\, C_{\mathrm{iso}}\, \frac{f}{m_\pi}\, (M_R \pm M_N) \left\{ \begin{array}{c} \gamma^5 \\ \mathbb{1}_4 \end{array} \right\} u(p) \frac{\sqrt{2} f_\pi q^\mu}{q^2 - m_\pi^2}\,. \qquad \text{(F.12)}
\end{aligned}$$

By comparing Eq. (F.10) with Eq. (F.12) we can identify

$$\frac{F_P}{M_N} q^\mu = C_{\mathrm{iso}}\, \frac{f}{m_\pi}\, (M_R \pm M_N) \frac{\sqrt{2} f_\pi q^\mu}{q^2 - m_\pi^2}\,, \qquad \text{(F.13)}$$

so that

$$F_P = -C_{\mathrm{iso}}\, \sqrt{2} f_\pi \frac{f}{m_\pi} \frac{(M_R \pm M_N) M_N}{Q^2 + m_\pi^2}\,, \qquad \text{(F.14)}$$

Then, $\partial_\mu A^\mu_{1/2\pm}$ reads

$$\begin{aligned}
\partial_\mu A^\mu_{1/2\pm} &= \mathrm{i}\bar{u}(p') \left[F_A(M_R \pm M_N) + \frac{F_P}{M_N} q^2 \right] \left\{ \begin{array}{c} \gamma^5 \\ \mathbb{1}_4 \end{array} \right\} u(p) \\
&= \mathrm{i}\bar{u}(p') \left[F_A(M_R \pm M_N) - C_{\mathrm{iso}}\, \sqrt{2} f_\pi \frac{f}{m_\pi} \frac{(M_R \pm M_N)}{Q^2 + m_\pi^2} q^2 \right] \left\{ \begin{array}{c} \gamma^5 \\ \mathbb{1}_4 \end{array} \right\} u(p) \\
&\xrightarrow{m_\pi \to 0} \mathrm{i}\bar{u}(p') \left[F_A(M_R \pm M_N) + C_{\mathrm{iso}}\, \sqrt{2} f_\pi \frac{f}{m_\pi} (M_R \pm M_N) \right] \left\{ \begin{array}{c} \gamma^5 \\ \mathbb{1}_4 \end{array} \right\} u(p). \qquad \text{(F.15)}
\end{aligned}$$

It vanishes if

$$F_A(M_R \pm M_N) = -C_{\mathrm{iso}}\, \sqrt{2} f_\pi \frac{f}{m_\pi} (M_R \pm M_N), \qquad \text{(F.16)}$$

which yields the Goldberger-Treiman relation

$$F_A = -C_{\mathrm{iso}}\, \sqrt{2} f_\pi \frac{f}{m_\pi}, \qquad \text{(F.17)}$$

which defines our axial coupling, $F_A(0)$, for the spin 1/2 resonances (summarized in Table 5.4 on page 44).

F.2.2 Resonances with spin 3/2

For the spin 3/2 resonances, we proceed in the same way as for the spin 1/2 resonances. Here, the axial current is given by

$$\begin{aligned}
A^{\mu}_{3/2\pm} =& \left\langle R(p') \left| A^{\mu}_{3/2\pm}(0) \right| N(p) \right\rangle \\
=& \bar{\psi}_{\alpha}(p') A^{\alpha\mu}_{3/2} \left\{ \begin{array}{c} \gamma^5 \\ \mathbb{1}_4 \end{array} \right\} u(p) \\
=& \bar{\psi}_{\alpha} \left(- \left[\frac{C_3^A}{M_N}(g^{\alpha\mu} \not{q} - q^{\alpha}\gamma^{\mu}) + \frac{C_4^A}{M_N^2}(g^{\alpha\mu} q\cdot p' - q^{\alpha} p'^{\mu}) \right.\right. \\
& \left.\left. + C_5^A g^{\alpha\mu} + \frac{C_6^A}{M_N^2} q^{\alpha} q^{\mu} \right] \gamma^5 \left\{ \begin{array}{c} \gamma^5 \\ \mathbb{1}_4 \end{array} \right\} \right) u(p),
\end{aligned} \tag{F.18}$$

where we have used in the last line the definition of $A^{\alpha\mu}_{3/2}$ given in Eq. (5.15) on page 46. $A^{\alpha\mu}_{3/2}$ needs to be multiplied by γ^5 for positive parity states, thus, the upper (lower) operator holds for positive (negative) parity.

The divergence of the axial current $A^{\mu}_{3/2\pm}$ reads

$$\begin{aligned}
\partial_{\mu} A^{\mu}_{3/2\pm} =& -\mathrm{i} q_{\mu} A^{\mu}_{3/2\pm} \\
=& \mathrm{i}\bar{\psi}_{\alpha} \left[\frac{C_3^A}{M_N} q_{\mu}(g^{\alpha\mu} \not{q} - q^{\alpha}\gamma^{\mu}) + \frac{C_4^A}{M_N^2} q_{\mu}(g^{\alpha\mu} q\cdot p' - q^{\alpha} p'^{\mu}) \right. \\
& \left. + C_5^A q_{\mu} g^{\alpha\mu} + \frac{C_6^A}{M_N^2} q_{\mu} q^{\alpha} q^{\mu} \right] \left\{ \begin{array}{c} \mathbb{1}_4 \\ \gamma^5 \end{array} \right\} u(p) \\
=& \mathrm{i}\bar{\psi}_{\alpha} \left[0 + 0 + C_5^A q^{\alpha} + \frac{C_6^A}{M_N^2} q^{\alpha} q^2 \right] \left\{ \begin{array}{c} \mathbb{1}_4 \\ \gamma^5 \end{array} \right\} u(p) \\
=& \mathrm{i}\bar{\psi}_{\alpha} q^{\alpha} \left[C_5^A + \frac{C_6^A}{M_N^2} q^2 \right] \left\{ \begin{array}{c} \mathbb{1}_4 \\ \gamma^5 \end{array} \right\} u(p).
\end{aligned} \tag{F.19}$$

The PCAC hypothesis introduced in Section 2.3.2 implies that this divergence should vanish if $m_{\pi} \to 0$. This is not realized for the first term in Eq. (F.19) but when the induced pseudoscalar term, C_6^A has a pion pole. The pion pole contribution is

obtained from Eq. (F.1) with Eq. (F.8)

$$\begin{aligned} A^{\mu}_{\pi,3/2} &= \bar{\psi}_{\alpha}(p')(-\mathrm{i})\ C_{\mathrm{iso}}\ \frac{f}{m_{\pi}}\ \left\{ \begin{array}{c} \mathbb{1}_4 \\ \gamma^5 \end{array} \right\}\ \partial^{\alpha}\phi\ u(p)\frac{\sqrt{2}f_{\pi}q^{\mu}}{q^2-m_{\pi}^2} \\ &= \bar{\psi}_{\alpha}(p')(-\mathrm{i})\ C_{\mathrm{iso}}\ \frac{f}{m_{\pi}}\ \left\{ \begin{array}{c} \mathbb{1}_4 \\ \gamma^5 \end{array} \right\}\ (-\mathrm{i}q^{\alpha})\ u(p)\frac{\sqrt{2}f_{\pi}q^{\mu}}{q^2-m_{\pi}^2} \\ &= -\bar{\psi}_{\alpha}(p')\ C_{\mathrm{iso}}\ \frac{f}{m_{\pi}}\ \left\{ \begin{array}{c} \mathbb{1}_4 \\ \gamma^5 \end{array} \right\}\ q^{\alpha}\ u(p)\frac{\sqrt{2}f_{\pi}q^{\mu}}{q^2-m_{\pi}^2}\ . \end{aligned} \tag{F.20}$$

Comparing Eq. (F.18) with Eq. (F.20) yields

$$\frac{C_6^A}{M_N^2}q^{\alpha}q^{\mu} = C_{\mathrm{iso}}\ \frac{f}{m_{\pi}}\ q^{\alpha}\ \frac{\sqrt{2}f_{\pi}q^{\mu}}{q^2-m_{\pi}^2}\ , \tag{F.21}$$

and thus

$$C_6^A = -C_{\mathrm{iso}}\ \sqrt{2}f_{\pi}\ \frac{f}{m_{\pi}}\ \frac{M_N^2}{Q^2+m_{\pi}^2}\ . \tag{F.22}$$

Consequently, we find

$$\begin{aligned} \partial_{\mu}A^{\mu}_{3/2\pm} &= \mathrm{i}\bar{\psi}_{\alpha}q^{\alpha}\left[C_5^A + \frac{C_6^A}{M_N^2}q^2\right]\ \left\{ \begin{array}{c} \mathbb{1}_4 \\ \gamma^5 \end{array} \right\}\ u(p) \\ &= \mathrm{i}\bar{\psi}_{\alpha}q^{\alpha}\left[C_5^A - C_{\mathrm{iso}}\ \sqrt{2}f_{\pi}\ \frac{f}{m_{\pi}}\ \frac{1}{Q^2+m_{\pi}^2}q^2\right]\ \left\{ \begin{array}{c} \mathbb{1}_4 \\ \gamma^5 \end{array} \right\}\ u(p) \\ &\xrightarrow{m_{\pi}\to 0} \mathrm{i}\bar{\psi}_{\alpha}q^{\alpha}\left[C_5^A + C_{\mathrm{iso}}\ \sqrt{2}f_{\pi}\ \frac{f}{m_{\pi}}\right]\ \left\{ \begin{array}{c} \mathbb{1}_4 \\ \gamma^5 \end{array} \right\}\ u(p)\ , \end{aligned} \tag{F.23}$$

which is zero when

$$C_5^A = -C_{\mathrm{iso}}\ \sqrt{2}f_{\pi}\ \frac{f}{m_{\pi}}. \tag{F.24}$$

The final results for the axial couplings $C_5^A(0)$ are collected in Table 5.7 on page 50.

G

Uncertainties in the neutrino-nucleon cross section

This chapter addresses two sources of uncertainties which affect the neutrino-nucleon cross section.

G.1 W dependence of the resonance form factors

As stated in Appendix E, our form factors for resonance excitation depend only on Q^2, and any dependence on the invariant mass W has been neglected so far. However, as pointed out by Buss [Bus09], this approximation fails for Compton scattering, i.e., $\gamma N \to \gamma N$.

Using the very same model as in this thesis, Buss fits the mass dependence of the Δ-resonance form factor to Compton-scattering data assuming a dominant s-channel. The matrix element for Compton scattering, $\gamma(q)N(p) \to \gamma(q')N(p')$, via Δ excitation in the s-channel reads

$$M = \bar{u}(s', p')\epsilon^{\star}_{\alpha}(\lambda', q')\tilde{\Gamma}^{\beta\alpha}(p', q')G_{\beta\nu}(p_{\Delta})\Gamma^{\nu\mu}(p, q)\epsilon_{\mu}(\lambda, q)u(s, p); \tag{G.1}$$

ϵ denotes the photon-polarization vectors, otherwise the notation is identical to that used in Section 5.2.1. The $\gamma N \to \Delta$ vertex factor $\Gamma^{\nu\mu}$ is parametrized in terms of form factors (cf. Eq. (5.14)), for which we now introduce an explicit mass dependence by setting

$$C_i(W, Q^2) = C_i(Q^2)f(W), \tag{G.2}$$

where $C_i(Q^2)$ are the standard Δ form factors used throughout this work. The W dependence is encoded in the form factor $f(W)$, which is chosen as [Bus09, Pos04]

$$f(W) = \frac{\Lambda^4 + \frac{1}{4}(s_0 - M_\Delta^2)^2}{\Lambda^4 + \left(W^2 - \frac{1}{2}(s_0 + M_\Delta^2)\right)^2}, \tag{G.3}$$

with $s_0 = (m_\pi + M_N)^2$.

It is shown in Fig. 2 of Ref. [Bus09], that the Compton-scattering data are clearly overestimated for $f(W) = 1$, i.e., no W dependence. By introducing a finite Λ, Buss has been able to improve the correspondence with data — a best fit yields $\Lambda = 1.071\,\text{GeV}$.

To investigate the impact on our results, let us first go back to our special treatment of the single-pion background. It has been defined as the difference between data and resonance contribution (details were given in Chapter 6). Thus, by construction, the W dependence has no impact at all on the total cross section, it simply shifts strength from the resonance contribution to the background. For electron and photon scattering, this is shown explicitly in Figs. 3 and 4 of Ref. [Bus09].

However, this statement applies only to channels *with* non-resonant background and not to the ones where the background has been neglected. This has been the case in the isospin 3/2 channel, which has been used to fit the Δ axial form factor (see Fig. 5.6). The corresponding observable is shown in the left panel of Fig. G.1 and, thanks also to the invariant-mass cut at 1.4 GeV, no difference between the two options for the W dependence is observed. Thus, introducing $f(W) \neq 1$ has no influence on the extraction of the axial form factor for the Δ. The integrated cross section for the same channel and without any cut on the invariant mass is plotted in the right panel of Fig. G.1. Also there, the differences, apparent only at higher E_ν, are small and still within the accuracy limits of the available data. We thus conclude that the neglect of $f(W)$ in our work has little or no impact on our results.

G.2 Neglect of DIS

In Section 3.1 we discussed the various contributions to the lepton-nucleon cross section. Being interested in neutrino reactions up to beam energies of around 2 GeV, we have neglected deep inelastic scattering as it is of major importance only at higher energies. Before we quantify this statement, we give a brief introduction to the treatment of DIS in elementary ℓN reactions in the GiBUU approach.

The final state of the initial lepton-nucleon reaction is modeled by the event generator PYTHIA (version 6.420) [SMS06]. There, the high-energy interactions lead to the excitation of one or more hadronic strings which fragment according to the Lund

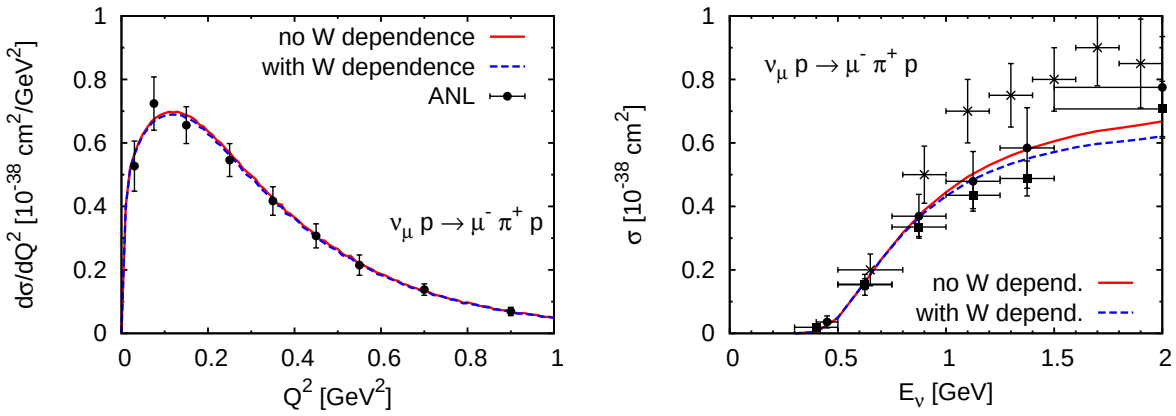

Figure G.1: Left panel: differential cross section $\mathrm{d}\sigma/\mathrm{d}Q^2$ averaged over the ANL flux applying an invariant mass cut at $W < 1.4\,\mathrm{GeV}$. Data are taken from Ref. [B$^+$77]. Right panel: integrated $p\pi^+$ production cross sections without any cut on the invariant mass. Data are taken from ANL (Refs. [B$^+$79] (•) and [R$^+$82] (■)) and BNL ([K$^+$86] (×)). The curves were obtained with and without W dependence of the form factor as detailed in the text.

fragmentation scheme implemented in PYTHIA. PYTHIA includes also direct interaction processes such as diffraction and vector-meson dominance. We refer the reader to the recent works of Gallmeister *et al.* [FCGM04, GF05, GM08] for details on the application of PYTHIA in the GiBUU framework, mainly in connection with high-energy (virtual) photon scattering.

To include DIS in our model, we modify Eq. (3.1) (see page 26) such that

$$\mathrm{d}\sigma_{\mathrm{tot}} = \mathrm{d}\sigma_{\mathrm{QE}} + \sum_{\mathrm{R}} \mathrm{d}\sigma_{\mathrm{R}} + \begin{cases} \mathrm{d}\sigma_{\mathrm{BG}} & \text{for } W < 1.6\,\mathrm{GeV} \\ \mathrm{d}\sigma_{\mathrm{DIS}} & \text{for } W > 1.6\,\mathrm{GeV} \end{cases} . \tag{G.4}$$

In this way we allow the resonances to spread to arbitrarily large W, while we cut the phenomenological background at $W = 1.6\,\mathrm{GeV}$. This cut in W is required to avoid double counting of single-pion final states: as our background is fitted to data and not based on a microscopic model, it contains also contributions from underlying DIS processes. For invariant masses of the lepton-nucleon system larger than 1.6 GeV, DIS is "switched on" and gives also rise to single-pion final states. The specific choice of 1.6 GeV is motivated by the fact that the same approach leads to reasonable results in electron-nucleon scattering where plenty of data are available to compare with [Galb].

First results are presented in Fig. G.2 for muon neutrino scattering off protons (left) and neutrons (right panel).[1] The cross section on the proton is dominated by pion production through the excitation of the Δ resonance (largest contribution to the dashed

[1] The DIS results were provided by K. Gallmeister.

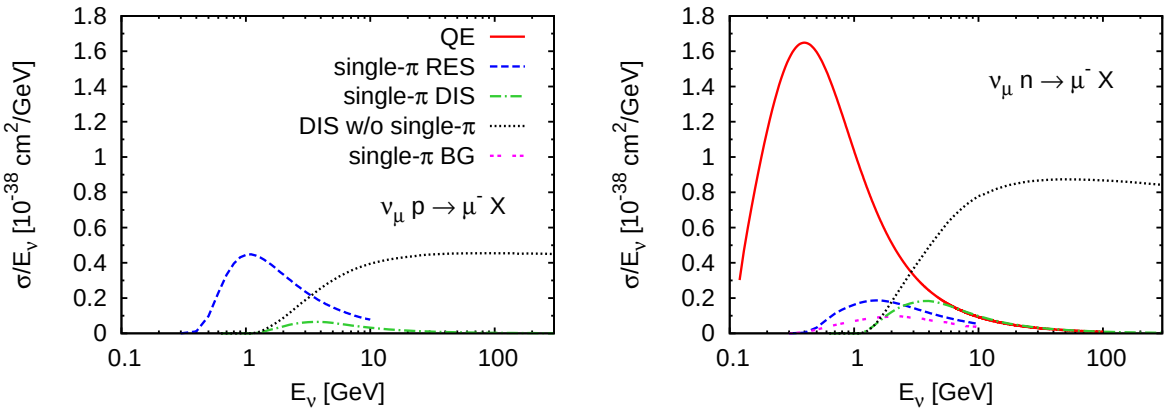

Figure G.2: Total CC neutrino cross sections for $\nu_\mu p \to \mu^- X$ (left) and $\nu_\mu n \to \mu^- X$ (right panel) as a function of the neutrino energy decomposed in the contributions of quasielastic scattering (QE), single-π production through various ways (resonance [dashed], non-resonant background [double-dashed] and DIS [dash-dotted]) and the DIS contribution which leads to final states other than 1π (dotted lines).

line) and by DIS, setting in at around 1.5 GeV neutrino energy. The non-resonant background is set to zero by definition, and also the fraction of DIS leading to single-π final states is negligible. A different picture emerges on the neutron. Most dominant is QE scattering at low and DIS at high energies. Single-π production contains contributions from all three interaction types.

This can be investigated further by enlarging the energy region of interest in the present work: in Fig. G.3 we show the single-π production cross sections on protons (top) and neutrons (middle and bottom panels). The solid lines include both resonances and non-resonant background (agree with the solid lines in Fig. 6.2). The dashed lines include in addition single-π final states through DIS, following Eq. (G.4). They become increasingly more important for energies larger than 1.5 GeV but can safely be neglected below.

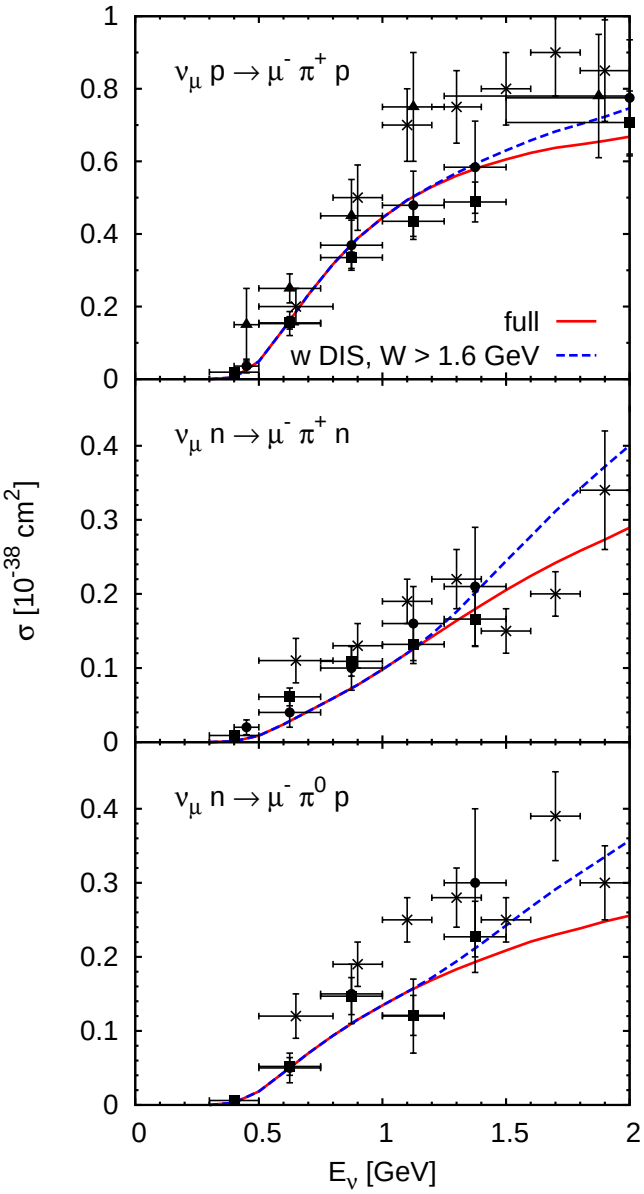

Figure G.3: Total CC pion production cross sections as a function of the neutrino energy compared to the pion production data of of ANL (Refs. [B$^+$79] (•) and [R$^+$82] (■)) and BNL ([K$^+$86] (×)). The solid lines denote the our result including resonance excitation and non-resonant background according to Eq. (3.1). The dashed lines include in addition single-π final states through DIS following Eq. (G.4).

Bibliography

[A$^+$87] L. A. Ahrens *et al.*, *Measurement of neutrino-proton and anti-neutrino-proton elastic scattering*, Phys. Rev. D **35**, 785 (1987).

[A$^+$90] D. Allasia *et al.*, *Investigation of exclusive channels in neutrino / anti-neutrino deuteron charged current interactions*, Nucl. Phys. B **343**, 285 (1990).

[A$^+$95] M. Anghinolfi *et al.*, *Inclusive electron scattering from an oxygen and argon jet target*, J. Phys. G **21**, L9 (1995).

[A$^+$96] M. Anghinolfi *et al.*, *Quasielastic and inelastic inclusive electron scattering from an oxygen jet target*, Nucl. Phys. A **602**, 405 (1996), arXiv:nucl-th/9603001.

[A$^+$09] C. Andreopoulos *et al.*, *The GENIE neutrino Monte Carlo generator*, arXiv:0905.2517.

[A404] F. E. Maas *et al.* [A4 Collaboration], *Measurement of strange quark contributions to the nucleon's form factors at* $Q^2 = 0.230\,(GeV/c)^2$, Phys. Rev. Lett. **93**, 022002 (2004), arXiv:nucl-ex/0401019.

[ABB$^+$97] W. M. Alberico, M. B. Barbaro, S. M. Bilenky, J. A. Caballero, C. Giunti, C. Maieron, E. Moya de Guerra and J. M. Udias, *Inelastic ν and $\bar{\nu}$ scattering on nuclei and strangeness of the nucleon*, Nucl. Phys. A **623**, 471 (1997), arXiv:hep-ph/9703415.

[ABB$^+$98] W. M. Alberico, M. B. Barbaro, S. M. Bilenky, J. A. Caballero, C. Giunti, C. Maieron, E. Moya de Guerra and J. M. Udias, *The ratio of p and n yields in NC ν ($\bar{\nu}$) nucleus scattering and strange form factors of the nucleon*, Phys. Lett. B **438**, 9 (1998), arXiv:hep-ph/9712441.

[ABB$^+$99] W. M. Alberico, M. B. Barbaro, S. M. Bilenky, J. A. Caballero, C. Giunti, C. Maieron, E. Moya de Guerra and J. M. Udias, *Strange form factors of the proton: a new analysis of the ν ($\bar{\nu}$) data of the BNL-734 experiment*, Nucl. Phys. A **651**, 277 (1999), arXiv:hep-ph/9812388.

[ABC+05] J. E. Amaro, M. B. Barbaro, J. A. Caballero, T. W. Donnelly, A. Molinari and I. Sick, *Using electron scattering superscaling to predict charge-changing neutrino cross sections in nuclei*, Phys. Rev. C **71**, 015501 (2005), arXiv:nucl-th/0409078.

[ABCD06] J. E. Amaro, M. B. Barbaro, J. A. Caballero and T. W. Donnelly, *Superscaling and neutral current quasielastic neutrino-nucleus scattering*, Phys. Rev. C **73**, 035503 (2006), arXiv:nucl-th/0602053.

[ABL08] I. G. Aznauryan, V. D. Burkert and T.-S. H. Lee, *On the definitions of the $\gamma^* N \to N^*$ helicity amplitudes*, arXiv:0810.0997.

[ABM02] W. M. Alberico, S. M. Bilenky and C. Maieron, *Strangeness in the nucleon: neutrino nucleon and polarized electron nucleon scattering*, Phys. Rept. **358**, 227 (2002), arXiv:hep-ph/0102269.

[ACS09] M. S. Athar, S. Chauhan and S. K. Singh, *$CC1\pi^+$ to CCQE cross sections ratio at accelerator energies*, arXiv:0908.1442.

[Adl68] S. L. Adler, *Photoproduction, electroproduction and weak single pion production in the (3,3) resonance region*, Ann. Phys. **50**, 189 (1968).

[ADT81a] S. A. Adjei, D. A. Dicus and V. L. Teplitz, *Charged current two pion production from nucleons*, Phys. Rev. D **24**, 623 (1981).

[ADT81b] S. A. Adjei, D. A. Dicus and V. L. Teplitz, *Neutral current two pion production from nucleons*, Phys. Rev. D **23**, 672 (1981).

[AFGM01] P. Alberto, M. Fiolhais, B. Golli and J. Marques, *N* electroproduction amplitudes in a model with dynamical confinement*, Phys. Lett. B **523**, 273 (2001), arXiv:hep-ph/0103171.

[AH96] I. J. R. Aitchison and A. J. G. Hey, *Gauge theories in particle physics* (Institute of Physics Publishing, 1996).

[AHNV09] J. E. Amaro, E. Hernandez, J. Nieves and M. Valverde, *Theoretical study of neutrino-induced coherent pion production off nuclei at T2K and MiniBooNE energies*, Phys. Rev. D **79**, 013002 (2009), arXiv:0811.1421.

[ALNT07] C. Alexandrou, T. Leontiou, J. W. Negele and A. Tsapalis, *The axial N to Δ transition form factors from lattice QCD*, Phys. Rev. Lett. **98**, 052003 (2007), arXiv:hep-lat/0607030.

[And07] C. Andreopoulos, *Overview of progress in neutrino-nucleus simulation codes*, AIP Conf. Proc. **967**, 31 (2007).

[And09a] C. Anderson, *Neutral current $1\pi^0$ production at MiniBooNE*, talk given at NUINT09, May 17-22, 2009, Sitges, Spain, available online at http://nuint09.ifae.es/Agenda.html.

[And09b] C. Andreopoulos, *The GENIE neutrino Monte Carlo generator*, lectures given at 45th Karpacz Winter School in Theoretical Physics, February 2-11, 2009, Lądek-Zdrój, Poland, available online at http://wng.ift.uni.wroc.pl/karp45.

[Ank08] A. M. Ankowski, *Breakdown of the impulse approximation and its consequences: the low-Q^2 problem*, PoS **NUFACT08**, 118 (2008), arXiv:0810.1167.

[ANP74] S. L. Adler, S. Nussinov and E. A. Paschos, *Nuclear charge exchange corrections to leptonic pion production in the (3,3) resonance region*, Phys. Rev. D **9**, 2125 (1974).

[AR] L. Alvarez-Ruso, private communication.

[ARBDM03] L. Alvarez-Ruso, M. B. Barbaro, T. W. Donnelly and A. Molinari, *Nuclear response functions for the N - N*(1440) transition*, Nucl. Phys. A **724**, 157 (2003), arXiv:nucl-th/0303027.

[ARBLM09] L. Alvarez-Ruso, O. Buss, T. Leitner and U. Mosel, *Quasielastic scattering at MiniBooNE energies*, arXiv:0909.5123.

[ARGHVV07] L. Alvarez-Ruso, L. S. Geng, S. Hirenzaki and M. J. Vicente Vacas, *Charged current neutrino induced coherent pion production*, Phys. Rev. C **75**, 055501 (2007), arXiv:nucl-th/0701098.

[ARGVV07] L. Alvarez-Ruso, L. S. Geng and M. J. Vicente Vacas, *Neutral current coherent pion production*, Phys. Rev. C **76**, 068501 (2007), arXiv:0707.2172.

[ARSVV98] L. Alvarez-Ruso, S. K. Singh and M. J. Vicente Vacas, *Charged current weak electroproduction of the Delta resonance*, Phys. Rev. C **57**, 2693 (1998), arXiv:nucl-th/9712058.

[ARSVV99] L. Alvarez-Ruso, S. K. Singh and M. J. Vicente Vacas, *$\nu d \to \mu^- \Delta^{++} n$ reaction and axial vector $N - \Delta$ coupling*, Phys. Rev. C **59**, 3386 (1999), arXiv:nucl-th/9804007.

[AS08] A. M. Ankowski and J. T. Sobczyk, *Construction of spectral functions for medium nuclei*, Phys. Rev. C **77**, 044311 (2008), arXiv:0711.2031.

[ASAS06] S. Ahmad, M. Sajjad Athar and S. K. Singh, *Neutrino induced charged current $1\pi^+$ production at intermediate energies*, Phys. Rev. D **74**, 073008 (2006), arXiv:nucl-th/0607069.

[B$^+$77] S. J. Barish *et al.*, *Study of neutrino interactions in hydrogen and deuterium. 1. Description of the experiment and study of the reaction $\nu d \to \mu^- pp(s)$*, Phys. Rev. D **16**, 3103 (1977).

[B$^+$79] S. J. Barish *et al.*, *Study of neutrino interactions in hydrogen and deuterium: inelastic charged current reactions*, Phys. Rev. D **19**, 2521 (1979).

[B$^+$81] N. J. Baker *et al.*, *Quasielastic neutrino scattering: a measurement of the weak nucleon axial vector form factor*, Phys. Rev. D **23**, 2499 (1981).

[B$^+$83] P. Barreau *et al.*, *Deep inelastic electron scattering from carbon*, Nucl. Phys. A **402**, 515 (1983).

[B$^+$85] S. V. Belikov *et al.*, *Quasielastic neutrino and anti-neutrinos scattering: total cross sections, axial vector form factor*, Z. Phys. A **320**, 625 (1985).

[B$^+$90] J. Brunner *et al.*, *Quasielastic nucleon and hyperon production by neutrinos and anti-neutrinos with energies below 30 GeV*, Z. Phys. C **45**, 551 (1990).

[BABB08] A. Bodek, S. Avvakumov, R. Bradford and H. S. Budd, *Vector and axial nucleon form factors:a duality constrained parameterization*, Eur. Phys. J. C **53**, 349 (2008), arXiv:0708.1946.

[BARLM06] O. Buss, L. Alvarez-Ruso, A. B. Larionov and U. Mosel, *Pion induced double charge exchange reactions in the Delta resonance region*, Phys. Rev. C **74**, 044610 (2006), arXiv:nucl-th/0607016.

[BARMM06] O. Buss, L. Alvarez-Ruso, P. Muehlich and U. Mosel, *Low-energy pions in nuclear matter and 2π photoproduction within a BUU transport model*, Eur. Phys. J. A **29 (2)**, 189 (2006), arXiv:nucl-th/0603003.

[BCF04] A. Blondel, M. Campanelli and M. Fechner, *Energy reconstruction in quasielastic events unfolding physics and detector effects*, Nucl. Instrum. Meth. A **535**, 665 (2004).

[BD67] J. D. Bjorken and S. D. Drell, *Relativistische Quantenmechanik* (Bibliographisches Institut, Mannheim, 1967).

[BDPD+96] M. B. Barbaro, A. De Pace, T. W. Donnelly, A. Molinari and M. J. Musolf, *Probing nucleon strangeness with neutrinos: nuclear model dependences*, Phys. Rev. C **54**, 1954 (1996), arXiv:nucl-th/9605020.

[BDS08] O. Benhar, D. Day and I. Sick, *Inclusive quasielastic electron-nucleus scattering*, Rev. Mod. Phys. **80**, 189 (2008), arXiv:nucl-ex/0603029.

[BDW67] F. A. Berends, A. Donnachie and D. L. Weaver, *Photoproduction and electroproduction of pions. 1. dispersion relation theory*, Nucl. Phys. B **4**, 1 (1967).

[BEM02] V. Bernard, L. Elouadrhiri and U. G. Meissner, *Axial structure of the nucleon*, J. Phys. G **28**, R1 (2002), arXiv:hep-ph/0107088.

[BFN+05] O. Benhar, N. Farina, H. Nakamura, M. Sakuda and R. Seki, *Electron- and neutrino-nucleus scattering in the impulse approximation regime*, Phys. Rev. D **72**, 053005 (2005), arXiv:hep-ph/0506116.

[BG88] G. F. Bertsch and S. D. Gupta, *A guide to microscopic models for intermediate energy heavy ion collisions*, Phys. Rep. **160**, 189 (1988).

[BGG+] O. Buss, T. Gaitanos, K. Gallmeister, A. Larionov, T. Leitner, U. Mosel and J. Weil, *Giessen Boltzmann-Uehling-Uhlenbeck transport model*, in preparation .

[BGPR96] S. Boffi, C. Giusti, F. D. Pacati and M. Radici, *Electromagnetic response of atomic nuclei* (Oxford University Press, Oxford, Great Britain, 1996).

[BK73] E. Byckling and K. Kajantie, *Particle kinematics* (John Wiley & Sons, 1973).

[BK84] G. F. Bertsch and H. Kruse, *Boltzmann equation for heavy ion collisions*, Phys. Rev. C **29**, 673 (1984).

[BK07] A. V. Butkevich and S. A. Kulagin, *Quasielastic neutrino charged-current scattering cross sections on oxygen*, Phys. Rev. C **76**, 045502 (2007), arXiv:0705.1051 [nucl-th].

[BLMAR07] O. Buss, T. Leitner, U. Mosel and L. Alvarez-Ruso, *Influence of the nuclear medium on inclusive electron and neutrino scattering off nuclei*, Phys. Rev. C **76**, 035502 (2007), arXiv:0707.0232.

[BM05] A. V. Butkevich and S. P. Mikheyev, *Test of Fermi gas model and plane-wave impulse approximation against electron nucleus scattering data*, Phys. Rev. C **72**, 025501 (2005), arXiv:hep-ph/0505008.

[BM06] O. Benhar and D. Meloni, *How well do we know the nucleon structure functions in the Delta production region?*, Phys. Rev. Lett. **97**, 192301 (2006), arXiv:hep-ph/0604071.

[BM07] O. Benhar and D. Meloni, *Total neutrino and anti-neutrino nuclear cross sections around 1 GeV*, Nucl. Phys. A **789**, 379 (2007), arXiv:hep-ph/0610403.

[BPY05] A. Bodek, I. Park and U.-K. Yang, *Improved low Q^2 model for neutrino and electron nucleon cross sections in few GeV region*, Nucl. Phys. Proc. Suppl. **139**, 113 (2005), arXiv:hep-ph/0411202.

[BR81] A. Bodek and J. L. Ritchie, *Fermi motion effects in deep inelastic lepton scattering from nuclear targets*, Phys. Rev. D **23**, 1070 (1981).

[BS07] C. Berger and L. M. Sehgal, *Lepton mass effects in single pion production by neutrinos*, Phys. Rev. D **76**, 113004 (2007), arXiv:0709.4378.

[BS09] C. Berger and L. M. Sehgal, *PCAC and coherent pion production by low energy neutrinos*, Phys. Rev. D **79**, 053003 (2009), arXiv:0812.2653.

[Bus08] O. Buss, *Photon- and pion-induced nuclear reactions in a transport approach*, PhD thesis, Justus-Liebig-Universität Gießen, 2008, available online at http://theorie.physik.uni-giessen.de/.

[Bus09] O. Buss, *Compton scattering and the mass dependence of the Delta form factor*, internal report, Justus-Liebig-Universität Gießen (2009), available online at http://gibuu.physik.uni-giessen.de/GiBUU/wiki/Xsections/Compton.

[But08] A. V. Butkevich, *Analysis of quasielastic neutrino charged-current scattering off ^{16}O and neutrino energy reconstruction*, Phys. Rev. C **78**, 015501 (2008), arXiv:0804.4102.

[Cas02] D. Casper, *The NUANCE neutrino physics simulation, and the future*, Nucl. Phys. Proc. Suppl. **112**, 161 (2002), arXiv:hep-ph/0208030.

[CG98] F. Cano and P. Gonzalez, *A consistent explanation of the Roper phenomenology*, Phys. Lett. B **431**, 270 (1998), arXiv:nucl-th/9804071.

[CJ00] W. Cassing and S. Juchem, *Semiclassical transport of particles with dynamical spectral functions*, Nucl. Phys. A **665**, 377 (2000), arXiv:nucl-th/9903070.

[CNS] CNS Data Analysis Center, http://gwdac.phys.gwu.edu/.

[CPSS97] F. Cardarelli, E. Pace, G. Salme and S. Simula, *Electroproduction of the Roper resonance and the constituent quark model*, Phys. Lett. B **397**, 13 (1997), arXiv:nucl-th/9609047.

[CSTL04] W.-T. Chiang, B. Saghai, F. Tabakin and T. S. H. Lee, *Dynamical coupled-channel model of kaon hyperon interactions*, Phys. Rev. C **69**, 065208 (2004), arXiv:nucl-th/0404062.

[CVL96] J. Cugnon, J. Vandermeulen and D. L'Hote, *Simple parametrization of cross sections for nuclear transport studies up to the GeV range*, Nucl. Instrum. Meth. B **111**, 215 (1996).

[D$^+$80] M. Derrick *et al.*, *Study of the reaction* $\nu n \to \nu p \pi^-$, Phys. Lett. B **92**, 363 (1980).

[DF83] T. De Forest, *Off-shell electron nucleon cross sections. The impulse approximation*, Nucl. Phys. A **392**, 232 (1983).

[DJDVDV74] C. W. De Jager, H. De Vries and C. De Vries, *Nuclear charge and magnetization density distribution parameters from elastic electron scattering*, Atom. Data Nucl. Data Tabl. **14**, 479 (1974).

[Dju06] Z. Djurcic, *Backgrounds in neutrino appearance signal at MiniBooNE*, AIP Conf. Proc. **842**, 828 (2006), arXiv:hep-ex/0601014.

[DKT07] D. Drechsel, S. S. Kamalov and L. Tiator, *Unitary isobar model - MAID2007*, Eur. Phys. J. A **34**, 69 (2007), arXiv:0710.0306.

[DONUT01] K. Kodama *et al.* [DONUT Collaboration], *Observation of* τ *neutrino interactions*, Phys. Lett. B **504**, 218 (2001), arXiv:hep-ex/0012035.

[DP79] T. W. Donnelly and R. D. Peccei, *Neutral current effects in nuclei*, Phys. Rept. **50**, 1 (1979).

[DSFB99] Y. B. Dong, K. Shimizu, A. Faessler and A. J. Buchmann, *Description of the electroproduction amplitudes of the Roper resonance in a relativistic quark model*, Phys. Rev. C **60**, 035203 (1999).

[DSG86] V. Dmitriev, O. Sushkov and C. Gaarde, Δ *formation in the H-1 (He-3, H-3)* Δ^{++} *reaction at intermediate-energies*, Nucl. Phys. A **459**, 503 (1986).

[DT92] D. Drechsel and L. Tiator, *Threshold pion photoproduction on nucleons*, J. Phys. G **18**, 449 (1992).

[Dyt09] S. Dytman, *Final state interactions (GENIE)*, lectures given at 45th Karpacz Winter School in Theoretical Physics, February 2-11, 2009, Lądek-Zdrój, Poland, available online at http://wng.ift.uni.wroc.pl/karp45.

[EBM99] M. Effenberger, E. L. Bratkovskaya and U. Mosel, e^+e^- *pair production from* γA *reactions*, Phys. Rev. C **60**, 044614 (1999), arXiv:nucl-th/9903026.

[ECM+94] A. Engel, W. Cassing, U. Mosel, M. Schafer and G. Wolf, *Pion - nucleus reactions in a microscopic transport model*, Nucl. Phys. A **572**, 657 (1994), arXiv:nucl-th/9307008.

[Eff99] M. Effenberger, *Eigenschaften von Hadronen in Kernmaterie in einem vereinheitlichten Transportmodell*, PhD thesis, Justus-Liebig-Universität Gießen, 1999, available online at http://theorie.physik.uni-giessen.de/.

[EM99] M. Effenberger and U. Mosel, *Off-shell effects on particle production*, Phys. Rev. C **60**, 051901 (1999), arXiv:nucl-th/9906085.

[EM00] M. Effenberger and U. Mosel, *Photoproduction of mesons in nuclei at GeV energies*, Phys. Rev. C **62**, 014605 (2000), arXiv:nucl-th/9908078.

[EW88] T. E. O. Ericson and W. Weise, *Pions and nuclei* (Clarendon Press, Oxford, 1988).

[FCGM04] T. Falter, W. Cassing, K. Gallmeister and U. Mosel, *Hadron attenuation in deep inelastic lepton nucleus scattering*, Phys. Rev. C **70**, 054609 (2004), arXiv:nucl-th/0406023.

[FK97] T. C. Ferree and D. S. Koltun, *Inelastic nucleon contributions in* (e, e') *nuclear response functions*, Phys. Rev. C **55**, 253 (1997), arXiv:nucl-th/9512021.

[FKR71] R. P. Feynman, M. Kislinger and F. Ravndal, *Current matrix elements from a relativistic quark model*, Phys. Rev. D **3**, 2706 (1971).

[FN79] G. L. Fogli and G. Nardulli, *A new approach to the charged current induced weak one pion production*, Nucl. Phys. B **160**, 116 (1979).

[FN80] G. L. Fogli and G. Nardulli, *Neutral current induced one pion production: a new model and its comparison with the experiment*, Nucl. Phys. B **165**, 162 (1980).

[Fur02] K. Furuno, *BNL 7-foot bubble chamber experiment - neutrino deuterium interactions*, talk given at NUINT02, December 12-15, 2002, Irvine, California, available online at http://www.ps.uci.edu/~nuint/sessions.htm.

[G005] D. S. Armstrong *et al.* [G0 Collaboration], *Strange quark contributions to parity-violating asymmetries in the forward G0 electron proton scattering experiment*, Phys. Rev. Lett. **95**, 092001 (2005), arXiv:nucl-ex/0506021.

[Gala] H. Gallagher, private communication.

[Galb] K. Gallmeister, private communication.

[Gal02] H. Gallagher, *The NEUGEN neutrino event generator*, Nucl. Phys. Proc. Suppl. **112**, 188 (2002).

[Gal09] H. Gallagher, *Neutrino event generator review*, talk given at NUINT09, May 17-22, 2009, Sitges, Spain, available online at http://nuint09.ifae.es/Agenda.html.

[GCHS05] H. Gallagher, D. Casper, Y. Hayato and P. Sala, *Event generator comparisons*, Nucl. Phys. Proc. Suppl. **139**, 278 (2005).

[GENIE] GENIE, http://www.genie-mc.org/.

[GF05] K. Gallmeister and T. Falter, *Space-time picture of fragmentation in PYTHIA / JETSET for HERMES and RHIC*, Phys. Lett. B **630**, 40 (2005), arXiv:nucl-th/0502015.

[GiBUU] GiBUU, http://gibuu.physik.uni-giessen.de/GiBUU.

[GKKL92] G. T. Garvey, S. Krewald, E. Kolbe and K. Langanke, *Strange quark contributions to neutrino induced quasielastic scattering*, Phys. Lett. B **289**, 249 (1992).

[GLW93] G. T. Garvey, W. C. Louis and D. H. White, *Determination of proton strange form factors from neutrino p elastic scattering*, Phys. Rev. C **48**, 761 (1993).

[GM08] K. Gallmeister and U. Mosel, *Time dependent hadronization via HERMES and EMC data consistency*, Nucl. Phys. A **801**, 68 (2008), arXiv:nucl-th/0701064.

[GM09] K. Gallmeister and U. Mosel, *Production of charged pions off nuclei with 3...30 GeV incident protons and pions*, Nucl. Phys. A **826**, 151 (2009), arXiv:0901.1770.

[GMCARVV08] L. S. Geng, J. Martin Camalich, L. Alvarez-Ruso and M. J. Vicente Vacas, *Nucleon-to-Delta axial transition form factors in relativistic baryon chiral perturbation theory*, Phys. Rev. D **78**, 014011 (2008), arXiv:0801.4495.

[GNO97] A. Gil, J. Nieves and E. Oset, *Many body approach to the inclusive (e, e') reaction from the quasielastic to the Delta excitation region*, Nucl. Phys. A **627**, 543 (1997), arXiv:nucl-th/9711009.

[GS08a] K. M. Graczyk and J. T. Sobczyk, *Form factors in the quark resonance model*, Phys. Rev. D **77**, 053001 (2008), arXiv:0707.3561.

[GS08b] K. M. Graczyk and J. T. Sobczyk, *Lepton mass effects in weak CC single pion production*, Phys. Rev. **D77**, 053003 (2008), arXiv:0709.4634.

[HAPPEX01] K. A. Aniol *et al.* [HAPPEX Collaboration], *New measurement of parity violation in elastic electron proton scattering and implications for strange form factors*, Phys. Lett. B **509**, 211 (2001), arXiv:nucl-ex/0006002.

[HAPPEX06] K. A. Aniol *et al.* [HAPPEX Collaboration], *Constraints on the nucleon strange form factors at Q^2 approx. 0.1 GeV^2*, Phys. Lett. B **635**, 275 (2006), arXiv:nucl-ex/0506011.

[HARP] HARP, http://harp.web.cern.ch/harp/.

[Haw02] E. Hawker, *Single pion production in low energy neutrino-carbon interactions*, talk given at NUINT02, December 12-15, 2002, Irvine, California, available online at http://www.ps.uci.edu/~nuint/sessions.htm.

[Haw04] E. Hawker, *Data checks of FSI models in NUANCE*, talk given at NUINT04, March 17-21, 2004, Gran Sasso, Italy, available online at http://nuint04.lngs.infn.it/.

[Haw05] E. A. Hawker, *NUANCE at MiniBooNE*, Nucl. Phys. Proc. Suppl. **139**, 260 (2005).

[Hay] Y. Hayato, private communication.

[Hay02] Y. Hayato, *NEUT*, Nucl. Phys. Proc. Suppl. **112**, 171 (2002).

[Hay09] Y. Hayato, *NEUT*, lectures given at 45th Karpacz Winter School in Theoretical Physics, February 2-11, 2009, Lądek-Zdrój, Poland, available online at http://wng.ift.uni.wroc.pl/karp45.

[HCTM99] A. Hombach, W. Cassing, S. Teis and U. Mosel, *Analysis of flow effects in relativistic heavy-ion collisions within the CBUU approach*, Eur. Phys. J. A **5**, 157 (1999), arXiv:nucl-th/9812050.

[HKMP93] C. J. Horowitz, H.-C. Kim, D. P. Murdock and S. Pollock, *Neutrino-nucleus quasifree neutral current reactions and the nucleon strange quark content*, Phys. Rev. C **48**, 3078 (1993).

[HNS$^+$08] E. Hernandez, J. Nieves, S. K. Singh, M. Valverde and M. J. Vicente Vacas, *Neutrino induced threshold production of two pions and N*(1440) electroweak form factors*, Phys. Rev. D **77**, 053009 (2008), arXiv:0710.3562.

[HNV07] E. Hernandez, J. Nieves and M. Valverde, *Weak pion production off the nucleon*, Phys. Rev. D **76**, 033005 (2007), arXiv:hep-ph/0701149.

[IZ05] C. Itzykson and J. B. Zuber, *Quantum field theory* (Dover Publications, New York, 2005), reprint of the work originally published by McGraw-Hill, New York, in 1980.

[JRHR99] N. Jachowicz, S. Rombouts, K. Heyde and J. Ryckebusch, *Cross sections for neutral-current neutrino-nucleus interactions: Applications for C-12 and O-16*, Phys. Rev. C **59**, 3246 (1999).

[K$^+$78] W. Krenz *et al.*, *Experimental study of exclusive one pion production in all neutrino induced neutral current channels*, Nucl. Phys. B **135**, 45 (1978).

[K$^+$86] T. Kitagaki *et al.*, *Charged current exclusive pion production in neutrino deuterium interactions*, Phys. Rev. D **34**, 2554 (1986).

[K$^+$90] T. Kitagaki *et al.*, *Study of* $\nu d \to \mu^- pp(s)$ *and* $\nu d \to \mu^- \Delta^{++}(1232)n(s)$ *using the BNL 7-foot deuterium filled bubble chamber*, Phys. Rev. D **42**, 1331 (1990).

[K$^+$04] B. Krusche *et al.*, *Photoproduction of π^0-mesons from nuclei*, Eur. Phys. J. A **22**, 277 (2004), arXiv:nucl-ex/0406002.

[K$^+$05] C. Kraus *et al.*, *Final results from phase II of the Mainz neutrino mass search in tritium β decay*, Eur. Phys. J. C **40**, 447 (2005), arXiv:hep-ex/0412056.

[K2K] K2K, http://neutrino.kek.jp/.

[K2K03] M. H. Ahn *et al.* [K2K Collaboration], *Indications of neutrino oscillation in a 250 km long-baseline experiment*, Phys. Rev. Lett. **90**, 041801 (2003), arXiv:hep-ex/0212007.

[K2K05a] M. Hasegawa *et al.* [K2K Collaboration], *Search for coherent charged pion production in neutrino carbon interactions*, Phys. Rev. Lett. **95**, 252301 (2005), arXiv:hep-ex/0506008.

[K2K05b] S. Nakayama *et al.* [K2K Collaboration], *Measurement of single π^0 production in neutral current neutrino interactions with water by a 1.3 GeV wide band muon neutrino beam*, Phys. Lett. B **619**, 255 (2005), arXiv:hep-ex/0408134.

[K2K06] R. Gran *et al.* [K2K Collaboration], *Measurement of the quasielastic axial vector mass in neutrino oxygen interactions*, Phys. Rev. D **74**, 052002 (2006), arXiv:hep-ex/0603034.

[K2K08] A. Rodriguez *et al.* [K2K Collaboration], *Measurement of single charged pion production in the charged-current interactions of neutrinos in a 1.3 GeV wide band beam*, Phys. Rev. D **78**, 032003 (2008), arXiv:0805.0186.

[Kal07] D. Kalok, *The influence of in-medium modifications on quasielastic electron and neutrino scattering on nuclei*, Diploma thesis, Justus-Liebig-Universität Gießen, 2007, available online at http://theorie.physik.uni-giessen.de/.

[KamLAND03] K. Eguchi *et al.* [KamLAND Collaboration], *First results from KamLAND: Evidence for reactor anti- neutrino disappearance*, Phys. Rev. Lett. **90**, 021802 (2003), arXiv:hep-ex/0212021.

[Kat09] T. Katori, *Measurement of muon neutrino charged current quasielastic (CCQE) double differential cross section in MiniBooNE*, talk given at NUINT09, May 17-22, 2009, Sitges, Spain, available online at http://nuint09.ifae.es/Agenda.html.

[KATRIN01] A. Osipowicz *et al.* [KATRIN Collaboration], *KATRIN: A next generation tritium beta decay experiment with sub-eV sensitivity for the electron neutrino mass*, arXiv:hep-ex/0109033.

[KB94] L. Kadanoff and G. Baym, *Quantum statistical mechanics* (Addison Wesley Publishing Company, 1994).

[KLK94] E. Kolbe, K. Langanke and S. Krewald, *Neutrino induced reactions on C-12 within the continuum random phase approximation*, Phys. Rev. C **49**, 1122 (1994).

[KLN04] K. S. Kuzmin, V. V. Lyubushkin and V. A. Naumov, *Lepton polarization in neutrino nucleon interactions*, Mod. Phys. Lett. A **19**, 2815 (2004), arXiv:hep-ph/0312107.

[KLN08] K. S. Kuzmin, V. V. Lyubushkin and V. A. Naumov, *Quasielastic axial-vector mass from experiments on neutrino-nucleus scattering*, Eur. Phys. J. C **54**, 517 (2008), arXiv:0712.4384.

[Kop09] S. E. Kopp, *Accelerator neutrino beams as used in cross section experiments*, talk given at NUINT09, May 17-22, 2009, Sitges, Spain, available online at http://nuint09.ifae.es/Agenda.html.

[Kur09] Y. Kurimoto, *SciBooNE's neutral current π^0 production measurement*, talk given at NUINT09, May 17-22, 2009, Sitges, Spain, available online at http://nuint09.ifae.es/Agenda.html.

[Ladek09] *Neutrino interactions: from theory to Monte Carlo simulations, 45th Karpacz Winter School in Theoretical Physics, Lądek-Zdrój, Poland, February 2-11, 2009*, Acta Physica Polonica B **40**, 2379 (2009), see also http://wng.ift.uni.wroc.pl/karp45.

[Lar] A. Larionov, private communication.

[LARM06a] T. Leitner, L. Alvarez-Ruso and U. Mosel, *Charged current neutrino-nucleus interactions at intermediate energies*, Phys. Rev. C **73**, 065502 (2006), arXiv:nucl-th/0601103.

[LARM06b] T. Leitner, L. Alvarez-Ruso and U. Mosel, *Neutral current neutrino-nucleus interactions at intermediate energies*, Phys. Rev. C **74**, 065502 (2006), arXiv:nucl-th/0606058.

[LBARM09] T. Leitner, O. Buss, L. Alvarez-Ruso and U. Mosel, *Electron- and neutrino-nucleus scattering from the quasielastic to the resonance region*, Phys. Rev. C **79**, 034601 (2009), arXiv:0812.0587.

[LBGM07] A. B. Larionov, O. Buss, K. Gallmeister and U. Mosel, *Three-body collisions in Boltzmann-Uehling-Uhlenbeck theory*, Phys. Rev. C **76**, 044909 (2007), arXiv:0704.1785.

[LBL92] Z.-p. Li, V. Burkert and Z.-j. Li, *Electroproduction of the Roper resonance as a hybrid state*, Phys. Rev. D **46**, 70 (1992).

[LBMAR07] T. Leitner, O. Buss, U. Mosel and L. Alvarez-Ruso, *Neutrino interactions with nuclei*, AIP Conf. Proc. **967**, 192 (2007), arXiv:0709.0244.

[LBMAR08] T. Leitner, O. Buss, U. Mosel and L. Alvarez-Ruso, *Neutrino scattering with nuclei — theory of low energy nuclear effects and its applications*, PoS **NUFACT08**, 60 (2008), arXiv:0809.3986.

[LBMAR09] T. Leitner, O. Buss, U. Mosel and L. Alvarez-Ruso, *Neutrino-induced pion production at energies relevant for the MiniBooNE and K2K experiments*, Phys. Rev. C **79**, 038501 (2009), arXiv:0812.1787.

[Leh03] J. Lehr, *In-Medium-Eigenschaften von Nukleonen und Nukleonenresonanzen in einem semiklassischen Transportmodell*, PhD thesis, Justus-Liebig-Universität Gießen, 2003, available online at http://theorie.physik.uni-giessen.de/.

[Lei05] T. Leitner, *Neutrino interactions with nucleons and nuclei*, Diploma thesis, Justus-Liebig-Universität Gießen, 2005, available online at http://theorie.physik.uni-giessen.de/.

[LEM00] J. Lehr, M. Effenberger and U. Mosel, *Electron and photon induced reactions on nuclei in the nucleon resonance region*, Nucl. Phys. A **671**, 503 (2000), arXiv:nucl-th/9907091.

[Leu00] S. Leupold, *Towards a test particle description of transport processes for states with continuous mass spectra*, Nucl. Phys. A **672**, 475 (2000), arXiv:nucl-th/9909080.

[LLLM02] J. Lehr, H. Lenske, S. Leupold and U. Mosel, *Nuclear matter spectral functions by transport theory*, Nucl. Phys. A **703**, 393 (2002), arXiv:nucl-th/0108008.

[LM03] A. B. Larionov and U. Mosel, *The $NN \to N\Delta$ cross section in nuclear matter*, Nucl. Phys. A **728**, 135 (2003), arXiv:nucl-th/0307035.

[LM05] A. B. Larionov and U. Mosel, *Kaon production and propagation at intermediate relativistic energies*, Phys. Rev. C **72**, 014901 (2005).

[LMW09] T. Leitner, U. Mosel and S. Winkelmann, *Neutrino-induced coherent pion production off nuclei reexamined*, Phys. Rev. C **79**, 057601 (2009), arXiv:0901.2837.

[LMZ95] J. Liu, N. C. Mukhopadhyay and L.-S. Zhang, *Nucleon to Delta weak excitation amplitudes in the nonrelativistic quark model*, Phys. Rev. C **52**, 1630 (1995), arXiv:hep-ph/9506389.

[LP05] O. Lalakulich and E. A. Paschos, *Resonance production by neutrinos. J = 3/2 resonances*, Phys. Rev. D **71**, 074003 (2005), arXiv:hep-ph/0501109.

[LPM03] J. Lehr, M. Post and U. Mosel, *In-medium modifications of the S11(1535) resonance and eta photoproduction*, Phys. Rev. C **68**, 044601 (2003), arXiv:nucl-th/0306024.

[LPP06] O. Lalakulich, E. A. Paschos and G. Piranishvili, *Resonance production by neutrinos: the second resonance region*, Phys. Rev. D **74**, 014009 (2006), arXiv:hep-ph/0602210.

[LS72] C. H. Llewellyn Smith, *Neutrino reactions at accelerator energies*, Phys. Rept. **3**, 261 (1972).

[LSND95] C. Athanassopoulos *et al.* [LSND Collaboration], *Candidate events in a search for anti-muon-neutrino → anti-electron-neutrino oscillations*, Phys. Rev. Lett. **75**, 2650 (1995), arXiv:nucl-ex/9504002.

[LSND01] A. Aguilar *et al.* [LSND Collaboration], *Evidence for neutrino oscillations from the observation of $\bar{\nu}_e$ appearance in a $\bar{\nu}_\mu$ beam*, Phys. Rev. D **64**, 112007 (2001), arXiv:hep-ex/0104049.

[M$^+$73] W. A. Mann *et al.*, *Study of the reaction $\nu n \to \mu^- p$*, Phys. Rev. Lett. **31**, 844 (1973).

[M$^+$76] J. Mougey *et al.*, *Quasifree (e, e' p) scattering on C-12, Si-28, Ca-40 and Ni-58*, Nucl. Phys. A **262**, 461 (1976).

[M$^+$84] D. MacFarlane *et al.*, *Nucleon structure functions from high-energy neutrino interactions with iron and QCD results*, Z. Phys. C **26**, 1 (1984).

[MAID] MAID, http://www.kph.uni-mainz.de/MAID.

[Mar99] J. Marteau, *Effects of the nuclear correlations on the neutrino oxygen interactions*, Eur. Phys. J. A **5**, 183 (1999), arXiv:hep-ph/9902210.

[MCGP03] A. Meucci, F. Capuzzi, C. Giusti and F. D. Pacati, *Inclusive electron scattering in a relativistic Green function approach*, Phys. Rev. C **67**, 054601 (2003), arXiv:nucl-th/0301084.

[MFM04] P. Muhlich, T. Falter and U. Mosel, *Inclusive omega photoproduction off nuclei*, Eur. Phys. J. A **20**, 499 (2004), arXiv:nucl-th/0310067.

[MGP04a] A. Meucci, C. Giusti and F. D. Pacati, *Neutral-current neutrino-nucleus quasielastic scattering*, Nucl. Phys. A **744**, 307 (2004), arXiv:nucl-th/0405004.

[MGP04b] A. Meucci, C. Giusti and F. D. Pacati, *Relativistic Green's function approach to charged-current neutrino nucleus quasielastic scattering*, Nucl. Phys. A **739**, 277 (2004), arXiv:nucl-th/0311081.

[MGP06] A. Meucci, C. Giusti and F. D. Pacati, *Neutrino-nucleus quasielastic scattering and strange quark effects*, Nucl. Phys. A **773**, 250 (2006), arXiv:nucl-th/0601052.

[MicroBooNE] MicroBooNE, http://www-microboone.fnal.gov/.

[MINERvA04] D. Drakoulakos *et al.* [MINERvA Collaboration], *Proposal to perform a high-statistics neutrino scattering experiment using a fine-grained detector in the NuMI beam*, arXiv:hep-ex/0405002.

[MiniBooNE] MiniBooNE, http://www-boone.fnal.gov/.

[MiniBooNE07a] A. A. Aguilar-Arevalo *et al.* [MiniBooNE Collaboration], *Constraining muon internal bremsstrahlung as a contribution to the MiniBooNE low energy excess*, arXiv:0710.3897.

[MiniBooNE07b] A. A. Aguilar-Arevalo *et al.* [MiniBooNE Collaboration], *A search for electron neutrino appearance at the* $\Delta m^2 \sim 1\ eV^2$ *scale*, Phys. Rev. Lett. **98**, 231801 (2007), arXiv:0704.1500.

[MiniBooNE08a] A. A. Aguilar-Arevalo *et al.* [MiniBooNE Collaboration], *First observation of coherent* π^0 *production in neutrino-nucleus interactions with* $E_\nu < 2\ GeV$, Phys. Lett. B **664**, 41 (2008), arXiv:0803.3423.

[MiniBooNE08b] A. A. Aguilar-Arevalo *et al.* [MiniBooNE Collaboration], *Measurement of muon neutrino quasielastic scattering on carbon*, Phys. Rev. Lett. **100**, 032301 (2008), arXiv:0706.0926.

[MiniBooNE09a] A. A. Aguilar-Arevalo *et al.* [MiniBooNE Collaboration], *Measurement of the ν_μ charged current π^+ to quasielastic cross section ratio on mineral oil in a 0.8 GeV neutrino beam*, Phys. Rev. Lett. **103**, 081801 (2009), arXiv:0904.3159.

[MiniBooNE09b] A. A. Aguilar-Arevalo *et al.* [MiniBooNE Collaboration], *The MiniBooNE detector*, Nucl. Instrum. Meth. A **599**, 28 (2009), arXiv:0806.4201.

[MiniBooNE09c] A. A. Aguilar-Arevalo *et al.* [MiniBooNE Collaboration], *The neutrino flux prediction at MiniBooNE*, Phys. Rev. D **79**, 072002 (2009), arXiv:0806.1449.

[MiniBooNE09d] A. A. Aguilar-Arevalo *et al.* [MiniBooNE Collaboration], *Search for electron anti-neutrino appearance at the $\Delta m^2 \sim 1\ eV^2$ scale*, Phys. Rev. Lett. **103**, 111801 (2009), arXiv:0904.1958.

[MiniBooNE09e] A. A. Aguilar-Arevalo *et al.* [MiniBooNE Collaboration], *Unexplained excess of electron-like events from a 1 GeV neutrino beam*, Phys. Rev. Lett. **102**, 101802 (2009), arXiv:0812.2243.

[MiniBooNE09f] R. H. Nelson [MiniBooNE Collaboration], *$CC\pi^0$ event reconstruction at MiniBooNE*, arXiv:0909.1238.

[MINOS] MINOS, http://www-numi.fnal.gov/.

[Mit07] G. Mitsuka, *NEUT*, AIP Conf. Proc. **967**, 208 (2007).

[MLJ$^+$06] M. C. Martinez, P. Lava, N. Jachowicz, J. Ryckebusch, K. Vantournhout and J. M. Udias, *Relativistic models for quasielastic neutrino scattering*, Phys. Rev. C **73**, 024607 (2006), arXiv:nucl-th/0505008.

[MM06] P. Muhlich and U. Mosel, *omega attenuation in nuclei*, Nucl. Phys. A **773**, 156 (2006), arXiv:nucl-th/0602054.

[MMCU03] C. Maieron, M. C. Martinez, J. A. Caballero and J. M. Udias, *Nuclear model effects in charged current neutrino-nucleus quasielastic scattering*, Phys. Rev. C **68**, 048501 (2003), arXiv:nucl-th/0303075.

[Mos99] U. Mosel, *Fields, symmetries, and quarks* (Springer, Berlin, 1999).

[MS92] D. M. Manley and E. M. Saleski, *Multichannel resonance parametrization of πN scattering amplitudes*, Phys. Rev. D **45**, 4002 (1992).

[MS93] F. Mandl and G. Shaw, *Quantenfeldtheorie* (AULA-Verlag, Wiesbaden, 1993).

[MuCap07] V. A. Andreev *et al.* [MuCap Collaboration], *Measurement of the rate of muon capture in hydrogen gas and determination of the proton's pseudoscalar coupling* g_P, Phys. Rev. Lett. **99**, 032002 (2007), arXiv:0704.2072.

[NAV04] J. Nieves, J. E. Amaro and M. Valverde, *Inclusive quasielastic neutrino reactions*, Phys. Rev. C **70**, 055503 (2004), arXiv:nucl-th/0408005.

[NOGR93] J. Nieves, E. Oset and C. Garcia-Recio, *A theoretical approach to pionic atoms and the problem of anomalies*, Nucl. Phys. A **554**, 509 (1993).

[NOMAD08] V. Lyubushkin *et al.* [NOMAD Collaboration], *A study of quasielastic muon neutrino and anti-neutrino scattering in the NOMAD experiment*, arXiv:0812.4543.

[Nor28] L. W. Nordheim, *On the kinetic method in the new statistics and its application in the electron theory of conductivity*, Proc. R. Soc. Lond. A **119**, 689 (1928).

[NPKO90] H. W. L. Naus, S. J. Pollock, J. H. Koch and U. Oelfke, *Electron scattering from a bound nucleon*, Nucl. Phys. A **509**, 717 (1990).

[NSNB07] H. Nakamura, M. Sakuda, T. Nasu and O. Benhar, *Inclusive electron spectrum in the region of pion production in electron-nucleus scattering and the effect of the quasielastic interaction*, Phys. Rev. C **76**, 065208 (2007), arXiv:0705.3884.

[NUINT09] *6th International Workshop on Neutrino-Nucleus Interactions in the Few-GeV Region (NUINT09), May 17-22, 2009, Sitges, Spain*, http://nuint09.ifae.es/Agenda.html.

[NVVV06] J. Nieves, M. Valverde and M. J. Vicente Vacas, *Inclusive nucleon emission induced by quasielastic neutrino-nucleus interactions*, Phys. Rev. C **73**, 025504 (2006), arXiv:hep-ph/0511204.

[OPERA] OPERA, http://operaweb.lngs.infn.it/.

[OS87] E. Oset and L. L. Salcedo, *Delta selfenergy in nuclear matter*, Nucl. Phys. A **468**, 631 (1987).

[P$^+$79a] M. Pohl *et al.*, *Experimental study of single pion production in charged current neutrino interactions*, Lett. Nuovo Cim. **24**, 540 (1979).

[P$^+$79b] M. Pohl *et al.*, *Experimental study of the reaction $\nu n \to \mu^- p$*, Lett. Nuovo Cim. **26**, 332 (1979).

[Pas] E. A. Paschos, private communication.

[Pat04] S. F. Pate, *Determination of the strange form factors of the nucleon from νp, $\bar{\nu} p$, and parity-violating $\vec{e} p$ elastic scattering*, Phys. Rev. Lett. **92**, 082002 (2004), arXiv:hep-ex/0310052.

[Pat05] S. F. Pate, *Don't forget to measure $\Delta(s)$*, Eur. Phys. J. A **24S2**, 67 (2005), arXiv:nucl-ex/0502014.

[PDG08] C. Amsler *et al.* [Particle Data Group Collaboration], *Review of particle physics*, Phys. Lett. B **667**, 1 (2008).

[PDT07] B. Pasquini, D. Drechsel and L. Tiator, *Invariant amplitudes for pion electroproduction*, Eur. Phys. J. A **34**, 387 (2007), arXiv:0712.2327.

[Pen02] G. Penner, *Vector meson production and nucleon resonance analysis in a coupled channel approach*, PhD thesis, Justus-Liebig-Universität Gießen, 2002, available online at http://theorie.physik.uni-giessen.de/.

[PLJR09] C. Praet, O. Lalakulich, N. Jachowicz and J. Ryckebusch, *Δ-mediated pion production in nuclei*, Phys. Rev. C **79**, 044603 (2009), arXiv:0804.2750.

[PLM98] W. Peters, H. Lenske and U. Mosel, *Coherent photoproduction of pions on nuclei in a relativistic, non-local model*, Nucl. Phys. A **640**, 89 (1998), arXiv:nucl-th/9803009.

[PMP08] S. F. Pate, D. W. McKee and V. Papavassiliou, *Strange quark contribution to the vector and axial form factors of the nucleon: combined analysis of G0, HAPPEX, and Brookhaven E734 data*, Phys. Rev. C **78**, 015207 (2008), arXiv:0805.2889.

[PNK96] S. Pollock, H. W. L. Naus and J. H. Koch, *The electron-nucleon cross section in $(e, e'p)$ reactions*, Phys. Rev. C **53**, 2304 (1996), arXiv:nucl-th/9512043.

[Pol08] C. Polly, *Updates to the low energy excess in MiniBooNE*, talk given at FNAL Wine & Cheese, August 1, 2008, available online at http://www-boone.fnal.gov/slides-talks/conf-talk/polly/Polly_FermilabWC_full.pdf.

[Pos04] M. Post, *Hadronic spectral functions in nuclear matter*, PhD thesis, Justus-Liebig-Universität Gießen, 2004, available online at http://theorie.physik.uni-giessen.de/.

[PPY00] E. A. Paschos, L. Pasquali and J.-Y. Yu, *Single pion production in neutrino reactions and estimates for charge exchange effects*, Nucl. Phys. B **588**, 263 (2000), arXiv:hep-ph/0005255.

[Pra09] C. Praet, *Modeling quasi-free neutrino-nucleus reactions for accelerator-based experiments*, PhD thesis, Universiteit Gent, 2009, available online at http://inwpent5.ugent.be/papers/phdchristophe.pdf.

[PS09] E. A. Paschos and D. Schalla, *Coherent pion production*, Phys. Rev. D **80**, 033005 (2009), arXiv:0903.0451.

[PSY07] E. A. Paschos, I. Schienbein and J. Y. Yu, *Single pion electro- and neutrinoproduction on heavy targets*, arXiv:0704.1991 [hep-ph].

[R$^+$82] G. M. Radecky *et al.*, *Study of single pion production by weak charged currents in low-energy neutrino d interactions*, Phys. Rev. D **25**, 1161 (1982).

[Rav71] F. Ravndal, *Electroproduction of nucleon resonances in a relativistic quark model*, Phys. Rev. D **4**, 1466 (1971).

[RC53] F. Reines and C. L. Cowan, *Detection of the free neutrino*, Phys. Rev. **92**, 830 (1953).

[Rei95] F. Reines, *The neutrino: From poltergeist to particle*, Nobel Lecture, December 8, 1995, available online at http://nobelprize.org/nobel_prizes/physics/laureates/1995/reines-lecture.pdf.

[Ros80] R. Rosenfelder, *Quasielastic electron scattering from nuclei*, Annals Phys. **128**, 188 (1980).

[RS81] D. Rein and L. M. Sehgal, *Neutrino excitation of baryon resonances and single pion production*, Ann. Phys. **133**, 79 (1981).

[RS83] D. Rein and L. M. Sehgal, *Coherent π^0 production in neutrino reactions*, Nucl. Phys. B **223**, 29 (1983).

[S$^+$89] R. M. Sealock *et al.*, *Electroexcitation of the Delta(1232) in nuclei*, Phys. Rev. Lett. **62**, 1350 (1989).

[SAA06] S. K. Singh, M. S. Athar and S. Ahmad, *Weak pion production from nuclei*, Pramana **66**, 689 (2006), arXiv:nucl-th/0507016.

[SACSVV08] M. Sajjad Athar, S. Chauhan, S. K. Singh and M. J. Vicente Vacas, *Neutrino-nucleus cross sections*, arXiv:0808.1437.

[SAMPLE04] D. T. Spayde *et al.* [SAMPLE Collaboration], *The strange quark contribution to the proton's magnetic moment*, Phys. Lett. B **583**, 79 (2004), arXiv:nucl-ex/0312016.

[Sch08a] D. W. Schmitz, *A measurement of hadron production cross sections for the simulation of accelerator neutrino beams and a search for muon-neutrino to electron-neutrino oscillations in the $\Delta m^2 \sim 1\ eV^2$ region*, PhD thesis, Columbia University, 2008, available online at http://lss.fnal.gov/archive/thesis/fermilab-thesis-2008-26.pdf.

[Sch08b] T. Schwetz, *The LSND puzzle in the light of MiniBooNE results*, arXiv:0805.2234.

[SciBooNE] SciBooNE, http://www-sciboone.fnal.gov/.

[SciBooNE06] A. A. Aguilar-Arevalo *et al.* [SciBooNE Collaboration], *Bringing the SciBar detector to the Booster neutrino beam*, arXiv:hep-ex/0601022.

[SciBooNE08] K. Hiraide *et al.* [SciBooNE Collaboration], *Search for charged current coherent pion production on carbon in a few-GeV neutrino beam*, Phys. Rev. D **78**, 112004 (2008), arXiv:0811.0369.

[Sel97] W. G. Seligman, *A next-to-leading order QCD analysis of neutrino - iron structure functions at the Tevatron*, PhD thesis, Columbia University, 1997, available online at http://lss.fnal.gov/archive/thesis/1900/fermilab-thesis-1997-21.pdf.

[SL01] T. Sato and T. S. H. Lee, *Dynamical study of the Delta excitation in $N(e,e'\pi)$ reactions*, Phys. Rev. C **63**, 055201 (2001), arXiv:nucl-th/0010025.

[SLMP05] V. Shklyar, H. Lenske, U. Mosel and G. Penner, *Coupled-channel analysis of the omega-meson production in πN and γN reactions for cm energies up to 2 GeV*, Phys. Rev. C **71**, 055206 (2005), arXiv:nucl-th/0412029.

[SM72] R. A. Smith and E. J. Moniz, *Neutrino reactions on nuclear targets*, Nucl. Phys. B **43**, 605 (1972).

[SMS06] T. Sjostrand, S. Mrenna and P. Skands, *PYTHIA 6.4 Physics and Manual*, JHEP **05**, 026 (2006), arXiv:hep-ph/0603175.

[SNO01] Q. R. Ahmad *et al.* [SNO Collaboration], *Measurement of the charged current interactions produced by B-8 solar neutrinos at the Sudbury Neutrino Observatory*, Phys. Rev. Lett. **87**, 071301 (2001), arXiv:nucl-ex/0106015.

[SO92] S. K. Singh and E. Oset, *Quasielastic neutrino (anti-neutrino) reactions in nuclei and the axial vector form factor of the nucleon*, Nucl. Phys. A **542**, 587 (1992).

[Sob09] J. Sobczyk, *Comparisons of neutrino-nucleus cross section calculations*, talk given at NUINT09, May 17-22, 2009, Sitges, Spain, available online at http://nuint09.ifae.es/Agenda.html.

[SOVVGR88] L. L. Salcedo, E. Oset, M. J. Vicente Vacas and C. Garcia-Recio, *Computer simulation of inclusive pion nuclear reactions*, Nucl. Phys. A **484**, 557 (1988).

[SSAA06a] S. K. Singh, M. Sajjad Athar and S. Ahmad, *Nuclear effects in neutrino induced coherent pion production at K2K and MiniBooNE*, Phys. Rev. Lett. **96**, 241801 (2006).

[SSAA06b] S. K. Singh, M. Sajjad Athar and S. Ahmad, *Nuclear cross sections in O-16 for beta beam neutrinos at intermediate energies*, Phys. Lett. B **641**, 159 (2006), arXiv:nucl-th/0603001.

[Ste07] B. Steinmüller, *Eine neue Initialisierung des Atomkerns für GiBUU*, Diploma thesis, Justus-Liebig-Universität Gießen, 2007, available online at http://theorie.physik.uni-giessen.de/.

[Sto93] P. Stoler, *Baryon form factors at high Q^2 and the transition to perturbative QCD*, Phys. Rept. **226**, 103 (1993).

[SUL03] T. Sato, D. Uno and T. S. H. Lee, *Dynamical model of weak pion production reactions*, Phys. Rev. C **67**, 065201 (2003), arXiv:nucl-th/0303050.

[Super-K98] Y. Fukuda *et al.* [Super-K Collaboration], *Evidence for oscillation of atmospheric neutrinos*, Phys. Rev. Lett. **81**, 1562 (1998), arXiv:hep-ex/9807003.

[SvH73] P. A. Schreiner and F. von Hippel, *Neutrino production of the Delta(1236)*, Nucl. Phys. B **58**, 333 (1973).

[SVVO98] S. K. Singh, M. J. Vicente Vacas and E. Oset, *Nuclear effects in neutrinoproduction of Delta at intermediate energies*, Phys. Lett. B **416**, 23 (1998).

[T2K] T2K, http://jnusrv01.kek.jp/public/t2k/.

[TAR] L. Tiator and L. Alvarez-Ruso, private communication.

[TCE+97] S. Teis, W. Cassing, M. Effenberger, A. Hombach, U. Mosel and G. Wolf, *Pion-production in heavy-ion collisions at SIS energies*, Z. Phys. A **356**, 421 (1997), arXiv:nucl-th/9609009.

[TDK+04] L. Tiator, D. Drechsel, S. Kamalov, M. M. Giannini, E. Santopinto and A. Vassallo, *Electroproduction of nucleon resonances*, Eur. Phys. J. A **19**, 55 (2004), arXiv:nucl-th/0310041.

[Tei97] S. Teis, *Transporttheoretische Beschreibung von relativistischen Schwerionenkollisionen bei SIS-Energien*, PhD thesis, Justus-Liebig-Universität Gießen, 1997, available online at http://theorie.physik.uni-giessen.de/.

[TH95] I. S. Towner and J. C. Hardy, Currents and their couplings in the weak sector of the Standard Model, in *Symmetries and fundamental interactions in nuclei*, edited by W. C. Haxton and E. M. Henley, p. 183, World Scientific, Singapore, 1995.

[Tia] L. Tiator, private communication.

[TK06] L. Tiator and S. Kamalov, *MAID analysis techniques*, arXiv:nucl-th/0603012.

[TW01] A. W. Thomas and W. Weise, *The structure of the nucleon* (Wiley-VCH, Berlin, 2001).

[UU33] E. A. Uehling and G. E. Uhlenbeck, *Transport phenomena in Einstein-Bose and Fermi-Dirac gases. I*, Phys. Rev. **43**, 552 (1933).

[Val] M. Valverde, private communication.

[VAN06] M. Valverde, J. E. Amaro and J. Nieves, *Theoretical uncertainties on quasielastic charged-current neutrino nucleus cross sections*, Phys. Lett. B **638**, 325 (2006), arXiv:hep-ph/0604042.

[vdVP04] B. I. S. van der Ventel and J. Piekarewicz, *Quasielastic neutrino-nucleus scattering*, Phys. Rev. C **69**, 035501 (2004), arXiv:nucl-th/0310047.

[vdVP06] B. I. S. van der Ventel and J. Piekarewicz, *Strange-quark contribution to the ratio of neutral- to charged-current cross sections in neutrino-nucleus scattering*, Phys. Rev. C **73**, 025501 (2006), arXiv:nucl-th/0506071.

[VVKM94] M. J. Vicente Vacas, M. K. Khankhasaev and S. G. Mashnik, *Inclusive pion double charge exchange above 0.5 GeV*, arXiv:nucl-th/9412023.

[Was09] M. Wascko, *Recent experimental data*, lectures given at 45th Karpacz Winter School in Theoretical Physics, February 2-11, 2009, Lądek-Zdrój, Poland, available online at http://wng.ift.uni.wroc.pl/karp45.

[Wil09] M. Wilking, *First $CC\pi^+$ cross section results from MiniBooNE*, talk given at NUINT09, May 17-22, 2009, Sitges, Spain, available online at http://nuint09.ifae.es/Agenda.html.

[Win08] S. Winkelmann, *Neutrinoinduzierte, kohärente Pionproduktion*, Diploma thesis, Justus-Liebig-Universität Gießen, 2008, available online at http://theorie.physik.uni-giessen.de/.

[WLM05] M. Wagner, A. B. Larionov and U. Mosel, *Kaon and pion production in relativistic heavy-ion collisions*, Phys. Rev. C **71**, 034910 (2005), arXiv:nucl-th/0411010.

[WPK+88] G. M. Welke, M. Prakash, T. T. S. Kuo, S. D. Gupta and C. Gale, *Azimuthal distributions in heavy ion collisions and the nuclear equation of state*, Phys. Rev. C **38**, 2101 (1988).

[WSPR90] M. Warns, H. Schroder, W. Pfeil and H. Rollnik, *Calculations of electromagnetic nucleon form factors and electroexcitation amplitudes of isobars*, Z. Phys. C **45**, 627 (1990).

[YRCT06] R. D. Young, J. Roche, R. D. Carlini and A. W. Thomas, *Extracting nucleon strange and anapole form factors from world data*, Phys. Rev. Lett. **97**, 102002 (2006), arXiv:nucl-ex/0604010.

[Zel] G. P. Zeller, private communication.

[Zel03] G. P. Zeller, *Low energy neutrino cross sections: comparison of various Monte Carlo predictions to experimental data*, arXiv:hep-ex/0312061.

[Zel08] G. P. Zeller, *Low energy neutrino cross sections (K2K, MiniBooNE, SciBooNE, Minerva)*, talk given at Neutrino 08, May 25-31, 2008, Christchurch, New Zealand, available online at http://www2.phys.canterbury.ac.nz/~jaa53/presentations/Zeller.pdf.

[Zel09] G. P. Zeller, *Some thoughts on Monte Carlo convergence*, talk given at NUINT09, May 17-22, 2009, Sitges, Spain, available online at http://nuint09.ifae.es/Agenda.html.

Deutsche Zusammenfassung

Motivation und Stand der Forschung

Die Neutrinophysik nahm ihren Anfang im Jahre 1930, als Wolfgang Pauli ein neues Teilchen — das Neutrino — postulierte, um so die Erhaltung von Energie und Impuls im β-Zerfall zu retten. Erst 1953 wurde dessen Existenz experimentell durch Reines und Cowan nachgewiesen. Heute ist nicht nur der sichere Nachweis dreier Neutrinoarten erbracht, sondern ihre Wechselwirkungen bieten einzigartige Möglichkeiten, fundamentale Fragen in vielen Bereichen der Physik zu untersuchen. Neutrinoreaktionen werden im Rahmen des Standard-Modells der Teilchenphysik beschrieben. Sie wechselwirken ausschließlich schwach durch den Austausch geladener W-Bosonen (charged current, CC) oder neutraler Z-Bosonen (neutral current, NC).

Seit Neutrino-Oszillationen in unterschiedlichsten Experimenten bestätigt wurden [Super-K98, SNO01, K2K03, KamLAND03] besteht kein Zweifel mehr, dass Neutrinos zwar eine kleine und immer noch unbekannte, aber doch von Null verschiedene Ruhemasse besitzen. Gegenwärtig sind weltweit mehrere Long-Baseline-Experimente (LBL) mit Neutrinoenergien von einigen hundert MeV bis hin zu mehreren GeV im Betrieb [MINOS, K2K, MiniBooNE, OPERA] oder im Aufbau [T2K]. Sie untersuchen einerseits fundamentale Fragen wie CP-Verletzung und die Existenz von sterilen Neutrinos, andererseits ist das Ziel eine präzise Vermessung der Oszillationsparameter wie Massendifferenzquadrate und Mischungswinkel.

Der Erfolg dieser Experimente ist eng an ein gutes Verständnis der Neutrino-Kern-Wechselwirkung verknüpft: Neutrinos wechselwirken mit sehr kleinen Querschnitten und sind nur über die durch ihre Wechselwirkung mit Materie erzeugten Teilchen nachweisbar, im Falle von neutralen Strömen (NC) sogar nur durch die produzierten Hadronen. Um den Wirkungsquerschnitt zu vergrößern, werden oft Targets mit hoher Massenzahl A verwendet. Im Hinblick auf die LBL-Experimente ergeben sich daraus Probleme: Teilchen, die durch die Neutrino-Wechselwirkung im Kern erzeugt werden, unterliegen Endzustandswechselwirkungen (final-state interactions, FSI), bevor sie detektiert werden. Insbesondere durch nukleare Effekte wie Absorption und Rückstreuung können sich die detektierten Raten erheblich ändern, was zu fehlerhaften Interpretationen führen kann.

Ein quantitatives Verständnis der Wechselwirkung von Neutrinos mit Kernen ist auch für die Messung der Oszillationsparameter erforderlich, da diese — bei fest-

er, bekannter Entfernung zwischen Quelle und Detektor — direkt proportional zur Energie der Neutrinos sind. Die Neutrinos werden im Wesentlichen über die Reaktion $pA \to \pi X$ und den darauf folgenden Pionenzerfall erzeugt, was einen einige 100 MeV bis hin zu einigen GeV breiten Neutrinostrahl ergibt. In ν_μ disappearance-Experimenten etwa misst man, wie sich das Neutrinoenergie-Spektrum an einem entfernten Ort im Vergleich zur Neutrinoquelle geändert hat, d. h. man vergleicht das "oszillierte" mit dem "nicht-oszillierten" Spektrum und gewinnt so Informationen über die Oszillationsparameter. Für die Interpretation dieser Experimente und einer darauf basierenden Präzisionsmessung der Oszillationsparameter ist es daher wichtig, die Energieverteilung der Neutrinos genau zu kennen. Die Energie der Neutrinos muss dazu aus den gemessenen Energien des auslaufenden Leptons und der Hadronen im Endzustand rekonstruiert werden. Üblicherweise wird dazu die quasielastische Streuung, $\nu_\ell n \to \ell p$, verwendet, die bei Neutrinoenergien um 1 GeV dominierend ist. Im nuklearen Medium kann diese Reaktion durch die FSI jedoch nicht immer klar identifiziert werden.

Inklusive quasielastische Streuung am Kern wurde z. B. im Rahmen relativistischer Fermigas-Modelle untersucht, welche die Fermibewegung der Nukleonen im Kern, das Pauliverbot und die nukleare Bindung berücksichtigen [SM72, DP79, HKMP93, BDPD$^+$96, ABB$^+$97, ABB$^+$98]. Andere Ansätze gehen über die Ebene-Wellen-Näherung hinaus und verwenden z. B. realistischere Wellenfunktionen [ABB$^+$97, ABB$^+$98, JRHR99, MGP04a, MLJ$^+$06, vdVP06, MGP06] oder benutzen eine sogenannte "Scaling"-Analyse der Elektron-Streudaten für die Vorhersage der Neutrino-Querschnitte [ABC$^+$05]. Weiterhin können die Nukleon im nuklearen Medium stoßverbreitert sein; Benhar *et al.* [BFN$^+$05] zum Beispiel berechnen deren Spektralfunktionen mithilfe eines aufwendigen NMBT-Verfahrens.

Semi-inklusive Prozesse wie quasielastischer Nukleonen-Knockout, bei dem das Nukleon aus dem Kern herausgeschlagen wird, sind von Interesse insbesondere für NC-Experimente, da das auslaufende Neutrino nicht detektiert werden kann. Hierzu benötigt man eine gute Beschreibung der Endzustandswechselwirkungen. Dies wird oft entweder ganz vernachlässigt [HKMP93, BDPD$^+$96, vdVP06] oder nur absorptiv behandelt (optisches Potential oder Glauber-Modell) [ABB$^+$97, ABB$^+$98, MGP04a, MLJ$^+$06, MGP06, vdVP04]. Dabei wird nicht berücksichtigt, dass es durch Kollisionen der Nukleonen im Kern zu Energieverlusten, Richtungsänderungen, Ladungsaustausch und auch zu Mehrfach-Nukleon-Knockout kommen kann. Dies kann nur im Rahmen von Monte-Carlo-Modellen beschrieben werden [NVVV06]. Beiträge zum Nukleonen-Knockout kommen jedoch nicht nur von quasielastischen Prozessen, sondern auch von Ereignissen, bei denen zunächst eine Resonanz angeregt wird, aber nach den FSI nur ein Nukleon detektiert wird, da das Pion aus dem Resonanzzerfall absorbiert wird. Diese 'Fake-QE-Prozesse' sind von großer Bedeutung für Experimente, da sie Einfluss auf die Energierekonstruktion haben. Ein Verständnis dieser

Prozesse ist nur im Rahmen einen 'Coupled-Channel'-Modells möglich, welche vielfältige Wechselwirkungen beinhaltet. Keines der oben genannten Modelle kann dies leisten.

Andere Experimente suchen nach ν_e appearance, also dem Erscheinen von einem Elektron-Neutrino in einem Muon-Neutrino-Strahl. Der Flavor des Neutrinos kann jedoch auch nur über die in der Wechselwirkung erzeugten, nachweisbaren Teilchen bestimmt werden. Insbesondere neutrale Pionen spielen eine wichtige Rolle bei der Flavoridentifikation: So kann etwa ein (eventuell sogar durch Endzustandswechselwirkung erzeugtes) durch ν_μ NC-induziertes π^0 im Detektor durch seinen Photon-Zerfall ein ν_e-Ereignis simulieren.

Wesentlich für die Interpretation von Neutrino-Oszillationsexperimenten ist also auch das Verständnis der Pionenerzeugung durch Neutrinos. Bis zu Neutrinoenergien von etwa 1.5 GeV verläuft die Pionproduktion hauptsächlich über die Anregung und den darauf folgenden Zerfall der Δ-Resonanz, mit steigender Neutrinoenergie tragen höhere Resonanzen und auch nicht-resonanter Untergrund bei. Bislang gab es nur wenige Untersuchungen zur neutrino-induzierten Pion-Produktion am Kern: Singh *et al.* [SVVO98] haben gezeigt, dass neben 'simplen' Medium-Effekten wie Fermibewegung, Pauli-Verbot und Bindung der Nukleonen im Kernpotential, insbesondere die medium-modifizierte Breite des Δ's (Stoßbreite) den Absorptionsquerschnitt beeinflusst. Semi-inklusive Prozesse wurden sonst einzig in Ref. [PPY00] im Rahmen des ANP-Modells behandelt.

Um die aktuellen Neutrinoexperimente interpretieren zu können, benötigt man also ein Modell, das sowohl die anfängliche Neutrino-Kern-Wechselwirkung als auch die Endzustandswechselwirkung der produzierten Teilchen gut beschreibt — und das in allen angesprochenen Energieregionen. Da keine der obigen Arbeiten dies leistet, wurden Eventgeneratoren speziell für die Simulation der jeweiligen Experimente entwickelt (z. B. NUANCE [Cas02], NEUT [Hay02] und GENIE [A$^+$09]), um die im Kern ablaufenden Reaktionen quantitativ zu verfolgen. Trotz erheblicher Unterschiede ist allen Modellen gemeinsam, dass sie auf Monte-Carlo Simulationen des Reaktionsprozesses aufbauen. Diese Codes enthalten im Allgemeinen Beiträge sowohl von quasielastischen wie auch inelastischen Prozessen, insbesondere wird für die Resonanzanregung meist das Modell von Rein und Sehgal [RS81] verwendet. Weiterhin wird bei allen Generatoren ein Fermigas-Modell verwendet, allerdings meistens mit konstantem, also insbesondere nicht dichteabhängigem, Fermi-Impuls und konstanter Bindungsenergie. Endzustandswechselwirkungen werden mit einem Kaskaden-Modell beschrieben, wobei die Wechselwirkungsquerschnitte der intranuklearen Streuung und Absorption speziell auf die zu verwendeten Targets angepasst wurden. Ihr kernphysikalischer Gehalt ist oft zweifelhaft; problematisch ist außerdem, dass alle diese Eventgeneratoren ausschließlich für bestimmte Neutrinoexperimente entwickelt wurden und kaum an anderen, vergleichbaren Reaktionen (z. B. an Elek-

troproduktionsexperimenten) getestet wurden.

Neutrino-Streuung im GiBUU-Modell

Das Ziel der vorliegenden Arbeit war die Entwicklung eines Modells, welches Neutrino-Kern-Streuung sowohl in der quasielastischen (QE) als auch in der Resonanzregion zuverlässig beschreibt, d. h. für Neutrinoenergien bis etwa 2 GeV anwendbar ist. Eine gute Beschreibung der Neutrino-Nukleon-Reaktion ist dabei ebenso wichtig wie die korrekte Behandlung der Medium-Modifikationen und der Endzustandswechselwirkungen. Auf beides wurde gleichermaßen Wert gelegt.

Wie bei Photon- und Elektron-induzierten Reaktionen üblich, arbeiten wir in der 'impulse approximation' und betrachten die Neutrino-Kern-Streuung als Zwei-Stufen-Prozess: Das Neutrino wechselwirkt also zunächst mit einem gebundenen Nukleon, die erzeugten bzw. angestoßenen Teilchen unterliegen dann bei ihrer Propagation aus dem Kern Endzustandswechselwirkungen.

Die elementare QE-Reaktion wird mit einem relativistischen Formalismus beschrieben (siehe Kapitel 4), die benötigten Formfaktoren wurden neuesten Analysen von Bodek *et al.* [BABB08] und Kuzmin *et al.* [KLN08] entnommen, die für die Vektor-Anteile auf den in jüngster Zeit erfolgten Messungen am JLAB beruhen. Auch die Neutrino-induzierte Resonanzanregung, diskutiert in Kapitel 5, die den Großteil der Pion-Produktion ausmacht, beschreiben wir mit einem Formfaktorformalismus. Die Vektorformfaktoren haben wir dabei aus Helizitätsamplituden bestimmt, die aus einer aktuellen MAID-Analyse der JLAB-Daten extrahiert wurden [MAID], ähnlich dem zuerst von Fogli et al. [FN79] angewandten Verfahren. Dieses Verfahren wurde in neuerer Zeit auch von Lalakulich *et al.* [LP05] benutzt, um die Vektorformfaktoren der 4 niedrigst-liegenden Resonanzen zu bestimmen. Allerdings wurden in Ref. [LP05] die axialen Formfaktoren nicht neu bestimmt, obwohl dies bei einer Änderung der Vektoranteile für eine optimale Beschreibung der Daten nötig ist. Wir haben dieses Modell weitgehend erweitert (von 4 auf 13 Resonanzen bis zu einer invarianten Masse von 2 GeV) und auch die axialen Formfaktoren neu angepasst; die Annahme von 'partial conservation of the axial current' (PCAC) liefert dabei die Kopplungen der axialen Formfaktoren. Wir berücksichtigen weiterhin einen phänomenologisch motivierten Ein-Pion-Untergrund, dessen Vektoranteil ebenfalls auf der MAID-Analyse basiert (siehe Kapitel 6).

Medium-Modifikationen und Endzustandswechselwirkungen der produzierten Teilchen werden mithilfe des GiBUU-Modells beschrieben. Dieses Verfahren beruht auf der Boltzmann-Uehling-Uhlenbeck (BUU) Gleichung, die sich von den genannten Neutrino-Eventgeneratoren durch die konsistente Berücksichtigung von Selbstenergien aller beteiligten Teilchen (Real- und Imaginärteile) unterscheidet. Die Fermibewegung im Targetkern wird hier mit einer lokalen Thomas-Fermi Näherung dichter

an die empirischen Verteilungen angepasst als dies in den Eventgeneratoren üblicherweise der Fall ist; auch die Besetzung im Ortsraum folgt empirischen Dichteverteilungen.

Mit dem Gießener BUU-Modell, beschrieben in Kapitel 7, ist anfänglich die Erzeugung verschiedenster Teilchen (Photonen, Dileptonen, Pionen, Kaonen, Vektormesonen etc.) in Schwerionen-Reaktionen sehr erfolgreich beschrieben worden [TCE$^+$97, HCTM99, LM03, LM05, WLM05]. Später wurde das Modell auf elementare Proben erweitert und Proton-, Pion-, Photon- und Elektron-induzierte Teilchenproduktion [ECM$^+$94, EBM99, EM00, LEM00, LPM03, MFM04, K$^+$04, BARMM06, BARLM06, MM06, Bus08, LBARM09, FCGM04, GF05] an Kernen über einen weiten Energiebereich konsistent unter Verwendung derselben theoretischen Verfahren und Codes berechnet. Insbesondere die Untersuchungen Photon-induzierter Reaktionen haben gezeigt, dass eine detaillierte, quantitativ zuverlässige Beschreibung der Messdaten nur dann möglich ist, wenn die Endzustandswechselwirkungen der erzeugten Hadronen realistisch beschrieben werden. Insbesondere müssen die Effekte gekoppelter Kanäle berücksichtigt werden, die zu einem 'Sidefeeding' des beobachteten Kanals beitragen können. Sehr sensitiv auf Details der Pion-Wechselwirkung ist der Prozess des doppelten Ladungsaustauschs (DCX). Dessen korrekte Behandlung ist damit ein wichtiger Test der Zuverlässigkeit unseres FSI-Modells, welche durch die erfolgreiche Beschreibung der Daten bestätigt wurde [BARLM06]. Die korrekte Berücksichtigung des Imaginärteils der Selbstenergien der erzeugten Teilchen, d. h. ihre Absorption durch Wechselwirkung mit dem Kern, ist bei allen diesen Rechnungen wichtig. Zudem können wir, im Gegensatz zu den meisten anderen Transport- und Kaskaden-Verfahren, die im Allgemeinen stoßverbreiterten Baryonen konsistent propagieren. Damit gehen wir über andere Ansätze hinaus, in denen insbesondere Resonanzen überhaupt nicht transportiert werden, sondern sofort zerfallen oder absorbiert werden. Ein wichtiger Punkt der vorliegenden Arbeit war die Implementierung des sogenannten Off-shell-Potentials. Damit stellen wir sicher, dass die stoßverbreiterten Baryonen im Vakuum wieder zu ihrer Vakuumspektralfunktion zurückgekehrt sind.

Das GiBUU-Modell unterscheidet sich deutlich von den oben genannten Eventgeneratoren nicht nur durch seine theoretische Fundierung; es ist das einzige Verfahren, dessen physikalischer Inhalt an einer breiten Klasse von unterschiedlichen Reaktionstypen getestet worden ist. Dabei sind die Tests anhand von Experimenten zu Elektron-/Photon-induzierten Reaktionen am Kern besonders wichtig, weil in diesen der elektrische Sektor der elektroschwachen Wechselwirkung und die da darauf folgenden Endzustandswechselwirkungen an "gut messbaren" Prozessen überprüft werden können.

In Kapitel 9 haben haben wir mit unserem Formalismus sowohl Neutrino- als auch inklusive Elektron-Kernquerschnitte berechnet. Außer der Fermibewegung und dem Pauli-Blocking sind vor allem zwei Punkte für eine erfolgreiche Beschreibung der

Elektron-Streudaten entscheidend: Die Impulsabhängigkeit des Mean-Field-Potentials führte zu einer signifikanten Verbreiterung und Absenkung der QE-Peaks. Diese Effekte werden noch verstärkt durch die In-Medium-Modifikationen des Nukleons und der Resonanzen. Deren Spektralfunktionen haben wir konsistent, d. h. mit den in den BUU-Rechnungen verwendeten Stoßquerschnitten, in einer Niedrig-Dichte-Näherung bestimmt. Dabei haben wir sowohl Real- als auch Imaginärteile der Selbstenergien berücksichtigt. Erstere äußern sich in Potentialen der beteiligten Baryonen, letztere in den Breiten. Die gute Beschreibung der inklusiven Elektronstreuung im gleichen Modell dient uns daher als Qualitäts-Check der Neutrinorechnungen.

Neutrino-induzierte Teilchenproduktion haben wir in Kapitel 10 und 11 sowohl für geladene (CC) als auch für neutrale Ströme (NC) untersucht. Erheblicher Einfluss der Endzustandswechselwirkung ist bei der Pionproduktion zu beobachten. Bei CC-Prozessen werden aufgrund von Isospineffekten zu Beginn deutlich mehr π^+ produziert, bei NC-Prozessen π^0. Diese Pionen können nun absorbiert werden oder auch elastisch, evtl. mit Ladungsaustausch, rückstreuen. Das führt insbesondere bei kleinen Pionenergien zu einer überproportionalen Population des π^0-Kanals bei CC, und der $\pi^\pm$-Kanäle bei NC (Sidefeeding). Da gerade die π^0 Mesonen verantwortlich für falsche Flavor-Identifikation sind, ist dieser Effekt für die Interpretation der Neutrinoexperimente von hoher Bedeutung. In unseren Rechnungen sehen wir zudem deutlich, dass QE-Prozesse über die FSI zur Pionproduktion beitragen. Wesentlich wichtiger ist allerdings der umgekehrte Effekt: wird z. B. das Pion aus einem Resonanzzerfall durch FSI absorbiert, erscheint das Ereignis im Detektor wie QE-Streuung und wird mit zur Energierekonstruktion herangezogen, und verfälscht damit möglicherweise das sowohl die Messung des QE-Wirkungsquerschnitts als auch das Oszillationsergebnis. Eine korrekte und realistische Beschreibung der durchaus komplizierten FSI ist also für Oszillationsexperimente wichtig.

Unsere Ergebnisse zum Nukleonen-Knockout zeigen ebenso einen mehr als deutlichen Einfluss der FSI. Auch hier konnten wir wieder Sidefeeding vom dominanten in den unterdrückten Kanal beobachten (bei CC von Protonen zu sekundären Neutronen). Doch nicht nur QE-Streuung führt letztlich zu Nukleon-Knockout, sondern auch Resonanzproduktion im Anfangszustand. Wird bei letzterem das Pion absorbiert, ist der Prozess experimentell von der QE-Streuung nicht mehr zu unterscheiden, und kann — nicht nur bei NC-Experimenten, die sich alleine auf die auslaufenden Hadronen beziehen — zu Fehlinterpretationen führen, denn insbesondere die saubere Identifikation von QE-Prozessen ist für die Neutrinoenergie-Rekonstruktion von entscheidender Bedeutung. Eine korrekte und realistische Beschreibung der durchaus komplizierten FSI ist jedoch für Oszillationsexperimente wichtig. Es ist daher ein besonders wichtiges Ergebnis unserer Rechnungen, dass bei Neutrinoenergien oberhalb von etwa 1 GeV der Beitrag der Δ-Anregung zum Nukleonen Knockout mit dem QE Knockout vergleichbar ist. Nichtberücksichtigung dieser Tatsache führt zu zu großen

'quasielastischen' Querschnitten und verfälscht damit die Extraktion von Formfaktoren und der axialen Masse des Nukleons.

Schließlich haben wir diverse Anwendungen unseres Modells im Hinblick auf aktuelle und zukünftige LBL-Experimente (kurz vorgestellt in Kapitel 12) aufgezeigt: Die Verschränkung von quasielastischen Prozessen und Pionproduktion sowie mögliche Konsequenzen für aktuelle ν_μ disappearance-Experimente haben wir in Kapitel 13 anhand einiger konkreter Beispiele diskutiert. Insbesondere haben wir gezeigt, wie die Neutrinoenergie rekonstruiert werden kann und dass dafür die korrekte Identifikation der quasielastischen Streuereignisse besonders wichtig ist. Den Einfluss der FSI auf ν_e appearance-Experimente haben wir in Kapitel 14 untersucht. In Kapitel 15 geben wir Vorhersagen und vergleichen, soweit möglich, mit Neutrino-Streudaten des MiniBooNE und des K2K-Experiments. Unsere Rechnungen unterschätzen jedoch die MiniBooNE-Daten deutlich. Wir haben verschiedene mögliche Ursachen studiert — weitere Daten, auch von anderen Experimenten und so Modell-unabhängig wie möglich, sind zur Klärung der Diskrepanz nötig.

In der vorliegenden Arbeit wurde erstmals quasielastische Streuung und Resonanzproduktion in einem verlässlichen FSI-Modell zusammen untersucht und die Implikationen, insbesondere im Hinblick auf ihre Verschränkung, für aktuelle Neutrino-Oszillationsexperimente diskutiert. Abgesehen von den empirisch-phänomenologischen Eventgeneratoren gibt es bis heute keine gemeinsame Beschreibung von QE und Pionenproduktion am Kern außer dem hier präsentierten Modell. Unsere Untersuchungen zeigen zudem klar, dass die In-Medium-Effekte und vor allem die Endzustandswechselwirkungen erheblichen Einfluss auf die gemessenen Ereignisraten haben und daher korrekt beschrieben werden müssen. Unabhängige Tests der Modelle sind dabei obligatorisch.